NATURE AND ORIGIN OF SECONDARY MINERAL COATINGS ON VOLCANIC ROCKS OF THE BLACK MOUNTAIN, STONEWALL MOUNTAIN, AND KANE SPRINGS WASH VOLCANIC CENTERS, SOUTHERN, NEVADA

ORIGINAL CONTAINS
COLOR ILLUSTRATIONS

Dr. James V. Taranik, Principal Investigator
Dr. Liang C. Hsu, Co-Investigator
Dr. David M. Spatz, Co-Investigator
Mr. Michael J. Chenevey, Co-Investigator

Mackay School of Mines
Department of Geological Sciences
University of Nevada, Reno
Reno, Nevada 89557

October, 1989

CONTRIBUTORS

The following individuals were actively involved in this project and made important contributions:

Dr. Sandra Feldman
Dr. Donald Noble
Mr. James Sjoberg
Mr. William Aymard
Dr. Amy Hutsinpilar Collins
Dr. Marcus Borengasser
Mr. John Perry

ACKNOWLEDGEMENTS

ORGANIZATION

This report is organized into 4 parts. Part I deals with the main objectives of the original proposal. Parts II, III, and IV test results and hypotheses developed in Part I and expand the data base and knowledge with regard to sensors, spectral range and geographic exposure.

PART I

PART I

GENETIC, SPECTRAL, AND LANDSAT THEMATIC MAPPER IMAGERY RELATIONSHIPS BETWEEN DESERT VARNISH AND TERTIARY VOLCANIC HOST ROCKS, SOUTHERN NEVADA

David M. Spatz, Principle Author
Mackay School of Mines
University of Nevada, Reno
Reno, Nevada 89557

ABSTRACT

Desert varnish on volcanic rock assemblages of southern Nevada is composed largely of iron, manganese, silica, and alumina rich amorphous compounds. Thin section and scanning electron microscope observation reveals that desert varnish occurs chiefly as thin discontinuous translucent films that impregnate rock surfaces intergranularly to depths typically of 0.1-0.3mm. Varnish encrustations and laminations are less common and tend to concentrate in minute recesses. Manganese is commonly concentrated at the coating-air interface and within coating interlayers. Iron exhibits more consistent background levels but is often concentrated at the coating-rock interface. Higher iron/manganese ratios and total combined iron and manganese in coatings on mafic rocks, and high cerium levels in coatings on rocks enriched in cerium and other rare earth elements, suggest a genetic relationship with underlying host rocks.

Mass balance calculations indicate sufficient background levels of both iron and manganese in the substrate of most rocks investigated to provide all manganese and iron requirements for desert varnish formation from only a few mm depths. An iron-manganese depletion zone and secondary layer of cementation near tuff surfaces point to a possible solution front leach origin similar to that which forms caliche in aridic soils.

Desert varnish is absorbent relative to felsic host rocks at wavelengths below about 0.7 to 1.3um, depending on mafic affinity of the sample, and less absorbent than mafic host rocks at higher wavelengths. The thin discontinuous nature of desert varnish results in dominance of lithologic spectral response in the longer wavelength Landsat thematic mapper (TM) bands and high TM 5/2 values over felsic units that support extensive desert varnish. Portable spectroradiometer measurements of variably coated felsic rock surfaces indicate a linear relationship to radiation absorption by varnish within the TM band 2-4 range, but about half that at longer wavelengths and a pronounced reduction in varnish absorption on surfaces with less than "heavy" varnish development. Reflectance divergence is pronounced in band 3. Rock-varnish albedo differences (RVAD) help identify rocks with extensive varnish, using visible/near infrared imagery.

Highly evolved late magmatic differentiates, enriched in large ion lithophile and other "incompatible" elements, exhibit unusually steep spectral curves (positive slopes) from about 1.5 to 2.2um, leading to anomalously low 5/7 values. A binary decision rule flow-diagram and table of imagery characteristics for a general igneous rock classification is presented.

TABLE OF CONTENTS

   A: Landsat TM scene ID's and dates
   B: TM Sensor and platform orbit description
   C: Computer processing components
   D: IDIMS software functions
   E: Analytical geochemistry procedures
   F: Additional geochemical analyses,
       Stonewall Flat Tuff
   G: Additional geochemical analyses, Black Mountain
       caldera formations
   H: Additional geochemical analyses, Kane Springs
       Wash volcanic center
   I: Landsat TM subscene image statistics
   J: Class statistics for supervised
       classification of lithologies
   K: DN statistics for lithologic training sites
   L: Summary of X-ray diffraction analyses

LIST OF FIGURES

LIST OF PLATES

LIST OF TABLES

CHAPTER I

INTRODUCTION AND OBJECTIVES

This dissertation documents results of research into the nature, composition, morphology, distribution, origin, spectra, and relationships of Landsat imagery to secondary mineral coatings (chiefly desert varnish) on a diverse suite of volcanic host rocks derived from three Tertiary calderas in southern Nevada. The study included original mapping at one of the study sites; correlation of volcanic lithologic, petrochemical, spectral, and Landsat 5 thematic mapper (TM) data; and extensive laboratory instrumental analyses. Imagery enhancement and classification techniques were employed to document the application of remote sensing data to geologic mapping problems in volcanic terrain.

STATEMENT OF PROBLEM

This research effort developed out of concern over the degree to which secondary mineral coatings might affect remote sensing reflectance measurements. Fundamental to answering this question was development of an improved understanding of the nature and origin of secondary mineral coatings and the degree to which variations in chemical composition and other properties of coatings correlate with host lithologies. The study, therefore, was designed to

better understand the nature and origin of desert varnish and other secondary weathering, cooling, and alteration products. As such, data and information provided by this investigation could be important to several geoscience disciplines and related fields, including geochronology, geomorphology, and archaeology as well as geologic mapping and visible/near infrared remote sensing applications. Detailed evidence is presented in Chapter V to help explain the source of iron and manganese in desert varnish.

Reflected electromagnetic sensing techniques measure reflectance from surficial cover only. Cover classes in most natural Earth circumstances include consolidated rock outcrop, detritus, vegetation, and soil. Outcrop and rock detritus surfaces are altered to varying degrees by normal oxidation weathering processes. Secondary mineral and amorphous compounds result through complex organic and inorganic chemical processes that vary with climate, physiography, topography, sun orientation, and rock type.

These secondary rock and soil surface weathering considerations bear importantly on interpretations of reflectance data and spectral information collected over them. In the case of outcrop and rock detritus, surficial coatings resulting primarily from secondary weathering processes are detected to varying degrees depending on intensity and distribution of secondary coatings and the

wavelength of the measured radiation.

GENERAL EXPERIMENTAL APPROACH

A six-phase investigative program was pursued: 1) A-priori imagery analysis without significant familiarity with the geology of the study sites; 2) field investigations involving sampling of lithologies and coatings, portable visible/near-IR spectral measurements, general observations, and ground based photography; 3) further imagery analysis based on field experience and mapping results; 4) laboratory instrumental analysis; 5) correlation of spectral and imagery data with lithologic, petrochemical, and desert varnish characteristics and; 6) final field and imagery correlation and verification.

MAJOR SCIENCE QUESTIONS ADDRESSED

The following major science questions were addressed by this study for the volcanic rock assemblages at each of the 3 study sites:

1. What secondary mineral and amorphous phases occur on the surface of the diverse volcanic rock assemblages?

2. What is the nature, morphology, composition, extent, distribution, and compositional and morphological zoning relationships of secondary mineral coatings?

3. What is the origin of desert varnish and other secondary mineral coatings and the source of component elements?

4. What correlation exists between variations in desert varnish and host rock lithologic and petrochemical properties?

5. Can desert varnish or other secondary mineral coatings be detected and mapped by Landsat thematic mapper imagery?

6. To what extent does desert varnish and variations in varnish maturity influence the lithologic discrimination of Landsat thematic mapper imagery?

7. How are visible/near-infrared spectra of volcanic rock assemblages affected by variations in rock lithology and petrochemistry?

8. What thematic mapper imagery processing techniques could be applied to enhance the discrimination and mapping of volcanic rock assemblages in diverse global environments based on the spectral influence of both rock properties and desert varnish?

RESEARCH ACCOMPLISHMENTS

The following points are central to the major accomplishments resulting from this investigation:

1. Secondary mineral coatings on the various volcanic rock assemblages were identified and characterized.

2. Desert varnish compositions, morphology, vertical and horizontal zoning characteristics, and distribution were observed and documented.

3. A model for the origin of desert varnish was formulated. It suggests a likely source for iron and manganese.

4. Lab and field spectral measurements were collected over various volcanic rock assemblages with varying degrees of varnish distribution and intensity.

5. Genetic and spectral relationships were characterized between desert varnish and host rock lithologies and petrochemistries.

6. Correlations were documented between rock lithology and petrochemistry and lab and field spectra.

7. Landsat thematic mapper imagery models, tables, and binary decision flow diagrams were outlined to aid volcanic rock discrimination and mapping.

8. Rock-varnish albedo difference was utilized to assist varnish detection using Landsat thematic mapper product tape digital data and imagery.

9. The effects of varying degrees of varnish intensity and distribution on thematic mapper band reflectance values were outlined.

10. Imagery-unit maps were correlated with volcanic rock assemblages at each of the 3 study sites and related to petrochemistry and desert varnish.

11. The Stonewall Mountain-Mount Helen calderas area was mapped to a scale of about 1:60,000 using Landsat imagery as a base.

12. Results of this investigation were reviewed in context of potential global and planetary applications.

13. The investigation helps focus attention on areas where additional research is needed to further both scientific understanding and remote sensing applications.

STUDY SITES

RATIONALE FOR SELECTION

The three study sites selected for investigation (Figure 1) provide superior settings in terms of outcrop exposure, structural and stratigraphic preservation, volcanic rock type diversity, and a pre-existing data base collected by previous researchers at The Mackay School of Mines, principally Professor Donald C. Noble. These special attributes are largely a consequence of both location – the semiarid southwest U.S. – and relatively youthful origins. Each of the 3 principal study areas is approximately 14.6 x 14.6km square, encompassed for convenience exactly within a 512 x 512 pixel Landsat 5 TM subscene.

These study sites exhibit similarities as well as diversities. Each site centers on or straddles a well defined youthful caldera structure with discrete ash flow tuff deposits and associated lavas, flow domes, and subvolcanic intrusive bodies. Each center was the source of multiple outflow ash sheets that extend from the calderas up to 30 km distally. Some of these major pyroclastic deposits are distinct petrochemically, mostly in regard to iron content, both divalent and trivalent forms. Devitrification, vapor-phase alteration, and welding history also vary from unit to unit and within

120°   114°

—42°

WINNEMUCCA

ELKO

N

EUREKA

CARSON
CITY

TONOPAH

STONEWALL MTN
CALDERA

KANE SPRINGS WASH
CALDERA

BLACK MTN
CALDERA

NEVADA

0   50   100   200
Kilometers

LAS VEGAS

—36°
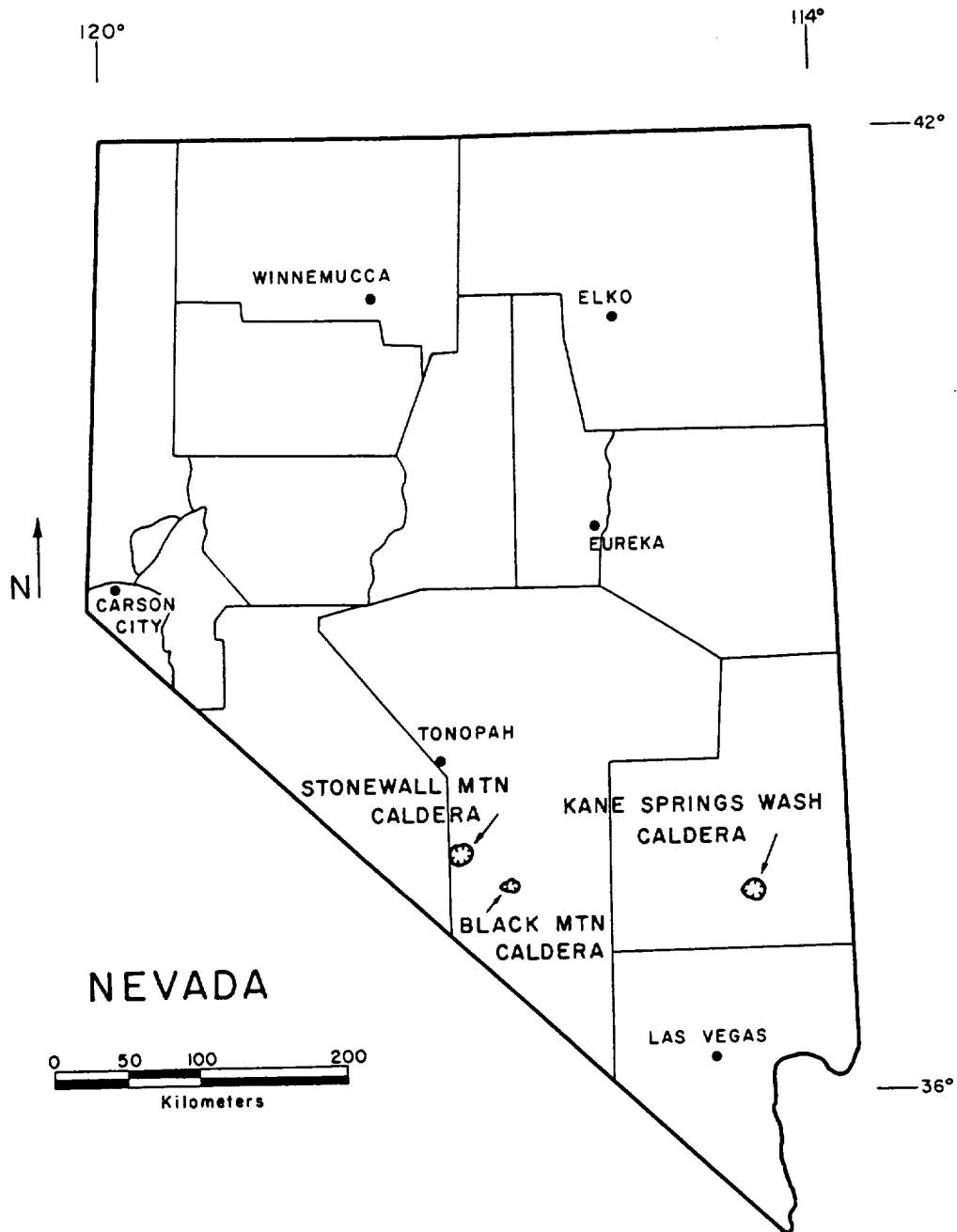
FIGURE 1. Location of the study sites within Nevada, U.S.A.: Kane Springs Wash caldera, Stonewall Mountain caldera, and Black Mountain caldera.

units. Intracaldera lavas and shallow volcanic intrusive rocks, moreover, exhibit even greater diversity of chemical and textural properties. Calc-alkalic suites, ranging from rhyolite to basalt, occur at both the Stonewall Mountain site, where they interfinger with more unusual peralkaline flows from the Stonewall Mountain eruptive event, and at the Kane Springs Wash volcanic center.

Both the climate (semiarid) and the physical and chemical diversity of rock types provide an ideal setting to study desert varnish and other secondary mineral coatings and their effect on remote sensing measurements. Vegetation is sparse - typically less than 30% of ground cover with virtually no overhanging canopy - and soil development relatively inorganic. Thus spectral response is largely lithologically driven. Cloud cover is normally minimal during most of the year, but snow caps mountain peaks throughout Nevada most of December to April. Desert varnish is pervasive and well developed. The diverse physical and chemical properties of the volcanic host rocks provided an excellent laboratory for study of varnish formation, its distribution, and its relationship to host rocks under diverse host rock conditions.

LOCATION AND TOPOGRAPHY

The Kane Springs Wash volcanic center is located in southern Lincoln County, approximately 110 air km NNE of

Las Vegas in the Delamar Mountain Range (Figure 2). Access is facilitated by an excellent graded dirt road that connects the town of Caliente due south with Federal Highway 93 about 30km south of Alamo. Roads within the study area are sparse, poor, and unimproved. Topographic relief is moderate to high. Elevations vary from about 1070 to 1980m.

The Stonewall Mountain study site (Figure 3) is located in western Nye County 35 air km SE of Goldfield, Nevada. The project boundary straddles the eastern margin of the Stonewall Mountain caldera and the western margin of the Mount Helen caldera. The actual mountain of "Stonewall" itself lies west of the study site. The property is wholly within the Nellis Air Force Base bombing range which has "active" status throughout the year. Access is by prior arrangement with the Range Commander at Nellis in Las Vegas subject to security clearance, during brief nonactive times such as weekends or range clean-up periods. Military escort is normally required. Topographic relief is modest: elevation varies mostly within 200m with two isolated elevation extremes at about 1520 and 1830mfor the low and the high. The majority of the area is relatively flat.

The NW corner of the Black Mountain study site (Figure 3) lies 8km SE of the Stonewall Mountain project boundary. The site centers on Black Mountain and the Black Mountain
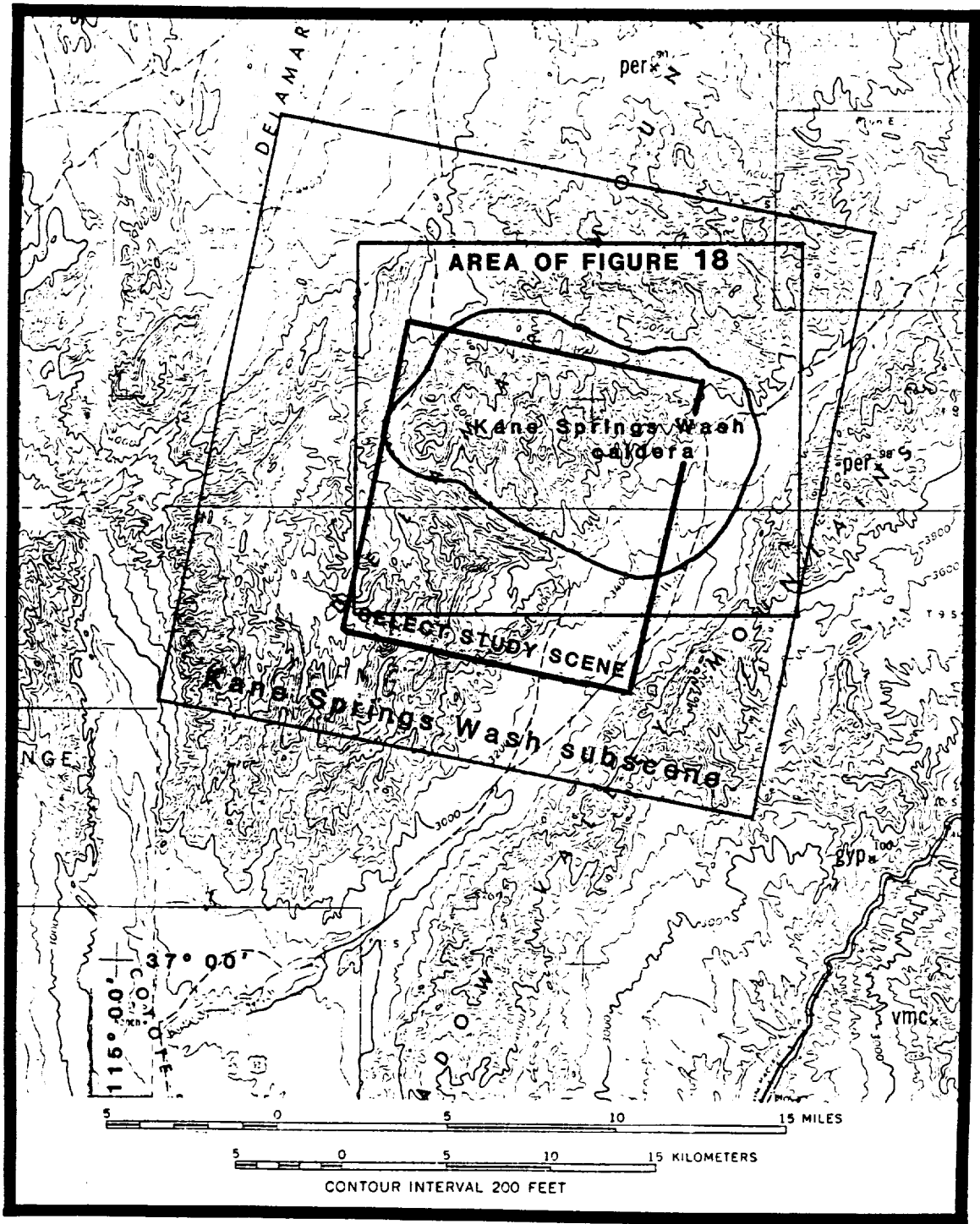
FIGURE 2. Location of the Kane Springs Wash Volcanic Center showing Landsat STM subscenes.
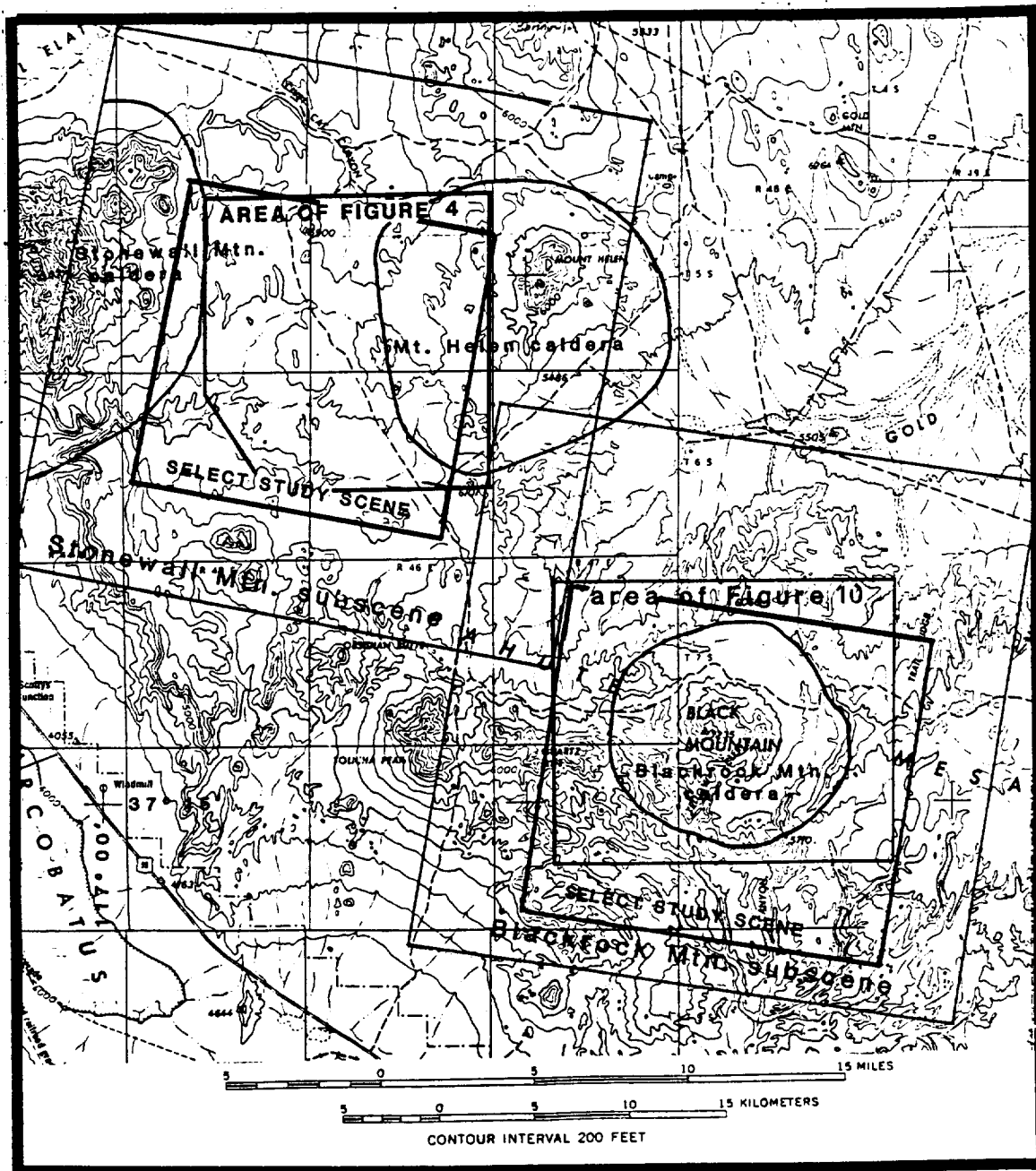
FIGURE 3. Location of the Stonewall Mountain and Black Mountain study sites, showing Landsat ᐁTM subscenes.

caldera structure. Access is, again, as with the Stonewall Mountain site, through the Commander at Nellis Air Force Base in Las Vegas. The site is a "manned area" not subject to bombing exercises, so field parties are not restricted to weekends and other rare isolated "nonactive" periods. Military escort is, however, normally required. Topography is more rugged than at Stonewall. Elevation ranges from about 1830m on the pediment NW of Black Mountain (Gold Flat) to 2205m at its summit.

CLIMATE, VEGETATION AND SOIL

The climate throughout the Basin and Range province in which the study areas lie is classified semiarid. High desert conditions prevail. Annual rainfall varies from about 7-15cm on average at Stonewall and lower elevations at Kane Springs Wash to slightly more at higher altitudes at Kane Springs and Black Mountain. Winter temperature at the study sites is mild but can reach freezing during the early morning hours or for a few days at a time. Summer days are hot - commonly in excess of 32 degrees C and can exceed 38 degrees C for a few days at a time.

Vegetation types at Stonewall Mountain and Black Mountain have been identified and compiled by Helen Cannon of the U.S.G.S. (Noble, et al., 1964). At the Stonewall Mountain area, which is dominated by alluvial and colluvial material rather than saltier soils proximal to playas and

by a dearth of moisture at least within the study scene, the following xerophytic halophytes dominate: winterfat (Eurotia lanata), narrowleaf saltbush (Atriplex linearis), horsebrush (Tetradymia sp), budsage (Artemisia spinescens), and shadscale (Atriplex confertifolia). At the somewhat higher elevations of Pahute Mesa which includes Black Mountain, shrubs include: Mormon tea (Ephedra sp), rabbitbrush (Chrysothamnus sp), horsebrush (Tetradymia sp), gooseberry (Ribes montegenum), sagebrush (Artemisia sp), bitterbrush (Purshia tridentata), Stansburys cliffrose (Cowania stansburiana), snowberry (Symphoricarpos parishii), four-wing saltbush (Atriplex canescens), skunkbush (Rhus trilobata), and mountain mahogany (Cercocarpus ledifolius). Herbs include: lupine (Lupinus), cryptantha (Cryptantha), heliotrope (Phacelia), penstemon (Penstemon), paintbrush (Castilleja), sandwort (Arenaria), groundsel (Senecio), rockcress (Arabis), primrose (Oenothera) gilia (Gilia), and wild buckwheat (Eriogonum). At higher elevations on the slopes of Black Mountain trees include pinyon, juniper, and Gambels oak (Pinus monophylla, Juniperus osteosperma, and Quercus gambelli, respectively). Grasses are represented chiefly by foxtail and cheat grass.

Surface cover at both the Black Mountain and Stonewall Mountain areas is dominated by soil, rock float, and rock/mineral detritus, rather than vegetation. Typical

terrain at the Stonewall site supports sagebrush as the dominant vegetative type. Proportion of sagebrush cover is typically 25-30%, rarely greater. At Stonewall sagebrush is by far the most dominant vegetation component, and of the 3 study sites, Stonewall is the most barren. At Black Mountain, where average annual precipitation is greater, both sagebrush and atriplex are heartier, larger, and locally more dense. On the slopes of Black Mountain a sharp line commonly demarks a zone where foxtail and cheat grasses persist upslope toward the crest of Black Mountain where rabbitbrush and mormon tea are prevalent. The mesas immediately west of Black Mountain, which are underlain by Gold Flat Tuff, sport juniper and pinyon trees at a proportion of cover up to 10-15% in places.

Relief at Kane Springs Wash is more extreme than at the other 2 study sites and peaks and mesas attain greater elevations. The site is "rockier" in general, with more precipitous slopes and greater outcrop exposure; however, the remote sensing advantage of greater rock exposure is countered by shadowing and vegetation. Vegetative types are dominated by sagebrush, single-leaf pinyon, and juniper. More alkalic and rocky soils support shadscale, greasewood, and rabbit brush. Foxtail is a dominant grass. Lower elevations, particularly the higher alluvial fan regions at canyon mouths and canyon floors, are populated by creosote, black brush, agave, yucca, cholla and prickly

pear cactus.

Imagery over higher elevations (northern portion of the study scene) at Kane Springs is influenced significantly by moderately dense groves of pinyon and juniper (30-40%). Canyon floors and local drainage basins with relatively high moisture containment and consequent riparian representatives are also locuses of spectral contamination.

Soils at these study sites are dominantly aridisols. They are relatively dry, sandy, mineral rich alkalic soils with low organic accumulations. Soil composition, color, and spectral characteristics, therefore, are dominated by rock source material. Variably but typically minor accumulation of salts and sulfates is characteristic. Caliche horizons are evident at many sites at Stonewall Mountain. Azonal soils (entisols) are present in washes and recent alluvial plains. More organic rich mollisols correlate with the riparian growth in the washes and other small localized containment basins at Kane Springs and on mesas and elevated zones at Black Mountain and Kane Springs Wash.

CHAPTER II

METHOD OF INVESTIGATION

This section and accompanying appendices detail research activities and the investigative techniques of each of the major phases of study: Landsat data acquisition, field work, imagery processing techniques, and laboratory analytical methods.

LANDSAT DATA ACQUISITION AND SENSOR DESCRIPTION

The 3 study areas are encompassed within 4 contiguous Landsat 5 thematic mapper (TM) scenes. Appendix A lists scene identification data and satellite collection dates for products acquired for this research. Data for all bands (1-7) were requested on regular consumer product computer compatible tapes (CCT's). For the most part, scenes acquired in mid-summer through fall are of better quality due to abatement of vegetative activity, clear skies, and low atmospheric moisture.

Scenes were read onto disk and preliminary examination was conducted in the winter, 1986, at the Mackay School of Mines' image processing center. Subscenes, 1024 x 1024 pixels in dimension, were selected over each study site. Cloud cover in each of these imagery takes is virtually nil and Rayleigh scatter in the lower wavelength bands is minimal. Water vapor absorption effects in bands 2, 3, 4,

5 and 7 appear unimportant for our study objectives.

Both histogram and black body (deep shadow zone) methods of determining atmospheric scatter were applied. In each scene, atmospheric scatter was extreme in TM band 1 but was not detected in bands 2 and greater. Although minor atmospheric scatter is likely in band 2, decreasing exponentially through higher band numbers, it does not appear significant. This observation may be due largely to sensor sensitivity variation within band intervals. Peak sensor response in band 2 is at the maximum wavelength for the band interval 0.595um (Markham and Barker, 1985). Subscenes were further reduced to 512 x 512 pixel dimensions for most detailed imagery processing to maximize monitor resolution, data integrity, and field control. These final subscenes are approximately 14.6km square and adequately cover the areas of interest.

LANDSAT IMAGERY APPLICATIONS IN TERRAIN ASSESSMENT

Descriptions of the thematic mapper remote sensing system have been presented by Engel (1980), Engel and Weinstein (1982), Engel et al. (1983), and Sabins (1987). Taranik (1978a) and Taranik and Trautwein (1977) describe in detail geologic remote sensing applications of Landsat multispectral data. Computer processing techniques were further outlined by Taranik (1978b). A series of papers by Hunt (1977), Hunt and Ashley (1979), Hunt and Salisbury

(1970), and Hunt, Salisbury, and Lenhoff (1973a, 1973c, and 1974), present spectral data and mineral and rock spectral libraries for visible and near-infrared reflectance. Earlier work on silicate mineral spectra was published by Clark (1957).

In general, the thematic mapper instrument, mounted on the Landsat 4 and 5 satellites launched in 1982 and 1984, respectively, is an advanced Multispectral Scanner System (MSS). Sensor details are presented in Appendix B. These satellites were launched in polar orbit at an altitude of 705km. Fourteen and a half orbits are accomplished each day with a 7.6% overlap at the equator and overflight at 40 degree latitude at approximately 10:30 local sun time. The thematic mapper makes solar reflectance measurements over the 0.45 to 2.35um spectral region in 6 discrete bands. Another broad thermal band measures emitted radiation between 10.4 and 2.35um at 120m ground resolution. The thermal region is not being considered in this study. The sensor operates by the cross-track scan principle, utilizing an oscillating scan mirror at a scan angle or angular field of view of 14.9 degrees, collecting data over a 185.2km swath. Scenes are truncated at 170km north to south. The instantaneous field of view is 0.043 mrad resulting in a ground resolution cell of 30 x 30m. There is no on-board data recording system. Data is either transferred to one of several Tracking and Data Relay

Satellites (TDRS) which relays the data to ground based antennas, or is directly transmitted to the ground.

Computer processing techniques are used to better display differences in spectral reflectance thereby enhancing select lithologies and surface alteration types. Overall rock reflectivity tends to increase in the visible and near-IR interval of the electromagnetic spectrum to a maximum typically at about 1.5um (TM band 5). Reflectivity of reddish colored iron oxide minerals is greatest in the red portion of the visible spectrum, .6-.7um (TM band 3). Secondary clay minerals, which exhibit relatively intense reflectivities throughout the visible spectrum, register an absorption peak at about 2.2um (TM band 7). Other hydrous minerals, sulfates, and carbonates possess similar spectral properties, with absorption minima also near 2.2 - 2.3um (Hunt and others, 1970, 1973a, 1979).

By selecting bands positioned at maximum spectral contrasts for various surface cover types, computer enhancement techniques can be used to improve tonal contrast or provide distinctive color contrast on false color composites (Taranik, 1978b and Trautwein and Taranik, 1978). Lithologic differences detected using visible and near-infrared spectra are related to iron content (Baird, 1984a and 1984b, and Rowan et al., 1974 and 1977). Discrimination of hydrothermal and supergene alteration using narrow band visible and near-infrared reflectance

data has been reported by Abrams et al. (1977), Farr (1981), Podwysocki et at. (1983), and Segal (1983). The intensity, saturation, and hue (ISH) transform has been successfully applied to TM data for cover type discrimination recently by Borengasser et al. (1984) and Haydn et al. (1982).

Manipulation of bands and transform images in various combinations both by trial and error and by analysis of spectral bands with unique properties helped identify certain bands, complex transformations, and hybrid image combinations that provide superior lithologic enhancement at the study sites. Reflected electromagnetic remote sensing techniques detect surficial spectral phenomena (less than about 50um depths for clay minerals and goethite at 0.9um radiation, according to Buckingham and Sommer, 1983). Thematic mapper band 3 spectral reflectances of the iron oxide minerals and reflectance in band 7 are related to variations in composition of clay and other secondary hydrous minerals. Band 5 has proven to provide best spectral separation for most cover types. These 3 bands provide superior spectral contrast between lithologies of the 3 project areas for reasons addressed in Chapters VII and VIII. Hybrid ratio color composites and ratios that include one or more of these 3 bands enhance spectral contrast between lithologies and display these differences as unique colors on images. Principal component (PC)

analysis is an especially effective means by which to display spectral variability. The first principal component (PC1) contains by far the majority (typically 85-95%) of variance between bands largely as a function of topographic reflectance effects. It is a very high contrast single "band" image. Spectral variability displayed by subsequent PC's is less influenced by topographic effects and tends to exhibit reflectance intensities related to surface cover. Because the project sites are dominated by rock and rock product cover, PC2 largely displays spectral variance associated with lithology. Spectral variations displayed by PC3 correspond quite closely with 4/3 ratios, which tend to display spectral effects related to vegetation. Vegetation is very bright on 4/3 images.

ISH transformations seem to work well in the project areas with bands 3, 5 and 7. Combining ISH transformations with individual bands or band ratios (always contrast enhanced) results in high contrast images. An intensity parameter image of bands 1-2-4 combines well with bands 3 and 5 or 7 and circumvents redundancy of spectral information. ISH saturation or hue images with bands 2-4-7 in combination with bands 3 and 5 or 3/1 and 5 is another effective example.

ANALYSIS OF IMAGERY DATA

Imagery analysis was conducted on the Mackay School of Mines' VAX 11/780 based Electromagnetic Systems Laboratories (ESL, a subsidiary of TRW Inc.) Interactive Digital Image Manipulation System (IDIMS) and a compact personal computer image analysis station (Appendix C). The IDIMS software package contains over 250 application functions (Appendix D) implemented by command language or menu.

Prior to conducting the field phase, and in advance of any significant knowledge of the study areas, image analysis was conducted on each of the 512 x 512 subscenes described in the section on "Data Acquisition" above. This a-priori approach was intended to result in delineation of remote sensing units without bias from field experience. Subsequent field sampling was then designed, based in part on units delineated spectrally. Sample sites were selected to include distinctive remote sensing units in terms of color, tone, texture, or pattern characteristics. Further imagery processing was then conducted in the fall of 1986, after the previous summer's field work. The aim of subsequent imagery manipulation and assessment was to refine enhancement techniques and to maximize contrast between rock units with benefit of direct field experience with coatings and lithologies.

For each subscene the images presented in Table 1 were

TABLE 1.
LANDSAT 5 THEMATIC MAPPER
IMAGES AND IMAGERY COMPOSITES ROUTINELY
ANALYZED AT THE STUDY SITE

INDIVIDUAL BANDS: 1,2,3,4,5,7

BAND RATIOS: 4/3, 3/1 or 3/2, 5/1 or 5/2, 5/7, 5/4

SIMPLE BAND COMPOSITES: 3-2-1, 3-5-7, 5-3-1, 3/1-5/7-4,
                        2-4-7, 2-4-7, 5/7-5/4-3/1

ISH: individual intensity (I), saturation (S), hue (H)
      on bands 3-5-7 and 1-3-5

ISH COMPOSITES: bands 3-5-7, 1-3-5, 1-2-4, 2-4-5

PRINCIPLE COMPONENTS: individual PC's 1,2,3,4,5,& 6

COMPOSITE PC's: 1-2-3, 2-3-4, 1-2-4, 1-2-5, 2-4-5

COMPLEX COMPOSITES: bands 3-5 or 7-I,S or H (bands 1-2-4;
                    3/1-7-I, S or H (bands 2-4-5;
                    3/1-5/7-I, S or H (bands 2-4-5;
                    3 or 3/1, 5 or 5/7, PC 1 or 2

produced and photographed with the system's Dunn camera peripheral on 35mm film. Although image composites other than those listed in Table 1 were reviewed, these band relationships and imagery renditions were determined to represent best contrast relationships between lithologies and desert varnish. Rationale behind the selection of these bands and the enhancement techniques will follow in subsequent chapters. Each individual band image and composite image was linearly contrast stretched, using the IDIMS scaling function (Appendix D) usually at a .5 truncation of brightness values at either end of the brightness range. All composites were color encoded, using the three primary colors, red, green, and blue. Some of the more effective images were spacially enhanced by an edge enhancement technique to sharpen boundaries between imagery units and to enhance linear features.

FIELD INVESTIGATION

Field work was accomplished during the summers, 1986 and 1987. Approximately 490 samples were collected from 230 sites (Plates 1, 2, and 3). Samples included bags of thin chips hosting desert varnish and other secondary surface coatings; petrographic samples for character reference, thin section, scanning electron microscope (SEM) observation, energy dispersive X-ray analysis (SEM-EDX), and geochemical analysis; and larger (15x15cm) slabs for

Plate 1

CALDERA MARGIN

CALDERA MARGIN

CACTUS SPRING, NEV.
 QN3730-W11645/15

LOUICHA PEAK, NEV.
N3715-W11645/15
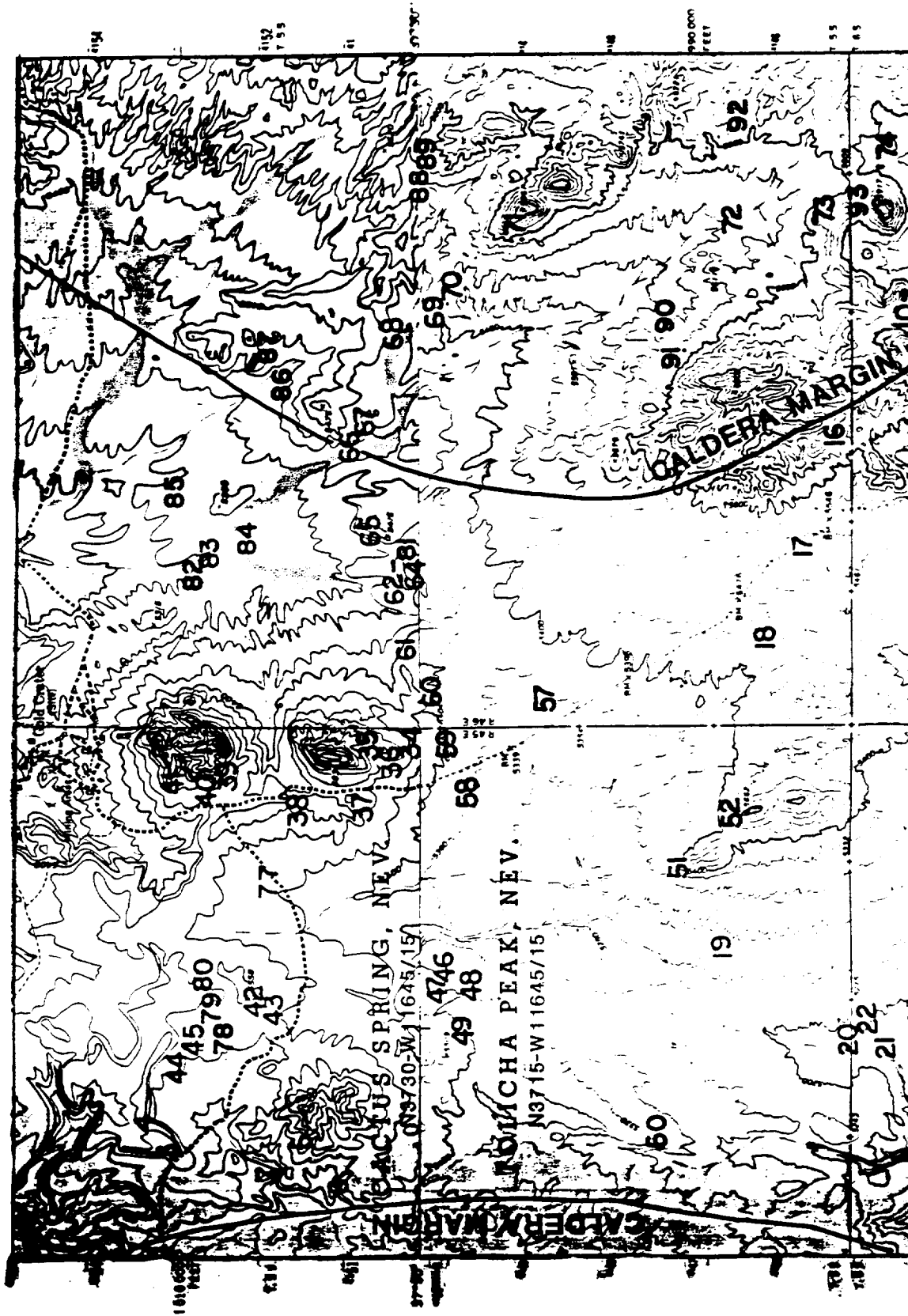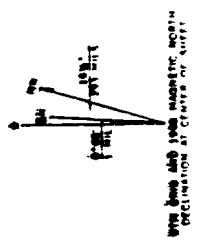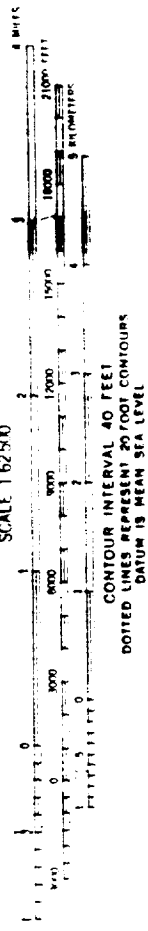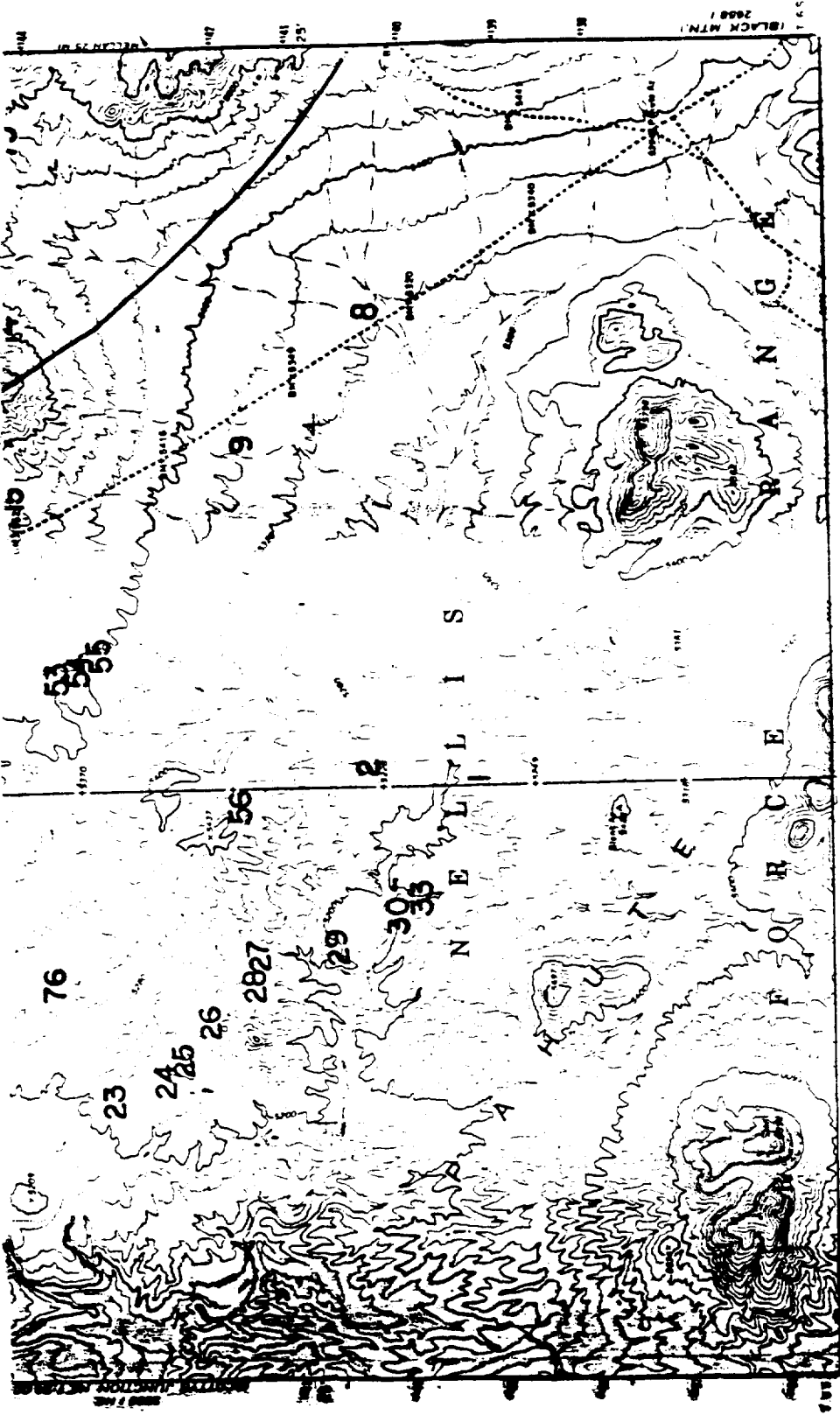
FOLDOUT FRAME

SAMPLE LOCATION MAP–STONEWALL MOUNTAIN AREA

BASE:U.S.G.S.Topographic quadrangles, cut and spliced

SCALE 1:62500

CONTOUR INTERVAL 40 FEET
DOTTED LINES REPRESENT 20 FOOT CONTOURS
DATUM IS MEAN SEA LEVEL

Plate 2
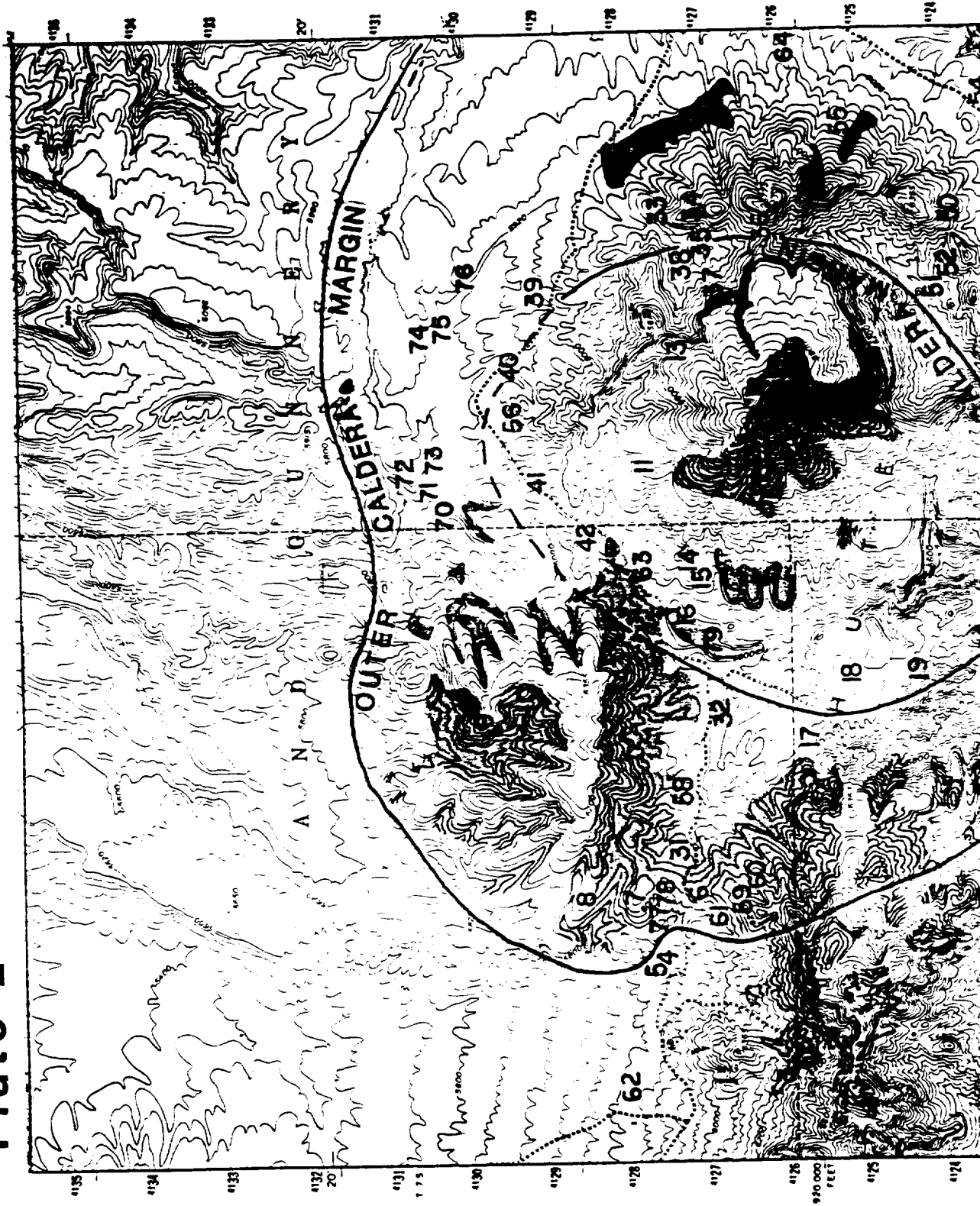
FOLDOUT FRAME

SAMPLE LOCATION MAP–BLACK MOUNTAIN AREA
BASE:U.S.G.S. Topographic quadrangles,cut and spliced
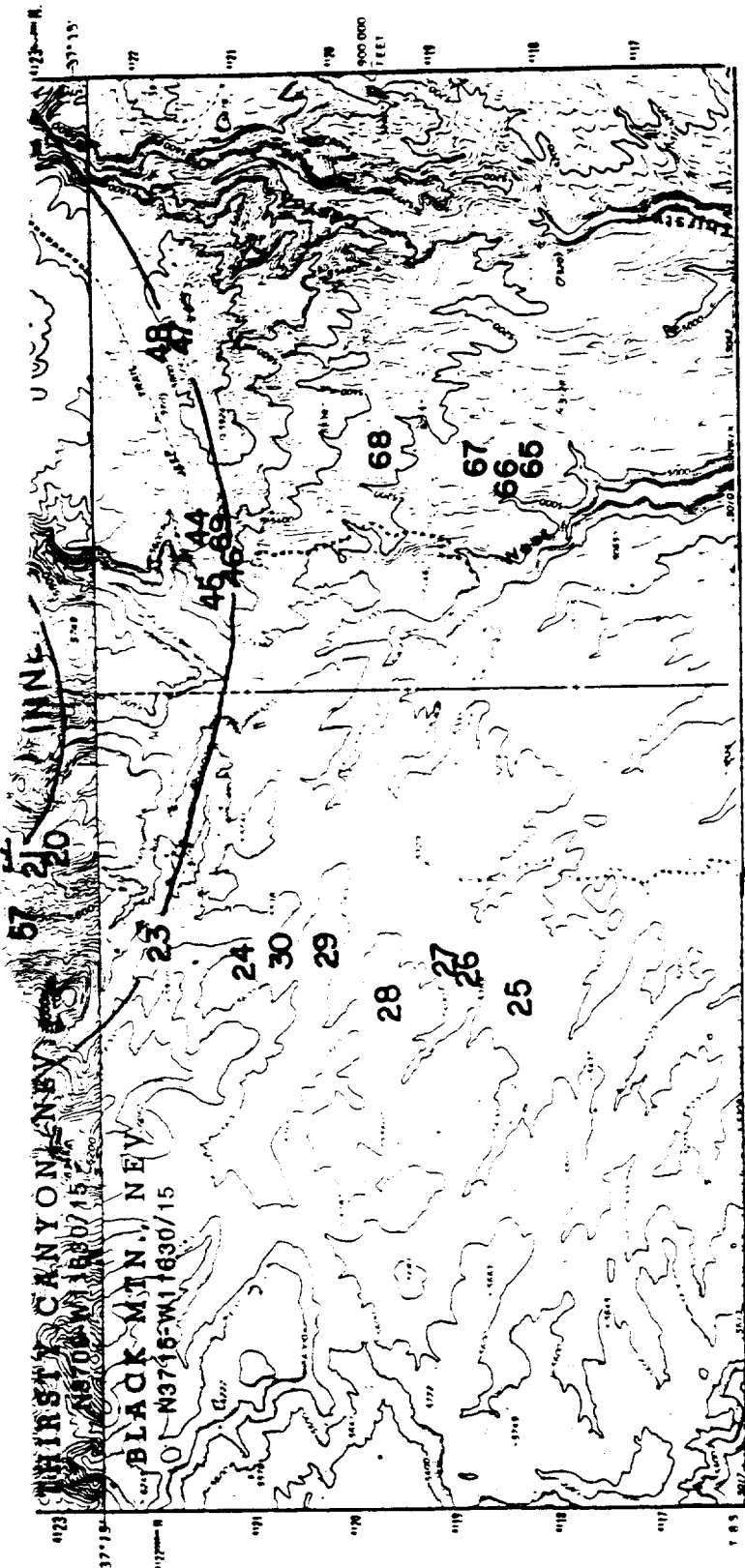
SCALE 1:62500
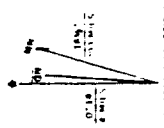
CONTOUR INTERVAL 40 FEET
DASHED LINES REPRESENT 20-FOOT CONTOURS
DATUM IS MEAN SEA LEVEL

FOLDOUT FRAME 2

Plate 3

CALDERA MARGIN

DELAMAR 3 NE QUADRANGLE
NEVADA-LINCOLN CO.
7.5 MINUTE SERIES (TOPOGRAPHIC)

FOLDOUT FRAME
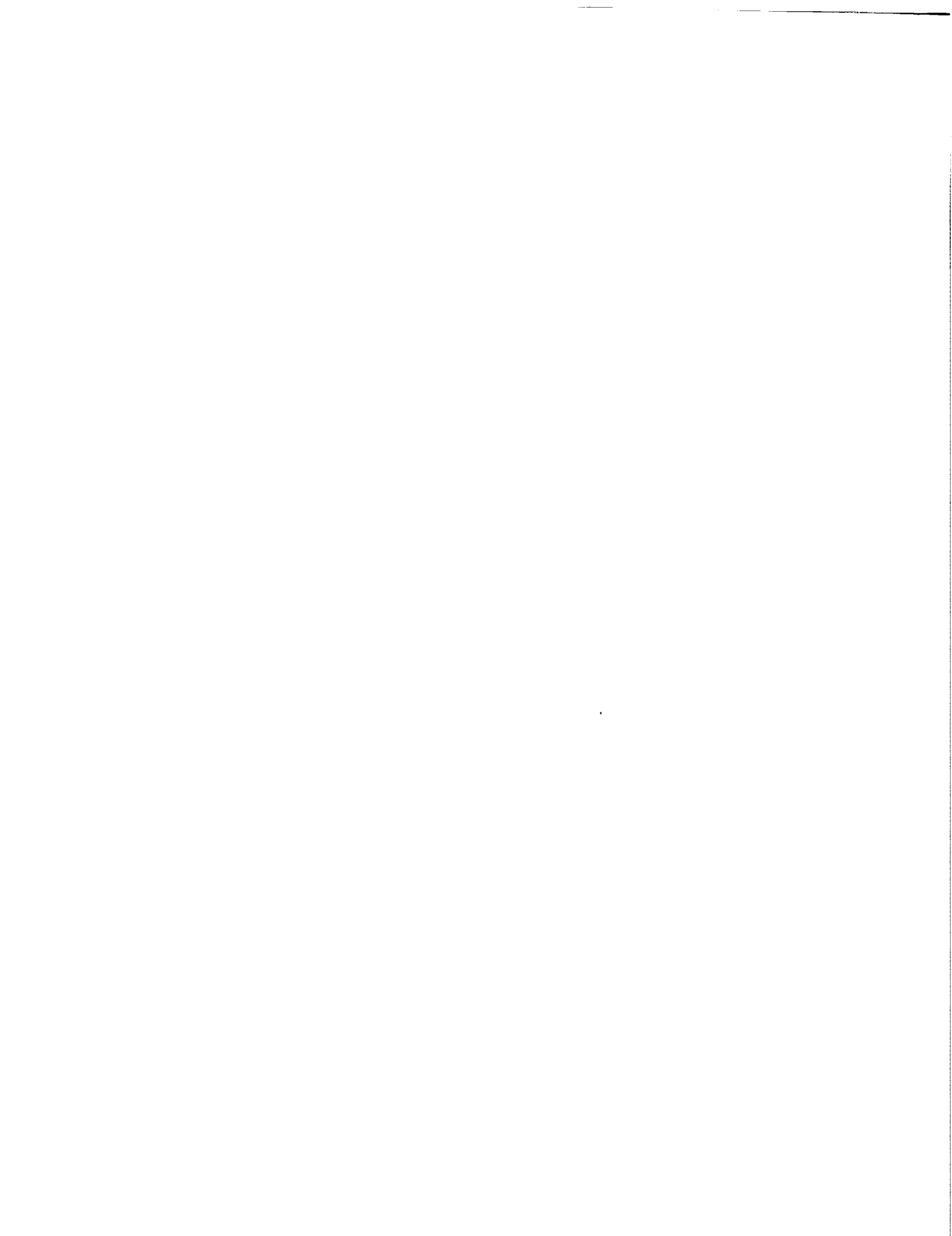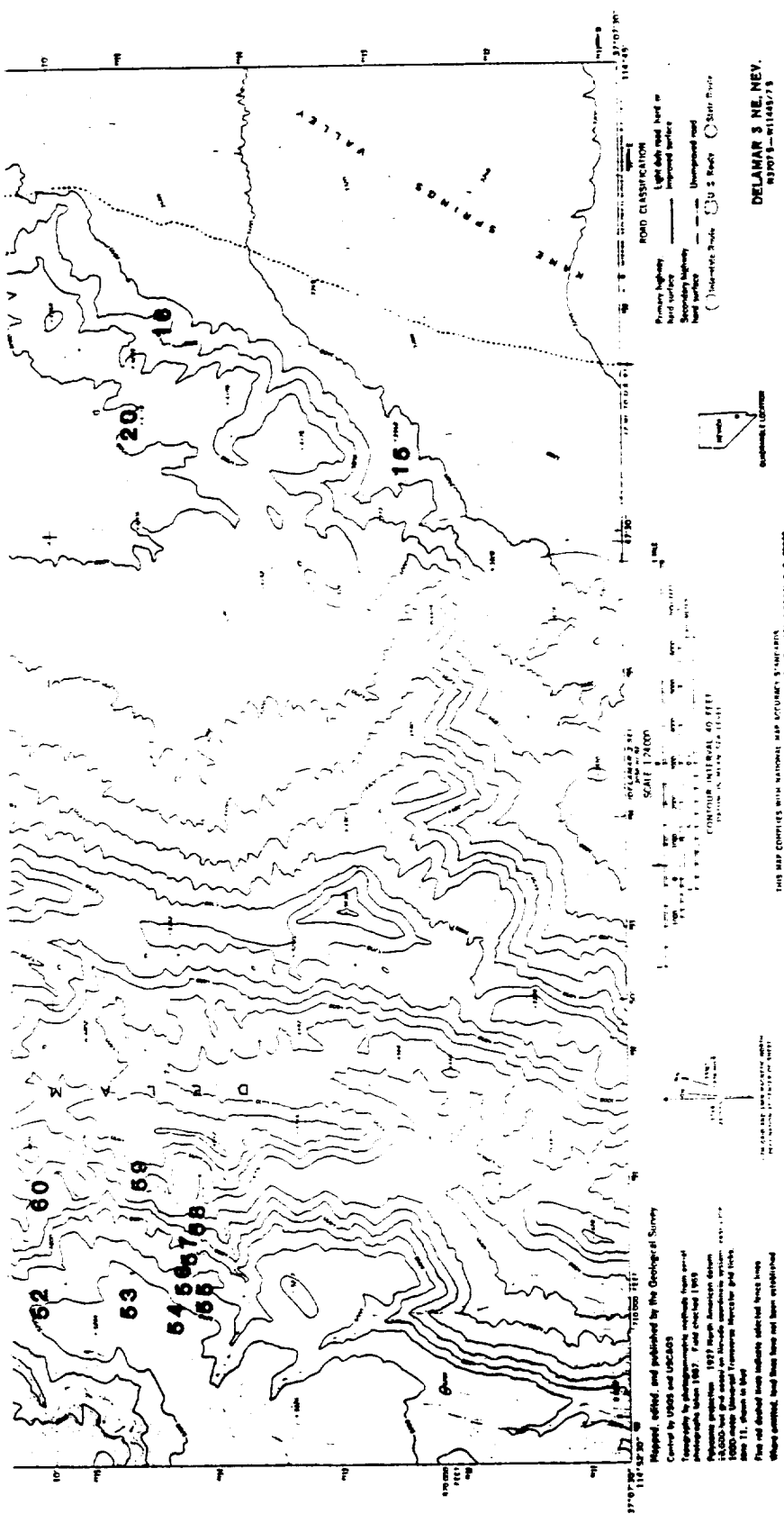
SAMPLE LOCATION MAP—KANE SPRINGS WASH AREA

BASE: U.S.G.S. Topographic quadrangle, reduced 50%

FOLDOUT FRAME

spectrographic measurements. Most sites were photographed.

An attempt was made to acquire reasonably complete sample coverage from both imagery and lithologic perspectives. Thus, distinct imagery units (color and gray level contrast), discerned from the initial pre-field image processing phase, were sampled as well as formationally differentiated units shown on the geologic maps available for each area. Samples of unmapped units, including ash flow members, subvolcanic intrusives, vapor-phase altered zones, densely welded zones, air-fall tuffs, and basal glasses, were also collected. A 7.5 minute topographic quadrangle base map was used for sample site notation at Kane Springs and 15 minute quadrangle maps used at both Stonewall Mountain and Black Mountain. Scale of the 15 minute quadrangle maps compares well with 8x10 inch enlargements of 35mm photos taken by the Dunn camera peripheral.

Ground-based 35mm photographs were "framed" to encompass representable scenes including outcrop, soil, regolith, and vegetation to serve primarily as reference logs to scene spectral compositions. Distance shots were also collected to show both stratigraphic relationships and sample locations.

Field spectra were collected during the 1987 field season from 95 samples at over 50 sites from the Stonewall Mountain and Black Mountain study areas. Spectral samples

were collected from some plants as well as rock surfaces and from surfaces with variably developed desert varnish on a common host rock. Due to both field and tape retrieval problems only 81 spectral curves were recovered. A portable infrared imaging spectroradiometer (IRIS) built by Geophysical Environmental Research, New York, N.Y. was used. The sensor head mounts on a tripod. It is a dual beam system that looks at both reference and sample targets simultaneously to reduce fluctuation in source energy. Incoming radiation is modulated in phase by a tuning fork chopper and directed through the optical system to two parallel input detector modules. The system operates over the spectral range from 350nm to 3.0um and alternates gratings on a motor-driven mount. A CMOS microcomputer operates and digitizes the measurements and stores them in CPU memory. Data is output on magnetic tape.

LABORATORY RESEARCH

Analytical investigations of coatings began in the fall of 1986. Since then 87 thin sections have been cut and studied to varying degrees of detail and 58 X-ray diffraction (XRD) analyses completed. Scanning electron microscope (SEM) studies have been conducted on over 30 samples, most of which were probed compositionally with the systems energy dispersive X-ray system (EDX). These analytical probes focused on secondary mineral coating

compositions and underlying rock compositional zoning within weathering cortexes. Infrared spectrometric analyses were performed on 22 samples. Geochemical analyses including inductively coupled plasma (ICP), X-ray fluorescence (XRF), neutron activation (NAA), and wet chemical methods (all performed by Chemex Labs, Inc., Vancouver) were run on 69 samples including a complete profile of 26 for 60 elements, and major and trace element analyses on weathering rinds and powders of desert varnish. Specific gravity measurements (picnometer) were taken on 25 samples for mass balance considerations. Beckman lab spectra (visible and near-IR) were run on 23 samples. Density slice gray level measurements were collected from 6 coating photographs and SEM images. The suite of samples selected for these applications represent the major volcanic units present at each of the 3 study sites as well as the diverse coating types observed. Detail on the specific methods employed are presented below.

INSTRUMENTAL TECHNIQUES

THIN SECTION PETROGRAPHY. Some 86 thin sections were prepared. Most were cut perpendicular to the rock surface and exhibit surface coatings. Sections typically extend down into the host rock a centimeter or two. In this geometry boundaries between surface coatings and underlying host can be observed and relationships noted. Each section

was prepared by a Nevada Bureau of Mines and Geology technician with explicit instructions to maintain section edges and edge thicknesses in order to preserve coatings. Petrographic investigations were conducted on a standard binocular petrographic microscope.

X-RAY DIFFRACTION. Coating materials from surface ships and subsurface zones of 58 representative rock units were extracted for X-ray diffraction (XRD) analysis. The extractive technique involved briskly and lightly vibrating fine powder-size material from the rock surface with an electric scribe mounted with a carbide steel tip. Some of the extraction was accomplished under a Baush and Lombe zoom binocular scope. Although the scribe has both diamond and tungsten carbide tips available, these harder points were avoided since they tend to drill deeper beneath the surface coatings into underlying fresher rock. Still, much of the coating compositions collected in this manner contain primary rock contaminants. To improve sample purity, powders were screened to 100 mesh to exclude coarser particles likely to involve underlying primary minerals, then ground in an agate mortar prior to mounting on a glass slide for X-ray analysis. (Greater than 90% by volume of the particles extracted from the rocks were less than 100 mesh, 0.147mm before grinding.) Thus only minor material beyond this thickness (0.2mm) appears to

contaminate the samples.

All samples were X-rayed on one of Mackay's Philips Norelco XRD instruments and 2 theta measurements calibrated to a known quartz standard. Samples were saved in numbered glass vials.

SEM. Scanning electron microscope studies were conducted on a JEOL T300 scanning electron microscope, equipped with an energy dispersive X-ray system (EDX), at the U.S. Bureau of Mines Reno Research Center. Over 30 samples were scanned and compositional probes tabulated for coatings, weathering rinds, subsurface zones of calcium enrichment, fresh rock interiors, and individual mineral grains. Both standard polished sections and polished thin sections were created for sample mounts. Textures were observed in low KeV mode and photographed. Coating encrustations were photographed and compositional line scans and color composition maps plotted. The EDX system measures the characteristic line spectra emitted from the sample when the instrument is placed in high KeV mode. The unit is equipped with a Peak Instruments wavelength spectrometer for carbon analysis. The imagery processing peripheral is manufactured by Princeton Gamma Tech.

INFRARED SPECTROPHOTOMETRY. Twenty-two samples including coating powders, subsurface weathering bands,

rock interiors, and 2 opal and manganese oxide standards were scanned on the University of Nevada Chemistry Department's Perkin-Elmer model 599 Infrared Spectrophotometer. Samples were mixed with and made into a KBr pellet and compared to a pure KBr pellet. A 3-minute scan time was used from 2.5 to 50um (4000-200 wavenumber) and graphed on a log scale.

DENSITY SLICE. Gray level density slice measurements of 6 photographs of ash flow tuff surfaces hosting moderately mature coatings were collected on a Dapple Systems optical image analysis system at the U.S. Bureau of Mines. The unit utilizes a Panasonic movie camera and an Apple IIe image processing peripheral. Gray level histograms are presented on a scale of 0-255. Gray levels thought visually to represent coated surfaces were compared to gray levels of fresh rock surfaces exposed within the photographic frame.

VISIBLE/NEAR-INFRARED LAB SPECTRA. Visible and near-IR spectral measurements, comparing coated to uncoated surfaces, were plotted on the Jet Propulsion Lab's Beckman UV5240 UV-Visible-NIR spectrophotometer. The instrument uses a diffraction grating as its dispersion element, a tungsten source lamp and a halogen reference tube. Twenty-three samples, representing some of the more variable rock

types at the study sites were measured for spectral character between 0.4 and 2.5um.

CHEMICAL ANALYSES. Inductively coupled plasma (ICP) analyses of coatings, weathering rinds, rock interiors, and one carefully prepared subsurface weathering band, were analyzed for major elements, H_2O, CO_2, S, and selected trace elements. In addition, 26 whole rock samples were analyzed by diverse methods (Appendix E) for 60 elements. Analyses for rare earth elements (REE) were performed by neutron activation analysis (NAA). Analyses were performed by Chemex Laboratories in B.C., Canada. ICP is an especially effective type of atomic spectroscopy in which samples are "atomized" by a super heated argon gas plasma and emission spectra analyzed for absorption peaks representative of the various elements present. NAA is a relatively new analytical procedure based on production of radioactive nuclei from stable nuclei subjected to irradiation by a flux of neutrons of variable energies. Activation of the sample is followed by direct measurement of the induced gamma or X-radiation, using a gamma-ray spectrometer. X-ray fluorescence (XRF) operates through excitation of atoms by primary X-rays of known continuous energies. Emitted fluorescent radiations from the sample are diagnostic for the elements and the intensity directly related to the elements proportion in the sample.

CHAPTER III

GEOLOGY OF THE STUDY SITES

All three study sites are located in southern Nevada in the center of the Basin and Range province (Figure 1). Regional tensional stresses initiated in mid-Tertiary time are usually invoked to explain the province's characteristic topography and neotectonic setting. More than 20 major volcanic ash flow sheets and 8 caldera collapse structures have been recognized (Eckel, 1968; Ekren, et al., 1971; and Byers, et al., 1976). A relatively young (mid to late Miocene), chiefly silicic volcanic caldera structure with associated intracaldera lavas and tuffs and outflow sheets of ash flow characterizes each of the three study sites. Moreover, these 3 volcanic centers are members of a suite of unusual peralkaline rhyolitic deposits present in the western U.S. (Noble and Parker, 1974). Each area is well preserved and well exposed. Pre-Tertiary rocks consist primarily of mio-eugeosynclinal Paleozoic rocks.

Inasmuch as this investigation has focused on the origin of secondary mineral coatings and the relationships they bear with underlying host rocks and Landsat TM imagery, this chapter will concentrate on detailed descriptions of individual volcanic units. Petrochemical properties of the units will be correlated independently

with Landsat TM imagery in Chapter VI and VII. Rock assemblages at each site are described in order of decreasing age, insofar as relative ages are understood.

STONEWALL MOUNTAIN AREA

The study area at Stonewall Mountain actually involves two separate and independent caldera structures - the Stonewall Mountain caldera and the slightly older Mount Helen caldera east of Stonewall. Caldera margin faults are approximately 6 miles apart and the Landsat work scene selected for this site overlaps both (Figure 3). The geology of the area was mapped at a gross scale (Figure 4) and described by Ekren et al. (1971). Figures 5 and 6 are ground-based photographs of the area.

Stonewall Mountain itself consists of an intracaldera complex composed of a complicated sequence of pyroclastics, volcanic breccias, and flow dome complexes (Foley, 1978). The eruptive event was quite young, relative to the southern Nevada volcanic field in general - 6 to 6.3 Ma (Noble et al., 1984). The study site encompasses a two-component outflow ash sheet from the Stonewall volcanic system - the Stonewall Flat Tuff, which consists of a lower pumice rich ash flow deposit, the Spearhead Member, overlain by a thinner, typically more densely welded ash flow member, the Civet Cat Canyon Tuff. The Civet Cat Canyon Member was auto-oxidized during deposition and is a

Base: Landsat 5 TM Images

EXPLANATION

OLDER ROCKS OF MOUNT HELEN

THIRSTY CANYON TUFF

QTa	Alluvium and colluvium
Tby	Basalt of Basalt Ridge
Tffs	Stonewall Flat Tuff
Tbs	Basalt of Stonewall Mountain Area
Tha	Alluvium- Younger rocks of Mount Helen
Tmr	Rainier Mesa Member Of Timber Mountain Tuff
Ts	Sedimentary Rocks and bedded tuff
Tbp	Rhyolite of Ocher Ridge and Belted Peak
Tto	Tuff of Tolicha Peak
Ttos	Sedimentary rocks and tuff of Tolicha Peak

Tqp	Quartz latite: includes rhyodacite, stippled where intrusive
Tbh	Andesitic basalt
Tfgp	Fanglomerate
	Tuffs of Antelope Springs
Oe	Ordovician Eureka Limestone
QTb	Basalt
Tpb	Paintbrush Tuff

Fault, ball on downthrown side

Geologic contact, approximate

Strike and dip

GEOLOGIC MAP OF THE STONEWALL MOUNTAIN STUDY AREA

Modified after Ekren and others, 1971

FIGURE 4

1 Mile
1.61 Kilometer

Figure 5. Stonewall Mountain area. Photo taken on outcrop of Antelope Springs rhyolite, central eastern edge of study site looking west. Stonewall Mountain is in background. Note orangy to brown mineral coatings on the rhyolite. Bright orange patches are lichen.
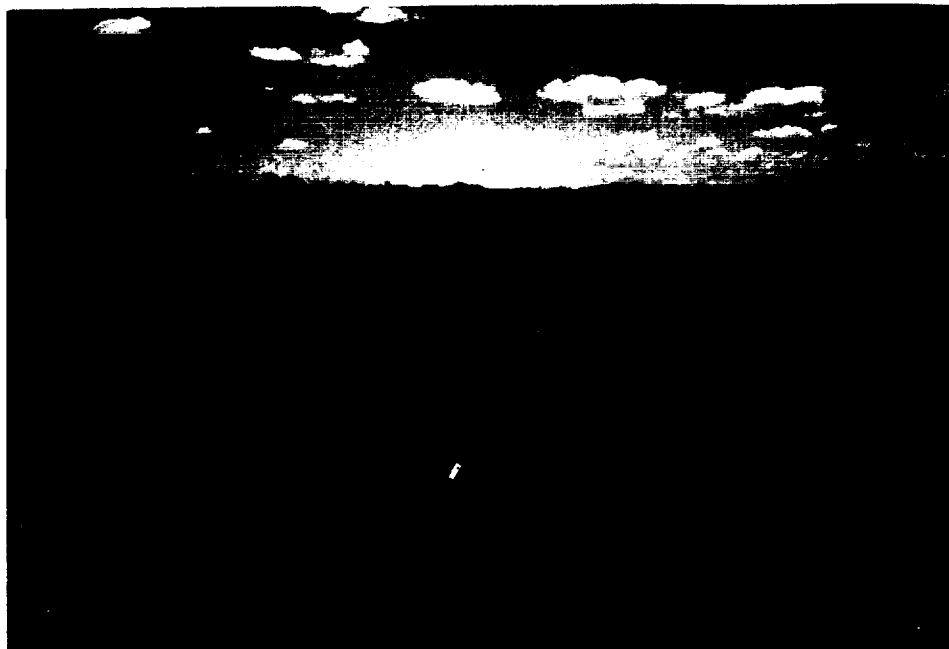
Figure 6. Stonewall Mountain area. Outcrop of densely welded Civet Cat Canyon Tuff, showing an example of well developed but typically discontinuous desert varnish. Photo taken at western border of study site, looking north.

distinctive deep reddish maroon brown color which forms a dark chocolate brown supergene coating. Both ash flow members are underlain in places by whitish pumice-rich airfall tuff of varying thickness, and both are composed of composite intraformational units within one major cooling unit. More descriptive lithologic detail is presented in the following section. Outcrops within the Stonewall study area are subordinated by alluvium and shallow regolith. Enhanced imagery tends to emphasize rock talus and detritus adjacent to outcrop as well as outcrops themselves.

Flows from the Mount Helen caldera are dominated by a felsic suite of tuff and lava ranging in composition from rhyolitic to latitic. Ekren et al. (1971) named the entire section the Antelope Springs Formation. The Antelope Springs appears to be older than the Stonewall Flat tuff of Stonewall Mountain since the Spearhead Tuff was observed overlying and onlapping the Antelope Springs Rhyolite at localities both in the eastern and western parts of the study area. Younger basalt flows, possibly part of the Mount Helen eruptive event, are present at two isolated localities within the work area. The basalt is younger than the prominent Mount Helen caldera rim fault, which it overlies at an isolated occurrence recognized on Landsat TM images.

The collapsed western margin of the Mount Helen caldera is delineated by a normal fault distinctly shown on Landsat

images. The fault is bound on the west by quartzite pebble/cobble gravel, probably old pre-caldera alluvial deposits and on the east by the felsic Mount Helen flows. Table 2 lists the important volcano-tectonic events in chronological order thought to have occurred at the Stonewall site.

The Stonewall study site is covered with sparse (25-30% average), low plant growth, chiefly sagebrush. The area is unique among the 3 in monotony and dearth of vegetative cover. Bright orange lichen does, however, populate the felsic deposits of the Mount Helen center.

ANTELOPE SPRINGS FORMATION

Rhyolitic to latitic tuffs and lavas, whose source is believed to be the Mount Helen caldera since unit distribution centers on that volcanic center, occur over much of the Stonewall study area. Ekren et al. (1971) assigned these rhyolitic to rhyodacitic rocks to Tuffs of Antelope Springs. The usual sequence within the project area is dense quartz porphyry rhyolite lava capping friable, poorly welded, fine grained tuff which overlies reddish ferruginous crystal rich latitic flows. Shallow, subvolcanic intrusive varieties are also present. These two lithologies are distinct and mappable; however, their designation as upper and lower Antelope Springs is project oriented and not intended as a formal stratigraphic

SEQUENCE OF VOLCANO-TECTONIC EVENTS AT
THE STONEWALL MOUNTAIN STUDY SITE

Intracaldera Deposits of Stonewall Mountain
Complex sequence of intracaldera extrusive and subvolcanic rhyolitic to latitic flows
and breccia bodies.

.

STONEWALL MOUNTAIN CALDERA COLLAPSE

Civet Cat Canyon Tuff of Stonewall Flat Tuff
Slightly peralkaline trachyte to high silica rhyolite ash flow tuff with a glassy cap
rock.

Spearhead Tuff member of Stonewall Flat Tuff
Slightly peralkaline, highly evolved rhyolite ash flow tuff.

Late Basalt
Vesicular, olivine basalt flows, intra and extracaldera, possibly sourced from Mount
Helen caldera from a later structure.

MOUNT HELEN CALDERA COLLAPSE

Rhyolite Porphyry of Antelope Springs Formation
Densely welded ash flow tuffs and quartz porphyry lavas, commonly hydrothermally
altered, underlain by less dense tuffs.

Quartz Latite Porphyry of Antelope Springs Formation
Crystal rich extrusive and subvolcanic latitic lavas and tuffs.

TABLE 2. Volcanic and structural evolution of the Stonewall and Mount Helen study site
(compiled with help from Ekren et al., 1971, and Noble et al., 1984).

assignment. The section is typically faulted, fractured, and often hydrothermally altered.

QUARTZ LATITE PORPHYRY. In the project area the lowermost Antelope Springs unit forms latitic crystal rich lava and shallow subvolcanic intrusive bodies. The formation is a mottled cream color with lacy dark to pastel red iron oxide staining. From thin section, albitic plagioclase phenocrysts (An=apx.5% by a-normal method) comprise about 15-30% of the rock. Rounded quartz phenocrysts make up approximately 5-10%, set in a very fine aphanitic groundmass. In some parts of the unit resorption is displayed by abundant cellularly textured plagioclase and heavily embayed quartz phenocrysts. The groundmass exhibits devitrification spherules and radiating fans of feldspar. Resorbed, fragmented biotite crystals at about 1% proportions were observed. The weathering surface is unstable and secondary mineral coatings poorly developed. The unit forms low hummocky hills and weathers to a friable to moderately dense pebble to cobble size float. Sagebrush is the dominant vegetative cover with some grasses. Whole rock and trace element geochemistry for units from the Mount Helen caldera are given in Table 3 and general comparisons among all major Stonewall site units tabulated in Table 4. This basal (within the project site) Antelope Springs deposit is a high silica, potassium rich latite to

TABLE 3. MAJOR AND TRACE ELEMENT ANALYSES* FROM
THE MOUNT HELEN CALDERA
(Sample location in parenthesis)

	(41) Latite	(52) Rhyolite	(10) Rhyolite	(94) Rhyolite	(39) Latite	(89) Latite	(12) Basalt	(93) Basalt
SiO_2	68.00	74.70	75.47	73.16	68.00	66.00	48.00	47.80
Al_2O_3	7.36	5.52	13.07	13.66	7.52	7.05	8.09	7.89
Fe_2O_3*	2.60	0.58	0.77	0.55	1.98	2.75	6.01	5.92
CaO	0.89	1.19	0.32	0.63	0.75	.70	3.64	3.33
MgO	0.10	0.17	0.07	0.12	0.24	0.35	1.00	1.34
TiO_2	0.33	0.07	0.30	0.32	0.27	0.35	1.00	1.34
Mn	663	110	<.01%	0.01%	300	437	1330	1285
Na_2O	0.35	1.23	0.99	0.97	0.75	2.50	2.07	2.68
K_2O	4.89	4.52	9.31	10.10	5.36	2.27	0.83	1.01
FeO	----	----	0.23	----	----	----	----	----
P	960	220	0.12%	0.21%	850	940	1700	2680
La	58	41	----	38	61	51	33	30
Ce	96	74	----	72	107	88	70	68
Sm	7.2	7.0	----	3.6	4.3	6.6	7.2	15.1
Eu	1.0	0.6	----	0.4	1.1	1.1	2.1	1.9
Tb	0.3	0.2	----	0.1	0.4	0.1	1.4	1.3
Yb	0.8	0.9	----	1.7	1.1	0.7	3.1	2.9
Lu	0.3	0.4	----	0.3	0.3	0.3	0.9	0.8
Nd	22	21	----	22	29	28	26	25
Sc	6.2	2.9	----	----	4.7	6.8	25.9	24.9
Ta	<.2	<2	----	----	<.2	<2	<.2	<2
Th	14.0	19.0	----	24	15.0	12.0	2	2.0
U	5.2	3.8	----	10	3.8	2.9	1	0.6
Hg ppb	120	280	----	----	30	30	40	30
Mo	6	6	----	----	4	7	4	1
Ni	3	<1	----	----	1	2	84	51
Nb	14	14	----	----	13	14	16	19
Rb	140	210	----	----	190	100	10	16
Se	0.2	0.2	----	----	0.2	0.2	0.2	0.2
Ag	0.5	0.5	----	----	0.5	0.5	0.5	0.5
Sr	206	182	----	----	354	785	485	765
S%	0.09	<.001	0.057	----	0.37	0.34	0.26	<.001
Te	<.05	<.05	----	----	<.05	<.05	0.20	<.05
Tl	0.4	0.7	----	----	0.6	0.4	0.10	0.10
Sn	1.0	1.0	----	----	1	1	1	1
W	7	4	----	----	3	4	2	2
V	62	6	----	----	56	78	176	223
Y	33	58	----	----	42	35	25	37
Zn	28	11	----	----	25	58	77	101
Zr	220	110	----	----	170	215	180	225
CO_2%	----	----	<.01	----	----	----	----	----
$+H_2O$%	----	----	0.34	----	----	----	----	----
$-H_2O$%	----	----	0.20	----	----	----	----	----
F	300	750	----	----	530	590	430	480
Sb	1.2	0.8	----	----	0.8	0.1	0.2	1.4
As	27	16	----	----	3	5	3	3
Ba	1460	240	----	----	1230	1660	710	670
Be	1.3	1.2	----	----	1.3	2.0	1.3	1.4
Bi	0.1	0.1	----	----	0.1	0.1	0.1	0.1
B	20	40	----	----	20	20	<10	<10
Br	<1.0	2.0	----	----	<1.0	1.0	<1.0	1.0
Ca	0.1	0.3	----	----	0.2	0.2	0.1	0.1
C%	0.26	0.61	----	----	0.22	0.35	0.06	0.06
Ca	8.0	12.0	----	----	9.0	25.0	<2.0	<2.0
Cr	16	13	----	----	19	16	82	83
Co	7	1	----	----	3	7	35	35
Cu	1	2	----	----	2	3	28	25
Dy	5	6	----	----	4	4	7	6
Ga	13	12	----	----	14	14	11	12
Ge	5	5	----	----	5	5	5	5
Au ppb	<5	<5	----	----	<5	<5	<5	<5
Hf	5	4	----	----	6	6	6	4
Pb	40	28	----	----	24	22	14	12
Li	36	29	----	----	32	30	6	9

* Oxides reported in percent and elements in ppm unless noted otherwise. Analytical methods are in appendix. Rhyolite and latite are from the Antelope Springs Formation. Fe_2O_3 represents total iron.

SUMMARY OF VOLCANIC UNITS OF THE
STONEWALL STUDY SITE

UNIT	LITHOLOGY	PETROCHEMISTRY MAJOR	PETROCHEMISTRY MINOR*	FIELD CHARACTER	DESERT VARNISH DEVELOPMENT**	DOMINANT VEGETATION ASSOCIATION
Civet Cat Canyon Tuff Cap Rock	Vitrophyre with sanidine/anorthoclase and biotite phenocrysts	Rhyolite peralkaline	Slightly high F, low Sr, Cr, Cu Ni, Mg	Dark grey-brown and rouge-red, densely welded glass. Forms mesa caps. Thin-platted float.	Sparse, poorly developed.	Sagebrush, grasses.
Civet Cat Canyon Tuff	Crystal ash-flow with sanidine/anorthoclase and biotite phenocrysts.	Rhyolite slightly peralkaline	slightly high Th, Be, REE, slightly low Sr, V, Mg	Very dark red-brown very densely welded, ledge former. Thin-platted float.	Moderate to well developed, dark chocolate brown.	Sagebrush, grasses, some juniper.
Spearhead Tuff	Pumice rich ash-flow with sanidine/anorthoclase phenocrysts.	Rhyolite slightly peralkaline	High REE, Zn, Zr, Be, Ce, Low Sr, Mg, Ba, Co, Ni, V	Pale buff to buff grey, moderately welded, ledge former. Thick rough, slabby float.	Highly variable, well to poorly developed, brown to grey buff.	Sagebrush, grasses.
Basalt Flows	Dense flow, minor vesiculation, microporphyritic olivine and plagioclase.	Low silica basalt	High P, Sc, V, low U, Th	Very dark grey very dense, massive mesa cap in places.	Moderate to well developed, very dark grey with silvery sheen.	Grass, some sagebrush.
Antelope Springs Rhyolite	Dense quartz porphyry intrusives, flows and welded ash-flows(?) underlain by friable tuff. Commonly hydrothermally altered.	Rhyolite, slightly alkaline	slightly high Mg, Tl, Th	Very light cream-colored. Forms steep slopes, cliffs and knobs. Joint-bound blocky float.	Moderate to poorly developed. Brown to orange brown.	Grasses, some sagebrush, abundant orange lichen.
Antelope Springs Latite	Massive crystal rich flows and subvolcanic intrusive bodies with albitic plagioclase phenocrysts and frayed biotite.	Latite High silica, potassic latite to subalkaline rhyolite.	slightly high Ce, Ba	Reddish brown color. Form low, hummocky hills. Weathers to friable cobble-size float.	Poorly developed, brown to reddish brown.	Grasses, sagebrush.

* Amounts (high or low) are relative to other rock assemblages at the study site.
** Desert varnish is by nature, highly discontinuous and irregular in these study sites.

TABLE 4. Summary of lithological, petrochemical, and field characteristics of volcanic units from the Stonewall Mountain study site.

subalkaline rhyolite.   The unit contains slightly high

cesium and barium.

RHYOLITE PORPHYRY. Capping latite of Tuffs of Antelope Springs is a distinctively light colored rhyolite sequence consisting of friable white pumice lapilli tuffs commonly overlain by densely welded quartz porphyry tuff (Figure 5). The lava sequence contains abundant (50%) medium grained quartz-eye phenocrysts, sanidine, and alkali feldspar. Breccia textures are present in places. Coatings on the felsic rocks are immature and very poorly developed. They are yellowish orange, cream to buff in color with rare patches of thin gray to very dark gray patina. The lavas are quite dense and tend to develop a thin (1-2mm) porcelaneous rind in the immediate subsurface (few mm) below weathered surfaces. Bleached rinds indicate depletion of ferromagnesian constituents. One of the more conspicuous features of the felsic deposits in outcrop is the presence of abundant rosettes of orange lichen. In places they blanket outcrop and float to greater than 30% areally and must contribute somewhat to the spectral composition. Another feature significant to remote sensing is the common presence of shallow alluvial outwash detritus adjacent to felsic rock outcrops. These unconsolidated deposits can be spectrally identical to adjacent outcrop. The unit forms steep slopes, cliffs and knobs where it is

either densely welded tuff or intrusive in origin. Float from the unit tends to be joint-bound and blocky. Vegetation is typical for the Stonewall site in general - mostly sagebrush - and indistinct (Table 4). Petrochemically, Antelope Springs rhyolite is a somewhat alkaline rhyolite with slightly high mercury, thallium, and thorium (Table 3).

LATE BASALT

Alkali olivine basalt, probably derived from the Mount Helen caldera, occurs at three sites in the Stonewall study area. Each is a relatively small exposure (less than 2km in any dimension), but the unit stands out in stark spectral contrast to surrounding rock types. The basalt is very dark gray, aphanitic and vesicular. It forms thin gently dipping flows that onlap the flanks of two ridges supported by Tuff of Antelope Springs. The basalt overlies and is younger than the prominent Mount Helen caldera margin fault that transects, north-south, the eastern half of the study area. In thin section the basalt is characterized by thin laths of plagioclase in a trachytic texture with some biotite and other mafic minerals in a microcrystalline groundmass. Desert varnish tends to form very thin shiny coatings with a characteristic conspicuous silvery sheen. The basalt is dense and massive and occurs as salient cliffs along mesa ledges and rough "mal pais"

flats strewn with subangular boulders. This unit is relatively low in silica with high amounts of phosphorous, scandium, vanadium and low amounts of uranium and thorium relative to other deposits at the Stonewall site (Table 3 and 4).

STONEWALL FLAT TUFF

The Stonewall Flat Tuff is the outflow sheet from the Stonewall Mountain caldera. The formation was characterized stratigraphically by Noble and others (1984) and includes two members: Spearhead Tuff and younger Civet Cat Canyon Tuff. Each member is a separate cooling unit composed of several subflows. Whole rock, minor, and trace element analyses for Stonewall Flat Tuff are compiled in Table 5 and Appendix F.

SPEARHEAD MEMBER. The Spearhead Tuff is the lowermost member of the Stonewall Flat Tuff. In the project area the member is composed of moderate to densely welded flows of rhyolitic ash flow tuff (Figure 7). Outcrops are typically grayish brown to grayish tan, occurring either as densely welded prominent mesa top ledges or less welded, less resistant slope formers. The unit consists of moderate to abundant and variously deformed pumice fragments up to several inches in length and contains 5 to 10% phenocrysts of sanidine with minor quartz and albitic plagioclase

TABLE 5. MAJOR AND TRACE ELEMENT ANALYSES*
FROM THE STONEWALL MOUNTAIN CALDERA
(Sample location in parenthesis)

	(81) Civet Cat Canyon Cap	(20) Civet Cat Canyon Tuff	(81) Civet Cat Cap-Red	(50) Civet Cat Canyon Tuff	(86) Spearhead Tuff	(27) Spearhead Tuff	(82) Spearhead Glass Base	(91) Spearhead Dense Base
SiO_2	65.44	70.87	68.90	72.36	72.84	75.63	66.80	73.70
Al_2O_3	14.06	14.41	6.64	14.04	12.41	13.14	6.63	5.79
Fe_2O_3*	2.42	2.71	1.53	2.55	2.59	2.51	1.48	2.56
CaO	2.12	1.87	1.31	1.90	2.17	0.51	1.91	1.08
MgO	0.42	1.00	0.17	0.37	0.33	0.14	0.48	0.16
TiO_2	0.32	0.33	0.19	0.30	0.34	0.16	0.16	0.16
MnO	0.12	0.10	707	0.10	0.02	0.09	659	1265
Na_2O	4.31	4.20	3.17	4.16	2.21	4.30	2.75	2.86
K_2O	5.50	5.31	4.00	5.10	4.80	4.75	4.20	4.38
FeO	----	0.12	----	0.23	----	0.08	----	----
P	0.21%	0.22%	310	0.26%	0.23%	0.27%	410	470
La	76	----	79	----	----	----	77	104
Ce	142	----	146	----	----	----	148	210
Sm	8.8	----	8.8	----	----	----	9.3	20.5
Eu	0.4	----	1.0	----	----	----	0.8	0.5
Tb	1.2	----	0.9	----	----	----	0.9	2.7
Yb	4.3	----	3.2	----	----	----	3.3	5.8
Lu	0.6	----	0.7	----	----	----	0.8	0.9
Nd	58	----	35	----	----	----	37	47
Sc	----	----	6.0	----	----	----	5.1	5.4
Ta	----	----	2	----	----	----	2	2
Th	16	----	15.0	----	----	----	17.0	14.0
U	4	----	4.5	----	----	----	3.7	4.1
Hg ppb	----	----	40	----	----	----	30	30
Mo	----	----	4	----	----	----	5	9
Ni	----	----	<1	----	----	----	<1	<1
Nb	----	----	35	----	----	----	38	44
Rb	----	----	140	----	----	----	150	120
Se	----	----	0.2	----	----	----	0.2	0.2
Ag	----	----	0.5	----	----	----	0.5	0.5
Sr	----	----	81	----	----	----	120	63
S%	----	<.001	<.001	<.001	----	<.001	0.036	.001
Te	----	----	<.05	----	----	----	<.05	<.05
Tl	----	----	0.5	----	----	----	0.4	0.4
Sn	----	----	1	----	----	----	1	1
W	----	----	1	----	----	----	1	5
V	----	----	<1	----	----	----	<1	8
Y	----	----	68	----	----	----	72	91
Zn	----	----	73	----	----	----	77	168
Zr	----	----	460	----	----	----	385	545
CO_2	----	0.63	----	0.56	----	<.01	----	----
$+H_2O$	----	0.52	----	0.24	----	0.11	----	----
$-H_2O$	----	0.37	----	0.25	----	0.10	----	----
F	----	----	730	----	----	----	630	160
Sb	----	----	0.2	----	----	----	0.2	0.3
As	----	----	3	----	----	----	3	23
Ba	----	----	620	----	----	----	500	190
Be	----	----	2.8	----	----	----	3.7	4.0
Bi	----	----	0.1	----	----	----	0.1	0.1
B	----	----	20	----	----	----	50	40
Br	----	----	1.0	----	----	----	2.0	<1.0
Cd	----	----	0.2	----	----	----	0.2	0.3
C%	----	----	0.31	----	----	----	0.60	0.39
Cs	----	----	16.0	----	----	----	16.0	5.0
Cr	----	----	3	----	----	----	7	16
Co	----	----	<1	----	----	----	<1	1
Cu	----	----	<1	----	----	----	6	4
Dy	----	----	11	----	----	----	10	15
Ga	----	----	15	----	----	----	15	21
Ge	----	----	5	----	----	----	5	5
Au ppb	----	----	<5	----	----	----	<5	<5
Hf	----	----	11	----	----	----	12	14
Pb	----	----	36	----	----	----	26	30
Li	----	----	16	----	----	----	26	18

* Oxides reported in percent and elements in ppm unless noted otherwise. Analytical methods are in appendix. Fe_2O_3 represents total iron.
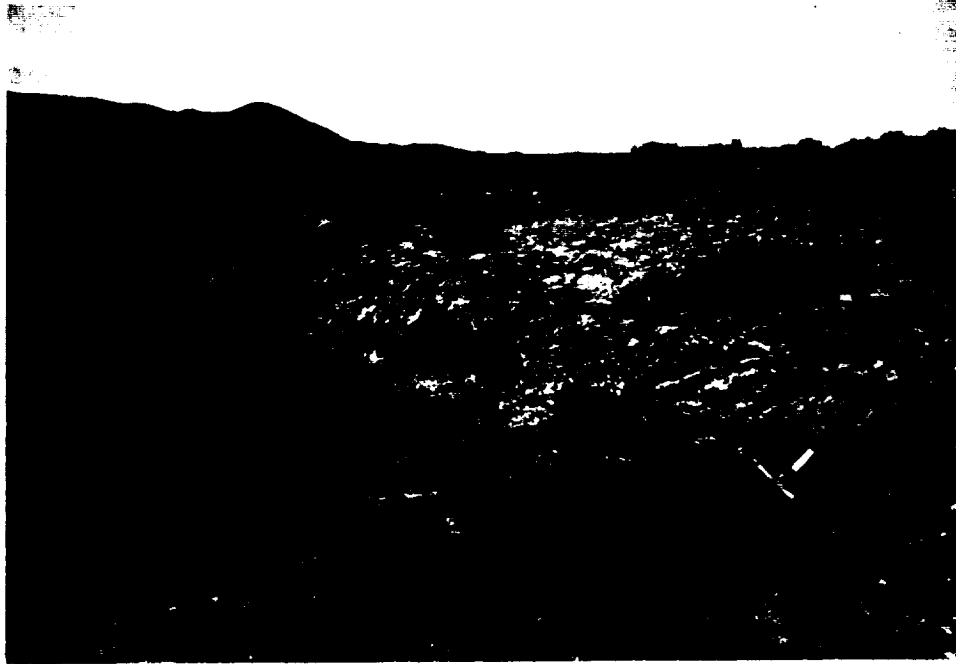
Figure 7. Stonewall Mountain study area. Outcrop of welded Spearhead Tuff. Welded zone forms ledge overlying glassy base. Photo taken at northern boundary of study site, looking north.
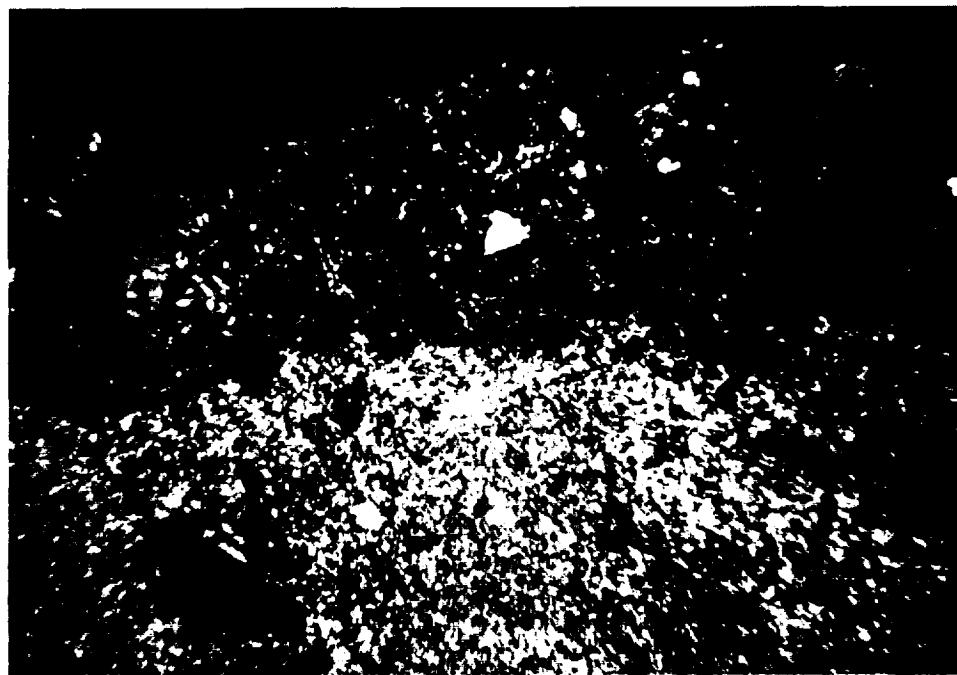
Figure 8. Photomicrograph of Spearhead Tuff from Stonewall Mountain. Crossed nichols at 10x. Light colored birefringent mass in lower half of photo is secondary calcite. Note vaguely darker fringe of desert varnish at the top of the sample.

(Figure 8). Rare clinopyroxene, olivine (fayalitic), sodic amphibole, and Fe-Ti oxides are reported by Noble and others (1984). Geochemical investigations by Noble and Parker (1974) and Noble (1979) indicate the tuff is slightly peralkaline, very highly evolved, with low europium/europium*, extremely low strontium, magnesium, barium, cobalt, and nickel and relatively high in the rare earth elements, zinc, zirconium, beryllium, and cerium (Table 5 and Appendix F). Hafnium content is exceptionally high. Coatings are grayish tan on moderate to poorly welded zones, very dark chocolate brown on densely welded zones. The unit sheds thick, rough slabby float and is dominated by sagebrush growth (20-30% of cover).

CIVET CAT CANYON MEMBER. The Civet Cat Canyon Tuff is the uppermost member of the Stonewall Flat Tuff and overlies the Spearhead Member (Figure 6). The unit was the subject of a focused investigation by Weiss (1987), who conducted detailed mapping west of the project boundary. Civet Cat Canyon Tuff is separated from Spearhead Tuff by basal vitrophyre and locally by white pumice-rich airfall tuff. In outcrop and hand specimen the Civet Cat Canyon Tuff is a distinctive brick-red brown to reddish chocolate in color due to microscopic secondary amorphous iron oxide that is believed to have formed during auto-oxidation of the unit during or immediately after deposition (Figure 9).

Figure 9. Photomicrograph of Civet Cat Canyon Tuff cut normal to and including the weathered surface. Plane light at 10x. Dark reddish brown patches at top of photo are desert varnish. Dark irregular streaks in lower third of photo are interstitial primary (autooxidation) hematite, characteristic of Civet Cat Canyon Tuff.

The unit is very densely welded and granophyrically crystallized. It occurs primarily as mesa caps in the study area. Thicknesses range from about 2 to 5m. Civet Cat Canyon Tuff is a slightly peralkaline crystal ash flow rhyolite tuff with about 10-15% phenocrysts of sanidine-anorthoclase and is distinctive from the Spearhead Tuff Member in hand specimen most reliably by the presence of biotite phenocrysts. Clinopyroxene, monazite, and Fe-Ti oxides are accessory minerals. Coatings are usually well developed and very dark chocolate brown to dark gray chocolate. A thin glassy cap rock, dark gray brown to a striking pastel red in color occurs at several localities. This unit was differentiated as the cap rock of Civet Cat Canyon by Hausback and Frizzell (1986) and where red or orange in color it produces striking imagery contrast with surrounding cover. Civet Cat Canyon Tuff discards thin platy float a few inches to a few feet across. It supports sagebrush and grasses, and vegetation is indistinct for the unit. The unit contains slightly high amounts of thorium, barium, and rare earth elements, and low amounts of strontium, vanadium, and magnesium relative to other rock assemblages at the site (Table 5). The cap rock subunit contains slightly higher fluorine.

BLACK MOUNTAIN CALDERA

The Black Mountain study site consists of a concise

well exposed, relatively small caldera complex, the margin of which is completely encompassed within the work area (Figure 10). The geology has been described by Cornwall (1972), Noble et al., (1964, 1968, and 1984), and Noble and Christiansen (1968 and 1974). Volcanic units are more numerous and diverse than at the Stonewall Mountain study area and were apparently produced in part by multi-collapse events. The center is believed to have been active between about 6.5 to 8.5 Ma ago. Ground-based photographs of the Black Mountain area are exhibited in Figure 11 and 12.

The Black Mountain eruptive sequence overlies older lavas and tuffs, felsic in composition. The only other non-Black Mountain unit at the site is a small isolated outcrop of Paleozoic limestone. The Black Mountain volcanic pile consists of intracaldera lavas and tuffs and an outflow ash sheet - The Thirsty Canyon Tuff (Noble, et al., 1964). Table 6 tabulates volcanic and structural events at Black Mountain, taken from Noble and Christiansen (1974). Four collapse events appear to be represented at the caldera, each preceded by major ash flow eruptions. The flows alternated initially between subalkaline and comenditic (light colored peralkaline volcanics) compositions with a general trend toward greater peralkalinity upsection. Intracaldera and outer rim lava flows followed caldera collapse. Compositions of lavas vary, but often resemble those of preceding ash flow
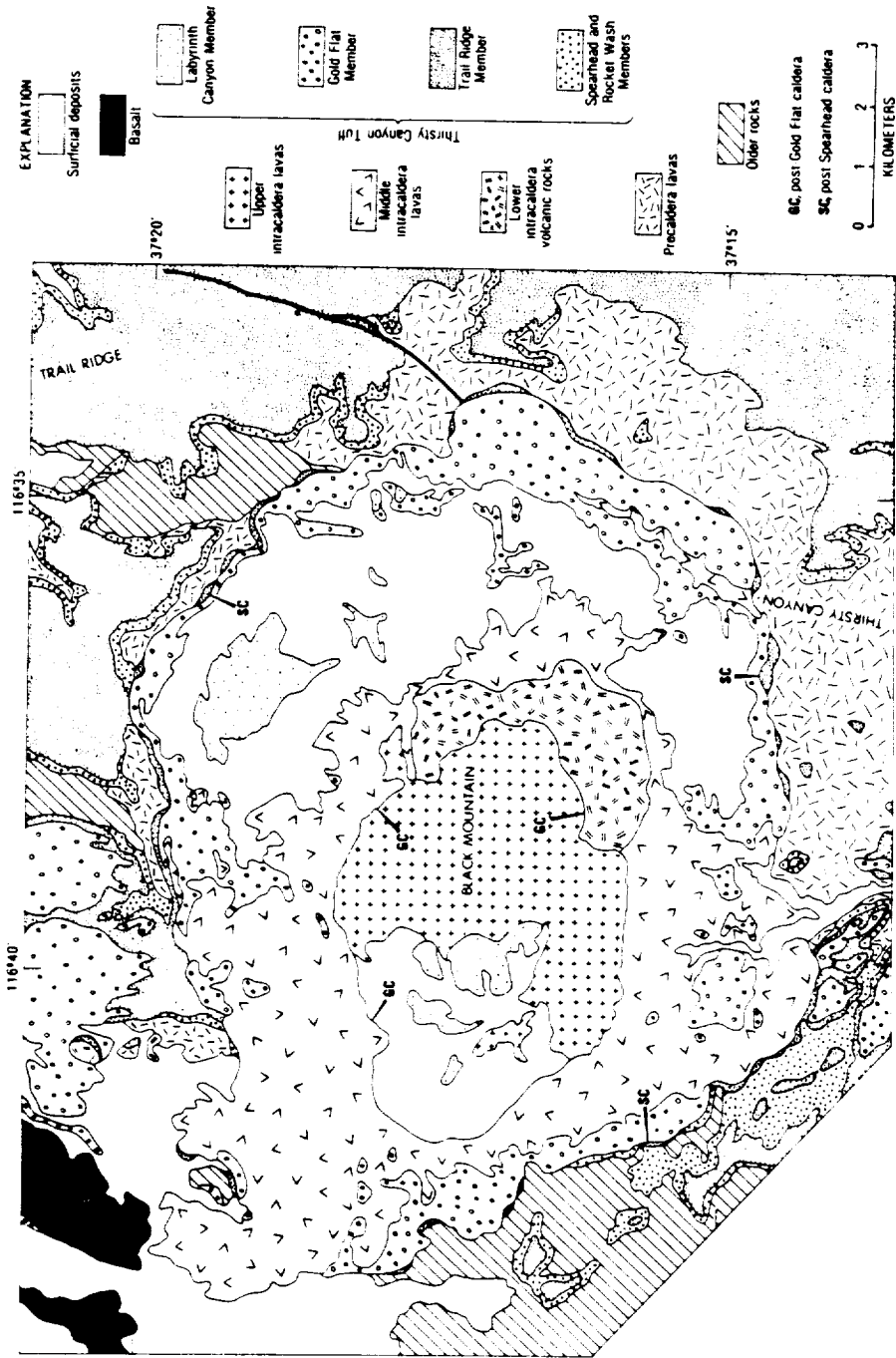
Figure 10. Geologic map of the Black Mountain caldera, Southern Nevada, from Christiansen, 1979. (Compiled from Christiansen and Noble, 1968; Noble and Christiansen 1968; O'Connor and others, 1966; and unpublished mapping by R.L. Christiansen and D.C. Noble.)
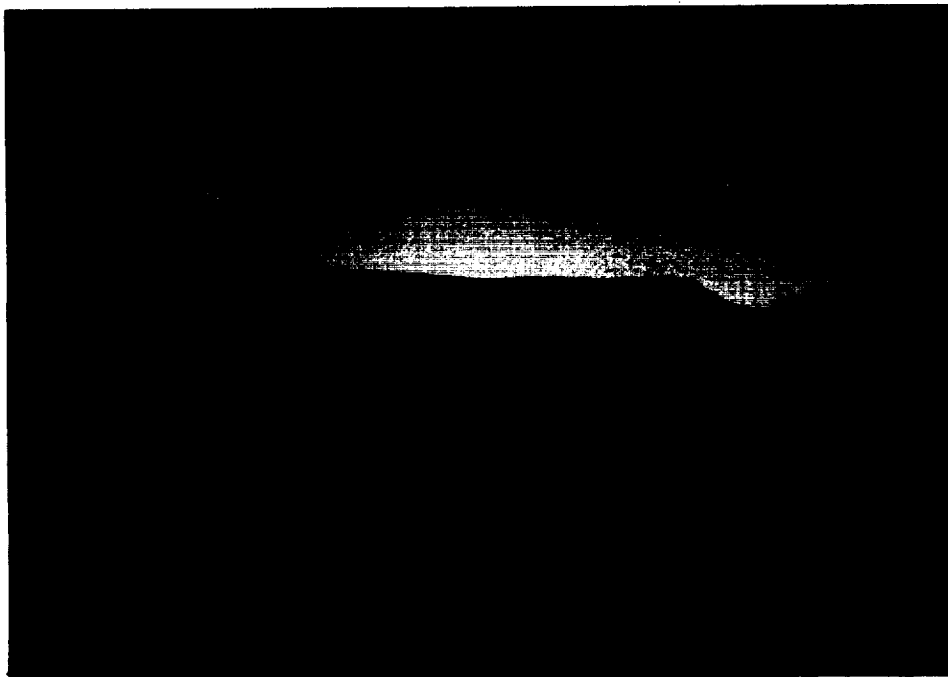
Figure 11. Black Mountain study site. Photo taken from the SE border of the study scene looking west at stratified Gold Flat ash flow beds in the foreground and the summit of Black Mountain underlain by Trachyte of Hidden Cliff in the background.

Figure 12. Photograph of the Black Mountain study site showing outcrop of vapor phase altered Gold Flat Tuff. Photo taken in west central part of study site, looking north.

TABLE 6.   OUTLINE OF THE VOLCANIC AND STRUCTURAL EVOLUTION
OF THE BLACK MOUNTAIN VOLCANIC CENTER, SOUTHERN NEVADA.
ARRANGED IN ASCENDING ORDER OF AGE.
(From Noble and Christiansen, 1974)

Basalt of Basalt Ridge
     K-rich hypersthene normative

Labyrinth Canyon Tuff (Distal Spearhead Tuff from the Stonewall Caldera)
     Comendite; probably erupted from central vent of Hidden Cliff volcano.

Trachyte of Hidden Cliff
     Trachyte and mafic trachyte with peralkaline potential; forms central volcano within
     post-Gold Flat caldera.

                              CALDERA COLLAPSE

Gold Flat Member of the Thirsty Canyon Tuff
     Pantellerite produced by extreme fractionation of comendite magma.

Lavas of Pillar Springs
     Trachyte with peralkaline potential; subalkaline and peralkaline silicic lavas; forms
     central volcano within caldera.

                          PROBABLE CALDERA COLLAPSE

Trail Ridge Member of the Thirsty Canyon Tuff   .
     Compositionally zoned from subalkaline rhyolite to quartz latite.

                         POSSIBLE CENTRAL RESURGENCE

Rocks of Yellow Cleft and Unnamed Lavas
     Trachyte and syenite with peralkaline potential to comendite; mafic trachyte; forms
     central volcanic complex within caldera.

                            MAJOR CALDERA COLLAPSE

Pahute Mesa Member of the Thirsty Canyon Tuff
     Vertically zoned upwards from comendite to quartz latite.

Unnamed Comendite Lavas
     Found as lithic fragments in the Spearhead Member.

                          PROBABLE CALDERA COLLAPSE

Rocket Wash Member of the Thirsty Canyon Tuff
     Subalkaline and/or transitional rhyolite and low-silica rhyolite.

Lavas of Ribbon Cliff
     Subalkaline trachyte to quartz latite; forms a low volcanic edifice centered where
     caldera later formed.

eruptions suggesting cogenetic magmas. Two to three generations of scalloped caldera margin scarps and associated talus were recognized by Noble and Christiansen (1968), indicating repeated instability of the caldera margin in some places.

In brief, the depositional history of Black Mountain can be represented by alternating sequences of lava and ash flow eruptions. Prior to the initial caldera formation, Lavas of Ribbon Cliff extruded to form a low volcanic edifice (Noble and Christiansen, 1974). The unit is present in the western half of the study area. After Lava of Ribbon Cliff was deposited, the lowermost member of the Thirsty Canyon Tuff, the Rocket Wash Tuff, was extruded, then minor lava flows and Pahute Mesa Tuff, then the first definite caldera collapse. These units are represented by minor exposures in the study area. They are spectrally indistinct and undifferentiated for our purposes. These tectono-volcanic activities were followed by intracaldera lava eruption (Rocks of Yellow Cleft), then deposition of the Trail Ridge Member of Thirsty Canyon Tuff, which was likely followed by caldera collapse. After Trail Ridge Tuff deposition, a chemically and spectrally similar lava flow, Lavas of Pillar Springs, were erupted. They form a significant portion of surface cover along the north and the eastern portions of the study area. Finally, the Gold Flat Member of Thirsty Canyon Tuff was deposited. Gold

59

Flat Tuff is the youngest ash flow at the volcanic center. It postdates final caldera collapse and is a rare unit compositionally (pantellerite, Noble, 1965). The formation is a highly evolved peralkaline comendite end-member with greater than 4% iron content.

The final event at Black Mountain was central volcano fill by dark trachyte and mafic trachyte lavas with peralkaline affinities. The Labyrinth Canyon ash flow deposit which occurs in isolated intracaldera patches on the flank of the central volcano was later reassigned on the basis of both geochemical and paleomagnetic deduction (Noble, et al., 1984) to distal Spearhead Member of the Stonewall Flat Tuff. Ash flow members of Stonewall Flat Tuff tend to have lower concentrations of hafnium, thorium, ytterbium, lanthanum, and rare earth elements. Hafnium is thought by Noble and others (1984) to be especially diagnostic of Spearhead Tuff.

The ash flow deposits at Black Mountain exhibit vertical zoning indicative of a chemically zoned magma chamber. The Pahute Mesa Member for example grades upward from high silica, high ytterbium, and high heavy rare earth elements and low light rare earth elements to low silica, low ytterbium, and both low heavy and low light rare earth elements. The lower zone would seem therefore to represent more evolved magma.

Vegetative cover is greater at Black Mountain than at

Stonewall and exerts a greater influence on Landsat radiance measurements. There are three general mappable vegetative cover classes at Black Mountain: sagebrush and atriplex dominant, grass dominant (chiefly foxtail and cheat grass), and mixed zones with juniper and pinyon. Vegetation will be discussed in more detail below as it influences spectral response over individual units. Since some of the lavas and tuffs at Black Mountain are indistinct in terms of imagery character, they are grouped together in the categories that follow. In general, however, units are described in order of decreasing age. Geochemical analyses are tabulated in Tables 7, 8, and 9 and Appendix G. General characteristics of units are compared in Table 10.

OLDER LAVAS AND TUFFS

Deposits of the Black Mount Caldera overlie older lavas and tuffs, which are exposed in the western portion of the study area (underlying Quartz Ridge). These units are distinctive in outcrop and hand specimen. They are relatively silicic, leucocratic, and coarsely granular as a result of abundant phenocrysts of quartz and alkali feldspar. They are more heavily fractured and tend to host more yellowish limonitic coatings than other units at the Black Mountain site. Breccia textures and hydrothermal alteration occur locally. The older lavas and tuffs

TABLE 7. MAJOR AND TRACE ELEMENT ANALYSES* OF LAVAS
FROM THE BLACK MOUNTAIN CALDERA
(Sample locations in parenthesis)

	(1) Pre-Black Mountain Volcanics	(2) Pre-Black Mountain Volcanics	(13) Trachyte Hidden Cliff	(11) Trachyte Hidden Cliff	(17) Lava of Pillar Springs	(35) Lava of Yellow Cleft	(38) Lava of Yellow Cleft
SiO2	74.90	70.90	58.21	59.50	70.40	79.50	65.70
Al2O3	5.96	7.18	17.37	7.97	6.80	5.35	6.88
Fe2O3*	0.91	1.45	7.38	4.05	2.48	0.81	1.64
CaO	0.50	1.11	5.28	2.18	0.42	0.49	1.19
MgO	0.08	0.23	1.96	0.85	0.11	0.07	0.43
TiO2	0.09	0.18	1.07	0.55	0.19	0.06	0.19
Mn	78	497	0.16%	1305	959	383	656
Na2O	2.15	3.15	4.97	3.89	3.63	2.32	2.46
K2O	4.73	3.66	4.06	3.78	4.29	3.47	3.94
FeO	----	----	3.59	----	----	----	----
P	180	310	0.78%	2750	150	300	590
La	51	77	----	112	215	47	78
Ce	84	124	----	206	367	83	141
Sm	27.7	3.8	----	5.2	10.1	19.7	3.7
Eu	0.5	0.9	----	1.4	<0.5	<.05	1.1
Tb	0.5	1.4	----	1.6	3.7	1.4	1.1
Yb	1.6	2.1	----	4.4	10.6	3.0	3.4
Lu	0.4	0.4	----	0.7	1.5	0.4	0.5
Nd	27	36	----	63	121	22	41
Sc	1.8	2.3	----	8.1	4.8	0.9	5.3
Ta	<2	2	----	2	5	<2	<2
Th	21	17	----	18	48	15	11
U	3.2	3.5	----	2.0	4.1	4.1	2.3
Hg ppb	80	40	----	50	40	20	40
Mo	6	6	----	7	7	7	3
Ni	2	<1	----	<1	<1	4	1
Nb	20	25	----	55	120	28	29
Rb	80	72	----	36	97	120	24
Se	0.2	0.2	----	0.2	0.2	0.2	0.2
Ag	0.5	0.5	----	0.5	0.5	0.5	0.5
Sr	154	317	----	355	29	87	348
S%	0.05	.001	----	.007	<.001	.052	<.001
Te	<.05	<.05	.005	<.05	<.05	<.05	<.05
Tl	1.2	0.5	----	0.1	0.6	0.1	0.3
Sn	1	1	----	1	3	1	1
W	6	1	----	2	4	5	2
V	8	11	----	34	<1	2	2
Y	53	51	----	71	155	55	46
Zn	14	62	----	112	166	36	56
Zr	185	255	----	590	830	140	450
CO2	----	----	1.09	----	----	----	----
+H2O	----	----	0.20	----	----	----	----
-H2O	----	----	0.32	----	----	----	----
F	100	500	----	1200	1950	160	520
Sb	2.4	0.2	----	0.2	0.6	0.1	0.2
As	14	3	----	3	4	3	3
Ba	630	1060	----	1160	110	290	750
Be	2.4	2.5	----	3.4	11.0	3.0	2.8
Bi	0.1	0.1	----	0.1	0.1	0.1	0.1
B	20	10	----	<10	10	30	10
Br	<1	<1	----	<1	<1	<1	<1
Cd	0.2	0.2	----	0.1	0.2	0.2	0.2
C%	0.32	0.08	----	0.22	0.04	0.13	0.21
Cs	<1	3.0	----	1.0	4.0	3.0	2.0
Cr	18	14	----	2	15	25	14
Co	1	2	----	7	1	1	1
Cu	6	2	----	7	<1	3	<1
Dy	3	4	----	7	9	6	6
Ga	15	16	----	17	22	15	16
Ge	5	5	----	5	5	5	5
Au ppb	<5	5	----	<5	<5	<5	<5
Hf	4	5	----	8	18	3	6
Pb	22	28	----	34	54	30	24
Li	15	9	----	14	26	7	11

* Oxides reported in percent and elements in ppm unless noted otherwise. Analytical methods are in appendix. Fe2O3 represents total iron.

TABLE 8. MAJOR AND TRACE ELEMENT ANALYSES* OF ASH FLOW TUFFS FROM THE BLACK MOUNTAIN CALDERA
(Sample location in parenthesis)

	(67) Trail Ridge Tuff	(60) Gold Flat Tuff	(65) Gold Flat Tuff	(46) Rocket Wash Tuff	(14) Labyrinth Canyon	(15) Glassy Base Labyrinth C.	(16) Labyrinth Canyon
SiO_2	62.70	70.43	62.60	71.72	75.10	72.30	72.60
Al_2O_3	7.62	11.92	4.80	12.52	6.31	6.40	5.23
Fe_2O_3*	2.24	6.54	3.22	3.78	1.57	1.52	1.27
CaO	2.52	0.88	4.96	0.85	0.51	0.35	1.27
MgO	0.46	0.25	----	0.77	0.31	0.34	0.54
TiO_2	0.30	0.31	0.15	0.22	0.09	0.09	0.07
Mn	1114	0.17%	----	0.14%	796	478	579
Na_2O	3.91	5.00	3.27	5.02	3.20	2.52	2.69
K_2O	4.70	4.75	3.23	4.55	3.80	4.12	3.33
FeO	----	0.93	----	0.57	----	----	----
P	810	0.17	670	0.13	1260	110	710
La	88	----	287	----	76	74	68
Ce	159	----	548	----	143	138	131
Sm	30.5	----	8.0	----	10.8	10.9	11.0
Eu	1.7	----	0.6	----	<0.5	<0.5	<0.5
Tb	1.1	----	8.3	----	2.1	2.2	2.0
Yb	3.0	----	26.5	----	5.3	5.4	4.4
Lu	0.6	----	3.8	----	0.8	0.9	0.6
Nd	48	----	139	----	11	49	49
Sc	8.2	----	2.0	----	1.5	1.4	1.4
Ta	<2	----	14	----	3	3	3
Th	10.0	----	110	----	19	19	18
U	2.9	----	22.0	----	5.1	4.8	10
Hg ppb	30	----	30	----	120	60	70
Mo	5	----	4	----	6	7	4
Ni	3	----	5	----	7	<1	3
Nb	32	----	325	----	52	59	51
Rb	28	----	170	----	130	170	120
Se	0.2	----	0.2	----	0.2	0.2	0.2
Ag	0.5	----	0.5	----	0.5	0.5	0.5
Sr	53	----	194	----	51	34	53
S%	.022	<.001	0.23	----	.021	<.001	.054
Te	<.05	----	<.05	.008	<.05	<.05	<.05
Tl	0.2	----	1.3	----	0.4	1.8	0.6
Sn	1	----	1	----	1	1	2
W	3	----	6	----	5	1	4
V	<1	----	31	----	14	<1	10
Y	52	----	370	----	105	105	86
Zn	92	----	361	----	111	137	102
Zr	520	----	2950	----	375	395	360
CO_2	----	0.42	----	0.39	----	----	----
$+H_2O$	----	0.20	----	0.25	----	----	----
$-H_2O$	----	0.25	----	0.45	----	----	----
F	460	----	2100	----	290	1040	290
Sb	0.2	----	0.5	----	0.8	0.2	0.3
As	4	----	17	----	5	3	7
Ba	630	----	290	----	260	60	140
Be	3.0	----	21.0	----	5.1	5.1	4.8
Bi	0.1	----	0.1	----	0.1	0.1	0.1
B	30	----	60	----	40	30	30
Br	<1	----	<1	----	<1	<1	<1
Cd	0.1	----	0.5	----	0.3	0.2	0.3
C	0.69	----	1.87	----	0.30	0.08	0.6
Cs	1.0	----	4.0	----	3.0	3.0	2.0
Cr	14	----	14	----	13	<1	7
Co	2	----	2	----	3	<1	1
Cu	2	----	10	----	5	1	4
Dy	10	----	35	----	5	13	5
Ga	15	----	22	----	19	21	19
Ge	5	----	5	----	5	5	5
Au ppb	<5	----	<5	----	<5	<5	<5
Hf	11	----	76	----	7	8	7
Pb	24	----	100	----	48	48	32
Li	10	----	84	----	22	27	27

* Oxides reported in percent and elements in ppm unless noted otherwise. Analytical methods are in appendix. Fe_2O_3 represents total iron.

Table 9.
BLACK MOUNTAIN CALDERA MAJOR ELEMENT ANALYSES
(From Noble and Christiansen, 1974)

	Trachyte Hidden Cliff	Ribbon Cliff Lava	Pillar Spring Lava	Pillar Spring Lava	Gold Flat Tuff	Pahute Mesa Tuff
SiO_2	54.8	61.08	63.6	69.15	69.30	66.9
Al_2O_3	16.8	17.51	16.8	14.32	9.05	16.0
Fe_2O_3	3.5	3.39	2.7	2.76	3.73	2.6
FeO	4.4	1.71	1.7	0.77	2.60	0.84
MgO	3.2	1.03	0.87	0.23	0.01	0.47
CaO	6.1	3.19	2.0	0.66	0.10	0.72
Na_2O	4.7	5.14	4.9	5.08	7.04	5.1
K_2O	3.3	4.55	5.0	5.36	4.37	5.8
H_2O^+	0.45	0.34	0.72	0.23	0.13	0.46
H_2O^-	0.17	0.32	0.50	0.25	0.02	0.18
TiO_2	1.3	0.88	0.88	0.36	0.25	0.42
P_2O_5	0.70	0.34	0.38	0.05	0.01	0.10
MnO	0.17	0.12	0.14	0.16	0.20	0.18
CO_2	0.24	0.02	<0.05	0.01	0.00	<0.05
Cl	0.01	0.02	——	0.01	0.77	0.01
F	0.13	0.16	——	0.33	1.35	0.04

SUMMARY OF MAJOR VOLCANIC UNITS OF THE BLACK MOUNTAIN
CALDERA STUDY SITE

UNIT	LITHOLOGY	PETROCHEMISTRY MAJOR	MINOR*	FIELD CHARACTER	DESERT VARNISH DEVELOPMENT**	DOMINANT VEGETATION ASSOCIATION
Labyrinth Canyon Tuff (Spearhead)	Fine ash-flow tuff with pebble size pumice and alkali feldspar.	Peralkaline rhyolite	High Hf, Mg, Rb, Tl, B. Low Sr, Ba	Tan in color, densely to moderately welded thin, platy ledge former.	Poor to moderate development. Pale orangy buff to dull gray brown.	Sagebrush, grasses and some low juniper.
Trachyte of Hidden Cliff	Variably vesicular, lava flow with minor plagioclase and olivine phenocrysts	Mafic trachyte	High P, Sc, Sr, Mn Ti, V, Be, Eu, Co, Mg. Low Rb, B	Dark gray, rough, hummocky boulders confined largely to Black Mountain.	Distinctively gray-light to medium. Moderately well developed.	Sagebrush, atriplex, rabbit brush, some low juniper grasses 10% moss green lichen.
Gold Flat Tuff	Eutaxitic ash flow with pumice and phenocrysts of anorthoclase Na-rich pyroxene and amphibole and fayalite.	Peralkaline pantellerite	High REE, Be, Pb, Sn, Th, Nb, Rb, Ta, U, Zr, An, As, B, Ce, C, Cu, F, Li	Pale olive gray moderately welded. Forms blocky slabs in float. Tops mesas.	Grey brown to dark grayish chocolate, moderately well developed.	Sagebrush, grasses, some juniper and pinyon.
Lavas of Pillar Spring	Coarse granitic lava flow with alkali feldspar and minor quartz and biotite.	Slightly subalkaline rhyolite to trachyte	Slightly high HREE, Th, Sn, Zn, Zr, Be, F, Hf	Dull gray brown rounded "beehive" outcrops of exfoliated flow layered granular lava. Forms low hills of rugged "fortresses".	Dull gray, gray brown and reddish brown, moderately to poorly developed.	Mostly grasses with sagebrush and atriplex.
Trail Ridge Tuff	Ash flow tuff with pumice fragments and alkali feldspar phenocrysts.	slightly peralkaline to subalkaline rhyolite to latite.	slightly high Sc, Eu, Mn	Dark chocolate brown poorly to moderately welded thin bedded. Forms shallow ledges on slopes.	Dark brown to gray brown, moderately well developed.	Sagebrush, atriplex, grasses
Rocks of Yellow Cleft	Dense flows and breccias with quartz and alkali feldspar phenos.	Latite to high silica rhyolite.	Silicic variety. High Sm, Cr. Low Sc, Ti, Ti, Zr, Sb, Ce, F, Hf	Dense, light colored cream, angular, blocky jointed outcrops in arcuate basin (moat).	Poorly developed, very discontinuous, yellowish to orangy.	Mostly grasses some sagebrush.
Older Lavas and Tuffs	Granular, granitic, crystal rich lavas and tuffs with quartz and alkali feldspar phenocrysts, some hydrothermal alteration.	Subalkaline rhyolite.	Slightly high As, Sb; low Mn and Mg (altered)	Mostly rounded, sloping outcrops, large, rounded exfoliated boulders.	Poorly developed pale to dark orangy brown.	Grasses with some sage, juniper, and pinyon.

* Amounts (high or low) are relative to other units within the study site.
** Desert varnish is by nature highly discontinuous and irregular in these study sites.
TABLE 10. Summary of lithological, petrochemical, and field characteristics of volcanic units of the Black Mountain study site.

weather like granite, forming rounded sloping outcrops and large exfoliated boulders. They are responsible for the rugged, mountainous terrain of Quartz Mountain in the western project area. Vegetation is largely grasses with some low evergreens. The section is basically subalkaline with slightly high arsenic and antimony and low manganese and magnesium where altered by hydrothermal solutions (Table 7).

LAVAS OF RIBBON CLIFF AND PILLAR SPRINGS. Two major extrusions of lava preceded ash flow sheets between each of the 3 or 4 caldera collapse events. (Noble and Weiss, 1986, now believe there were 3.) They are, from older to younger, Lavas of Ribbon Cliff and Lavas of Pillar Springs. Each unit is composed chiefly of trachyte. Lavas of Ribbon Cliff include latitic flows (Noble and Christiansen, 1974). Lavas of Pillar Springs tend toward peralkaline character (Nobel and Christiansen, 1974) and are similar to Trail Ridge Tuff geochemically (Tables 7 and 8) and spectrally. They form "beehive" mounds in outcrop due to exfoliation-like weathering parallel to viscous contorted flow structure. Coarse granitic textures are a consequence of abundant alkali feldspar phenocrysts with minor quartz and biotite. Coatings are generally poorly developed on these flows whose surfaces are unstable, subject to rapid, mechanical degradation. Desert varnish, where present, is

dull brown to dull reddish brown in color. Lavas of Pillar Springs form rugged terrain with a labyrinth of short canyons and a fortress-like geomorphology (Figure 13). The unit can contain slightly high thorium, tin, zinc, zirconium, beryllium, fluorine, hafnium, and rare earth elements (Table 7).

ROCKS OF YELLOW CLEFT. The latites of Yellow Cleft are intracaldera flows, conspicuously dense and light in color. They contain quartz and alkali feldspar phenocrysts and are brecciated and recemented locally. Coatings are very thin, yellowish to orangy, discontinuous and poorly developed. The unit occurs in one coherent arcuate depression in the eastern caldera moat. It probably erupted after Pahute Mesa Tuff, preceding Trail Ridge Tuff deposition. Outcrops are angular, jointed, and blocky, present only in one broad depression. Float is mostly cobble to small boulder size and very angular. Grasses dominate vegetative growth over the unit with subordinate sagebrush. The unit is a latite to high silica rhyolite with high amounts of samarium, and chromium and low thallium, titanium, zirconium, antimony, cerium, fluorine, and hafnium (Table 7).

TRAIL RIDGE TUFF. Trail Ridge Tuff is the middle member of the Thirsty Canyon Tuff Formation - the outflow sheet from the Black Mountain caldera. The unit occurs in

Figure 13. Black Mountain study site. Rugged outcrop area of Pillar Springs Lava. Photograph taken just southwest of the outer caldera rim, looking west.

Figure 14. Photomicrograph of basal glass of the Gold Flat Tuff from Black Mountain. Plane light at 10x. Note dark reddish layer of desert varnish at the sample's upper surface.

a few small isolated patches in the study area, commonly overlain by Gold Flat Tuff. It overlies the Rocket Wash and Pahute Mesa members, which are represented even more sparsely in the study area, and where they are present they are quite thin in outcrop and virtually indistinguishable on imagery from the lavas. The Trail Ridge member is a subalkaline rhyolite to quartz latite ash flow tuff. It tends to be moderately to densely welded. It is a brownish gray tuff with pumice fragments and alkali feldspar phenocrysts. Coatings are brownish to gray brown and darker and more maturely developed in general than those on the lavas. Trail Ridge Tuff forms short, stepped ledges on low hills and ridges. It is bedded and slightly welded within the study area. It weathers mostly to a fine scree with some platy slabs. The formation supports sagebrush, atriplex, grasses, and indistinct canopy. Scandium, europium, and manganese are slightly higher relative to other units at Black Mountain (Appendix G).

GOLD FLAT TUFF. The Gold Flat Tuff is the uppermost ash flow sheet of the Thirsty Canyon Tuff and the most thoroughly studied formation in the project area. Noble (1965) identified the unit as pantellerite and a highly evolved differentiate of the Black Mountain magmatic system. It is a thin, moderately welded outflow sheet that caps mesas west and south of Black Mountain summit and the

inner caldera rim (Figure 12). A thin basal vitrophyre (Figure 14) separates it from Trail Ridge Member. Lithologically the unit exhibits eutaxitic structure and contains 10-20% broken phenocrysts of anorthoclase, quartz, and sodic plagioclase with minor phenocrysts of clinopyroxene, aegirine-augite, amphibole, and olivine (fayalitic). Density slice imagery on an SEM image indicated 7.5-9.5% aegirine-augite content. Cerium- and lanthanum-rich monazite, cerianite, and zircon were identified by SEM-EDX probes. Groundmass is devitrified, presently composed largely of very fine alkali feldspar and cristobalite. Whole rock and minor and trace element analyses are given in Table 8 and 9 and Appendix G. The iron/magnesium ratio of olivine and amphibole is high. Concentrations of beryllium, niobium, lead, tin, thorium, and the rare earth elements are also anomalously high, up to 10 times that of comenditic glass from the Spearhead Tuff (Noble, 1965). Alkali/alumina and Na_2O/K_2O ratios are elevated as well. The unit is very pale olive gray in hand specimen. Coatings are gray brown to dark grayish chocolate and moderately well developed. The unit is moderately welded throughout the study site, is the latest deposit of any volume and areal extent at the site, and caps mesas and ridges, forming ledges and short cliff faces at their fringes. It produces blocky slabs of float. South of Black Mountain summit, the Gold Flat Tuff is host

to about 25% sagebrush cover. West of the caldera rim, a mixed growth of grasses merging into juniper and pinyon and sagebrush are present.

TRACHYTE OF HIDDEN CLIFF. After final collapse and extrusion of the Gold Flat ash tuff, mafic trachytic lavas filled the volcano and formed what is now the high edifice over Black Mountain. Mafic trachyte is dark gray, variably vesicular, largely aphyric with 5% plagioclase and alkali feldspar phenocrysts with some fayalitic olivine, clinopyroxene, and ilmenite (SEM-EDX probes). The unit exhibits peralkaline trends geochemically (Tables 7 and 9 and Appendix G). Outcrops on Black Mountain host about 10% dusty moss green to greenish gray lichen. Coatings are distinctively gray - light to medium - and moderately well developed. Trachyte of Hidden Cliff forms rough, hummocky, boulder strewn surfaces (Figure 15). There is a diverse floral association with the formation of Black Mountain where grasses dominate with rabbit brush and other low shrubs including sagebrush and scattered evergreens. Trace element geochemistry is typically mafic - low rubidium and boron for example (Table 7).

LABYRINTH CANYON TUFF (DISTAL SPEARHEAD). The Labyrinth Canyon Tuff was reassigned (Noble, et al., 1984)
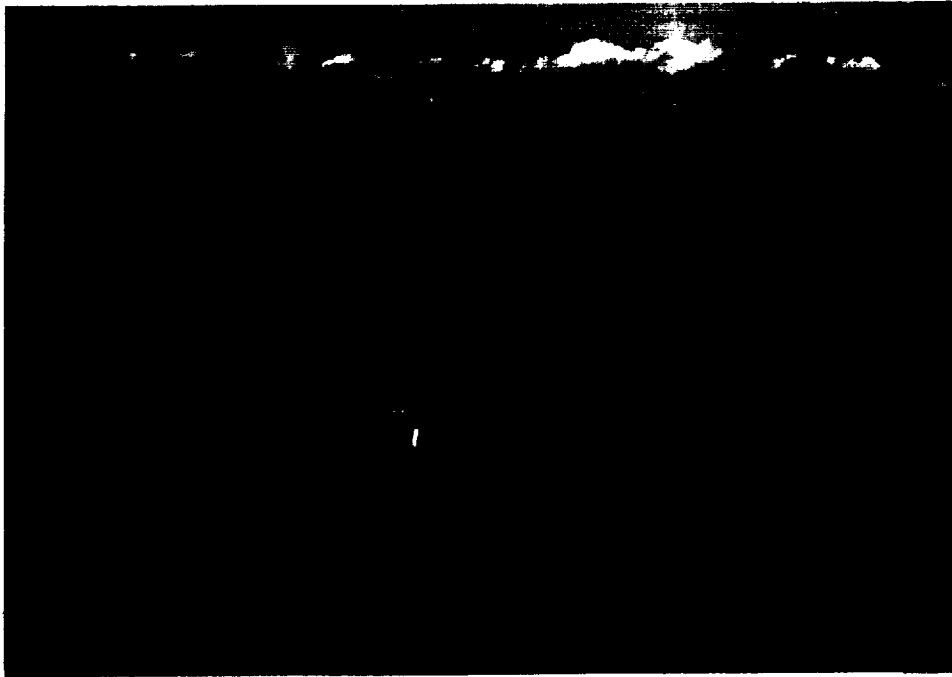
Figure 15. Black Mountain study site. Photograph taken on the flank of Black Mountain, looking north and showing outcrop of Trachyte of Hidden Cliff.

to distal Spearhead Tuff of Stonewall Flat Tuff based on geochemical and paleomagnetic data. Trace element signatures are consistent with Spearhead, particularly hafnium content. (The name Labyrinth Canyon is retained here to save confusion over imagery descriptions between the two calderas and to conform with normal practice which is to retain first-assigned formal formational names.) The Labyrinth Canyon Tuff is a thin somewhat platy ash flow. It is a fine grained, very pale orangy buff peralkaline rhyolite with sparse granule to pebble sized pumice fragments and alkali feldspar crystals (Figure 16). Basal vitrophyre separates it from underlying mafic trachyte lava. Coatings on the unit tend to be weak to moderately well developed and pale orangy buff to dull gray brown (Figure 17). In the project area, the Labyrinth Canyon Tuff caps a group of small mesas on the west flank of Black Mountain. The unit forms short cliff faces along the mesa margins. It weathers to thin, platy cobble sized float and supports grasses and sagebrush, dominantly. Relatively high hafnium, mercury, rubidium, thallium, and boron and low strontium and barium characterize the formation (Table 8).

KANE SPRINGS WASH

The Kane Springs Wash volcanic center was described in

Figure 16. Photomicrograph of the Labyrinth Canyon Tuff (distal Spearhead Tuff). Plane light, 10x. Thin section is cut normal to and including the weathered surface. Dark reddish desert varnish occurs sporadically on and near the rock-air (balsam) interface.
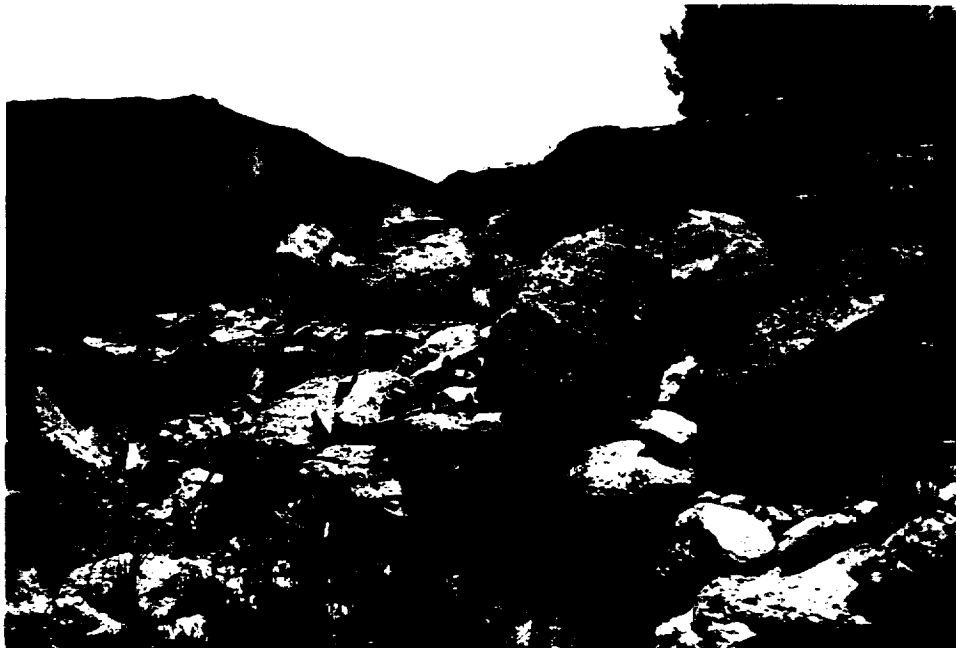
Figure 17. Black Mountain study site. Outcrop of the Labyrinth Canyon Tuff (distal Spearhead Tuff) with Black Mountain in the background. The unit is moderately welded with well develped desert varnish. The rock hammer is hanging on light gray basal glass.
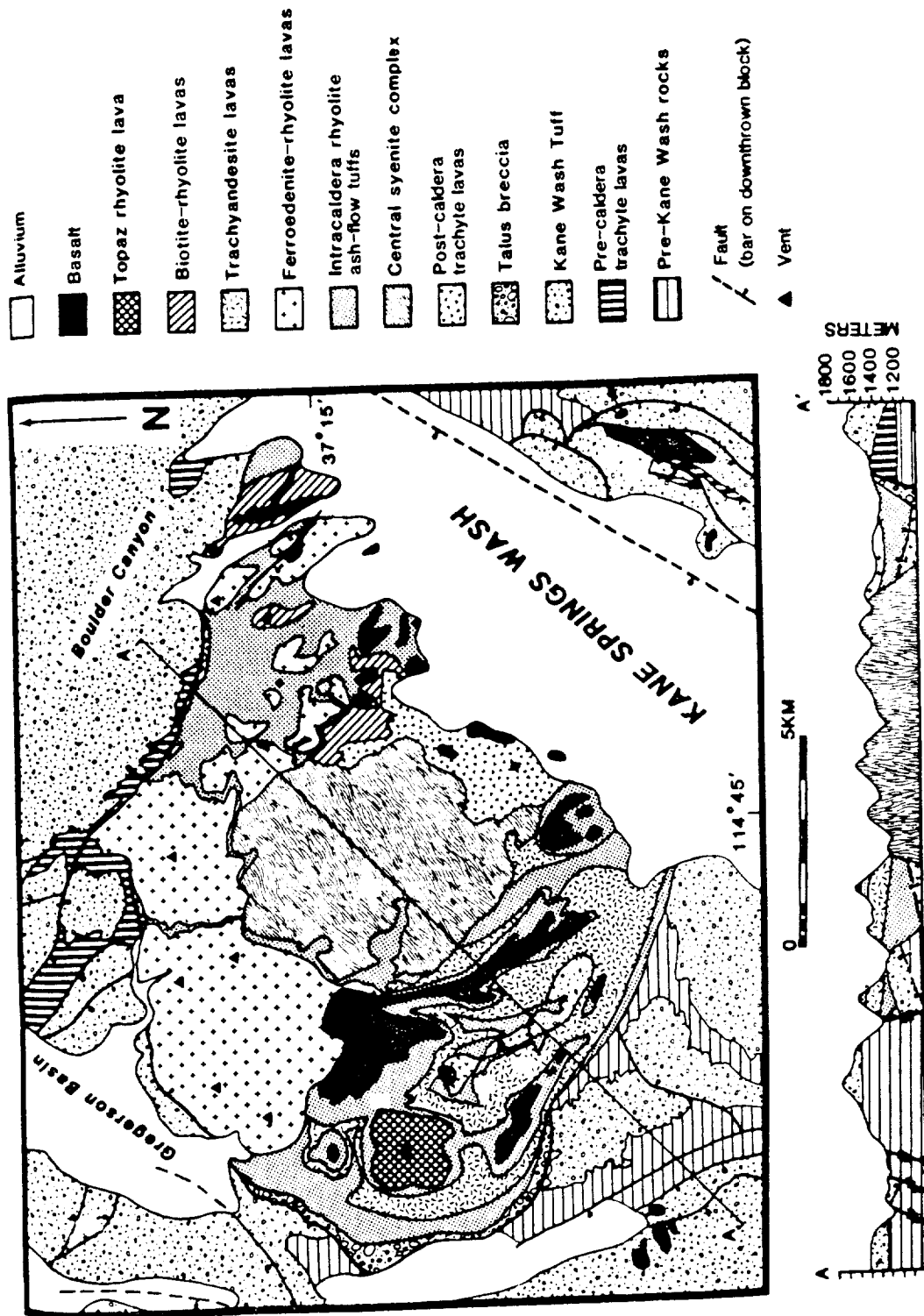
Figure 18. Geologic map and cross section of the Kane Springs Wash volcanic center (after Novak, 1984).

a general way by Cook (1966) and Noble (1968). Detailed mapping and geochemical studies were conducted by Novak (1984 and 1985). Figure 18 from Novak (1984) shows area geology; ground-based photographs of the Kane Springs Wash area are displayed in Figures 19 and 20; and major volcano-tectonic events are outlined in Table 11.

The Kane Springs Wash volcanic center consists of a well defined central caldera collapse structure filled with a complex sequence of diverse intracaldera lavas, tuffs, and flow dome deposits that straddle the collapse event in time. The outflow sheet within the study area comprises at least 3 distinct ash flow cooling units, ranging in composition from subalkaline to peralkaline rhyolite with a pantelleritic trend. K-Ar ages (Novak, 1984) place the eruptive event between about 14 and 11 Ma. Volcanism may have been controlled by the Pahranagat left-lateral strike-slip shear system to the west. Basin and Range faulting in the area appears younger.

The caldera rim fault is quite pronounced on the west and south edge of the caldera, and a prominent scarp demarks striking contrast between intracaldera lithologies and outflow deposits. Intracaldera deposits consist of dark trachyandesite flows overlain primarily by white pumice-rich air fall tuff. Dark late basalt caps the intracaldera mesas. Intrusive through this sequence but pre-basalt are flow dome complexes of topaz bearing
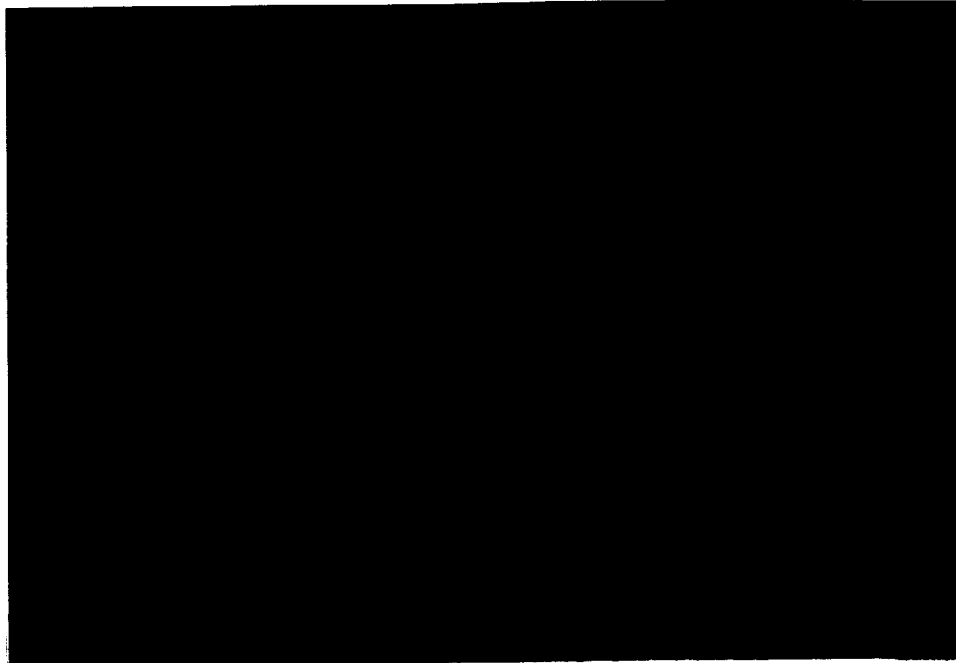
Figure 19. Kane Springs Wash study site. Photo shows stratigraphic section with Hiko Tuff (H) at base overlain by lower Kane Wash Tuff members O and W, capped by upper Kane Wash Tuff V member ash flows.
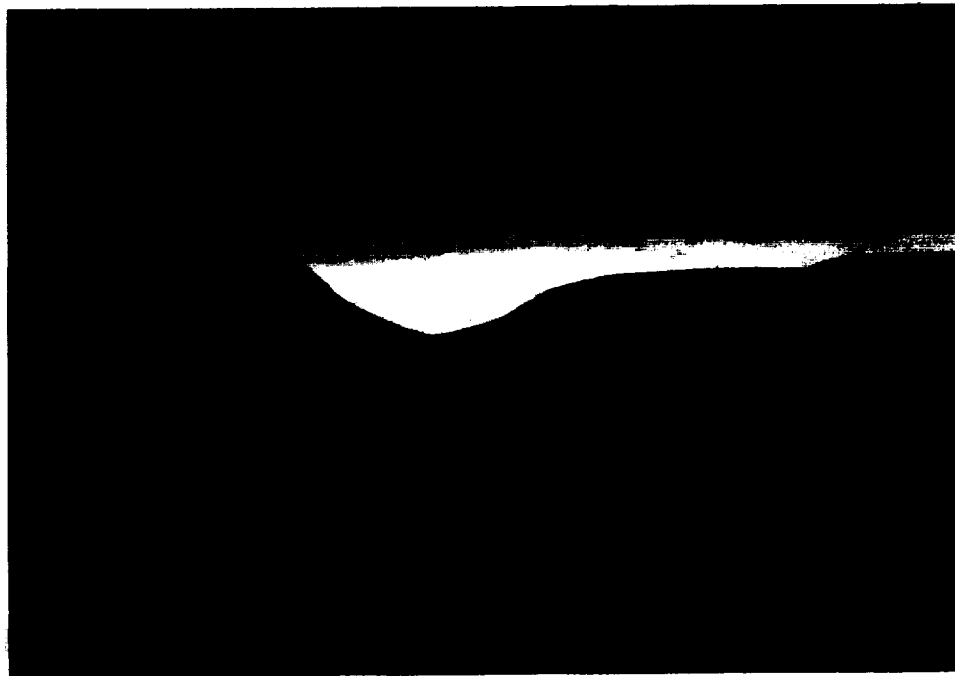
Figure 20. Kane Springs Wash volcanic center. Photo shows intracaldera units within the caldera looking west. R - topaz rhyolite, B - late basalt, T - trachyandesite lava, A - air fall tuff.

SEQUENCE OF VOLCANO-TECTONIC EVENTS AT THE
KANE SPRINGS WASH VOLCANIC CENTER

Late Basalt

Intra and extracaldera olivine basalt flows.

Rhyolite Flow-Domes

Ferroedenite and topaz-bearing exogenous intracaldera flow-domes.

Trachyandesite Lavas

Slightly vesicular to dense basalt to trachyandesite.

Rhyolite Lavas and Pyroclastics

High silica ferroedenite moat rhyolites and ash-flow tuffs.

Central Syenite Complex

Subcircular intracaldera extrusive to subvolcanic syenite.

Trachyte Lavas

Vesicular coarsely porphyritic intracaldera trachyte.

CALDERA COLLAPSE

Member V3

Densely welded comenditic ash-flow tuff with a vitrophyric base grading upward to vapor phase altered tuff.

Member V2 of Kane Wash Tuff

Welded vapor-phase-altered crystal-poor, ash-rich comenditic ash-flow tuff zoned upward to more mafic tuff.

Member V1 of Kane Wash Tuff

Nonwelded ash-rich rhyolitic base zoned upward to densely welded trachytic tuff.

Members O and W of Kane Wash Tuff

Fayalite-bearing rhyolite ash-flow tuff, possibly sourced from separate caldera SW of the Kane Springs Wash center.

PRE-KANE WASH VOLCANICS

Hiko Tuff

Subalkaline dacitic to latitic crystal-rich ash-flow tuff.

TABLE 11. Volcanic and structural evolution of the Kane Springs Wash Volcanic Center arranged in ascending order of age (compiled largely from Novak, 1984).

rhyolite. In the NE portion of the caldera is a sequence of complexly emplaced silica-poor tuffs and syenite domes which formed late in the depositional history, but which do not appear to have caused resurgent doming. The outflow sheet is a comenditic ash flow deposit with typical welding, vapor phase, and vitric zonal relationships. It has been named the Kane Wash Tuff and includes three members: V1, V2, and V3 from base to top, each a separate cooling unit. Noble (1968) included underlying ash flow deposits, designated O and W, with the Kane Wash Formation as part of the Kane Wash sheet. Novak (1984), however, disputes the inclusion of the O and W cooling units with Kane Wash Formation on the basis of unit thicknesses and clast size, which he observed increasing away from the Kane Spring Wash Center. The established stratigraphic subdivision of Noble was, nevertheless, retained by Novak. The Kane Wash deposits and the O and W ash flow units overlie older Hiko tuff. White air fall tuff occurs interstratified between some of the ash flow formations.

Although the Kane Springs Wash Formation includes several outflow sheets with distinctive chemistry, varying from subalkaline rhyolite to peralkaline iron-enriched rhyolite (Noble, 1968), these units do not seem to differ enough petrochemically to cause significant spectral variation. Rather, imagery characteristics appear to depend more on coating development and perhaps vegetation

diversity as a function, partially, of welding intensities within individual sheets. Moreover, remote sensing differentiation is facilitated by the presence of conspicuous high albedo inter-sheet air fall tuffs. The Kane Springs volcanic center is unique among the 3 study areas inasmuch as post caldera flows are abundant at Kane Springs Wash and confined to the intracaldera basin.

HIKO FORMATION. The Kane Wash Formation overlies an older felsic tuff. This pre-Kane Springs Wash basement is a crystal-rich ash flow deposit. It weathers and exfoliates like granite and forms mounds or "beehives" in places. Hiko Tuff contains about 50% broken sanidine-anorthoclase crystals with some plagioclase, quartz, biotite, and amphibole (Figure 21). Pumice and other lithics are sparse. The unit contains densely welded zones sequenced stratigraphically between less densely welded interzones. Coatings are more pronounced on densely welded portions of the tuff. They tend to be dull brown with variable tints of orange and gray, but mostly very pale orangy buff. Whole rock, minor, and trace element analyses for Kane Springs Wash units are presented in Table 12, 13, and 14 and Appendix H. Where sampled, Hiko Tuff is subalkaline and latitic in composition (Table 12). It contains slightly high strontium and barium and slightly low boron relative to other units at Kane Springs. The
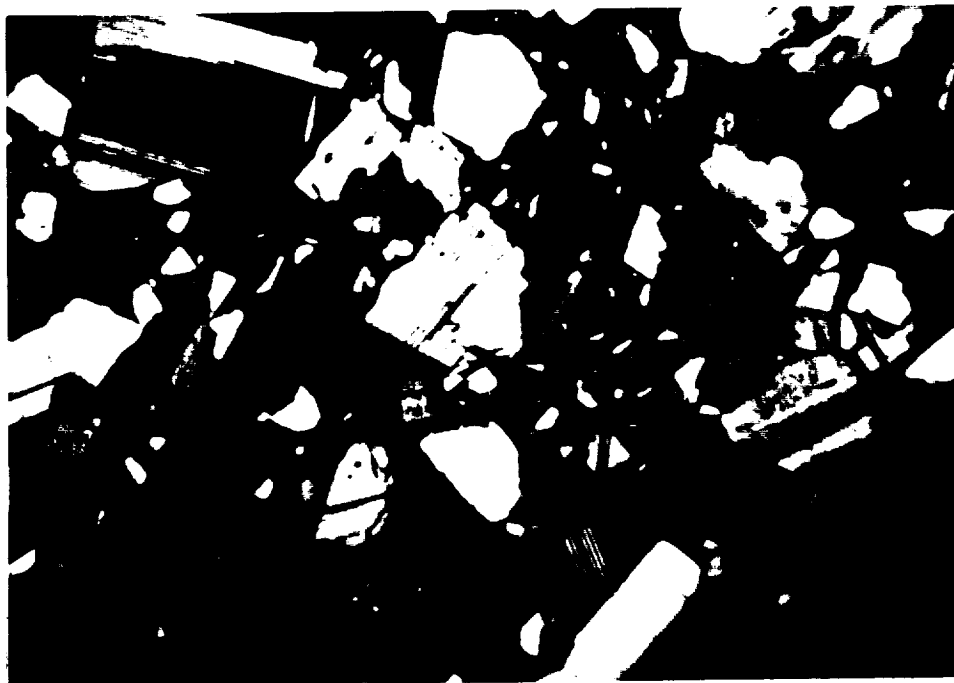
Figure 21. Photomicrograph of Hiko Tuff. Crossed nichols at 10x. Hiko Tuff is coarse and granular. Photo shows broken crystals of plagioclase, alkali feldspar, quartz and biotite with opaque magnetite in a mesostasis of devitrified glass.

Figure 22. Kane Springs Wash study site. Outcrop of Kane Wash Tuff V1 Member, moderately welded. Photo taken on east side of study area, looking north. (Cholla cactus is about 1m high.)

TABLE 12. MAJOR AND TRACE ELEMENT ANALYSES* OF
ASH FLOW TUFFS FROM THE KANE SPRINGS WASH CENTER
(Sample location in parenthesis)

	(19) Hiko Tuff	(50) Hiko Tuff	(18) Kane Wash V1	(26a) Syenite Complex	(26b) Syenite Complex
SiO_2	65.30	63.50	78.40	69.58	68.50
Al_2O_3	6.34	6.76	11.84	15.12	7.13
Fe_2O_3*	2.03	2.22	2.10	5.14	2.95
CaO	2.36	2.67	0.66	0.77	0.36
MgO	0.72	0.68	0.14	0.14	0.08
TiO_2	0.26	0.30	0.14	0.50	0.22
Mn	407	441	0.04%	0.05%	1055
Na_2O	2.25	2.42	3.67	4.90	3.63
K_2O	2.36	2.47	4.53	5.38	4.39
FeO	----	----	0.31	0.33	----
P	800	920	0.25%	0.20%	520
La	61	52	----	----	131
Ce	104	98	----	----	280
Sm	3.9	10.8	----	----	22.7
Eu	1.3	1.3	----	----	0.5
Tb	1.8	0.4	----	----	1.4
Yb	2.0	1.2	----	----	4.4
Lu	0.3	0.4	----	----	1.2
Nd	28	24	----	----	68
Sc	5.9	5.9	----	----	4.0
Ta	<2	<2	----	----	3
Th	13.0	12.0	----	----	13.0
U	3.4	3.0	----	----	3.7
Hg ppb	50	30	----	----	60
Mo	5	4	----	----	8
Ni	4	5	----	----	<1
Nb	14	19	----	----	58
Rb	48	68	----	----	110
Se	0.2	0.2	----	----	.02
Ag	0.5	1.0	----	----	0.5
Sr	543	581	----	----	38
S%	.015	.003	<.001	.047	<.001
Te	.05	<.05	----	----	0.10
Tl	0.3	0.2	----	----	0.3
Sn	1	1	----	----	1
W	3	3	----	----	4
V	41	45	----	----	<1
Y	34	35	----	----	80
Zn	48	51	----	----	101
Zr	230	230	----	----	565
CO_2	----	----	0.14	<.01	----
$+H_2O$	----	----	0.26	0.33	----
$-H_2O$	----	----	0.25	0.31	----
F	620	560	----	----	1250
Sb	0.2	0.1	----	----	0.2
As	3	3	----	----	9
Ba	1140	1260	----	----	430
Be	1.6	1.8	----	----	2.8
Bi	0.1	0.1	----	----	0.6
B	<10	10	----	----	20
Br	<1.0	<1.0	----	----	2.0
Cd	0.1	0.2	----	----	0.3
C%	0.43	0.44	----	----	0.05
Cs	2.0	7.0	----	----	10.0
Cr	23	22	----	----	14
Co	7	7	----	----	1
Cu	8	8	----	----	<1
Dy	2	2	----	----	18
Ga	13	12	----	----	22
Ge	5	5	----	----	5
Au ppb	<5	<5	----	----	<5
Hf	4	6	----	----	14
Pb	28	24	----	----	30
Li	11	7	----	----	12

* Oxides reported in percent and elements in ppm unless noted otherwise. Analytical methods
are in appendix. Fe_2O_3 represents total iron.

TABLE 13. MAJOR AND TRACE ELEMENT ANALYSES* OF LAVAS
FROM THE KANE SPRINGS WASH VOLCANIC CENTER
(Sample location in parenthesis)

	(7) Rhyolite Dome	(10a) Rhyolite Dome	(10b) Rhyolite Dome	(24a) Syenite Dome	(24b) Syenite Dome	(25) Syenite Dome	(32) Basalt	(21) Basalt
SiO_2	75.20	75.40	76.43	66.50	67.46	64.70	48.00	54.89
Al_2O_3	5.98	6.43	13.38	7.05	15.16	7.10	6.84	17.15
Fe_2O_3*	0.73	0.91	1.16	2.81	5.13	3.26	6.06	9.18
CaO	1.09	1.12	0.94	0.58	1.51	1.02	6.06	7.71
MgO	0.15	0.17	0.12	0.24	0.45	0.43	3.40	4.46
TiO_2	0.02	0.05	0.04	0.35	0.65	0.49	1.00	1.48
Mn	258	317	0.03%	764	0.13%	702	984	0.12%
Na_2O	2.86	3.11	4.29	3.57	5.05	3.19	2.07	3.09
K_2O	3.57	3.54	4.42	4.03	5.10	3.78	0.83	1.94
FeO	----	----	0.28	----	0.70	----	----	5.98
P	240	210	0.09%	740	0.29%	1080	1700	0.47%
La	18	24	----	70	----	68	27	----
Ce	33	33	----	141	----	133	55	----
Sm	7.5	3.9	----	13.1	----	12.6	6.8	----
Eu	<0.5	<0.5	----	2.0	----	2.3	1.8	----
Tb	2.5	4.1	----	1.0	----	1.6	0.8	----
Yb	7.3	19.9	----	5.1	----	3.0	1.4	----
Lu	0.9	1.8	----	1.0	----	0.7	0.6	----
Nd	16	20	----	46	----	39	17	----
Sc	1.8	2.1	----	5.7	----	7.7	24.7	----
Ta	4	7	----	2	----	2	<2	----
Th	28.0	43.0	----	11.0	----	10.0	2.0	----
U	7.0	8.6	----	3.3	----	2.9	1.0	
Hg ppb	20	40	----	40	----	70	40	
Mo	5	6	----	6	----	10	4	----
Ni	3	3	----	<1	----	1	84	----
Nb	51	78	----	44	----	36	16	----
Rb	120	200	----	56	----	47	10	----
Se	0.2	0.2	----	0.2	----	0.2	0.02	----
Ag	1.0	0.5	----	0.5	----	1.0	0.5	----
Sr	14	76	----	84	----	151	485	----
S%	.006	<.001	<.001	<.001	.047	<.001	.026	<.001
Te	<.05	<.05	----	<.05	----	<.05	0.20	----
Tl	0.6	1.7	----	0.2	----	0.2	0.1	----
Sn	1	3	----	1	----	1	1	----
W	4	7	----	4	----	5	2	----
V	<1	3	----	<1	----	26	176	----
Y	115	220	----	70	----	59	25	----
Zn	50	74	----	110	----	96	77	----
Zr	110	115	----	390	----	360	180	----
CO_2	----	----	0.39	----	<.01	----	----	0.07
$+H_2O$	----	----	0.08	----	0.24	----	----	0.26
$-H_2O$	----	----	0.22	----	0.30	----	----	0.19
F	260	2500	----	630	----	770	320	----
Sb	0.2	0.5	----	0.3	----	0.2	0.1	----
As	5	5	----	3	----	3	4	----
Ba	40	180	----	1290	----	1280	450	----
Be	7.7	12.0	----	2.7	----	2.4	1.2	----
Bi	0.1	0.1	----	0.1	----	0.1	0.1	----
B	40	30	----	60	----	10	10	----
Br	<1.0	<1.0	----	<1.0	----	<1.0	1.0	----
Cd	0.1	0.1	----	0.1	----	0.2	0.1	----
C%	0.4	0.31	----	0.06	----	0.06	0.51	----
Cs	4.0	9.0	----	9.0	----	6.0	<2.0	----
Cr	18	17	----	14	----	21	163	----
Co	<1	1	----	1	----	5	34	----
Cu	2	3	----	<1	----	4	26	----
Dy	9	18	----	9	----	7	6	----
Ga	21	22	----	18	----	17	10	----
Ge	5	5	----	5	----	5	5	----
Au ppb	<5	<5	----	<5	----	<5	<5	----
Hf	6	7	----	11	----	9	3	----
Pb	44	52	----	30	----	28	14	----
Li	60	97	----	13	----	12	5	----

* Oxides reported in percent and elements in ppm unless noted otherwise. Analytical methods are in appendix. Fe_2O_3 represents total iron.

TABLE 14. KANE SPRINGS WASH VOLCANIC CENTER
MAJOR ELEMENT ANALYSES*
(From Novak, 1984)

	Basalt	Trachy-andesite	Postcald. Trachyte	Syenite	Precald. Trachyte	Kane Wash Tuff-W	Kane Wash Tuff V2	Rhyolite Dome	Rhyolite Lava
SiO_2	50.5	53.1	59.3	59.8	67.3	72.6	73.1	74.8	76.1
Al_2O_3	15.6	15.8	15.9	15.9	14.2	12.2	11.1	12.9	12.3
Fe_2O_3	10.6	10.4	6.57	6.39	3.37	1.28	2.72	0.87	1.24
MgO	7.60	3.86	1.73	1.59	0.27	<.10	0.10	0.12	0.11
CaO	8.83	7.04	3.60	3.62	1.15	0.65	0.26	0.42	0.49
Na_2O	2.98	3.76	4.36	4.50	4.12	3.85	4.04	3.84	3.32
K_2O	1.35	2.31	4.49	4.71	5.66	4.80	4.29	4.60	5.14
TiO_2	1.89	1.83	1.23	1.20	0.39	0.04	0.15	<.02	0.10
P_2O_5	0.49	0.39	0.44	0.42	0.06	<.05	<.05	<.05	<.05
MnO	0.15	0.17	0.15	0.14	0.07	<.02	0.04	0.03	<.02
L.O.I.	0.12	1.49	1.30	0.96	2.42	3.44	2.75	3.44	0.29
Total	100.11	100.15	99.07	99.23	99.01	98.86	98.55	101.02	99.09
F					0.08	0.13	0.34	0.49	0.17
Cl					0.08	<.05	0.17	0.05	0.06

* All analyses by x-ray fluorescence, except F and Cl,
which were determined by wet chemical methods. Results in %.

unit supports grasses, predominately, with variable sagebrush. A summary and a comparison of units from the Kane Wash site are tabulated on Table 15.

KANE WASH TUFF. In the Kane Springs Wash study area the Kane Wash Tuff consists of 5 rhyolite ash flow cooling units: a lowermost compound fayalite bearing cooling unit designated the "O" member, which overlies the Hiko Formation; a much thicker (up to 190m) compound cooling member - "W" - with a distinctive white basal glass, which overlies the "O" member; then the "V1", "V2", and "V3" members as the section is ascended (Figure 19). Although earlier workers (Noble, 1968) felt the "O" and "W" members were erupted from the Kane Springs center, Novak (1984, 1985), after conducting more extensive mapping decided their source was a vent near the southern end of the Hiko Range. All 5 of these members are similar in composition (Tables 12 and 14); however, the older Kane Wash Tuff members, "O" and "W" tend to form a singular coherent remote sensing unit. They are less welded in general than the "V" members and weather to form moderate slopes rather than ledges. Each unit contains phenocrysts of sanidine-anorthoclase, olivine (fayalitic), and pyroxene with some quartz. Sodic amphibole occurs in the vapor phase mineral assemblage of the "V" members. Pumice fragments comprise generally about 5% of these outflow sheets. The "V"

SUMMARY OF MAJOR VOLCANIC UNITS OF THE
KANE SPRINGS WASH STUDY SITE

UNIT	LITHOLOGY	PETROCHEMISTRY MAJOR	MINOR*	FIELD CHARACTER	DESERT VARNISH DEVELOPMENT**	DOMINANT VEGETATION ASSOCIATION
Late Basalt	Massive to vesicular flows with microporphyritic laths of plagioclase	Olivine basalt	High Ni, P, Sc, Ti, V, Cr, Co, Cu. Low Rb, Th, U, Li.	Very dark gray massive mesa caps. Forms blocky scree.	Moderate to well developed. Very dark gray with occasional silvery sheer.	Pinyon pine and juniper on mesa tops with some sagebrush and grasses.
Rhyolite Domes	Massive flow-banded lava, phenocrysts of quartz, sanidine, fayalite and Na-rich amphibole, vapor phase topaz.	High silica peralkaline rhyolite	High Rb, Ta, HREE, Th, Sn, U, Y, Be, F, Li. Low Ba, P, Eu.	Dense, domal, knobs light buff to flesh colored. Irregular platy to blocky float.	Poorly developed. Pale orange to dark brown.	Mostly grasses, some sage and juniper.
Trachyandesite Lava	Vesicular flows with plagioclase phenocrysts in dark, holocrystalline matrix.	Andesite to low silica andesite.	High Ni, Sc, Zr, Ga. Slightly low U, Th, Pb.	Dark gray, forms low, sloping, hummocky terrain. Float is irregular and rough.	Sporadic moderately well developed, dark gray.	Grass and sagebrush with 5-10% moss green lichen.
Syenite Complex	Fine grained porphyry with anorthoclase, quartz, and clinopyroxene phenos. Flow domes, intrusives, and minor tuff.	Syenite and trachyte.	High Mo, Zn, Zr, B slightly high REE, As, Be, F, Hf, La. Low C, Eu, V, Ni.	Cream colored domal knobs and rugged hills, weathers to exfoliated slabs and rough boulders.	Tan to brown to reddish brown. Some silky opaline silica. Moderately well developed.	Grasses and sage with some juniper.
Kane Tuff V1-3 Members	Ash flow tuffs with pumice and crystals of fayalite, Na-rich amphibole, sanidine, anorthoclase.	Peralkaline comenditic rhyolite to trachyte	High REE, Hf, F, Rb, Zr, Th, U. Low Sc, Ba.	Densely welded to vapor phase altered, forms, ledges, steps, and slopes. Weathers to thick, blocky slabs.	Brown to gray brown, poorly to moderately well developed.	Grasses and sagebrush, some juniper 10% moss green lichen and vapor phase altered.
Kane Tuff O & W Members	Ash-flow tuffs with pumice and lithic clasts and crystals of fayalite.	Subalkaline rhyolite	Low Mn, Mg, Ti	Distinctive white glassy tuff separates O from W. Moderately welded, slope former. Ledges minor in project area.	Brown to gray brown moderately well developed.	Mostly grasses, some sage.
Hiko Tuff	Ash-flow tuff Granular, granitic crystal rich with	Subalkaline latite	Slightly high Sr, Ba Slightly low B	Coarse granularity results in "beehive" exfoliated mounds.	Poorly developed. Dull gray brown to brown.	Mostly grasses, some sage.

* Amounts (high or low) are relative to other units within the study site.
** Desert varnish is by nature highly discontinuous and irregular in these study sites.

TABLE 15. Summary of lithological, petrochemical, and field characteristics of volcanic units of the Kane Springs Wash study site.

members (Figure 22) vary from densely welded to strongly vapor phase altered. In places the less welded vapor phase altered zones are covered with dusty green lichen overgrowth (15-20% of the outcrop surface). The V1 member attains thicknesses of 120m and contains lithics with dimensions up to 5cm across. Lithic fragments in the V2 member, in contrast, are about 1cm long and typically less abundant. Both members are zoned from densely welded to vapor phase altered up section. V1 is mineralogically zoned with about 55% crystal content near its base to 25% up section. Member V2 exhibits a stronger peralkaline tendency and grades from crystal-poor, ash-rich comendite at the base to a more trachytic composition with 5% phenocrysts of sanidine and quartz toward the top. V2 and V3 are mesa formers west and southwest of the caldera. V3 member is a thin, densely welded comendite virtually identical to V2 lithologically. These outflow sheets are separated by air fall deposits and basal vitrophyre. Coatings are quite well developed and a mature dark chocolate brown on densely welded layers. Less mature surfaces are ashen gray brown. The Kane Wash Tuff Formation supports grasses, generally foxtail, and sagebrush. At higher elevations juniper is present. The "V" members are relatively highly evolved petrochemically. They contain anomalously high amounts of the rare earth elements, hafnium, fluorine, rubidium, zirconium, thorium,

and uranium and low amounts of scandium and barium. The "O" and "W" members report low manganese, magnesium, and titanium.

AIR FALL TUFF. White, coarse, pumice-rich to very fine lapilli tuff with rare pumice lithics occurs between some of the ash flow members of Kane Wash Tuff described above, particularly the "O" and "W" members. A thick pumice-rich white ash deposit also occurs within the caldera interfingering with the trachyandesite lavas. These rhyolitic pyroclastics are unwelded, nonresistant, vitric, white to cream colored, and quite conspicuous, especially where coarse. Fine grained ash tends to be buff with pale orangy brown tints. Thicknesses vary from about 5 to 25m. Coatings are very poorly developed and seem to be composed largely of transported dust and organic material. These units form moderate slopes and vegetative cover is relatively sparse, dominated by grasses.

CENTRAL SYENITE COMPLEX. Following caldera collapse, a roughly circular complex of extrusive to subvolcanic intrusive syenite and trachyte erupted in the central part of the caldera (Novak, 1984). The complex is texturally and compositionally diverse, but is dominated by fine-grained, cream-colored porphyry with about 20% anorthoclase with some clinopyroxene and up to 5% quartz. The unit

forms a cumulo-dome, approximately 5km across, that is resurgent into the caldera floor. It contains syenitic flow dome complexes which resemble younger topaz rhyolite flow domes spectrally. Coatings are tan to brown to reddish brown. Milky amorphous silica was noted in coatings on one of the flow domes but is likely hydrothermal in part. The complex underlies rugged topography (Figure 23) with steep knobs and drainage channels. Sagebrush is common with some grasses and evergreens in the northern more elevated portion of the study site. Analyses of syenite samples (Tables 12 and 13) report relatively high contents of molybdenum, zinc, zirconium, boron; slightly high rare earth elements, arsenic, barium, fluorine, hafnium, and lanthanum; and low scandium and barium.

TRACHYANDESITE LAVA. Dark gray, vesicular mafic trachyte forms elongate lava tongues about 100-150m thick in the western moat area (Figure 20). The unit was deposited after caldera collapse. It contains about 15% phenocrysts of sieved plagioclase with olivine and clinopyroxene. The groundmass is holocrystalline and similar in mineralogy. Coatings are distinctively gray to rusty brown, usually dull, but occasionally dark with a silvery sheen. Secondary mineral coatings are sporadic but fairly well developed. They are lighter in color than coatings on basalt, but typically darker than coatings on
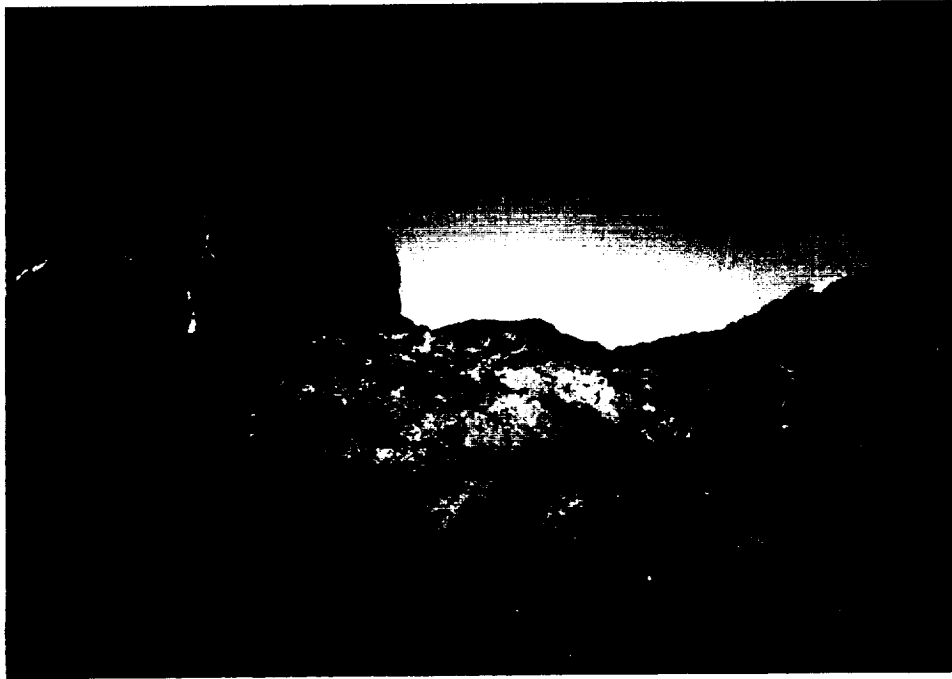
Figure 23. Kane Springs Wash study site. Photograph of syenite dome taken at northeastern side of study area, looking north.

Figure 24. Kane Springs Wash study site. Photograph of intracaldera area underlain by trachyandesite. Photo taken in west central part of study area, looking east.

the tuffs and rhyolites. Trachyandesite tends to host a relatively dense population of moss green to gray lichen similar to the lichen overgrowth on mafic trachyte of Black Mountain. It occupies elongate topographic lows within the moat area and weathers to irregular rugged boulders and smaller float, strewn over a hummocky surface. (Figure 24). Foxtail grasses dominate the vegetative canopy. Trachyandesite is relatively low in uranium, thorium, and lead and high in nickel, scandium, zirconium, and gallium (Appendix H).

RHYOLITE DOMES. Flow-layered rhyolite flow domes occur in the western caldera moat (Figure 20). These deposits are annular and appear exogenous over trachyandesite or intracaldera pyroclastics where they occur within the study site. They are pale flesh in color, quite dense, and form prominent knolls which likely represent paleovents. Grasses are the dominant growth, juniper occurs on north slopes. Flow layering near dome centers is subvertical. The white, pumice-rich pyroclastics which fill the western moat probably erupted just prior to emplacement of these high silica rhyolites. Rhyolite domes contain phenocrysts of quartz, sanidine, plagioclase, fayalite, sodic amphibole, and Fe-Ti oxides. Vapor phase topaz crystals up to 2mm long have been observed within a central lithophysal core (Novak, 1984). These deposits are relatively high in

the heavy rare earth elements, tantalum, tin, uranium, beryllium, lithium, fluorine, rubidium, thorium, and yttrium (Tables 13 and 14 and Appendix H). Novak (1985) reports large negative europium anomalies (Eu/Eu*=0.0020) in topaz rhyolite from Kane Springs Wash. Coatings on the rhyolite domes are chiefly pale orangy brown to moderately dark brown.

LATE BASALT. Late olivine basalt flows occur mainly as mesa caps within the westernmost area and around apparent late vents along the eastern border of the study site. Analytical data is presented in Tables 13 and 14 and Appendix H. Basalt overlies the white intracaldera pyroclastic deposit. Basalt is very dark gray and quite conspicuous in outcrop and talus scree. It is massive to vesicular. Coatings are gray to very dark with a silvery sheen. In thin section (Figure 25) the unit is characterized by thin laths to stubby broken crystals of plagioclase in a trachytic texture with pyroxene and amphibole in a microcrystaline groundmass. The unit typically supports juniper and pinyon (15-20%) and grasses, with minor sagebrush. Typical of basalt, nickel, phosphorous, scandium, titanium, vanadium, chromium, copper, and cobalt are relatively enriched and rubidium, thorium, uranium, and lithium are low (Table 13 and Appendix H).

Figure 25. Photomicrograph of Late Basalt of Kane Springs Wash. Crossed nichols at 10x. Note dark brown to yellowish desert varnish impregnating the rock surface, intergranularly.

CHAPTER IV

IMAGERY ANALYSIS

Landsat 5 thematic mapper bands in the visible and near infrared - bands 1, 2, 3, 4, 5, and 7 - were applied to this study. The thematic mapper instrument is the most advanced orbital visible/near-infrared sensor available, and it was felt that the near-infrared bands could help provide superior discrimination in terms of secondary alteration products. Moreover, previous investigations have shown that spectral variation among lithologic cover within typical low vegetation scenes is greatest in band 5, driven primarily by divalent iron variation. The earlier multi-spectral scanner (MSS) does not offer a similar band interval. The superior spatial resolution of TM over MSS was another consideration for applying TM.

Imagery analysis was conducted a-priori prior to field work and prior to any significant knowledge of surface geology. Imagery units were outlined in the first phase of the study program. Correlation with lithologic units followed field studies (Spatz, Taranik, and Hsu, 1987a). It turned out that imagery units correlated extremely well with lithologic units (greater than 90% for PC images), both with regard to outcrop and in some cases with regard to monolithologic detritus.

IMAGE STATISTICS

A multivariate statistical evaluation of pixel values for each scene was conducted with IDIMS function ISOCLS (Appendix I). Mean and standard deviations for each band and covariance matrices between bands were computed. Correlation coefficients between bands were derived by dividing covariance by the product of standard deviations of respective bands. Correlation coefficients provide a measure of the amount of spectral variance between bands. Bands with lowest correlation coefficients are the least correlated and contain greater spectral diversity. By selecting bands with least apparent spectral similarity, spectral contrast on image composites should be enhanced. The principal components (PC) transformation (Appendix C) takes variance and covariance to compute eigenvectors which are new data axes projected through multi-dimensional band data sets in progressively shorter axes. Each eigenvector is represented by a corresponding eigenvalue. Eigenvalues are a measure of the amount of variance contained in each PC. The tables in Appendix I show the relative contributions of each band to each PC and thus those bands most responsible for spectral variance in each PC. In general PC1 is dominated by reflectance variation due to topography. PC2 contains more subtle spectral variation of surface cover, in this case rock/soil dominated variance,

whereas PC3 variance is dominated largely by remaining spectral variance, in this case, vegetation. These relationships are supported by the fact that PC3 images tend to appear almost identical to 4/3 ratio images which highlight vegetation.

In this section imagery characteristics of each major volcanic unit at each of the 3 study sites are discussed with a view toward establishing effective imagery correlation and image combinations for lithologic discrimination and mapping. In all color composites, the encoded color sequence is red-green-blue (RGB). Our studies indicate vegetation (only 25-30% of surface cover) is subordinate as a significant spectral control in the images at Stonewall.

Imagery training sites were selected and class statistics computed with IDIMS function CLASFY (Appendix J) for each major lithologic unit. One set of training sites was used for the supervised classification computations which follow, another for representative band reflectance values (digital numbers or DN values) in each band for each unit. Band statistics for each unit are compiled in Table 16. Atmospheric corrections were not performed, since histogram and deep shadow methods of determining scatter indicated Raleigh scatter was significant only in band 1, and where used as a single band, band 1 is always stretched. Moreover, lithologic discrimination and other

Table 16   RAW LANDSAT DN VALUES OVER THE MAJOR LITHOLOGIC UNITS*

STONEWALL MOUNTAIN AREA

UNITS	TM BANDS						BAND RATIOS			
	1	2	3	4	5	7	3/2	5/2	5/4	5/7
Civet Cat Cap	137	66	96	86	202	125	1.45	3.06	2.35	1.62
Civet Cat Canyon	135	62	85	70	106	66	1.37	1.71	1.51	1.61
Spearhead Tuff	156	74	103	85	154	99	1.39	2.08	1.81	1.56
Basalt Flow	115	49	63	49	78	44	1.29	1.59	1.59	1.77
Antelope Springs										
Upper Rhyolite	182	98	150	128	237	148	1.53	2.42	1.85	1.60
Lower Latite	159	76	111	92	125	72	1.46	1.64	1.36	1.74
Quartzite Conglom.	134	62	91	76	114	70	1.47	1.83	1.50	1.63

THE BLACK MOUNTAIN CALDERA

UNITS	TM BANDS						BAND RATIOS			
	1	2	3	4	5	7	3/2	5/2	5/4	5/7
Labyrinth Canyon	133	64	98	93	188	113	1.53	2.94	2.02	1.66
Gold Flat Tuff	141	68	97	85	183	119	1.43	2.69	2.15	1.54
Trachyte, Hidden Clf.	124	58	84	77	155	89	1.45	2.67	2.01	1.74
Lava, Pillar Springs	108	49	64	62	110	62	1.31	2.24	1.77	1.77
Trail Ridge Tuff	122	55	75	63	112	69	1.36	2.04	1.78	1.62
Older Thirsty Canyon	137	64	92	80	159	99	1.44	2.48	1.99	1.61
Lavas, Ribbon Cliff	130	60	84	70	120	72	1.40	2.00	1.71	1.67
Lavas, Yellow Cliff	123	58	86	81	146	84	1.48	2.52	1.80	1.74
Pre-Thirsty Canyon										
Volcanics	144	70	101	90	173	104	1.44	2.47	1.92	1.66

THE KANE SPRINGS WASH VOLCANIC CENTER

UNITS	TM BANDS						BAND RATIOS			
	1	2	3	4	5	7	3/2	5/2	5/4	5/7
Topaz Rhyolite	151	76	111	96	180	108	1.46	2.37	1.88	1.67
Basalt	102	46	56	63	86	47	1.22	1.87	1.37	1.83
Trachyandesite	110	47	63	56	92	50	1.34	1.96	1.64	1.84
Hiko Tuff	144	71	104	90	172	100	1.47	2.42	1.91	1.72
Kane Tuff (V)	136	67	101	87	180	109	1.51	2.69	2.07	1.65
Syenite Complex	126	60	85	86	145	82	1.42	2.42	1.69	1.77
Kane Tuff (O-W)	134	62	88	75	125	75	1.42	2.02	1.67	1.67

*Pixel statistics for each unit are compiled in the Appendix

cover imagery signatures are quite good using the product digital values provided on the computer compatible tapes (CCTs).

STONEWALL MOUNTAIN AREA

Imagery over the Stonewall Mountain area is superior in quality for geologic remote sensing applications (Figures 26-29 and Plate 4), because vegetation and topography are subdued and outcrop/detritus/soil reasonably ubiquitous. Imagery from the Stonewall study site reflects a major normal fault in the eastern half, marked by a conspicuous curvilinear, that is thought to be the western margin of the Mount Helen caldera. Table 17 summarizes and compares imagery characteristics of Stonewall Mountain units.

CIVET CAT CANYON TUFF

Reflectance over Civet Cat is low in all bands over the main Civet Cat Canyon flow since Civet Cat Canyon Tuff is a relatively low albedo rock due to dark iron oxide matrix; however, over the spectrally distinctive Civet Cat Canyon cap rock, reflectance is relatively low in bands 1, 2, and 3 and high in bands 4, 5, and 7, increasingly so in the later 3 relative to other cover in the scene (Tables 16 and 17). These spectral relationships cause the cap rock zone

R45E | R46E

A

B

C

D

Qal Tad Tss Tar Tb Oe Tsc Tqc Ta Tad

Int scan 9 + 1

Backfile
11/1/17

Base: Landsat 5 TM Images

Tss

Tsc

Tsc

BM

1 Mile

1.61 Kilometer
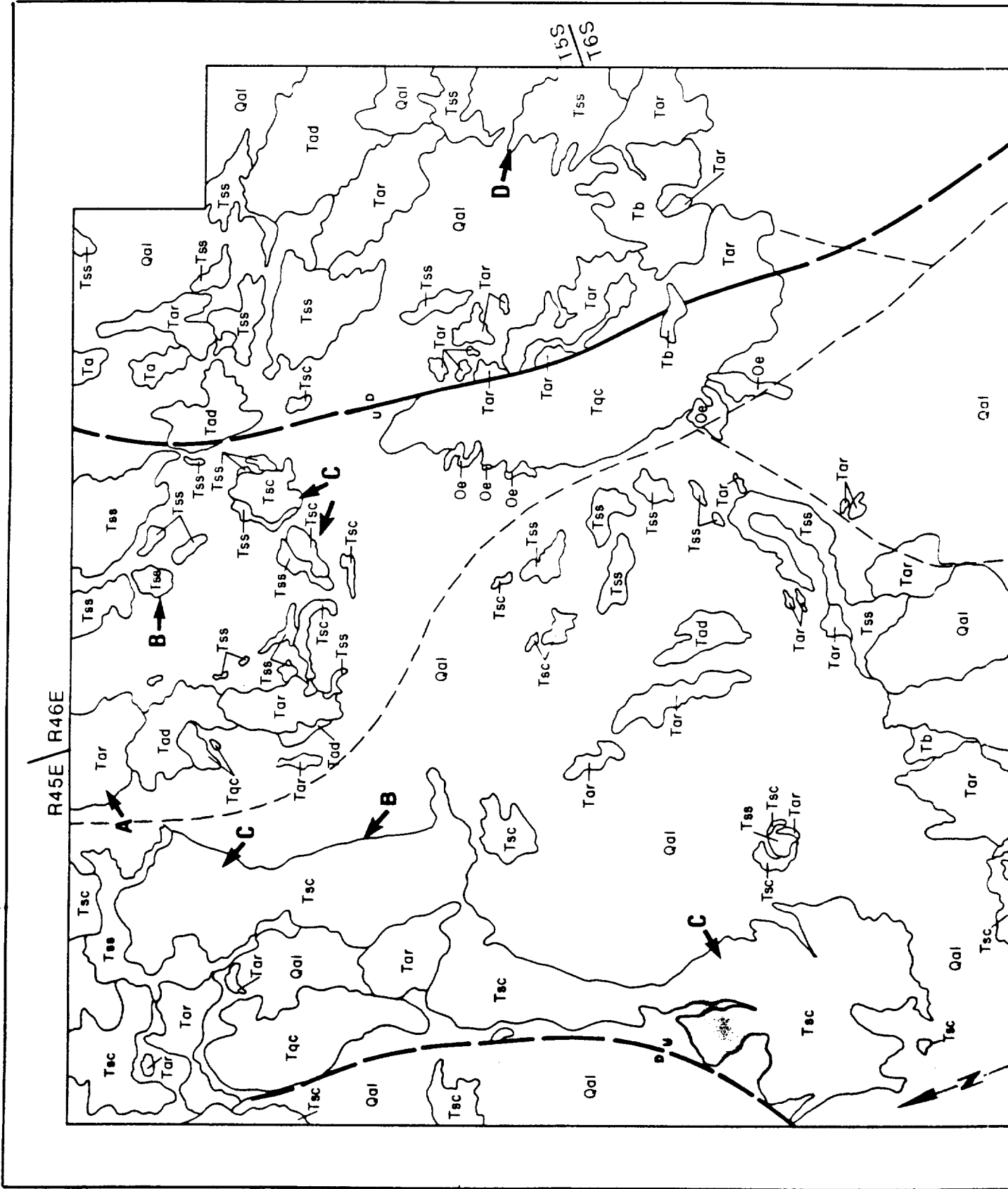
GEOLOGIC EXPLANATION

Qal Recent alluvial gravels. Includes some older Tertiary gravels.

Tb Basalt

Ts Stonewall Flat Tuff

Tsc Civet Cat Canyon Member

Tss Spearhead Member

Ta Antelope Springs Formation

Tar Upper white rhyolite (includes some Paintbrush Formation and older Mount Helen deposits)

Tad Lower red latite

Tqc Quartzite conglomerate

Oe Ordovician Eureka quartzite

UPPER MIOCENE

u/D

Lithologic contact, approximate, based on TM imagery

Dirt road

BM Bench mark

SPECIAL FEATURES HIGHLIGHTED BY ENHANCED IMAGERY

A Hydrothermal alteration

B Glassy base of ash flow tuff

C Glassy zone capping Civet Cat Canyon Tuff

D Densely welded lower Spearhead

Probable caldera margin fault showing relative displacement, dashed where uncertain

Geology by D. Spatz with reference to Ekren, et al, 1971, Noble, et al, 1984, and Frizzell and Hausback, 1986

PLATE 4 LITHOLOGIC MAP OF THE STONEWALL MOUNTAIN PROJECT SITE

Interpreted from Landsat TM imagery, supported by field study

Figure 26. Stonewall Mountain area. Landsat 5 TM 512x512 pixel band 2 image, contrast enhanced by scaling. Desert varnish is absorbant and dark in the lower TM wavelength range, so darker tones on the image tend to correspond with either more mafic rock assemblages or rocks with relatively well developed desert varnish.

Figure 27. Stonewall Mountain area. Landsat 5 TM 512x512 pixel subscene. Principal components (PC) image, with PC2, PC3, and PC4 color encoded red, green, blue, respectively. Variance in PC2 is lithologically dominated in this scene. Note striking peach color of glassy cap rock of Civet Cat Canyon Tuff, easily discriminated on the composite.

Figure 28. Stonewall Mountain area. Landsat 5 3/1 - 5/7 - PC2 image encoded red, green, blue, respectively. Subscene is 512x512 pixels. Each band was contrast enhanced with the SCALE function. Antelope Springs rhyolite, typically somewhat altered hydrothermally (argillic, pyritic, hematitic, limonitic), is distinctively yellow due to high DN values in both 3/1 and 5/7. Stonewall Flat Tuff, the outflow sheet from Stonewall Mountain, is purplish, its contacts fairly sharp in this composite.
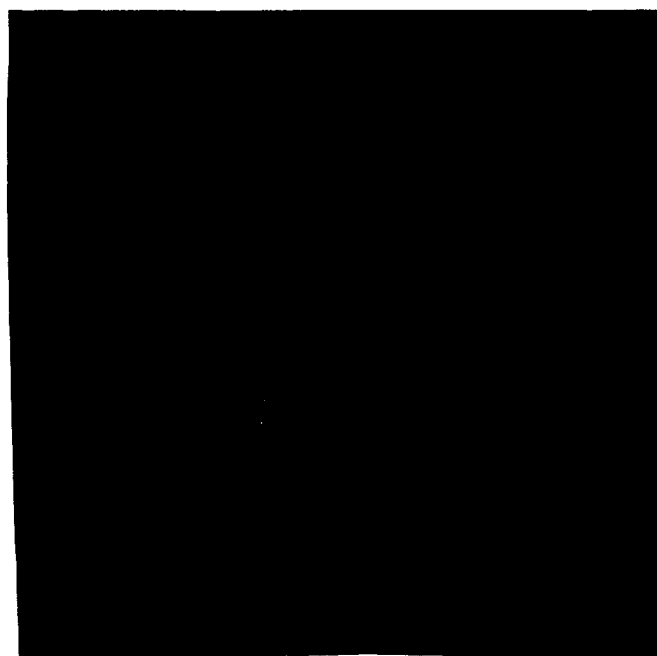
Figure 29. Stonewall Mountain area. Landsat 5 TM 512x512 pixel image. False color composite of bands 3, 5, and 7, each contrast enhanced with IDIMS function SCALE.

SUMMARY OF VOLCANIC UNITS OF THE STONEWALL STUDY SITE
WITH TM IMAGERY CHARACTERISTICS

UNIT	LITHOLOGY	PETROCHEMISTRY MAJOR	PETROCHEMISTRY MINOR*	FIELD CHARACTER	DESERT VARNISH DEVELOPMENT**	DOMINATE VEGETATION ASSOCIATION	TM IMAGERY RELATIONSHIPS*** BRIGHT	INDISTINCT	DARK
Civet Cat Canyon Tuff Cap Rock	Vitrophyre with sanidine/anorthoclase and biotite phenocrysts	Rhyolite peralkaline	Slightly high F, Low Sr, Cr, Cu Ni, Mg	Dark gray-brown and rouge-red, densely welded glass. Forms mesa caps. Thin-platted floats.	Sparse, poorly developed.	Sagebrush, grasses.	Bs 4,5,7, 5/2 5/4, PCs 2,3,5 ISM-(3-5-7)S,M ISM-(1-2-4)S	PC 4	Bs 1,2,3, 3/2 5/7, PC 1 ISM-(3-5-7)1 ISM(1-2-4)1,M
Civet Cat Canyon Tuff	Crystal ash-flow with sanidine/anortho-clase and biotite phenocrysts.	Rhyolite slightly peralkaline	Slightly high Th, Be, REE, slightly low Sr, V, Mg	Very dark red-brown very densely welded, ledge former. Thin-platted float.	Moderate to well developed, dark chocolate brown.	Sagebrush, grasses, some juniper.	PCs 2,4 ISM-(1-2-4)S,M	5/2,5/4,5/7 PC 3,5 ISM(3-5-7)S	Bs 1,2,3,4,5,7 3/2, PC1 ISM(3-5-7)1,M ISM(1-2-4)1
Spearhead Tuff	Pumice rich ash-flow with sanidine/anortho-clase phenocrysts.	Rhyolite slightly peralkaline	High REE, Zn, Zr, Be, Ce, Low Sr, Mg, Ba, Co, Ni, V	Pale buff to buff gray, moderately welded, ledge former. Thick rough, slabby float.	Highly variable, well to poorly developed, brown to gray buff.	Sagebrush, grasses.	3/2, PCs 2,3,4 ISM(3-5-7) M	Bs 3,4,5,7 5/2,5/7,PC 5 ISM(3-5-7)S ISM(1-2-4)S	Bs 1,2, PC 1 ISM(3-5-7)1 ISM(1-2-4)1,M
Basalt Flows	Dense flow, minor vesiculation, microporphyritic olivine and plagio-clase.	Low silica basalt	High P, Sc, V, low U, Th	Very dark gray very dense, massive mesa cap in pieces.	Moderate to well developed, very dark gray with silvery sheen.	Grass, some sagebrush.		3/2,5/2,5/4, 5/7 PCs 2,3,4,5 ISM(1-2-4)S,M S,M	Bs 1,2,3,4,5,7 PC 1 ISM(3-5-7) I, S,M ISM(1-2-4) I
Antelope Springs Rhyolite	Dense quartz porphyry intrusives, flows and welded ash-flows(?) underlain by friable tuff. Commonly hydro-thermally altered.	Rhyolite, slightly alkaline	Slightly high Mg, Tl, Th	Very light cream-colored. Forms steep slopes, cliffs and knobs. Joint-bound blocky float.	Moderate to poorly developed. Brown to orangy brown.	Grasses, some sagebrush, abundant orange lichen.	Bs 1,2,3,4,5,7 3/2,5/2,5/4,5/7 PC 1 ISM(3-5-7) I,S ISM)1-2-4) I	PCs 3,4,5 ISM(3-5-7) H	PC 2 ISM(1-2-4)S,M
Antelope Springs Latite	Massive crystal rich flows and subvolcanic intrusive bodies with albitic plagioclase phenocrysts and frayed biotite.	Latite High silica, potassic latite to subalkaline rhyolite.	Slightly high Ca, Ba	Reddish brown color. Form low, humocky hills. Weathers to friable cobble-size float.	Poorly developed, brown to reddish brown.	Grasses, sage-brush.	3/2, PCs 1, 3 ISM(1-2-4) M	5/2, 5/7 PCs 4, 5 ISM(1-2-4) I	Bs 1,2,3,4,5,7 5/4, PC 2 ISM(3-5-7) I, S, M ISM(1-2-4) S

* Amounts (high or low) are relative to other units in the study site.
** Desert varnish is by nature, highly discontinuous and irregular in these study sites.
*** ISM - Intensity, Saturation, and Hue (I,S,H,) on bands 3, 5, and 7.

Table 17. Summary of lithological, petrochemical, and field characteristics of volcanic units from the Stonewall Mountain study site.

to be subdued in 3/2 and 5/7 ratio images, but strikingly bright in the 5/2 image. High scene reflectance in band 7 creates high contrast turquoise blue over the unit in 3-5-7 images. The unit registers a dull, indistinct pale grayish green in the 3/1-5/4-4 image. There is a low intensity but high saturation and hue response for the cap rock in ISH computations with bands 3-5-7, resulting in a distinctive moss green hue in the composite ISH image. On ISH images with bands 1-2-4 the unit shows low values in intensity and hue, high values in saturation, but low contrast in all three modes. Red Civet Cat cap rock is strikingly bright in PC2 images, growing somewhat less so in PC's 3 and 4. This results in an impressive discriminating capacity over the unit in the PC2-PC3-PC4 and PC2-PC4-PC5 images. The unit is also rather anomalous on some of the more exotic composites, including especially the 1-4-Hue image, Hue computed on bands 3-5-7; the 3/1-5/7-PC2 images, and a 3-7-Hue (bands 1-2-4) composite. A 3/1-PC2-Hue (bands 3-5-7) is especially effective in highlighting the Stonewall Flat Tuff in general.

SPEARHEAD TUFF

The Spearhead Tuff exhibits little spectral variation throughout the visible and near-infrared (Table 16). It is relatively dark in all TM bands, particularly bands 1, 2, and 3, in contrast to surrounding alluvium and Antelope

Springs rhyolite which is a leucocratic high albedo unit. A darker trend tends to increase the tonal contrast somewhat in 5/7 images. Intensity increases slightly in 5/2 images. These band relationships, of course, control color characteristics in false color composite images. So in 3/1-5/7-4 images, encoded RGB, the unit is magenta indicating higher reflectance in the 3/1 and 4 images with relatively low reflectance in 5/7, and bluish gray in the 3/5/7 image due to higher reflectance in bands 3 and 7. In individual principle component images, the Spearhead Tuff is brightest in PC3 with high brightness also in PC2 and PC4. Thus in the 3/1-5/7-PC2 composite the formation is a distinctive dark purple. ISH computations on bands 3-5-7 result in indistinct low contrast tones over the unit in the saturation and hue modes, darker though in the intensity image. This results in a distinctive dull army green hue in the ISH composite. Indeed, basalt exposures, shadows, and the ash flow units with their dark desert varnish coatings tend to register high DN values in the saturation mode. Relationships are similar on ISH images of bands 1-2-4, thus a hue composite of bands 1-2-4 with scaled bands 3 and 7 results in distinctive bluish hues over the unit, green if intensity is used instead of hue in the same configuration. Imagery characteristics of Spearhead Tuff are summarized in Table 17 and compared with the other units at the Stonewall Mountain site.

ANTELOPE SPRINGS FORMATION

The Antelope Springs Formation in the study site consists of a lower reddish, ferruginous latitic member and a more felsic highly reflectant upper white rhyolite. Some of the formation appears intrusive and hydrothermal alteration consisting of hydrous secondary minerals occurs in places. The lower unit is relatively dark in all bands, because of relatively low albedo in comparison to adjacent white rhyolite (Table 16). The latite is more melanocratic due to higher relative mafic mineral constituents and also because of a lacy network of blood red ferruginous matrix. Antelope Springs latite is distinctive in many of the false color composites. The upper member exhibits high reflectivity in all bands with diminishing intensity in longer wavelength bands 5 and 7. Band ratios for the high albedo upper member tend to dampen intensities relative to other cover and enhance differences in iron oxide coatings and clay altered surfaces in certain locations. For example, several exposures are quite bright in 5/7 ratio images. The unit contrasts markedly with other formations in most color composite images. On 3-5-7 and 3/1-5/7-4 images the upper unit is cream colored with iron oxide stained areas light reddish. The lower latitic member in this rendition is red brown. On the ISH computations, bands 3-5-7, the upper unit is bright in saturation and intensity, light to medium gray in hue. In 1-2-4 ISH images the deposit is quite dark in hue and saturation,

light in the intensity mode. These felsic rocks respond with bright intensity in PC1 for the upper member, dark for the lower. The upper unit is dark and indistinct in PC2, and with only slight variation in higher PC's. Thus PC1 overpowers other bands in composites in which it is included, and PC composites without PC1 tend to obscure the upper member. In the 3/1-5/7-PC2 image the light colored upper unit is bright yellow to reddish and quite conspicuous. Perhaps the greatest overall contrast over the unit is exhibited by the 3-7-Hue (bands 1-2-4) image in which it is highlighted in bright yellow and the 3-5-7 ISH composite in which it is bright red.

LATE BASALT

Basalt, a low albedo lithology, is dark in all bands, decreasing slightly in brightness in longer wavelength bands 5 and 7 relative to adjacent cover (Table 16), due in part to the greater depth of penetration of the lower energy radiation and greater contribution of lithology, which is heavily absorbing to TM band 5 radiation as a result of divalent iron content. Higher energy radiation is more responsive to secondary mineral coatings. Basalt is thus medium gray and obscure in the 5/7 image and not appreciably changed by 3/2 and 5/2 ratios. On the 3/1-5/7-4 composite basalt is swamp green and well highlighted. It is dark brown on the 3-5-7 composite. In individual band modes of the 3-5-7 ISH transformation, the unit is dark.

In 1-2-4 ISH, saturation and hue images it is very bright. Thus on the 3-7-Hue (Hue on bands 1-2-4) composite basalt is purple and on the 3-5-7 ISH composite, greenish. It is very dark in PC1, obscure and indistinguishable in PC2, slightly brighter in PC's 3 and 4. It is highlighted, therefore, by blue in the PC1 PC2 PC4 composite, but cannot be discriminated on the PC2 PC4 PC5 image. On the 3/1-5/7-PC2 images the unit is dark green. Imagery characteristics of basalt are compared with imagery characteristics of other units at Stonewall Mountain in Table 17.

BLACK MOUNTAIN CALDERA

Imagery over the Black Mountain study area (Figures 30-33 and Plate 5) differs from that of the Stonewall area partly as a result of more diverse vegetative cover. Caldera structure is evident from the geometry of some narrow arcuate ash flow exposures that circumscribe the mountain, prominent arcuate scarps, and curvilinear topography. Lithologies are varied. Still the outflow sheets tend to be readily mappable with Landsat TM imagery. Vegetation over each unit was described in Chapter III. The 4/3 ratio image highlights zones with relatively heavy growth. This image is matched very closely by the PC3 image which also presents vegetation in strikingly bright contrast. Table 18 compares imagery of Black Mountain

T7S
T8S

R47E | R48E

Tu
Tu
Tu
Tss
Ty
x Black Mountain
Tgf
Tgf
Trc
Trc
Tfr
Tgf
Tgf
Tgf
Tgf
Tgf
Th
Th
Tss
Tss
Tss
Tss
Tu
Tgf
Tgf
Tgf
Tgf
Tfr
Tgf
Tu
Tfr
Tgf
Tgf
Tu
Tu
Tgf
To
Tfr
Tgf
Tfr
Tgf
Tgf
Tu
Tgf
Tgf
Tgf
Tgf
To
Tu
Tgf
Tgf
Tgf
Tu
Tu
Tgf
To

Base: Landsat 5 TM Imagery

Tgf
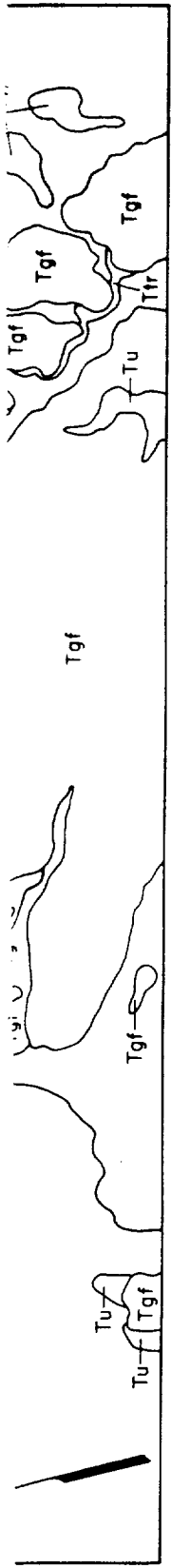
BLACK MOUNTAIN CALDERA ASH
SHEET COMPRISING THE THIRSTY
CANYON TUFF FORMATION

EXPLANATION

1 Mile
1.61 Kilometer

Tss	Spearhead Tuff (formerly Labyrinth Canyon)
Th	Trachyte of Hidden Cliff
Tgf	Gold Flat Tuff
Ty	Lavas of Yellow Cleft
Tu	Undifferentiated tuffs and lavas (pre-Gold Flat) of the Black Mountain Eruption. Includes recent alluvial-colluvial deposits. Mostly lavas of Pillar Springs.
Tfr	Trail Ridge Tuff
Trc	Lavas of Ribbon Cliff
To	Pre-Black Mountain rocks, mostly lavas and tuffs

Caldera rim fault, probable

Lithologic contact, approximate based on TM imagery

Dirt road

UPPER MIOCENE

PLATE 5

LITHOLOGIC MAP OF THE BLACK MOUNTAIN CALDERA

Interpreted from Landsat 5 TM Imagery units and field observations and based on geology by Noble and Christiansen, 1974
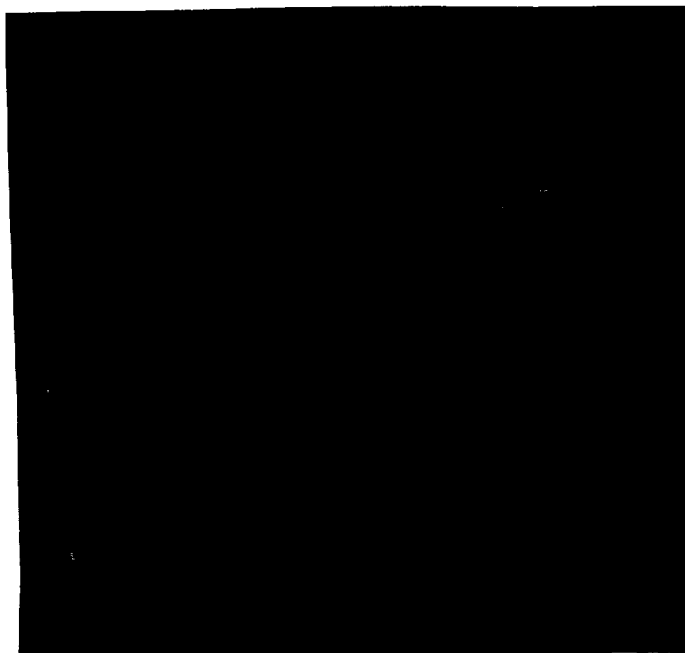
Figure 30. Black Mountain caldera. Landsat 5 TM 512x512
subscene. Band ratio 5/7 image, contrast enhanced by
function SCALE. The steep spectral slope, between about
1.5 and 2.2 micrometers, exhibited by Gold Flat Tuff
(Chapter VII) leads to low 5/7 values and quite dark tonal
contrast on this image.

Figure 31. Black Mountain caldera. Landsat 5 TM 512x512
pixel image. Composite of bands 3, 5, and 7, edge enhanced
and color encoded red, green, and blue, respectively. Note
distinctive powder blue hue over Gold Flat Tuff due to its
relatively high reflectance in band 7.
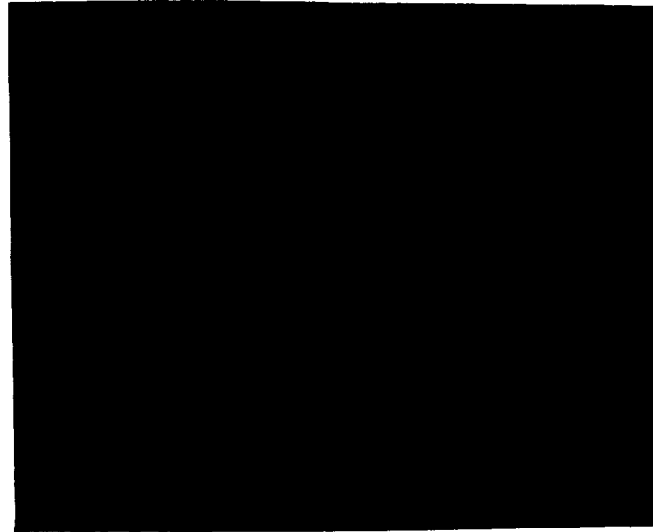
Figure 32. Black Mountain caldera. Landsat 5 TM 512x512 pixel subscene. Principal components image, PC1, PC2, and PC3 color encoded red, green, and blue, respectively and contrast enhanced by scaling. Linear, northwest trending Gold Flat Tuff southwest of Black Mountain is bluish due to vegetative contribution in PC3 (band 4 dominated, Appendix I). Crystal rich lavas and Trail Ridge Tuff are green, Trail Ridge tending to be slightly darker. Trachyte of Hidden Cliff on Black Mountain is purplish.

Figure 33. Black Mountain caldera. Landsat 5 TM 512x512 pixel subscene. Color composite image of bands 1 and 4 colored red and green, respectively with the hue band of an ISH transformation on bands 3, 5, and 7, colored blue. Each band is contrast enhanced by IDIMS function SCALE. Color contrast correlated well with lithologic contacts.

units with other characteristics and Table 16 lists raw DN values for each band by lithologic unit.

OLDER LAVAS AND TUFFS

The older felsic lavas and tuffs are the most reflectant cover in lower wavelength bands, 1-4 (Table 16). They are intermediate in reflectance at higher wavelengths. This is probably due to their relatively silicic tendency and lack of desert varnish. At lower wavelengths this unit is more reflectant than adjacent rock/detritus cover (Table 18) due to absence of varnish and at higher wavelengths it is less distinct since the lower energy radiation penetrates the varnish cover on adjacent felsic units which tend to support considerable desert varnish (Chapter VII). In the ratioed images the unit tends to be dull, intermediate in intensity and indistinct. Some areas over the unit, however, exhibit a brighter signature in the 3/2 image probably due to iron oxide staining observed in the field. Alluvial material and drainages down slope of these areas are also bright. The deposit is a distinctive rusty cream color on the 3-5-7 composite. It is bright on both the PC1 and PC2 images and therefore exhibits a yellow signature on composites combining PC's 1 and 2, or a reddish color if only one of them is in combination with other variables and encoded red. In the 5-7-PC2 composite the unit is a pastel purple due to high DN values in 5 and

SUMMARY OF VOLCANIC UNITS OF THE BLACK MOUNTAIN
CALDERA STUDY SITE WITH TM IMAGERY CHARACTERISTICS

UNIT	LITHOLOGY	PETROCHEMISTRY MAJOR	PETROCHEMISTRY MINOR[*]	FIELD CHARACTER	DESERT VARNISH DEVELOPMENT[**]	DOMINATE VEGETATION ASSOCIATION	TM IMAGERY RELATIONSHIPS[***] BRIGHT	INDISTINCT	DARK
Labyrinth Canyon Tuff (Spearhead)	Fine ash-flow tuff with pebble size pumice and alkali feldspar.	Peralkaline rhyolite	High Hf, Mg, Rb, Ti, B. Low Sr, Ba	Tan in color, densely to moderately welded thin, platy ledge former.	Poor to moderate development. Pale orangy buff to dull gray brown.	Sagebrush, grasses and some low juniper.	Bs 4,5,7, 3/2 5/2, 5/4, PC1 ISH-S,H	Bs 1,2,3,5/7 PC 5 ISH-I	PCs 2,3,4
Trachyte of Hidden Cliff	Variably vesicular, lava flow with minor plagioclase and olivine phenos	Mafic trachyte	High P, Sc, Sr, Mn Ti, V, Ba, Eu, Co, Mg. Low Rb, B	Dark gray, rough, hummocky boulders confined largely to Black Mountain.	Distinctively gray light to medium. Moderately well developed.	Sagebrush, atriplex, rabbit brush, some low juniper grasses 10% moss green lichen.	5/7, PCs 2,3	Bs 4,5,3/2, 5/2, PC 5 ISH-S	Bs 1,2,3,7 PCs 1,4 ISH-I,H
Gold Flat Tuff	Eutaxitic ash flow with pumice and pheno-crysts of anorthoclase Na-rich pyroxene and amphibole and feyalite.	Peralkaline pantellerite	High REE, Be, Pb, Sn, Th, Nb, Rb, Te, U, Zr, Sn, As, B, Ca, C, Cu, F, Li	Pale olive gray moderately welded, forms blocky slabs in float. Tops masses.	Gray brown to dark grayish chocolate, moderately well developed.	Sagebrush, grasses, some juniper and pinyon.	Bs 4,5,7 3/2,5/2,5/4 PC 1 ISH-S,H	Bs 1,2,3 PCs 4,5 ISH-I	5/7, PCs 2,3
Lavas of Pillar Spring	Coarse granitic lava flow with alkali feldspar and minor quartz and biotite.	Slightly subalkaline rhyolite to trachyte	Slightly high MREE, Th, Sn, Zn, Zr, Be, F, Hf	Dull gray brown rounded "beehive" outcrops of exfoliated flow layered granular lava. Forms low hills of rugged "fortresses".	Dull gray, gray brown and reddish brown, moderately to poorly developed.	Mostly grasses with sagebrush and atriplex.	3/2, PCs 2, 4	5/2, 5/7 PCs 3, 5 ISH-I	Bs 1,2,3,4,5,7 ISH-S,H
Trail Ridge Tuff	Ash flow tuff with pumice fragments and alkali feldspar phenocrysts.	Slightly peralkaline to subalkaline rhyolite to latite.	Slightly high Sc, Eu, Mn	Dark chocolate brown poorly to moderately welded thin bedded. Forms shallow ledges on slopes.	Dark brown to gray brown, moderately well developed.	Sagebrush, atriplex, grasses	PCs 2, 4	B 1, 3/2,5/2 PCs 3, 5 ISH-I	Bs 2,3,4,5,7 5/4, 5/7 PC 1 ISH-S,H
Rocks of Yellow Cleft	Dense flows and breccias with quartz and alkali feldspar phenocrysts.	Latite to high silica rhyolite.	Silicic variety. High Sm, Cr. Low Sc, Ti, Ti, Zr, Sb, Co, F, Hf	Dense, light colored cream, angular, blocky jointed outcrops in arcuate basin (moat).	Poorly developed, very discontinuous, yellowish to orangy.	Mostly grasses some sagebrush.	3/2, 5/7 ISH-I	Bs1,2,3,4,5,7 5/2, 5/4 PCs 3, 4, 5 ISH-H	Bs 1,2,3,4,5,7 PC 1 ISH-S
Older Lavas and Tuffs	Granular, granitic, crystal rich lavas and tuffs with quartz and alkali feldspar phenocrysts, some hydrothermal alteration.	Subalkaline rhyolite.	Slightly high As, Sb; low Mn and Mg (altered)	Mostly rounded, sloping outcrop on large, rounded exfoliated boulders.	Poorly developed pale to dark orangy brown.	Grasses with some sage, juniper, and pinyon.	Bs 1,2,3,4, 3/2, PCs 1,2 ISH-I, S	Bs 5, 7 5/2, 5/4, 5/7 PCs 3, 4, 5 ISH-H	

[*] Amounts (high or low) are relative to other units in the study site.
[**] Desert varnish is by nature highly discontinuous and irregular in these study sites.
[***] ISH - Intensity, Saturation, and Hue (I,S,H) on bands 3, 5, and 7.

Table 18. Summary of lithological, petrochemical, and field characteristics of volcanic units of the Black Mountain study site.

PC2 and low DN values in band 7. With ISH transform on bands 3-5-7 the unit is quite bright in the intensity mode relative to other cover, bright in saturation, but only medium in hue. Thus a distinctive yellow hue manifests over these rocks in the 1-4-Hue composite. (The hue parameter is subdued for this formation.)

LAVAS OF PILLAR SPRINGS AND RIBBON CLIFF

The inter-ash flow lavas at Black Mountain, the granular crystal rich Lava of Pillar Springs and Ribbon Cliff, form a generally coherent remote sensing unit at Black Mountain. These lavas are rhyolitic to trachytic with fairly high iron content, low in albedo relative to some adjacent rock cover, and thus darker in all bands, growing slightly darker with increasing wavelength (Tables 16 and 18). Lava of Ribbon Cliff seems to be slightly darker than Lava of Pillar Springs in bands 5 and 7. The units tend to be light to medium-light gray and indistinct in the ratio images. In the color composites 3/1-5/7-4 image the lavas are yellowish green and basically indistinguishable from Trachyte of Hidden Cliff. On the 3-5-7 image, however, they are greenish brown. Lavas of Ribbon Cliff are more reddish than the other lavas on this image, possibly reflecting a higher proportion of brighter superficial iron oxide staining. This distinction is mirrored on the 1-4-Hue (bands 3-5-7) image. On the 3-5-7

band ISH images, the lavas are dark in saturation and hue; indistinctive medium gray in the intensity mode. In the principal components transformation lavas are brightest relative to other cover in PC2 and PC4, dark in PC1. So in the PC composites, PC2 controls their contrast; in composite PC1 PC2 PC3 images they are greenish and in PC2 PC3 PC4, reddish. They contrast in the latter with Trachyte of Hidden Cliff which is emerald green probably due to the vegetative response of the summit area of Black Mountain. These imagery characteristics are compared with other units within the study scene in Table 18.

ROCKS OF YELLOW CLEFT

Rocks of Yellow Cleft are indistinct from the other units in all TM bands. DN values are intermediate (Table 16). The unit occurs in one contiguous arcuate depression, however, at the eastern edge of the central caldera moat. Its outline is distinguishable since it is surrounded by lower albedo units - Trachyte of Hidden Cliff and Lava of Ribbon Cliff. The unit is covered with grasses and sagebrush. Outcrop is sparse. Rocks of Yellow Cleft tend to be slightly darker than most other units on PC1 images and slightly bright on 3/2 and 5/7 images, the latter probably due to grassy cover. On ISH transforms with bands 3-5-7 the unit is somewhat bright on the intensity image, dark on the saturation image.

TRAIL RIDGE TUFF

Thematic mapper imagery over Trail Ridge Tuff is very similar to that over the Lavas of Pillar Springs, with which it is closely related both in time and space and in composition. The Pillar Springs Lava followed the Trail Ridge Tuff eruption. Trail Ridge tends to be slightly brighter in band 1, darker in 5/7 ratios, and brighter in PC2 images, which aids discrimination where the unit lies adjacent to Lavas of Ribbon Cliff.

GOLD FLAT TUFF

The Gold Flat TUff is an unusual rock petrochemically and is distinctive spectrally as well. This peralkaline deposit is very highly evolved magmatically and contains a high proportion of large ion lithophile elements and other incompatible elements that partition into late magmatic phases, including tantalum, rubidium, thorium, and the rare earths (Table 18). Reflectance increases as wavelength increases to brightest in band 7 relative to other units. For this reason the unit is distinctly dark in the 5/7 image and reddish to magenta in 3/1-5/7-4 false color composites. The unusually high reflectance in band 7 relative to other scene cover gives rise to a strikingly bright turquoise blue hue in the 3-5-7 composite. Gold Flat Tuff is bright in PC1, very dark and anomalous in PC2, and dark as well in PC3 except over its northern exposures

where it is masked by the bright response of vegetation. It is medium gray and indistinct in PC's 4, 5, and 6. The relationship among eigenvalues and hue images with ISH transformation on bands 3-5-7 is medium in intensity in the intensity mode. On the ISH false color composite Gold Flat Tuff is a very distinctive pale magenta. On the 5-7-PC2 composite, the formation is brilliant mustard yellow, but similar to Labyrinth Canyon Tuff, which also exhibits geochemical properties of highly evolved differentiates. It is light purple in the 1-4-Hue (bands 3-5-7), blue where vegetation includes golden grasses and scattered low evergreen trees.

TRACHYTE OF HIDDEN CLIFF

Mafic trachyte forms the central volcanic edifice and is very dark in all bands (Table 16) except 4 and 5 in which it is an indistinct medium gray contrast. Spectral response appears to be influenced by vegetation, in this case, largely cheat grasses and lichen. The unit is very bright relative to other cover in 5/7 and 4/3 images, forming a slightly striped pattern that apparently follows drainages and is probably caused by riparian vegetative reflectances in band 4. In individual PC's the deposit is quite dark in the first PC, very light due to vegetative interference in the third. Mafic trachyte is pinkish purple on the PC1 PC2 PC3 composite, yellowish green in the

PC2 PC3 PC4 rendition. It is indistinct from other lavas in the PC2 PC4 PC5 image. In the ISH transform of bands 3-5-7, the unit is very dark in intensity and hue, medium gray and indistinct in saturation. On the ISH composite it is purplish. In the 1-4-Hue (bands 3-5-7) image, mafic trachyte is dark forest green and a dull army green on the 3-5-Hue (bands 1-2-4) image.

LABYRINTH CANYON TUFF

The Labyrinth Canyon ash flow tuff, actually distal facies of Spearhead Tuff (Noble, et al., 1984), is spectrally similar to but distinct from Gold Flat Tuff partly due, as will be demonstrated in Chapters VI and VII, to the unusual trace element content of Gold Flat Tuff. It tends to be moderately to only slightly bright in bands 1-3, quite bright in bands 4 and 5, somewhat less so in band 7 than Gold Flat Tuff, which aids its discrimination in false color composite images that take this disparity into account. It is bright in the 3/2 image, possibly due to it's orangy buff color, and is medium gray in 5/7 images, but much lighter in tone from the Gold Flat Tuff. Labyrinth Canyon is a pale powder blue and distinct from Gold Flat in the 3-5-7 composite and unique in color contrast as well in 3/1-5/7-4 hybrids in which it is very pale pink. The unit is bright in PC1, dark in PC2. It appears masked by the bright vegetative

response of cheat grass in PC3. It is pale pinkish lavender on the PC1 PC2 PC3 composite and a bright orangy red on the PC1 PC2 PC4 configuration. Saturation and hue images of bands 3-5-7 give the unit a very bright signature, less so in the intensity mode. The deposit exhibits fair color contrast as well in the 1-4-Hue (bands 3-5-7) and the 3-5-Hue (bands 1-2-4) composites. Color is not unique for the unit on the PC2 composites with bands 5 and 7 and bands 3 and 7.

KANE SPRINGS WASH VOLCANIC CENTER

Imagery response of units at Kane Springs Wash is influenced much more strongly by topography and vegetation than that at the other 2 study sites. Topographic relief is almost 1000m and evergreen trees dot the mesa tops, particularly in the northern part of the caldera. Other vegetative cover is also denser (commonly 40%) throughout the scene, including foxtail grass, cheat grass, atriplex, sagebrush, and cactus (Chapter I). The study scene encompasses the southern part of the caldera where intracaldera subsidence and post caldera fill has left a prominent curvilinear and a conspicuous imagery feature. Figures 34-37 show enhanced images of the Kane Springs Wash study site. Plate 6 is a map of imagery units that correlate with lithology. Band DN values for each unit are

tabulated in Table 16 and a summary of unit imagery characteristics and comparison with other unit features is presented in Table 19.

HIKO TUFF

The Hiko Formation is the oldest unit in the Kane Springs Wash study scene. It is distinct chiefly due to image textural properties, namely alternating tonal bands which result from successions of alternating densely welded and vapor phase altered zones. The banded texture is enhanced by vegetation, chiefly grasses, which favor the gentler slope-forming, vapor phase altered zones, rather than ledges and shallow cliff faces which result from weathering of the densely welded layers. On some images, particularly the PC1 PC2 PC3 composite, alternating densely welded and vapor phase altered layering gives rise to red and white banding. Reflectance from Hiko Tuff increases in intensity in higher wavelength bands. The unit is bright in 3/2 and 5/2 ratio images, darker on a 5/7. It is indistinct in simple color composites and hybrid composites. The deposit is bright in PC1, obscured in other PC's. In the ISH transform, bands 3-5-7, the section is relatively bright in the intensity mode, medium gray in hue and saturation. Complex color composites tend to highlight the interval best. In PC1 PC2 PC3 and PC1 PC2 PC4 composites the formation is characterized by a reddish

Base: Landsat 5 TM Images
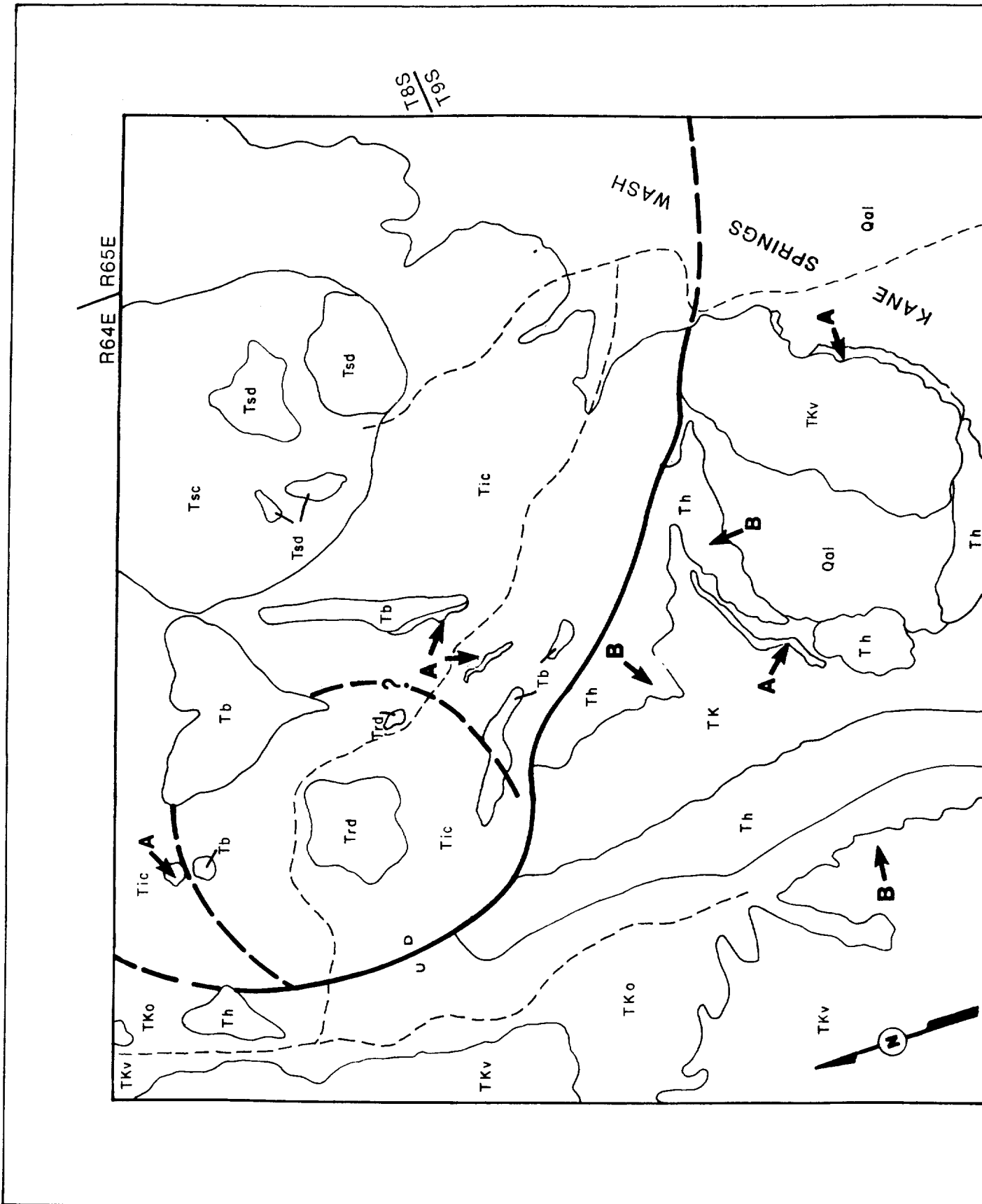
EXPLANATION

1 Mile
1.61 Kilometer

Qal   Recent Alluvial Gravels

Tb   Late Basalt

Trd   Rhyolite Flow Domes

Tic   Intracaldera Moat deposits: includes rhyolite lavas, trachyandesite lavas, and white airfall tuff

Tsc   Syenite Complex

Tsd   Syenite Flow Dome Complex

TKv   Kane Wash Tuff, undifferentiated

TKu   Ash Flow Tuffs, V1, V2, and V3

TKo   Ash Flow Tuffs, O and W

Th   Hiko Ash Flow Tuff

MID-MIOCENE KANE WASH CALDERA

D
U   Caldera Margin Fault showing relative displacement. Dashed where uncertain.

Lithologic Contact, approximate, based on TM imagery

Dirt Road

SPECIAL FEATURES HIGHLIGHTED BY ENHANCED IMAGERY

A   Airfall Tuff Deposits

B   Stripping reflecting repititious densely welded and vapor phase altered tuff zones

LITHOLOGIC MAP OF THE SOUTHERN PART OF THE KANE SPRINGS WASH VOLCANIC CENTER
Interpreted from Landsat 5 TM imagery units and field observation and based on geology by Novak, 1984

PLATE 6

FOLDOUT FRAME

Figure 34. Kane Springs Wash volcanic center. Landsat 5 TM 512x512 band 5 image, contrast enhanced with function SCALE and edge enhanced. High tonal contrast correlates generally with various volcanic rock assemblages on basis of divalent iron content or felsic tendency: leucocratic units are light; intracaldera melanocratic deposits dark.

Figure 35. Kane Springs Wash volcanic center. Landsat 5 TM 512x512 pixel image of band ratio 5/7, scaled. Dark annular area in the northwest quadrant is topaz rhyolite flow dome, and similarly dark zone in the southwest corner is Kane Wash Tuff Member V1. Both units are highly evolved peralkaline differentiates and exhibit steep spectral curves from TM band 5 through 7, resulting in low 5/7 values.

SUMMARY OF MAJOR VOLCANIC UNITS OF THE
KANE SPRINGS WASH STUDY SITE WITH TM IMAGERY CHARACTERISTICS

UNIT	LITHOLOGY	PETROCHEMISTRY MAJOR	PETROCHEMISTRY MINOR*	FIELD CHARACTER	DESERT VARNISH DEVELOPMENT**	DOMINATE VEGETATION ASSOCIATION	TM IMAGERY RELATIONSHIPS*** BRIGHT	INDISTINCT	DARK
Late Basalt	Massive to vesicular flows with microporphyritic laths of plagioclase	Olivine basalt	High Ni, P, Sc, Ti, V, Cr, Co, Cu. Low Rb, Th, U, Li.	Very dark gray massive mesa caps. Forms blocky scree, occasional silvery sheer.	Moderate to well developed. Very dark gray with	Pinion pine and juniper on mesa tops with some sagebrush and grasses.	5/7	PCa 2,3,4,5 ISH-S,H	Ba 1,2,3,4,5,7 3/2, 5/2, 5/4 PC 1, ISH-1
Rhyolite Domes	Massive flow-banded lava, phenocrysts of quartz, sanidine, fayalite and Na-rich amphibole, vapor phase topaz.	High silica peralkaline rhyolite	High Rb, Ta, HREE, Th, Sn, U, Y, Be, F, Li. Low Ba, P, Eu.	Dense, domal, knobs light buff to flesh colored. Irregular platy to blocky float.	Poorly developed. Pale orangy to dark brown.	Mostly grasses, some sage and juniper.	Ba1,2,3,4,5,7, 3/2, PCa 1,5 ISH-1	5/2, 5/4 PCa 3,4, ISH-S	5/7, PC 2 ISH-H
Trachyandesite Lava	Vesicular flows with plagioclase phenocrysts in dark, holocrystalline matrix.	Andesite to low silica andesite.	High Ni, Sc, Zr, Ga. Slightly low U, Th, Pb.	Dark gray, forms low, sloping, hummocky terrain. Float is irregular and rough.	Sporadic moderately well developed, dark gray.	Grass and sagebrush with 5-10% moss green lichen.	PC 2, 5/7 ISH-S		Ba 1,2,3,4,5,7 3/2, 5/2, 5/4 PC 1,3,4,5 ISH-1
Syenite Complex	Fine grained porphyry with anorthoclase, quartz, and clinopyroxene phenos. Flow domes, intrusives, and minor tuff.	Syenite and trachyte.	High Mo, Zn, Zr, B slightly high REE, As, Be, F, Hf, La. Low C, Eu, V, Ni.	Cream colored domal knobs and rugged hills, weathers to exfoliated slabs and rough boulders.	Tan to brown to reddish brown. Some silty opaline silica. Moderately well developed.	Grasses and sage with some juniper.	Ba 1,2,3,4,5,7 5/2	3/2,5/4,5/7 PCa 1,3,4,5 ISH-1,5	PC 2 ISH-H
Kane Tuff V1-3 Members	Ash flow tuffs with pumice and crystals of fayalite, Na-rich amphibole, sanidine, anorthoclase.	Peralkaline comenditic rhyolite to trachyte	High REE, Hf, F, Rb, Zr, Th, U. Low Sc, Ba.	Densely welded to vapor phase altered, forms, ledges, steps, and slopes. Weathers to thick, blocky slabs.	Brown to gray brown, poorly to moderately well developed.	Grasses and sagebrush, some juniper 10% moss green lichen and vapor phase altered.	Ba 5,7 3/2,5/2,5/4 PCa 3,4,5 ISH-S, H	Ba 1,2,3,4 PC 1 ISH-1	5/7, PC 2
Kane Tuff O & W Members	Ash-flow tuffs with pumice and lithic clasts and crystals of fayalite.	Subalkaline rhyolite	Low Mo, Mg, Ti	Distinctive white glassy tuff separates O from W. Moderately welded, slope former, ledges minor in project area.	Brown to gray brown moderately well developed.	Mostly grasses, some sage.	PC 3 ISH-S	Ba1,2,3,4,5,7 3/2, 5/2, 5/4 PCa 1,2,4,5 ISH-1, H	5/7
Hiko Tuff	Ash-flow tuff Granular, granitic crystal rich with sardine/anortho-clase.	Subalkaline latite	Slightly High Sr, Ba Slightly low B	Coarse granularity results in "beehive" exfoliated mounds. Forms large boulders and rugged terrain.	Poorly developed. Dull gray brown to brown.	Mostly grasses, some sage.	Ba 1,2,3,4,5,7 3/2, 5/2, 5/4 PC 1, ISH-1	PCa 2,3,4,5 ISH-S, H	

* Amounts (high or low) are relative to other units at the study site.
** Desert varnish is by nature highly discontinuous and irregular in these study sites.
*** ISH - Intensity, Saturation, and Hue (I,S,H,) on bands 3, 5, and 7.

Table 19. Summary of lithological, petrochemical, and field characteristics of volcanic units of the Kane Springs Wash study site.

123

banded image. It is light powder blue in the 1-4-Intensity (ISH, bands 30507) image. The 3-5-7- ISH Intensity parameter image exhibits the unit in relatively bright intensities.

KANE WASH TUFF (MEMBERS "O" AND "W")

The lower members of the Kane Wash Tuff Formation - "O" and "W" - are basically indistinct on images of the area. They are probably not part of the Kane Springs Wash caldera outflow sheet, but rather were extruded from a source to the northwest (Novak, 1984). The unit is subdued and indistinct on all images except for some brightness tendency on PC3 images, probably due to grass canopy and on saturation images from ISH transforms on bands 3-5-7.

KANE WASH TUFF ("V" MEMBERS)

Kane Wash Tuff members V1, V2, and V3 exhibit medium gray tones in lower wavelength bands, but are relatively bright in band 5, increasing in intensity in band 7 (Tables 16 and 19). These flows are relatively highly evolved petrochemically and exhibit relatively high brightness values in band 7, similar to the highly evolved Gold Flat Tuff of Black Mountain. The unit is quite bright in the 5/1 and 5/2 ratio images, rather dark on the 5/7 image. In the 3-5-7 composite the section is a distinctive powder blue. It is reddish but indistinct in the 3/1-5/7-4 image.

The tuffs are extremely bright in the hue mode of the 3-5-7 ISH transformation, dark in saturation, and medium gray in the intensity mode. They are a reasonably distinctive lavender in the ISH composite. In PC1 the Kane Wash Tuff is medium gray, in PC2 quite dark where densely welded, and relatively light in PC's 3-5. In composite PC's 1-2-3 and 2-3-4 the formation is distinct, especially in the latter in which it tends toward bright blue. In more complex renditions with ISH and simple band hybrids the section is typically highlighted with some characteristic tint. This appears to be due primarily to the presence of large areal exposures or platforms of densely welded zones.

AIR FALL TUFFS

The air fall tuffs which are very light in color are highly reflective in all wavelengths. This characteristic controls this unit's response in false color composite images. These tuffs are quite bright in PC1, even brighter in PC2. Tonal contrast is obscured in higher PCs. In all ISH transformations these glassy beds are bright in intensity mode, obscured in saturation and hue. The deposits are more uniquely highlighted by PC composites and the 1-4-Saturation (bands 3-5-7) image.

SYENITE COMPLEX

The syenite complex is distinguishable on images

primarily as anomalous textural patterns, involving tone and color variation, throughout a roughly annular zone. The pattern is created by irregular reflectance properties over relatively small areas throughout the complex. Reflectance is variable, but more consistently bright in the higher wavelength bands (Tables 16 and 19). In individual PC images the unit exhibits overall medium intensity brightness except in PC2, in which it is relatively dark. The subtly distinct "busy" or high frequency textural pattern tends to be mirrored in complex composites by highly variable hues and tints. Two subcircular zones within the complex exhibit relatively bright signatures similar in reflectance character and in many images to the topaz rhyolite domes described below. These zones reflect a syenitic flow dome complex within the syenite complex.

TRACHYANDESITE LAVAS

Trachyandesite lavas are exposed primarily in the canyons within the caldera complex. They are thus largely obscured by shadows with which they tend to blend. The unit is relatively nonreflectant and dark in all bands (Tables 16 and 19). It is tonally light in the 5/7 image. The deposit is light in tone in PC2, dark in all other PC's. The formation is anomalously dark in the hue mode of the 3-5-7 ISH transform and bright in saturation. It is a

reddish brown to greenish brown color in the 1-4-Hue (bands 3-5-7) image and the 1-4-Intensity composite.

RHYOLITE FLOW DOMES

Topaz Rhyolite flow domes are characterized by peralkaline tendency and high fluorine and chlorine as well as other incompatible elements that partition into highly evolved magmatic differentiates (Table 19). These domes tend to form concise small subcircular outlines. Tonal contrast and color patterns within these deposits are somewhat variable. In that regard they, thus, behave similarly to the syenite complex described above. The rhyolite and syenite flow domes are highly reflectant in all bands, but the rhyolite domes more so in band 7 (Table 16). For that reason rhyolite domes form a strikingly anomalous dark bullseye contrast on the 5/7 ratio image. They are brilliant red on the 3/1-5/7-4 composite. The formation is uniquely bright in PC5, quite bright also in PC1. It is darker in PC2. The unit tends to resemble the Kane Wash Tuffs on many of the composite images. It exhibits slight deviation from the latter, however, in the 1-4-Saturation and intensity (bands 3-5-7) composites. Perhaps the best images for discrimination are the individual bands, PC5, 5/7 ratio, and saturation with bands 3-5-7, in which the unit appears dark.

LATE BASALT

Basalt caps the mesas within the caldera. Its spectra are contaminated by vegetative cover, including sparse to moderately dense evergreens up to 35-40%. The basalt flows are dark in all bands, with a slight increase in band (Tables 16 and 19). The unit is rather light, however, in the 5/7 ratio image and therefore greenish on the 3/1-5/7-4 composite. In the 3-5-7 composite the lavas are blue to greenish. The unit is very dark in PC1, indistinct on other PC's. On the PC composites, 1-2-3 and 2-3-4, basalt is dark blue to dusty blue. On the intensity image of the ISH function of bands 3-5-7, the formation is dark but indistinct in hue and saturation. On the 1-4-ISH composites the basalt is a dark felty green. The unit is a rather distinctive purple on the 3/1-5-PC2 image.

Table 20 summarizes qualitative TM imagery relationships between the various volcanic units at each of the three study sites. Table 16 tabulates average DN values for each unit and Tables 17, 18, and 19 compare imagery characteristics over each rock assemblage with lithologic, compositional, and field relationships.

BASAL GLASS ENHANCEMENT

Identification of glassy zones within a pile of ash flow tuffs is paramount to stratigraphic separation among

TABLE 20. RELATIVE TM IMAGERY CONTRAST AMONG THE MAJOR VOLCANIC UNITS

B-Bright   D-Dark   I-Medium or Indistinct   V-Very

THE KANE SPRINGS WASH SITE

UNIT	TM BANDS						BAND RATIOS				PRINCIPLE COMPONENTS					ISH 3-5-7		
	1	2	3	4	5	7	3/2	5/2	5/4	5/7	1	2	3	4	5	I	S	H
Basalt	D	D	D	D	D	D	D	D	D	B	VD	I	I	I	I	D	I	I
Topaz Rhyolite	B	B	B	B	B	B	B	I	I	VD	B	D	I	I	B	B	I	D
Trachyande-site	D	D	D	D	D	D	D	D	D	B	D	B	D	D	D	D	B	VD
Syenite Complex	B	B	B	B	B	B	I	B	I	I	I	D	I	I	I	I	I	D
Kane Tuff V Members	I	I	I	I	B	B	B	B	B	VD	I	D	B	B	B	I	B	B
Kane Tuff O & W Units	I	I	I	I	I	I	I	I	I	D	I	I	B	I	I	I	B	I
Hiko Tuff	B	B	B	B	B	B	B	B	B	D	B	I	I	I	I	B	I	I

THE BLACK MOUNTAIN SITE

UNIT	TM BANDS						BAND RATIOS				PRINCIPLE COMPONENTS					ISH 3-5-7		
	1	2	3	4	5	7	3/2	5/2	5/4	5/7	1	2	3	4	5	I	S	H
Labyrinth Canyon	I	I	I	B	B	B	B	B	B	I	B	D	D	D	I	I	B	B
Trachyte Hidden Cliff	D	D	D	I	I	D	I	I	B	B	D	B	B	D	I	D	I	D
Gold Flat Tuff	I	I	I	B	B	VB	B	B	B	D	B	D	D	I	I	I	VB	VB
Lavas of Pillar Spr.	D	D	D	D	D	D	B	I	D	I	D	B	I	B	I	I	D	D
Trail Ridge Tuff	I	D	D	D	D	D	I	I	D	D	D	B	I	B	I	I	D	D
Rocks of Yellow Cleft	I	I	I	I	I	I	B	I	I	B	D	B	I	I	I	B	D	I
Older Lavas and Tuffs	B	B	B	B	I	I	B	I	I	I	B	B	I	I	I	B	B	I

THE STONEWALL MOUNTAIN SITE

UNIT	TM BANDS						BAND RATIOS				PRINCIPLE COMPONENTS					ISH 3-5-7			ISH 1-2-4		
	1	2	3	4	5	7	3/2	5/2	5/4	5/7	1	2	3	4	5	I	S	H	I	S	H
Civet Cat Canyon Tuff Cap Rock	D	D	D	B	B	B	D	B	VB	D	D	VB	B	I	B	D	B	B	D	B	D
Civet Cat Canyon	D	D	D	D	D	D	D	I	I	I	D	B	I	B	I	D	I	D	D	B	B
Spearhead Tuff	D	D	I	I	I	I	B	I	I	I	D	B	B	B	I	D	I	B	D	I	D
Basalt Flows	D	D	D	D	D	D	I	I	I	I	D	I	I	I	I	D	D	D	D	I	I
Antelope Spr Rhyolite	B	B	B	B	VB	B	B	B	B	B	B	D	I	I	I	B	B	I	B	D	D
Antelope Spr Latite	D	D	D	D	D	D	B	I	D	I	B	D	B	I	I	D	D	D	I	D	B

ash flow formations. Formational bases are designated by convention at glassy intervals which prove that the underlying deposit was cool prior to deposition of the overlying flow. Intervals between glassy zones are called cooling units. They are formally assigned formation status.

Directional filters were applied to a Stonewall Mountain contrast enhanced band 5 image in an attempt to highlight thin air fall tuff deposits and basal vitrophyres. Air fall tuffs (Plinian type) often precede ash flow deposition and basal vitrophyres may form at the bases of ash flows where bedrock was cool.

Filters (Appendix D) create a mask or "kernel" and then "convolve" it to the image. The mask or kernel is a two dimensional matrix, in this case a low-pass, 3 x 3 matrix, which centers on each pixel in the scene and weights the surrounding pixels according to preset amounts. The sum of the new weighted values of surrounding pixels is then compared to a new weighted value for the central pixel. If the value of the central pixel is less than the summed value of surrounding pixels, the central pixel value is changed to the latter. For edge enhancement, the technique tends to sharpen borders between areas of gradational tonal contrast. For our purposes, that of highlighting linear contrast of basal glass and air fall, a directional bias (Jensen, 1986) was applied in order to take advantage of

the general trend of ash flow deposits in the Stonewall scene.

Both southwest and northeast filters were successful in enhancing basal air fall deposits (Figure 38). Air fall at the base of Spearhead Tuff is apparent in Figure 38 at "A" and at the base of Civet Cat Canyon Tuff at "B". The air fall deposit at the base of Spearhead is also manifest on normal nonedge enhanced images; however, the basal glass exhibited under Civet Cat Canyon Tuff was not observed on other images.

SPECTRAL CLASSIFICATION

UNSUPERVISED CLASSIFICATION

Unsupervised classification was performed on each of the 3 study sites, using IDIMS function ISOCLS. ISOCLS applies a clustering algorithm to a multispectral image, in this case, 6-banded images, in order to partition multivariate data points into disparate categories with similar statistical properties. The function operates by "split" and "combine" interactions, involving the distance between data points and the cluster means. If a data point's standard deviation is greater than the default value of 4.5, "splitting" occurs and a new cluster is created. The maximum number of clusters for these classifications was set at 16, the default value.

Figure 38. Stonewall Mountain study area. Landsat 5 TM 512x512 pixel subscene. Directional filter applied to contrast enhanced (scaled) band 5 image. Edge enhancement was with a northeast biased 3x3 mask with a 0.4 add back to the original. Note the light toned ribbons at A and B. They are glassy basal air fall zones at the base of Civet Cat Canyon Tuff (A) and Spearhead Tuff (B).
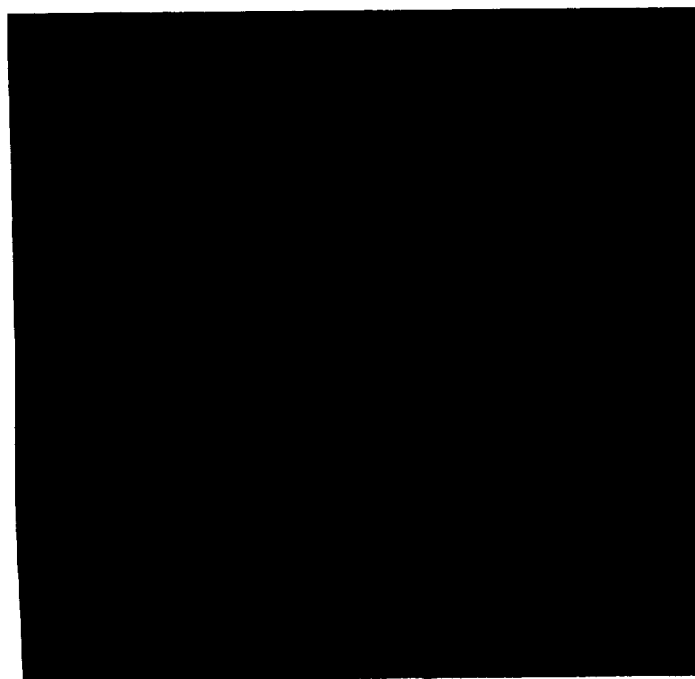
Figure 39. Unsupervised classification of the Stonewall Mountain study area. Landsat TM, bands 1, 2, 3, 4, 5, and 7. Classification performed by function ISOCLS (Appendix D), then contrast enhanced (scaled) and false colored. Sixteen classes are represented.

Comparison of the unsupervised classification images for each of the study sites (Figures 39, 40, and 41) with their corresponding geologic maps (Chapter III) seems to result in fairly weak lithologic correlation. Some units are fairly well represented, in part, by classes designated by the ISOCLS function - some basalt at Kane Springs Wash and some of the Gold Flat Tuff at Black Mountain, for example - but for the most part, spectra of the classified clusters include alluvium and pixels with mixed cover with many inconsistencies, thus resulting in only nominal lithologic correlation. The method seems to work best at the Stonewall Mountain area where vegetation and topographic relief provide least interference.

The unsupervised classification scheme at Stonewall Mountain was regrouped by IDIMS function RECLAS, which reclasses pixels if they differ from pixels in a surrounding 3 x 3 matrix. The algorithm results in a reduction of classes and a more generalized "smoothed" image which proves lithologic correlation.

SUPERVISED CLASSIFICATION

Supervised classification with IDIMS function CLASFY was applied at all 3 study sites. The training sites are shown in Figure 42 and class statistics compiled in Appendix J. The computer processing procedure involves definition of training sites on known cover types,
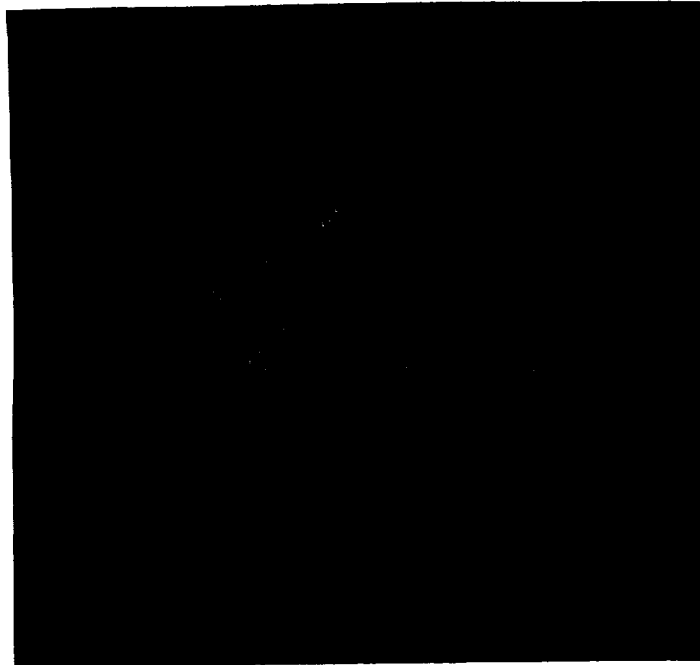
Figure 40. Unsupervised classification of the Black Mountain subscene. Landsat 5 TM bands 1, 2, 3, 4, 5 and 7, 512x512 pixel dimension. Image was classified into 16 classes with function ISOCLS, then reclassed into 8 by RECLAS. The image was scaled for contrast, then false colored.

Figure 41. Unsupervised classification of the Kane Springs Wash volcanic center. Landsat 5 TM bands 1, 2, 3, 4, 5 and 7. Classed by function ISOCLS into 16 classes, then reclassed with function RECLAS, contrast enhanced (scaled), then false colored. Image is a 512x512 pixel subscene.

assigning the training sites to a special file and performing statistical evaluation of the pixels within the training sites with the function STATS. CLASFY then evaluates all pixels according to a maximum likelihood decision rule based on class covariance matrices and mean vectors (Jensen, 1986).

The supervised method for the Stonewall and Black Mountain study sites (Figures 43 and 44) resulted in generally positive classification of pixels according to lithology (Figures 45, 46, and 47). Coherent groups of contiguous pixels correspond with mappable formations at a scale of about 1:50,000. Isolated pixels and narrow, dendritic, reticulate or erratic patterns do not typically reflect exposed or mappable bedrock. These pixels appear to be largely alluvium or detritus without distinct classes of their own.

Function RECLAS was also applied to the supervised classification images, resulting in less erratic, outlying, pixels. This method leads to better overall groupings for geologic mapping purposes at scales of about 1:50,000 and smaller.
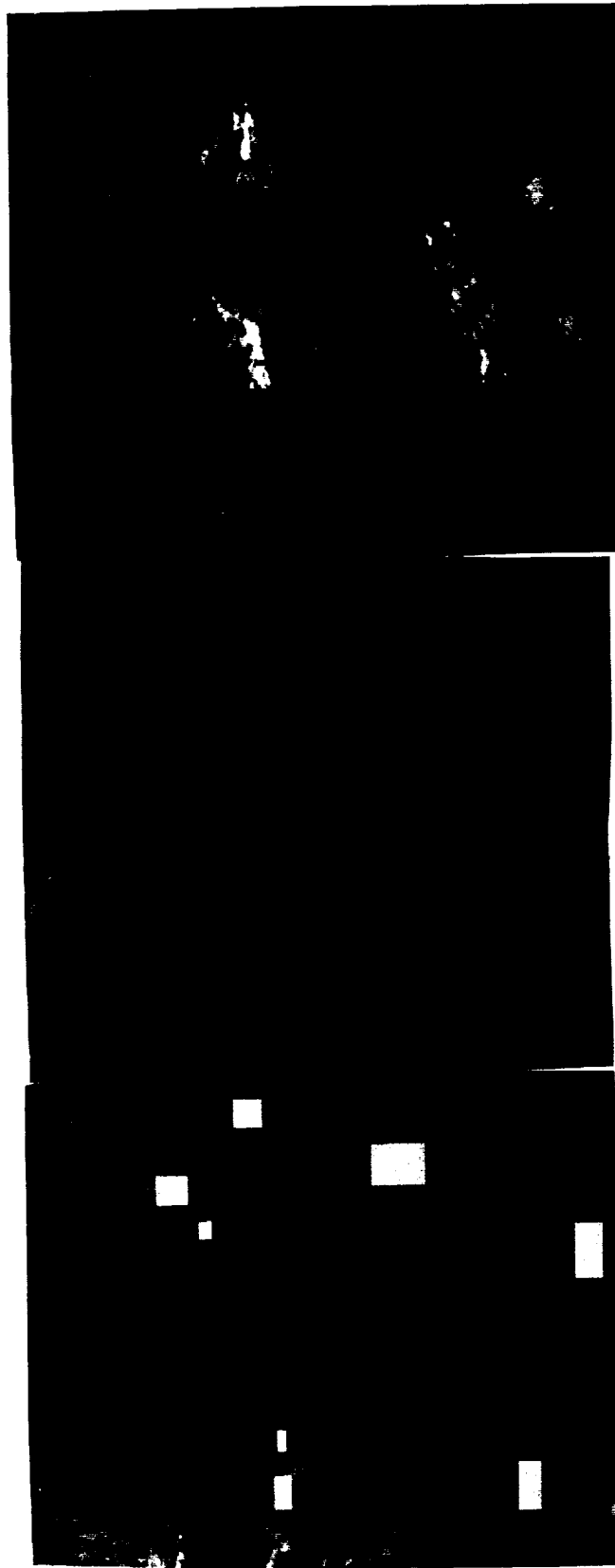
Figure 42. Indexes to supervised classification of each of the three study sites: Stonewall Mountain (top), Black Mountain (middle), and Kane Springs Wash (bottom). Trainings sites for each lithologic unit included in the classification are shown.

Figure 43. Supervised classification of the Stonewall Mountain subscene, using all 6 Landsat 5 TM bands (visible/near-IR). Index to classes is shown in Figure 42. Classification performed by function CLASFY, contrast enhanced with the SCALE function, then reclassified by RECLAS and false colored.

Figure 44. Supervised classification of the Black Mountain subscene using IDIMS function CLASFY on lithologic training sites shown in Figure 37. All 6 Landsat TM bands included on 512x512 pixel subscene. Image was contrast enhanced (scaled), reclassified by RECLAS and false colored.
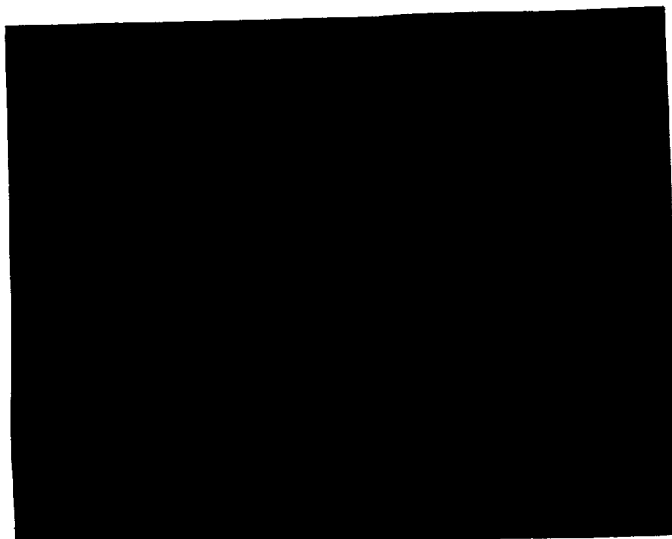
Figure 45. Supervised classification of the Stonewall Mountain study area showing Stonewall Flat Tuff: 4 classes all in red - 2 of red glassy cap of Civet Cat Canyon Tuff, 1 of underlying Civet Cat Canyon Tuff, and 1 of Spearhead Tuff. The maximum likelihood classification (CLASFY, Chapter 2) utilized all 6 Landsat 5 TM bands. The 512x512 pixel image was scaled.
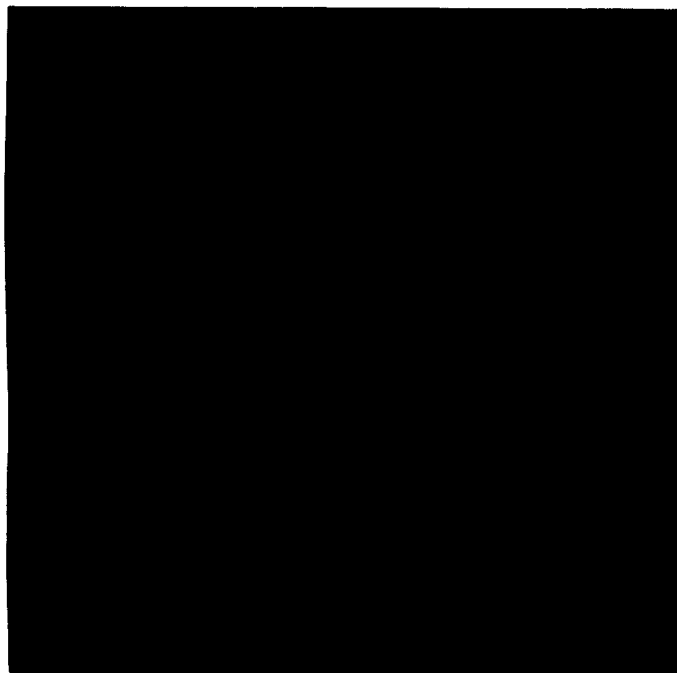
Figure 46. Supervised classification using IDIMS function CLASFY on 512x512 pixel Stonewall Mountain subscene. Image shows glassy red cap of Civet Cat Canyon Tuff - 2 training sites (Figure 37) - in orange and yellow. All 6 Landsat 5 TM bands were included. Image was contrast enhanced (scaled).
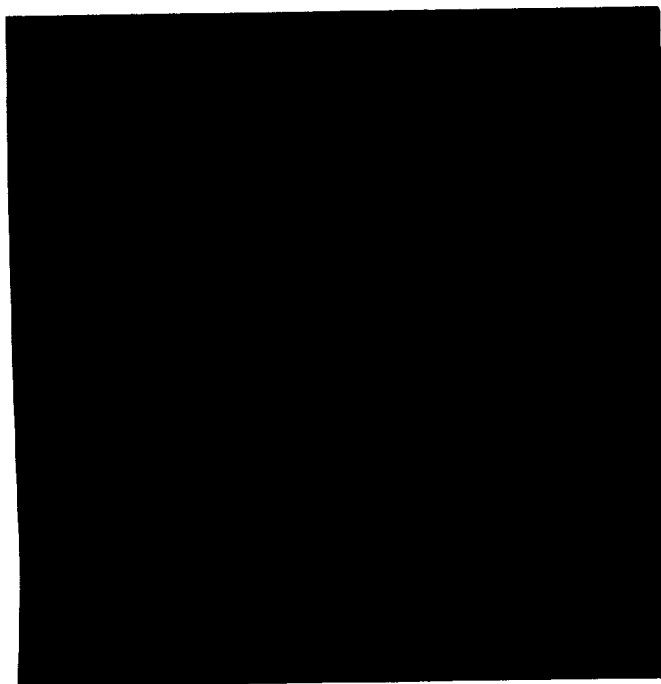
Figure 47. Supervised classification image of Stonewall Mountain by IDIMS function CLASFY (Appendix D) on 512x512 pixel Landsat 5 TM subscene using all 6 bands. Image is contrast enhanced (scaled) and shows Antelope Springs Formation. Upper rhyolitic porphyry is yellow. Lower latitic porphyry is orange. Groups of coherent colored pixels are meaningful. Scattered individual pixels are largely spurious.

CHAPTER V

SECONDARY MINERAL COATINGS

HISTORICAL PERSPECTIVE

Early attempts to describe surficial secondary mineral coatings in desert environments (predominately desert varnish) in a comprehensive fashion were published by White (1924), Laudermilk (1931), and Engel and Sharp (1958). A more quantitative approach to the study of desert varnish began in the mid-1970's and numerous workers have published their results since. Dorn and Oberlander (1981) in a fairly lengthy treatise on the topic do an excellent job of summarizing work on coatings up to that time, and Elvidge (1979) provides an exhaustive historical composition in his master's thesis.

Desert varnish is usually defined as the arid secondary phase of the weathered surface of rocks in arid to semi-arid environments. Taylor-George, et al. (1983) define desert varnish as a coating of ferromanganese oxide and clay. Perry and Adams (1978) found that varnishes they studied consisted of alternating bands with variable detrital minerals of clay, feldspar, quartz, and hematite. According to Dorn and Oberlander (1981), desert varnish averages 10-30um thick. (In my study areas, thicknesses of this magnitude were only rarely observed and in a very limited areal extent on a microscopic scale.) To most field

geologists desert varnish is that conspicuous dark rusty brown to shiny black stain that commonly coats prominent desert bluffs. Iron and manganese oxides are the distinctive components.

Previous workers who have attempted to firmly establish the ultimate source of varnish constituents differ in opinion. Engel and Sharp (1958) concluded that the components of desert varnish are derived from the underlying host rock, whereas Dorn and Oberlander (1981) state that the constituents of "all rock varnishes" are derived from sources external to the host rock. Source of varnish constituents and relative proportions of exposure of varnish to underlying rock bear significantly on remote sensing interpretations.

Varnish and probably all coatings seem to require considerable time to form. Hunt (1961) cites archaeological evidence to establish a threshold of about 2000 years for noticeable development. Exceptions may occur, however, and Engel and Sharp (1958) note one locality with noticeable varnish development over a 25 year period. Coatings tend to be amorphous and have a dark brown streak. Hardness of typical coatings on rocks of the Mojave Desert were measured at 4.5-5 (Laudermilk, 1931). Coatings adhere to their host tenaciously. They are insoluble in water, but readily soluble in hot, dilute hydrochloric acid. Varnishes often overlie light "limonitic" staining and light clay alteration.

Coating morphology varies from paint-thin films to lamellar successions of light and dark layers. Borns et al. (1980) observed microorganisms, either mold or fungus, with a scanning electron microscope (SEM) in lamellar varnishes. Staley, et al. (1982) describe abundant microcolonial structures of lichen, algae, and fungi on desert rock surfaces from the Southwest U.S. They point out that lichen and algae can derive their nutrients from their host, but fungi require an external source and speculate the external source is probably wind blown dust. By analysis with SEM-EDX (energy dispersive X-ray), Taylor-George, et al. (1983) discovered iron, aluminum and silica, three of the characteristic elements of varnish, in fungi on rock surfaces from the Sonoran Desert. They also identified manganese oxidizing bacteria in the varnish as well. Perry and Adams (1978) found cyclic manganese deposition in lamellar coatings.

Comprehensive chemical data on varnishes were published by Engel and Sharp (1958). Their wet chemical determinations from rocks of southern California established oxygen, hydrogen, silica, aluminum, iron, and manganese as the chief elemental components. Spectrographic analyses uncovered titanium, barium, and strontium in unusually high concentrations followed by other trace metals whose relative amounts seemed dependent on local geology. Compositional analysis of coatings by

SEM-EDX reveals MnO concentrations of up to 25% by weight (Hooke, et al., 1969; Allen, 1978; and Perry and Adams, 1978). This anomalously high amount is difficult to reconcile given background MnO concentrations in rock, soil, and dust on the order of 0.1%. Biological concentration is usually evoked to account for the MnO. SEM-EDX analyses by Hooke, et al. (1969) on varnishes from Death Valley revealed an outer layer rich in Fe and Mn, with Mn/Fe increasing toward the outer surface, and an inner zone enriched in SiO_2 and Al_2O_3. The total thickness of the varnish was 20-50um. Optical and SEM-EDX analysis by Allen (1978) on varnishes from Sonoran Desert rocks indicated high concentrations of magnesium as well as manganese and iron. This metal rich layer is approximately 20um thick and includes a "clay-like" matrix separated from the host rock by a 1mm thick weathered cortex. The cortex is composed of unoriented microcrystals probably derived from the host. These thin layers, also described by Engel and Sharp (1958) are attributed to the weathering process. Allen concluded the source for the metals is external to the host.

The significant contribution of both SiO_2 and Al_2O_3 to the chemical composition of coatings is attributed by Allen (1978) and Potter and Rossman (1977, 1979) to clay minerals. Potter and Rossman feel the iron and manganese oxides of varnish are in intimate association with mixed

layer illite-montmorillonite clay minerals. They still surmise, however, that the clay minerals are probably externally derived by wind. Farr and Adams (1984) and Curtiss, et al. (1985) discovered short lived hydrous alumina-silica coatings up to 5um thick on very fresh basalts in semi-arid parts of Hawaii.

Recent investigations stress a possible biological origin for some desert varnishes (Krumbein and Jens, 1981; Dorn and Oberlander, 1981; Taylor-George, et al., 1983; Staley, et al., 1983). It was noted above that some workers propose that all elemental constituents in varnish are derived externally. Neutron activation analyses by Knauss and Ku (1980) for trace elements and radioisotopes indicated that both uranium and associated thorium in desert varnishes from the Colorado Plateau in Utah were derived from sources external to the host rocks. In a contrary view, Glasby, et al. (1981) hold that varnish on dolerite from Antarctica is derived by leaching of elements from the substrate. They arrive at this conclusion by comparing analyses of whole rock with varnish compositions, the latter of which is not enriched in manganese as is the case with varnishes from the Southwest U.S.

The little previous work that has been conducted on the spectral characteristics of desert varnish and its influence on imagery has been rather general. Longshaw (1974) drew attention to the fact that secondary

environmental effects alter rock surfaces and can change their spectral character. Abrams and Siegal (1980) presented spectral curves comparing a fresh cut andesite surface to its weathered counterpart. They noted that the absorption peak at 1.9um was essentially smoothed-over on the altered surface. The spectral curve of the altered surface, furthermore, was quite steep, from 1.5 to 2.2um, in comparison to the fresh surface, a feature discovered in our samples (Chapter VII) but not mentioned by them. Farr (1981) compared curves of varnished surfaces with unvarnished surfaces and noted a general depression of reflectivity throughout the visible and near infrared. Podwysocki, et al. (1987) describe effects of desert varnish on thermal infrared multispectral scanner data (TIMS). They found that quartz mineral restrahlen minima, typically at 8.7um, move to slightly longer wavelengths with varnish cover. Although they attribute the shift to possible clay content in the varnish, the shift may be due to the high iron and manganese in the varnish.

DEFINITION

The term "coating" is used here to denote, more inclusively than desert varnish, all secondary surficial mineral products, regardless of origin. Mineral coatings are thus any inorganic secondary mantle or weathering product that occurs on the outer surface of rocks to an

indefinite depth and conceals to some degree fresh, primary lithologies. Coatings could conceivably consist of secondary replacement products developed by hydration, hydrolysis, or metasomatic ionic exchange with primary rock minerals, or precipitated or attached exogenous material. The term coating seems appropriate since we do not intend to include pervasive secondary products such as hydrothermal alteration or auto-oxidation of tuffs during cooling. Throughout this paper, the term coating is often used synonymously with desert varnish when desert varnish is the subject coating. The composition of any inorganics present is not to be treated except inasmuch as they serve as catalysts to help control the chemical environment of coating formation.

For purposes of remote sensing, we are concerned with the entire surface of any rock exposure, which may include both true desert varnish, subvarnish alteration zones, and relatively fresh rock with or without an incipient phase of alteration. Any given scene typically contains a combination of rock surface types, depending on host composition, textures, and topographic occurrence. Desert varnish is quite varied in maturity, darkness, and extent, even within a hand sample. One of the great lessons of this study is that the eye is deceiving. A hand sample of very well developed desert varnish - varnish that is extremely dark and pervasive - when viewed under a

binocular scope in thin section and at 30-200 power with the SEM, turns out to be surprisingly discontinuous. Results presented in this chapter lead to the conclusion that very heavy varnish over a 15x15cm slab of rock typically covers only about 50% of the surface to any significant extent.

A qualitative scale was selected for desert varnish comparison:

Very heavy - very dark chocolate brown or very dark gray, pervasive and complete coverage to the naked eye.

Heavy - very dark but coverage is only 50% - 75% to the naked eye, OR coverage is complete but intensity is very dark to moderate.

Moderate - dark varnish covers 30% - 50% of the rock surface OR intensity is moderate in comparison to heavily varnished surfaces.

Light - varnish is generally light in intensity or darkness and appears to cover 50% or more of the rock to the naked eye.

Very light - varnish is generally very light in color and appears to cover 30% or more of the rock surface.

Although one can readily select examples of desert varnish exhibiting variations that do not fit one of these categories ideally, for purposes of comparing coated

surfaces and collecting spectral measurements, compliance with the above classification scheme was useful. It is important to emphasize that this is a field classification with application by the unaided eye. It is generally a linear scale, each successive category representing approximately equal increments in varnish variation.

NATURE OF COATINGS IN THE PROJECT AREAS

Coatings on the volcanic rocks at Stonewall Mountain, Black Mountain, and Kane Springs Wash are typical of weathered surfaces on rocks throughout the semi-arid West and Southwest, U.S. This section addresses the nature, distribution, and compositional character of coatings in the 3 study areas. Analytical methods were described in Chapter II. Results of this research have been published previously by Spatz, Taranik, and Hsu (1987b and 1987c).

DISTRIBUTION

Coatings vary with underlying host rock in a manner generally congruous with host petrochemistry, degree of welding, devitrification, hyalinity, porosity, and other textural and physiochemical properties. Coatings may vary consistently enough from one formation to another to differentiate units in the field, inferentially. The basic observation and assumption is that darker, thicker coatings

represent the more mature accumulations, which correlate well with relatively dense insoluble rocks, resistant to chemical and mechanical degradation. Examples of coatings on outcrops of various volcanic rock assemblages are given in Figures 5, 6, 7, 12, 17 and 22.

Desert varnishes at these study sites tend to be thin, translucent films that resemble a stain at the rock surface (Figures 8, 9, and 16). Coatings penetrate into the substrate up to about 0.5mm, intergranularly between mineral grains and lithic fragments. Coated surfaces are underlain by a weathering rind or cortex that exfoliates, falling eventually from the outcrop, exposing an unvarnished surface that in time will redevelop varnish, and which in turn will be removed on another exfoliation surface. Thus any given outcrop of dense rock, like densely welded ash flows, basalt, and rhyolite flow domes that host mature coatings will also exhibit surfaces with varying degrees of desert varnish. Even within a zone of quite dense, mature varnish, fresh mineral grains are randomly exposed and varnish cover is discontinuous (Figures 48 and 49).

The case hardened weathering rinds that varnishes tend to ride upon vary in thickness from about .5-20mm. The underlying substrate on the ash flow tuffs is usually a cream, buff, or orangy buff variably calcareous zone, stained lightly in places with limonitic iron oxides. The
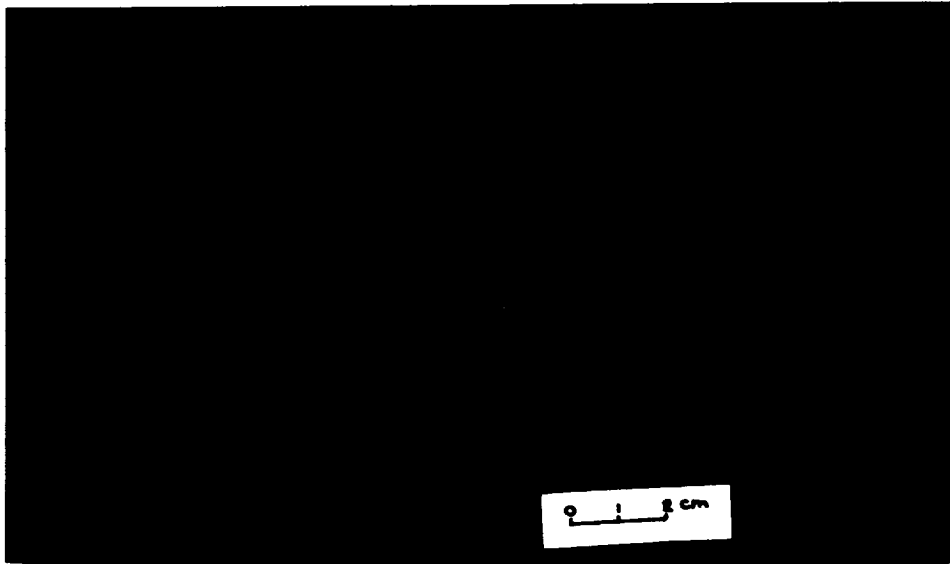
Figure 48. Hand specimen óf Spearhead Tuff of Stonewall Mountain, showing weathered desert varnish coated surface. Desert varnish concentrates in minute recesses and on a porous pumice fragment.
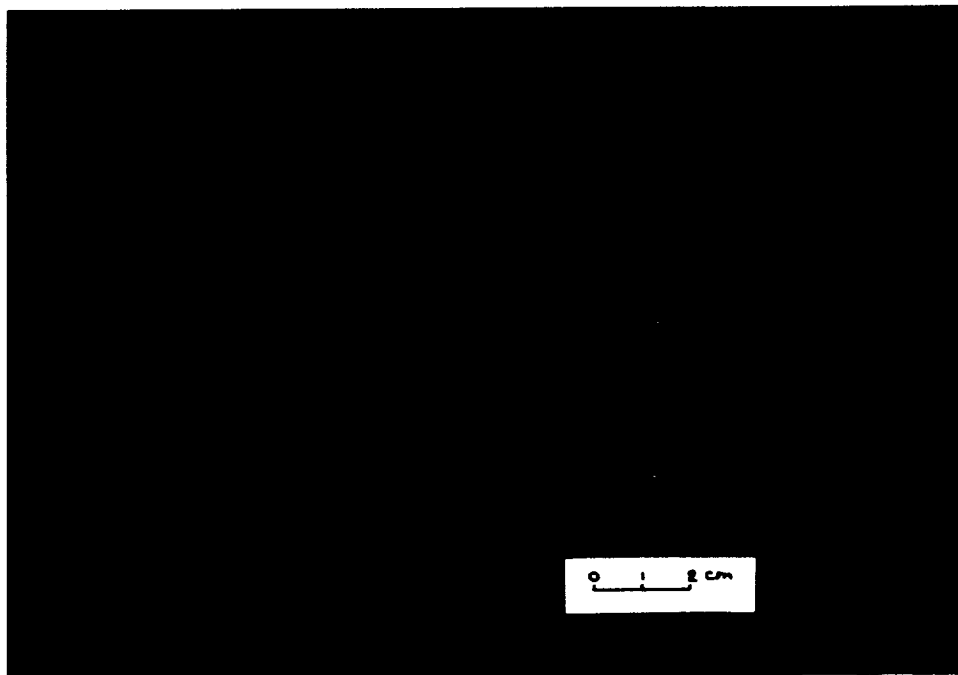
Figure 49. Hand specimen of topaz rhyolite of Kane Springs Wash, showing weathered surface and typical moderately well developed desert varnish.

zone is largely absent from most lavas and vitric tuffs, particularly the basalts and mafic trachytes. Thin section observation revealed that some subsurface zones contain a sublayer of secondary calcite (Figure 8).

Proportional density slices of a black and white photograph of densely welded Civet Cat Canyon Tuff (Figure 50) show the distribution of desert varnish within a surface exhibiting moderately mature coating development. In this example a fresh rock exposure is used for calibration, and surfaces that are darker and known from visual observation to be coated are segregated by density slicing to reveal coating distribution - in this case, 37%. Bear in mind that this represents a zone of outcrop with relatively mature coating development and that a significant proportion of any sizable outcrop contains uncoated surfaces.

Thin section and SEM observation reveal that rock surfaces with varnish encrustation or layering are relatively minor, most of the coating consisting of a thin, penetrative film (Figure 25). Where coating accumulation with layering has been observed, it tends to favor small recesses in the rock surface (Figures 14 and 51). Thicknesses observed vary from less than 5 to 50um but thicknesses greater than 10um are rare. There seems to be some tendency for coatings to accumulate at surface intersections with thin glassy zones in the tuffs, even

Figure 50. Gray level density slice (right) of black and white photograph (left) of Civet Cat Canyon Tuff with moderately well developed desert varnish. The gray level separation was controlled visually to distinguish fresh rock exposure (F) from darker desert varnish coatings. Note desert varnish cover is 37%.
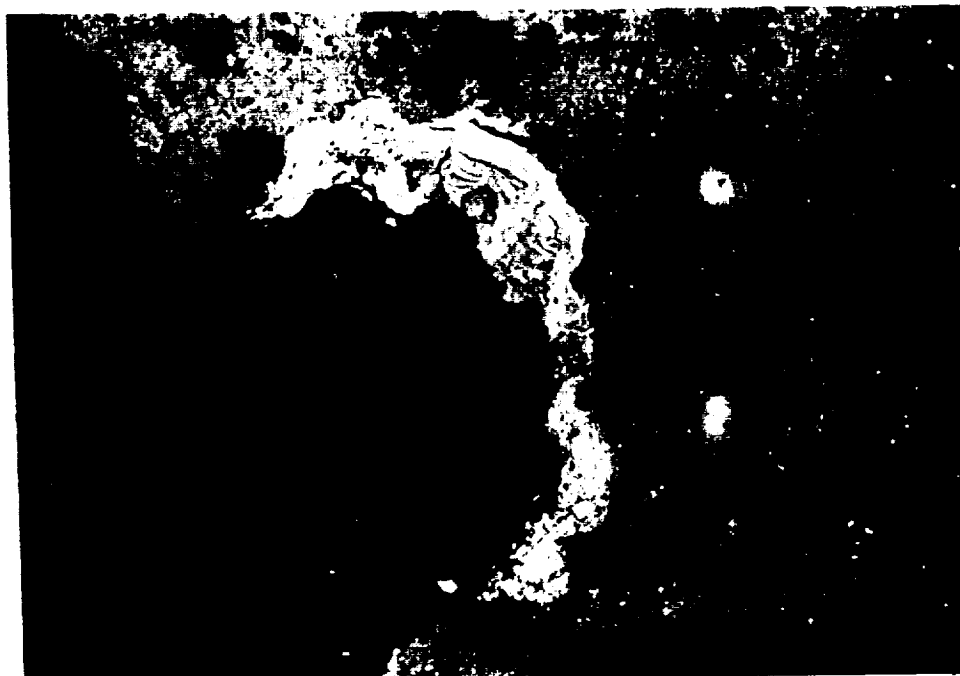
Figure 51. Scanning electron microscope backscatter image of a polished section of Civet Cat Canyon Tuff of Stonewall Mountain, showing exceptionally thick accumulation of desert varnish (light tone) in a protected recess. The varnish zone is very finely laminated due to successive increases and decreases of Fe and Mn relative to Al and Si.

though glassy units in general do not typically exhibit very continuous coatings due to their nonresistant nature. Figure 52 shows varnish distribution on a "heavily" varnished surface at high magnification. Compositional probes (Table 21) of variably varnished areas under high magnification show that a large proportion of the surface contains very little desert varnish.

CHEMICAL COMPOSITION

Coating compositions, in general, are consistent in major elements from unit to unit. SEM-EDX probes indicate desert varnish is composed chiefly of iron, manganese, silica, and aluminum (Figure 53 and Tables 21 and 22), iron and manganese accounting for roughly half. The coatings contain some titanium, calcium, potassium, and sodium. Calcium tends to be depleted more than sodium and potassium, relative to the underlying host rock. The coatings and the underlying weathering rind both contain higher H_2O and sulfur than the host rock (Table 23).

The Fe/Mn ratio in desert varnishes varies. The most consistent relationship seems to be that manganese forms laminar concentrations (Figure 54) and is commonly observed at a peak in concentration at the outer surface of the coating (Figure 55). Iron tends to remain fairly constant throughout the coating, and the Fe/Mn ratio usually increases toward lower levels of the coating.
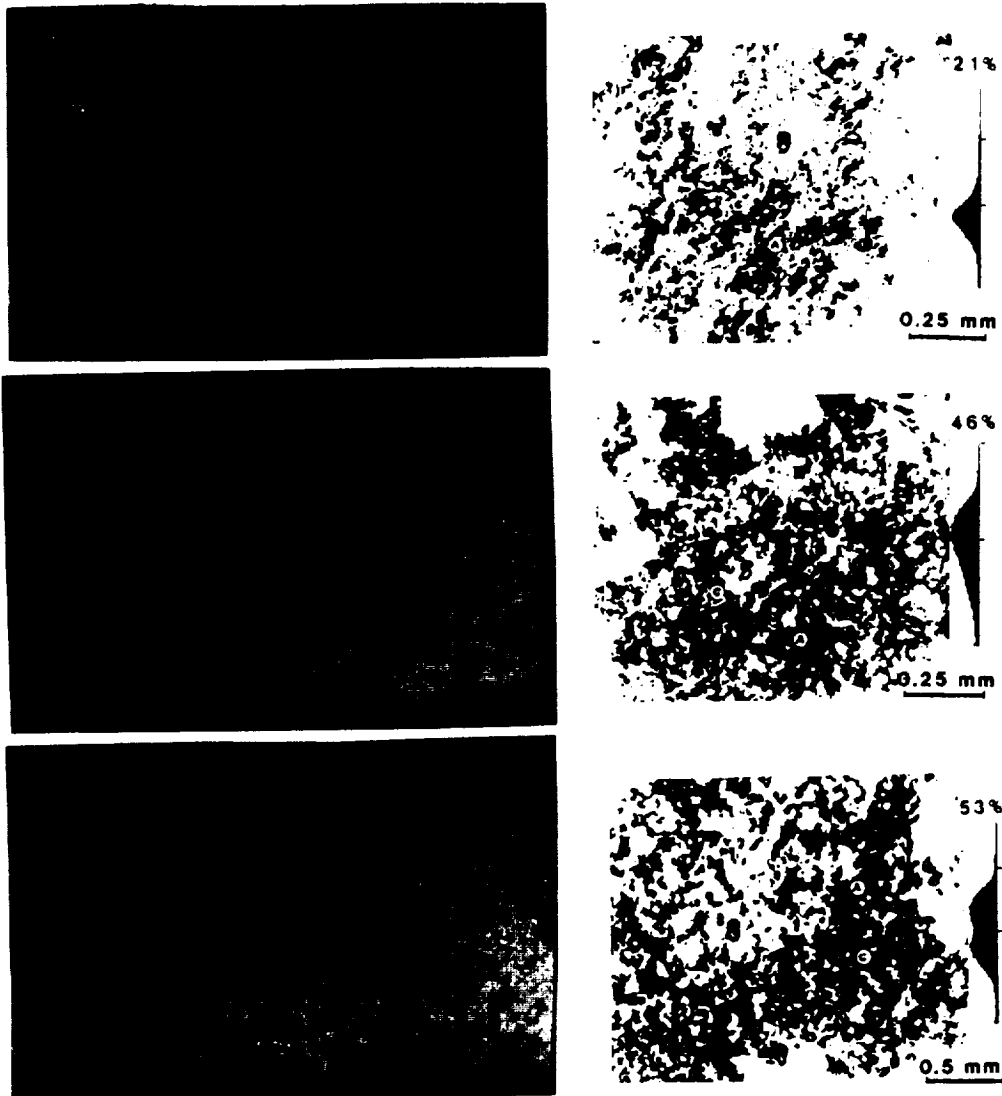
Figure 52. Scanning electron microscope image (backscattered primary electron) of 3 rock surfaces with heavy varnish development: Gold Flat Tuff (top), Spearhead Tuff (middle), and Civet Cat Canyon Tuff (bottom). Hand samples, density slice gray levels, and percent desert varnish cover are shown for each.
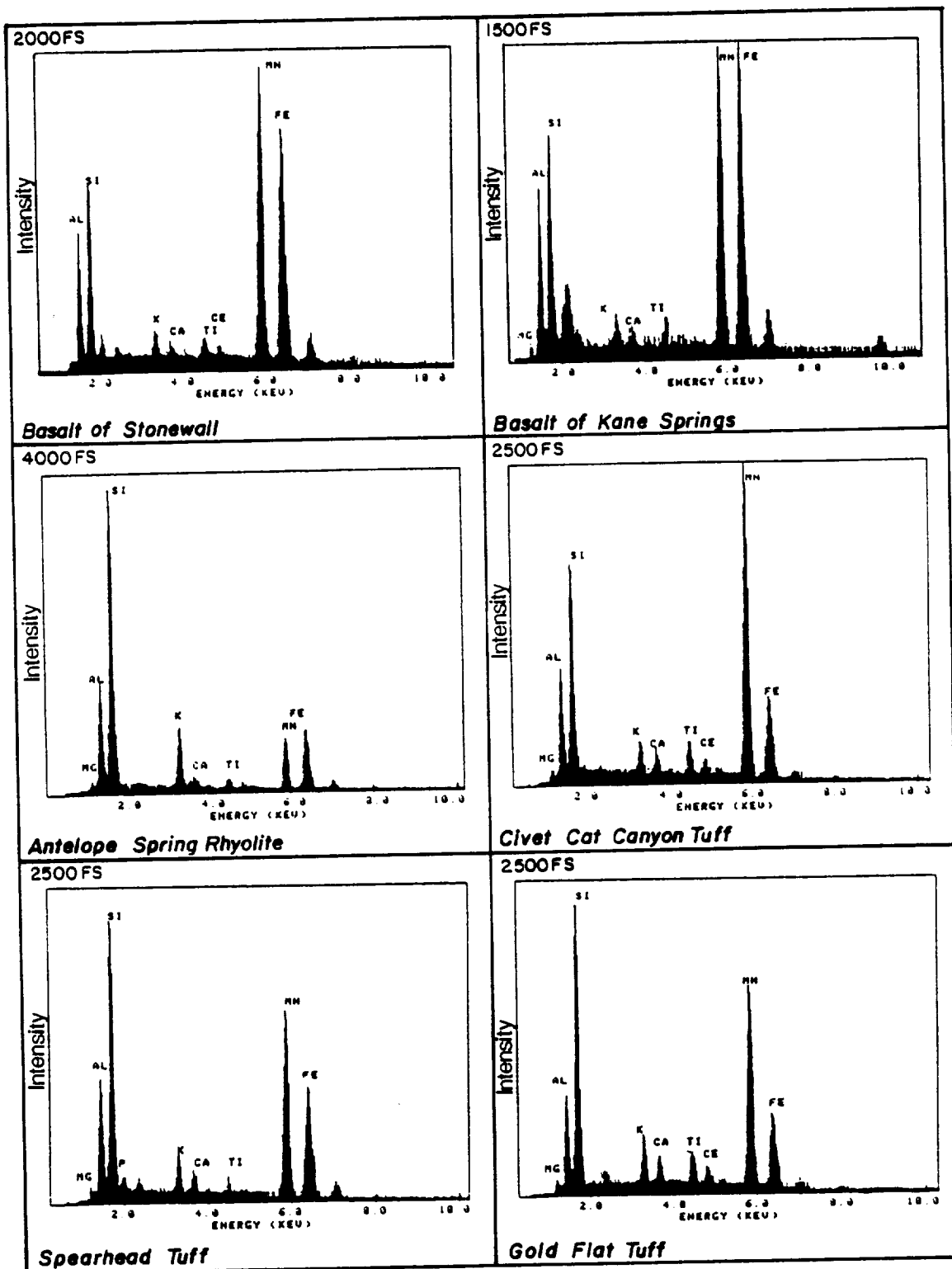
Figure 53. Scanning electron microscope probes (energy dispersive x-ray system) of desert varnish zones on 6 rock samples of various compositions. Element peaks record relative amounts.

TABLE 21. SEM-EDX COMPOSITIONAL PROBES OF DESERT VARNISH AND ADJACENT UNVARNISHED AREAS (FEW MICROMETER SEPARATION) WITHIN SAMPLE OF "HEAVY" VARNISH.

(Letters correspond with those of Figure 52.
Results in oxide %, sample numbers in parentheses.)

	CIVET CAT TUFF (20)			LABYRINTH TUFF (16)			SPEARHEAD TUFF (27)		
	A	B	C	A	B	C	A	B	C
Na	----	1.88	----	----	3.73	----	0.07	5.19	0.71
Mg	1.70	0.00	1.73	----	0.05	----	1.73	0.01	1.00
Al	16.76	13.13	17.77	16.42	17.34	19.17	17.15	17.89	17.94
Si	26.72	75.44	28.05	34.43	64.83	38.07	34.53	64.98	40.80
P	----	----	----	----	----	----	2.09	0.29	2.29
K	1.58	5.20	1.72	1.86	6.24	1.81	1.93	4.70	3.12
Ca	1.39	0.60	1.24	0.97	0.31	1.12	1.31	0.31	0.94
Ti	3.20	0.30	2.66	1.21	0.35	0.98	1.24	0.35	0.77
Mn	39.48	1.31	37.63	29.13	0.56	24.96	24.78	2.03	18.55
Fe	7.28	1.97	8.01	14.99	6.52	12.97	14.57	4.26	13.35
Ce	1.91	0.16	1.79	0.99	0.06	0.91	0.59	0.00	0.53

	GOLD FLAT TUFF (25)			ANTELOPE SPRING LATITE (39)		
	A	B	C	A	B	C
Na	0.00	2.68	0.14	0.00	0.00	0.35
Mg	2.06	0.01	2.97	3.23	1.28	1.77
Al	13.75	13.91	15.44	19.63	33.66	18.87
Si	37.01	72.47	38.79	42.99	55.01	49.27
P	----	----	----	1.04	----	----
K	2.57	4.98	2.23	2.49	0.66	4.85
Ca	1.86	0.52	1.87	1.54	0.54	0.81
Ti	3.50	0.12	2.72	1.25	1.03	1.43
Mn	27.77	0.28	24.15	18.63	3.96	9.68
Fe	8.98	5.02	9.57	8.33	3.12	12.25
Ce	2.49	0.00	2.13	0.87	0.74	0.72

A - Dense desert varnish   B - Very light to no desert varnish   C - Dense desert varnish

TABLE 22. SEM-EDX COMPOSITIONAL PROBES OF DESERT VARNISH
(Oxide %, totals to 100%, stoichiometrically,
sample numbers in parentheses.)

	CIVET CAT TUFF (20)			SPEARHEAD TUFF (27)		LATE BASALT (12) (Stonewall)			ANTELOPE SPR. RHYOLITE (10)
	1	2	3	1	2	1	2	3	
Na	----	----	----	----	0.07	----	----	----	0.01
Mg	1.71	1.70	1.73	1.63	1.73	0.91	0.87	----	1.29
Al	16.75	16.76	17.17	17.69	17.15	15.90	16.98	16.86	17.80
Si	40.08	26.72	28.05	33.86	34.53	18.40	19.88	19.56	32.00
P	----	----	----	----	2.09	2.26	2.63	2.09	----
S	----	----	----	----	----	----	1.36	----	----
K	2.84	1.58	1.72	1.84	1.93	1.14	1.08	1.05	1.70
Ca	2.99	1.39	1.24	2.80	1.31	0.67	0.76	0.72	1.14
Ti	0.87	3.20	2.66	1.35	1.24	1.93	1.62	1.78	0.98
Mn	25.36	39.48	37.63	29.63	24.78	33.77	32.31	31.35	29.30
Fe	9.40	7.28	8.01	11.19	14.57	23.64	21.59	25.32	15.77
Ce	----	1.91	1.79	----	0.59	1.37	0.91	1.27	----
Fe/Mn	.36	.18	.21	.38	.59	.70	.67	.81	.54

	GOLD FLAT TUFF(25)		LABYRINTH TUFF (16)		ROCKET WASH TUFF (46)	TRACHYTE OF HIDDEN CLIFF (11)		
	1	2	1	2		1	2	3
Na	0.00	0.14	----	----	----	----	----	----
Mg	2.06	2.97	----	----	1.94	1.58	0.12	1.34
Al	13.75	15.44	16.42	19.17	19.61	16.41	11.94	16.61
Si	37.01	38.79	34.43	38.07	38.41	31.37	22.83	31.35
P	----	----	----	----	----	1.86	0.49	1.75
S	----	----	----	----	----	1.16	0.44	1.55
K	2.57	2.23	1.86	1.81	2.77	1.55	1.71	1.59
Ca	1.86	1.87	0.97	1.12	1.10	1.79	2.21	1.71
Ti	3.50	2.72	1.21	0.98	1.11	2.07	2.67	2.29
Mn	27.70	24.15	29.13	24.96	20.31	32.11	42.43	30.36
Fe	8.98	9.57	14.99	12.97	14.76	8.59	13.07	9.85
Ce	2.49	2.13	0.99	0.91	----	1.50	2.08	1.58
Fe/Mn	.32	.40	.51	.52	.73	.27	.31	.32

	LATE BASALT KANE (21)	SYENITE (26)		NIKO TUFF (38)	ANTELOPE SPRING LATITE (39)	
		1	2		1	2
Na	----	----	----	----	0.35	0.00
Mg	2.20	1.95	----	1.18	1.77	3.23
Al	15.94	20.64	22.14	18.67	18.87	19.63
Si	18.24	20.52	23.58	36.30	49.27	42.99
P	----	4.10	3.41	----	----	1.04
S	----	1.19	0.63	----	----	----
K	0.83	0.69	0.33	1.56	4.85	2.49
Ca	0.59	0.48	0.78	0.65	0.81	1.54
Ti	2.18	0.73	0.05	1.28	1.43	1.25
Mn	28.13	33.69	33.18	28.39	9.68	18.63
Fe	31.88	15.49	15.89	11.96	12.25	8.33
Ce	----	0.52	----	----	0.72	0.87
Fe/Mn	1.13	.47	0.48	.42	1.27	.45

TABLE 23. ICP ANALYSES* OF WEATHERING RINDS OR CORTEXES (R), AND UNDERLYING FRESH ROCKS (W)

		CO_2	S	FeO	$+H_2O$	$-H_2O$	SiO_2	Al_2O_3	Fe_2O_3	MgO	CaO	Na_2O	K_2O	TiO_2	P_2O_5	MnO	LOI
BM-13 Trachyte of Hidden C.	(R)	0.88	0.033	4.21	0.27	0.37	57.42	17.17	7.39	2.11	5.18	4.91	3.99	1.060	0.72	0.17	1.61
	(W)	1.09	0.005	3.59	0.20	0.32	58.21	17.37	7.38	1.96	5.28	4.97	4.06	1.070	0.78	0.16	1.50
BM-46 Rocket Wash	(W)	0.39	0.008	0.57	0.25	0.45	71.72	12.52	3.78	0.77	0.85	5.02	4.55	0.220	0.13	0.14	1.29
	(R)	2.07	0.004	0.35	0.25	0.35	67.88	14.15	3.72	0.26	3.41	5.37	4.85	0.250	0.15	0.14	2.75
BM-60 Gold Flat Tuff	(R)	0.46	0.050	0.94	0.29	0.54	70.15	11.37	6.51	0.55	1.19	4.76	4.41	0.310	0.21	0.17	1.87
	(W)	0.42	<0.001	0.93	0.20	0.25	70.43	11.92	6.54	0.25	0.88	5.00	4.75	0.310	0.17	0.17	1.10
KS-10 Kane Topaz Rhyolite	(R)	1.44	<0.001	0.31	0.10	0.21	74.44	13.15	1.08	0.18	2.34	4.31	4.45	0.030	0.11	0.03	2.15
	(W)	0.39	<0.001	0.28	0.08	0.22	76.43	13.38	1.16	0.12	0.94	4.29	4.42	0.040	0.09	0.03	1.09
KS-18 Kane Wash Tuff	(R)	3.12	0.023	0.17	0.39	0.40	72.76	10.27	2.11	0.60	4.80	3.21	3.97	0.150	0.17	0.05	4.55
	(W)	0.14	<0.001	0.31	0.26	0.25	78.40	11.84	2.10	0.14	0.66	3.67	4.53	0.140	0.25	0.04	0.86
KS-21 Kane Wash Basalt	(R)	0.07	0.002	6.48	0.28	0.25	48.60	16.39	12.10	6.50	8.65	3.07	1.24	2.000	0.73	0.16	0.79
	(W)	0.07	<0.001	5.98	0.26	0.19	54.89	17.15	9.18	4.46	7.71	3.09	1.94	1.480	0.47	0.12	0.38
KS-24 Kane Syenite Dome	(R)	0.14	<0.001	0.65	0.35	0.33	69.39	15.08	4.86	0.61	0.82	4.75	5.32	0.520	0.25	0.14	1.05
	(W)	<0.01	0.047	0.70	0.24	0.30	67.46	15.16	5.13	0.45	1.51	5.05	5.10	0.650	0.29	0.13	1.14
KS-26 Kane Syenite	(R)	0.07	0.003	0.47	0.45	0.30	69.20	14.82	4.62	0.16	0.62	4.76	5.20	0.440	0.21	0.07	1.14
	(W)	0.07	<0.001	0.33	0.33	0.31	69.58	15.12	5.14	0.14	0.77	4.90	5.38	0.500	0.20	0.05	0.98
SW-10 Antelope Spr. Rhyolite	(R)	<0.01	<0.001	0.19	0.47	0.18	75.00	14.62	0.58	0.05	0.18	1.12	9.92	0.130	0.15	<0.01	1.10
	(W)	<0.01	0.057	0.23	0.34	0.20	75.47	13.07	0.77	0.07	0.32	0.99	9.31	0.300	0.12	<0.01	1.16
SW-20 Civet Cat Tuff	(R)	2.18	0.008	0.25	0.24	0.30	66.76	14.77	2.83	0.47	4.02	4.26	5.48	0.360	0.22	0.10	3.17
	(W)	0.63	<0.001	0.12	0.52	0.37	70.87	14.41	2.71	1.00	1.87	4.20	5.31	0.330	0.22	0.10	1.95
SW-27 Spearhead Tuff	(R)	3.39	0.033	0.11	0.46	0.36	70.50	10.61	2.01	0.49	5.73	3.53	4.03	0.120	0.19	0.07	5.34
	(R)	0.21	0.248	0.17	0.84	0.54	72.94	11.51	2.44	0.74	2.03	3.79	4.27	0.120	0.72	0.11	2.97
	(W)	<0.01	<0.001	0.08	0.11	0.10	75.63	13.14	2.51	0.14	0.51	4.30	4.75	0.160	0.27	0.09	0.44
SW-50 Civet Cat Tuff	(W)	0.14	0.005	0.16	0.33	0.20	71.61	14.79	2.79	0.31	1.34	4.23	5.45	0.310	0.42	0.11	0.83
	(R)	0.56	<0.001	0.23	0.24	0.25	72.36	14.04	2.55	0.37	1.90	4.16	5.10	0.300	0.26	0.10	1.42

* Analyses performed by Chemex labs. Results in %.

LSW30A WMN ▦
LSW30A WFE ⌒‿
LSW30B WCA ⋯⋯

SEM-EDX

600FS

EPOXY   COATING   ROCK INTERIOR

Mn

Fe

Intensity

0.0   16.7   33.3   50.0   66.7   83.3   100.0
%Fullscan
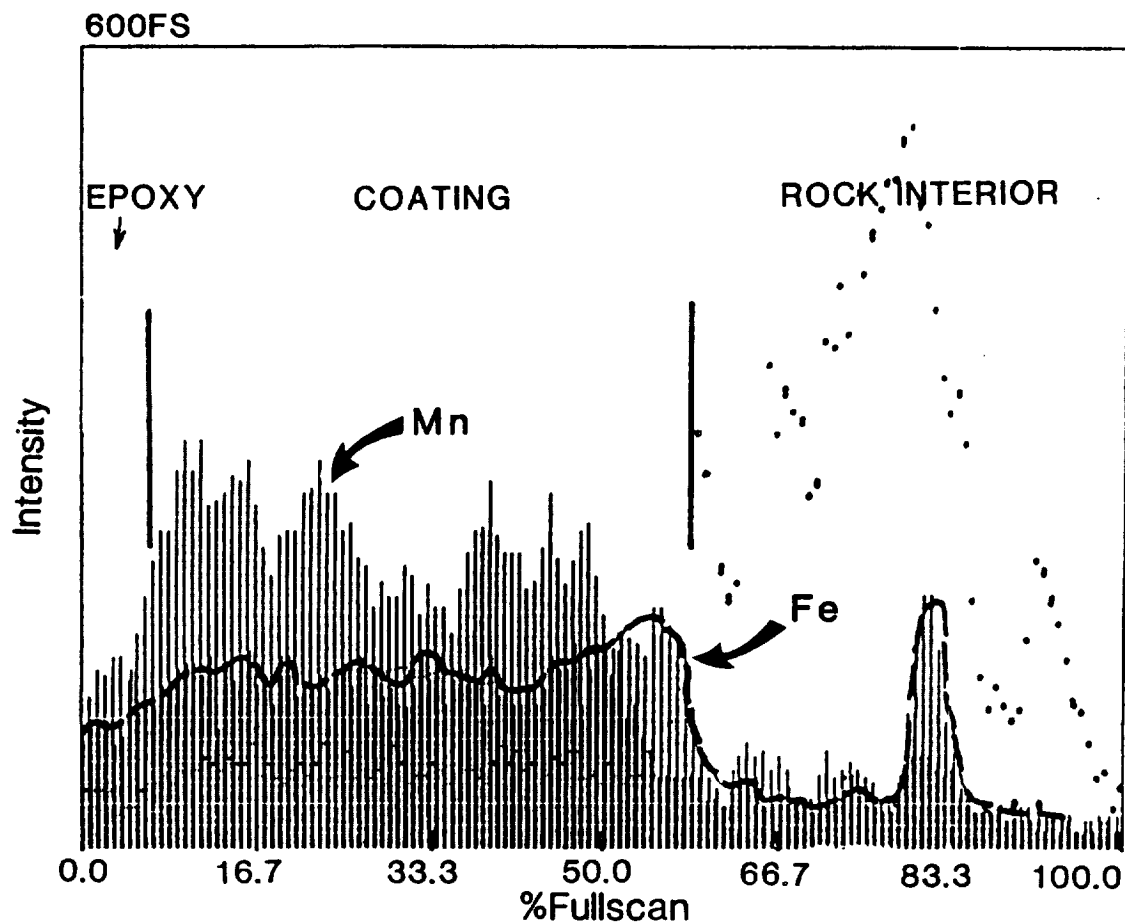
Figure 54. SEM-EDX compositional profile across desert varnish
zone on Spearhead Tuff of Stonewall Mountain. Laminations are
mirrored by Mn peaks, whereas Fe is present at a fairly constant
level. Note that Mn drops off at the rock interface before Fe,
resulting in a high Fe/Mn ratio.
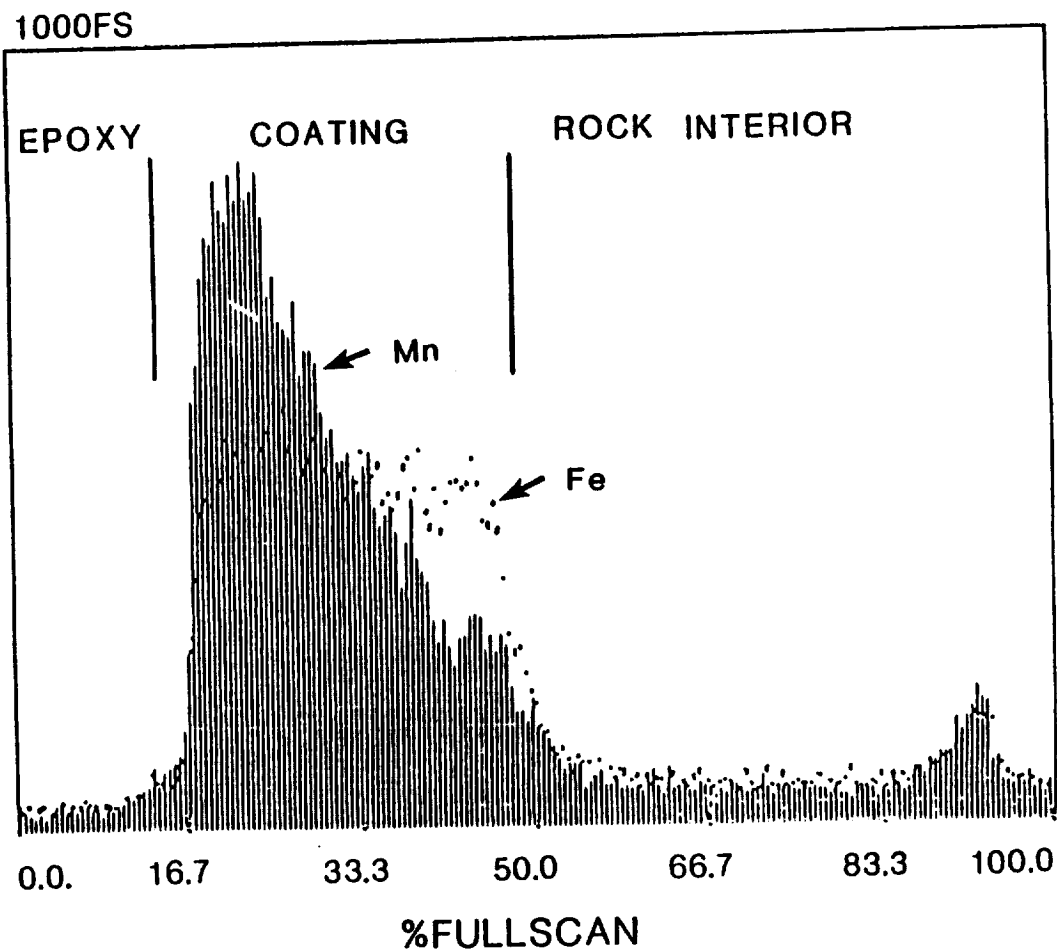
Figure 55. SEM-EDX compositional profile across desert varnish on Hiko Tuff of the Kane Springs Wash study site. Mn is concentrated at the rock-air interface, gradually decreasing toward the varnish base. Fe on the other hand is fairly constant throughout. A high Fe/Mn ratio occurs at the coating-rock interface.

Where coatings penetrate into the rock below encrusted layers, the Fe/Mn ratio is usually higher. Similar compositional zoning relationships are demonstrated by compositional SEM-EDX maps (Figures 56, 57, and 58). Table 24 compares compositional variation among desert varnishes on some of the rock units.

PHASES

Thin section observation, X-ray diffraction analysis, SEM-EDX probes, and IR spectrophotometry indicate that desert varnishes from the three study sites are composed of amorphous compounds. XRD curves are dominated by primary mineral phases, underlying and intermixed with the coatings (Appendix L). Elevation in XRD intensity over a broad area at a 2-theta value between 20 and 30 (Figure 59) indicates an amorphous "opaline" like compound. Two samples of coatings from older tuffs from Kane Springs Wash registered a 2-theta peak near a 2d spacing for the clay mineral. illite, but lacked most peaks characteristic of illite at other 2d spacings. The sample was run on the school's new Phillips XRG 3100 computerized XRD and compared with its disc powder file library. The only realistic mineral selected was a hydrous silicate - $H_2Si_2O_5H_2O$. It is likely the mineral is either a poorly ordered mixed-layer illitic clay or perhaps this hydrous silicate. Kaolinite is present in two coating samples from Stonewall Mountain -
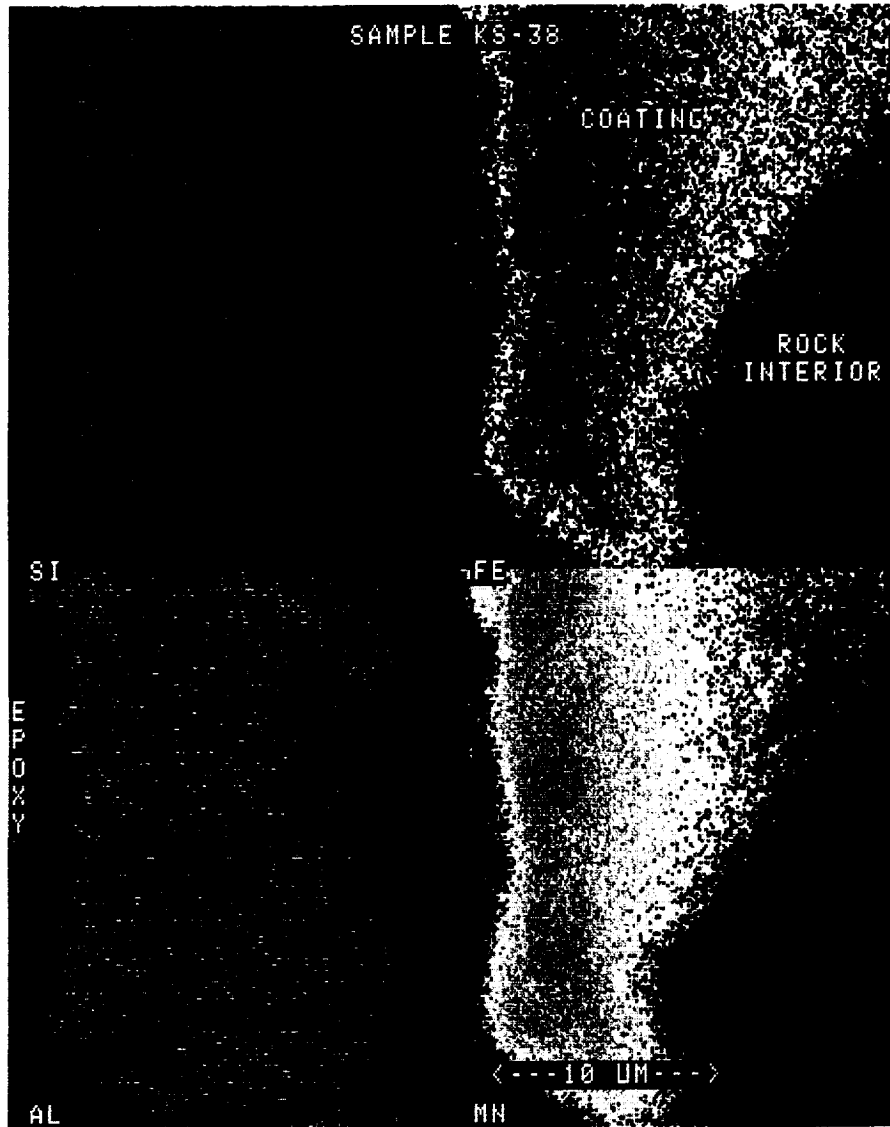
FIGURE 56. SEM-EDX compositional map of a polished section across desert varnish on the surface of Hiko Tuff, Kane Springs Wash volcanic center, showing concentrations of silica, aluminum. iron, and manganese. More intense colors track greater concentrations.

FIGURE 57. SEM-EDX compositional map of a polished section across desert varnish on Spearhead Tuff of Stonewall Mountain. More intense yellows reflect greater concentrations of iron, manganese, silica., and aluminunm.

SAMPLE SW-10
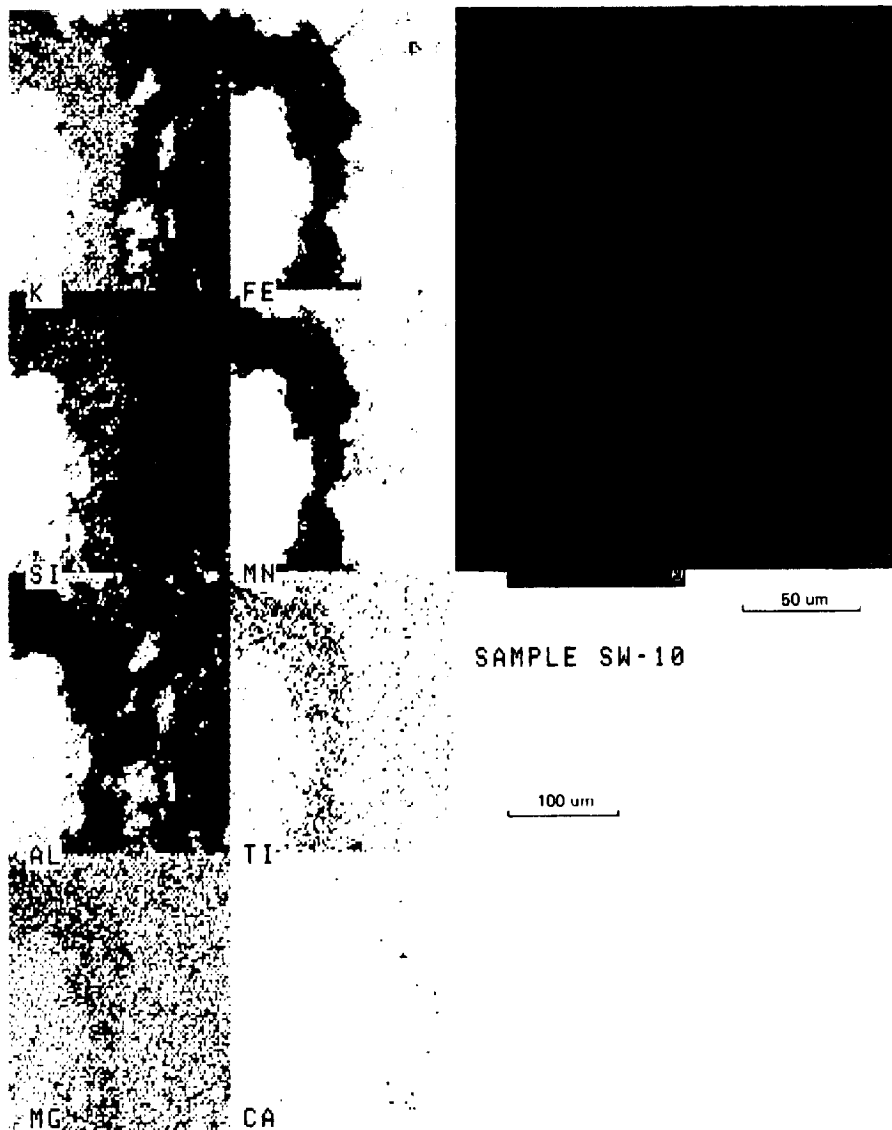
FIGURE 58. SEM-EDX compositional map of a polished section across desert varnish on Antelope Springs Rhyolite of Stonewall Mountain. More intense concentrations of potassium, silica, aluminum, magnesium, calcium, titanium, manganese, and iron are colored red, then green, and finally blue indicating lowest values. Larger image in upper right is nonselective backscatter image. Brighter blue hue indicates concentration of higher atomic number elements.
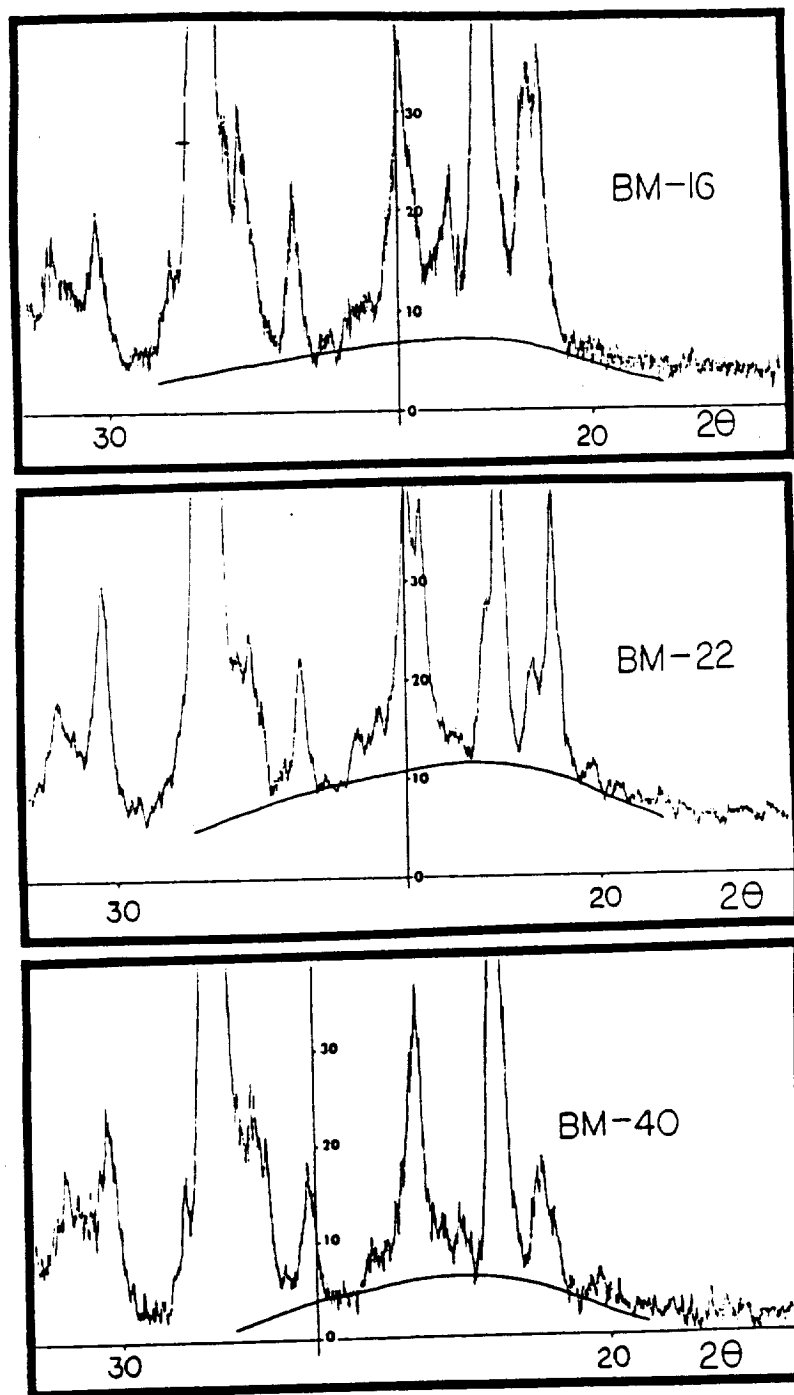
Figure 59.   X-ray diffraction curves of powders of rock surfaces with very heavy desert varnish deposits.   BM-40 is Trachyte of Hidden Cliff, BM-22 is Trail Ridge Tuff and BM-16 is Labyrinth Canyon Tuff.   Dark curved line demarks "amorphous hump" or broad zone where diffraction intensity increases due probably to presence of an opaline or amorphous substance.

TABLE 24. SUMMARY OF LITHOLOGICAL, PEROCHEMICAL, FIELD VARNISH,
TM IMAGERY, AND VARNISH COMPOSTIONAL CHARACTERISTICS

UNIT	PETROCHEMISTRY MAJOR	PETROCHEMISTRY MINOR*	FIELD VARNISH	IMAGERY HIGHLIGHTS BRIGHT	IMAGERY HIGHLIGHTS DARK	VARNISH COMPOSITIONAL HIGHLIGHTS*
Civet Cat Canyon Tuffs	Rhyolite slightly peralkaline	Slightly high Th, Be. REE, slightly low Sr, V, Mg	Very dark red-brown very densely welded, ledge former. Thin-platted float.	PCs 2,4 ISH-(1-2-4)S,H	Bs 1,2,3,4,5,7 3/2, PC1 ISH(3-5-7)I,H ISH(1-2-4)I	High K, Ce, Ti Low Fe/Mn
Spearhead Tuff	Rhyolite slightly peralkaline	High REE, Zn, Zr, Be, Ce. Low Sr, Mg, Ba, Co, Ni, V	Pale buff to buff gray, moderately welded, ledge former. Thick rough, slabby float.	3/2, PCs 2,3,4 ISH(3-5-7) H	Bs 1,2, PC 1 ISH(3-5-7)I ISH(1-2-4)I,H	High Na Low Fe/Mn
Basalt Flows Stonewall	Low silica basalt	High P, Sc, V, low U, Th	Very dark gray very dense, massive mesa cap in places.		Bs 1,2,3,4,5,7 PC 1 ISH(3-5-7) I, S,H ISH(1-2-4) I	High P, Fe/Mn Low Mg, Si, K
Antelope Springs Rhyolite	Rhyolite, slightly alkaline	Slightly high Hg, Tl, Th	Very light cream-colored. Forms steep slopes, cliffs and knobs. Joint-bound blocky float.	Bs 1,2,3,4,5,7 3/2,5/2,5/4,5/7 PC 1 ISH(3-5-7) I,S ISH)1-2-4) I	PC 2 ISH(1-2-4) H	Low Ti
Antelope Springs Latite	Latite High silica, potassic latite to subalkaline rhyolite.	Slightly high Cs, Ba	Reddish brown color. Form low, hummocky hills. Weathers to friable cobble-size float.	3/2, PCs 1, 3 ISH(1-2-4) H	Bs 1,2,3,4,5,7 5/4, PC 2 ISH(3-5-7) I, S, H ISH(1-2-4) S	High Si, Mg, K
Labyrinth Canyon Tuff (Spearhead)	Peralkaline rhyolite	High HF, Hg, Rb, Tl, B. Low Sr, Ba	Tan in color, densely to moderately welded thin, platy ledge former.	Bs 4,5,7, 3/2 5/2, 5/4, PC1 ISH-S,H	PCs 2,3,4	Low Ca, Ti
Trachyte of Hidden Cliff	Mafic trachyte	High P, Sc, Sr, Mn Ti, V, Ba, Eu, Co, Mg. Low Rb, B	Dark gray, rough, hummocky boulders confined largely to Black Mountain.	5/7, PCs 2,3	Bs 1,2,3,7 PCs 1, 4 ISH-I, H	High P, Mn, Ce Low Si, Mg, K Low Fe/Mn
Gold Flat Tuff	Peralkaline pantellerite	High REE, Be, Pb, Sn, Th, Nb, Rb, Ta, U, Zr, Sn, As, B, Ca, C, Cu, F, Li	Pale olive gray moderately welded, Forms blocky slabs in float. Tops mesas.	Bs 4,5,7 3/2,5/2,5/4 PC 1 ISH-S,H	5/7, PCs 2,3 PCs 4,5 ISH-I	High Na, Ti, Ce Low Fe, Mn
Late Basalt Kane Spr.	Olivine basalt	High Ni, P, Sc, Ti, V, Cr, Co, Cu. Low Rb, Th, U, Li.	Very dark gray massive mesa caps. Forms blocky scree.	5/7	Bs 1,2,3,4,5,7 3/2, 5/2, 5/4 PC 1, ISH-I	High Fe/Mn, Ti Low Si, K
Syenite Complex Kane Spr.	Syenite and trachyte	High Mo, Zn, Zr, B Slightly high REE, As, Ba, F, Hf, La. Low C, Eu, V, Ni.	Cream colored domal knobs and rugged hills, weathers to exfoliated slabs and rough boulders.	Bs 1,2,3,4,5,7 5/2	PC 2 ISH-H	High Al, P Low Si, K, Ca, Ti Low Fe/Mn
Hiko Tuff	Subalkaline latite	Slightly High Sr, Ba Slightly low B	Coarse granularity results in "beehive" exfoliated mounds. Forms large boulders and rugged terrain.	Bs 1,2,3,4,5,7 3/2, 5/2, 5/4 PC 1, ISH-I	5/7	High Si, Low Fe/Mn, Mg

* Amounts (high or low) are relative to other units.

rhyolite and latite of Antelope Springs Formation. No clays registered from coatings on the ash flow units. Analcime was detected in the coating sample from a minor air fall tuff unit at Stonewall. Corroborative analytical attempts indicated that these minerals are likely contaminates from the rock substrate.

Infrared spectrophotometry scans of coatings (Figure 60) do not reveal any mineral phases indigenous to coatings. A broad absorption zone between about 4 and 8um indicates amorphous compounds. Variations in the water absorption peak at 6um indicates a variable hydrous component in the coatings.

SEM images of horizontal surfaces of desert varnish (Figure 61) exhibit coating morphology in noncrystalline, amorphous-looking form. Coatings appear as minute botryoidal or mammillary mounds. Lacy interconnecting networks of apparently younger varnish deposits wind around the mounds on some of the samples.

Just beneath the surface of most outcrops of ash flow tuff in the project areas is a thin dark ribbon (layer), typically about 1 to 5mm thick and about 1 to 3mm below the rock surface (Figure 62). These secondary layers of accumulation or cementation are described in more detail in the section that follows. They are believed to bear significantly on the origin of desert varnish.
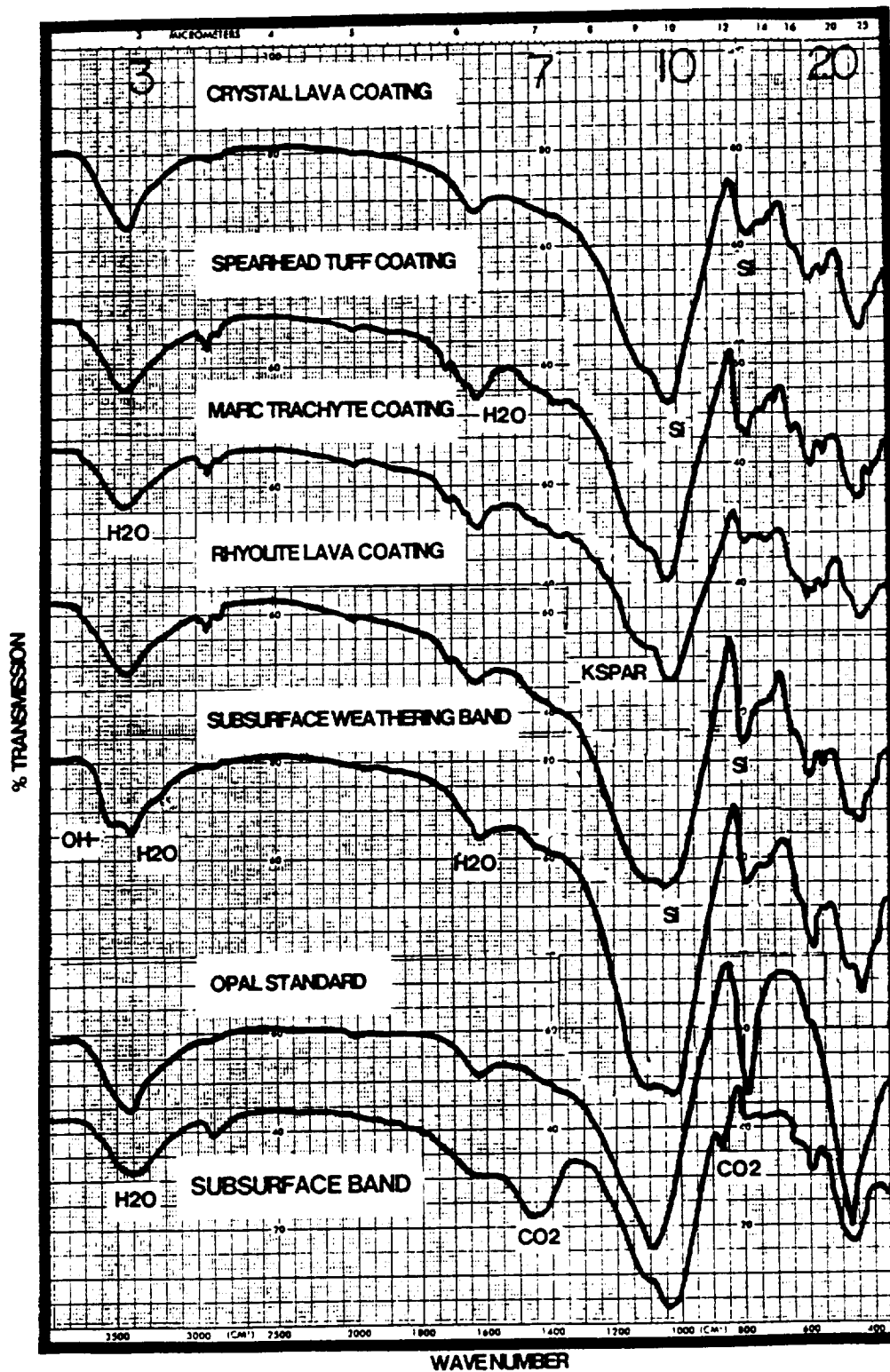
FIGURE 60. Infrared lab spectrophotometer curves of powder samples enclosed in KBr pellets. Absorption peaks for water, hydroxide, and possible carbonate are indicated.

169

ORIGINAL PAGE
COLOR PHOTOGRAPH

Figure 61. Scanning electron microscope image (secondary electrons at an instrument eV of less than 50) of exceptionally dense desert varnish on Civet Cat Canyon Tuff of Stonewall Mountain, showing lacy intergrowth of younger desert varnish (upper photo) and the generally noncrystalline amorphous appearance of desert varnish.
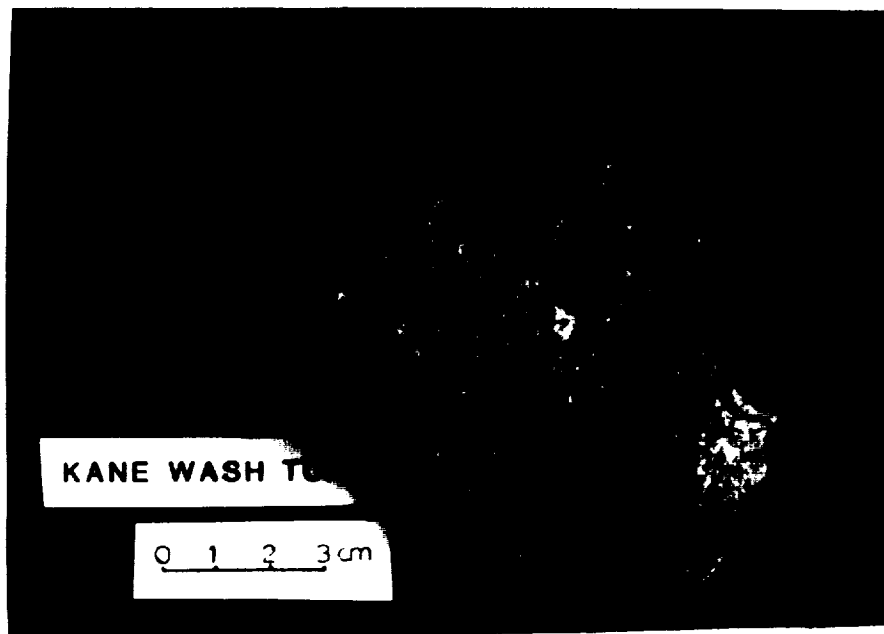
Figure 62. Cross section hand samples through weathered surface of Kane Wash Tuff, showing dark secondary layer of cementation developed just below the rock surface.

ORIGIN OF DESERT VARNISH

The following discussion reviews the analytical results obtained from coatings and the underlying rock substrate and the possible geochemical environments under which they formed. Speculation on genetic models is also presented.

Source of desert varnish elemental constituents is not known; however, most investigators believe the source is wind blown dust exogenous to the underlying host rock. The source of the iron and manganese in the coatings must ULTIMATELY be iron and manganese bearing minerals. The primary sources of wind blown dust that comes to rest on the rock surfaces is in the opinion of this author the very rocks themselves, a conclusion Engel and Sharp (1958) and Elvidge (1979) arrived at through general speculation as well, after considering alternative sources, including present day volcanic expulsion. It is likely, therefore, that the source of the iron and manganese in desert varnish is the rocks upon which they lie or rocks within the immediate vicinity. I have investigated the substrate below the coatings including the weathering rinds and the dark secondary layers they contain, as well as the coatings themselves, to explore a possible genetic connection.

From field observation, we know that mineral coatings and desert varnish are indeed products of the weathering environment. From considerations on the geochemistry of

C-3

natural waters, iron and manganese, we can establish a likely geochemical environment within which the relationships we observe make sense. Important considerations will include pH, Eh, and dissolved ions. My analytical research indicates that coatings are composed of amorphous compounds or poorly ordered hydroxides of manganese, iron, silica, and aluminum. Clay appears to be a minor constituent.

GEOCHEMISTRY OF IRON AND MANGANESE

Figure 63 shows Eh-pH relationships for both iron and manganese. Under moderately oxidizing conditions, both iron and manganese are soluble below a pH of about 6, but form oxides and hydroxides at higher alkalinities. Noncrystalline phases are favored by rapid precipitation which would be expected on the surface of rocks in semi-arid environments where dissolution and precipitation may follow pH fluctuations after rain showers. Manganese is more mobile than iron and thus precipitates more slowly. Manganese can remain soluble in aerated waters at pH values in excess of 9.0, whereas iron likely would be precipitated (Hem, 1964). This behavior probably accounts for the observed high concentration of manganese relative to iron at the outer desert varnish surface and manganese concentration in layers within the coatings when the whole system is viewed within a cyclic climatic condition
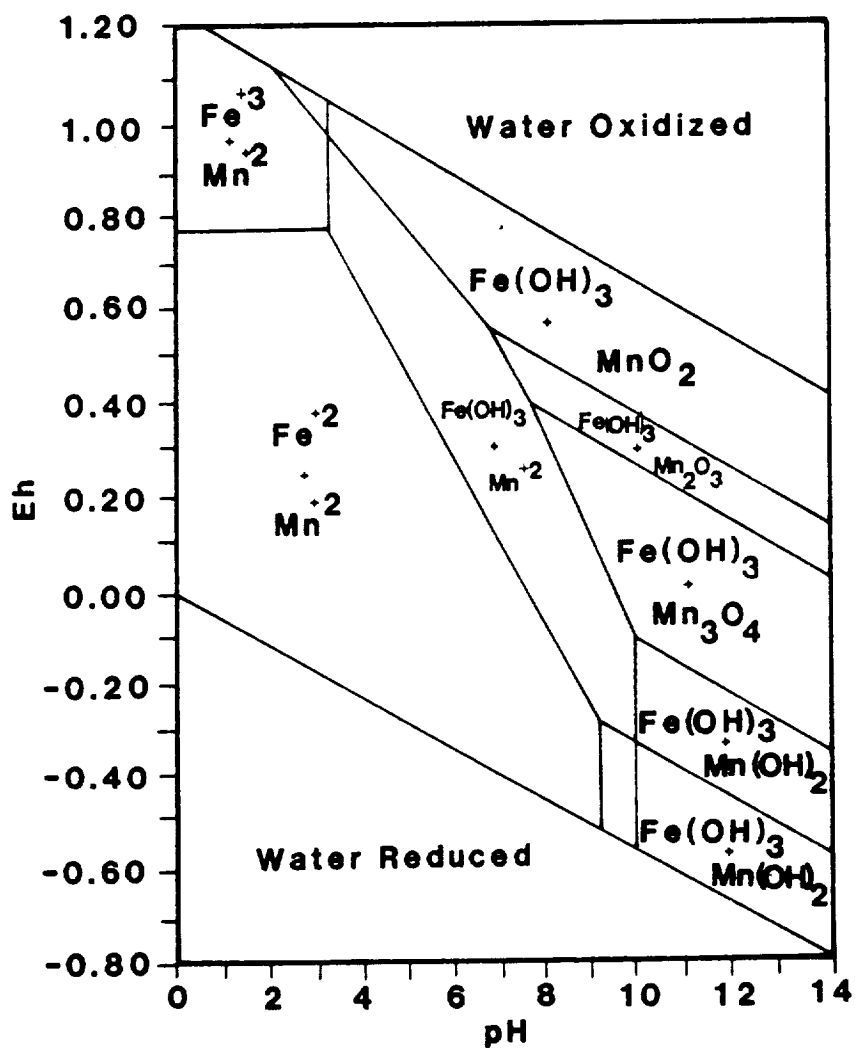
FIGURE 63. Eh-pH diagram for Fe and Mn at standard T and P. (Modified after Krauskopf, 1967)

involving either humidity or temperature. Slightly cooler climates may favor increased CO_2 concentration, prolonged acidic conditions, and greater dissolution and concentration of both iron and manganese.

Carbon dioxide as undissociated carbonic acid, and bicarbonate, and carbonate ion is the pH buffer of most natural waters (Hem, 1960). The atmosphere contains about 0.03 percent CO_2 by volume, but plants contribute further CO_2 by respiration and decay. According to Hem, only a small proportion of CO_2 dissolved in water forms carbonic acid. Thus rain water, falling and collecting on the surface of the volcanic rocks in southern Nevada, would likely be further enriched in CO_2 from lichen and other organics growing on the rocks. An acidic environment around lichen is supported by the general lack of desert varnish around lichen; however, Osborn (1960) mentions that crustose lichen metabolize iron and remove it from the rock. These relationships are further obscured by the fact that lichen in the Kane Springs Wash study area seem to favor poorly welded, vapor phase altered tuffs, which do not typically develop mature coatings anyway. Lichen tend to accumulate in the recesses of the rocks where water drains, collects, and resides the longest.

Hem (1963) found that precipitates of manganese, formed at pH values between 8 and 9, contained too little manganese to be manganese oxides, suggesting that the

precipitates contained water. He speculated that the solid phase was likely $Mn(OH)_3$. Hydrous precipitates of both iron and manganese lose water and grow increasingly less soluble with time. Johnston and Lewis (1983) found that with time ferrihydrite converts to hematite by a particle coalescing event.

WEATHERED CORTEXES AND DARK SUBSURFACE BANDS

A weathering rind develops on all the volcanic rock types studied (Figure 64). It is a 0.3-15mm thick plate that exfoliates outcrop surfaces and spalls off, carrying the coatings with it. Table 23 compares major element analyses of the rinds with their parent rocks.

Rinds are enriched in CO_2 relative to interiors on the tuffs but not relative to interiors of dense rhyolites or basalts. Rinds tend to contain more sulfur and both essential and nonessential H_2O. Rinds appear depleted in SiO_2 relative to underlying interiors. For the most part rinds show some apparent depletion in Al_2O_3, especially those of the more porous tuffs. For most cases there is a slight depletion in total iron (reported as Fe_2O_3) in the rinds. The major exceptions are basalt from Kane Springs Wash (KS-21) and other mafic units. MgO and CaO are enriched in rinds. MnO shows, if anything, a slight enrichment in the rinds. As will be discussed later, SEM-EDX probes indicate some geochemical stratification within

the weathered cortex itself.

From thin sections and application of hydrochloric acid to hand samples we know that the rinds contain carbonate which would account for their enrichment in CaO, MgO, and CO_2. The higher H_2O content of the rinds indicates hydration and apparent depletion in alkalis, and iron suggests leaching. The rinds are weathered cortexes and reflect geochemical interaction with the weathering environment. The extent to which they may relate to coatings is discussed below.

SEM-EDX analyses of the dark layers that occur within the weathered cortex (Figures 62 and 64) are tabulated in Table 25. Composition of the layers is similar to that of the weathering cortex (Table 23). Enrichment in CaO is the only consistent compositional difference between the secondary bands and the enclosing weathering cortex. From thin section petrography we know that some of the secondary layers are distinctly carbonate rich. Zeolites have been tentatively identified, but the association may be coincidental. Backscatter SEM imagery reveals that the layers are dense, less porous, and evidently zones of cementation (Figure 65). They appear harder to a knife blade as well. The layers seem to contain a distinct hydrous component (infrared spectra, Figure 60), and they appear cloudy in thin section suggesting presence of an amorphous compound, perhaps similar to that which
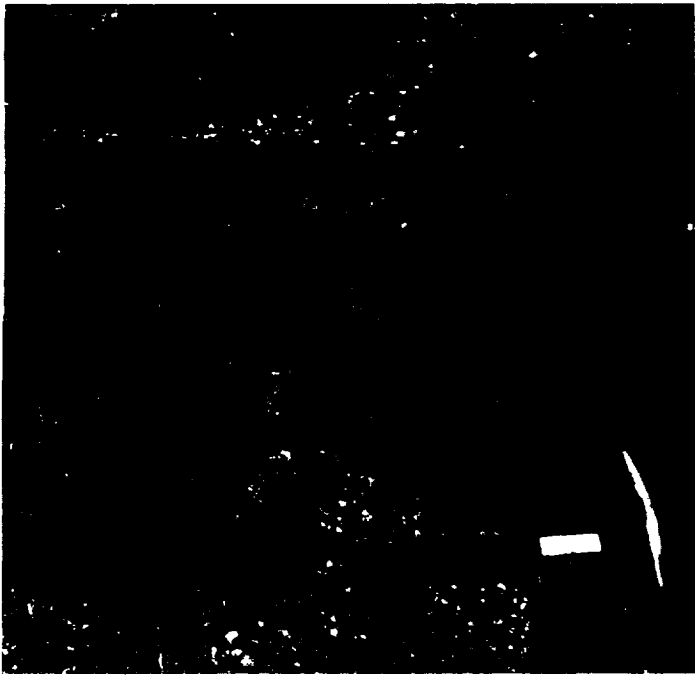
FIGURE 64. Artist's rendition (lower drawing) of outcrop of Civet Cat Canyon Tuff (upper photograph), showing relationships between desert varnish, weathering cortexes, and secondary subsurface layer of cementation and Ca enrichment.

CIVET CAT CANYON TUFF
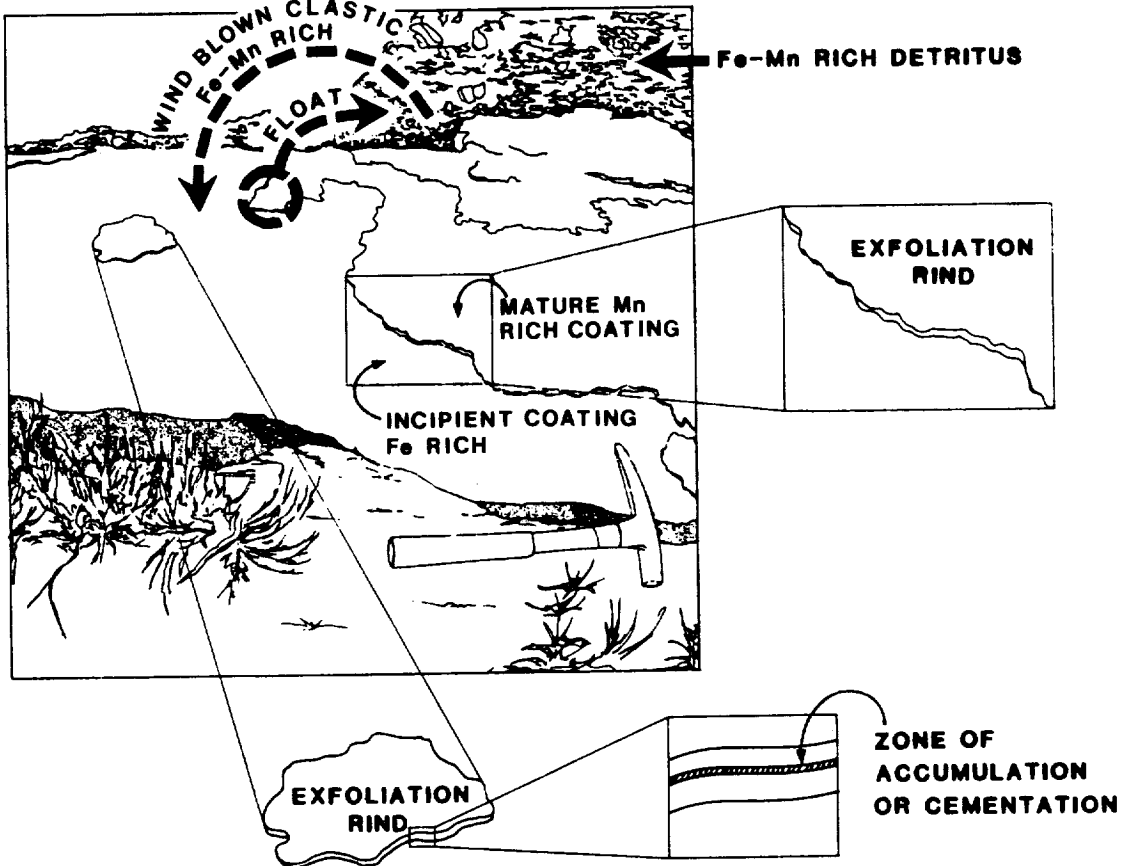
TABLE 25. SEM-EDX COMPOSITIONAL PROFILE THROUGH WEATHERED CORTEXES INCLUDING SECONDARY LAYER OF CEMENTATION

(Results in oxide %, totals computed stoichiometrically to 100%, sample numbers in parentheses)

	KANE WASH TUFF (57)				ROCKET WASH TUFF (46)				GOLD FLAT TUFF (S-2)		
	1	2	3	4	1	2	3	4	1	2	3
Na	1.06	0.46	0.58	0.92	2.15	1.50	1.55	2.06	5.44	4.88	6.76
Mg	0.00	0.81	0.00	0.00	0.18	2.21	0.00	0.00	0.40	1.67	2.12
Al	10.72	8.32	10.31	10.45	10.87	9.99	11.13	11.21	11.17	9.99	12.34
Si	75.99	69.03	75.41	79.48	67.80	64.72	76.06	67.44	74.52	67.97	61.21
K	5.92	4.48	6.06	5.98	4.95	5.13	4.92	4.82	4.22	3.77	4.40
Ca	3.89	15.21	5.31	0.86	9.23	12.44	1.39	9.97	0.96	8.79	9.72
Ti	----	----	----	----	0.65	0.29	0.29	0.22	0.16	0.34	0.15
Mn	0.07	0.04	0.15	0.19	0.25	0.24	0.49	0.30	0.20	0.15	0.30
Fe	2.35	1.65	2.16	2.20	3.92	3.48	4.17	3.97	2.93	2.43	3.00

	SPEARHEAD TUFF (30)			SPEARHEAD TUFF (72)			SPEARHEAD TUFF (83)			HIKO TUFF (38)		
	1	2	3	1	2	3	1	2	3	1	2	3
Na	0.62	0.27	0.57	2.48	0.59	0.34	5.77	5.29	5.59	0.00	2.38	0.20
Mg	0.00	0.00	0.00	----	----	----	0.57	0.78	0.90	0.00	0.00	0.00
Al	8.92	8.09	11.07	9.66	7.71	6.46	11.49	9.80	10.03	11.19	18.52	12.93
Si	81.72	78.00	75.66	78.39	62.03	69.49	68.49	65.33	72.83	79.16	68.87	77.05
K	4.91	4.39	5.75	4.21	3.64	3.06	4.38	3.71	3.85	5.82	2.93	6.83
Ca	1.68	7.24	4.22	2.86	23.60	18.66	7.26	13.05	4.27	2.03	6.39	1.60
Ti	0.16	0.02	0.17	----	----	----	0.18	0.14	0.32	0.42	0.22	0.39
Mn	0.11	0.04	0.30	0.01	0.36	0.19	0.07	0.16	0.19	----	----	----
Fe	1.88	1.94	2.27	2.39	2.07	1.79	1.78	1.74	2.01	1.37	0.68	0.99

1 - Leached zone
2 - Zone of accumulation or secondary cementation
3 - Rock immediately beneath zone of cementation
4 - Rock interior
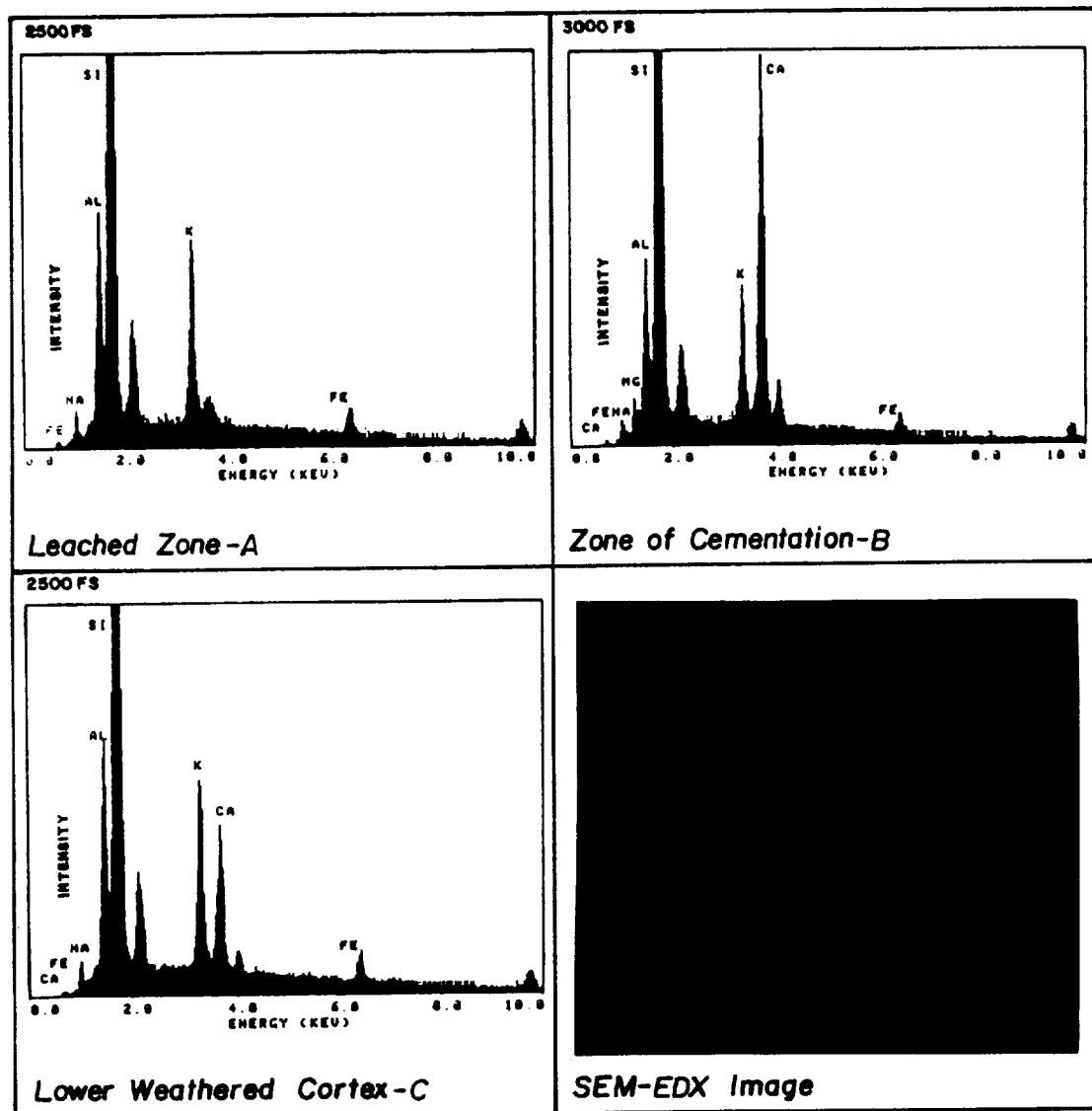
Figure 65. SEM secondary electron image of polished section of Civet Cat Canyon Tuff (lower right) showing dense layer of secondary cementation and Ca enrichment. SEM-EDX compositional analyses are shown for the zone of leaching, the lower weathered cortex and the secondary layer of cementation.

characterizes desert varnish.

Analcime (zeolite group) was detected by XRD in a porous air fall tuff from Stonewall Mountain. The occurrence of zeolites in tuffaceous rocks is well documented (Mumpton, edit., 1977). The origin of analcime, a sodium bearing zeolite commonly in association with alkaline rocks like those in the project areas, is not well understood (Hay, 1977) but reaction with meteoric waters is one popular hypothesis. Reaction of glass to form zeolites seems unequivocal (Hay and Sheppard, 1977). Deffeyes (1959) and Mumpton (1973) have shown that the reaction involves diagenetic solution of glass, then precipitation of zeolites rather than formation through devitrification. According to Mariner and Surdam (1970), an aluminosilicate gel may form first from the glass, from which zeolites grow. This relationship could account for the apparent association of zeolites with amorphous compounds in the secondary weathering layers described above. Zeolites are preferred over clays in this geochemical environment because of the cation/hydrogen ratio. Cations excluded from the zeolite structure could remain in solution for transport to other sites.

The carbonate mineralization which seems to correlate directly with tuff porosities and to concentrate in the weathered cortex resembles caliche zones and may follow principles of caliche formation. Aridic soils, in contrast

to humic soils, are characterized by concentrations of calcium salts somewhere in their profile (Krauskopf, 1967). Rain water soaks into soil and porous rocks, as well, and is later pumped back toward the surface by capillary action in response to an evaporative pressure gradient. Only the most soluble cations would be leached: namely sodium, potassium, and magnesium. Calcium would largely remain behind in a layer that represents a solution front. The distinct, dark layers may reflect the lower edge of the solution front's advance into the tuffs. The layers are enriched in calcium, and for some of the more porous tuffs the rock zone just above is slightly enriched in sodium.

SOURCES OF IRON AND MANGANESE

Coating distributions on rock surfaces have been described above from optical, SEM, and density slice methods. It was found that the amount of encrusting varnish 3-10um thick, rarely up to 50um thick, is greatly subordinated by thin films which coat the surface and impregnate the rock intergranularly, up to 0.5mm depths. For this reason ICP analyses of a thin surficial zone which includes the desert varnish layer (Table 26) record a maximum of only 1.15% MnO. These samples were extracted from the rock by a carbide scribe moved lightly over the surface. Samples were screened to minus 100 mesh to reduce contamination by extraneous mineral grains. Binocular

TABLE 26. ICP ANALYSES OF SURFICIAL COATING ZONES*

	S %	FeO %	+H$_2$O %	-H$_2$O %	SiO$_2$ %	Al$_2$O$_3$ %	Fe$_2$O$_3$ %	MgO %	CaO %	Na$_2$O %	K$_2$O %	TiO$_2$ %	P$_2$O$_5$ %	MnO %
Trachyte of Hidden C.	0.028	2.78	not/ss	0.21	51.67	24.23	6.32	1.68	3.12	4.32	4.26	1.250	0.43	0.66
Gold Flat Tuff	0.023	1.01	not/ss	0.58	62.13	16.25	5.30	0.40	0.64	4.24	5.16	0.520	0.11	1.06
Kane Wash Tuff	0.018	0.61	not/ss	not/ss	70.37	13.45	2.64	0.61	0.59	3.24	4.31	0.240	0.15	0.52
Kane Basalt	0.012	3.59	not/ss	0.60	46.23	15.06	12.80	6.39	6.10	2.18	1.65	2.210	1.27	1.15
Stonewall Basalt	0.007	3.98	not/ss	0.12	42.89	25.76	10.34	3.17	6.09	2.68	1.99	2.200	0.40	0.63
Civet Cat Tuff	0.025	0.79	not/ss	0.30	66.29	17.22	2.70	0.33	0.92	3.53	5.12	0.390	0.11	0.65
Civet Undercoat	0.008	0.27	not/ss	0.33	70.43	14.30	2.42	0.43	0.84	3.95	5.89	0.330	0.07	0.18
Antelope Spr. Rhyolite	0.022	0.41	not/ss	0.24	51.84	34.48	1.32	0.20	0.73	1.02	7.14	0.800	0.44	0.36
Spearhead Tuff	0.012	1.01	not/ss	0.20	54.49	27.74	3.24	0.29	0.72	3.14	5.07	0.580	0.10	0.57

	+H$_2$O %	Al %	Ag ppm	As ppm	Ba ppm	Be ppm	Bi ppm	Ca %	Cd ppm	Co ppm	Cr ppm	Cu ppm	Fe %	Ga ppm	Hg ppm	K %	La ppm
Gold Flat Tuff	1.82	0.62	<0.2	5	450	0.5	<2	0.43	1.5	18	4	22	1.55	<10	<1	0.15	90
Antelope Spr. Rhyolite	1.15	0.34	<0.2	20	280	<0.5	2	0.08	0.5	10	2	46	0.42	<10	<1	0.14	20
Civet Cat Tuff	0.99	0.60	<0.2	5	580	<0.5	<2	0.28	1.5	19	2	19	1.47	<10	<1	0.16	60
Spearhead Tuff	1.75	0.43	<0.2	<5	390	<0.5	<2	0.77	1.0	9	2	15	1.02	<10	<1	0.12	50

	Mo ppm	Na %	Ni ppm	P ppm	Pb ppm	Sb ppm	Se ppm	Sr ppm	Ti %	Rl ppm	U ppm	V ppm	W ppm	Zn ppm
Gold Flat Tuff	2	0.06	10	720	78	<5	<10	58	0.05	<10	<10	13	<5	166
Antelope Spr. Rhyolite	5	0.01	5	310	62	<5	<10	39	0.01	<10	<10	7	<5	57
Civet Cat Tuff	2	0.07	12	310	104	<5	<10	62	0.06	<10	<10	7	<5	152
Spearhead Tuff	1	0.03	6	580	68	<5	<10	56	0.02	<10	<10	12	<5	128

* Surficial coating zone represents a 0.25-0.50mm thick zone at the rocks surface which bears the desert varnish; desert varnish is discontinuous and much thinner on average.

scope optical examinations indicate that the samples represent depths averaging about 0.20mm thick and rarely include material below 0.5mm. Specific gravity comparisons between rock substrate, the surficial zone with desert varnish, and weathering rinds are listed in Table 27. Table 28 tabulates mass balance calculations for both iron and manganese in both surficial coating zones and underlying fresh rock.

From these data we can evaluate the rock substrate, particularly the weathered cortex, as a potential source of manganese and iron. From specific gravity measurements and geochemical analyses of the surficial zone, including the desert varnish, mass comparisons of both iron and manganese in gms/cm3 in both zones can be calculated (Table 28). Table 28 lists iron and manganese enrichment factors for three ash flow tuff deposits, one from each of the three study sites: Trachyte of Hidden Cliff from Black Mountain, basalt from the Stonewall Mountain site, and Antelope Springs rhyolite. Iron enrichment in desert varnish over underlying fresh rock varies from 2.3 times in basalt coatings to 1.3 times in Trachyte of Hidden Cliff. The average enrichment factor of iron is 2.1 for all the units, 2.2 for the three tuff samples. Manganese is enriched 10.7 times in desert varnish on the ash flow units and 8.5 times on average for all the samples. Manganese enrichment in varnish on Antelope Springs rhyolite, which does not tend

TABLE 27. SPECIFIC GRAVITY (S.G.) DETERMINATIONS
OF WEATHERING CORTEXES OR
RINDS (R), FRESH ROCKS (W), AND SURFICIAL COATING ZONES (C)*

	Gold Flat Tuff			Pahute Mesa Tuff			Kane Wash Tuff		
	W	R	C	W	R	C	W	R	C
S.G.	2.60	2.60	4.36	2.49	2.50	5.28	2.46	2.45	4.65

	Kane Springs Syenite			Spearhead Tuff			Trachyte Hidden Cliff		
	W	R	C	W	R	C	W	R	C
S.G.	2.62	2.57	2.73	2.49	2.45	3.82	2.65	----	4.22

	Lava of Pillar Spr.			Basalt-Stonewall			Antelope Spr. Rhyolite		
	W	R	C	W	R	C	W	R	C
S.G.	2.70	----	3.37	2.95	----	5.28	2.70	----	2.78

TABLE 28. MASS BALANCE COMPARISONS FOR FE AND MN
BETWEEN SURFICIAL COATING ZONES (C) AND FRESH ROCK (W)*

Unit		Specific Gravity	wt.% Fe_2O_3	wt.% MnO	gm/cm3 Fe_2O_3	gm/cm3 MnO	Enrichment Factor Fe	Enrichment Factor Mn
Gold Flat Tuff	C	4.36	5.30	1.06	0.23	0.046		
	W	2.60	4.30	0.17	0.11	0.005	2.1	9.2
Spearhead Tuff	C	3.82	3.24	0.57	0.12	0.022		
	W	2.49	2.55	0.08	0.06	0.002	2.0	11.0
Kane Wash Tuff	C	4.65	2.64	0.52	0.12	0.024		
	W	2.46	2.10	0.07	0.05	0.002	2.4	12.0
Trachyte	C	4.22	6.32	0.66	0.27	0.028		
	W	2.65	5.72	0.15	0.15	0.004	1.8	7.0
Basalt	C	5.28	10.34	0.63	0.55	0.033		
	W	2.95	8.01	0.13	0.24	0.004	2.3	8.3
Antelope Springs Rhyolite	C	2.78	1.32	0.36	0.04	0.010		
	W	2.70	0.63	0.01	0.02	0.003	2.0	3.3
					Average		2.1	8.5
					Average Tuffs		2.2	10.7

* Specific Gravity measurements performed by picnometer by Chemex Labs, Vancouver, B.C.
Surficial coating zone represents an approximately 0.25-0.5mm thickness at the rock
surface and includes the desert varnish.

to support well developed, continuous varnish, is only 3.3 times. On the basalt, manganese enrichment is 8.8 times.

Since the surficial sample including the desert varnish was about 0.2mm thick and quite conservatively less than 0.5mm thick, we can estimate thickness of rock substrate required to furnish all of the iron and manganese in the desert varnishes on these samples. Thicknesses required are equal to the enrichment factors shown in Table 28. Thus for the ash flow tuffs, which tend to develop more advanced stage and continuous desert varnish coatings, 10.7 times the surficial zone thickness would be required to furnish all the iron and manganese in the coating. If the 0.2mm thickness is applied, only 2.14mm of subsurface thickness contains enough manganese and a 0.44mm thick zone enough iron to account for all the iron and manganese distributed over the surface of these units. If the very conservative thickness of 0.5mm is applied, 5.35mm is required for manganese and still only 1.1mm for iron.

Leaching of course would not be expected to be 100% efficient. If only 25% efficient, then these thicknesses would increase by 4 times or to 8.56mm and 21.4mm for manganese, assuming 0.2mm and 0.5mm surficial zone thicknesses, respectively, and 1.76mm and 4.4mm for iron, also assuming 0.2mm and 0.5mm surficial zone thicknesses, respectively. In fact, depletion of both iron and manganese is evident from ICP analyses of weathering rinds

and underlying relatively fresh rock. Comparison of weathering rinds with rock interiors (Table 23) indicates that the rinds are relatively depleted in iron and manganese. One major exception is the basalt. Manganese appears significantly depleted in the subsurface zones of ash flow tuff samples BM-46, KS-57, and SW-30 (Table 23) relative to deeper zones within the rock. SEM-EDX compositional profiles through the coating zone and rock substrate down through the secondary zone of cementation also indicate iron and manganese depletion in a typically bleached zone just below the coating layer (Table 25). Manganese is depleted within the leached layer just below coatings by up to 50% to 65% in the ash flow tuffs (Table 25) and iron by 10% to 30%. Thus depletion appears congruous with the leach model mentioned above and developed more fully below.

GEOCHEMICAL MODEL

The zoning and ion concentration relationships observed in the data presented above support a leaching process in the weathered cortex of volcanic rocks at the study sites much like the solution front system described by Krauskopf (1967) for caliche formation in aridic soils. A leach mechanism is envisioned to initiate the derivation of desert varnish elemental constituents from rock substrate. Recycling of spalled-off rinds with desert varnish layers

would tend to enrich soils with iron and manganese. This iron- and manganese-rich dust could then form feedstock for progressive iron and manganese enrichment in desert varnish through time (Figure 64).

A slightly acidic carbon dioxide and carbonic acid enriched solution created from atmospheric interaction and biogenic processes at the rock's surface is envisioned soaking into the surface, permeating the porous tuffs to a greater extent than the more dense flows. Carbonate rich cortexes and dark hydration layers develop near the lower extent of solution front advance where magnesium rich calcite and amorphous, opaline deposits precipitate from a solution supersaturated in these components as a function of leaching the overlying substrate (the CO_2 was already present in the leachant) and evaporating the water which would move by capillary action back toward the surface and out of the rock. More soluble components remain in the retreating solution and are precipitated when supersaturation levels are reached as the solution regresses toward the rock surface. Sodium appears to concentrate very slightly in the upper part of the weathered cortex. Iron and manganese remain in solutionn to be precipitated at the rock surface. Figure 66 graphically represents this leach-solution pump model. Important outcrop relationships and recycling of desert varnish rich dust are depicted in Figure 64. The process

likely requires optimum wetting and drying cycles. Too much water influx too often would dispense leached iron and manganese into the rock.

The lamination relationships in layered desert varnish and the Fe/Mn ratio of coatings may be explained in context of this solution pump. Manganese tends to concentrate at the outer edge of the varnish and to form concentrated layers within some of the varnishes at lower levels. The Fe/Mn ratio generally increases toward the lower edge of the coatings and iron is sometimes concentrated in a layer at the rock interface. This relationship seems opposite to that which one might expect if all the iron and manganese were leached from surficial dust, since manganese is the more soluble and mobile of the two elements. If both iron and manganese were contained in a solution that was undergoing extraction out of the rock by evaporation, iron would be expected to precipitate at the rock-air interface in response to higher Eh conditions, possibly forming a poorly crystalline ferrihydrite phase which some workers (Johnston and Lewis, 1983) feel could be an important coating component. Manganese should remain in solution longer and precipitate out at the coating-air interface in response to evaporation and supersaturation.

Another explanation for the high manganese zone at the outer coating surface could be successive resolution and redeposition of the relatively mobile metal; however, one

WEATHERING PROFILE IN OUTER CORTEX OF
RHYOLITIC ASH FLOW TUFF

SOLUTION FRONT MODEL

- Acidic rain water leaches substrate. Acidity is both atmospheric and biogenic.

- Initial Fe and Mn from ferromags precipitate at air/rock interface from solution pumped to surface by evaporation.

- Further concentration promoted by recycling Fe-Mn rich dust derived from coating-encrusted float and biogenic activity.

- Solution front advances to zone of cementation.

- In response to evaporation and supersaturation, cations and colloids precipitate in a sequence inversely proportional to solubilities.

- Ca precipitates at solution front, then Mg. Na concentrated in zone of leaching as solution cycles back to surface.

ZONE

MINERAL COATING

Amorphous compounds of Si, Al, Fe, Mn. Occurs mostly as thin, discontinuous, intergranular impregnations up to 0.5 mm depths.

ZONE OF LEACHING

Minute quantities of cations leached from minerals and glass moved both up and down by solution front. Slight Na enrichment.

ZONE OF ACCUMULATION

Dense, cementing amorphous compounds, probably siliceous. Ca and some Mg enrichment. Can contain calcite and zeolites.

RELATIVELY UNALTERED ROCK

EXFOLIATION RIND

0.5 - 2.0 cm

FIGURE 66. Genetic model for origin of Fe and Mn in desert varnish.

might expect more dispersion in this case and manganese distribution to greater depths, like iron. A sensitive wetting-evaporation cycle is implied. If the water/evaporation ratio were too high, leaching would be progressive only without regressive transport, and desert varnish development would be thwarted. In this case a layer of diffuse iron enrichment would likely occur within the upper few mm of the rock surface. Another reason for manganese concentration at the surface, which other workers have suggested, is microbial fixation, possibly through ubiquitous bacterial activity.

Some correlation between underlying host rock and coatings and a possible genetic link is indicated from differences in iron and manganese relationships between the more mafic units and the more felsic units. Basalt coatings exhibit a higher Fe/Mn ratio than coatings from more felsic rocks and higher overall iron and manganese content as well (Table 22). Some geographical differences in desert varnish composition also were detected (Tables 21 and 22). Cerium, for example, is enriched in desert varnish on Gold Flat Tuff which contains high cerium, and other units within the Black Mountain study area reflect high cerium as well. This relationship suggests at least a partial underlying host rock origin rather than an exclusive exogenous wind blown dust source; however, such circumstances would not preclude dust which could originate

from the same unit.

Thus a leaching model is proposed to initiate both iron and manganese supply for desert varnish formation with continued concentration and development propelled by a wind cycled feed stock of dust derived from comminuted weathering rinds and rock surfaces.

CHAPTER VI

SPECTRAL CHARACTERISTICS

This chapter is devoted to a review of the spectral (reflected) properties of the rock types in each of the study areas and the effect of differential amounts of desert varnish on spectral measurements. Focus is on the TM interval. Twenty-two lab spectra, 81 field spectra, and over 80 TM band DN values and band ratio values for major rock assemblages, and band DN values vs petrochemistry plots were evaluated.

FUNDAMENTALS OF REFLECTED ROCK SPECTRA

Spectral profiles for most rock-forming minerals and many major rock types have been published by Hunt and Salisbury (1970); Hunt, Salisbury, and Lenoff (1973a, b, and c and 1974); Hunt (1977); and Hunt and Ashley (1979). These publications provide a spectral library for comparison and general reference.

Reflected rock spectra are controlled by the illuminating source and direction and by rock mineralogy (disregarding instrumentation). If illuminating source and direction are held constant, mineralogic variations are the fundamental control of reflectance. Minerals are crystalline solids composed of chemical compounds held together by definite and multiple proportions and are

electrically neutral. As long as the overall structure is held essentially intact, some ions can occur interchangeably at certain sites within the crystal lattice, either as discontinuous isomorphous exchange or as impurities. Some ions or molecules (water for example) cause characteristic spectral features. Thus, in the visible spectrum some mineral species can be any of several colors depending on trace element content or isomorphous element ratios. There are two fundamental interatomic and intermolecular processes that control mineral and rock spectra: electronic and vibrational (Hunt, 1980).

Excitation of electrons in the atomic structure causes transitions in energy levels. This process is called electronic (Hunt, 1980). Energy transitions are always at some multiple of Planck's constant or $E = vh$, where E=energy, v=frequency of the electromagnetic radiation, and h=Planck's constant. Energy absorption or absorption of incoming radiation at some given wavelength or frequency at the atomic level can occur when Planck's equation is satisfied. Thus for any electron orbiting within a shell or subshell with a set energy level, absorption will only occur at definite wavelengths. Spectral profiles are, in this way, altered characteristically, depending on composition of the target. Spectral features that can be used for identifying purposes include sharp absorption peaks at given wavelengths and changes in slope.

Transition metals, particularly iron, dominate electronic absorption phenomena in minerals. Electrons in the unfilled orbitals of transition metals in a mineral compound are unpaired and their energy is unbound as in the free ion state. Different energy levels are assumed by the d orbital electrons due to surrounding crystal field electronics and incoming radiation is absorbed accordingly (congruent with Planck's formula). Thus any transition metal can cause different absorption features depending on relationships with the surrounding mineral (or amorphous material), the nature of the mineral, and the transition metal itself. Ferrous iron, the most common transition metal in silicate minerals, causes a broad band absorption peak to about 1.0-1.1um. This property could retard reflectivity in TM band 5, causing steeper spectral slopes between band 5 and 7.

Molecules and anion groups such as OH and CO_3 vibrate at fundamental modes and at combinations of fundamental modes and overtones (Hunt, 1980). Vibrational behavior is caused by electronic instability between the molecule and the surrounding electronic field. Groups of anions tend to vibrate as a whole against the lattice structure. Vibrational absorption peaks tend to be quite sharp and those caused by fundamental modes occur at longer wavelengths than the TM limit at 2.5um.

LITHOLOGIES AND DESERT VARNISH

LAB SPECTRA

Twenty-two select samples of rock surfaces were scanned for visible/infrared spectral characteristics at the Jet Propulsion Lab on their Beckman lab spectrophotometer (Figures 67 and 68). Results from the lab spectra tend to support band reflectance relationships of TM imagery, exhibited in contrast enhanced single band images and hybrid composites involving band ratios. Of most significance (Figures 67 and 68):

1. Shorter wavelength bands are more absorbent to surfaces with desert varnish (coated).

2. At longer wavelengths - bands 5 and 7 - varnish absorption becomes less significant since lower E radiation penetrates deeper.

3. The progressively decreasing influence of varnish absorbance at longer wavelengths causes lower 5/7 ratio values for surfaces with varnish.
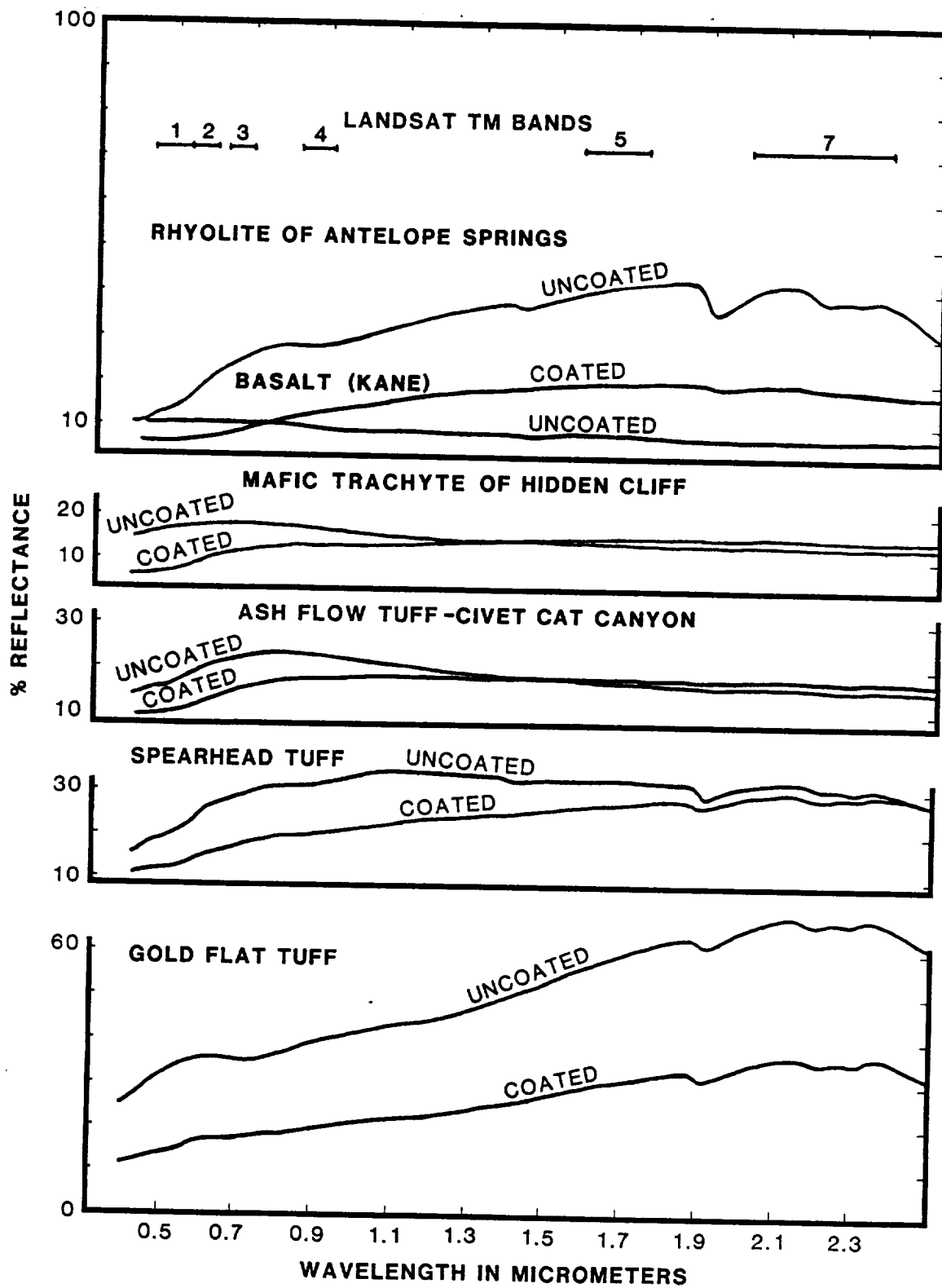
FIGURE 67 Beckman lab spectra (visible/ near infrared) , comparing uncoated weathered surfaces to surfaces with desert varnish (coated). (Only one uncoated sample shown for Antelope Springs Rhyolite.)
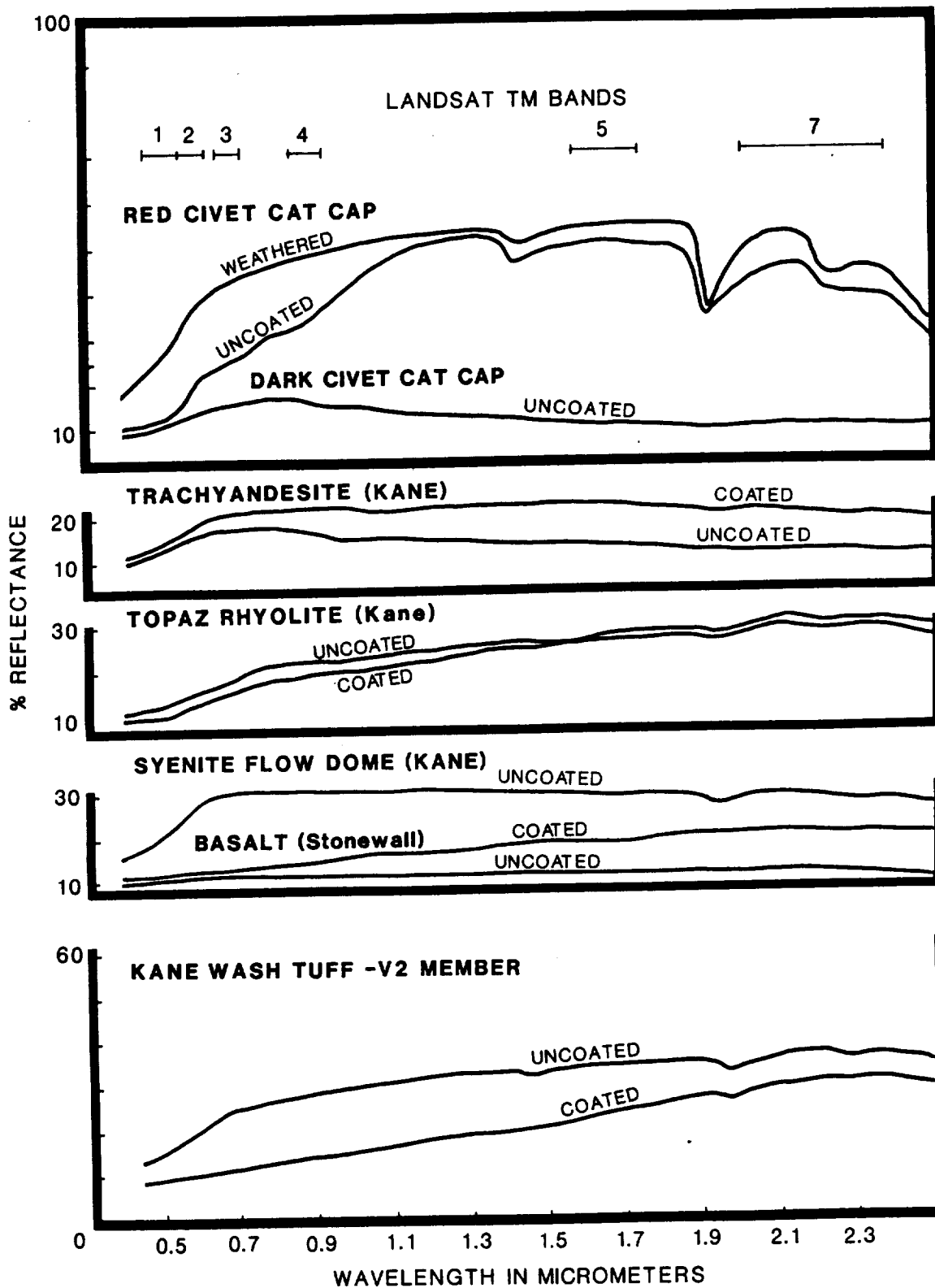
FIGURE 68. Beckman lab spectra (visible/ near infrared), comparing uncoated weathered surfaces to surfaces with desert varnish (coated). (Only one sample shown for Syenite flow and dark Civet Cat Cap samples.)

4. As varnish cover increases, 5/7 ratio values should decrease.

5. The slope of the reflectance curve for Gold Flat Tuff, a highly evolved unit with a high concentration of incompatible large-ion-lithophile elements, between bands 5 an 7 is quite steep, which should lead to very low 5/7 values.

6. Felsic units with a high concentration of varnish should exhibit higher 5/2 values.

These observations help explain imagery contrast and band relationships at each of the three study sites in instances where similar relationships exist between desert varnish occurrence, magmatic evolution, and petrochemistry. The following two sections present binary and ternary plots which exhibit these relationships, graphically.

FIELD SPECTRA

To help clarify radiance and TM imagery differences attributable to various cover types, 81 field spectra were collected with the Mackay School of Mines' Infrared Imaging Spectroradiometer (IRIS). Spectral measurements were made

of most major rock types as well as rock surfaces with varying amounts of desert varnish (Figure 69-86) at both the Stonewall Mountain and Black Mountain study sites. Field photographs of samples representative of IRIS spectral targets are presented in Figures 87 and 88. In addition, a few spectral graphs were plotted over some vegetation and soil cover as well (Figures 79, 85, 89, 90, and 91).

STONEWALL MOUNTAIN SITE. Reflectance variations of differential amounts of desert varnish on dense to moderately welded Civet Cat Canyon Tuff of Stonewall Mountain are shown in Figure 69. Civet Cat Canyon Tuff is an unusually dark rhyolitic ash flow tuff due to interstitial iron oxide produced during auto-oxidation effects upon deposition of an extremely hot ash flow. The primary rock spectrum is thus fairly low in reflectance due to low albedo. Spectral comparison of Figure 69 reveals superior discrimination within the TM band 5 interval with all variations of secondary mineral coatings bunched at lower wavelengths, and all but the moderately coated samples converging within the band 7 interval.

Reflectance spectra over glassy cap rock of Civet Cat Canyon Tuff (Figure 70) show that very heavily coated surfaces are relatively absorbent in lower wavelengths of the TM range but more reflectant beyond the band 4 region.

FIGURE 69. Field spectra comparing varying degrees of desert varnish coating on Civet Cat Tuff (welded).
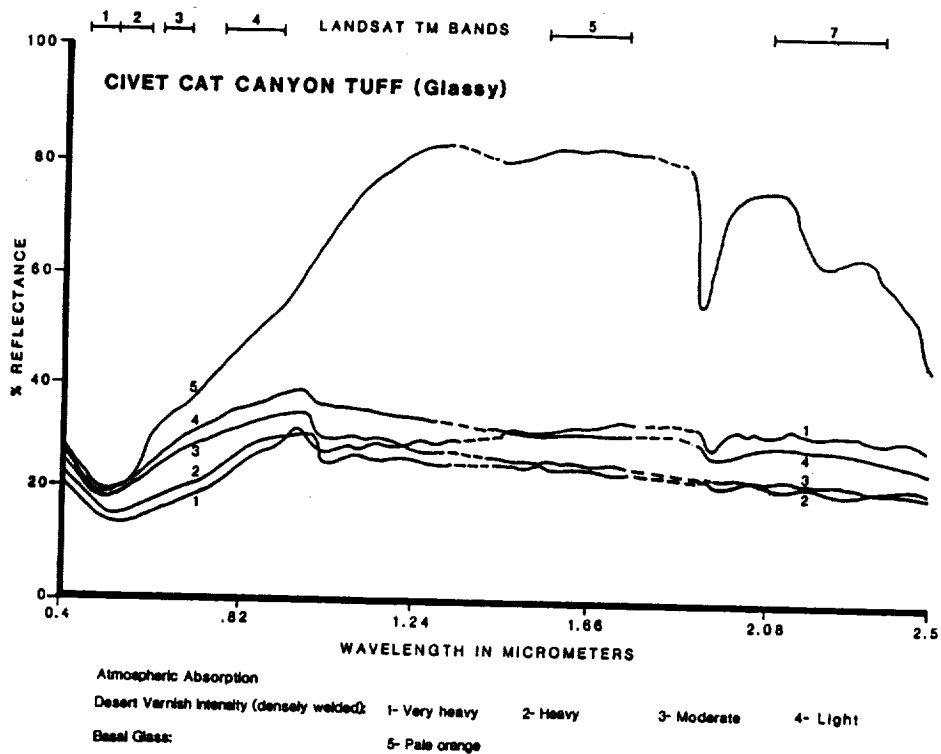
FIGURE 70. Field spectra comparing varying degrees of desert varnish coating on Civet Cat Tuff (glassy).

Spectral responses of heavily varnished surfaces are similar to very lightly coated surfaces. Sample 5 (Figure 70) is a glassy, orangy colored cap rock. It's spectral character is quite distinct. It responds similarly to vegetation: relatively reflectant in band 4 and 5.

Figure 71 shows reflectance spectra for glassy cap rock of Civet Cat Canyon Tuff. For this glassy unit absorption versus reflectance relationships are ideal: generally higher absorption in all bands over the most heavily varnished samples, and greatest reflectance over those with least varnish. Note the steep increase in the reflectance curve through the TM band 4 to 5 region for glass essentially devoid of coatings, a distinctive spectral characteristic of this unit.

Spectral curves of reflectance over Spearhead Tuff with variable varnish cover show a steeper curve in higher variation at other TM wavelengths (Figures 72 and 73). Spectral spread is greater for other varnish intensities at low wavelengths, especially within TM band 3 with convergence beyond TM band 4. The glassy unvarnished unit is highly reflectant relative to the other samples. The heavily varnished surface responds spectrally with a relatively steep slope between TM bands 5 and 7.

Antelope Springs rhyolite (Figure 74) shows the same steep spectral curve between bands 5 and 7 for heavily varnished divergent reflectance in the shorter wavelength
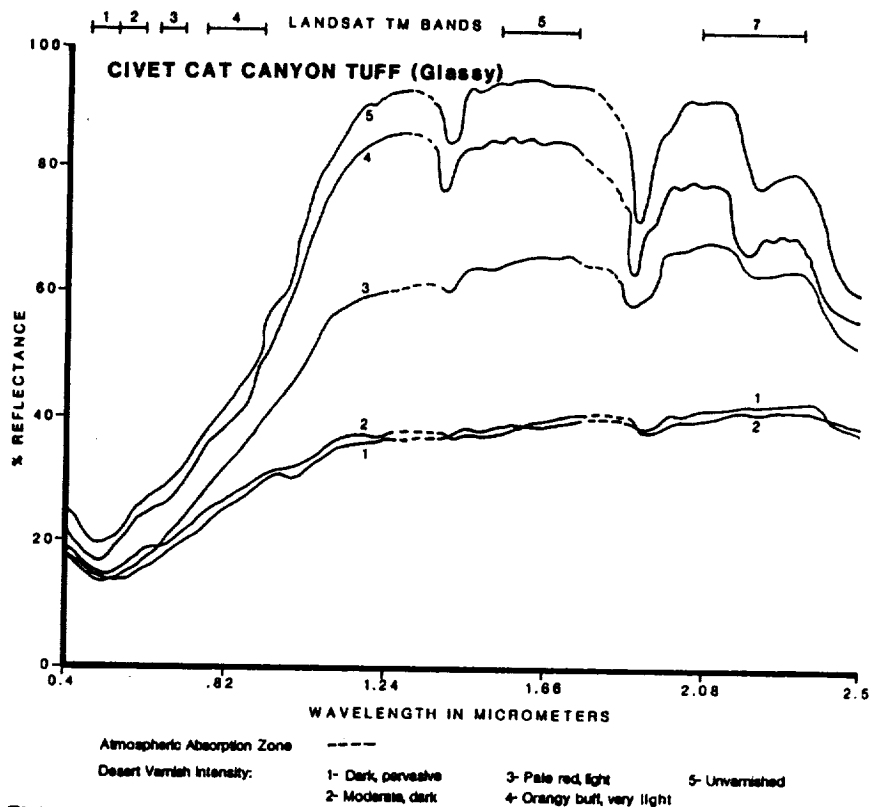
FIGURE 71. Field spectra comparing varying degrees of desert varnish coating on Civet Cat Canyon. Tuff
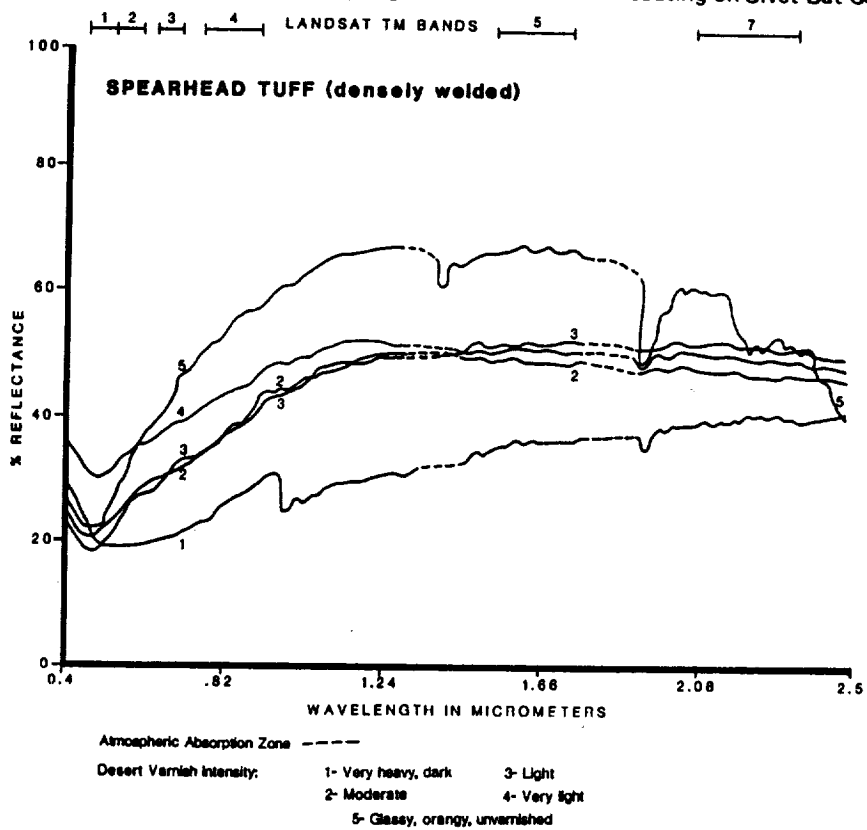
FIGURE 72. Field spectra comparing varying degrees of desert varnish coating on Spearhead Tuff (densely welded)
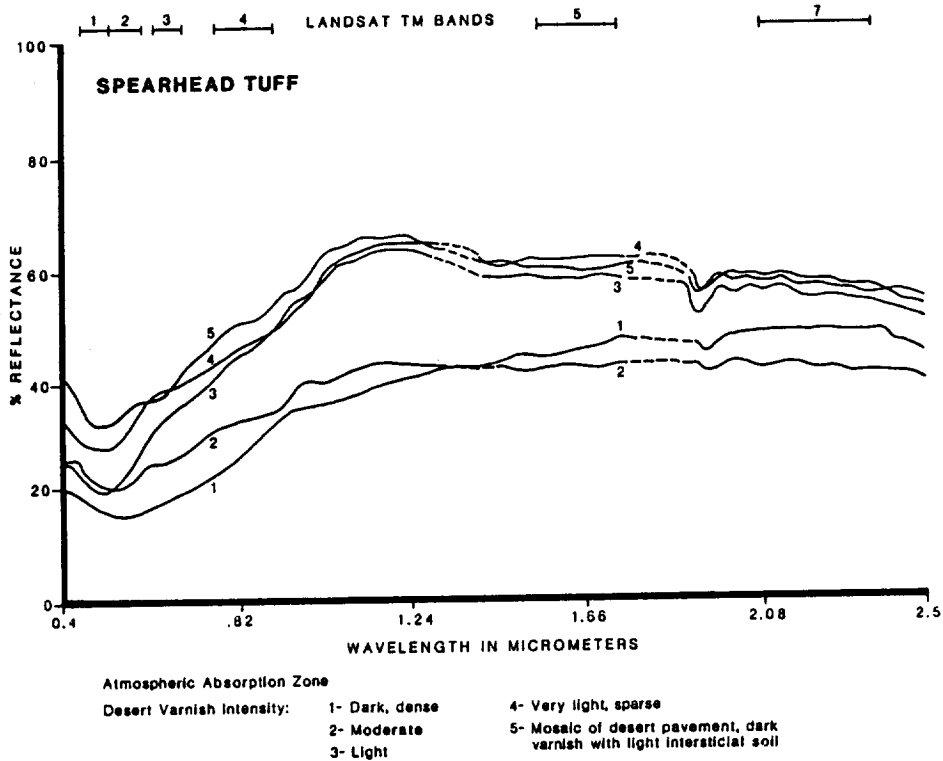
FIGURE 73. Field spectra comparing varying degrees of desert varnish coating on Spearhead Tuff.
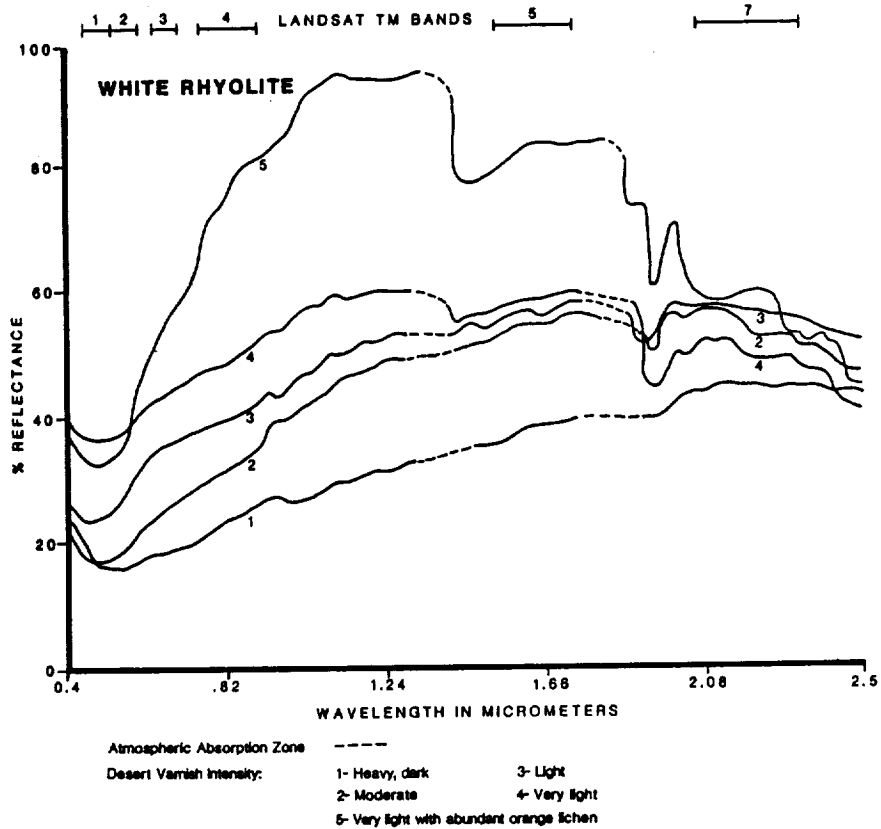
FIGURE 74. Field spectra comparing varying degrees of desert varnish coating on White Rhyolite.

TM bands, but bunched beyond band 4 except for the most heavily varnished sample. The very lightly varnished surface with abundant orange lichen responds spectrally much like vegetation.

Reflectance values for variably varnished basalt from Stonewall Mountain (Figure 75) exhibit relationships similar to those exhibited by lab spectra: heavily varnished surfaces are relatively absorbent in the lower wavelength region (TM bands 1-3) but increasingly more reflectant at higher wavelengths. For basalt, this relationship probably reflects either the different albedos of alumina- and silica-rich varnish versus the lower albedo spectral response of the underlying mafic rock, or trace metal content in the varnish.

BLACK MOUNTAIN CALDERA. Spectra for typical Gold Flat Tuff are presented in Figure 76. Varnished samples 1 and 2 (Figure 76) show expected variations: intense absorption over the heavily varnished sample (1) at short wavelengths (TM bands 1 and 2) with reflectance values converging at longer wavelengths. The satiny, glassy section exhibits relatively high reflectance in band 4, similar to glassy Civet Cat Canyon cap rock and more similar to vegetation than other rock types. Dull, orangy basal glass (Figure 77) also exhibits steep spectral slopes in this region. Heavily varnished vapor phase altered Gold Flat (Figure 78)
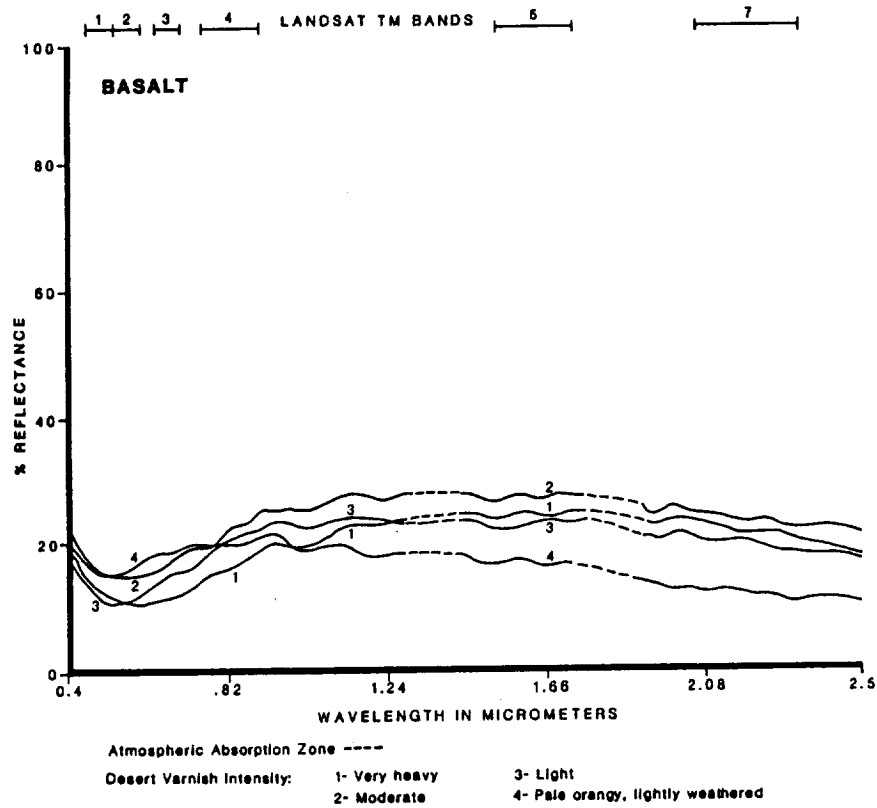
FIGURE 75. Field spectra comparing varying degrees of desert varnish coating on basalt.
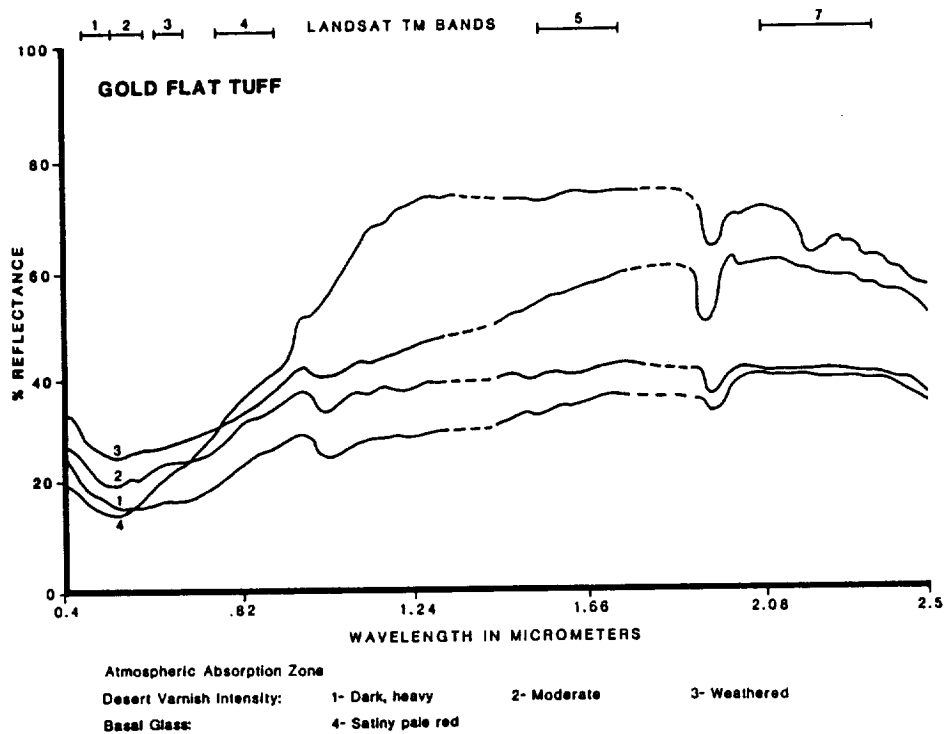
FIGURE 76. Field spectra comparing varying degrees of desert varnish coating on Gold Flat Tuff.
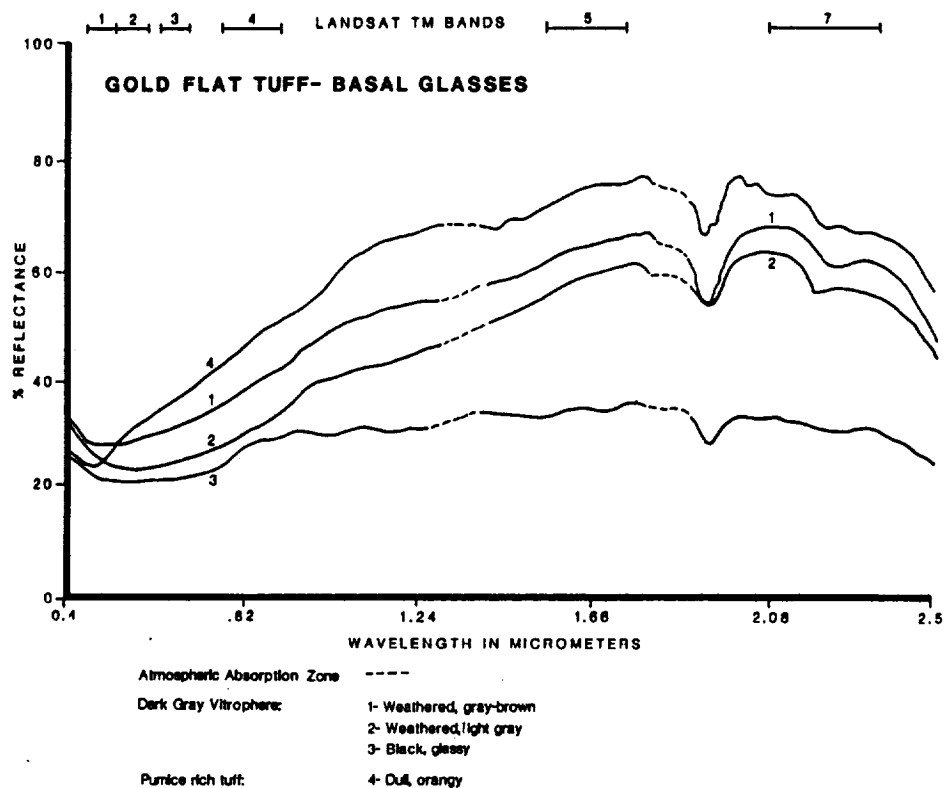
FIGURE 77. Field spectra comparing dark gray vitrophere and pumice rich tuff of Gold Flat Tuff- Basal Glasses.
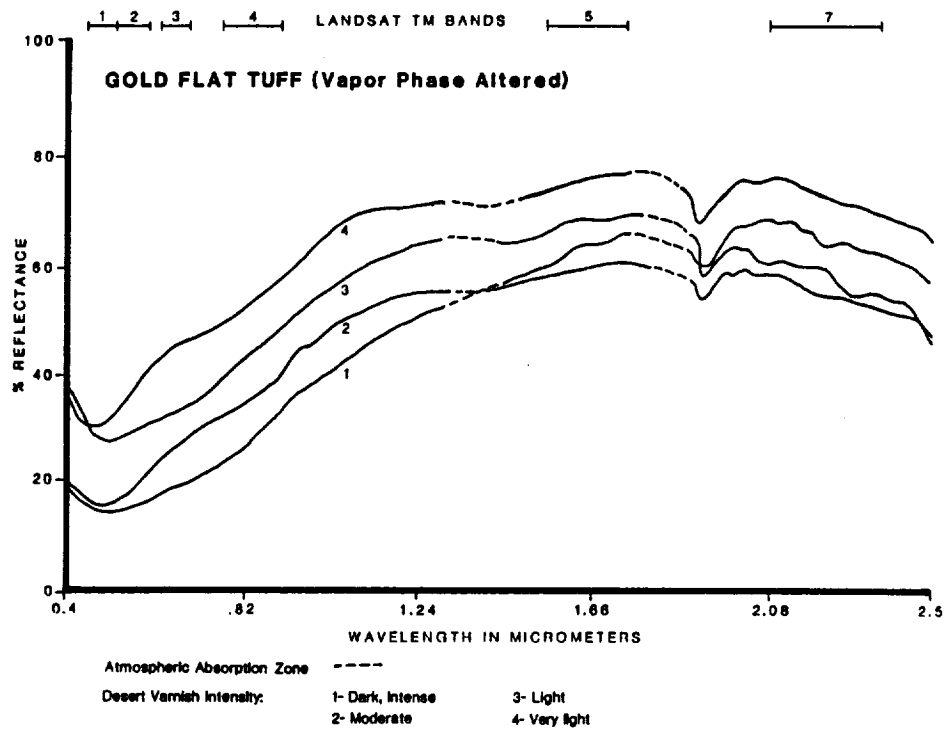
FIGURE 78. Field spectra comparing varying degrees of desert varnish coating on Gold Flat Tuff (Vapor phase altered).
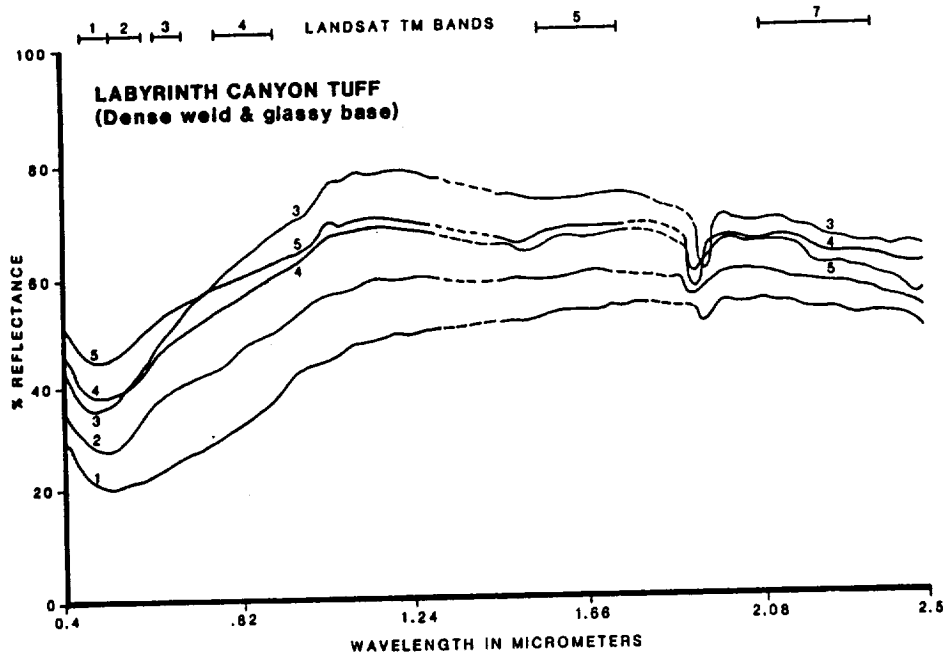
FIGURE 79. Field spectra comparing varying degrees of desert varnish coating on Labyrinth Canyon Tuff (dense weld & glassy base).
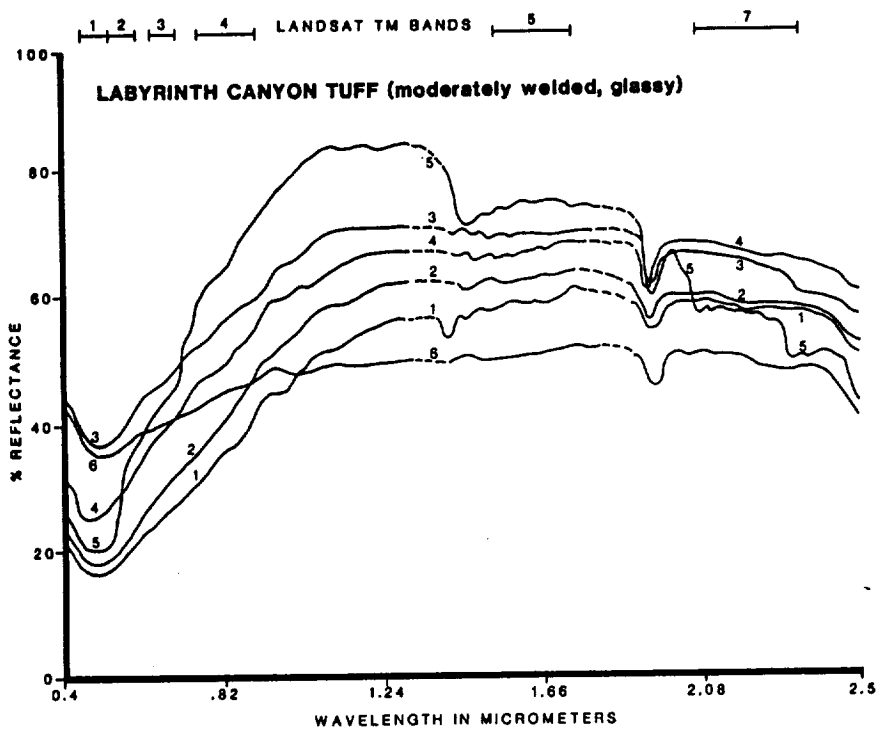
FIGURE 80. Field spectra comparing varying degrees of desert varnish coating on Labyrinth Canyon Tuff (moderately welded, glassy).
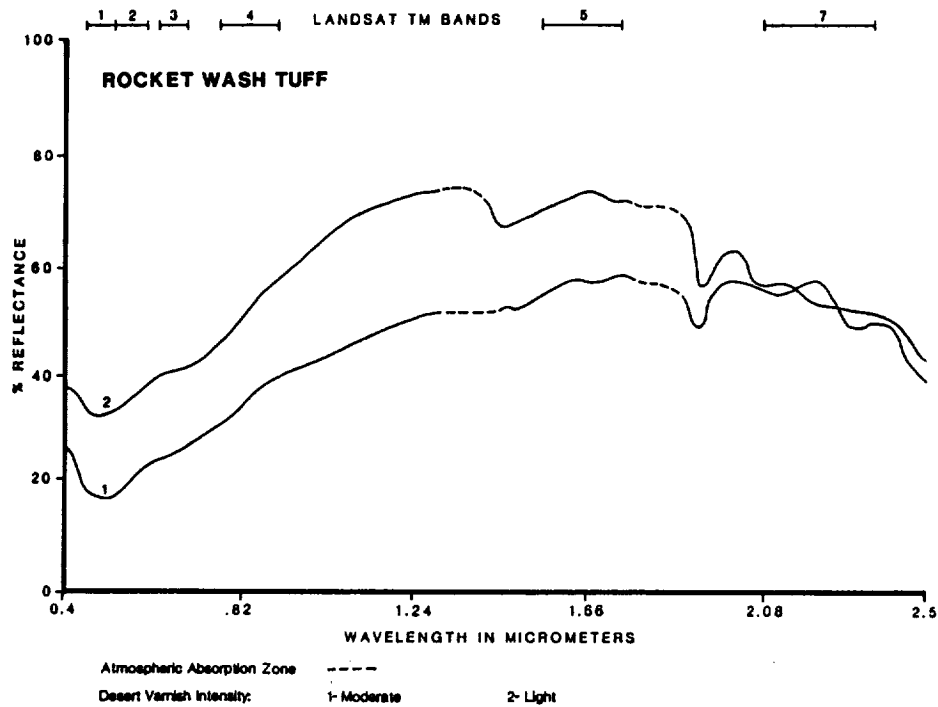
FIGURE 81. Field spectra comparing varying degrees of desert varnish coating on Rocket Wash Tuff.
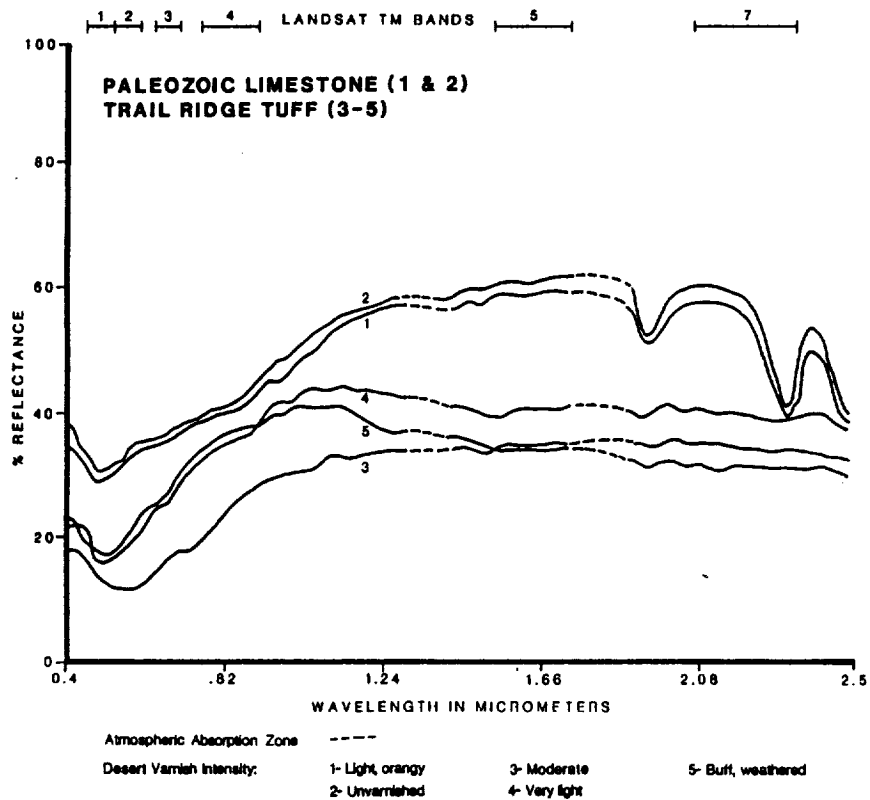
FIGURE 82. Field spectra comparing varying degrees of desert varnish coating on Trail Ridge Tuff (3-5), and Paleozoic Limestone (1&2).

Tuff shows expected high absorption at shorter wavelengths and steep curve and crossover of other spectra beyond TM band 4.

Similar relationships are shown by Labyrinth Canyon Tuff (Figures 79 and 80), Rocket Wash Tuff (Figure 81), and Trail Ridge Tuff (Figures 82 and 83). Variably varnished Labyrinth Canyon units show greater diversity of reflectance at shorter wavelengths, with convergence around bands 5 and 7. Heavily varnished Labyrinth Canyon (Figure 74), which is less reflectant than less varnished samples at TM bands 1 through 3, exhibits steeper curves beyond. Heavy lichen cover (Figure 80, spectra 5) behaves spectrally much like typical vegetation. Black vitrophyre is spectrally flat (Figure 80) and spectra tend to converge and cross over at wavelengths beyond 1.0um (Figures 79-82). Pronounced spectral divergence occurs in the TM band 3 region due to "red" radiance sensitivities to more reddish colors of lightly varnished surfaces. Limestone and pervasive hydrothermal alteration with characteristic high relative reflectivities at shorter wavelengths and absorption peaks around 2.2 to 2.3um are shown in Figures 82 and 83.

Spectra for lava deposits, including Trachyte of Hidden Cliff and Lava of Ribbon Cliff (Black Mountain caldera) are presented in Figures 84, 85, and 96. Relationships match those seen in laboratory spectra. Heavily varnished
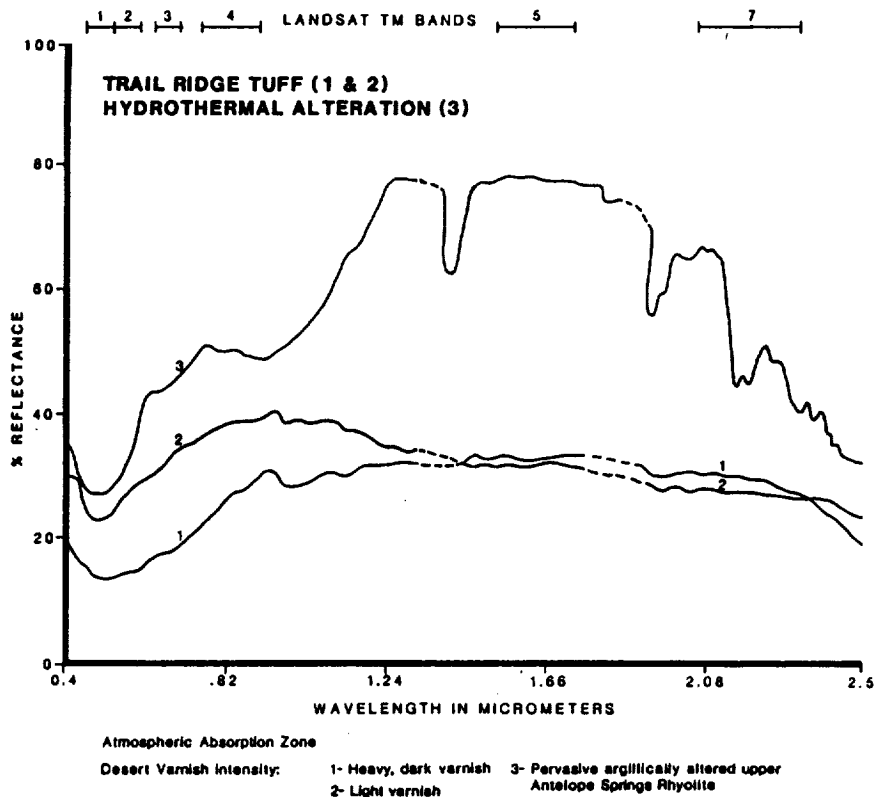
FIGURE 83. Field spectra comparing varying degrees of desert varnish coating on Trail Ridge Tuff (1&2), & Hydrothermal alteration (3).
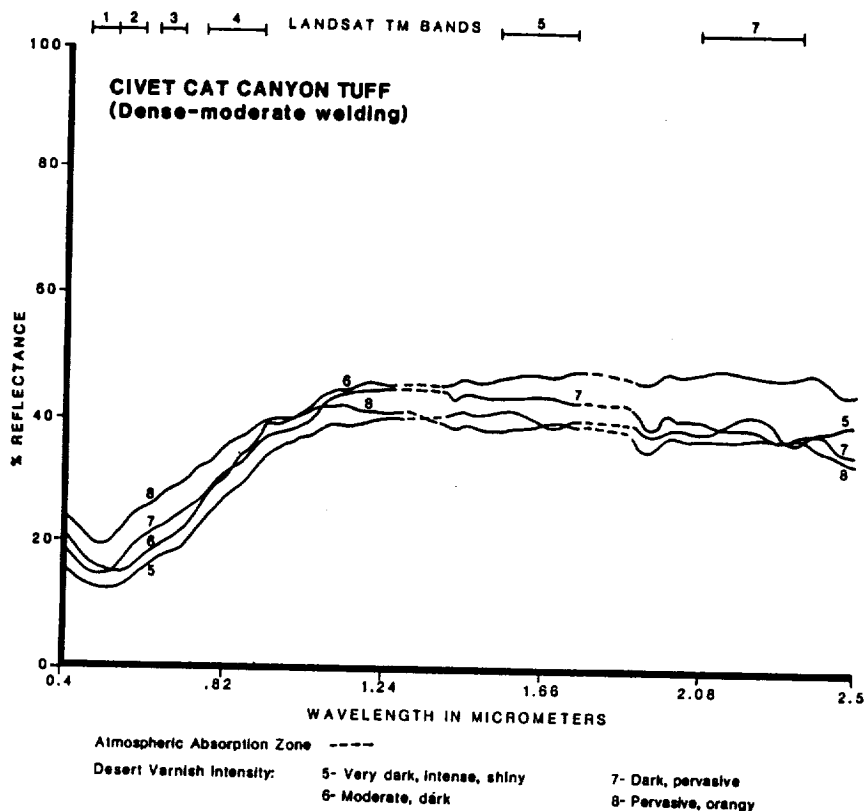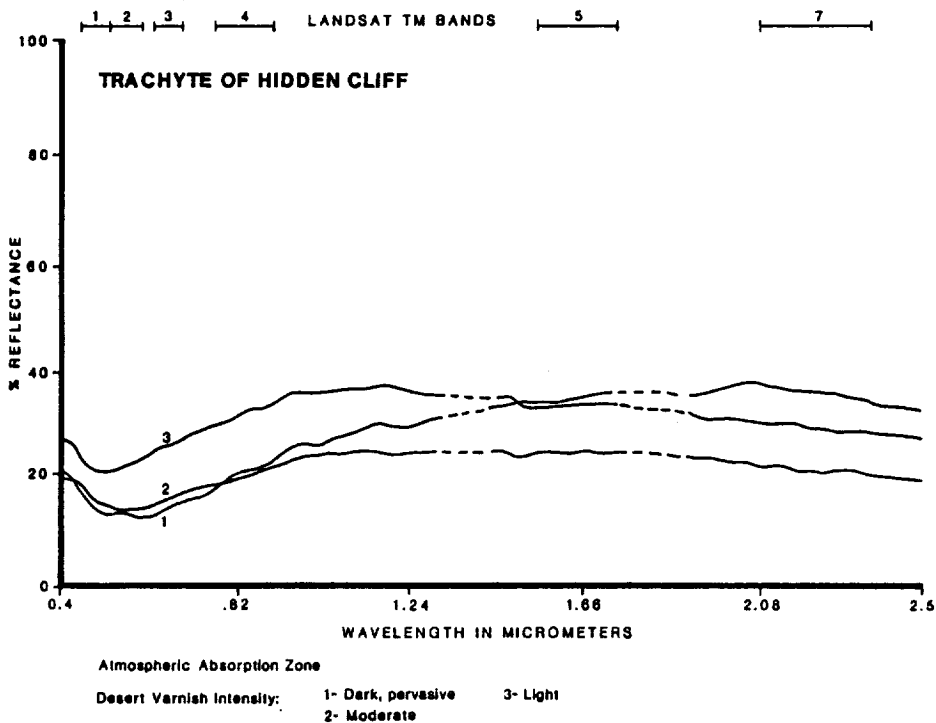

FIGURE 84. Field spectra comparing varying degrees of desert varnish coating on Trachyte of Hidden Cliff.
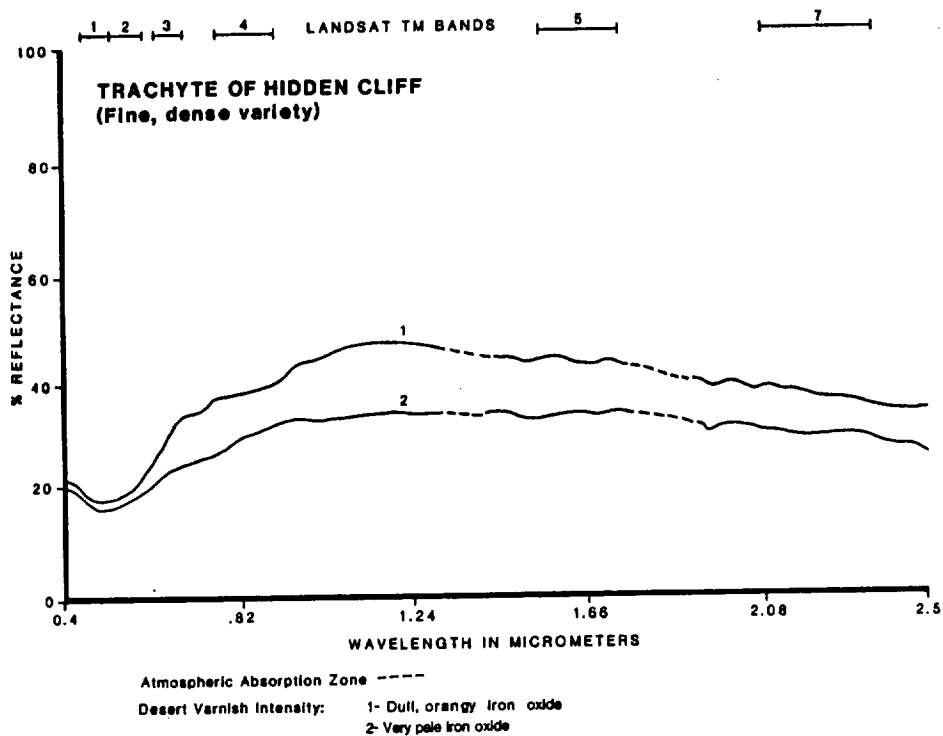
FIGURE 85. Field spectra comparing varying degrees of desert varnish coating on of Trachyte of Hidden Cliff (fine, dense variety).
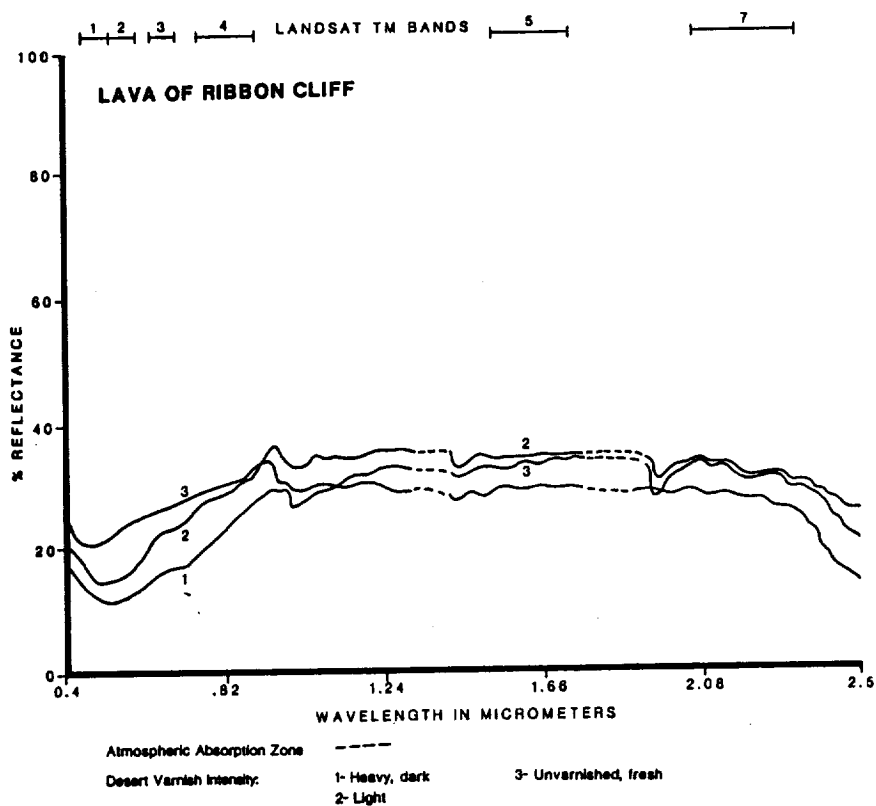
FIGURE 86. Field spectra comparing varying degrees of desert varnish coating of lava on Ribbon Cliff.

surfaces, slightly more absorbing at short wavelengths, are more reflectant in the TM band 5 and 6 region. Curves for low varnish varieties are flat.

Tables 29, 30, and 31 show spectral curves of many of the major rock units from the Stonewall Mountain, Black Mountain, and Kane Springs Wash study sites, respectively, and compare the spectra with lithologic and petrochemical properties of the units. Table 32 compares spectra of unvarnished rock surfaces with spectra of heavily varnished surfaces. The Table includes unit lithologic and petrochemical properties as well.

SOIL, DESERT PAVEMENT, VEGETATION

A few field spectra were collected over vegetation, soil, and one mosaic of desert pavement for comparison with rock spectra and to assess influence of these cover types on rock spectra. Sandy soil (Figure 89) whose source was mostly adjacent Labyrinth Canyon Tuff is spectrally quite similar to lightly varnished Labyrinth Canyon (Figure 79, spectra 3). Soil, regolith, and desert pavement could be expected to respond spectrally similar to their parent rock source, with variation attributable in part to variable desert varnish development, a relationship consistent with the correlation of alluvium and rock detritus with adjacent outcrop on TM imagery. Indeed, spectra of desert pavement

Table 29. COMPARISON OF SPECTRAL PROPERTIES OF STONEWALL MOUNTAIN UNITS
WITH LITHOLOGIC, PETROCHEMICAL AND IMAGERY CHARACTERISTICS

UNIT	LITHOLOGY	PETROCHEMISTRY MAJOR	MINOR*	FIELD OR LAB SPECTRA**
Civet Cat Canyon Red Cap	Vitrophyre with sanidine/anorthoclase and biotite phenocrysts	Rhyolite peralkaline	Slightly high F, low Sr, Cr, Cu	
Civet Cat Canyon Tuff	Crystal ash-flow with sanidine/anortho- clase and biotite phenocrysts.	Rhyolite slightly peralkaline	Slightly high Th, Be. REE, slightly low Sr, V, Mg	
Spearhead Tuff	Pumice rich ash-flow with sanidine/anortho- clase phenocrysts.	Rhyolite slightly peralkaline	High REE, Zn, Zr, Be, Ce. Low Sr, Mg, Ba, Co, Ni, V	
Basalt Flows	Dense flow, minor vesiculation, microporphyritic olivine and plagio- clase.	Low silica basalt	High P, Sc, V, low U, Th	
Antelope Springs Rhyolite	Dense quartz porphyry intrusives, flows and welded ash-flows(?) underlain by friable tuff. Commonly hydro- thermally altered.	Rhyolite, slightly alkaline	Slightly high Mg, Tl, Th	

Wavelength
(Micrometers)

* Amounts (high or low) are relative to other units within the study site.
** %R is % reflectance spectral measurements taken with Collins IRIS spectrometer.

Table 30. COMPARISONS OF SPECTRAL PROPERTIES OF BLACK MOUNTAIN UNITS
WITH LITHOLOGIC, PERTROCHEMICAL AND IMAGERY CHARACTERISTICS

UNIT	LITHOLOGY	PETROCHEMISTRY MAJOR	MINOR*	FIELD OR LAB SPECTRA**
Labyrinth Canyon Tuff (Spearhead)	Fine ash-flow tuff with pebble size pumice and alkali feldspar.	Peralkaline rhyolite	High HF, Hg, Rb, Tl, B. Low Sr, Ba	
Trachyte of Hidden Cliff	Variably vesicular, lava flow with minor plagioclase and olivine phenos	Mafic trachyte	High P, Sc, Sr, Mn Ti, V, Ba, Eu, Co, Mg. Low Rb, B	
Gold Flat Tuff	Eutaxitic ash flow with pumice and phenocrysts of anorthoclase Na-rich pyroxene and amphibole and fayalite.	Peralkaline pantellerite	High REE, Be, Pb, Sn, Th, Nb, Rb, Ta, U, Zr, An, As, B, Ca, C, Cu, F, Li	
Lavas of Pillar Spring	Coarse granitic lava flow with alkali feldspar and minor quartz and biotite.	Slightly subalkaline rhyolite to trachyte	Slightly high HREE, Th, Sn, Zn, Zr, Be, F, Hf	
Trail Ridge	Ash flow tuff with pumice fragments and alkali feldspar phenocrysts.	Slightly peralkaline to subalkaline rhyolite to latite.	Slightly high Sc, Eu, Mn	

Wavelength

* Amounts (high or low) are relative to other units within the study site.
** %R is % reflectance spectral measurements taken with Collins IRIS spectrometer.

Table 31. COMPARISONS OF SPECTRAL PROPERTIES OF KANE SPRINGS WASH UNITS
WITH LITHOLOGIC, PETROCHEMICAL AND IMAGERY CHARACTERISTICS

| UNIT | LITHOLOGY | PETROCHEMISTRY | | LAB SPECTRA** |
		MAJOR	MINOR*	
Late Basalt	Massive to vesicular flows with microporphyritic laths of plagioclase	Olivine basalt	High Ni, P, Sc, Ti, V, Cr, Co, Cu. Low Rb, Th, U, Li.	
Rhyolite Domes	Massive flow-banded lava, phenocrysts of quartz, sanidine, fayalite and Na-rich amphibole, vapor phase topaz.	High silica peralkaline rhyolite	High Rb, Ta, HREE, Th, Sn, U, Y, Be, F, Li. Low Ba, P, Eu.	
Trachyandesite Lava	Vesicular flows with plagioclase phenocrysts in dark, holocrystalline matrix.	Andesite to low silica andesite.	High Ni, Sc, Zr, Ga. Slightly low U, Th, Pb.	
Syenite Complex	Fine grained porphyry with anorthoclase, quartz, and clinopyroxene phenos. Flow domes, intrusives, and minor tuff.	Syenite and trachyte.	High Mo, Zn, Zr, B Slightly high REE, As, Ba, F, Hf, La. Low C, Eu, V, Ni.	
Kane Tuff V2 Members	Ash flow tuffs with pumice and crystals of fayalite, Na-rich amphibole, sanidine, anortho-clase.	Peralkaline comenditic rhyolite to trachyte	High REE, Hf, F, Rb, Zr, Th, U. Low Sc, Ba.	

Wavelength
(Micrometers)

*   Amounts (high or low) are relative to other units within the study site.
** %R is % reflectance spectral measurements

Table 32. COMPARISON OF PETROCHEMISTRY, VARNISH CHARACTER AND COMPOSITION, AND SPECTRA OF BOTH EXTENSIVELY VARNISHED SURFACES AND UNVARNISHED SURFACES

UNIT	PETROCHEMISTRY MAJOR	MINOR*	FIELD VARNISH	VARNISH COMPOSITION	FIELD & LAB SPECTRA**
Civet Cat Canyon Tuff	Rhyolite slightly peralkaline	Slightly high Th, Be. REE, slightly low Sr, V, Mg	Very dark red-brown very densely welded, ledge former. Thin-platted float.	High K, Ca, Ti Low Fe/Mn	(spectra: F, C)
Spearhead Tuff	Rhyolite slightly peralkaline	High REE, Zn, Zr, Be, Ce. Low Sr, Mg, Be, Co, Ni, V	Pale buff to buff gray, moderately welded, ledge former. Thick rough, slabby float.	High Na Low Fe/Mn	(spectra: F, C)
Basalt Flows Stonewall	Low silica basalt	High P, Sc, V, low U, Th	Very dark gray very dense, massive mesa cap in places.	High P, Fe/Mn Low Mg, Si, K	(spectra: C)
Antelope Springs Rhyolite	Rhyolite, slightly alkaline	Slightly high Mg, Tl, Th	Very light cream-colored. Forms steep slopes, cliffs and knobs. Joint-bound blocky float.	Low Ti	(spectra: F, C)
Labyrinth Canyon Tuff (Spearhead)	Peralkaline rhyolite	High Hf, Mg, Rb, Tl, B. Low Sr, Ba	Tan in color, densely to moderately welded thin, platy ledge former.	Low Ca, Ti	(spectra: F, C)
Trachyte of Hidden Cliff	Mafic trachyte	High P, Sc, Sr, Mn Ti, V, Be, Eu, Co, Mg. Low Rb, B	Dark gray, rough, hummocky boulders confined largely to Black Mountain.	High P, Mn, Ce Low Si, Mg, K Low Fe/Mn	(spectra: F)
Gold Flat Tuff	Peralkaline pantellerite	High REE, Be, Pb, Sn, Th, Nb, Rb, Ta, U, Zr, Sn, As, B, Ca, C, Cu, F, Li	Pale olive gray moderately welded, forms blocky slabs in float. Tops mesas.	High Na, Ti, Ce Low Fe, Mn	(spectra: F, C)
Late Basalt Kane Spr.	Olivine basalt	High Ni, P, Sc, Ti, V, Cr, Co, Cu. Low Rb, Th, U, Li.	Very dark gray massive mesa caps. Forms blocky scree.	High Fe/Mn, Ti Low Si, K	(spectra: C)
Syenite Complex Kane Spr.	Syenite and trachyte.	High Mo, Zn, Zr, B Slightly high REE, As, Ba, F, Hf, La. Low C, Eu, V, Ni.	Cream colored domal knobs and rugged hills, weathers to exfoliated slabs and rough boulders.	High Al, P Low Si, K, Ca, Ti Low Fe/Mn	(spectra: F)

Spectra axes: vertical 80, XR, 0; horizontal 0.4 to 2.5; Wavelength (Micrometers)

* Amounts (high or low) are relative to other units shown.
** X R is %. F - unvarnished surface. C - surface with heavy desert varnish

Figure 87. IRIS spectral samples from the Stonewall Mountain site. Top row: Antelope Springs rhyolite showing very heavy varnish coatings on left, then heavy to moderate, moderate, light to very light and finally a sample with lichen growth on the far right. Bottom row: basalt from the Stonewall site with very heavy desert varnish coating on the far left sample, then heavy, moderate and finally light desert varnish on the right.

Figure 88. Platy float weathered from glassy Civet Cat Canyon Tuff cap rock. (Pen in lower left for scale.) Note variable desert varnish coatings.
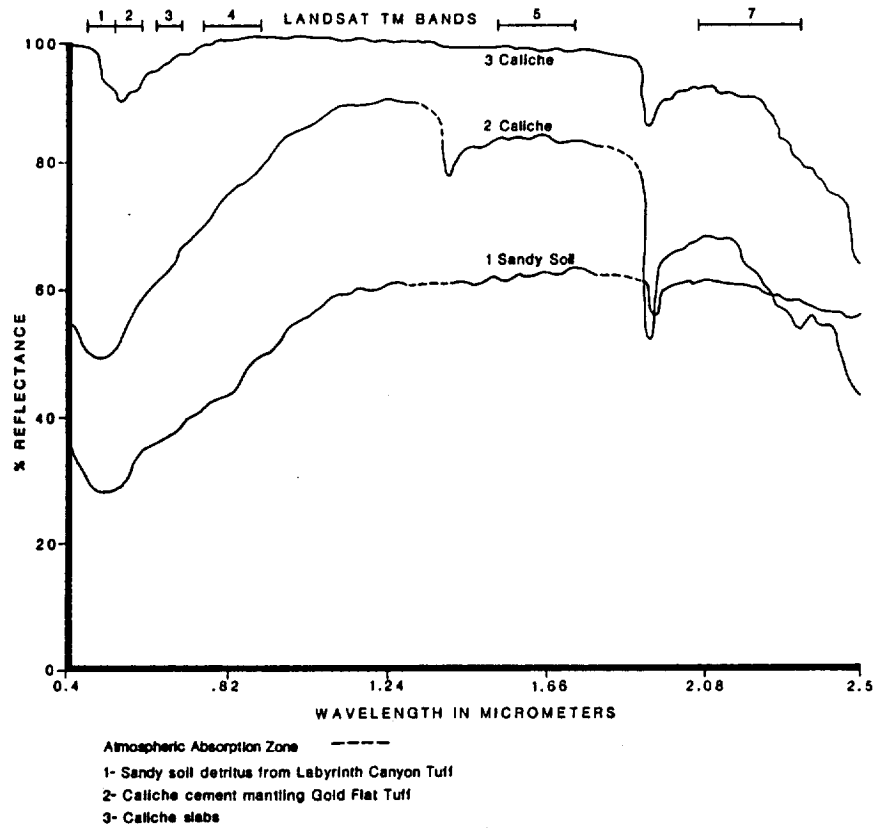
FIGURE 89. Field spectra of caliche and sandy soil.
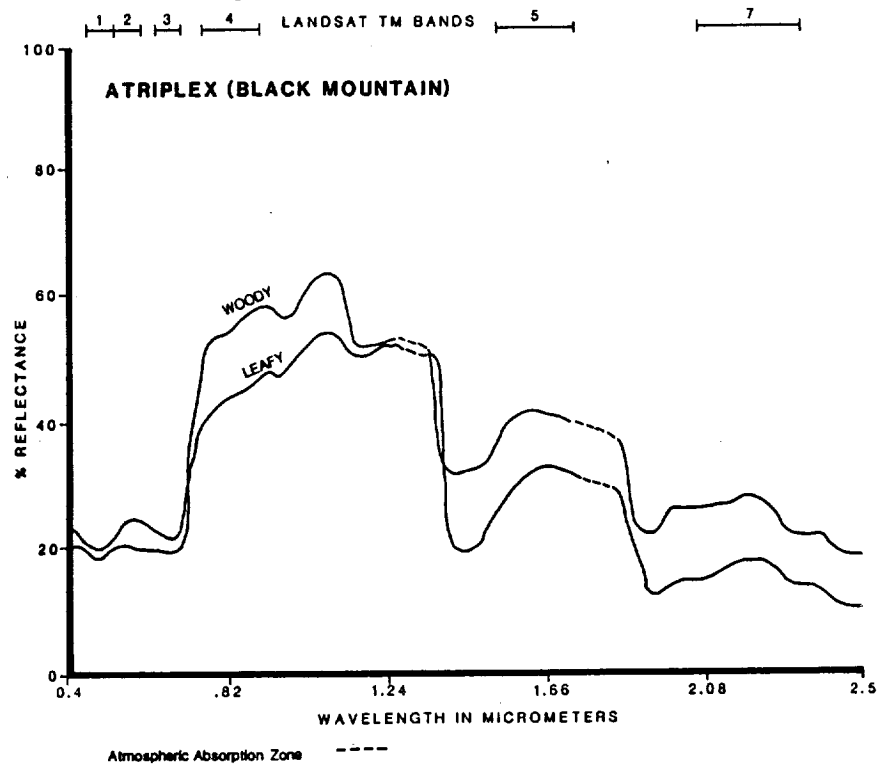
FIGURE 90. Field spectra of Atriplex (Black Mountain).

mosaic derived from Spearhead Tuff (Figure 73) are most similar to Spearhead spectra with heavy desert varnish cover. This observation should be expected inasmuch as desert pavement in general develops some of the more extensive and dark desert varnish present in the study sites. Spectra of caliche samples (Figure 89) exhibit very high overall reflectivities.

Lichen, a mixture of algae and fungi, which includes the common green variety known as moss, has been described over various rocks in the study areas in previous sections. Pale army green lichen is prevalent on much of the vapor phase altered tuffs of Kane Springs Wash where it can anchor efficiently and where a porous rock surface provides relatively abundant residual water after rain showers. It also occurs over much of the vesicular Trachyte of Hidden Cliff at Black Mountain. Bright orange lichen preferentially homesteads the Antelope Springs rhyolite at the Kane Springs Wash volcanic center. Although lichen undoubtedly influences surface spectra to some degree, it is a minor cover type when considered within the 30x30m pixel sized resolution cell of TM. Spectra of the distinctive orange lichen are shown in Figures 74 and 80 over Antelope Springs Rhyolite and Labyrinth Canyon Tuff, respectively. Lichen cover on these hand samples was exceptional - 60-70%. The spectral curves exhibit shapes typical for most types of vegetation - very steep curves

between TM bands 3 and 4, and high 4/5 ratios - quite different from rock spectra.

Spectra for sagebrush and atriplex (Figures 90 and 91) from the study areas also exhibit classic vegetation curves - very steep slopes between TM bands 3 and 4, and high 4/5 ratios compared with rock. The woodier atriplex specimen (Figures 90 and 91) is more reflective than a somewhat more leafy counterpart through the TM band 4 interval, but less reflective at longer wavelengths. Spectra for sagebrush are apparently indistinguishable from atriplex. The sample tested (Figure 81) exhibited spectra largely conformable to the interval between 2 atriplex samples, one more woody than the other (woodier in terms of exposure to the sensor).
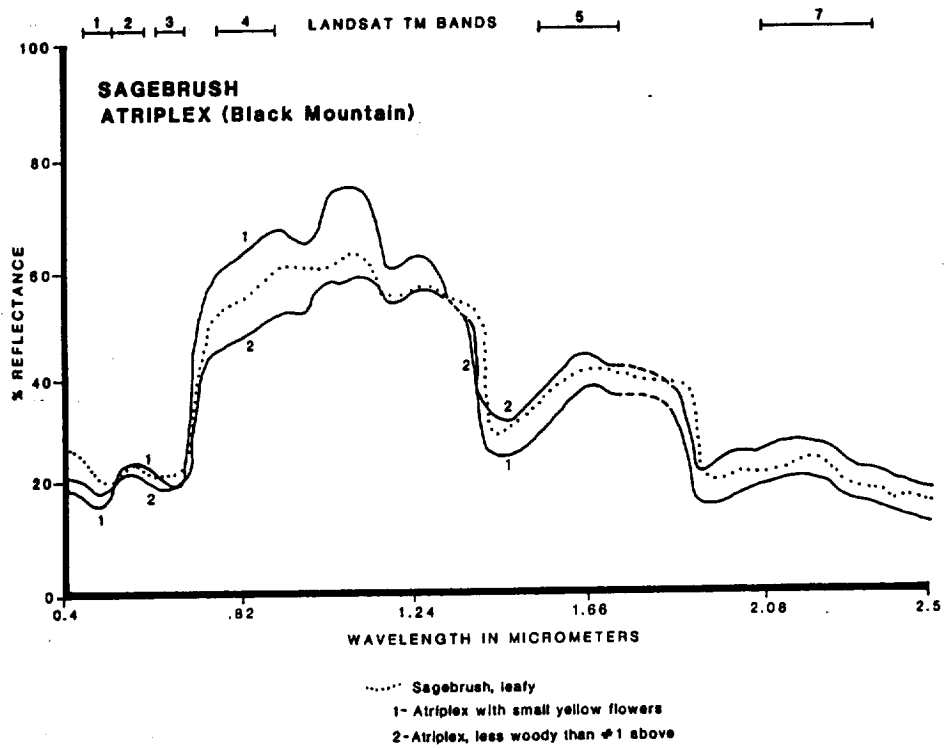
FIGURE 91. Field spectra comparing varying degrees of sagebrush and atriplex (Black Mountain).

CHAPTER VII

SPECTRAL INFLUENCES ON LANDSAT TM DATA

This chapter will address the influences of various cover types within the project areas on spectral compositions, focusing on lithologies and desert varnish and the Thematic Mapper band intervals. The study has revealed important relationships between rock petrochemistry and desert varnish and the influence both of these criteria and the variations and vagaries among them exert on visible/near-infrared spectra (Spatz, Taranik and Hsu, 1987b, 1987c and 1988, and Spatz and Taranik, 1988). Results bear importantly upon Landsat TM interpretations. This Chapter includes correlations of Landsat TM DN values with petrochemistry and desert varnish, discusses importance of rock-varnish albedo differences, and ends with a section on mapping applications.

LITHOLOGY AND PETROCHEMISTRY

Figures 92 and 93 present reflectance values for TM bands of most major lithologic units from each of the study sites. Appendix K contains pixel statistical information for each lithologic unit represented in the graphs. The ternary plots, on the other hand, were compiled from a different set of data, but relationships are consistent

BLACK MTN TM REFLECTANCE

Average DN Values vs **Thematic Mapper Bands**

Gold Flat Tuff   — ·· — ·· — ··· — ····

Labyrinth Tuff   ···············

Trachyte Lava   — — — — —

Pillar Spr. Lava   — · — ·· — · — · — ·

STONEWALL TM REFLECTANCE

Average DN Values vs **Thematic Mapper Bands**

Spearhead Tuff   — ·· — · — ·· — ····

Basalt Lava   ···············

Civet Cat Tuff   — — — — — —

Antelope Rhyolite   — ·· — · — ·· — · — · —

Civet Cat Cap   ——————
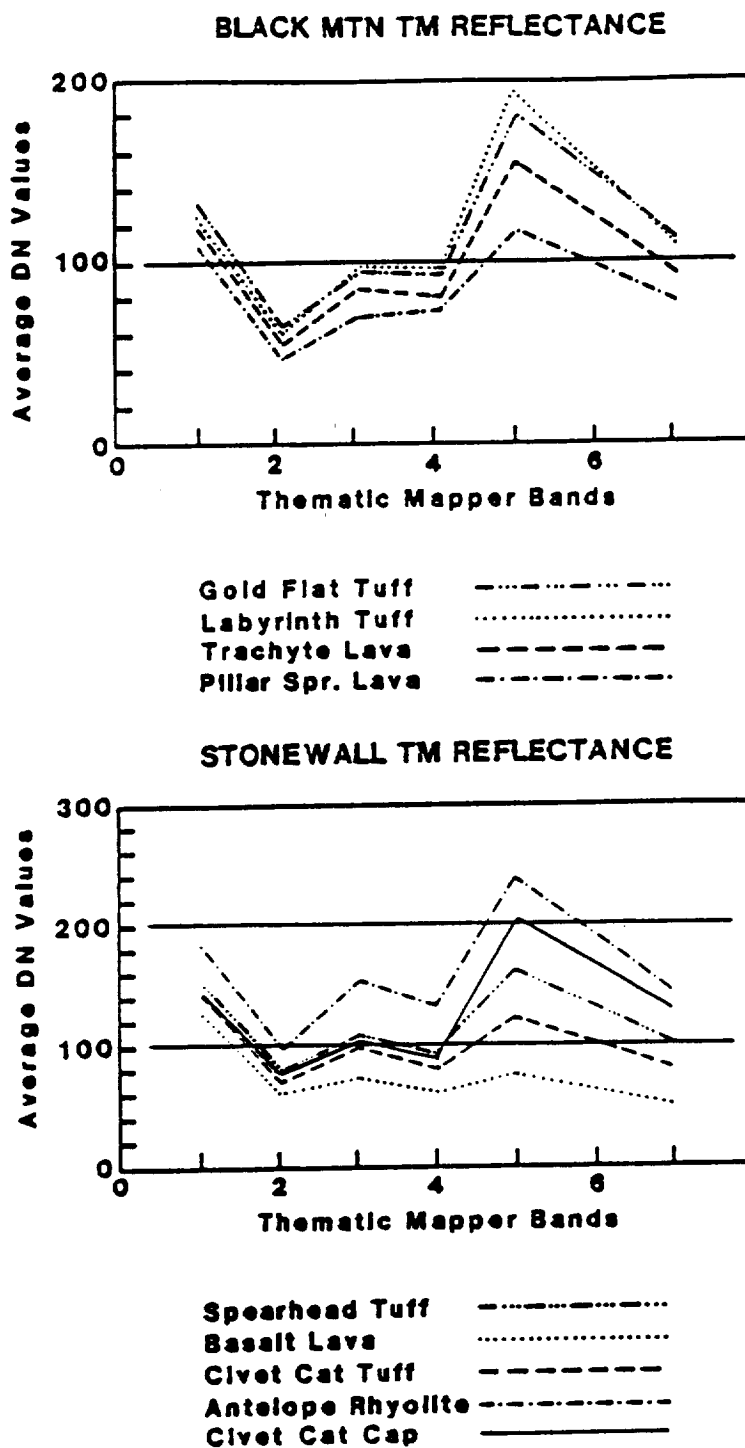
Figure 92. Graph of thematic mapper band DN values over the major
lithologic units of the Black Mountain caldera (top) and the
Stonewall Mountain study area (bottom). Raw values uncorrected
for additive path radiance.

KANE SPR. TM REFLECTANCE
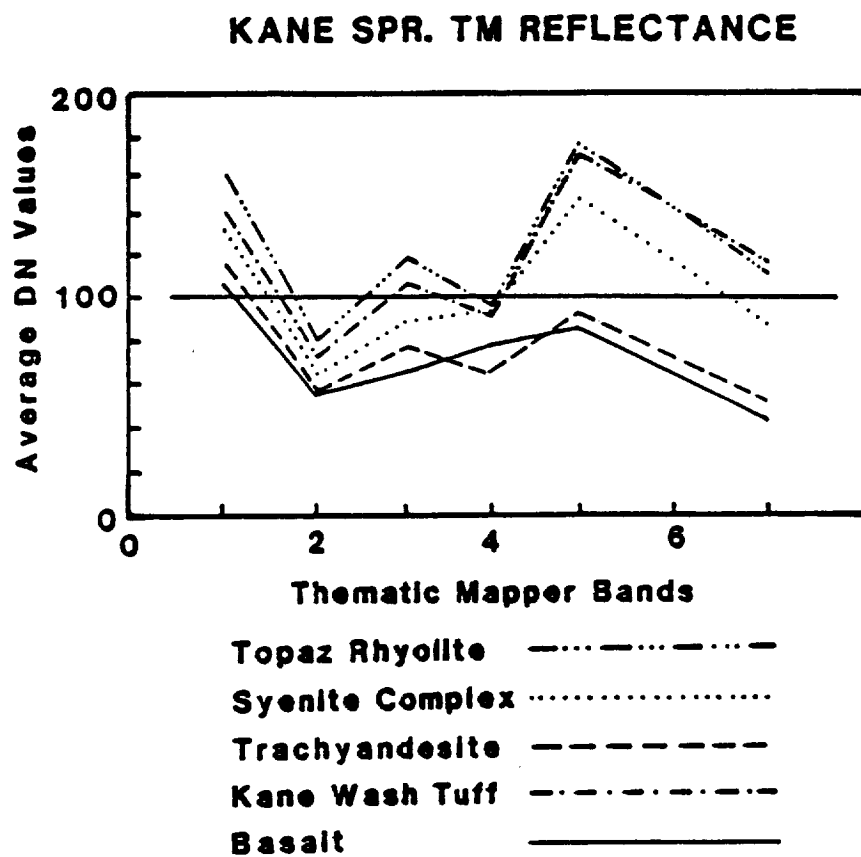
Figure 93. Graph of thematic mapper band DN values over the major lithologic units of the Kane Springs Wash volcanic center. Raw values uncorrected for additive path radiance.

with those from Appendix K. Both binary and ternary band vs band diagrams and band vs composition diagrams for units from each of the study sites follow. Emphasis in these plots is on bands and band relationships which have been most illuminating with respect to Landsat TM and laboratory and field spectra. Although points on the graphs are limited by the restricted number of mappable imagery units in the scenes, some otherwise unapparent trends and groupings of units can be delineated on the basis of relationships involving felsic tendencies, degree of magmatic evolution, and extent and maturity of desert varnish. The trends and groups that are interpreted on these diagrams and those that follow are consistent with the imagery and laboratory spectra presented in earlier sections.

A regression intersection method of adjusting image data for additive path radiance (Crippen, 1987) was applied to each scene to test atmospheric effect on band ratios. Raleigh scatter due to atmospheric interference is extreme in band 1, but histogram and deep shadow methods of measuring additive path radiance in band 2 proved negative and atmospheric scatter is considered unimportant for most of the applications described in the thesis. To test the effect of atmospheric interference on band ratios, particularly 5/2 ratios, Crippen's (1987) regression method was tested. It was found that DN values needed to be

adjusted downward 9 digital numbers in band 2 over the Kane Springs Wash study site and downward by 7 over both Black Mountain and Stonewall Mountain. Band 5 required a nominal adjustment of 3 digital numbers at Kane Springs Wash and 2 at the other two sites. The result does not alter relative positions of points on the graphs that follow, for example, 5/2 values for basalt, topaz rhyolite, and Kane Wash Tuff from the Kane Springs Wash study site using raw DN values (Table 16) are 1.87, 2.37, and 2.69, respectively. After the regression adjustment, values converted to 2.24, 2.70, and 3.05, respectively. The effect is slightly less at the other two sites. Values converge a little, but not enough to affect the interpretations that follow. Discrimination of rock assemblages or surface cover very similar in albedo within bands being used in ratioing, however, might benefit from adjustments for additive path radiance.

STONEWALL MOUNTAIN VOLCANICS

The more magmatically evolved late flows of the Stonewall Mountain caldera - the ash flow tuffs - show lower 5/7 values than the basalts and rhyolites derived from the Mount Helen caldera (Figure 94). Although a straight line albedo relationship exists among the units on the band 5 vs band 7 plot, divergence on the other graphs seem to follow 2 trends: one involving the ash flows of the Stonewall caldera, the other involving the units from
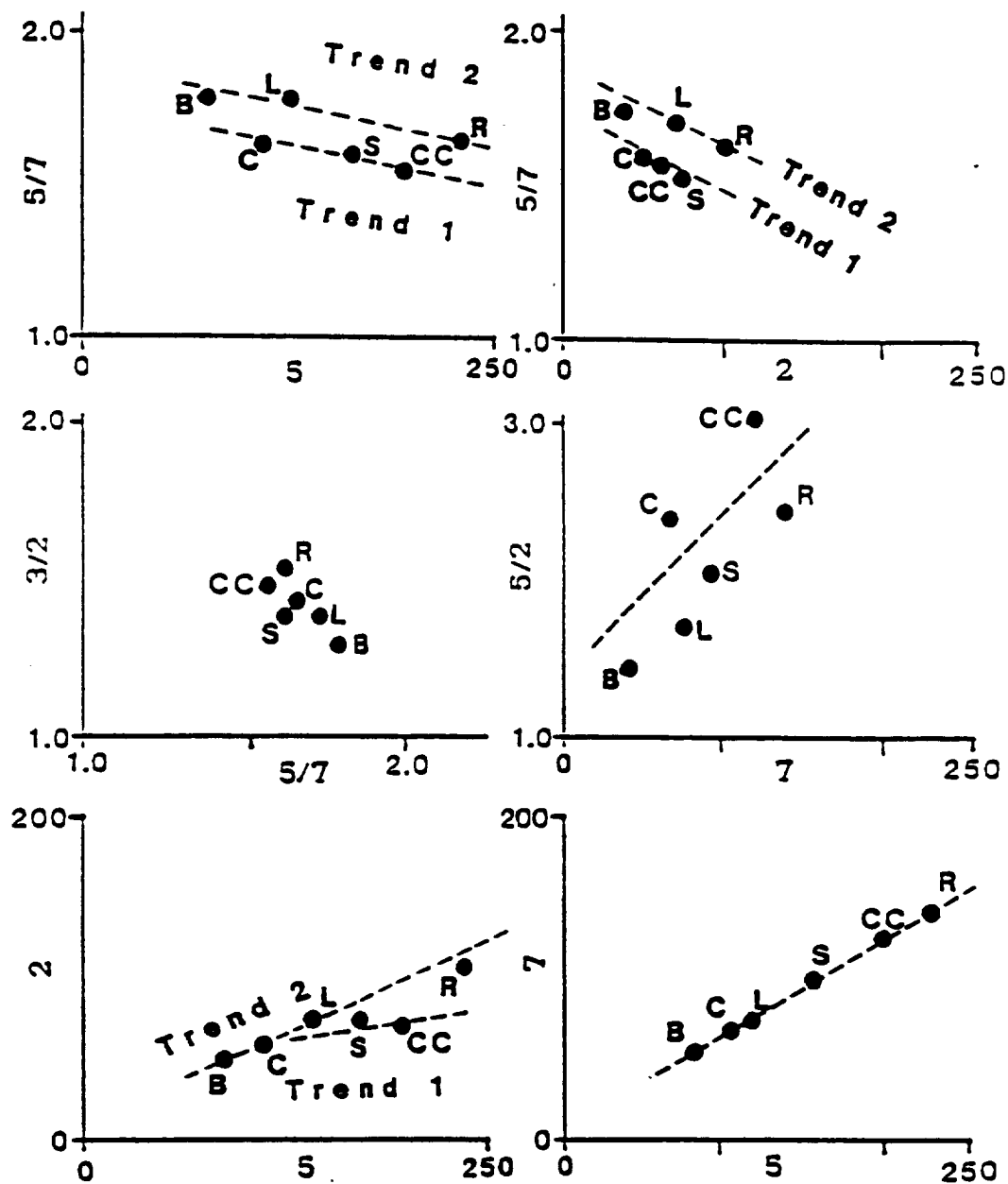
B - Late Basalt   CC - Civet Cat Canyon Cap Rock

S - Spearhead Tuff   R - Antelope Springs Rhyolite

C - Civet Cat Canyon Tuff   L - Antelope Springs Quartz Latite

Figure 94. Thematic mapper band DN plots for the major volcanic units of the Stonewall Mountain study area.

Mount Helen. The lower 5/7 values of the ash flow units of Stonewall are probably due both to the existence of more extensive, well developed desert varnish on these units and to the relatively high concentration of incompatible elements they contain. The two groups plot along separate trends on the band 2 vs band 5 graph, due apparently to absorption of varnish in band 2. The higher albedo of more felsic and evolved units leads to parallel trends within each of the two groups. The 5/2 vs band 7 diagram distributes the units in a broad relationship congruent with magmatic evolution - higher band 7 and 5/2 values.

Ternary band DN plots for the Stonewall units (Figure 95) distribute the deposits in predictable patterns according to relationships depicted in the binary diagrams. The linear distribution on the 5/2-5/7-3/2 triangle is believed to be due in part to both rock petrochemistry, with the highly evolved units plotting away from the 5/7 apex and toward the 5/2 apex, and to desert varnish, with the ash flow tuffs, which tend to develop more extensive varnish, falling toward the 5/2 apex. Figures 96 and 97 show band vs compositional diagrams for the Stonewall units. Distinct trends result from a correlation of albedo with felsic tendency; enrichment in incompatible elements, which indicates degree of magmatic evolution; and extent and intensity of desert varnish. It seems worthy to note that reflectivity trends of 5/7 and 5/2 ratios with respect
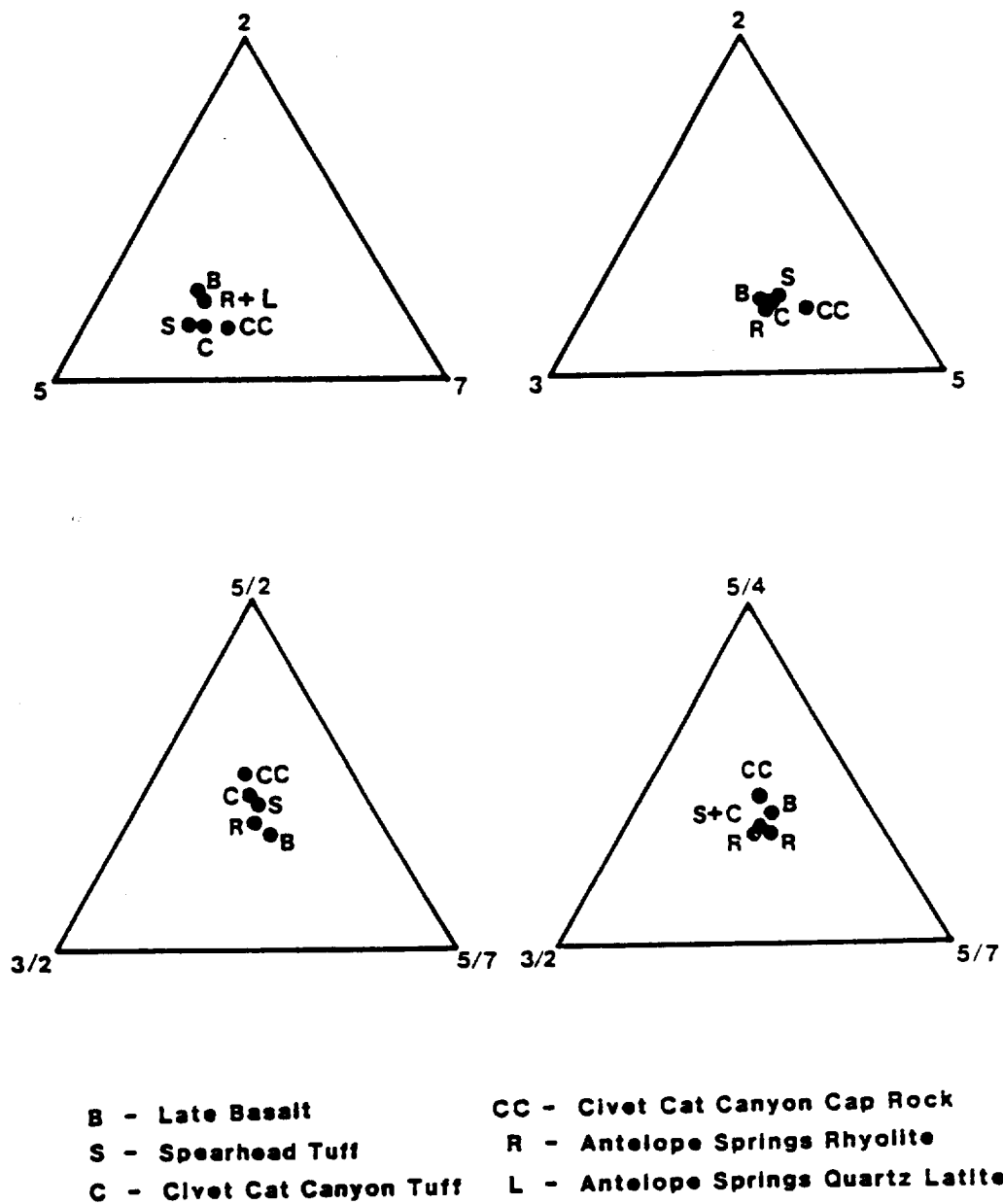
Figure 95. Thematic mapper band DN plots (ternary) for the major volcanic units of the Stonewall Mountain study area.

230
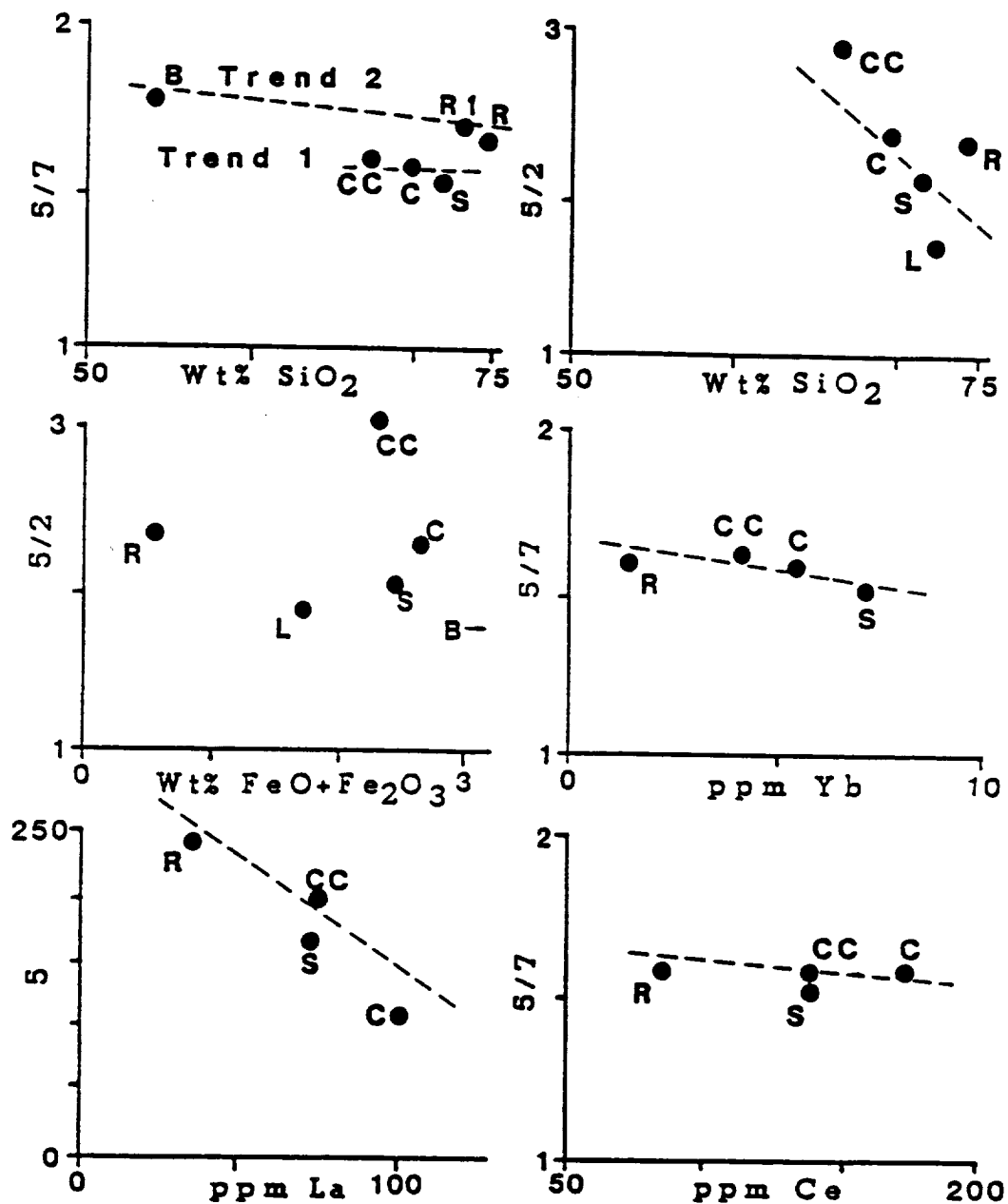
B   -   Late Basalt   CC -   Civet Cat Canyon Cap Rock
S   -   Spearhead Tuff   R -   Antelope Springs Rhyolite
C   -   Civet Cat Canyon Tuff   L -   Antelope Springs Quartz Latite

Figure 96.   Thematic mapper band DN plots versus petrochemistry for the major volcanic units of the Stonewall Mountain study area.
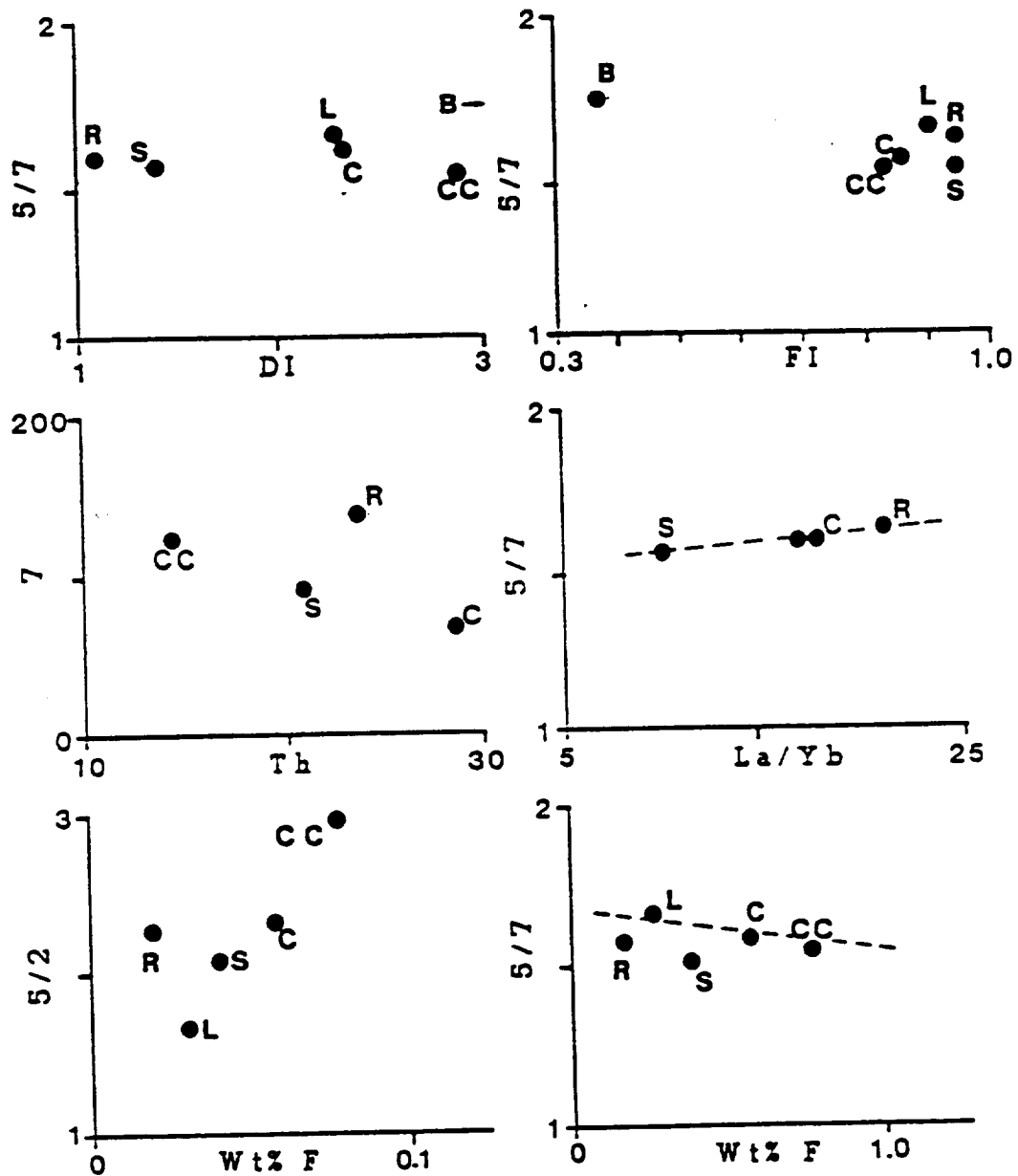
B - Late Basalt

S - Spearhead Tuff

C - Civet Cat Canyon Tuff

CC - Civet Cat Canyon Cap Rock

R - Antelope Springs Rhyolite

L - Antelope Springs Quartz Latite

FI [Felsic Index]: $Na_2O + K_2O / Na_2O + K_2O + CaO$

DI [Differentiation Index] : $100 \, MgO / MgO + FeO + Fe_2O_3 + Na_2O + K_2O$

Figure 97. Thematic mapper band DN plots versus petrochemistry for the major volcanic units of the Stonewall Mountain study area.

'to silica content indicate a slight negative slope and a decrease in 5/7 values with an increase in silica as expected, but 5/2 ratios decrease as well, and sharply, as silica increases. As we will see from plots of values from the other 2 study sites, an increase in 5/2 ratios seems to indicate an increase in magmatic evolution, more as measured by peralkaline tendency (higher Na_2O+K_2O), rather than silica. Band reflectivity plots against the rare elements reveal linear relationships, particularly between 5/7 values and fluorine. The correlation between reflectivity values and the trace elements is superior to linear relationships between reflectivity values and the major oxides, reflected in part (Figure 97) by the differentiation index (DI) and Felsic index (FI).

BLACK MOUNTAIN VOLCANICS

Similar relationships and trends can be found among the band vs band and band vs compositional plots for units from the Black Mountain and Kane Springs Wash study sites (Figures 98-105). At Black Mountain, highly evolved peralkaline Gold Flat Tuff and Labyrinth Canyon Tuff (distal Spearhead Tuff from the Stonewall caldera) form separate trends and groups since they both have relatively high albedo and exhibit relatively well developed desert varnish. Both units have high values in band 5, low values in band 2, thus a high 5/2 ratio (Figure 98). The Gold
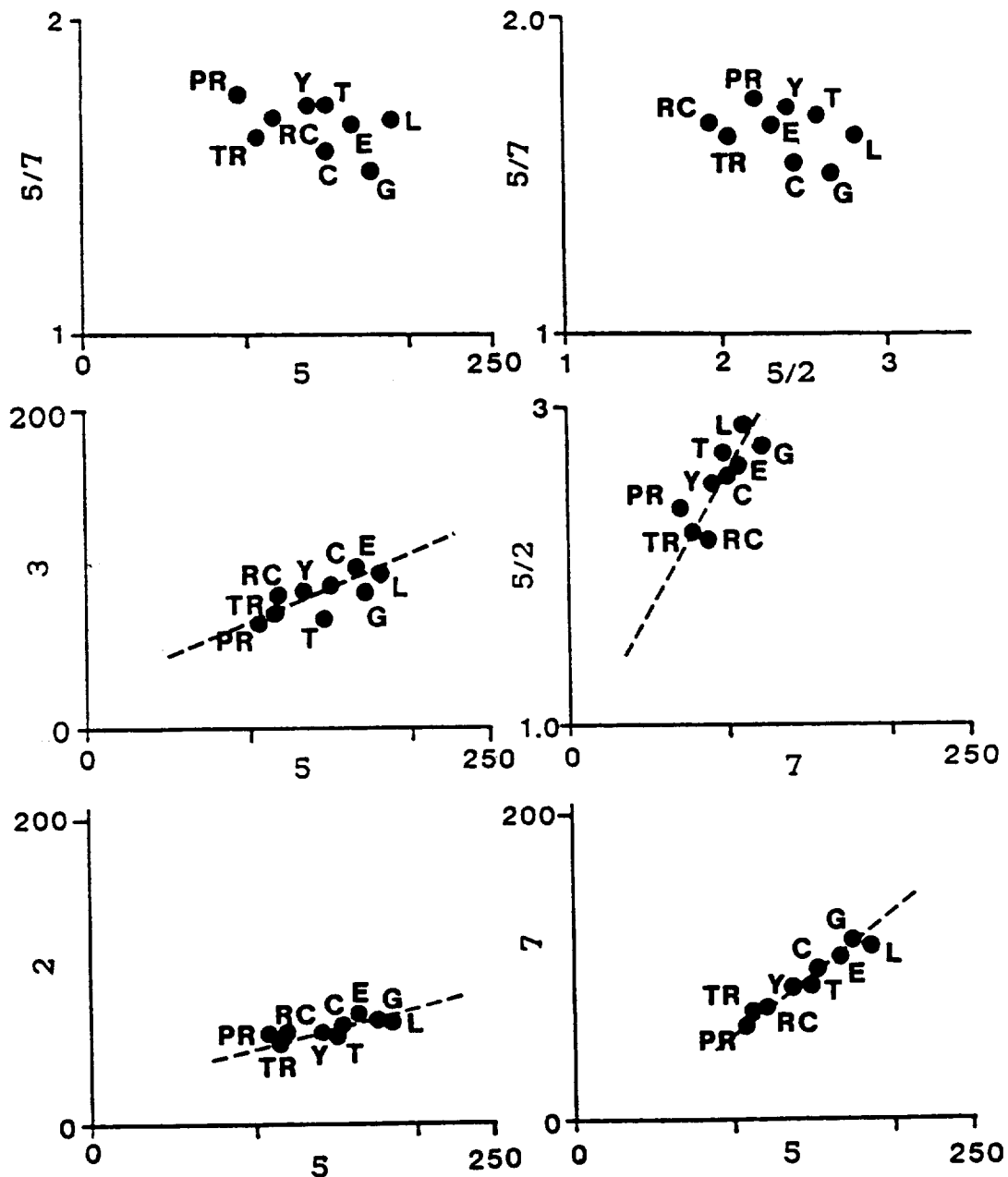
L - Labyrinth Canyon Tuff

G - Gold Flat Tuff

T - Trachyte of Hidden Canyon

C - Older Thirsty Canyon Tuffs

E - Pre-Black Mountian Volcanics

PR - Lava of Pillar Springs

TR - Trail Ridge Tuff

RC - Lava of Ribbon Cliff

Y - Rocks of Yellow Cliff

Figure 98. Thematic mapper band DN plots for the major volcanic units of the Black Mountain study area.

Figure 99. Thematic mapper band DN plots (ternary) for the major volcanic units of the Black Mountain study area.
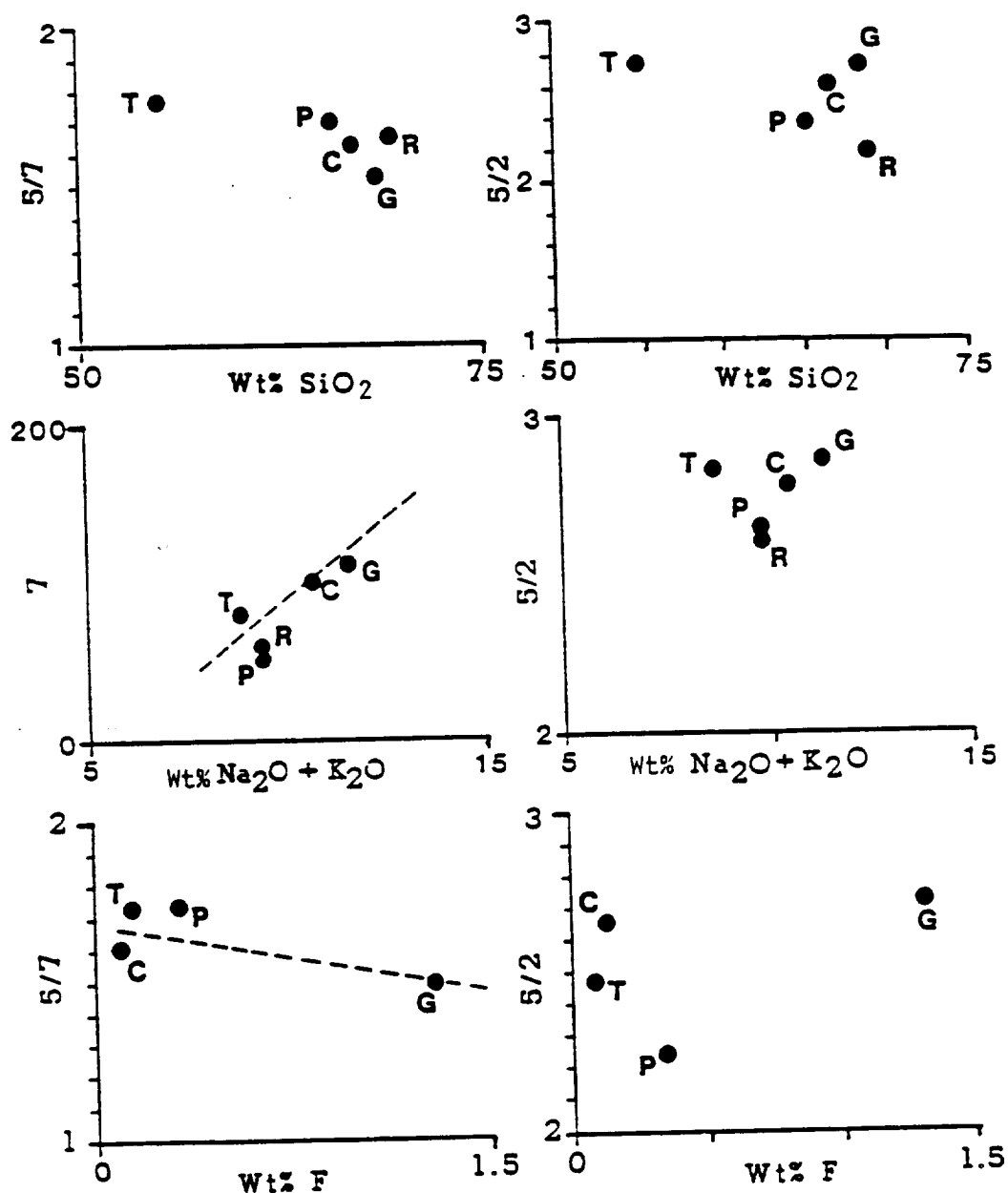
Figure 100. Thematic mapper band DN plots versus petrochemistry for the major volcanic units of the Black Mountain study area.

Figure 101. Thematic mapper band DN plots versus petrochemistry for the major volcanic units of the Black Mountain study area.

237
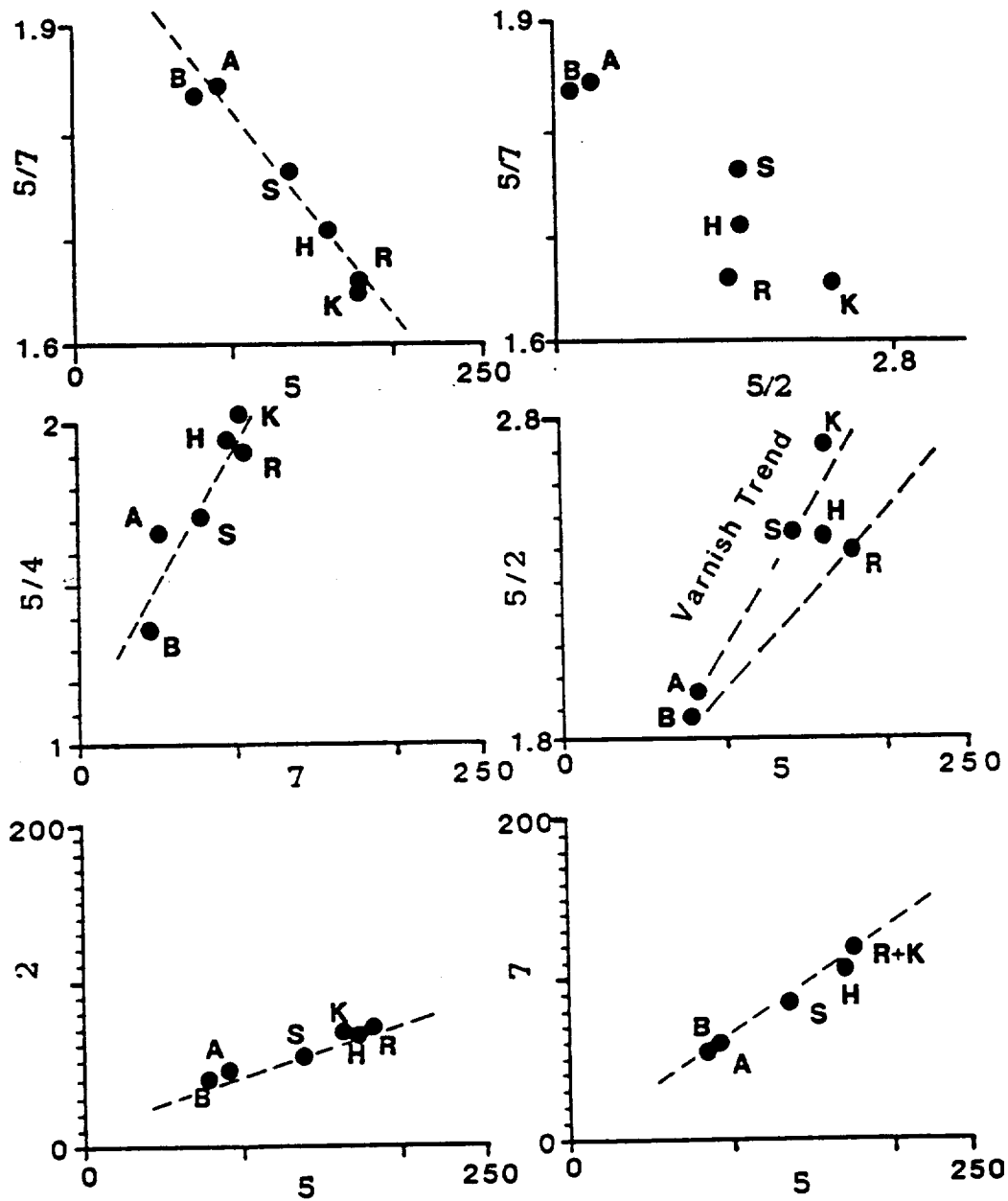
R - Topaz Rhyolite   H - Hiko Tuff
B - Basalt Flow   K - Kane Wash Tuff (V)
A - Trachyandesite   S - Syenite Complex

Figure 102. Thematic mapper band DN plots for the major volcanic units of the Kane Springs Wash study area.
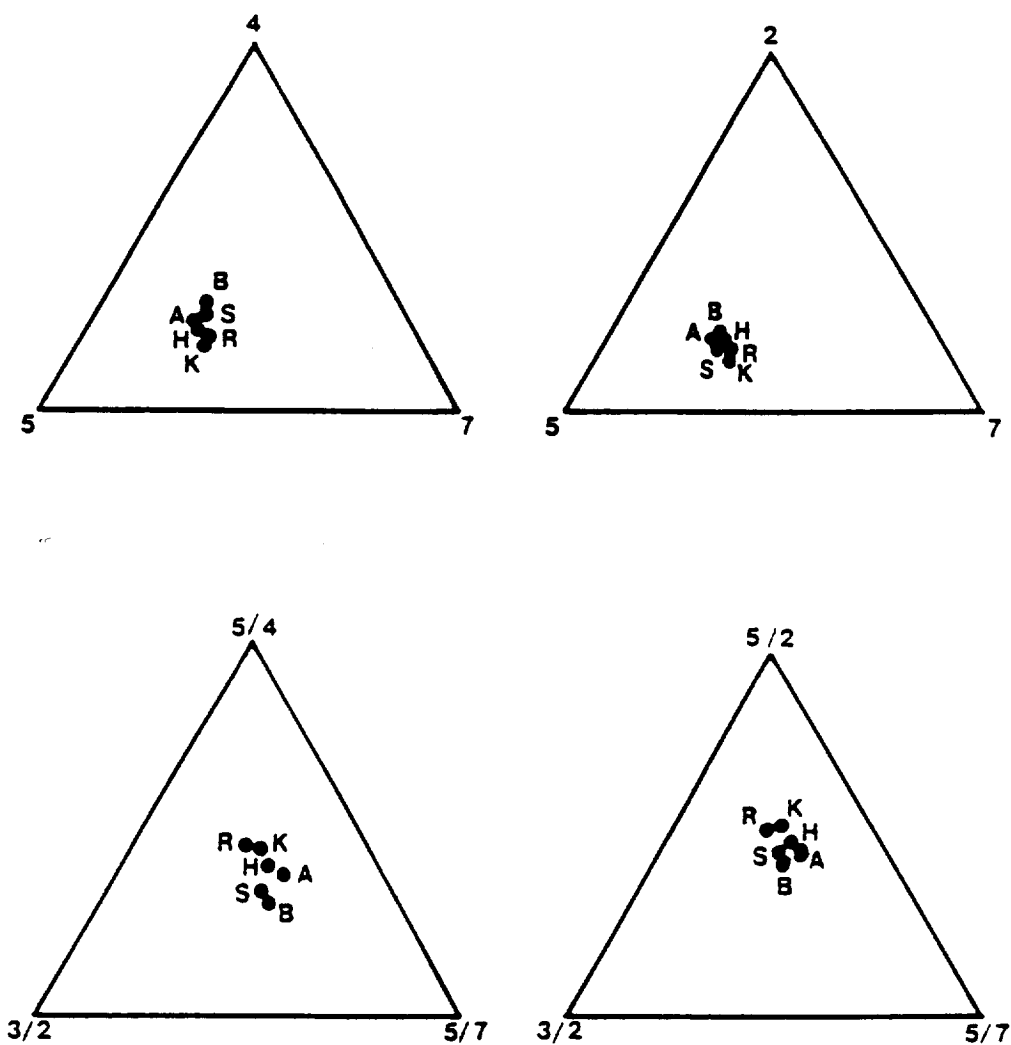
Figure 103. Thematic mapper band DN plots (ternary) for the major volcanic units of the Kane Springs Wash study area.
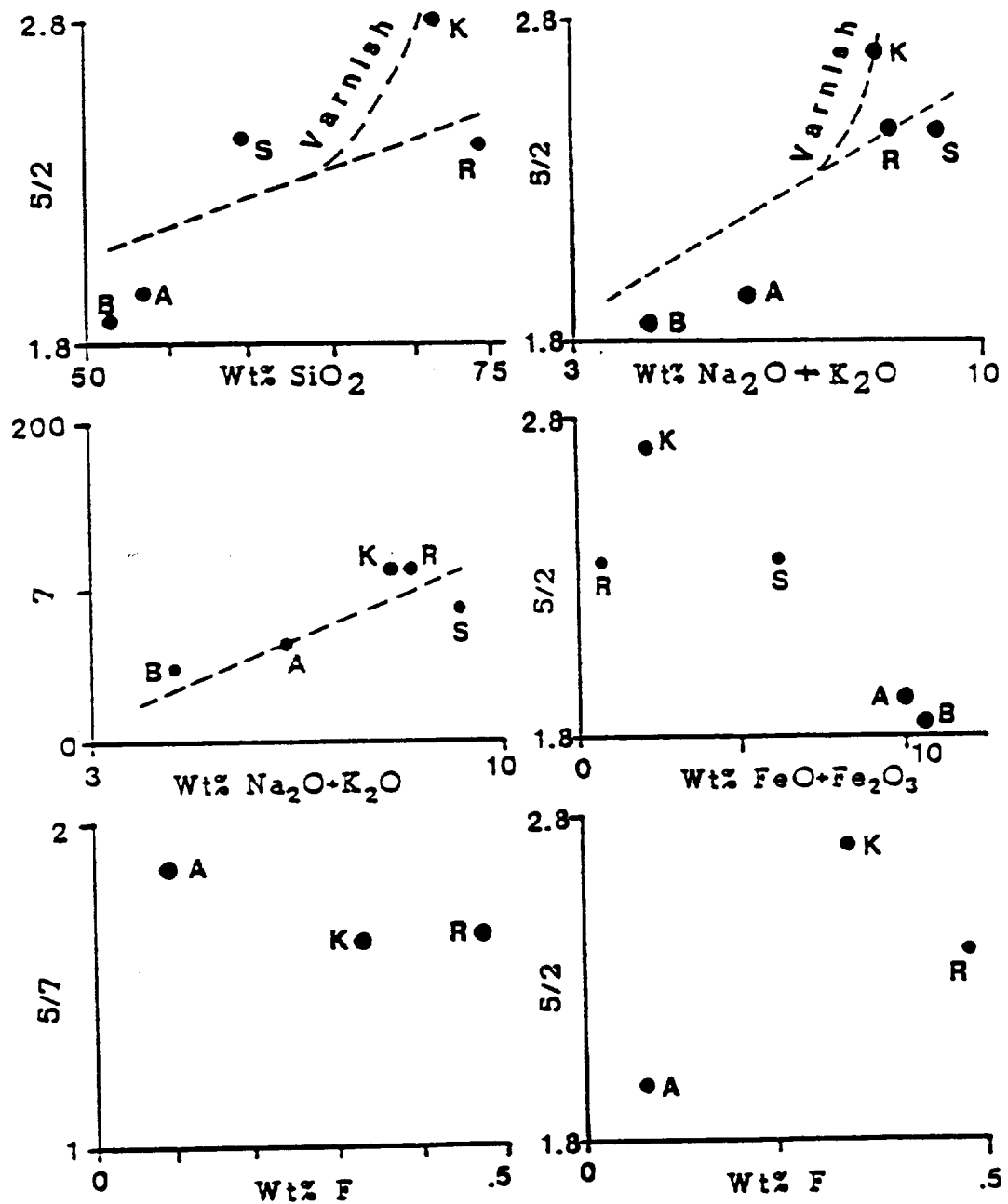
R – Topaz Rhyolite   H – Hiko Tuff
B – Basalt Flow   K – Kane Wash Tuff (V)
A – Trachyandesite   S – Syenite Complex

Figure 104. Thematic mapper band DN plots versus petrochemistry for the major volcanic units of the Kane Springs Wash study area.
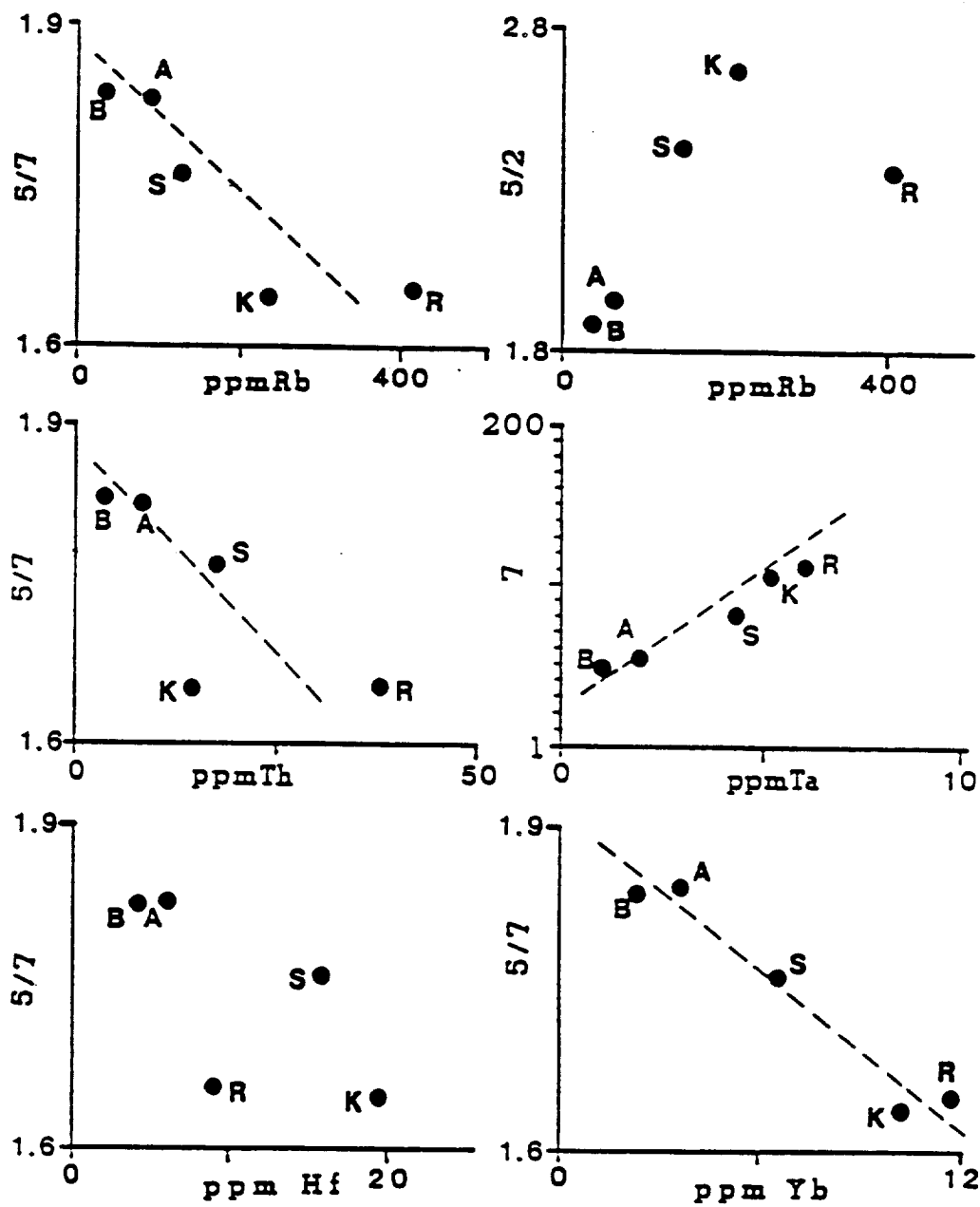
Figure 105. Thematic mapper band DN plots versus petrochemistry for the major volcanic units of the Kane Springs Wash study area.

Flat Tuff is an unusual, quite highly evolved late magmatic differentiate with a low 5/7 ratio and high relative fluorine and alkaline components (Figure 100). The ternary plot of 5/4-5/7-3/2 values distributes rock assemblages according to alkaline tendencies and incompatible element content, with lowest to highest from Trachyte of Hidden Cliff (T), Lavas of Pillar Springs and Trail Ridge Tuff (PR), older Thirsty Canyon Tuff (C), Labyrinth Canyon Tuff (L), to Gold Flat Tuff (G). The correlation between lower 5/7 values with degree of magmatic maturity is again apparent in reflectivities vs minor element plots, particularly thorium, rubidium, and fluorine (Figures 100 and 101).

KANE SPRINGS WASH VOLCANICS

At Kane Springs Wash interesting spectral characteristics are apparent between the 3 highest albedo units, the Hiko Tuff, Kane Springs Tuff, and Topaz Rhyolite which are congruent with differences in tendencies toward magmatic maturity and desert varnish formation. The final flow from the Kane Springs volcanic center was the Kane Springs Tuff which consists of 3 cooling units. Each is peralkaline and fairly well evolved. They were followed by intracaldera lava domes consisting of topaz rhyolite, also highly evolved. Divergence exits from the more typical plots established among the units at the other 2 study

sites. On a 5/7 vs band 5 plot, for example (Figure 103), a linear correlation emerges, compatible with magmatic evolution, whereas on the plot 5/7 vs 5/2 plots, Kane Wash Tuff and topaz rhyolite appear to plot along divergent trends due possibly to the greater development of desert varnish and higher 5/2 values on the former. More extensive varnish may account for the departure of Kane Wash Tuff from an otherwise linear distribution on the 5/2 vs Na_2O+K_2O and 5/2 vs SiO_2 diagrams (Figure 104). Again the large-ion-lithophile (LIL) elements and other incompatible elements provide positive correlation with band 7 and 5/7 plots. Particularly vivid linear relationships are exhibited with tantalum, rubidium, ytterbium, and fluorine.

DESERT VARNISH

Much has been presented in previous sections about desert varnish and secondary mineral coatings on volcanic rock assemblages at the three study sites. Nature, geochemistry, spectra, origin, and Landsat significance have been addressed. This section is intended to bring these observations and relationships together in a synopsis of the influence of desert varnish on surface spectral compositions and on Landsat imagery.

OCCURRENCE AND DISTRIBUTION

Desert varnish is characteristically thin translucent and discontinuous (Figures 8, 9, 14, 16, 50, 51, and 52). The coatings are a reddish brown to dark brown amorphous mass that tends to coat mineral grains at the surface and penetrate as a thin film intergranularly up to 1-1.5mm into the rock substrate. SEM scans reveal that the surface laminations or encrustations rarely exceed 10-20um and that even a well coated surface is dominated by much thinner films of coating. Thick 10-50um deposits are sporadic and discontinuous, concentrated in minute protected recesses.

Desert varnish develops to an advanced stage of maturity only where rock surfaces are resistant and durable. Horizontal and vertical discontinuity are characteristic. Where coated surfaces become breached by weathering or where deposits have not matured to an advanced state, relatively fresh rock is exposed. Over any given surface, 3x3m or so square, desert varnish rarely exceeds 50% by visual estimates. Removal of coated surfaces is expedited by development of weathering rinds, .25-2.0cm thick, which spall off outcrop surfaces. It is this process that leads to case hardening and exfoliation.

EFFECT ON TM SPECTRA

Penetration of electromagnetic energy within the TM range was studied by Buckingham and Sommer (1983) who found

that maximum penetration for pulverized samples of clay minerals was about 50um (Figure 106). A mixture of goethite and kaolinite - 75/25 - stopped penetration of 0.8-1.0um energy at around 25-30um. Amorphous, translucent compounds like those that make up the coatings of this study would transmit light further than crystalline mixtures of iron oxide and clays. In other words, light would penetrate in part (increasingly with increasing wavelength) completely through even the thickest concentrations of desert varnish yet discovered in this study reflecting to at least some degree the primary character of underlying rock to the extent that it is unaltered.

The effects of coatings on the spectral response of volcanic units in the project areas to the TM electromagnetic range were presented in preceding sections on lab and field spectra. Coated surfaces are compared to uncoated but somewhat weathered surfaces (Figures 67 and 68). Note that shorter wavelength energy is absorbed by desert varnish to a greater extent than longer wavelength energy. Beyond about 0.7-1.3um, depending on mafic affinity of the host rock, reflectance becomes less dependent on coatings for some units. In the case of the sample of Gold Flat Tuff, coatings tend to simply attenuate reflectance throughout the TM interval. (A similar relationship was reported by Farr, 1981.) The basalt,

Suite XIII   Goethite/Kaolinite   75/25   by weight

| Sample 1 | Sample 3 | Sample 5 | Sample 7 |

Thickness= 5umm   13 um   28 um   35 um

% Reflectance

100

50

900 um   900 nm   900 nm   900 nm

λ   λ   λ   λ
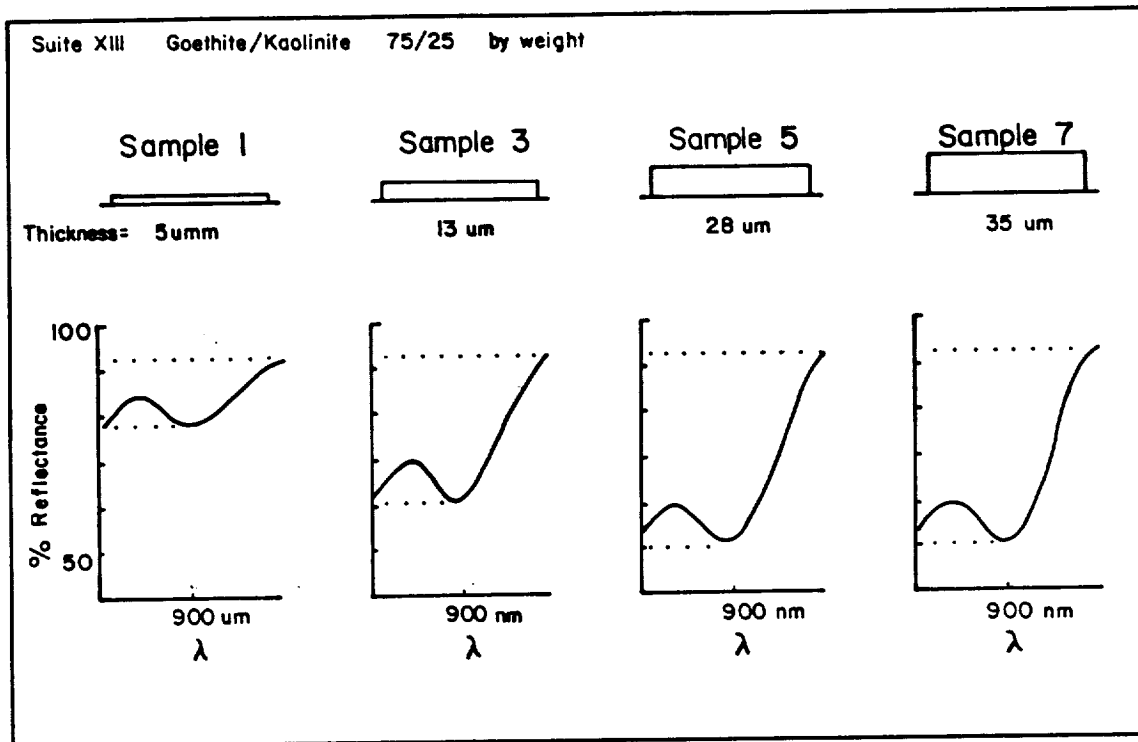
Absorption vs Sample Thickness
0.9 Micrometers

W.F. Buckingham and S.E. Sommer, 1983

FIGURE 106. Penetration measurements of 0.9 micrometer radiation. Target is mixture of goethite and kaolinite (75/25). Reflectance is affected by increasing thicknesses of target to 28 micrometers, then remains constant with greater thicknesses. (after Buckingham and Sommer, 1983).

mafic trachyte, and ash flow tuff (dark, ferruginous Civet Cat Canyon Tuff) samples show the typical absorption of coatings in the lower wavelength interval, but actually record higher reflectance beyond 0.7 to 1.3um for the coated samples. This relationship may be due in part to the relatively higher absorption and low albedo of fresh melanocratic rocks relative to coatings which consist of amorphous translucent compounds high in silica and aluminum. This relationship is supported by the general tendency for reflectance to increase with an increase in wave number for coated samples, but decrease or level off for the uncoated samples. Thus 5/7 values tend to decrease for coated samples relative to uncoated ones. This relationship is apparently inherent to spectra of desert varnish itself.

Field spectra, presented in Chapter VI, emphasize spectral contrasts of various lithologic units with variations in intensities of desert varnish development. Comparisons of reflectance values within Landsat TM bands for variably varnished surfaces for most of the units are tabulated in Table 33. Figures 107 and 108 show graphs of reflectance values for wavelengths within each TM band plotted against variable but unified and systematic differences in desert varnish development. Important relationships apparent from these graphs include:

TABLE 33. SPECTRORADIOMETER (IRIS) MEASUREMENTS
(in percent reflectance)
FOR VARIABLY VARNISHED ROCK SURFACES

FORMATION	WAVELENGTH (micrometers)				
	.56	.66	.83	1.65	2.21
Spearhead Tuff					
Heavy	19.1	20.2	26.5	36.0	39.3
Moderate	26.2	31.1	38.3	48.5	48.0
Light	24.3	31.2	38.5	52.4	51.9
Very Light	32.8	38.0	44.0	50.8	50.3
Civet Cat Canyon					
Very Heavy	15.4	18.2	28.0	40.0	40.0
Heavy	18.1	23.6	32.8	44.5	38.1
Moderate	16.0	20.8	31.9	46.7	47.9
Civet Cat Dark Glass					
Heavy	14.0	18.2	25.8	38.5	41.7
Moderate	15.6	19.3	26.5	39.4	40.9
Civet Cat Red Glass					
Light	14.8	20.6	33.0	64.7	61.9
Very Light	20.8	26.5	39.0	84.0	78.5
Fresh	22.0	29.4	42.8	92.7	79.5
Antelope Spr. Rhyolite					
Heavy	16.8	20.0	24.7	38.8	44.0
Moderate	19.9	26.5	32.7	54.6	52.6
Light	28.0	36.1	40.1	56.7	56.0
Very Light	38.8	44.2	48.9	58.9	49.7
Late Basalt					
Heavy	11.5	12.4	17.5	25.6	20.8
Moderate	15.6	18.0	22.8	27.0	23.6
Light	12.1	15.5	21.6	25.3	20.7
Very Light	16.7	18.5	20.0	16.8	14.5
Gold Flat Tuff					
Heavy	14.9	16.5	23.7	33.9	39.8
Moderate	20.1	22.8	31.2	40.3	40.6
Light	24.6	27.3	33.6	56.0	59.9
Labyrinth Canyon Tuff					
Heavy	19.3	26.4	36.1	58.3	56.1
Moderate	20.8	30.5	41.9	61.6	57.0
Light	30.5	40.0	51.0	66.8	65.4
Very Light	39.7	47.2	57.4	69.3	64.8
Ribbon Cliff Lava					
Heavy	12.0	16.3	24.2	33.0	30.5
Light	16.0	22.8	29.4	34.1	31.2
Fresh	23.7	26.7	30.3	29.2	27.2
Trachyte Hidden Cliff					
Heavy	11.8	12.9	19.8	32.6	35.0
Moderate	13.3	15.4	19.3	23.7	21.5
Light	21.5	24.6	31.1	32.2	28.1
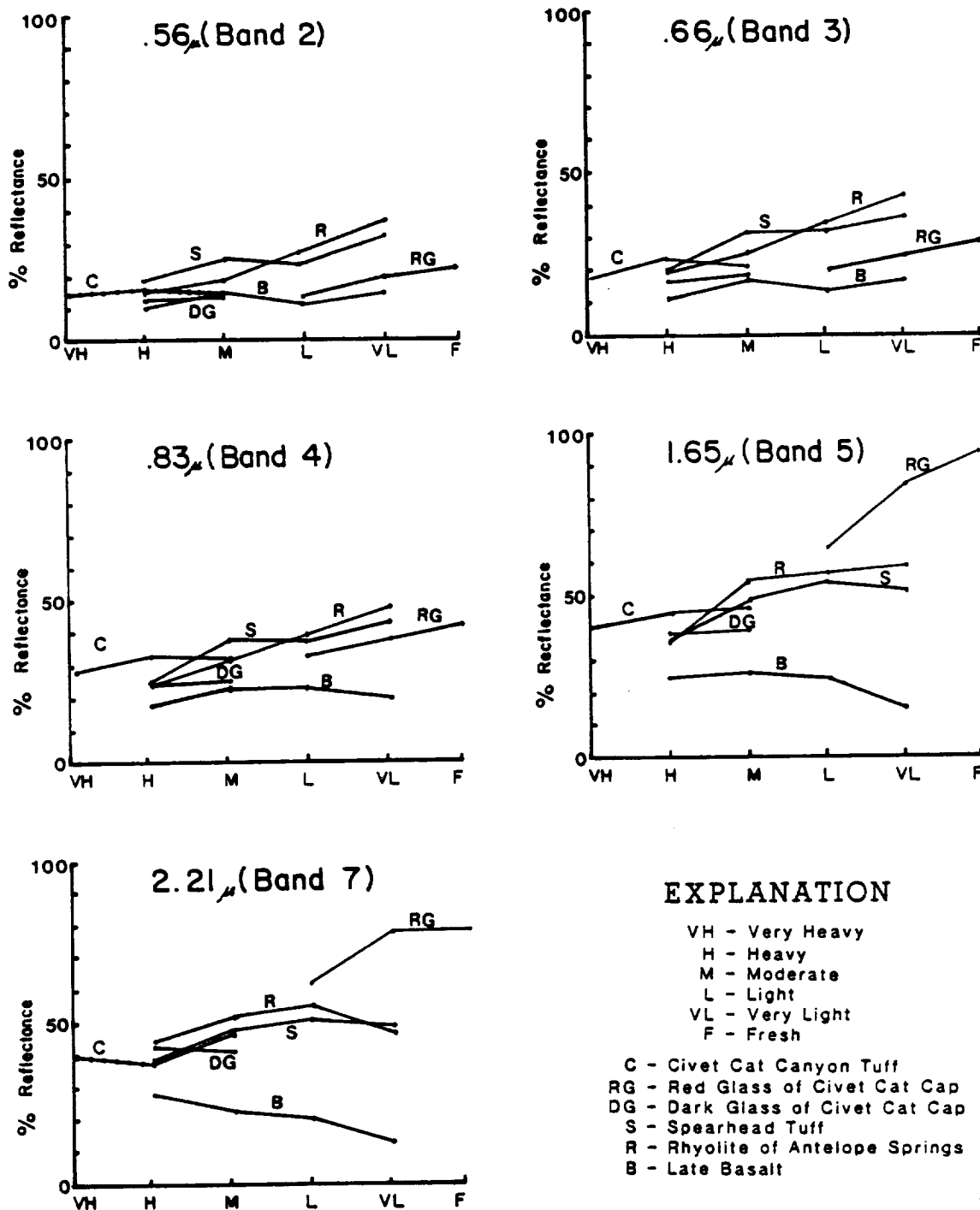
Figure 107. Effect of variable desert varnish at different visible/
near-infrared frequencies. Plots are for major volcanic units from
the Stonewall Mountain study site. Data from IRIS (Collins spectro-
radiometer) field measurements (Table 33).
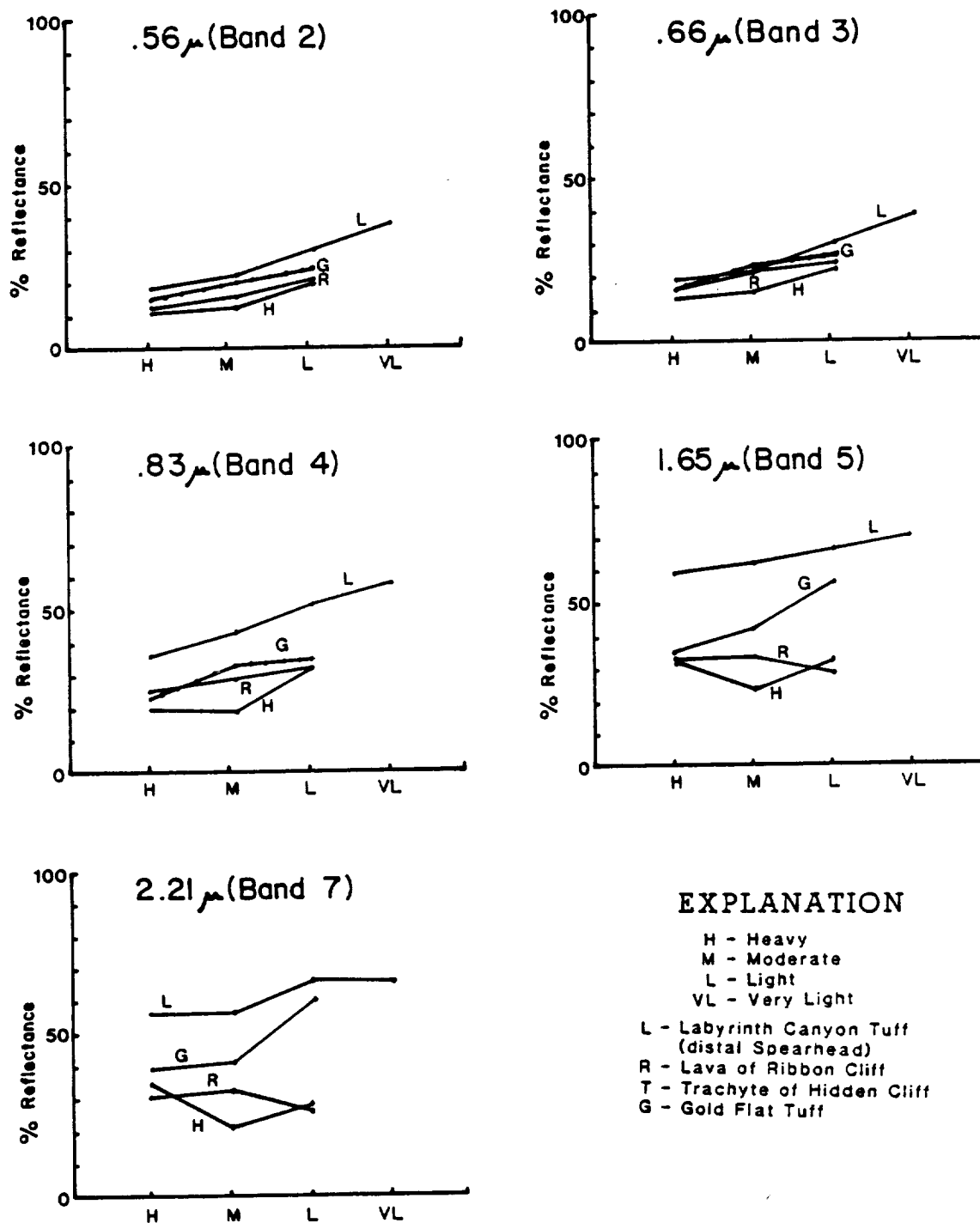
Figure 108. Effect of variable desert varnish at different
visible / near-infrared frequencies. Plots are for major
volcanic units from the Black Mountain study site. Data
from IRIS (Collins spectroradiometer) field measurements
(Table 33).

1. At shorter wavelengths (bands 2, 3, and 4) reflectance increases almost straight-line for the more felsic formations as the amount of varnish decreases, if curves are smoothed visually from high varnish to low varnish.

2. Reflectance increases about 6-10% or an average of about 8% at shorter wavelengths (bands 2-4) with each increment of the varnish scale. This relationship holds for the more felsic or low albedo units only. (Antelope Springs rhyolite, Spearhead Tuff, red glass of Civet Cat, and all units shown from Black Mountain) and for lower wavelengths - through TM band 4.

3. The slopes indicate about a 0.5% increase in reflectance with each percent decrease in varnish cover, if we assume 100% cover at the very heavy end of the varnish scale and no varnish at the fresh end; however, since very heavy varnish cover is only about 50% total rock cover in most instances, reflectance values would actually change about 1% with each 1% change in total varnish cover for the lower wavelength TM bands 1-3.

4. Radiation around TM bands 5 and 7 responds differently from the higher energy range. Reflectance slopes tend to increase between heavy and moderate varnish in the TM band 5 range for Antelope rhyolite and Spearhead Tuff, indicating a reflectance increase of around 1.5% for each percent decrease in varnish cover, again assuming about 50% varnish cover for very heavy varnish. At lower magnitudes of varnish distribution, however, the rate of change in reflectance decreases, and at wavelengths of 1.65um reflectance no longer seems affected by moderate to light varnish. This relationship was expected from lab and field spectra and 5/2 ratio plots over heavily varnished units. The longer wavelength bands are less attenuated by desert varnish which is much more absorbent to higher energy radiation.

5. Thus for longer wavelength radiation - 1.65 and 2.21um, reflectance does not appear affected except over the most intensely coated samples. This is most apparent with regard to more felsic or high albedo rocks. Basalt on the other hand exhibits decreasing

reflectance with decrease in varnish, a relationship, again, expected from laboratory spectra.

6. Reflectance divergence among units in both TM bands 5 and 7 is apparently caused by two factors: first, primary rock composition and second, higher reflectances of light to very light varnish which typically includes basal varnish clay and carbonate.

ROCK-VARNISH ALBEDO DIFFERENCE

With an increase in desert varnish formation on a given host, both in terms of intensity or thickness and pervasiveness, there would be a concomitant increase in the value of the TM 5/2 ratio if a significant difference exists between the composition and albedo of the varnish and that of the underlying host. As host felsic tendency increases so too would reflectance values as wavelength increases. With an increase in thickness of varnish, reflectance would be increasingly attenuated due to increased absorption by varnish relative to underlying host. Desert varnish on mafic rocks is indistinguishable due to similarities in albedo. The varnish divergence trends interpreted on the graphs above are controlled by

both the difference in composition between the varnish and host rock and the extent of varnish development. The 5/2 ratio can be a helpful measure of extent of varnish development. Its applicability increases with felsic tendency of host rock. Attenuation of reflectance by varnish is inversely proportional to wavelength. As varnish accumulates on a given host, TM bands 2 and 5 are disproportionately affected, with shorter wavelengths attenuated most. This should result in a hyperbolic curve if varnish thickness were plotted against a 5/2 ratio to a point where band 2 reflectance reaches a minimum and the curve slope stabilizes.

It seems useful to introduce a new concept that should aid discussions of TM imagery relationships involving desert varnish. Detection of desert varnish, according to principles outlined above, depends on the compositional difference between the varnish and the underlying host. This difference, perhaps best defined in terms of the ferromagnesian components, is herein termed the Rock-Varnish Albedo Difference (RVAD) which is controlled by mafic tendency of host rock and measured by the proportion of mafic constituents in varnish relative to underlying host rock or:

wt% Mn and Fe oxides in varnish/

wt% MnO + FeO + Fe_2O_3 + MgO in host rock

A plot of the 5/2 ratio and RVAD, represented by a mafic composition ratio between rock host and varnish, is represented in Figure 109, and data for unit 5/2 values and the RVAD are compiled in Table 34. Varnish compositions were probed by scanning electron microscope (SEM) with an energy dispersive X-ray system (EDX). Since SEM analysis is typically inaccessible to many investigators it is useful to realize that the FeO+MnO content of varnishes investigated remains fairly constant - 40-50% - on felsic units. The RVAD, therefore, for these suites of volcanic rocks is determined chiefly by the felsic tendency of host rather than by variations of iron and manganese in the varnish. For sake of desert varnish identification by TM imagery, which largely involves detecting a difference between varnish and host composition, we can say that the more felsic rocks have a high RVAD potential.

VEGETATION

Vegetation at each of the study sites was described in general in Chapter I and more specifically by rock units in Chapter III. Field spectra for sagebrush, atriplex, and lichen were presented inn Chapter VI. Vegetative cover varies markedly from study area to study area. TM band 4/3 and PC3 images highlight vegetation in bright tonal contrast, and these images help identify pixels with

TABLE 34.

ROCK-VARNISH INDEX OF MAJOR UNITS

VOLCANIC UNIT	DESERT VARNISH (wt%)		FRESH ROCK (wt%) (Average of several samples)			RVAD	TM BANDS 5/2
	FeO	MnO	FeO+Fe$_2$O$_3$	MgO	MnO		
Civet Cat (C)	7.28	39.48	2.63	0.69	0.10	13.67	1.71
Spearhead (S)	14.57	24.78	2.55	0.24	0.06	13.81	2.08
Antelope Spr. rhyolite (R)	15.77	29.30	0.63	0.12	0.01	59.30	2.42
Antelope Spr. latite (A)	8.33	18.63	1.44	0.47	0.04	13.83	1.64
Basalt from Stonewall (BS)	23.64	33.77	8.01	3.49	0.13	4.94	1.59
Labyrinth Canyon (L)	14.99	29.13	1.42	0.43	0.06	23.01	2.94
Trachyte H.C. (T)	13.07	42.43	5.72	1.41	0.15	7.62	2.67
Rocket Wash (RW)	14.76	20.31	3.78	0.77	0.14	7.48	2.10
Gold Flat (G)	8.98	27.77	4.88	0.25	0.17	6.83	2.69
Hiko Tuff (H)	11.96	28.39	2.13	0.70	0.04	14.06	2.42
Kane Wash Tuff (K)	12.13	28.67	2.10	0.66	0.04	14.57	2.69
Basalt from Kane Spr. (B)	31.88	28.13	7.62	3.93	0.11	5.15	1.87
Syenitic Complex (SC)	15.49	33.69	4.05	0.11	0.05	11.68	2.42

* RVAD is measured by wt% FeO+MnO in varnish, divided by wt% Fe$_2$O$_3$+MgO+MnO in underlying host. (Iron oxides represent total iron.)
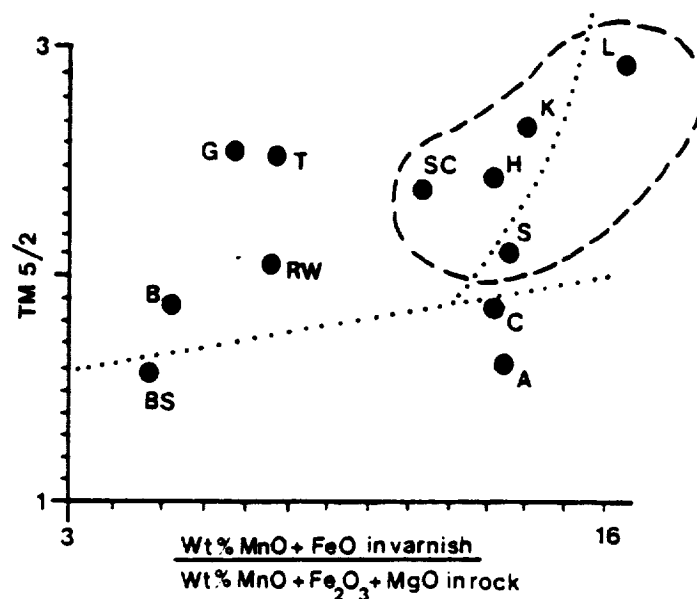
TOTAL IRON (Iron in varnish was reported as FeO)
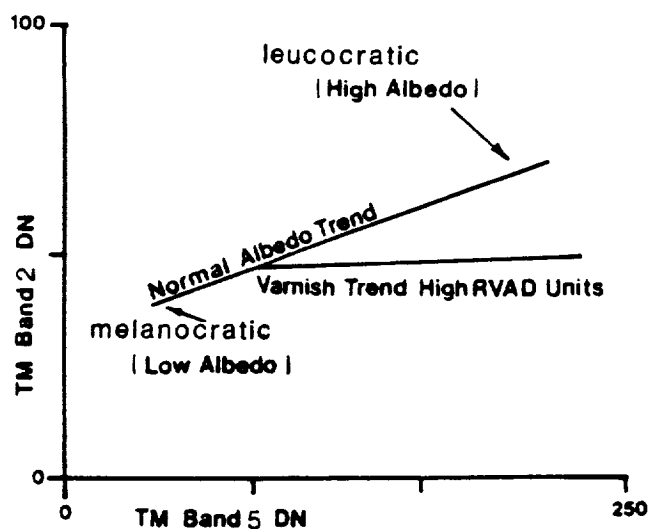
SIGNIFICANCE OF ROCK VARNISH ALBEDO DIFFERENCE

For explanation to graph symbols see Table 34.

Figure 109. Relationship of rock-varnish albedo difference (RVAD) to thematic mapper band 5/2 values. Letters on the upper graph stand for major volcanic rock units from the three study sites and correspond with Table 34. Note field of high 5/2 values and high RVAD's (dashed line) as measured by the ratio of Fe and Mn in varnish to Fe, Mn, and Mg in the host. Rock assemblages which fall in this field are leucocratic felsic units with well developed desert varnish, typically ash flow tuffs. Gold Flat Tuff (G) plots out of the field due partly to the unusually high iron content of this pantellerite. The plot of Trachyte of Hidden Cliff (T) is anomalous due to high 5/2 values resulting from vegetative spectral contamination. The dotted line on the upper graph is an interpretation of predicted linear relationships between units without extensive desert varnish development and a steep divergence off the linear up through units with well developed desert varnish which separates high RVAD units with high 5/2 values due to varnish cover.

vegetation dominated spectra. This section will describe vegetation influence on TM imagery, focusing on Black Mountain where relationships were most instructive.

There are three gross mappable vegetative cover classes at Black Mountain: sagebrush and atriplex dominant, foxtail and cheat grass dominant, and zones with low juniper and other evergreens. Vegetation varies considerably over the Gold Flat Tuff. Sagebrush/atriplex dominate over the broad Gold Flat capped mesa in the southern part of the project area, whereas the unit supports foxtail and other grasses with low evergreen shrubs where it forms an elongate north-northwest ridge in the west central portion of the study scene. As will be demonstrated later, these two vegetation types can be discriminated in some composite vegetation sensitive images but are virtually indistinguishable on certain lithologically dominated composites involving TM bands 5 and 7.

Outcrops of Trachyte of Hidden Cliff on Black Mountain host about 10% dusty moss green to greenish gray lichen with some bright orange lichen as well. Coatings are distinctively gray - light to medium - and moderately well developed. Inasmuch as Trachyte of Hidden Cliff underlies the summit of Black Mountain and its flanks, vegetation with higher altitude affinities, such as shrubs and scattered scrub evergreens are present. The western flank

258

of the mountain, however, tends to be dominated by golden grasses which extend over Labyrinth Canyon Tuff without discernible distinction from a distance. It will be shown later, however, that band composites with lithologically dominated spectra effectively differentiate Trachyte of Hidden Cliff from Labyrinth Canyon Tuff.

Labyrinth Canyon Tuff forms mesas which lap onto the western flank of Black Mountain. In spite of a golden grass canopy which overlies Labyrinth Canyon Tuff and its contact with underlying Trachyte, the two units exhibit distinctive spectra which are easily contrasted on some of the composite images. Orange lichen can be considerable - up to 15% of cover - on some outcrops.

Gold Flat Tuff is an unusual rock petrochemically and is distinctive spectrally as well. Gold Flat Tuff is relatively bright in bands 5 and 7 and PC1, very dark and anomalous in PC2, and dark as well in PC3 except over its northern exposures where it is masked by the bright response of vegetation due to dominant contribution of band 4 reflectance in PC3.

Mafic trachyte forms the central volcanic edifice and is very dark in all bands except 4 and 5 in which it is an indistinct medium gray. Spectral response appears to be influenced by vegetation, which in this case is chiefly foxtail grass and lichen with some scrub evergreen and rabbit brush at higher elevations. The unit is very bright

relative to other cover in the scene in the 5/7 and 4/3 images in a slightly stripped pattern that apparently follows drainages and is probably caused by high vegetative reflectances in bands 4 and 7. In individual PC's the deposit is quite dark in the first PC, very light due to vegetative interference in the third. It is indistinct from other lavas in the PC2-PC4-PC5 image, due apparently to absence of a parameter responsive to vegetative reflectance.

Labyrinth Canyon Tuff is spectrally similar to Gold Flat Tuff. It tends to be moderately to only slightly bright in TM bands 1, 2, and 3, quite bright in bands 4 and 5, somewhat less so in band 7. It is slightly less reflectant in band 7 than Gold Flat which aids its discrimination in false color composite images which incorporate this relationship. The unit is bright in PC1, dark in PC2. It appears masked by the bright vegetative response of golden grasses in PC3.

Contrast enhanced composite TM images of longer wavelength bands, particularly bands 3, 5, and 7 and composite images of these three bands in contrast enhanced mode (scaled), provide striking lithologic contrast among most volcanic deposits at both the Black Mountain and Stonewall Mountain areas. Over most pixel sized areas, vegetative cover is subordinate to rock/soil, especially at Stonewall Mountain where vegetation rarely exceeds 30% of

cover. Since some formations are uniquely exhibited in color contrast on some images, yet bear diverse vegetative canopies, it is apparent that the unique color contrast is more a result of lithologic spectral response than a vegetative control. The longer wavelength bands (bands 5 and 7 especially), PC2, and intensity and hue images of bands 3, 5, and 7 isolate reflective spectral contrasts that highlight lithologic character at the Black Mountain site. Color composites involving vegetation enhancement bands help distinguish vegetative influence and explain diversity among many of the composite images.

CHAPTER VIII

CONCLUSIONS AND APPLICATIONS

This final chapter emphasizes conclusions drawn from the research and data analysis described in preceding sections. Chapter I includes a list of the major scientific questions addressed by this study, to which the reader is referred.

Results of this investigation bear importantly on concepts of the origin of desert varnish, desert varnish occurrence and distribution, its spectral characteristics and influence on TM imagery, and variations in the physical and chemical properties of desert varnish or other secondary mineral coatings that could be dependent on underlying host rock and which might be used as an aid to specific lithologic discrimination on TM imagery. A geochemical model for the origin of iron and manganese in desert varnish has been proposed (Chapter V). Whole rock and trace element analyses of a wide range of volcanic rock assemblages at each of the three study sites have been correlated with both laboratory and field spectra, resulting in a better understanding of the lithologic and petrochemical spectral controls which lead to distinctive contrast on TM imagery. Rock-Varnish Albedo Differences (RVAD) help identify units with extensive, spectrally important, desert varnish development, using standard

product TM data. An applications section incorporating much of the findings of this study is included at the end of this section. It includes a summary chart and a binary decision rule flow diagram to aid TM imagery applications in volcanic terrain. Details of these findings are expanded below. Each section addresses those questions outlined from the original objective and listed in Chapter I.

NATURE AND ORIGIN OF DESERT VARNISH

Although this study included an investigation of all secondary mineral coatings, including any thought to have formed diagenetically or during the cooling phase of volcanic flow deposition as well as products of weathering, classical desert varnish was the only secondary coating type (save some hydrothermal alteration) of any consequence identified within the 3 study sites. Secondary coatings that could be construed as distinct from desert varnish - light reddish iron oxides and minor secondary clay - appear instead to be early stages or phases of desert varnish formation. Clay minerals are stable at the weathering rind/underlying rock interface due to greater humidity, longer moisture residence time and higher hydrogen activities. When exfoliated minor caliche also coats some surfaces.

Desert varnish encrustations are an extremely thin, less than 0.1mm thick deposit at the rock-air interface. X-ray diffraction, infrared spectrophotometry, and microscope petrographic analyses of desert varnishes and the very shallow subsurface beneath varnishes (0.5mm thicknesses) indicate that amorphous silica, alumina, iron and manganese enriched compounds are the chief constituents. Most desert varnishes contain some potassium and titanium and occasionally calcium and cerium. Clay minerals - kaolinite and illite - although identified in 3 samples of coatings by XRD do not appear to be important in the varnish zone. Analcime was identified in one sample of coating from Gold Flat Tuff of Black Mountain.

Compositional zoning within desert varnish crusts was evaluated with the SEM-EDX instrument. Iron was found to be fairly consistent throughout laminated encrustations. Manganese, on the other hand, is enriched in discrete layers. The layering within laminated varnish is probably due to periodic increases in manganese concentration in response to climatic changes. One hypothesis is that increases in precipitation lead to higher acidity and leachant strength, greater wind disturbance, and increases in atmospheric dust content. Under these conditions higher levels of manganese would be put into solution and made available for subsequent precipitation in the desert varnish zone. Mn/Fe ratios tend to decrease throughout

coating thicknesses to the coating-rock interfaces where iron is highly enriched relative to manganese. This relationship is apparent from outcrop observation as well, where extracted exfoliation rinds carrying desert varnish are followed closely in time by development of thin bright reddish iron oxide staining on the newly exhumed rock surface.

An attempt was made to identify differences between desert varnishes on different rock assemblages (physical character or composition) that could be correlated with underlying host lithologies. Desert varnish within these study areas is impressively monotonous for the most part except that varnishes on basalt were found to be higher in total combined iron and manganese and Fe/Mn ratios, implying some genetic association with host rock. Also, desert varnish on Gold Flat Tuff of the Black Mountain caldera is anomalous in cerium, a trace element characteristic of that unit and other highly evolved peralkaline deposits. The presence of cerium in desert varnish on other units at the Black Mountain study site (Trachyte of Hidden Cliff for example) may provide a genetic trace to source tuffs such as the Gold Flat tuff.

Secondary layers of mineral accumulation or cementation were discovered in the near surface substrate of most rocks studied, especially the more porous ash flow tuffs. These thin secondary layers - typically 1-3mm thick - occur just

below the weathered surface of the outcrop and conform stratigraphically with current weathered surface contours. The layers are darker than enclosing rock, porcelaneous in luster, and dense. They appear opaline megascopically and cloudy in thin section. SEM-EDX probe work documented consistently high calcium concentrations in these layers and less consistently high magnesium as well. Thin section observation identified carbonate cementation in the layers in a few instances. XRD analysis was inconclusive. These secondary layers are apparently accumulations of amorphous siliceous compounds similar to secondary surficial coatings with variable concentrations of calcium and magnesium carbonate. SEM-EDX analyses revealed that sodium concentrations occur occasionally in a lighter colored bleached zone just above these dark secondary zones.

The secondary layers of cementation apparently form much in the same way as caliche horizons in aridic soils, a model which bears importantly on source considerations for the iron and manganese in desert varnish. An acidic solution, originating as rain water with relatively low pH, attributable in part to contact with surficial lichen and other organic remains, leaches the rock substrate soaking deeper into the more porous rocks. Analytical profiles observed within surficial sections cut through these layers are consistent with element solubilities under these geochemical conditions. Calcium and magnesium would be

expected to leach more readily and be transported to greater depths within the rock. A solution front is created which would begin to retreat as source water starts to dry up under the influence of evaporative pressure in semiarid environments. As the solution is pumped back out of the rock by capillary action in response to evaporation, calcium would likely precipitate first, followed by magnesium and then sodium. When the surface of the rock is reached, the more mobile iron would precipitate in response to higher Eh conditions at the rock-air interface. Manganese could remain in solution longer and travel furthest - to the outer rock-coating-air interface - a relationship consistent with observations both in the field and with the SEM.

Desert varnish develops on unstable exfoliation surfaces that spall off the outcrop leading to a cyclic process with important consequences for desert varnish development. The caliche model presented in the previous paragraph probably accounts for incipient concentrations and the initial origin of iron and manganese in desert varnish; however, a recycling mechanism from regenerated surfaces due to exfoliation probably enhances iron and manganese concentrations. Exfoliation surfaces, which are discarded from the outcrop, carry mature desert varnish accumulations with them. This anomalously rich iron and manganese crust degrades to detritus and dust which then

becomes a potential wind-storm feedstock for redeposition back on the rock surface as minute particles. Iron and manganese are available from the wind blown dust for dissolution during rain showers and for deposition and incremental accretion within the desert varnish. This local source model for the iron and manganese in desert varnish places constraints on speculation regarding concepts of desert varnish genesis that might be applied to age considerations and geochronological interpretations.

SPECTRA AND DISTRIBUTION OF DESERT VARNISH
INFLUENCE ON TM IMAGERY

The distribution of desert varnish in our study areas was found to be discontinuous and limited. Heavy, thick encrustations of varnish are relatively unimportant to overall surface spectral compositions within the spatial resolution of Landsat. Even within hand-sample sized areas of moderate to heavy desert varnish accumulations, fresh mineral grains and zones of very light varnish stain are present. Indeed, SEM scans and gray level density slices of hand samples indicate dense varnish, even on the "heavily" varnished samples, rarely exceeds 50%. Field observations also indicate limited heavy to moderate desert varnish formation over any approximately 5x5mm sized area. In addition, radiation penetration studies by other workers

(Buckingham and Sommer, 1983) indicate that a 0.9um wavelength penetrates to over 25um depths, well below most desert varnish accumulations. Results of these observations lead to the conclusion that desert varnish exerts minimal radiance influence on any Landsat pixel sized area, particularly within longer wavelength bands.

Laboratory and field spectral profiles over variably varnished rock surfaces show that desert varnish is relatively absorbent at shorter wavelengths within the TM range, bands 1-3, but generally unimportant to spectral compositions at longer wavelengths. Spectral measurements over varnished surfaces selected at regular increments of varnish development show a generally straight line reflectance increase with decrease in varnish extent and intensity. Reflectance decrease is approximately 1% for each percent increase in varnish cover for TM bands 2, 3, and 4. At longer wavelengths, heavily varnished surfaces exert some attenuating influence on reflectance over felsic units but for surfaces with moderate to light varnish cover reduction in reflectance is about 0.5% for each approximate percent increase in varnish cover. Since desert varnish attenuates radiation penetration of felsic rocks in decreasing proportion to wavelength, spectral curves of varnished surfaces tend to exhibit steeper slopes toward longer wavelengths. This relationship causes lower TM band 5/7 values.

C-4

The Rock-Varnish-Albedo-Difference (RVAD) was described in Chapter VII and defined generally as the ratio of ferromagnesian constituents in desert varnish to ferromagnesian constituents in underlying host rock. Since the proportion of iron and manganese in desert varnish is fairly constant and, moreover, overwhelmed by differences in iron, manganese, and magnesium in host rock, RVAD is primarily a measure of a rock's felsic tendency. Thus rocks with low ferromagnesian content, the felsic leucocratic igneous rocks, would have high RVAD potential. Rocks with high RVAD and with extensive desert varnish cover can be discriminated from low albedo deposits by TM 5/2 ratios which tend to be higher on felsic rocks with extensive desert varnish due to preferential absorption of band 2 relative to band 5 by varnish. Rocks with low RVAD do not exhibit similar relative reflectance differences between bands 2 and 5 regardless of varnish development because both varnish and rock tend to be dark.

LITHOLOGY AND PETROCHEMISTRY - INFLUENCE ON SPECTRA AND TM IMAGERY

Results of imagery processing at the 3 project sites proved that TM data is quite effective at discriminating certain volcanic lithologies. In general, rock assemblages may exhibit characteristic spectra in the visible and near-

infrared as a function of iron content or felsic index. These major whole rock petrochemical properties give rise to differences in rock color index and albedos resulting typically in straight line reflectance increases throughout the TM range from high frequency to low.

This investigation of secondary mineral coatings, including field observation, SEM imagery, hand specimen description, density slicing of tonal variation, and microscopic petrography, indicates that desert varnish is discontinuous, thin, translucent and less important to rock spectral composition than one might suspect from the misleading visual conspicuousness of desert varnish on the outcrop. Still, desert varnish, we have observed, is relatively absorbent to shorter TM wavelengths - bands 1 and 2 especially - and dark tones on band 1 and 2 images can help map areas with anomalous desert varnish accumulations; however, low albedo rocks such as mafic igneous formations are also dark on these images. A TM 5/2 image helps identify relatively extensive desert varnish on rocks with high rock-varnish albedo differences, basically felsic or leucocratic rock assemblages.

The relatively high reflectance around 2.2um in both laboratory and field spectra for certain of the more highly evolved flows of each study area is reflected in TM band 7. Rock assemblages expressing this property include Kane Wash Tuff "V" series tuffs, Topaz Rhyolite of Kane Springs Wash,

Gold Flat Tuff of Black Mountain, and to a lesser degree, glassy cap rock of Civet Cat Canyon Tuff of Stonewall Mountain. This relationship leads to low 5/7 values and dark tonal contrast on 5/7 images. Plots of 5/7 values against rock chemistry reveal excellent correlation with high concentrations of certain incompatible trace elements, especially fluorine, rubidium, ytterbium, and the rare earth element suite, and fair correlation with peralkalinity and total K_2O and Na_2O content. Although some correlation is apparent with regard to whole rock SiO_2 and other major elements, consistency is inferior when compared with the trace elements, and some correlation should be expected anyway, since the more felsic and siliceous deposits tend to be the more evolved differentiates with anomalous concentrations of incompatible trace elements and large-ion-lithophile elements (LIL). It appears that high sodium minerals, iron, and the incompatible trace elements including the transition metals and some LIL elements are likely sources of the unusually high reflectance in TM band 7 and low 5/7 values for the highly evolved late magmatic differentiates of the three study sites. Ferruginous, glassy zones at the base of some of the ash flow tuff deposits are relatively reflectant in TM band 4 and behave much like vegetation in 5/4 and 4/5 ratio images.

Thus, congruency between imagery contrast, band DN

values over the various lithologic units, lab spectra, and binary and ternary plots of band vs band and band vs composition for the various volcanic rock formations lead to discrimination potential based largely on straight line albedo differences in the longer wavelength bands and on 5/7 and 5/2 ratios. Figure 110 is a binary decision rule flow-diagram for TM imagery analysis of volcanic settings in arid to semi-arid environments based on these relationships.

IMPLICATIONS FOR GEOLOGIC MAPPING

Lithologic mapping applications of Landsat and other narrow band sensors have not been studied in great detail. The spectral data published by Hunt and Salisbury (1970); Hunt, Salisbury, and Lenoff (1973 a, b, and c, and 1974); Hunt (1977) and Krohn (1985) have had inferential value for Landsat imagery applications. Other workers have discussed lithologic mapping using Landsat imagery, including Taranik and Trautwein (1977), Abrams and Siegal (1980), Baird (1984), and Davis and others (1987). Sultan and others (1987) contrasted lithologic criteria of some lithologies with TM band DN values and band ratios.

The cause for the unusually steep spectral slope between about 1.0 and 2.2um likely lies in electronic processes involving the incompatible and LIL elements and

their matrices. Contributing factors may be mafic mineral content and transitional relationships of iron which cause absorption over a broad band at about 1.2um (Hunt and Salisbury, 1970). Energy absorption by iron at these frequencies causes depression of spectral curves in the TM band 5 range, which could effectively lead to steeper spectral slopes beyond and low 5/7 values. Spectral plots for biotite and hornblende-bearing plutonic rocks (granite, monzonite, and diorite, for example) exhibit similar spectral relationships (Hunt and others, 1973b); however, absorption by amphibole at 2.3-2.4um would increase its 5/7 value. This could partially explain relatively high band 7 and low 5/7 values over Civet Cat Canyon Tuff, which is anomalously high in biotite; however, the relationship is not as pronounced in Antelope Springs latite or Hiko Tuff, both of which contain appreciable biotite, so I suspect the spectral characteristic is more a result of trace element content in glass matrix, devitrified glass, or late groundmass minerals. Since desert varnish tends to decrease 5/7 values as well due to steepening of the spectral slope from around 1.0 to 2.2um as a result of gradual decrease in desert varnish absorption at longer wavelengths, some varnish coatings would enhance these features.

Other possible mineralogic causes for high reflectivity in TM band 7 and low 5/7 values might include chloritic

content and chloritic alteration of mafic minerals, such as in a diabase whose amphiboles have altered to chlorite. Such rocks exhibit steep spectral curves between the TM band 5 and 7 interval; however, they also produce absorption peaks at about 2.3um, which tends to counter a low 5/7 tendency. Acidic rocks in general show steeper curves throughout the near IR region. A number of compositional characteristics in sedimentary rocks can produce such spectra, but they will not be considered here. Clay minerals, muscovite, oxide minerals and hydroxides produce flat spectral curves throughout this interval. Titanium bearing minerals possess similar spectra - rutile and titaniferous andradite garnet for example. Titanium is a transition metal with unpaired d orbital electrons with special absorption properties similar to iron. Other parallel spectral geometries include iron-rich epidote; hornblende; augite; titanium-, sodium-, and iron-rich jadeite; sphene in which thorium, strontium, barium, and rare earth elements substitute for calcium and OH and fluorine replace oxygen; tourmaline with fluorine, lithium, iron, manganese, boron, and sodium. Riebeckite is one of the characteristic accessory minerals of Gold Flat Tuff and its thorium, yttrium, titanium, cerium, and lanthanum produce parallel spectra to that of the highly evolved magmatic differentiates of the study sites. Of published rock spectra, close parallels include nepheline syenite, rich in sodium. Trachyte and syenite do not correlate

well. The fit for anorthoclase is reasonable, less so for orthoclase and quartz. Andesine produces an excellent parallel.

To recap, it appears that high sodium minerals, iron, and incompatible elements are likely sources of the unusually high reflectance in TM band 7 and low 5/7 values of the highly evolved late magmatic differentiates at the 3 study sites. Congruency between rock assemblages and imagery units, band DN values, laboratory spectra, and binary and ternary plots of band vs band and band vs compositional criteria lead to lithologic identification and differentiation potential based largely on straight line albedo differences in the longer wavelength bands and on 5/7 and 5/2 ratios. Figure 110 is a binary decision rule flow-diagram for analysis of volcanic caldera settings in arid to semi-arid environments based on these findings. Table 35 summarizes important imagery features for a general igneous rock classification scheme. These summary exhibits utilize the observation that rocks with a high rock-varnish albedo difference (RVAD) are felsic relative to desert varnish and thus bear potential for varnish identification. RVAD and high 5/2 values seem potentially applicable also to discrimination of matrix iron resulting from autooxidation or other secondary effects from more mafic units with low straight line albedos and low 5/2 values. They also depend heavily on the observation that magmatically evolved units tend to be relatively reflectant

Figure 110. Flow chart (binary decision rule) for identification and discrimination of general volcanic lithologies, using Landsat thematic mapper imagery or DN data.
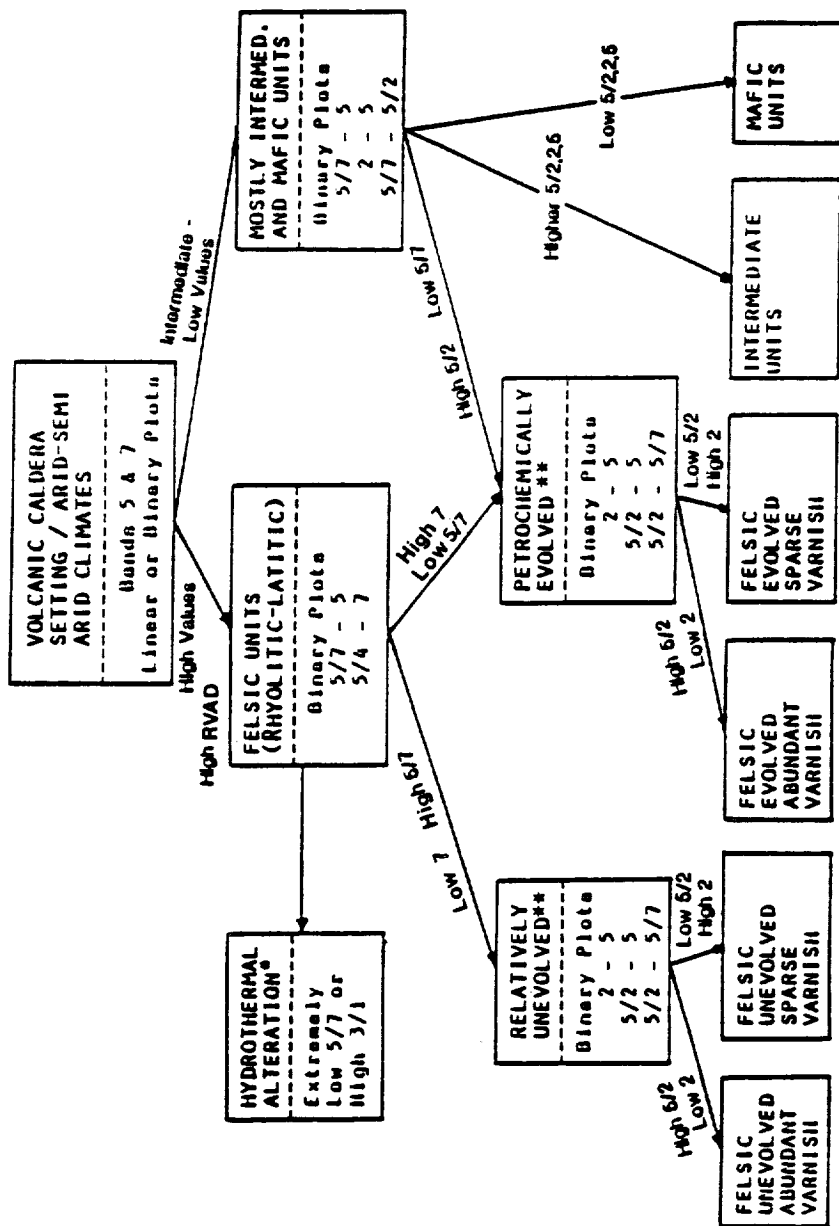
* Typically pervasive argillic, sericitic, silicic, or alunitic alteration with pyrite

** Evolved relative to peralkaline tendency and trace element content, particularly F, Rb, Ta, and REE

TABLE 35. LIKELY TM IMAGERY CHARACTERISTICS AND INFLUENCE
OF DESERT VARNISH BY GENERAL IGNEOUS ROCK CATEGORY*

IGNEOUS CATEGORY	GENERAL PETROCHEMISTRY	RVI POTENTIAL**	INFLUENCE OF DESERT VARNISH ON REFLECTANCE		TYPICAL TM IMAGERY CHARACTERISTICS
			2-4 TM BANDS 5-7		
Highly evolved (magmatically)	High in LIL and other incompatible elements (Rb, Ta, F, REE, Th, Ce, U, etc) High SiO_2	High	Regular gradational decrease with varnish increase	Steep (20-25%) decrease in values with increase in varnish cover but less decrease (5-10%) from moderate-heavy varnish	Bright in Bands 4, 5, PC1, 3/2, 5/2 and 5/4 ratios. Very bright in band 7. Dark in PC 2, PC 3 and very dark in 5/7
Peralkaline	$K_2O+Na_2O>Al_2O_3$	High	Regular gradational decrease with varnish increase	Little change with light to moderate varnish. 30-40% drop with moderate-heavy varnish	Bright in bands 4, 5, 7, 5/2, 3/2 and 5/4 Dark in PC 2, PC 3 and 5/7
Felsic (Alkalic and Alkali-Calcic)	$SiO_2>68\%$ typically $K_2O>Na_2O$ or $K_2O+Na_2O>CaO$	High	Regular gradational decrease with varnish increase	Little change with light to moderate varnish. 30-40% drop with moderate-heavy varnish	Bright in bands 1, 2, 3, 4, 5, 7, PC 1, 3/2, 5/2, 5/4 and 5/7. Dark in PC 2
Intermediate (Calc-alkalic)	$SiO_2>55\%$ (typically) $CaO>K_2O+Na_2O$ or $Na_2O>K_2O$	Intermediate	Regular but slight decrease with varnish increase	Little change with light to moderate varnish. Slightly greater decrease with moderate-heavy varnish	Moderate albedos should lead to intermediate reflectance values and indistinct contrast
Mafic	$SiO_2<55\%$ High FeO, MgO or CaO	Low	Little variation. Slight general decrease in values, with varnish increase	Reflectance increase, with varnish increase	Bright to indistinct in 5/7 Dark in bands 1, 2, 3, 4, 5, Dark to indistinct in 3/2, 5/2, 5/4 and PC 1

*   Relative reflectance comparisons for volcanic rock groups within volcanic terrain in semi-arid environments.

** Rock-varnish index (RVI) increases with an increase in felsic tendency of host rock. Since desert varnish attenuates, reflectance proportional to both varnish intensity and extent and wavelength frequency, TM 5/2 ratio images can be expected to record relatively brighter tonal contrast over felsic units with appreciable varnish coatings. They should appear relatively dark in bands 1 and 2; bright in bands 5 and 7.

in TM band 7 and produce low 5/7 values. Figure 110 expresses a bias toward TM bands 5 and 7 which contain strongly lithologically driven radiance values.

The principles described above should apply to any volcanic rock assemblages, regardless of age. This study has shed further light on the importance of rock compositional variation in controlling reflectance differences. Of course older volcanic terrain is more likely to have been subjected to tectonic strain and possibly metamorphic effects which could alter mineralogies and composition and concomitant spectral properties. Although these study sites are in a semi-arid environment and subject to minimal vegetative interference (25-40% of cover), spectral controls of other Landsat images could be controlled by other dominant cover types and by variations in spectral composition. If surface cover is vegetation dominant but reasonably consistent in type, spectral variation could be rock/soil dominant, and lithologic imagery contrast still apparent. Lithologic interpretation without ground control and spectral mixing models under high vegetation conditions would be more difficult and dubious. Under more humid conditions or over terrain with subtle differences in rock composition, atmospheric correction could improve imagery performance.

Although these principles were developed with volcanic subjects and obviously are most applicable to volcanic

terrain, they should also apply to some degree to any igneous terrain involving rock assemblages with compositional and mineralogical differences and also to metamorphic terrain with either pervasive metamorphic mineral assemblages or which were derived from igneous protoliths.

As we have seen, desert varnish does not exert appreciable radiance influence in the longer wavelength TM bands (bands 3-7). Application of the RVAD principle and 5/2 ratios for detection of surfaces with extensive desert varnish could be effective in any arid to semiarid environment where desert varnish is present. Quaternary geologists concerned with variable ages of alluvial fans or archaeologists interested in surface disturbance in desert environments might find this application useful.

Applications to extraterrestrial situations should also follow similar principles. Most planet surfaces are igneous in origin with minimal sedimentary features. Inasmuch as rock assemblages vary in composition and mineralogies, spectral character would also vary. Lithologic boundaries would likely be discernible and mappable, particularly since vegetation is absent. On Mars, the Mariner missions (6 and 7) detected hydrated minerals from infrared spectrometry (King, 1976). According to King (1976) rocks on Mars are dominantly basaltic with possibly minor differentiated varieties.

Spectral variation among these rocks based on petrochemical differences is likely, and longer wavelength TM bands or principal component images should display the contrast. The presence of hydrated minerals might lead to absorption peaks in band 7, resulting in further radiance differences and imagery differentiation. Hapke (1966) conducted irradiation experiments on a volcanic rock suite, variable in composition from rhyolite to basalt. He found that bombardment with both gamma and hydrogen ion radiation darkened all samples, effectively lowering albedos. So for extraterrestrial surfaces albedos could be expected to be lower and radiance differences obscured or converged. Imagery enhancement techniques and complex statistical transformations like principal components might be required to discriminate lithologic variation.

It is unlikely that any desert varnish is present on the surfaces of rocks on Mars and Venus. Development of desert varnish on Earth appears dependent on rather sensitive annual precipitation rates. Elvidge (1979) discovered that desert varnish does not tend to accumulate where precipitation levels exceed 25cm per year; however, desert varnish formation is believed to be dependent on some rainfall. The lower the precipitation levels the more extended the likely period for varnish development. There is no detectable water in the atmosphere of Mars (Mutch, 1976). Surface temperature and pressure are too low for

water to be stable. There are, however, semi-permanent polar ice caps of H_2O, and the presence of dendritic scarps indicates surface water has been active on Mars. A problem with extraterrestrial surfaces, however, including Mars and Venus, is the higher rate of meteorite impact, as evidenced by ubiquitous surface breccias, and on Mars extreme wind velocities which lead to abnormal surface abrasion. We know that varnishes at the Earth's surface are recycled on unstable exfoliation surfaces. It is likely the surfaces on other planets may be even more unstable. The presence of desert varnish at the Earth's surface today is dependent on constant varnish accumulation and regeneration. The Martian surface is likely not developing desert varnish currently and what varnish may be present is subject to constant erosional influence by meteoritic impact and wind abrasion. Surfaces with extensive desert varnish development on Mars are unlikely.

Other workers have conjectured that bacteria and other organics may be a necessary component in the formation of desert varnish on Earth. If true, desert varnish would not be expected on most extraterrestrial surfaces, at least not on our moon, or other planets in our solar system, since organic life does not appear present (King, 1976). Mercury is thought to have no atmosphere to speak of, and Venus' atmosphere is largely CO_2 with surface temperatures at 450 degrees C. Liquid H_2O would not exist on Venus either,

within current atmospheric pressure ranges.

FUTURE RESEARCH

This investigation followed several different lines of research interest, focusing on implications for remote sensing, but with specific applications to other related earth science fields as well. To better understand relationships and concepts that have resulted from this research and to address new related questions, future investigative efforts in the following areas could prove illuminating:

DESERT VARNISH

The distribution and occurrence of desert varnish is difficult to document because of the extreme discontinuity of varnish and its variable thickness and mode of occurrence (encrustations vs impregnating films). Radiation penetration experiments and radiance measurements at varied visible/near-infrared frequencies directed at mm square surface areas with thickness controls by SEM observation would move the general conclusions we can draw from this study into a much more detailed and quantitative arena. Suites of rocks of variable composition and variable varnish thicknesses could be evaluated. Instrumentation would require a highly focused beam at

specific wavelengths.

This study resulted in a genetic model for derivation of iron and manganese in desert varnish. The study is lithologic specific - Tertiary volcanic caldera deposits involving extensive porous ash flow tuffs. Although I have observed the secondary layer of Ca enrichment in volcanic rock assemblages all over the American Southwest, a similar investigation and search for secondary layers of Ca enrichment or accumulation of leached elements in non-Tertiary or sedimentary terrain would help establish whether or not this is a localized (geographic or lithologic) phenomenon or is a model with broad application to desert varnish formation.

SPECTRA

There is a need for more reference spectra for the less common rock types. We know that a few 100ppm of boron, manganese, chromium, iron, and other elements, especially the transition elements, cause spectral shifts in minerals and glass (Nassau, 1983). This study revealed special spectral properties for the highly evolved late magmatic differentiates, characterized by peralkaline tendencies and anomalous amounts of the incompatible and LIL elements. Ferruginous glass also exhibited unique spectra. Extensive laboratory and field spectral measurements of rocks and glassy tuffs or fabricated glass with compositional

controls would help advance correlations of Landsat radiance measurements and DN relationships with lithologic cover and help provide a base for spectral mixing models.

As a corollary to the above need for further reference spectra of rocks, research into the fundamental causes of spectra at the atomic level would aid not only theoretical explanations of radiance origins, but help advance predictive models as well. If we knew more about the vibrational effects of a given element both within different mineral lattices and within other atomic environments, we could speculate on spectral properties and ultimately predict sensor responses.

IMAGE ANALYSES

We have adequate data at the 3 sites investigated in this study to compose spectral mixing models to compare with Landsat TM data. Knowing some cover types, their relative proportions, and spectral characteristics of each, we could effectively subtract the radiance contributions of knowns to arrive at spectral properties of unknowns. If the remaining spectral contribution is thought to be lithologic dominant, we could compare residual spectra with a computer reference file of rock spectra to arrive at likely candidates, similar to SPAM software for AIS and other very narrow band sensors. Models for desert varnish and petrochemistry could be compiled in a reference file

and evoked by an operator for comparison.

In concert with computer programs to help analyze surface cover as proposed in the above paragraph, algorithms incorporating textural variations, spacial frequencies, and geometric and tonal pattern configurations could begin to advance computer analyses of terrain to a near human interpretive capacity or at least provide alternative computer tests to aid interpreters with varied backgrounds.

REFERENCES

Abrams, M.J., Ashley, R.P., Rowan, L.C., Goetz, A.F.H., and Kahle, A.B., 1977, Mapping of hydrothermal alteration in the Cuprite mining district, Nevada, using aircraft scanner images for the spectral region 0.46 to 2.36: Geology, v.5, p.713-718.

Abrams, M.J. and Siegal, B.S., 1980, Lithologic mapping IN Siegal, B.S and Gillespie, A,R, edit. Remote Sensing in Geology, John Wiley and Sons, New York, N.Y. p. 381-418.

Abrams, M.J., Brown, David, Lipley, Larry, and Sadowski, Ray, 1983, Remote Sensing for porphyry copper deposits in southern Arizona: Econ. Geol., v.78, no.4, p.591-604.

Allen, C.C., 1978, Desert varnish of the Sonoran Desert: optical and electron probe microanalyses: Jour. of Geol., v.86, p.743-752.

Baird, A.K., 1984a, Iron variation within a granitic pluton as determined by near-IR reflectance: Jour. Geol. 92, p.344-350.

Baird, A.K., 1984b, Granitic terrains viewed remotely by shuttle IR radiometry: Jour. Geoph. Res., v.89, B11, p.9433-9447.

Berner, R.A., and Holdren, G.R.,Jr., 1977, Mechanism of feldspar weathering: some observational evidence: Geology, v.5, p.369-372.

Borengasser, M.X., Brandshaft, D.R., and Taranik, J.V., 1984, Geological application of enhanced Landsat 4 TM imagery of south central Nevada: Int. Symp. on Remote Sensing of Envir., Third Thematic Conf., Remote Sensing for Explor. Geolo., Colorado Springs, Colo., 8p.

Borns, D.J., Adams, J.B., Curtiss, B., Farr, T., Palmer, F., Satley, J., and Taylor-George, S., 1980, The role of micro-organisms in the formation of desert varnish and other rock coatings: SEM study: GSA Abst., v.12, p.390.

Buckingham, W.F. and Sommer, S.E., 1983, Mineralogical characterization of rock surfaces formed by hydrothermal alteration and weathering - application to remote sensing: Econ. Geol., v.78, p.664-674.

Byers, F.M., et al., 1976, Volcanic suites and related cauldrons of Timber Mountain-Oasis Valley caldera complex, southern Nevada: U.S.G.S. Prof. Pap. 919, 70p.

Buchanan, M.D., 1979, Effective utilization of color in multidimensional data presentations: SPIE, v.199, p.9-18.

Christiansen, Robert L., 1979, Cooling units and composite sheets in relation to caldera structure: Geol. Soc. of America Special Paper 180, p.29-42.

Clark, S.P., 1957, Absorption spectra of some silicates in the visible and near infrared: Amer. Mineralogist, v.42, p.732-741.

Cook, E.F., 1965, Stratigraphy of Tertiary volcanic rocks in eastern Nevada: Nev. Bur. Mines Rept. No. 11, 61p.

Cornwall, H.R., 1972, Geology and mineral deposits of southern Nye County, Nev.: Nev. Bur. Mines and Geol. Bull. 77, 49p.

Crippen, Robert E., 1986, The regression intersection method of adjusting image data for band ratioing: proceedings fifth thematic conference on remote sensing for exploration geology, Reno, Nevada, Sept. 29-Oct. 2, 1986.

Crippen, Robert E., 1988, The dangers of underestimating the importance of data adjustments in band ratioing: preprint submitted to Internat. Jour. of Remote Sensing.

Curtiss, B., Adams, J.B., and Ghiorso, M.S., 1985, Origin, development and chemistry of silica-alumina rock coatings from the semi-arid region of the Island of Hawaii: Geoch. Et Cosmoch. Acta, Jan., Preprint, 258p.

Davis, J.C., 1973, Statistics and data analysis in geology: John Wiley & Sons, N.Y., N.Y., 2nd edit. 550p.

Davis, P.A., Berlin, G.L., and Chavez, P.S.,Jr., 1987, Discrimination of altered basaltic rocks in the southwestern United States by analysis of Landsat thematic mapper data: Photogrammetric Engineering and Remote Sensing, v.53, n.1, Jan. 1987, p.45-55.

Deffeyes, K.S., 1959, Zeolites in sedimentary rocks: Jour. Petrol., v.29, p.602-609.

Dorn, R.I. and Oberlander, T.M., 1981, Microbial origin of desert varnish: Science, v.213, p.1245-1247.

Dorn, R.I. and Oberlander, T.M., 1982, Rock varnish: Prog. in Phys. Geog., v.6, p.317-367.

Eckel, E.B., edit., 1968, Nevada test site: GSA Mem. 110, 290p.

Ekren, E.B., Anderson, R.E., Rogers, C.L., and Noble, D.C., 1971, Geology of northern Nellis Air Force Base Bombing and Gunnery Range, Nye County, Nev.: U.S.G.S. Prof. Pap. 651, 91p.

Elvidge, C., 1979, Distribution and formation of desert varnish in Arizona (MS Thesis): Tempe, Ariz., Arizona State Univ., 109p.

Engel, J.L., 1980, Thematic mapper - an interim report on anticipated performance: Santa Barbara Research Center, 13p.

Engel, J.L. and Weinstein, O., 1982, The Thematic Mapper - an overview: Insti. of Electrical and Electronics Eng., 8p.

Engel, J.L. Lansing, J.C., Brandshaft, D.G., and Marks, B.J., 1983, Radiometric performance of the Thematic Mapper: presentation at the seventeenth Intern. Symp. on Remote Sensing of Envir., Ann Arbor, Mich., May 9-13, 1983, 25p.

Engel, C.G. and Sharp, R.P., 1958, Chemical data on desert varnish: GSA Bull., v.69, p.487-518.

Farr, T.G., 1981, Surface weathering of rocks in semiarid regions and its importance for geologic remote sensing (Ph.D. thesis): Seattle, Wash., Univ. of Washington, 149p.

Farr, T.G. and Adams, J.B., 1984, Rock coatings in Hawaii: GSA Bull., v.95, p.1077-1083.

Foley, D., 1978, The geology of the Stonewall Mountain volcanic center, Nye County, Nev.: Unpub. Ph.D. thesis, Ohio State Univ., Columbus, Oh., 139p.

Fontanel, A., Blanchet, C., and Lallemand, C., 1975, Enhancement of Landsat imagery by combination of multispectral classification and principal component analysis: Proceedings NASA Earth Res. Sur. Symp., July 1975, Houston, Tex., TMX-58168, p.991-1012.

Frazzell, Virgil and Hausback, Brian, 1986, Southeastern Stonewall Mountain caldera, Nye County, Nevada: volcanic stratigraphy and structure, abstract IN Transactions, American Geophysical Union, v.67, no.44, Nov. 4, 1986, p.1261.

Glasby, G.P., McPherson, J.G., Kohn, B.P., Johnston, J.H., Keys, J.R., Freeman, A.G., and Tricker, M.J., 1981, Desert varnish in Southern Victoria Land, Antarctica: New Zealand Jour. of Geol. and Geoph., v.24, p.389-397.

Hapke, B.W., 1966, Optical properties of the Moon's surface IN The Nature of the Lunar Surface, Hess and others edit., Johns Hopkins Press, p.141-154.

Hay, R.L., 1977, Geology of zeolites in sedimentary rocks IN Mumpton, F.A. edit. Mineralogy and geology of natural zeolites: Miner. Soc. Amer. short course notes, v.4, p.53-64.

Hay, R.L. and Sheppard, R.A., 1977, Zeolites in open hydrologic systems IN Mumpton, F.A. edit. Mineralogy and geology of natural zeolites: Miner. Soc. Amer. short course notes, v.4, p.93-102.

Haydn, R., Dalke, G.W., Henkel, J., and Bare, J.E., 1982 Application of the ISH color transform to the processing of multisensor data and image enhancement: presented at the Inter. Symp. on Remote Sensing of Arid and Semiarid Lands, Cairo, Egypt, Jan. p.599-616.

Hem, J.D., 1960, Restraints on dissolved ferrous iron imposed by bicarbonate redox potential, and pH: U.S.G.S. Water Supply Pap. 1459-B, p.33-55.

Hem, J.D., 1963, Chemical equilibria and rates of manganese oxidation: U.S.G.S. Water Supply Pap. 1667-A, 64p.

Hem, J.D., 1964, Deposition and solution of manganese oxides: U.S.G.S. Water Supply Pap. 1667-B, 42p.

Hem, J.D. and Cooper, W.H., 1959, Survey of ferrous-ferric chemical equilibria and redox potentials; U.S.G.S. Water Supply Pap. 1459-A, 30p.

Hooke, R.LeB., Yang, H., and Weiblen, P.W., 1969, Desert varnish: an electron probe study: Jour. of Geol., v.77, p.275-288.

Hunt, C.B., 1954, Desert varnish: Science, v.120, p.183-184.

Hunt, C.B., 1961, Stratigraphy of desert varnish: U.S.G.S. Prof. Pap. 424-B, p.194-195.

Hunt, G.R., 1977, spectral signatures of particulate minerals in the visible and near infrared: Geophysics, v.42, p.501-513.

Hunt, G.R., 1980, Electromagnetic radiation: the communication link in remopte sensing IN Siegel, Barry S. and Gillespie, Alan R. edit. Remote Sensing in Geology, John Wiley & Sons, New York, N.Y. p.5-46.

Hunt, G.R. and Ashley, R.P., 1979, Spectra of altered rocks in the visible and near infrared: Econ. Geol., v.74, p.1613-1629.

Hunt, G.R. and Salisbury, J.W., 1970, Visible and near infrared spectra of minerals and rocks: I. Silicate minerals: Modern Geol., v.1, p.282-300.

Hunt, G.R. Salisbury, J.W., and Lenhoff, C.J., 1973a, Visible and near infrared spectra of minerals and rocks: VI. Additonal silicates: Modern Geol., v.4, p.85-106.

Hunt, G.R., Salisbury, J.W., and Lenhoff, C.J., 1973b, Visible and near infrared spectra of minerals and rocks: VII. Acidic igneous rocks: Modern Geol., v.4, p.217-224.

Hunt, G.R., Salisbury, J.W., and Lenhoff, C.J., 1973c, Visible and near infrared spectra of minerals and rocks: VIII. Intermediate igneous rocks: Modern Geol., v.4, p.237-244.

Hunt, G.R., Salisbury, J.W., and Lenhoff, C.J., 1974, Visible and near infrared spectra of minerals and rocks: IX. Basic and ultrabasic igneous rocks: Modern Geol., v.5, p.15-22.

Jensen, J.R., 1986, Introductory digital imagery processing: Prentice-Hall, Englewood Cliffs, N.J., 379p.

Johnston, J.H. and Lewis, D.G., 1983, A detailed study of the transformation of ferrihydrite to hematite in an aqueous medium at 92 degrees C: Geoch. Et Cosmoch. Acta, v.47, p.1823-1831.

Joreskog, K.G., Klovan, J.E., and Reyment, R.A., 1976, Geological factor analysis: Elsevier Scient. Pub. Co., N.Y., N.Y., 178p.

Keller, W.D., 1977, Scanning electron micrographs of kaolins collected from diverse environments of origin: Clays and Clay Mineralogy, v.25, p.347-364.

King, E.A., 1976, Space Geology, John Wiley and Sons, New York, N.Y., 349p.

Knauss, K.G. and Ku, T., 1980, Desert varnish: potential for age dating via uranium-series isotopes: Jour. of Geol., v.88, p.95-100.

Krauskopf, K.B., 1967, Introduction to geochemistry: Mcgraw-Hill Book Co., New York, N.Y., 721p.

Krohn, M.D., 1985, Spectral properties (0.4 to 25 microns) of selected rocks associated with disseminated gold and silver deposits in Nevada and Idaho: U.S.G.S. Open-file Rep. 85-576, 23p.

Krumbein, W.E. and Jens, K., 1981, Biogenic rock varnishes of the Negev Desert (Israel): an ecological study of iron and manganese transformation by cyanobacteria and fungi: Oecologia (Berl.), v.50, p.25-38.

Laudermilk, J.D., 1931, On the origin of desert varnish: Amer. Jour. of Science, v.21, p.51-66.

Longshaw, T.G., 1974, Field spectroscopy of multispectral remote sensing: an analytical approach: Applied Optics, v.13, p.1487-1493.

Mariner, R.H. and Surdam, R.C., 1970, Alkalinity and formation of zeolites in saline alkaline lakes: Science, v.170, p.977-980.

Markham, Brian L. and Barker, John L., 1985, Spectral characterization of the Landsat thematic mapper sensors: Int. Jour. Remote Sensing, v.6, no.5, p.697-716.

Mumpton, F.A., 1973, Scanning electron microscopy and the origin of sedimentary zeolites: Molecular sieves, Proc. 3rd Int. Cont. Mol. Sieves, Uytterhoeven, J.B., edit. Leuven Univ. Press, p.56-61.

Mumpton, F.A., edit., 1977, Mineralogy and geology of natural zeolites: Miner. Soc. Amer. short course notes, v.4, 233p.

Mutch, T.A. and others, 1976, The geology of Mars, Princeton Univ. Press, 400p.

Nassua, Kurt, 1983, The physics and chemistry of color; the fiftenn causes of color: John Wiley & Sons, New York, N.Y., 454p.

Noble, D.C., 1965, Gold Flat member of the Thirsty Canyon Tuff - a pantellerite ash-flow sheet in southern Nevada: U.S.G.S. Prof. Pap. 525-B, p.885-890.

Noble, D.C., Anderson, R.E., Ekren, E.B., and O'Connor, J.T., 1964, Thirsty Canyon Tuff of Nye and Esmeralda Counties, Nevada: U.S.G.S. Prof. Pap. 475-D, p.24-27.

Noble, D.C., 1968, Kane Springs Wash volcanic center, Lincoln County, Nev: GSA Mem. 110, p.109-116.

Noble, D.C., Bath, G.D., Christiansen, R.L., and Orkild, P.P., 1968, Zonal relationships and paleomagnetism of the Spearhead and Rocket Wash members of the Thirsty Canyon Tuff, southern Nevada: U.S.G.S. Prof. Pap. 600-C, p.61-65.

Noble, D.C. and Christiansen, R.L., 1968, Geologic map of the southwest quarter of the Black Mountain quadrangle, Nye County, Nevada: U.S.G.S. Misc. Geol. Invest. Map I-562.

Noble, D.C. and Christiansen, R.L., 1974, Black Mountain volcanic center: in Guidebook to the geology of four Tertiary volcanic centers in central Nevada: Nev. Bur. Mines and Geol. Rept. 19, p.22-26.

Noble, D.C. and Parker, D.F., 1974, Peralkaline silicic volcanic rocks of the western U.S.: Bull. Volcanology, v.38, p.803-827.

Noble, D.C., Vogel, T.A., Weiss, S.I., Erwin, J.W., McKee, E.H., and Younker, I.W., 1984, Stratigraphic relationships and source areas of ash-flow sheets of the Black Mountain and Stonewall Mountain volcanic centers, Nev: Jour. Geoph. Res., v.89, p.8593-8602.

Noble, D.C. and Weiss, S.I., 1986, Stratigraphy of the Thirsty Canyon Tuff and its bearing on the eruptive history of the Black Mountain volcanic center, southern Nevada ABST. IN Transactions, American Geophysical Union, v.67, no.44, Nov.4, 1986, p.1261.

Novak, S.W., 1984, Eruptive history of the Kane Springs Wash volcanic center, Nevada: Jour. Geoph. Res., v.89, p.8603-8615.

Novak, S.W., 1985, Geology and geochemical evolution of the Kane Springs Wash volcaninc center, Lincoln County, Nevada: Unpub. Ph.D. thesis, Stanford Univ., Stanford, Calif. 173p.

O'Connor, J.T., Anderson, R.W., and Lipman, P.W., 1966, Geologic map of the Thirsty Canyon quadrangle, Nye County Nevada: U.S.G.S. Quad. Map GQ-524.

Osborn, E.T. and Hem, J.D., 1961, Microbiological factors in the solution and transport of iron: U.S.G.S. Water Supply Pap. 1459-H, p.213-235.

Perry, R.S. and Adams, J.B., 1978, Desert varnish: evidence for cyclic deposition of manganese: Nature, v.276, p.489-491.

Podwysocki, M.H., Gunther, F.J., and Blodget, H.W., 1977, Discrimination of rock and soil types by digital analysis

of Landsat data: NASA Goddard Space Flight Center, X-923-77-17, 37p.

Podwysocki, M.H., Segal, D.B., and Abrams, M.J., 1983, Use of multispectral scanner images for assessment of hydrothermal alteration in the Marysvale, Utah mining area: Econ. Geol., v.78, p.675-687.

Podwysocki, M.H., 1987, Application of combined Landsat Thematic Mapper and airborne thermal infrared multispectral scanner data to lithologic mapping in Nevada: Summaries, 21st internat. symp. on remote sensing, Ann Arbor, Mich., Oct. 25-30, 1987, p.20-21.

Potter, R.M. and Rossman, G.R., 1977, Desert varnish: the importance of clay minerals: Science, v.196, p.1446-1448.

Potter, R.M. and Rossman, G.R., 1979, The manganese and iron oxide mineralogy of desert varnish: Chemical Geology, v.25, p.79-94.

Rogers, C.L., Ekren, E.B., Noble, D.C., and Weir, J.E., 1968, Geologic map of the northern half of the Black Mountain quadrangle, Nye County, Nevada: U.S.G.S. Misc. Geol. Invest. Map I-545.

Ross, C.S. and Smith, R.L., 1961, Ash flow tuffs: U.S.G.S. Prof. Pap. 366, 81p.

Rowan, L.C., Wetlaufer, P.H., Goetz, A.F.H., Billingsley, F.C., and Steward, J.H., 1974, Discrimination of rock types and detection of hydrothermally altered areas in south-central Nevada by the use of computer-enhanced ERTS images: U.S.G.S. Prof. Pap. 883, 35p.

Sabins, F.F., 1987, Remote Sensing: W.H. Freeman and Company, New York, N.Y., 449p.

Schwertmann, U. and Fischer, W.R., 1973, Natural "amorphous" ferric hydroxide: Geoderma, v.10, p.237-247.

Segal., D.B., 1983, Use of Landsat multispectral scanner data for the definition of limonitic exposures in heavily vegetated areas: Econ. Geol., v.78, p.711-722.

Spatz, D.M., Taranik, J.V., and Hsu, L.C., 1987a, Application of TM imagery to mapping volcanic rock assemblages at Tertiary calderas of the Basin and Range province: IGARSS 1987 symposium digest, Ann Arbor, Mich., May 1987, p.1299-1308.

Spatz, D.M., Taranik, J.V., and Hsu, L.C., 1987b, Influence

of mineral coatings and vegetation on TM imagery over Tertiary calderas of the Basin and Range province, western U.S.: ASPRS Technical Papers, Fall Convention, Reno, Nevada, October 4-9, p.13-25.

Spatz, D.M., Taranik, J.V., and Hsu, L.C., 1987c, Desert varnish on volcanic rocks of the Basin and Range province - composition, morphology, distribution, origin, and influence on Landsat imagery IN proceedings of ERIM fall convention, Ann Arbor, Michigan, October, 1987, apx.10p.

Spatz, D.M. and Taranik, J.V., 1988, Identification and mapping of volcanic lithologies genetically or spatially associated with precious metal deposits of the western U.S., using Landsat Imagery models IN proceed. 6th Thematic Conference on Remote Sensing, Houston, Texas, May 16-19, 1988, apx.10p.

Spatz, D.M., Taranik, J.V., and Hsu, L.C., 1988, Differentiating volcanic rock assemblages using Landsat TM data - influence of petrochemistry and desert varnish IN proceed. XXVII Committee on Space Research, Espoo, Finland, July 18-29, 1988, apx.10p.

Staley, J.T., Palmer, F., and Adams, J.B., 1982, Microcolonial fungi: common inhabitants of desert rocks: Science, v.213, p.1093-1094.

Sultan, M., Arvidson, R.E., Sturchio, N.C., and Guinness, E.A., 1987, Lithologic mapping in arid regions with Landsat thematic mapper data: Meatiq dome, Egypt: Geol. Soc. of Amer. Bull., v.99, p.748-762.

Taranik, J.V., 1978a, Characteristics of the Landsat multispectral data system: U.S.G.S. Open-file Rep. 78-187, 76p.

Taranik, J.V., 1978b, Principles of computer processing of Landsat data for geologic applications: U.S.G.S. Open-file Rep. 78-117, 50p.

Taranik, J.V., and Trautwein, C.M., 1977, Integration of geological remote sensing techniques in subsurface analysis: In LeRoy Edit, Subsurface Geology, Colorado School of Mines Pub., Golden, Colo., p.767-787.

Trautwein, C.M. and Taranik, J.V., 1978, Analytical and interpretive procedures for remote sensing data: U.S.G.S. Open-file Rep. 78-119, 52p.

Taylor-George, S., Palmer, F., Staley, J.T., Borns, D.J., Curtiss, B. and Adams, J.B., 1983, Fungi and bacteria

involved in desert varnish formation: Microb. Ecol., v.9, p.227-245.

Tschanz, C.M. and Pampeyan, E.H., 1970, Geology and mineral deposits of Lincoln County, Nev.: Nev. Bur. Mines and Geol. Bull. 73, 188p.

Weiss, S.I., 1987, Stratigraphy and paleomagnetic studies of ash-flow tuffs of the Black Mountain and Stonewall Mountain volcanic centers: Unpub. MS thesis, University of Nevada, Reno, Nev.

White, C.H., 1924, Desert varnish: Amer. Jour. Sci., v.7, 5th ser., p.413-420.

APPENDIX A

**Identities and dates of Landsat TM
scenes used in this study**

PATH	ROW	QUADRANT	SCENE ID	DATE OF ACQUISITION	PRODUCT
39	34	1,3,4	50139-17440	July 18,1984	P,T(no band4),N(band 4), B/W print,1:250,000
			50475-17451	June 19,1985	P,N,B/W print,1:1,000,000
			50491-17450	July 5,1985	P
			50539-17444	Aug. 22,1985	P,N
40	33	3,4	50066-17481	May 6,1984	P,N,B/W print,1:250,000
			50466-17512	June 10,1985	P,N
			50482-17510	June 26,1985	N
			50530-17503	Aug. 13,1985	P,N
40	34	1,2,3,4	50466-17515	June 10,1985	P,N
			50482-17512	June 26,1985	P,N
			50530-17510	Aug. 13,1985	P,N
			50546-17505	Aug. 29,1985	P
			50578-17502	Sept. 30,1985	P
			50594-17501	Oct. 16,1985	P
			50562-17503	Sept. 14,1985	P
41	33	3,4	50121-17553	June 30,1984	P,T(bands 3,6),N(bands 1, 2,4,5,7),B/W print,1:250000
41	34	1,2,4	50409-17575	April 14,1985	B/W print,1:1,000,000
			50457-17573	June 1,1985	P
			50473-17573	June 17,1985	P
			50489-17573	July 3,1985	P
			50569-17564	Sept. 21,1985	P,N

Landsat 5 TM Data Acquisitions

APPENDIX B

**Landsat 5 thematic mapper
instrument and orbit information**
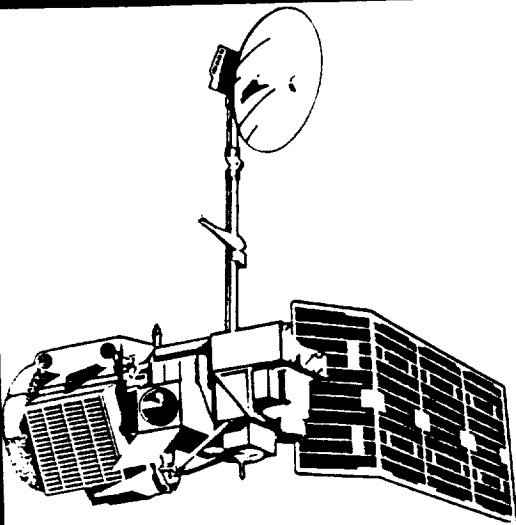
Satellite platform of Landsats 4 and 5.
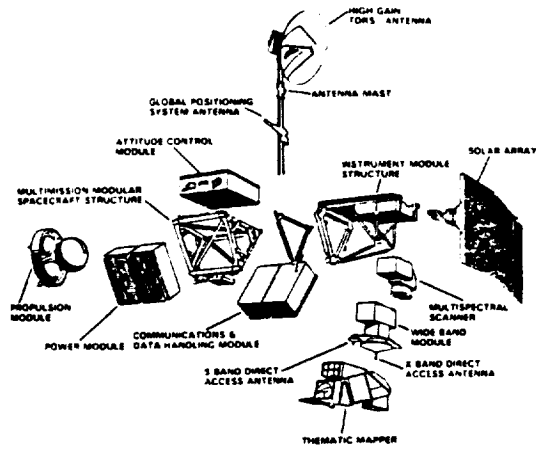
Components of the platform of Landsats 4 and 5.
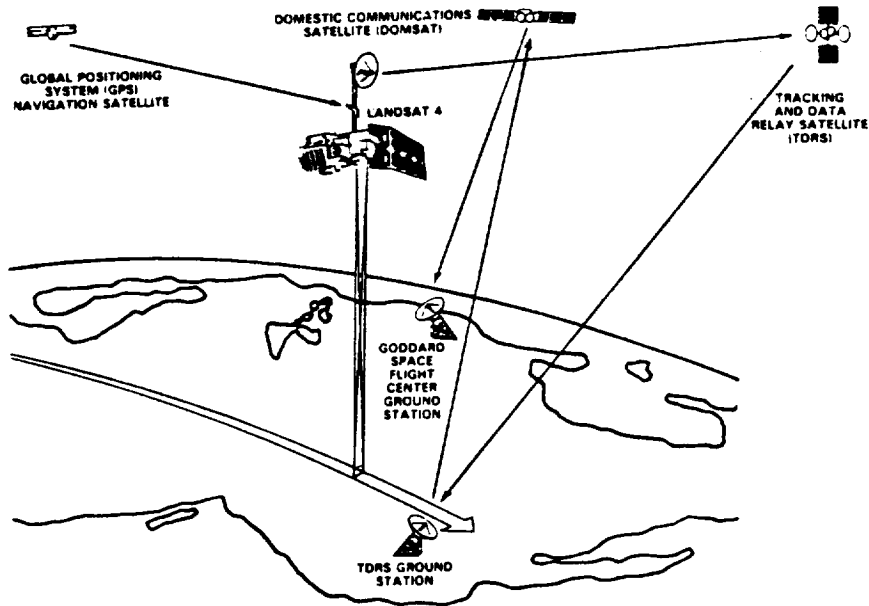
Communications network for Landsats 4 and 5.

Platforms and orbits of first and second generations of Landsat

	Landsats 1, 2, and 3	Landsats 4 and 5
Altitude	918 km	705 km
Orbits per day	14	14.5
Number of orbits (paths)	251	233
Image sidelap at equator	14 percent	7.6 percent
Crosses 40°N latitude at (local sun time, approximate)	9:30 a.m.	10:30 a.m.
Operational from	1972 to 1984	1982 to future
On-board data storage	Yes	No
Imaging systems:		
Multispectral scanner	Yes	Yes
Return-beam vidicon, panchromatic	Yes (Landsat 3)	No
Thematic mapper	No	Yes

Characteristics of Landsat imaging systems

	Multispectral scanner (MSS)	Return-beam vidicon (RBV)	Thematic mapper (TM)
Spectral region			
Visible and reflected IR	0.5 to 1.1 μm	0.50 to 0.75 μm	0.45 to 2.35 μm
Thermal IR (TM band 6)	—	—	10.5 to 12.5 μm
Spectral bands	4	1	7
Terrain coverage			
East-west direction	185 km	99 km	185 km
North-south direction	185 km	99 km	170 km
Instantaneous field of view			
Visible and reflected IR	0.087 mrad	0.043 mrad	0.043 mrad
Thermal IR (TM band 6)	—	—	0.17 mrad
Ground resolution cell			
Visible and reflected IR	79 by 79 m	40 by 40 m	30 by 30 m
Thermal IR (TM band 6)	—	—	120 by 120 m
Number of picture elements			
Single band	7.6×10^6	6.1×10^6	39×10^6
All bands	30.4×10^6	6.1×10^6	273×10^6

Thematic-mapper system.

Spectral bands for TM and MSS systems. Reflectance curves for vegetation, unaltered rocks, and hydrothermally altered rocks. From Sabins (1983, Figure C-5).
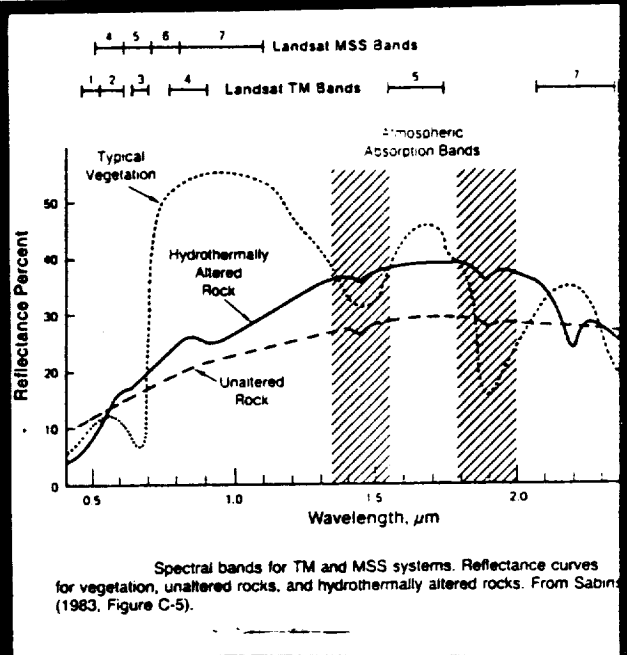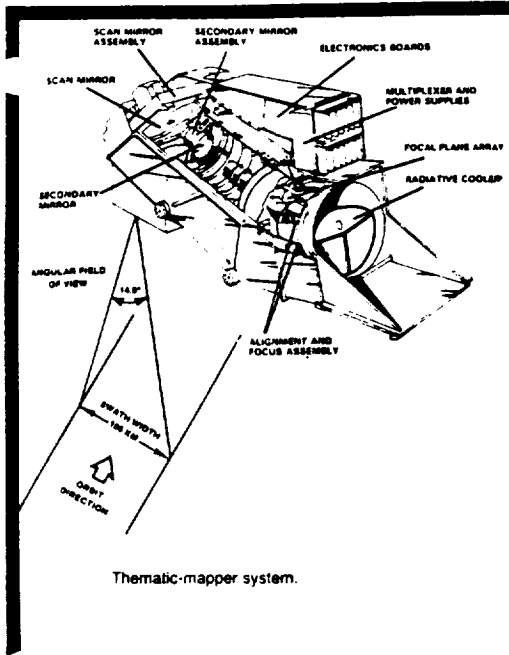
Thematic-mapper spectral bands

Band	Wavelength, μm	Characteristics
1	0.45 to 0.52	Blue-green—no MSS equivalent. Maximum penetration of water, which is useful for bathymetric mapping in shallow water. Useful for distinguishing soil from vegetation and deciduous from coniferous plants.
2	0.52 to 0.60	Green—coincident with MSS band 4. Matches green reflectance peak of vegetation, which is useful for assessing plant vigor.
3	0.63 to 0.69	Red—coincident with MSS band 5. Matches a chlorophyll absorption band that is important for discriminating vegetation types.
4	0.76 to 0.90	Reflected IR—coincident with portions of MSS bands 6 and 7. Useful for determining biomass content and for mapping shorelines.
5	1.55 to 1.75	Reflected IR. Indicates moisture content of soil and vegetation. Penetrates thin clouds. Good contrast between vegetation types.
6	10.40 to 12.50	Thermal IR. Nighttime images are useful for thermal mapping and for estimating soil moisture.
7	2.08 to 2.35	Reflected IR. Coincides with an absorption band caused by hydroxyl ions in minerals. Ratios of bands 5 and 7 are potentially useful for mapping hydrothermally altered rocks associated with mineral deposits.

APPENDIX C

Mackay School of Mines
Image processing system components

FACILITIES AND DATA PROCESSING EQUIPMENT

Mackay School of Mines has acquired a VAX-based Electromagnetic Systems
Laboratories (ESL) Interactive Digital Image Manipulation (IDIMS) System and a
personal computer image data analysis laboratory consisting of the following:

Manuf.	Model	Description
DEC	780XA-AE	VAX 11/780 CPU with 8 MB memory, (256KB Boards)
DEC	BA-DO-11	Expansion Box and expansion backplane
DEC	FP780-AA	Floating Point Accelerator
DEC	RUA81-CA	456 MB Fixed Disks (2 each)
DEC	RUA60	205 MB Removable Disk
SI	9700-53	800/1600/6250 BPI, 125 ips Tape Drives (2 each)
DEC	A100-8A	Decwriter Terminal
DEC	VT100-AA	2-Video Terminals
DEC	LP11-AA	300 lpm Printer
DEC	11/24-OC	LSI 11/24 Controller with 1MB Memory
DEANZA	IP8500	Gould-DeAnza Image Array Processor
DEANZA	IP85-M	8-Image Memory (512x512x8 Bit) Planes
DEANZA	IP85-DVP	Digital Video Processor with Tracball and Assoc. Interfaces
CONRAC	7211	19" High Resolution Monitor
ESL	-------	IDIMS, GES, ERIS, Data Catalog Software License
DEC	QE100-VZ	Fortran License
DEC	QE126-VZ	Pascal License
DUNN	634	Color Camera
CALCOMP	9160	Digitizing Station
DEC	DECNET	Ethernet
SYNTAX	SP-245/253	Network Softare
3 COM	501C	Network Hardware
IBM	P-AT	IBM PC-AT with 30 MB Hard Disk No. 9 Graphics Board, AST Preview Card, Monchrome Monitor, Electronome Color Monitor, Summamouse, and 80287 Chip, (16 Terminals)
MDA	MERIDIAN	MacDonald Detweiler Interactive Display and Analysis Software

APPENDIX D

IDIMS Landsat data processing functions

IMAGERY PROCESSING FUNCTIONS

COMMONLY USED IN THIS INVESTIGATION

The following list provides a brief description of some of the IDIMS software functions utilized for this project and should help clarify captions on images presented in preceding sections. Discussions of image enhancement techniques have been presented by Taranik (1978b) and Sabins (1987).

SCALE. Each band was linearly stretched using IDIMS function "scale", whereby an arbitrary amount of both the high and low tails of the brightness range distribution of pixels for each band is assigned to the maximum and minimum values respectively, and remaining intensity values stretched throughout the complete scale of 256. For final computation a histogram is calculated by the function. Experimentation yielded a consistently attractive value for truncation of 0.5 for most image manipulation applications. For principal component analysis, however, a truncation value of 0.2 proved superior. The result is a contrast enhanced image with brightness values extending the entire range of system resolution capacity, thus providing maximum brightness contrast between cover types.

RATIOS. Band ratios (Band x/Band y) are computed

through IDIMS function "divide" and involve dividing pixel intensity values in the numerator band by corresponding pixel intensity values for the band in the denominator. Resulting values tend to smooth out topographic reflectance and provide relative brightness values representative of cover type.

KERNEL. Edge enhancement techniques or filters involve either coarse or fine scale adjustments to smooth out contrast variations or sharpen them. For our purposes, the edge enhancement function sharpens the edges of remote sensing units by increasing the contrast at unit boundaries. A "kernel" or mask is produced by IDIMS function KERNEL. A 3 x 3 pixel size area was selected for the mask. The mask centers on each pixel in the scene and weights the surrounding pixels according to preset amounts. The sum of the new weighted values of surrounding pixels is then compared to a new weighted value for the central pixel. If the value of the central pixel is less than the summed value of surrounding pixels then the central pixel value is changed to the latter. The kernel is moved over each pixel by the function "CONVOL". Directional filters operate similarly, except that the values of the kernel grid are biased directionally to give resulting edge enhancements with linear bias.

ISH. The ISH transformation is a commonly applied computerized image manipulation technique which subdivides colors in color composite images into the optical parameters - intensity (I), saturation (S), and hue (H) (Buchanan, 1979; Haydn, et al., 1982). Red, green, and blue are transformed to intensity, saturation, and hue, and resulting 3 image composites thus represent I, S, and H, rather than the individual input bands. (Three input bands are allowed.) The IDIMS function ISH applied throughout this project plots the three primary colors at the vertices of an equilateral triangle. Intensity is defined as the average of the intensities of each color (each of the original bands). Saturation indicates the purity of a color with respect to departure from achromatic (white) which plots at the center of the triangle. Saturation would thus be at a minimum at the center, a maximum on triangle apexes. Hue is defined in relation to color. It begins at red (minimum), increasing toward green, then blue, and up to a maximum at red again. Each parameter - I, S, and H - ranges from 0-255. An RGB function IDIMS converts ISH to red, green, blue.

PRINCIPAL COMPONENTS. Descriptions of principal components statistical analysis (PC's) are given by Davis (1973) and Joreskog, et al. (1976). Application to remote sensing imagery transformation has been described by Fontanel, et al. (1975); Podwysocki, et al (1977); and

Taranik (1978). PC's, the basis of modern factor analysis schemes, are the eiginvectors of a variance-covariance matrix. The variance of two variables, in this case intensity values of two bands, is plotted on an x-y coordinate system. A point is then located perpendicular from each coordinate at the variance value extending a distance equal to the covariance. An ellipse is plotted with its center at the coordinate origin and bound near one end by the two points. The vector from origin to the apex of the ellipse is PC1 and all intensity values are regressed to that vector. PC2 is perpendicular to PC1, extends through the coordinate origin, and is bound by the ellipse. It is always much shorter than PC1 and resultant intensity values considerably lower. Podwysocki (1977) describes resultant values as "new variables (components) which are linear combinations of the original variables; each component contains uncorrelated information". All six TM bands may be entered and a complex principal components analysis computed, resulting in 6 PC's. The IDIMS function KLTRANS takes a covariance matrix computed through function ISOCLS and computes PC's. The principal components transformation typically provides maximum contrast between cover types and PC composites aid distinction between lithologies, vegetation, and topographic effects.

PICSTAT. PICSTAT computes statistics on a designated

image. The image can be outlined by only a few pixel dimensions for class identification. The algorithm calculates maximum and minimum values, mean average values, and the standard deviation for each band.

HISTOG. HISTOG provides image histograms. Histogram plots for all bands of an image can be evoked and outputted on the line printer or monitor screen. The plot shows frequencies of occurrence for each digital number value in the image.

ISOCLS. ISOCLS applies a clustering algorithm to a multispectral image, in this case, 6-banded images, in order to partition multivariate data points into disparate categories with similar statistical properties. The function operates by "split" and "combine" iterations, involving the distance between data points and the cluster means. If a data point's standard deviation is greater than the default value of 4.5, "splitting" occurs and a new cluster is created. The maximum number of clusters computed for images presented herein was 16, the default value. The result is an unsupervised classified image. ISOCLS statistics are utilized by the KLTRANS function which produces the PC images.

CLASFY. CLASFY is a classifying algorithm that

operates on statistics generated by STATS and stores in a statistics file for the image. CLASFY evaluates all pixels according to a maximum likelihood decision rule based on class covariance matrices and mean vectors. The procedure involves definition of training sites using display function, TR and TA, which are then assigned to a special file by IRRECV. Training sites are typically based on previous operator identification of cover types. The result is supervised classified image with as many classes as designated by the operator.

RECLAS. Classified images can be smoothed by reassigning erratic or extraneous pixels (individual pixels surrounded by a different class) by function RECLAS. A 3 x 3 grid is usually selected as a kernel and moved over the image. Any central pixel in the grid, which differs from surrounding pixels of a different but unified class, is reassigned to the class of the surrounding pixels.

APPENDIX E

Analytical geochemistry procedures

ANALYTICAL PROCEDURES

CHEMEX CODE	NUMBER SAMPLES	DESCRIPTION	METHOD	DETECTION LIMIT	UPPER LIMIT
5 9 2	5	SiO_2 %: Whole rock	ICP–AES	0.01	99.00
5 9 4	5	Al_2O_3 %: Whole rock	ICP–AES	0.01	99.00
5 8 6	5	Fe_2O_3(total) %: Whole rock	ICP–AES	0.01	99.00
5 9 3	5	MgO %: Whole rock	ICP–AES	0.01	99.00
5 8 8	5	CaO %: Whole rock	ICP–AES	0.01	99.00
5 9 9	5	Na_2O %: Whole rock	ICP–AES	0.01	99.00
8 2 1	5	K_2O %: Whole rock	ICP–AES	0.1	99.0
5 9 5	5	TiO_2 %: Whole rock	ICP–AES	0.01	99.00
5 9 7	5	P_2O_5 %: Whole rock	ICP–AES	0.01	99.00
5 9 6	5	MnO %: Whole rock	ICP–AES	0.01	99.00
5 4 2	5	BaO %: Whole rock	ICP–AES	0.01	99.00
4 7 5	5	L.O.I. %: Loss on ignition	FURNACE	0.01	99.00
5 4 0	5	Total %	CALCULATION	0.01	N/A

ANALYTICAL PROCEDURES

CHEMEX CODE	NUMBER SAMPLES	DESCRIPTION	METHOD	DETECTION LIMIT	UPPER LIMIT
1 3 1	3	U ppm: Gamma counting	NAA	1	10000
1 5 0	3	Th ppm: Trace rock, soil	NAA	1	1000
1 1 0	3	La ppm: Trace rock, soil	NAA	1	1000
1 3 5	3	Ce ppm: Trace rock, soil	NAA	2	10000
1 3 4	3	Sm ppm: Trace rock, soil	NAA	0.1	500
1 3 7	3	Eu ppm: Trace rock, soil	NAA	0.5	100.0
1 4 1	3	Tb ppm: Trace rock, soil	NAA	0.1	1000
1 3 8	3	Yb ppm: Trace rock, soil	NAA	0.1	1000
1 3 6	3	Lu ppm: Trace rock, soil	NAA	0.1	500
1 2 8	3	Nd ppm: Trace rock, soil	NAA	5	1000

ANALYTICAL PROCEDURES

CHEMEX CODE	NUMBER SAMPLES	DESCRIPTION	METHOD	DETECTION LIMIT	UPPER LIMIT
8 1 8	4			0.01	100.00
9 2 1	4	Al %: 32 element. soil & rock	ICP-AES	0.01	15.00
9 2 2	4	Ag ppm: 32 element. soil & rock	ICP-AES	0.2	200
9 2 3	4	As ppm: 32 element. soil & rock	ICP-AES	5	10000
9 2 4	4	Ba ppm: 32 element. soil & rock	ICP-AES	10	10000
9 2 5	4	Be ppm: 32 element. soil & rock	ICP-AES	0.5	100.0
9 2 6	4	Bi ppm: 32 element. soil & rock	ICP-AES	2	10000
9 2 7	4	Ca %: 32 element. soil & rock	ICP-AES	0.01	15.00
9 2 8	4	Cd ppm: 32 element. soil & rock	ICP-AES	0.5	100.0
9 2 9	4	Co ppm: 32 element. soil & rock	ICP-AES	1	10000
9 3 0	4	Cr ppm: 32 element. soil & rock	ICP-AES	1	10000
9 3 1	4	Cu ppm: 32 element. soil & rock	ICP-AES	1	10000
9 3 2	4	Fe %: 32 element. soil & rock	ICP-AES	0.01	15.00
9 3 3	4	Ga ppm: 32 element. soil & rock	ICP-AES	10	10000
9 5 1	4	Hg ppm: 32 element. soil & rock	ICP-AES	1	10000
9 3 4	4	K %: 32 element. soil & rock	ICP-AES	0.01	10.00
9 3 5	4	La ppm: 32 element. soil & rock	ICP-AES	10	10000
9 3 6	4	Mg %: 32 element. soil & rock	ICP-AES	0.01	15.00
9 3 7	4	Mn ppm: 32 element. soil & rock	ICP-AES	1	10000
9 3 8	4	Mo ppm: 32 element. soil & rock	ICP-AES	1	10000
9 3 9	4	Na %: 32 element. soil & rock	ICP-AES	0.01	5.00
9 4 0	4	Ni ppm: 32 element. soil & rock	ICP-AES	1	10000
9 4 1	4	P ppm: 32 element. soil & rock	ICP-AES	10	10000
9 4 2	4	Pb ppm: 32 element. soil & rock	ICP-AES	2	10000
9 4 3	4	Sb ppm: 32 element. soil & rock	ICP-AES	5	10000
9 5 2	4	Se ppm: 32 element. soil & rock	ICP-AES	10	10000
9 4 4	4	Sr ppm: 32 element. soil & rock	ICP-AES	1	10000
9 4 5	4	Ti %: 32 element. soil & rock	ICP-AES	0.01	5.00
9 4 6	4	Tl ppm: 32 element. soil & rock	ICP-AES	10	10000
9 4 7	4	U ppm: 32 element. soil & rock	ICP-AES	10	10000
9 4 8	4	V ppm: 32 element. soil & rock	ICP-AES	1	10000
9 4 9	4	W ppm: 32 element. soil & rock	ICP-AES	5	10000
9 5 0	4	Zn ppm: 32 element. soil & rock	ICP-AES	1	10000

ANALYTICAL PROCEDURES

CHEMEX CODE	NUMBER SAMPLES	DESCRIPTION	METHOD	DETECTION LIMIT	UPPER LIMIT
573	28	Al %: 24 element, rock & core	ICP-AES	0.01	25.0
22	28	Sb ppm: HCl-KClO3 digest, extrac	AAS-BKGD CORR	0.2	1000
13	28	As ppm: HNO3-aqua regia digest	AAS-HYDRIDE/EDL	1	10000
565	28	Ba ppm: 24 element, rock & core	ICP-AES	1	10000
34	28	Be ppm: HClO4-HNO3-HF digestion	AAS	0.1	1000
23	28	Bi ppm: HCl-KClO3 digest, extrac	AAS-BKGD CORR	0.1	1000
40	28	B ppm	FUSION-ICP	10	10000
154	28	Br ppm: Trace rock, soil	NAA	0.5	1000
7	28	Cd ppm: HNO3-aqua regia digest	AAS-BKGD CORR	0.1	200
576	28	Ca %: 24 element, rock & core	ICP-AES	0.01	25.0
367	28	C %: Leco induction furnace	LECO-IR DETECTOR	0.01	100.0
135	28	Ce ppm: Trace rock, soil	NAA	2	10000
158	28	Cs ppm: Trace rock, soil	NAA	2.0	10000
569	28	Cr ppm: 24 element, rock & core	ICP-AES	1	10000
563	28	Co ppm: 24 element, rock & core	ICP-AES	1	10000
577	28	Cu ppm: 24 element, rock & core	ICP-AES	1	10000
140	28	Dy ppm: Trace rock, soil	NAA	1	500
137	28	Eu ppm: Trace rock, soil	NAA	0.5	100.0
21	28	F ppm: Carbonate-nitrate fusion	SPECIFIC ION	20	10000
31	28	Ga ppm: HClO4-HNO3-HF dig., ext	AAS-BKGD CORR	1	10000
41	28	Ge ppm: HClO4-HNO3-HF digestion	AAS	5	10000
100	28	Au ppb: Fuse 10 g sample	FA-AAS	5	10000
107	28	Hf ppm: Trace rock, soil	NAA	2	1000
566	28	Fe %: 24 element, rock & core	ICP-AES	0.01	25.0
110	28	La ppm: Trace rock, soil	NAA	1	1000
560	28	Pb ppm: 24 element, rock & core	ICP-AES	2	10000
27	28	Li ppm: HClO4-HNO3-HF digestion	AAS	1	10000
136	28	Lu ppm: Trace rock, soil	NAA	0.1	500
570	28	Mg %: 24 element, rock & core	ICP-AES	0.01	25.0
568	28	Mn ppm: 24 element, rock & core	ICP-AES	1	10000

ANALYTICAL PROCEDURES

CHEMEX CODE	NUMBER SAMPLES	DESCRIPTION	METHOD	DETECTION LIMIT	UPPER LIMIT
20	28	Hg ppb: HNO3-HCl digestion	AAS-FLAMELESS	5	100
554	28	Mo ppm: 24 element, rock & core	ICP-AES	1	10000
128	28	Nd ppm: Trace rock, soil	NAA	5	1000
564	28	Ni ppm: 24 element, rock & core	ICP-AES	1	10000
191	28	Nb ppm	XRF	5	10000
559	28	P ppm: 24 element, rock & core	ICP-AES	10	10000
584	28	K %: 24 element, rock & core	ICP-AES	0.01	20.0
30	28	Rb ppm: HClO4-HNO3-HF digestion	AAS	1	10000
134	28	Sm ppm: Trace rock, soil	NAA	0.1	500
103	28	Sc ppm: Trace rock, soil	NAA	0.1	1000
16	28	Se ppm: HCl-KClO3 digest, ext	AAS-BKGD CORR	0.2	1000
378	28	SiO2 %: Carbonate fusion	GRAVIMETRIC	0.01	100.00
573	28	Ag ppm: 24 element, rock & core	AAS	0.5	500
583	28	Na %: 24 element, rock & core	ICP-AES	0.01	10.00
582	28	Sr ppm: 24 element, rock & core	ICP-AES	1	10000
330	28	S %: Leco induction furnace	LECO-IR DETECTOR	0.001	100.0
151	28	Ta ppm: Trace rock, soil	NAA	2	10000
24	28	Te ppm: HBr-Br2 digest, extrac	AAS-BKGD CORR	0.05	100.0
141	28	Tb ppm: Trace rock, soil	NAA	0.1	1000
39	28	Tl ppm: HClO4-HNO3-HF dig., ext	AAS-BKGD CORR	0.1	1000
150	28	Th ppm: Trace rock, soil	NAA	0.5	1000.0
19	28	Sn ppm: NH4I sublimation, extrac	AAS	2	1000
579	28	Ti %: 24 element, rock & core	ICP-AES	0.01	10.00
18	28	W ppm: K pyrosulfate fusion	COLORIMETRIC	2	1000
152	28	U ppm: Trace rock, soil	NAA	0.2	1000
572	28	V ppm: 24 element, rock & core	ICP-AES	1	10000
138	28	Yb ppm: Trace rock, soil	NAA	0.1	1000
801	28	Y ppm	XRF	5	10000
558	28	Zn ppm: 24 element, rock & core	ICP-AES	1	10000
914	28	Zr ppm	XRF	5	10000

APPENDIX F

Geochemical analyses of Stonewall Flat Tuff of
Stonewall Mountain (unpublished data from
Professor D.C. Noble and Steve Weiss, 1987)

MAJOR AND TRACE ELEMENT ANALYSES
FROM THE STONEWALL MOUNTAIN STUDY AREA
(From D. C. Noble, 1986, unpublished data)

	Spearhead Tuff	Spearhead Tuff	Spearhead Tuff	Spearhead Tuff	Spearhead Tuff	Civet Cat	Civet Cat	Average of Spearhead
SiO_2	74.60	69.1	74.1	72.8	71.8	72.7	71.3	72.48
Al_2O_3	12.4	13.9	12.8	12.7	13.5	13.8	13.0	13.06
Fe_2O_3	2.07	2.32	2.16	2.13	2.37	2.2	2.02	2.21
CaO	0.45	0.41	0.32	0.42	0.47	0.94	1.73	0.41
MgO	0.50	0.50	0.12	0.11	0.08	0.18	0.16	0.17
TiO_2	0.13	0.15	0.13	0.14	0.15	0.28	0.23	0.14
MnO	0.08	0.09	0.07	0.07	0.10	0.09	0.10	0.08
Na_2O	3.96	5.20	4.05	4.21	4.97	4.83	4.79	4.49
K_2O	5.37	5.52	4.39	5.53	5.01	5.43	4.90	5.16
P_2O_5	0.20	0.03	0.01	0.03	0.02	0.06	0.08	0.02
Total	99.76	97.22	98.15	98.14	98.47	100.51	98.31	-----
La	46.43	80.43	72.33	78.98	104.0	102.7	98.82	76.43
Ce	111.10	156.2	132.96	147.50	192.5	164.4	176.80	147.95
Sm	7.31	11.92	10.69	9.75	13.4	9.95	11.19	10.61
Eu	-----	0.064	0.03	0.03	0.05	0.78	0.42	0.43
Tb	1.43	1.61	1.47	1.65	1.51	1.23	1.26	1.53
Yb	6.56	6.69	6.95	7.52	6.99	5.07	5.90	6.94
Lu	0.88	1.23	1.24	1.32	1.29	0.91	1.12	1.19
Be	-----	----	----	----	----	4.20	4.30	----
Co	----	----	----	----	----	4.0	3.0	----
Cu	----	----	----	----	----	3.0	6.9	----
Pb	----	----	----	----	----	40.0	15.0	----
Ni	----	----	----	----	----	4.0	4.0	----
Sr	----	----	----	----	----	51.80	95.2	----
Th	----	----	----	----	----	27.00	32.0	----
Zr	----	----	----	----	----	158.00	303.0	----
V	----	----	----	----	----	11.30	4.8	----
Zn	----	----	----	----	----	81.00	102.0	----

Major oxides reported in %, trace elements in ppm.

MAJOR ELEMENT ANALYSES OF ROCKS OF THE CIVET CAT CANYON MEMBER OF THE STONEWALL FLAT TUFF

Sample #	1[1]	2[1]	3[1]	4[1]	5[1]	6[1]	7[1]	8[2]	9[2]	10[3]	11[3]	12[3]	13[1]
Subunit	Tsco	Tsco	Tsco	Tsco	Tsco	Tsco	Tsco	Tsco	Tscm	Tscm	CI	Tscu	ST
SiO_2	72.7	71.3	71.3	72.92	67.8	67.8	66.12	63.25	59.82	60.8	51.3	66.1	72.8
Al_2O_3	13.8	13.0	14.5	13.50	15.7	12.4	16.28	17.0	16.64	17.3	16.5	16.1	13.8
FeO^*	1.98	1.82	2.14	1.76	2.72	1.58	2.51	3.31	5.27	2.42	7.23	2.31	1.83
MgO	0.18	0.16	0.28	0.15	0.42	0.08	0.39	0.84	0.85	1.35	3.36	0.63	0.20
CaO	0.94	1.73	0.85	0.80	1.40	1.04	1.83	2.07	2.58	3.13	7.19	1.41	1.0
Na_2O	4.83	4.79	4.1	4.37	5.01	4.52	4.93	5.23	4.80	4.78	3.73	5.03	4.0
K_2O	5.43	4.90	5.3	5.28	6.30	5.00	6.05	6.45	6.30	5.07	2.69	5.68	4.8
K_2O+	----	----	0.45	0.23	----	----	0.15	----	----	----	----	----	----
K_2O-	----	----	0.19	0.21	----	----	0.17	1.15[4]	----	----	----	----	----
TiO_2	0.28	0.23	0.22	0.15	0.48	0.14	0.48	0.63	1.06	0.91	1.14	0.39	0.16
MnO_2	0.09	0.10	0.08	0.08	0.13	0.07	0.12	0.10	0.12	0.12	0.17	0.10	0.08
P_2O_5	0.06	0.08	0.06	0.01	0.13	0.03	0.11	0.16	0.31	0.32	0.50	0.12	0.04
CO_2	----	----	0.33	0.10	----	----	0.51	----	----	----	----	----	0.23
Cl	----	----	----	0.04	----	----	0.01	----	----	----	----	----	0.05
F	----	----	----	0.17	----	----	0.06	----	----	----	----	----	0.11
LOI	----	----	----	----	----	----	----	----	----	0.39	1.31	1.16	----
Total	100.5	98.3	99.8	99.86	100.4	92.8	100.0	100.5	98.2	99.0	96.8	99.4	99.1

$\underline{FeO^*}$
$\dfrac{FeO^*}{FeO^*+MgO}$

	0.848	0.862	0.811	0.862	0.792	0.917	0.778	0.687	0.777	0.500	0.549	0.667	0.839

$\underline{Na+K}$
$\dfrac{Na+K}{Al}$

	1.002	1.014	0.861	0.956	0.959	1.036	0.900	0.917	0.887	0.772	0.548	0.896	0.853

Note: Values are in weight % except FeO^*/FeO^*+MgO and Na+K/Al ratios, FeO^* = total FE as FeO. ST=Shard Tuff, CI = congnate inclusions extracted from sample #10. [1] = unpublished data from Noble, D.C., pers. comm., 1984. Samples 1, 2, 5 and 6 by Barringer-Magenta using ICP methods, 3 and 13 by rapid-rock methods (Shapiro and Brannock, 1962) and 4 and 7 by wet chemical methods (Peck, 1964). 2 = data from Foley (1978), Fe, FeO, MnO, MgO and P_2O_5 by wet chemical methods, SiO_2, Al_2O_3, TiO_2 and CaO by X-ray fluorescence methods and Na and K by single-flame photometry. 3 = new data by X-RAL Ltd., using $Li-BO_3$ fusion with X-ray fluorescence methods. 4 = total volatiles, ---- = not measured. (After Weiss, 1987). Tsco = outflow sheet; Tscm and Tscu = near vent tuffs.

APPENDIX G

Geochemical analyses of volcanics from the
Black Mountain caldera (unpublished data from
Professor D.C. Noble)

MAJOR AND TRACE ELEMENT ANALYSES FROM
THE BLACK MOUNTAIN CALDERA
(From D. C. Noble, 1986, unpublished data)

	Pahute Mesa Tuff	Rocket Wash Tuff	Trail Ridge Tuff	Trail Ridge Tuff	Trachyte Hidden Cliff	Trachyte Hidden Cliff	Ribbon Cliff Lava	Gold Flat Tuff
SiO_2	73.60	65.90	68.80	72.40	55.74	60.70	62.67	61.60
Al_2O_3	12.40	11.20	13.30	12.80	17.09	17.56	17.70	14.60
Fe_2O_3	3.49	1.82	2.65	3.65	7.68	5.45	4.59	4.28
CaO	1.06	1.48	0.57	0.42	5.90	2.94	2.88	1.55
MgO	0.21	0.02	0.24	0.56	3.25	4.42	0.88	0.29
TiO_2	0.23	0.08	0.21	0.23	1.32	0.96	0.84	0.30
MnO	0.14	0.05	0.09	0.11	0.17	0.14	0.10	0.13
Na_2O	4.30	4.25	4.43	4.21	4.78	5.18	5.23	6.05
K_2O	5.88	4.50	5.89	5.70	3.86	5.08	4.77	5.47
P_2O_3	0.03	0.02	0.02	0.01	0.71	0.57	0.32	0.08
Total	101.34	89.32	96.20	100.09	100.50	103.00	99.98	94.35
Sc	2.22	0.22	2.06	4.34	13.96	8.48	6.89	1.93
Zn	232.60	236.50	150.70	128.30	98.21	123.30	131.20	260.40
Rb	247.10	496.70	312.40	151.90	81.17	123.10	145.80	403.30
Sb	0.66	0.76	0.56	0.54	1.00	0.17	0.22	0.76
Cs	5.11	7.46	5.30	8.82	0.04	0.67	1.54	6.24
Hf	35.62	29.37	20.54	17.30	10.25	14.14	16.81	55.88
Ta	6.38	9.83	7.94	2.51	1.82	2.72	4.51	12.82
Th	35.02	51.28	37.57	21.94	9.49	17.89	17.44	75.25
La	188.50	51.33	93.88	147.60	82.94	114.10	109.00	229.90
Ce	374.50	103.70	199.00	266.40	153.90	201.80	194.80	438.20
Sm	19.24	9.46	13.65	13.35	8.53	11.82	11.68	25.38
Eu	0.26	0.04	0.15	1.93	2.17	1.87	2.35	0.89
Tb	2.61	3.06	2.08	1.28	1.07	1.26	1.22	3.47
Yb	12.93	15.76	11.76	5.88	4.16	5.45	5.07	19.94
Lu	2.49	2.65	1.66	0.89	0.03	0.23	0.80	3.51
Be	10.20	22.60	11.10	4.00	0.00	11.50	0.00	20.20
Co	14.00	7.00	4.00	15.00	0.00	7.00	0.00	13.00
Cu	5.40	7.60	1.20	3.40	0.00	4.00	0.00	4.20
Pb	35.00	65.00	40.00	25.00	0.00	35.00	0.00	55.00
Ni	3.00	2.00	10.00	42.00	0.00	58.00	0.00	6.00
Sr	16.60	14.40	34.30	13.40	0.00	12.70	0.00	150.00
Th	65.00	65.00	45.00	50.00	0.00	45.00	0.00	105.00
Zr	1130.00	659.00	523.00	1294.00	0.00	558.00	0.00	2080.00
V	4.30	0.10	8.50	4.10	0.00	0.80	0.00	7.40
Zn	207.00	244.00	160.00	187.00	0.00	132.00	0.00	222.00

Major oxides reported in %, trace elements in ppm.

APPENDIX H

Geochemical analyses of volcanics from the
Kane Springs Wash volcanic center (Novak, 1985)

Table 2 Chemical analyses of Kane Springs volcanic rocks

	Basalts				Intracaldera mafic lavas		
Sample	370	392	19	317	139	144	364
SiO$_2$*	52.4	47.9	50.4	51.5	49.0	56.9	60.5
Major element analyses							
SiO$_2$	51.1	46.9	50.5	51.0	53.1	55.9	58.5
Al$_2$O$_3$	14.8	16.9	15.6	16.6	15.8	15.5	15.2
ΣFe$_2$O$_3$	9.50	10.7	10.6	10.4	10.4	9.14	7.75
MgO	7.54	6.71	7.60	4.98	3.86	3.78	2.30
CaO	8.20	11.6	8.83	7.43	7.04	6.14	4.57
Na$_2$O	2.59	2.99	2.98	3.24	3.76	3.77	3.88
K$_2$O	1.74	.33	1.35	2.24	2.31	2.82	3.62
TiO$_2$	1.34	1.29	1.89	2.01	1.83	1.48	1.20
P$_2$O$_5$	.49	.16	.49	.77	0.39	0.27	0.23
MnO	.13	.14	.15	.15	0.17	0.16	0.13
H$_2$O+	1.40	-	.68	-	0.28	1.02	-
Total	100.1	99.5	97.7	98.9	98.9	100.0	97.4
XRF analyses							
Rb	44	7.4	24	44	19	57	82
Sr	683	333	577	626	524	288	243
Zr	208	109	186	298	200	454	525
Y	26	25	30	36	34	45	50
Nb	15	5.5	24	25	15	28	33
Ni	206	107	136	57	52	30	28
Zn	92	77	84	90	109	96	107
Ga	20	17	17	21	21	24	28
Pb	12	3	7	12	5	12	14
INAA Analyses							
La	39.6	8.51	28.2	50.8	27.7	55.7	63.8
Ce	86.4	19.3	61.7	110	62.9	118	137
Nd	43.8	14.5	32.8	53.2	36.1	52.4	61.0
Sm	8.52	3.69	7.02	10.36	8.05	10.24	11.8
Eu	2.15	1.30	2.05	2.75	2.81	2.40	2.34
Tb	.93	.66	.92	1.21	1.17	1.40	1.58
Tm	.34	.36	.37	.49	.45	.70	.75
Yb	2.33	2.36	2.44	3.07	3.10	4.40	5.12
Lu	.37	.39	.39	50	49	71	.80
Sc	24.5	33.5	24.4	20.0	22.9	20.1	16.5
Cr	465	320	270	104	31	80	66
Co	42.7	45.8	47.3	31.7	46.5	33.4	16.0
Hf	5.16	2.48	4.38	6.78	4.80	10.0	11.7
Ta	1.04	.28	1.45	1.58	1.14	2.27	2.12
Th	5.38	67	3.84	5.60	2.39	7.93	10.2
U	1.38	-	.90	1.27	0.89	1.87	2.14

Table 2, continued

	Postcaldera trachyte	Central complex	Precaldera trachyte	Ash-flow tuffs			Early moat rhyolite	Late moat rhyolite
				V2	V3	V2		
Sample	1	270	301	204	99	326	354	352
SiO_2*	61.0	70.9	69.6	76.3	75.9	67.3	77.1	76.0
Major element analyses								
SiO_2	59.3	70.1	67.3	74.4	75.2	65.3	76.1	75.3
Al_2O_3	15.9	13.7	14.2	11.2	10.9	14.2	12.3	12.5
ΣFe_2O_3	6.57	3.88	3.37	2.94	3.41	4.95	1.24	0.94
MgO	1.73	0.24	0.27	0.21	0.09	0.55	0.11	0.18
CaO	3.60	3.62	1.15	0.15	0.13	1.53	0.49	0.44
Na_2O	4.36	4.28	4.12	3.73	4.27	4.67	3.32	3.59
K_2O	4.49	5.31	5.66	4.91	4.77	5.55	5.14	5.45
TiO_2	1.23	0.42	0.39	0.15	0.19	0.48	0.10	0.05
P_2O_5	0.44	0.03	0.06	<.05	<.05	0.09	<.02	0.01
MnO	0.15	0.11	0.07	0.05	0.08	0.18	0.19	0.04
H_2O+	0.91	-	-	-	-	0.56	0.04	-
Total	98.8	99.5	97.7	97.7	98.2	99.3	98.1	98.5
XRF analyses								
Rb	66	138	204	373	306	155	160	439
Sr	268	48	74	6	57	4	20	3.5
Zr	343	611	695	1165	1238	900	150	107
Y	42	64	60	124	109	55	42	123
Nb	26	62	53	146	119	41	25	72
Zn	96	82	99	237	223	164	-	-
INAA analyses								
La	66.1	81.4	114	-	-	130.1	75.9	8.60
Ce	138.5	194	239	-	-	260	141	28.0
Nd	64	74.7	91.4	-	-	114	51	22
Sm	10.9	14.3	16.1	-	-	17.4	10.2	9.18
Eu	2.80	1.43	1.12	-	-	1.0	0.174	0.0115
Tb	1.43	1.85	2.03	-	-	2.2	1.36	2.79
Yb	3.97	6.92	7.28	-	-	6.8	5.05	11.86
Lu	0.63	1.12	1.17	-	-	1.00	0.732	1.79
Sc	10.23	4.03	4.57	-	-	5.81	1.90	2.01
Cr	5.7	<10	<10	-	-	2.0	<2	<1.5
Co	9.13	0.77	<10	-	-	2.43	0.45	0.04
Hf	9.35	17.3	18.9	-	-	20.9	6.39	7.92
Ta	1.90	4.45	5.37	-	-	3.50	2.92	6.35
Th	8.25	19.3	24.0	-	-	15.7	24.6	33.7
U	1.75	5.51	6.63	-	-	3.6	4.6	10.8

Table 10. Chemical analyses of intracaldera mafic and intermediate lavas.

Rock type	AB	AB	AB	TB	TA	TA	TA	A	A
Sample#	142	140	139	143	365	144	364	417	282
SiO_2*	48.1	48.3	49.0	49.5	54.3	56.9	60.5	62.4	63.7
XRF major-element analyses									
SiO_2	47.9	48.2	47.5	50.4	53.1	55.9	58.5	61.7	61.8
Al_2O_3	15.8	16.2	15.6	15.6	15.8	15.5	15.2	14.4	14.0
ΣFe_2O_3	13.8	13.9	13.6	14.4	10.4	9.14	7.75	7.99	7.98
MgO	4.78	4.64	4.73	3.72	3.86	3.78	2.30	1.67	1.43
CaO	8.68	8.24	8.33	7.01	7.04	6.14	4.57	4.77	4.44
Na_2O	3.55	3.57	3.48	3.84	3.76	3.77	3.88	2.98	2.89
K_2O	1.31	1.27	1.35	2.00	2.31	2.82	3.62	3.16	3.15
TiO_2	2.76	2.79	2.77	2.97	1.83	1.48	1.20	1.43	1.36
P_2O_5	0.62	0.63	0.65	0.59	0.39	0.27	0.23	0.50	0.51
MnO	0.18	0.18	0.18	0.19	0.17	0.16	0.13	0.14	0.11
H_2O+	-	-	1.10	-	1.33	0.28	1.02	-	0.86
H_2O-	-	-	0.46	-	0.54	0.16	0.46	-	-
Total	100.7	99.4	99.6	99.8	100.5	99.4	98.7	98.7	98.5
XRF trace-element analyses (ppm)									
Rb	17	-	19	25	-	57	82	-	82
Sr	515	-	524	432	-	288	243	-	327
Zr	181	-	200	248	-	454	525	-	330
Y	32	-	34	35	-	45	50	-	39
Nb	14	-	15	18	-	28	33	-	23
Ni	48	-	52	26	-	30	28	-	-
Zn	102	-	109	102	-	96	107	-	90
Ga	20	-	21	24	-	24	28	-	22
Pb	5	-	5	5	-	12	14	-	16
INAA analyses (ppm)									
La	-	-	28	-	-	56	64	-	-
Ce	-	-	63	-	-	118	137	-	-
Nd	-	-	36	-	-	52	61	-	-
Sm	-	-	8	-	-	10	12	-	-
Eu	-	-	2.8	-	-	2.4	2.3	-	-
Tb	-	-	1.17	-	-	1.40	1.58	-	-
Tm	-	-	0.45	-	-	0.70	0.75	-	-
Yb	-	-	3.1	-	-	4.4	5.1	-	-
Lu	-	-	0.49	-	-	0.71	0.80	-	-
Sc	-	-	22.9	-	-	20.1	16.5	-	-
Cr	-	-	31	-	-	80	66	-	-
Co	-	-	46	-	-	33	16	-	-
Ba	-	-	750	-	-	800	900	-	-
Hf	-	-	4.8	-	-	10	12	-	-
Ta	-	-	1.1	-	-	2.3	2.1	-	-
Th	-	-	2.4	-	-	7.9	10.2	-	-
U	-	-	0.9	-	-	1.9	2.1	-	-

AB=alkali basalt; TB=trachybasalt; TA=trachyandesite; A=Fe-rich andesite; SiO_2*=SiO_2 when normalized volatile free and with molar Fe^{+3}/Fe^{+2}=0.15.

325

Table 11. Chemical analyses of precaldera trachytes and Kane Wash Tuff.

	Precaldera trachytes		Kane Wash Tuff					
			V1-B	V2-B	V2-B	V2-M	V2-TF	V3-M
Sample#	223	301	245	89	204	171	326	98
SiO_2*	63.3	69.6	75.5	76.5	76.3	76.5	67.3	76.3
A.I.	0.79	0.93	0.96	1.05	1.05	1.05	0.99	1.04
XRF major-element analyses								
SiO_2	63.8	67.3	71.8	73.1	74.4	76.3	65.3	75.7
Al_2O_3	15.4	14.2	12.1	11.1	11.2	11.3	14.2	11.1
ΣFe_2O_3	6.77	3.37	2.39	2.72	2.94	2.78	4.95	2.89
MgO	1.19	0.27	0.16	0.10	0.21	0.09	0.55	0.22
CaO	2.66	1.15	0.72	0.26	0.15	0.21	1.53	0.43
Na_2O	4.50	4.12	3.97	4.04	3.73	4.12	4.67	3.91
K_2O	4.44	5.66	4.69	4.29	4.70	4.91	5.55	4.70
TiO_2	1.31	0.39	0.23	0.17	0.15	0.15	0.48	0.19
P_2O_5	0.44	0.06	<.02	<.05	<.05	<.03	0.09	<.05
MnO	0.15	0.07	0.04	0.04	0.05	0.06	0.18	0.07
H_2O+	-	0.91	-	1.02	-	1.7	0.54	0.56
F	-	0.08	-	0.08	-	0.34	0.20	0.06
Cl	-	0.08	-	0.06	-	0.17	<.05	<.05
Sum	100.7	97.7	96.1	97.0	97.7	101.9	98.2	99.8
O=F,Cl	-	0.05	-	0.04	-	0.18	0.05	0.03
Total	-	97.6	-	97.0	-	101.7	98.1	99.8
XRF trace-element analyses (ppm)								
Rb	112	204	246	351	373	342	155	243
Sr	223	74	24	10	6	6	74	28
Zr	458	695	497	1110	1165	980	900	900
Y	44	60	72	148	124	152	55	80
Nb	35	53	70	137	146	130	41	67
Zn	-	99	-	218	237	203	164	188
Ga	-	24	-	28	30	30	25	21
Pb	-	27	-	50	38	44	32	40
INAA analyses (ppm)								
La	82	114	116	106	-	-	130	95
Ce	173	239	239	242	-	-	260	225
Nd	77	91	106	101	-	-	114	93
Sm	13	16	17	21	-	-	17	17
Eu	2.3	1.1	0.23	0.32	-	-	1.0	0.23
Tb	1.8	2.0	2.8	3.9	-	-	2.2	3.1
Yb	5.3	7.3	10.3	14.6	-	-	6.8	11.9
Lu	0.82	1.2	1.6	2.2	-	-	1.0	1.8
Sc	10.1	4.6	1.4	0.5	-	-	5.8	0.4
Cr	1.5	<10	1.0	<1	-	-	2.0	<1
Co	9.8	-	0.4	0.2	-	-	2.4	0.1
Ba	1165	365	70	55	-	-	442	<50
Hf	14.6	18.9	21.2	35.6	-	-	20.9	31.8
Ta	2.9	5.4	6.7	9.1	-	-	3.5	6.8
Th	12.7	24.0	30.5	44.1	-	-	15.7	31.2
U	3.1	6.6	8.1	11.3	-	-	3.6	8.1

A.I.=agpaitic index (Molar Na+K/Al). B=basal vitrophyre; M=middle; T=top; TF=trachyte flamme.

Table 14. Chemical analyses of trachytes, syenites, and alkali syenites of the central complex.

Sample#	1	274	328	292	330	298	396	273	339	270	345	297
SiO$_2$*	61.0	61.2	62.9	63.0	65.8	66.2	66.5	67.7	68.0	70.1	75.7	76.9
A.I.	0.78	0.79	0.80	0.78	0.86	0.87	0.88	0.86	0.82	0.93	1.00	0.99
XRF major-element analyses												
SiO$_2$	59.3	59.8	63.3	63.6	65.5	67.1	67.4	69.4	68.3	70.1	73.7	75.1
Al$_2$O$_3$	15.9	15.9	15.6	16.7	17.1	16.8	16.6	14.5	15.7	13.7	11.6	11.2
ΣFe$_2$O$_3$	6.57	6.39	6.26	6.40	4.90	4.45	4.70	3.97	4.28	3.88	2.88	2.83
MgO	1.73	1.59	0.52	0.68	0.36	0.23	0.25	0.26	0.12	0.24	0.15	0.13
CaO	3.60	3.62	2.33	2.23	1.25	0.69	0.57	1.36	1.41	0.67	0.35	0.14
Na$_2$O	4.36	4.50	4.67	4.62	4.86	4.79	4.94	4.31	4.26	4.28	3.93	3.68
K$_2$O	4.49	4.71	5.14	5.00	5.81	6.25	5.92	5.41	5.39	5.31	4.74	4.66
TiO$_2$	1.23	1.20	1.18	1.19	0.80	0.66	0.63	0.54	0.67	0.42	0.23	0.19
P$_2$O$_5$	0.44	0.42	0.40	0.39	0.24	0.16	0.14	0.16	0.15	0.08	<.05	<.05
MnO	0.15	0.14	0.11	0.09	0.10	0.10	0.15	0.19	0.06	0.11	0.06	0.04
H$_2$O+	0.91	0.58	-	-	-	-	-	-	-	-	0.28	0.45
Sum	98.8	98.9	100.5	100.9	100.9	101.0	101.3	100.1	100.3	99.5	97.9	98.6
XRF trace-element analyses (ppm)												
Rb	66	74	-	-	52	91	86	-	158	138	231	-
Sr	268	217	-	-	113	57	44	-	125	48	17	-
Zr	343	282	-	-	215	378	335	-	386	611	804	-
Y	42	37	-	-	23	42	33	-	46	64	91	-
Nb	26	25	-	-	19	34	28	-	33	62	80	-
Zn	96	-	-	-	-	91	-	-	-	82	-	-
Ga	24	-	-	-	-	27	-	-	-	28	-	-
Pb	16	-	-	-	-	45	-	-	-	23	-	-
INAA analyses (ppm)												
La	68	-	-	-	63	69	82	-	-	81	-	-
Ce	139	-	-	-	129	126	164	-	-	194	-	-
Nd	64	-	-	-	55	62	69	-	-	75	-	-
Sm	10.9	-	-	-	9.06	10.5	11.1	-	-	14.3	-	-
Eu	2.8	-	-	-	3.3	2.2	1.7	-	-	1.4	-	-
Tb	1.4	-	-	-	1.1	1.3	1.4	-	-	1.9	-	-
Yb	4.0	-	-	-	3.0	4.1	4.7	-	-	6.9	-	-
Lu	0.63	-	-	-	0.47	0.65	0.76	-	-	1.12	-	-
Sc	10.2	-	-	-	6.8	6.1	5.1	-	-	4.0	-	-
Cr	5.7	-	-	-	1.2	<1.7	<1.1	-	-	-	-	-
Co	9.1	-	-	-	1.7	0.8	0.7	-	-	0.8	-	-
Ba	1500	-	-	-	2230	890	660	-	-	-	-	-
Hf	9.4	-	-	-	6.7	10.0	11.7	-	-	17.3	-	-
Ta	1.9	-	-	-	1.3	2.1	2.4	-	-	4.5	-	-
Th	8.3	-	-	-	5.3	8.6	10.0	-	-	19.3	-	-
U	1.8	-	-	-	1.4	2.1	2.3	-	-	5.5	-	-

A.I.=agpaitic index.

Sample 1, F=0.08; sample 274, F=0.09.

Table 16. Chemical analyses of late moat rhyolites.

Sample#	347	352	355	284
SiO_2*	76.6	76.0	77.0	76.7
A.I.	0.84	0.91	0.92	0.90
XRF major-element analyses				
SiO_2	75.1	75.3	75.5	74.8
Al_2O_3	12.2	13.0	12.5	12.9
ΣFe_2O_3	1.36	0.94	0.93	0.87
MgO	0.24	0.18	0.04	0.12
CaO	0.78	0.44	0.44	0.42
Na_2O	2.59	3.59	3.85	3.84
K_2O	5.58	5.45	4.77	4.60
TiO_2	0.14	0.05	0.03	<.02
P_2O_5	0.03	0.01	<.01	<.05
MnO	0.03	0.04	0.03	0.03
Sum	98.1	99.0	98.1	100.5
XRF trace-element analyses (ppm)				
Rb	158	439	359	524
Sr	47	4	10	16
Zr	101	107	96	156
Y	22	123	92	109
Nb	14	72	58	89
INAA analyses (ppm)				
La	-	8.6	-	12
Ce	-	28	-	38
Nd	-	22	-	23
Sm	-	9.2	-	9.5
Eu	-	0.012	-	0.008
Tb	-	2.8	-	2.6
Yb	-	11.9	-	14.4
Lu	-	1.8	-	2.3
Sc	-	2.0	-	2.2
Co	-	0.04	-	0.02
Ba	-	15	-	25
Hf	-	7.9	-	10.8
Ta	-	6.4	-	8.3
Th	-	38.7	-	45.8
U	-	10.8	-	13.2

Sample 284: H_2O+=2.4, F=0.49, Cl=0.05

APPENDIX I

Scene data statistics for each
of the three study sites

IMAGE STATISTICS
FOR THE STONEWALL MOUNTAIN SUBSCENE (512x512)*

COVARIANCE MATRIX FOR CLUSTER 1

BANDS	1	2	3	4	5	6
1	281.98					
2	187.56	130.57				
3	281.88	197.20	306.89			
4	220.05	154.54	241.63	194.74		
5	404.28	286.89	447.76	363.63	812.86	
6	189.81	135.00	211.03	172.99	402.59	222.75

TOTAL NUMBER OF POINTS =   262144   ITERATION # 1
                                          CLUSTER 1

SYMBOL	POINTS IN CLUSTER
1	262144

MEANS

BAND 1	BAND 2	BAND 3	BAND 4	BAND 5	BAND 6
162.74	81.15	117.54	97.43	165.83	99.75

STANDARD DEVIATIONS

BAND 1	BAND 2	BAND 3	BAND 4	BAND 5	BAND 6
16.79	11.43	17.52	13.95	28.51	14.92

CORRELATION MATRIX (R)

BANDS	1	2	3	4	5	6
1	1.00	2				
2	.98	1.00				
3	.96	.98	1.00			
4	.94	.97	.98	1.00		
5	.84	.88	.89	.92	1.00	
6	.76	.79	.81	.83	.95	1.00

R = Covariance/(stand. dev. x)(stand. dev. y)

IMAGE STATISTICS
FOR THE BLACK MOUNTAIN SUBSCENE (512x512)*

COVARIANCE MATRIX FOR CLUSTER 1

BANDS	1	2	3	4	5	6
1	130.57					
2	79.23	51.37				
3	120.77	80.20	136.23			
4	88.18	61.04	109.05	100.12		
5	160.74	106.63	186.15	173.81	523.03	
6	112.54	73.97	123.71	107.46	353.06	260.27

TOTAL NUMBER OF POINTS = 262144   ITERATION # 1

CLUSTER 1

SYMBOL	POINTS IN CLUSTER
1	262144

MEANS

BAND 1	BAND 2	BAND 3	BAND 4	BAND 5	BAND 6
129.04	61.00	87.69	78.38	146.99	89.85

STANDARD DEVIATIONS

BAND 1	BAND 2	BAND 3	BAND 4	BAND 5	BAND 6
11.43	7.17	11.67	10.01	22.87	16.13

CORRELATION MATRIX

BANDS	1	2	3	4	5	6
1	1.00					
2	.97	1.00				
3	.90	.96	1.00			
4	.77	.85	.93	1.00		
5	.62	.65	.70	.76	1.00	
6	.61	.64	.65	.67	.96	1.00

*Statistics computed by IDIMS function ISOCLS

IMAGE STATISTICS
FOR THE KANE SPRINGS WASH SUBSCENE (512x512)*

COVARIANCE MATRIX FOR CLUSTER 1

BANDS	1	2	3	4	5	6
1	160.25					
2	97.40	62.26				
3	165.61	105.83	185.68			
4	96.22	65.26	111.88	100.99		
5	238.10	157.85	279.01	197.79	564.53	
6	159.22	103.68	183.28	116.92	354.47	237.11

TOTAL NUMBER OF POINTS = 262144   ITERATION # 1
                                     CLUSTER 1

SYMBOL   POINTS IN CLUSTER
  1   262144

MEANS

BAND 1	BAND 2	BAND 3	BAND 4	BAND 5	BAND 6
124.34	57.39	80.62	71.66	125.67	71.78

STANDARD DEVIATIONS

BAND 1	BAND 2	BAND 3	BAND 4	BAND 5	BAND 6
12.66	7.89	13.63	10.05	23.76	15.40

CORRELATION MATRIX

BANDS	1	2	3	4	5	6
1	1.00					
2	.96	1.00				
3	.96	.98	1.00			
4	.76	.82	.82	1.00		
5	.79	.84	.86	.83	1.00	
6	.82	.85	.87	.76	.97	1.00

*Statistics computed by IDIMS function ISOCLS

PRINCIPAL COMPONENTS STATISTICS

STONEWALL MOUNTAIN AREA

I	EIGENVALUE (I)
1	1797.656250
2	118.011215
3	17.116089
4	12.925664
5	2.660455
6	1.412745

TRANSFORMATION MATRIX (EIGENVECTORS)

0.368303	0.257569	0.398771	0.319566	0.657626	0.323108
-0.506020	-0.285845	-0.380288	-0.223752	0.512003	0.453217
0.518041	0.058601	-0.241535	-0.287526	-0.359411	0.676766
0.488046	0.004007	-0.404738	-0.436638	0.419167	-0.481278
0.277976	-0.571174	-0.382229	0.670561	-0.014871	-0.022747
-0.156429	0.722676	-0.572811	0.353322	-0.016803	-0.006083

BLACK MOUNTAIN CALDERA

I	EIGENVALUE (I)
1	1005.116760
2	151.754028
3	31.079649
4	10.118806
5	2.476775
6	1.044413

TRANSFORMATION MATRIX (EIGENVECTORS)

0.276864	0.181794	0.307719	0.268180	0.701000	0.481959
0.529437	0.329714	0.498072	0.303647	-0.404013	-0.327843
-0.531388	-0.157900	0.179655	0.634960	0.237252	-0.448281
-0.436464	0.030353	0.352061	0.178230	-0.496493	0.637464
-0.269929	0.041677	0.661288	-0.632469	0.198914	-0.220261
-0.311942	0.911400	-0.252405	-0.030350	0.054876	-0.066354

KANE SPRINGS WASH

I	EIGENVALUE (I)
1	1185.295044
2	81.124763
3	32.253185
4	6.022783
5	5.215764
6	0.892326

TRANSFORMATION MATRIX (EIGENVECTORS)

0.328391	0.213222	0.373145	0.250498	0.675531	0.434013
0.595729	0.305867	0.464812	0.085820	-0.519128	-0.242165
-0.191788	-0.002714	-0.058222	0.883454	0.067267	-0.418096
-0.300434	0.010174	0.124051	0.325236	-0.512271	0.725291
0.596664	-0.057100	-0.737487	0.194919	-0.083320	0.227836
-0.232841	0.926073	-0.286440	-0.074986	0.016611	-0.015090

Statistics computed with IDIMS function KLTRANS

APPENDIX J

Lithologic class statistics for
supervised image classification

MULTISPECTRAL CHARACTERISTICS FOR TRAINING CLASS ALLUVIUM
DETERMINANT = 0.27414330E+09
CONSTANT TERM = -15.2282
MEANS = 121.76   127.55   138.54   137.64   136.82   165.71
INVERSE COVARIANCE MATRIX
```
      0.04
     -0.01    0.07
      0.00   -0.02    0.08
     -0.02   -0.03   -0.05    0.10
     -0.01    0.00    0.00   -0.01    0.06
      0.00    0.00    0.00    0.00   -0.02    0.03
```

MULTISPECTRAL CHARACTERISTICS FOR TRAINING CLASS ALLUVIUM 2
DETERMINANT = 0.29319542E+10
CONSTANT TERM = -16.4131
MEANS = 92.06   89.50   93.47   100.58   98.78   109.68
INVERSE COVARIANCE MATRIX
```
      0.04
     -0.03    0.07
     -0.02   -0.02    0.08
      0.01   -0.01   -0.05    0.07
     -0.01    0.00    0.02   -0.03    0.05
      0.00    0.00    0.00    0.00   -0.02    0.04
```

MULTISPECTRAL CHARACTERISTICS FOR TRAINING CLASS ALLUVIUM 3
DETERMINANT = 0.17139729E+10
CONSTANT TERM = -16.1447
MEANS = 167.83   166.40   171.43   173.82   183.50   173.43
INVERSE COVARIANCE MATRIX
```
      0.03
     -0.01    0.05
     -0.01   -0.02    0.07
      0.00   -0.01   -0.04    0.07
      0.00    0.00    0.00   -0.03    0.06
      0.00    0.01   -0.01    0.00   -0.02    0.03
```

MULTISPECTRAL CHARACTERISTICS FOR TRAINING CLASS ALLUVIUM 4
DETERMINANT = 0.56491412E+10
CONSTANT TERM = -16.7410
MEANS = 170.55   179.95   188.29   189.48   204.61   222.26
INVERSE COVARIANCE MATRIX
```
      0.03
     -0.01    0.05
     -0.01   -0.02    0.06
      0.00   -0.01   -0.03    0.06
      0.00    0.00    0.00   -0.02    0.06
      0.00    0.00   -0.01    0.01   -0.02    0.03
```

STONEWALL MOUNTAIN SITE
MAXIMUM LIKELIHOOD STATISTICS GENERATED USING STATFILE: SWSTAT TRAINING CLASS STATISTICS

MULTISPECTRAL CHARACTERISTICS FOR TRAINING CLASS BASALT
DETERMINANT = 0.29841322E+08
CONSTANT TERM = -14.1193
MEANS = 13.37   11.59   8.55   6.76   6.37   4.70
INVERSE COVARIANCE MATRIX
```
      0.06
     -0.06    0.14
     -0.02   -0.11    0.33
      0.01    0.04   -0.21    0.24
      0.00   -0.02   -0.02   -0.02    0.19
      0.01   -0.01    0.04   -0.06   -0.13    0.17
```

MULTISPECTRAL CHARACTERISTICS FOR TRAINING CLASS CIVET CAT CANYON TUFF CAP ROCK
DETERMINANT = 0.35306072E+08
CONSTANT TERM = -14.2034
MEANS = 44.77   5=47.73   53.98   76.33   181.69   214.52
INVERSE COVARIANCE MATRIX
```
      0.05
     -0.03    0.10
     -0.01   -0.06    0.16
     -0.02    0.01   -0.12    0.17
      0.01   -0.02    0.03   -0.04    0.09
      0.00    0 01   -0.02    0.01   -0.05    0.07
```

MULTISPECTRAL CHARACTERISTICS FOR TRAINING CLASS CIVET CAT CANYON TUFF CAP ROCK 2
DETERMINANT = 0.15651370E+09
COSTANT TERM = -14.9480
MEANS = 67.16   61.68   56.68   73.84   157.00   207.52
INVERSE COVARIANCE MATRIX
```
      0.07
      0.00    0.07
     -0.02   -0.01    0.11
     -0.02   -0.06   -0.06    0.14
      0.00    0.02    0.01   -0.04    0.04
     -0.01   -0.02   -0.01    0.04   -0.02    0.04
```

MULTISPECTRAL CHARACTERISTICS FOR TRAINING CLASS CIVET CAT CANYON TUFF
DETERMINANT = 0.37945651E+09
CONSTANT TERM = -15.3908
MEANS = 26.95   17.85   12.94   10.14   9.67   18.65
INVERSE COVARIANCE MATRIX
```
      0.03
     -0.01    0.10
     -0.02   -0.05    0.11
      0.00   -0.03   -0.04    0.11
      0.01    0.01    0.00   -0.05    0.08
     -0.01   -0.01    0.00    0.01   -0.04    0.03
```

STONEWALL MOUNTAIN SITE
MAXIMUM LIKELIHOOD STATISTICS GENERATED USING STATFILE: SWSTAT TRAINING CLASS STATISTICS

MULTISPECTRAL CHARACTERISTICS FOR TRAINING CLASS ANTELOPE SPRINGS LATITE
DETERMINANT = 0.11579347E+12
CONSTANT TERM = -18.2512
MEANS = 142.08   136.54   124.43   114.20   81.05   91.47
INVERSE COVARIANCE MATRIX
```
  0.01
 -0.01   0.04
  0.00  -0.03   0.05
 -0.01   0.00  -0.02   0.04
  0.00   0.00   0.01  -0.01   0.04
  0.00   0.00   0.00   0.00  -0.03   0.03
```

MULTISPECTRAL CHARACTERISTICS FOR TRAINING CLASS QUARTZITE CONGLOMERATE
DETERMINANT = 0.66484742E+09
CONSTANT TERM = -15.6712
MEANS = 18.65   20.84   26.16   30.25   19.64   23.16
INVERSE COVARIANCE MATRIX
```
  0.04
 -0.04   0.09
 -0.01  -0.02   0.08
  0.01  -0.02  -0.04   0.07
 -0.01   0.02   0.00  -0.03   0.09
  0.00   0.00  -0.01  -0.01  -0.04   0.05
```

MULTISPECTRAL CHARACTERISTICS FOR TRAINING CLASS ANTELOPE SPRINGS RHYOLITE
DETERMINANT = 0.13391469E+13
CONSTANT TERM = -19.4752
MEANS = 192.41   199.63   204.09   201.99   220.31   209.78
INVERSE COVARIANCE MATRIX
```
  0.01
 -0.01   0.03
 -0.01  -0.01   0.05
  0.00  -0.01  -0.03   0.05
  0.00   0.00   0.00  -0.01   0.02
  0.00   0.00   0.00   0.00  -0.01   0.01
```

MULTISPECTRAL CHARACTERISTICS FOR TRAINING CLASS HYDROTHERMALLY ALTERED RHYOLITE
DETERMINANT = 0.45164626E+11
CONSTANT TERM = -17.7804
MEANS = 121.22   141.26   147.09   151.80   198.59   168.41
INVERSE COVARIANCE MATRIX
```
  0.01
 -0.01   0.07
  0.00  -0.03   0.08
  0.00  -0.02  -0.03   0.06
  0.00   0.00  -0.01   0.00   0.01
  0.00   0.00   0.00  -0.01  -0.01   0.02
```

MULTISPECTRAL CHARACTERISTICS FOR TRAINING CLASS SPEARHEAD TUFF
DETERMINANT = 0.94269430E+10
CONSTANT TERM = -16.9970
MEANS = 86.02   73.88   64.59   64.61   87.55   118.15
INVERSE COVARIANCE MATRIX
```
  0.03
 -0.01   0.06
 -0.01  -0.03   0.10
 -0.01  -0.01  -0.06   0.08
  0.01   0.00   0.00  -0.03   0.05
  0.00   0.00   0.00   0.02  -0.03   0.02
```

BLACK MOUNTAIN CALDERA
MAXIMUM LIKELIHOOD STATISTICS GENERATED USING STATFILE: BMSTAT TRAINING CLASS STATISTICS

MULTISPECTRAL CHARACTERISTICS FOR TRAINING CLASS ALLUVIUM
DETERMINANT = 0.19168639E+05
CONSTANT TERM = -10.4441
MEANS = 136.50   67.31   101.09   89.92   156.79   97.14
INVERSE COVARIANCE MATRIX
```
      0.27
     -0.27    1.07
     -0.05   -0.26    0.50
      0.04   -0.05   -0.37    0.43
     -0.02   -0.08    0.04   -0.06    0.19
      0.02    0.06   -0.07    0.08   -0.14    0.19
```

MULTISPECTRAL CHARACTERISTICS FOR TRAINING CLASS GOLD FLAT TUFF
DETERMINANT = 0.40926318E+04
CONSTANT TERM = -9.6721
MEANS = 138.05   65.24   91.19   79.50   180.65   120.10
INVERSE COVARIANCE MATRIX
```
      0.27
     -0.26    1.14
     -0.11   -0.21    0.72
      0.05   -0.24   -0.56    0.85
      0.01    0.02   -0.01   -0.09    0.15
     -0.02   -0.06   -0.03    0.08   -0.12    0.29
```

MULTISPECTRAL CHARACTERISTICS FOR TRAINING CLASS LABYRINTH CANYON TUFF
DETERMINANT = 0.27733371E+05
CONSTANT TERM = -10.6288
MEANS = 132.30   63.57   96.65   91.21   191.06   114.96
INVERSE COVARIANCE MATRIX
```
      0.46
     -0.47    1.17
     -0.18   -0.30    0.76
      0.04    0.01   -0.31    0.27
      0.01    0.06   -0.02   -0.05    0.12
     -0.03   -0.10   -0.05    0.07   -0.13    0.24
```

MULTISPECTRAL CHARACTERISTICS FOR TRAINING CLASS BASEMENT LAVAS
DETERMINANT = 0.80552481E+06
CONSTANT TERM = -12.3133
MEANS = 150.10   73.41   106.04   91.90   168.05   104.31
INVERSE COVARIANCE MATRIX
```
      0.18
     -0.22    0.95
     -0.04   -0.28    0.43
      0.01   -0.10   -0.25    0.44
      0.01    0.02    0.02   -0.07    0.05
     -0.03   -0.06   -0.03    0.07   -0.06    0.12
```

MULTISPECTRAL CHARACTERISTICS FOR TRAINING CLASS PILLAR SPRINGS LAVA
DETERMINANT = 0.20427334E+06
CONSTANT TERM = -11.6272
MEANS = 118.81   53.09   72.42   64.25   119.01   72.46
INVERSE COVARIANCE MATRIX
```
      0.21
     -0.24    1.06
     -0.08   -0.30    0.45
      0.04   -0.19   -0.15    0.39
     -0.04    0.03    0.04   -0.09    0.08
      0.04   -0.03   -0.09    0.07   -0.08    0.14
```

BLACK MOUNTAIN CALDERA
MAXIMUM LIKELIHOOD STATISTICS GENERATED USING STATFILE: BMSTAT TRAINING CLASS

MULTISPECTRAL CHARACTERISTICS FOR TRAINING CLASS PILLAR SPRINGS LAVA 2
DETERMINANT = 0.12400005E+05
CONSTANT TERM = -10.2264
MEANS = 117.28   53.49   74.76   71.22   133.13   78.33
INVERSE COVARIANCE MATRIX
```
 0.29
-0.28    1.08
-0.09   -0.29    0.40
 0.04   -0.16   -0.06    0.56
-0.01    0.03    0.06   -0.16    0.16
 0.00   -0.03   -0.14    0.04   -0.17    0.34
```

MULTISPECTRAL CHARACTERISTICS FOR TRAINING CLASS RIBBON CLIFF LAVA
DETERMINANT = 0.64728887E+05
CONSTANT TERM = -11.0526
INVERSE COVARIANCE MATRIX
```
 0.24
-0.22    1.16
-0.09   -0.46    0.52
 0.00   -0.03   -0.15    0.43
 0.00   -0.04    0.06   -0.15    0.14
-0.01    0.04   -0.10    0.06   -0.12    0.24
```

MULTISPECTRAL CHARACTERISTICS FOR TRAINING CLASS TRACHYTE OF HIDDEN CLIFF
DETERMINANT = 0.20943572E+04
CONSTANT TERM = -9.3371
MEANS = 122.72   55.17   74.74   61.77   106.84   65.69
INVERSE COVARIANCE MATRIX
```
 0.03
-0.26    0.98
-0.20   -0.14    0.65
 0.12   -0.25   -0.32    0.85
-0.03   -0.02    0.05   -0.14    0.12
 0.05    0.06   -0.15   -0.07   -0.12    0.41
```

MULTISPECTRAL CHARACTERISTICS FOR TRAINING CLASS LAVAS OF YELLOW CLEFT
DETERMINANT = 0.26728738E+06
CONSTANT TERM = -11.7617
MEANS = 125.04   59.46   87.11   82.20   147.54   85.09
INVERSE COVARIANCE MATRIX
```
 0.20
-0.34    1.28
-0.01   -0.47    0.44
 0.06   -0.09   -0.06    0.13
-0.04    0.10    0.00   -0.05    0.10
 0.08   -0.10   -0.11    0.04   -0.12    0.24
```

KANE SPRINGS WASH VOLCANIC CENTER
MAXIMUM LIKELIHOOD STATISTICS GENERATED USING STATFILE: KSSTAT TRAINING CLASS STATISTICS

MULTISPECTRAL CHARACTERISTICS FOR TRAINING CLASS ALLUVIUM

DETERMINANT = 0.73323921E+04
CONSTANT TERM =   -9.9637
MEANS = 134.69   64.08   93.70   77.63   155.02   92.74
INVERSE COVARIANCE MATRIX

```
  0.19
 -0.21    1.27
 -0.04   -0.39    0.62
 -0.01   -0.25   -0.41    0.83
  0.03    0.03    0.03   -0.07    0.16
  0.01   -0.01   -0.05   -0.03   -0.19    0.37
```

MULTISPECTRAL CHARACTERISTICS FOR TRAINING CLASS ALLUVIUM 2

DETERMINANT = 0.48772394E+03
CONSTANT TERM =   -8.6085
MEANS = 133.10   60.42   84.65   66.84   118.16   70.16
INVERSE COVARIANCE MATRIX

```
  0.33
 -0.17    1.30
 -0.15   -0.30    0.72
 -0.06   -0.27   -0.36    1.23
  0.01    0.04   -0.01   -0.28    0.22
 -0.03   -0.11   -0.12    0.02   -0.09    0.42
```

MULTISPECTRAL CHARACTERISTICS FOR TRAINING CLASS BASALT

DETERMINANT = 0.40190681E+04
CONSTANT TERM =   -9.6630
MEANS = 103.04   46.64   61.40   63.61   91.85   51.44
INVERSE COVARIANCE MATRIX

```
  0.34
 -0.19    1.37
 -0.18   -0.30    0.50
  0.09   -0.29   -0.12    0.48
 -0.04   -0.01    0.01   -0.06    0.20
  0.05   -0.01   -0.13    0.04   -0.23    0.38
```

MULTISPECTRAL CHARACTERISTICS FOR TRAINING CLASS TOPAZ RHYOLITE

DETERMINANT = 0.25917345E+07
CONSTANT TERM = -12.8976
MEANS = 132.99   63.80   91.92   82.08   152.23   87.76
INVERSE COVARIANCE MATRIX

```
  0.17
 -0.26    1.03
 -0.02   -0.30    0.38
 -0.01   -0.16   -0.14    0.36
  0.02    0.05   -0.01   -0.06    0.06
  0.00   -0.03   -0.05    0.04   -0.07    0.15
```

MULTISPECTRAL CHARACTERISTICS FOR TRAINING CLASS AIRFALL TUFF

DETERMINANT = 0.17174088E+06
CONSTANT TERM = -11.5405
MEANS = 177.96   94.00   142.54   116.58   217.42   130.15
INVERSE COVARIANCE MATRIX

```
  0.27
 -0.30    2.40
 -0.03   -0.48    0.49
  0.06   -1.10   -0.19    1.22
  0.01   -0.01    0.00    0.00    0.02
 -0.05    0.21   -0.01   -0.16   -0.02    0.10
```

KANE SPRINGS WASH VOLCANIC CENTER
MAXIMUM LIKELIHOOD STATISTICS GENERATED USING STATFILE: DSSTAT TRAINING CLASS STATISTICS

MULTISPECTRAL CHARACTERISTICS FOR TRAINING CLASS HIKO TUFF
DETERMINANT = 0.93255602E+05
CONSTANT TERM = -11.2352
MEANS = 142.42   69.12   101.11   87.09   167.36   96.38
INVERSE COVARIANCE MATRIX

```
 0.18
-0.18    0.94
-0.06   -0.21    0.43
-0.02   -0.25   -0.27    0.69
-0.01    0.04    0.00   -0.08    0.11
 0.05   -0.04   -0.06    0.02   -0.13    0.26
```

MULTISPECTRAL CHARACTERISTICS FOR TRAINING CLASS KANE WASH TUFF Q & W MEMBERS
DETERMINANT = 0.27231275E+05
CONSTANT TERM = -10.6197
MEANS = 131.14   61.62   89.55   78.90   134.24   78.58
INVERSE COVARIANCE MATRIX

```
 0.29
-0.28    1.07
-0.08   -0.19    0.48
 0.04   -0.23   -0.35    0.65
-0.04    0.00    0.05   -0.05    0.08
 0.02    0.03   -0.07   -0.03   -0.12    0.34
```

MULTISPECTRAL CHARACTERISTICS FOR TRAINING CLASS SYENITE COMPLEX
DETERMINANT = 0.43274295E+07
CONSTANT TERM = -13.1539
MEANS = 118.64   53.81   73.46   71.24   119.50   65.84
INVERSE COVARIANCE MATRIX

```
 0.20
-0.25    0.97
-0.04   -0.29    0.28
 0.02   -0.13   -0.02    0.14
-0.02    0.05    0.01   -0.08    0.09
 0.02   -0.05   -0.07    0.09   -0.12    0.20
```

MULTISPECTRAL CHARACTERISTICS FOR TRAINING CLASS TRACHYANDESITE
DETERMINANT = 0.92584875E+05
CONSTANT TERM = -11.2316
MEANS = 113.44   51.64   71.71   67.01   113.09   59.26
INVERSE COVARIANCE MATRIX

```
 0.29
-0.13    1.30
-0.13   -0.54    0.52
-0.01   -0.04   -0.17    0.41
 0.00    0.04    0.07   -0.11    0.10
-0.03   -0.07   -0.11    0.09   -0.16    0.38
```

MULTISPECTRAL CHARACTERISTICS FOR TRAINING CLASS KANE WASH TUFF V MEMBERS
DETERMINANT = 0.91330488E+04
CONSTANT TERM = -10.0735
MEANS = 137.39   68.56   102.50   87.87   180.52   109.59
INVERSE COVARIANCE MATRIX

```
 0.27
-0.29    1.23
-0.04   -0.26    0.66
-0.05   -0.29   -0.44    1.00
 0.02    0.08   -0.03   -0.12    0.12
 0.02   -0.08   -0.07   -0.02   -0.10    0.28
```

APPENDIX K

Statistic of training site data (pixel groups)
over the major volcanic formations
at the three study sites

STONEWALL MOUNTAIN AREA

UNITS	NL	NS	BND	MINIMUM			MAXIMUM			MEAN	VARIANCE
				LINE	SAMP	VALUE	LINE	SAMP	VALUE		
Civet Cat Canyon Cap Rock	5	5	1	1	1	1.3300E+02	4	5	1.4400E+02	1.3720E+02	9.9202E+00
	5	5	2	1	1	6.1000E+01	5	5	7.1000E+01	6.5760E+01	4.7424E+00
	5	5	3	1	2	9.2000E+01	5	5	1.0300E+02	9.5880E+01	8.5059E+00
	5	5	4	4	1	8.3000E+01	4	5	9.0000E+01	8.5800E+01	3.9201E+00
	5	5	5	3	4	1.9700E+02	1	1	2.1000E+02	2.0188E+02	8.4250E+00
	5	5	6	4	4	1.2300E+02	1	1	1.3000E+02	1.2520E+02	2.1604E+00
Civet Cat Canyon Tuff	5	5	1	5	1	1.1900E+02	4	4	1.4400E+02	1.3484E+02	3.0614E+01
	5	5	2	5	1	5.5000E+01	4	4	6.7000E+01	6.1600E+01	8.0800E+00
	5	5	3	5	1	7.3000E+01	4	5	9.2000E+01	8.4640E+01	2.0950E+01
	5	5	4	4	2	6.5000E+01	1	1	7.6000E+01	7.0000E+01	8.8000E+00
	5	5	5	1	4	9.9000E+01	2	1	1.1600E+02	1.0572E+02	2.1962E+01
	5	5	6	1	4	6.1000E+01	1	2	7.2000E+01	6.5920E+01	8.7137E+00
Spearhead Tuff	10	10	1	2	10	1.4400E+02	9	10	1.6800E+02	1.5611E+02	2.7878E+01
	10	10	2	1	10	6.7000E+01	8	10	8.3000E+01	7.4220E+01	1.3332E+01
	10	10	3	1	10	9.3000E+01	9	10	1.1900E+02	1.0346E+02	3.3389E+01
	10	10	4	1	7	7.6000E+01	9	10	9.9000E+01	8.4920E+01	2.4074E+01
	10	10	5	1	7	1.3200E+02	3	1	1.7000E+02	1.5360E+02	1.0684E+02
	10	10	6	1	7	8.4000E+01	3	1	1.0800E+02	9.8610E+01	4.2598E+01
Basalt	5	5	1	2	1	1.0700E+02	4	1	1.2300E+02	1.1528E+02	2.1802E+01
	5	5	2	2	1	4.3000E+01	1	5	5.4000E+01	4.8640E+01	8.6304E+00
	5	5	3	1	3	5.4000E+01	5	3	7.0000E+01	6.3200E+01	1.9440E+01
	5	5	4	1	3	4.1000E+01	1	5	5.3000E+01	4.8880E+01	8.4255E+00
	5	5	5	2	2	6.7000E+01	5	5	1.0300E+02	7.8200E+01	5.9680E+01
	5	5	6	4	1	3.6000E+01	5	5	6.1000E+01	4.4280E+01	3.1642E+01
Antelope Springs Rhyolite	5	5	1	1	1	1.6300E+02	4	2	1.8900E+02	1.8164E+02	3.7431E+01
	5	5	2	1	1	8.5000E+01	1	5	1.0300E+02	9.7880E+01	1.8666E+01
	5	5	3	1	1	1.2900E+02	2	5	1.6300E+02	1.4956E+02	5.4167E+01
	5	5	4	1	1	1.1100E+02	1	5	1.3500E+02	1.2796E+02	3.2598E+01
	5	5	5	1	1	2.0700E+02	5	3	2.5000E+02	2.3664E+02	1.0735E+02
	5	5	6	1	1	1.2600E+02	1	5	1.5900E+02	1.4828E+02	6.2602E+01
Antelope Springs Latite	5	5	1	2	1	1.4900E+02	4	5	1.7000E+02	1.5936E+02	2.4711E+01
	5	5	2	3	1	7.0000E+01	4	5	8.2000E+01	7.5960E+01	7.3984E+00
	5	5	3	3	1	1.0100E+02	1	2	1.1900E+02	1.1072E+02	1.9482E+01
	5	5	4	2	1	8.4000E+01	1	2	1.0000E+02	9.2080E+01	1.7433E+01
	5	5	5	3	1	1.1200E+02	1	2	1.4000E+02	1.2544E+02	5.5766E+01
	5	5	6	2	1	6.5000E+01	1	2	8.0000E+01	7.1640E+01	1.6070E+01
Quartzite Conglomerate	10	10	1	1	5	1.2700E+02	4	4	1.4100E+02	1.3358E+02	1.2484E+01
	10	10	2	3	9	5.8000E+01	5	4	6.8000E+01	6.2400E+01	5.6600E+00
	10	10	3	2	10	8.3000E+01	4	5	1.0000E+02	9.0850E+01	1.5908E+01
	10	10	4	2	10	6.7000E+01	5	4	8.4000E+01	7.5960E+01	1.3337E+01
	10	10	5	2	10	1.0100E+02	8	9	1.2900E+02	1.1439E+02	3.1658E+01
	10	10	6	3	10	6.1000E+01	8	9	8.0000E+01	7.0140E+01	1.3940E+01

BLACK MOUNTAIN CALDERA

UNITS	NL	NS	BND	MINIMUM			MAXIMUM			MEAN	VARIANCE
				LINE	SAMP	VALUE	LINE	SAMP	VALUE		
Labyrinth Canyon Tuff	5	5	1	5	3	1.2600E+02	3	2	1.3800E+02	1.3300E+02	9.2805E+00
	5	5	2	5	1	6.0000E+91	3	2	6.7000E+01	6.4120E+01	3.9457E+00
	5	5	3	5	1	9.3000E+01	4	4	1.0300E+02	9.7720E+01	7.2414E+00
	5	5	4	1	3	8.8000E+01	4	2	9.9000E+01	9.2680E+01	8.1376E+00
	5	5	5	1	4	1.7900E+02	4	4	1.9600E+02	1.8784E+02	1.8934E+01
	5	5	6	1	4	1.0600E+02	3	3	1.1900E+02	1.1288E+02	1.0826E+01
Gold Flat Tuff	10	10	1	9	3	1.3100E+02	8	8	1.5400E+02	1.4088E+02	2.0446E+01
	10	10	2	10	2	6.2000E+01	8	8	7.5000E+01	6.7960E+01	8.6784E+00
	10	10	3	10	2	8.8000E+01	7	7	1.1100E+02	9.7110E+01	2.7598E+01
	10	10	4	8	4	7.7000E+01	8	8	9.5000E+01	8.4730E+01	1.8097E+01
	10	10	5	8	3	1.7400E+02	6	7	1.9300E+02	1.8342E+02	2.4823E+01
	10	10	6	10	1	1.1300E+02	7	9	1.2500E+02	1.1898E+02	6.4196E+00
Trachyte of Hidden Cliff	10	10	1	1	1	1.1800E+02	9	10	1.3200E+02	1.2440E+02	7.3802E+00
	10	10	2	1	1	5.4000E+01	8	10	6.3000E+01	5.7840E+01	2.6344E+00
	10	10	3	5	2	7.9000E+01	9	10	9.2000E+01	8.4450E+01	5.8075E+00
	10	10	4	1	1	7.3000E+01	9	10	8.5000E+01	7.7110E+01	4.2781E+00
	10	10	5	6	9	1.4600E+02	9	8	1.6600E+02	1.5479E+02	1.6686E+01
	10	10	6	1	1	8.2000E+01	10	9	9.7000E+01	8.9140E+01	8.5204E+00
Pillar Springs Lava	5	5	1	5	2	9.7000E+01	2	2	1.1500E+02	1.0840E+02	2.2000E+01
	5	5	2	5	2	4.0000E+01	1	3	5.2000E+01	4.8720E+01	8.2816E+00
	5	5	3	5	2	5.4000E+01	2	4	7.1000E+01	6.3800E+01	1.8400E+01
	5	5	4	5	2	4.9000E+01	2	5	6.9000E+01	6.1640E+01	3.1110E+01
	5	5	5	5	2	9.0000E+01	3	1	1.2500E+02	1.1000E+02	6.2560E+01
	5	5	6	5	2	5.2000E+01	3	1	7.2000E+01	6.1880E+01	1.9786E+01
Trail Ridge Tuff	5	5	1	2	2	1.1900E+02	1	4	1.2400E+02	1.2208E+02	1.8338E+00
	5	5	2	4	5	5.3000E+01	1	5	5.7000E+01	5.4960E+01	9.9840E-01
	5	5	3	3	5	7.3000E+01	1	5	7.7000E+01	7.5000E+01	8.8018E-01
	5	5	4	1	2	6.2000E+01	4	1	6.4000E+01	6.2640E+01	3.1043E-01
	5	5	5	1	3	1.0700E+02	4	1	1.1700E+02	1.1172E+02	7.6420E+00
	5	5	6	4	4	6.6000E+01	5	2	7.3000E+01	6.8840E+01	4.2945E+00
Older Thirsty Canyon Tuffs	3	3	1	2	3	1.3300E+02	1	1	1.4000E+02	1.3680E+02	7.4321E+00
	3	3	2	3	1	6.1000E+01	1	1	6.6000E+01	6.3889E+01	2.7655E+00
	3	3	3	3	1	8.9000E+01	1	1	9.8000E+01	9.1889E+01	7.4323E+00
	3	3	4	2	3	7.7000E+01	1	1	8.4000E+01	8.0000E+01	5.5557E+00
	3	3	5	2	3	1.5100E+02	1	1	1.6600E+02	1.5900E+02	1.9334E+01
	3	3	6	3	1	9.6000E+01	1	1	1.0400E+02	9.9222E+01	5.7286E+00
Basement Volcanics	10	10	1	4	3	1.3400E+02	4	10	1.5900E+02	1.4418E+02	2.5868E+01
	10	10	2	5	2	6.1000E+01	4	10	8.0000E+01	6.9710E+01	1.1326E+01
	10	10	3	1	2	9.0000E+01	3	10	1.1400E+02	1.0087E+02	2.5873E+01
	10	10	4	1	8	8.3000E+01	4	10	9.8000E+01	8.9810E+01	1.0514E+01
	10	10	5	6	2	1.5500E+02	4	10	1.9500E+02	1.7273E+02	7.8937E+01
	10	10	6	1	2	9.2000E+01	3	10	1.2300E+02	1.0425E+02	4.8588E+01
Lava of Yellow Cleft	10	10	1	2	4	1.1700E+02	4	1	1.3600E+02	1.2344E+02	1.1886E+01
	10	10	2	1	9	5.5000E+01	4	1	6.7000E+01	5.8440E+01	4.7664E+00
	10	10	3	6	1	7.9000E+01	4	1	1.0000E+02	8.5670E+01	1.1281E+01
	10	10	4	4	8	7.4000E+01	5	1	8.8000E+01	8.0560E+01	6.9065E+00
	10	10	5	1	6	1.3400E+02	8	5	1.6200E+02	1.4641E+02	3.5262E+01
	10	10	6	1	6	7.7000E+01	5	7	9.3000E+01	8.4480E+01	1.1950E+01
Ribbon Cliff Lava	10	10	1	1	1	1.2300E+02	8	3	1.3700E+02	1.3002E+02	7.0999E+00
	10	10	2	1	1	5.7000E+01	3	4	6.4000E+01	5.9830E+01	2.0212E+00
	10	10	3	1	2	7.8000E+01	5	4	9.0000E+01	8.4090E+01	5.8819E+00
	10	10	4	7	10	6.6000E+01	3	3	7.4000E+01	7.0270E+01	3.6572E+00
	10	10	5	1	10	1.0700E+02	4	3	1.3000E+02	1.1999E+02	2.8410E+01
	10	10	6	1	7	6.6000E+01	5	1	7.9000E+01	7.2230E+01	1.0217E+01

KANE SPRINGS WASH VOLCANIC CENTER

UNITS	NL	NS	BND	MINIMUM			MAXIMUM			MEAN	VARIANCE
				LINE	SAMP	VALUE	LINE	SAMP	VALUE		
Topaz Rhyolite	5	5	1	1	5	1.3800E+02	5	2	1.6500E+02	1.5160E+02	6.0400E+01
	5	5	2	1	5	6.8000E+01	5	2	8.5000E+01	7.5640E+01	2.0790E+01
	5	5	3	1	5	1.0000E+02	5	3	1.2600E+02	1.1116E+02	3.8934E+01
	5	5	4	1	5	8.6000E+01	5	3	1.0600E+02	9.5680E+01	2.1418E+01
	5	5	5	1	5	1.6300E+02	5	3	1.9600E+02	1.8008E+02	5.7914E+01
	5	5	6	1	4	9.8000E+01	5	1	1.1800E+02	1.0824E+02	3.6742E+01
Basalt	5	5	1	3	5	9.8000E+01	2	3	1.0600E+02	1.0272E+02	3.7215E+00
	5	5	2	2	5	4.5000E+01	2	1	4.7000E+01	4.6280E+01	4.4163E-00
	5	5	3	5	3	5.7000E+01	3	3	6.2000E+01	5.9560E+01	1.6866E+00
	5	5	4	5	2	6.1000E+01	1	1	6.4000E+01	6.2960E+01	8.3850E-01
	5	5	5	1	4	8.3000E+01	2	4	8.7000E+01	8.5480E+01	1.4496E+00
	5	5	6	1	1	4.4000E+01	1	4	5.0000E+01	4.6400E+01	2.4800E+00
Hiko Tuff	10	10	1	7	10	1.3200E+02	2	10	1.6200E+02	1.4435E+02	4.9048E+01
	10	10	2	7	10	6.2000E+01	1	10	8.2000E+01	7.0680E+01	2.0238E+01
	10	10	3	7	10	9.2000E+01	2	9	1.2100E+02	1.0410E+02	4.6430E+01
	10	10	4	7	10	7.9000E+01	2	9	1.0100E+02	8.9480E+01	2.8190E+01
	10	10	5	6	5	1.5500E+02	2	9	1.9200E+02	1.7233E+02	7.5242E+01
	10	10	6	6	6	8.9000E+01	2	9	1.1000E+02	9.9550E+01	2.4008E+01
Trachyandesite	10	10	1	7	9	1.0200E+02	1	5	1.1900E+02	1.0956E+02	1.5067E+01
	10	10	2	2	9	4.2000E+01	1	4	5.2000E+01	4.7090E+01	6.8619E+00
	10	10	3	6	10	5.5000E+01	1	5	7.2000E+01	6.3110E+01	1.7618E+01
	10	10	4	10	10	4.9000E+01	1	5	6.3000E+01	5.5560E+01	1.1766E+01
	10	10	5	10	10	7.8000E+01	1	5	1.0500E+02	9.2200E+01	4.0880E+01
	10	10	6	1	10	4.1000E+01	1	6	6.0000E+01	5.0140E+01	1.7860E+01
Kane Wash Tuff, V Members	10	10	1	2	6	1.2700E+02	8	3	1.4300E+02	1.3563E+02	1.0393E+01
	10	10	2	3	6	6.2000E+01	7	3	7.2000E+01	6.7380E+01	5.5356E+00
	10	10	3	7	8	9.1000E+01	7	3	1.0800E+02	1.0091E+02	1.5342E+01
	10	10	4	6	7	7.9000E+01	1	10	9.2000E+01	8.6640E+01	8.0504E+00
	10	10	5	7	8	1.6100E+02	4	10	1.9000E+02	1.8038E+02	2.9656E+01
	10	10	6	7	7	9.8000E+01	5	3	1.1700E+02	1.0879E+02	1.4926E+01
Syenite Dome	5	5	1	2	5	1.1800E+02	1	1	1.3300E+02	1.2656E+02	1.7606E+01
	5	5	2	1	5	5.6000E+01	1	1	6.5000E+01	5.9840E+01	6.6945E+00
	5	5	3	2	5	7.6000E+01	1	1	9.3000E+01	8.4480E+01	1.8010E+01
	5	5	4	5	1	7.8000E+01	5	4	9.1000E+01	8.6080E+01	1.2954E+01
	5	5	5	4	2	1.3400E+02	5	4	1.5600E+02	1.4460E+02	4.1120E+01
	5	5	6	1	5	7.2000E+01	5	4	9.1000E+01	8.1640E+01	2.4710E+01
Kane Wash Tuff, O & W Members	10	10	1	9	3	1.2800E+02	2	7	1.4200E+02	1.3401E+02	1.2610E+01
	10	10	2	1	3	5.9000E+01	4	1	6.7000E+01	6.2050E+01	3.5675E+00
	10	10	3	2	2	8.2000E+01	4	1	9.6000E+01	8.7860E+01	7.9604E+00
	10	10	4	10	9	7.0000E+01	4	1	8.1000E+01	7.4700E+01	4.5100E+00
	10	10	5	1	2	1.1800E+02	2	7	1.3100E+02	1.2519E+02	7.0337E+00
	10	10	6	1	2	7.0000E+01	2	7	7.9000E+01	7.4680E+01	3.4577E+00
Syenite Porphyry	10	10	1	10	10	1.0500E+02	8	6	1.3300E+02	1.2017E+02	2.2701E+01
	10	10	2	4	1	4.8000E+01	8	6	6.2000E+01	5.6230E+01	7.4572E+00
	10	10	3	10	10	6.2000E+01	1	4	9.4000E+01	7.9970E+01	3.0629E+01
	10	10	4	2	9	6.9000E+01	3	2	9.1000E+01	8.0010E+01	2.1910E+01
	10	10	5	10	10	1.0200E+02	8	9	1.4400E+02	1.2657E+02	7.0045E+01
	10	10	6	10	10	5.0000E+01	7	9	8.0000E+01	6.8860E+01	3.5340E+01

APPENDIX L

Summary of X-ray diffraction analyses

COATING SAMPLES ANALYZED BY X-RAY DIFFRACTION

Sample	Minerals Detected
Stonewall Mountain	
44 felsic tuff	Q, AF
42 Civet Cat Tuff	Q, AF
50 Stonewall Tuff	Q, AF
51 rhyolite Q por	Q, AF
12 basalt	AF
30 Spearhead Tuff	Q, AF
13 air fall tuff	Q, AF, Analcime
20 Spearhead Tuff	Q, AF
31 divitrified glass	Q, AF
34 rhyolite Q por	Q, AF
37 rhyolite Q por	Q, AF, Kaolinite
39 andesite por	Q, AF, Kaolinite
33 vitric ash	Glass
32 vitrophyre	Glass, Minor Q, AF
Black Mountain	
57 Trail Ridge Tuff	Q, AF
59 Gold Flat Tuff	Q, AF
58 crystal lava	Q, AF
61 Divitrified glass	Q, AF
56 crystal lava	Q, AF
22 Trail Ridge Tuff	Q, AF
11 trachyte	AF
62 allulvial gravel	Q, AF
25 Gold Flat Tuff	Q, AF
16 Labyrinth Tuff	Q, AF
60 Gold Flat Tuff	Q, AF
21 divitrified glass	Q, AF
24 Rocket Wash Tuff	Q, AF
20 Gold Flat Tuff	Q, AF
23 Trail Ridge Tuff	Q, AF
15 basal vitrophyre	Glass
27 Trail Ridge Tuff	Q, AF
10 Trail Ridge Tuff	AF
40 trachyte	Q, AF
55 crystal lava	Q, AF
Kane Springs	
52 Kane Wash Tuff	Q, AF
48 Kane Wash Tuff	Q, AF
47 Kane Wash Tuff	Q, AF
49 Kane Wash Tuff	Q, AF
56 Kane Wash Tuff	Q, AF
54 Kane Wash Tuff	Q, AF
53 Kane Wash Tuff	Q, AF
24 syenite dome	Q, AF

8	trachyandesite	AF
10	rhyolite dome	Q, AF
21	basalt	AF
11	trachyandesite	AF
53	Kane Wash Tuff	AF
38	Hiko ash flow	Q, AF, Illite (?)
40	Kane Wash Tuff	Q, AF
26	trachytic ash	Q, AF
4	vitric tuff	Glass, Minor Q
39	pumice air fall	Q, AF, Illite (?)

Q - Quartz,   AF - Alkali Feldspar, mostly sanadine and anorthoclase (potassian albite)

PART II

PART II

RECONNAISSANCE GEOLOGIC MAPPING OF THE KANE SPRINGS WASH VOLCANIC CENTER, LINCOLN COUNTY, NEVADA, USING MULTISPECTRAL THERMAL INFRARED IMAGERY

Michael J. Chenevey, Principle Author
Mackay School of Mines
University of Nevada, Reno
Reno, Nevada 89557

Abstract

The present study investigates the usefulness of Thermal Infrared Multispectral Scanner (TIMS) imagery for reconnaissance geologic mapping. The effects of rock coatings and vegetation on image interpretations are also evaluated. A decorrelation stretched TIMS image (using channels 1, 3, and 5) of the Kane Springs Wash study area allowed geologic mapping of basalt, limestone, dolomite, and some ash-flow tuff units on a small scale. Laboratory spectra of rock coatings obtained from volcanic rocks in the study area showed a dominance of spectral features attributed to illite/montmorillonite mixed-layer clays. When present in sufficient quantity, rock coatings can mask rock signatures measured with the TIMS. The reststrahlen feature of felsic rocks shifts to longer wavelengths, while the reststrahlen feature of ultramafic rocks will shift to shorter wavelengths. Some mafic rocks, although completely coated, do not show spectral differences due to the close proximity of the reststrahlen features of the mafic minerals and the clays. Vegetated areas produced lower brightness values than non-vegetated pixels due to evapotranspirative cooling. Pinyon-juniper vegetation lowers the emittance in TIMS channel 5 relative to TIMS channels 1 and 3.

Table of Contents

Table of Contents, Continued

Table of Contents, Continued

List of Tables

List of Figures

Table of Contents, Continued

Figures in Appendix Two

Table of Contents, Continued

Figures in Appendix Three

List of Appendices

Table of Contents, Continued

Chapter One

Introduction

The following study addresses the usefulness of Thermal Infrared Multispectral Scanner (TIMS) data for geologic mapping. Rock coatings and vegetation are possible hindrances to mapping with remotely sensed thermal infrared imagery. These two are evaluated in order to determine their influence on emittance received by the TIMS, and, consequently, geologic interpretations made from the data.

Many studies have utilized emissivity variations found in the 8 to 12 micrometer (thermal infrared) portion of the electromagnetic spectrum for mineralogic, and therefore litho-logic, discrimination (Lyon, 1965; Hunt et al., 1974, 1975, 1976; Vincent and Thompson, 1972; Lyon and Green, 1975; Vincent et al., 1975; Hunt, 1980; Salisbury et al., 1987; Salisbury et al., 1988; Bartholomew et al., 1988, Chenevey and Perry, 1989; etcetera).

Geologists mapping from ground-based observations can frequently miss significant lithologic features, since complete ground coverage of an area is many times impossible. Airborne multiband sensors measuring in the thermal infrared region provide a synoptic view of lithologic variations (provided the study area is free or nearly free of vege-tation), and thus are useful for reconnaissance geologic mapping.

The TIMS has been used for many geologic studies (Kahle et al., 1980; Kahle and Goetz, 1983; Gillespie, 1985; Kahle,

1987; and Kahle et al., 1989). TIMS data contains both temperature and emissivity information, and can be processed in such a way to enhance relative emissivity differences for a given area. Emissivity variations are dependent on mineralogical composition, and can be used to discriminate between silicate rock types (Lyon, 1965; Lyon and Green, 1975).

The present study consists of two parts. The first part focusses on the usefulness of TIMS imagery for mapping volcanic and sedimentary lithologies. The second part concentrates on the influence of rock coatings and vegetation on mid-infrared spectra and TIMS measurements, and how these coatings may affect interpretations made with TIMS imagery.

The Kane Springs Wash volcanic center is the study area for this project. The center is located in south central Lincoln county, Nevada, approximately 70 miles northeast of Las Vegas (Figure 1). TIMS imagery was acquired over an area of approximately 27 km by 18 km centered over the caldera complex on September 14, 1987.

Four geologic maps of the study area exist: a 1:100,000 scale county map (Tschanz and Pampeyan, 1970), a detailed map of the caldera complex (Novak, 1984), a "sketch" map of the caldera complex (Noble, 1968), and a detailed map of the northeast portion of the image area (Scott et al., 1988). The most detailed geologic maps are only applicable to part of the imaged area, thus much of this project involves original geologic interpretation based on the TIMS imagery and the author's field excursions to the study area.
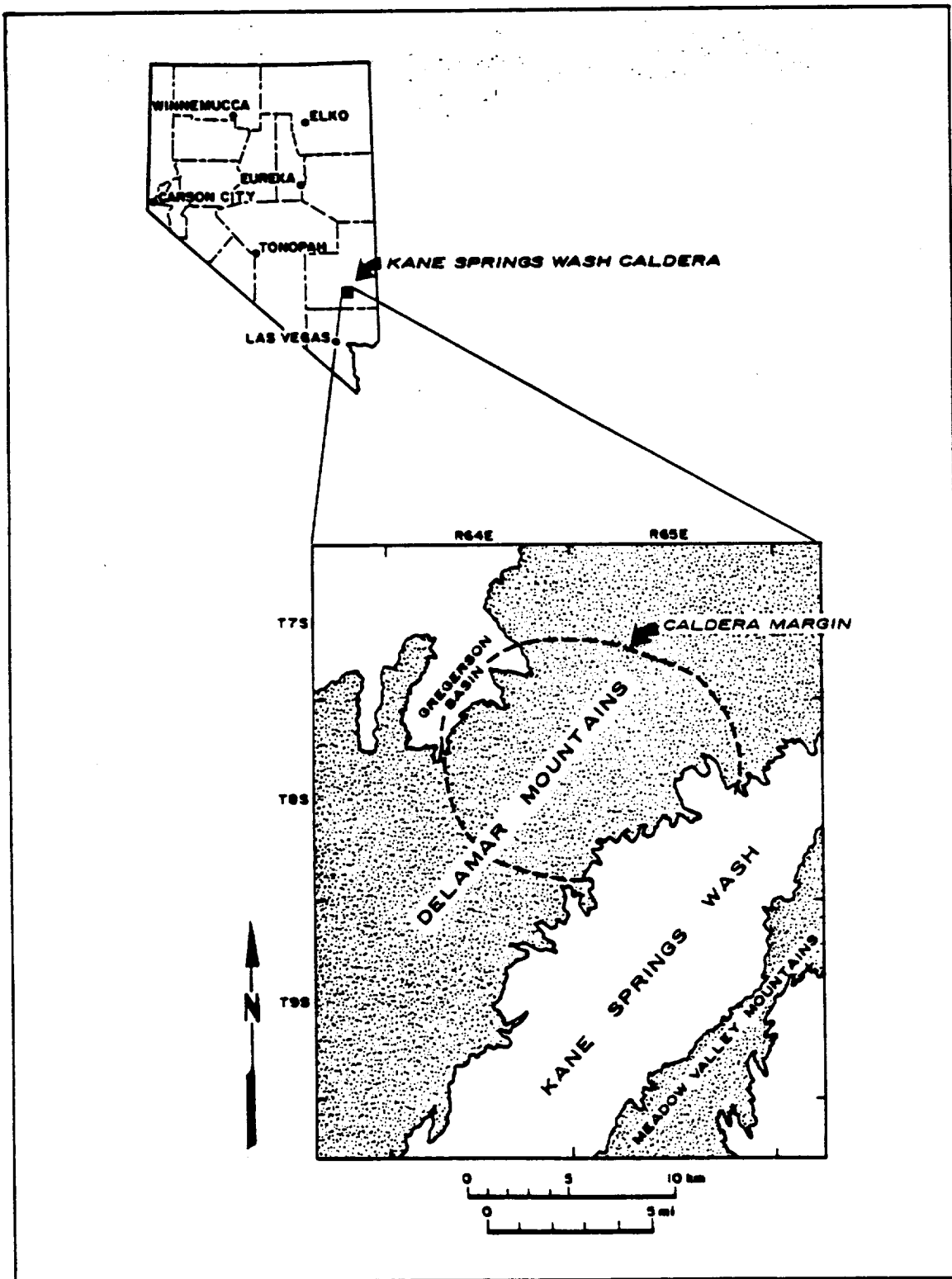
Figure 1. Location and geography of the Kane Springs Wash study area, south-central Lincoln County, Nevada.

Rock coatings and vegetation are two of the many factors which may obscure geologic information in TIMS imagery. Previous spectral studies of rock coatings have dealt with desert varnish in the western United States (Potter and Rossman, 1979a; Elvidge and Collet, 1982; Buckingham and Sommer, 1983; Adams et al., 1984; Spatz, 1988; Kahle et al., 1989; Bartholomew et al., 1989) and silica-based coatings in Hawaii (Kahle et al., 1989). Nine studies have utilized mid-infrared spectral data of rock coatings (Chenevey, 1989; Kahle et al., 1989; Bartholomew et al., 1989; Potter and Rossman, 1979a, 1979b; Christensen et al., 1986; Kahle et al., 1986; Kahle, 1987; and Podwysocki et al., 1987).

Over one hundred spectral measurements were acquired with two mid-infrared reflectance spectrometers and one portable emission spectrometer during the course of this investigation. Every major geologic unit in the study area that supported rock coatings was measured in order to determine the influence of rock coatings on mid-infrared spectral measurements and TIMS interpretations.

Thermal variations have been the most studied aspect of vegetation in the mid-infrared region (Langran, 1985; Sader, 1985; Pelletier and Ochoa, 1985; Sabins, 1987). Spectral studies of vegetation using mid-infrared wavelengths are few (Gates and Tantraporn, 1952; Fuchs and Tanner, 1966; Wong and Blevin, 1967; Gates, 1980; Salisbury, 1986; Salisbury and Milton, 1988; Elvidge, 1988). Only Salisbury and Milton (1988) and Elvidge (1988) have published continuous high resolution mid-infrared spectra of plant material. A study of the influence of vegetation on decorrelation stretched TIMS data has never been published.

Description of the Study Area

The geography of the Kane Springs Wash study area is
shown in Figure 1. The southern Delamar Mountains, which range
in elevation from approximately 3000 feet to 7500 feet,
dominate the study area. The Gregerson Basin is a small
depression approximately three miles in diameter found on the
western side of the Delamar Mountains (northwestern part of
the area). The Kane Springs Wash is the major drainage, and
crosses the study area from the northeast to the southwest.
Part of Delamar Valley is within the boundary of the study
area to the northwest. The Meadow Valley Mountains frame the
area to the southeast.

The study area is located in the northern Mojave desert,
and is arid. Temperature and rainfall data for a ten year
period (1978 to 1988) for three stations near the study area
are given in Table 1.

Vegetation in the study area ranges from rabbitbrush and
creosote in the lower washes to big sage in the upper washes
to pinyon-juniper woodland in the higher parts of the Delamar
Mountains. Vegetation coverage ranges widely. Coverage
averages from 5 to 25% desert scrub in the valleys and washes
to 25 to 50% and sometimes up to 100% pinyon-juniper in the
mountains.

Geologic Units Within the Study Area

Geologic units exposed in the study area include those
related to the Miocene Kane Springs Wash caldera complex and
older Tertiary and Paleozoic rocks. Paleozoic units are found

Table One

Average temperature and precipitation data
for three stations near the study area: Caliente,
Elgin, and Pahranagat Wildlife Refuge
(From NOAA annual summaries, Nevada)

	Ave. Temperature (^{O}C)	Ave. Precipitation (in.)
1978	12.9	20.8
1979	12.9	10.6
1980	15.0	13.0
1981	15.5	10.1
1982	13.2	12.9
1983	13.9	14.9
1984	14.4	13.4
1985	13.8	6.4
1986	16.0	8.3
1987	13.9	10.8
1988	14.0	7.2
Mean	14.1^{O}C	11.7 in.

most extensively in the southern quarter of the study area, and range in age from Cambrian to Permian. No Mesozoic units crop out in the study area. Cenozoic units are confined predominantly to the Tertiary period. They consist of older ash flow sheets from westerly sources, and those units which formed as a result of the Kane Springs Wash caldera activity. Quaternary units are found most extensively in the Kane Springs Wash, Delamar Valley, and Gregerson Basin.

The following is a brief description of the major lithologic units in the study area. More detailed descriptions of the units are presented by Cook (1965), Tschanz and Pampeyan (1970), Novak (1984 and 1985) and Spatz (1988).

Paleozoic Units

Cambrian

Limestone and Dolomite

Cambrian Limestone and Dolomite mapped by Tschanz and Pampeyan (1970) occur in the central northern portion of the study area, surrounding a Tertiary granite porphyry. No description of these units is given in the Lincoln county report. Field inspection showed that this unit is largely dolomite with some unidentifiable silicified fossils and does not display noticeable contact metamorphism with the granite stock.

Upper Cambrian Limestone and Dolomite, Undifferentiated

Upper Cambrian Limestone and Dolomite are found in limited exposures in the study area. The only occurrence of these rocks is in the southwestern corner of the study area. The units consist of a lower silty or cherty fossiliferous limestone and an upper cherty dolomite (Tschanz and Pampeyan, 1970).

Devonian

Simonson Dolomite

The Simonson Dolomite occurs in the Meadow Valley Mountains in the southeastern portion of the study area. It lies along a northwest trending fault contact with Tertiary volcanics lying to the west.

Guilmette Formation

The Guilmette Formation occurs in the southern part of the study area and overlies the Simonson Dolomite (unconformably?). The basal unit consists of a laminated, silty dolomite, and is overlain generally by massive limestone beds.

Mississippian

Upper Mississippian Clastic Rocks

The "clastic rocks" lie along a northwest-trending thrust contact with structurally lower Guilmette limestones to the west, as mapped by Tschanz and Pampeyan (1970). No description of this unit was presented in the Lincoln county report. The author has visited this locality in the Meadow Valley Mountains and found a continuous outcropping of northwest-trending quartz sandstone, approximately 1 m wide, which may be part of this unit. If the sandstone is in fact in the upper plate of the thrust, it may be the Scotty Wash Quartzite, as described by Tschanz and Pampeyan (1970).

Pennsylvanian and Permian

Limestone

Massive gray limestones occur at several localities in the southern part of the imaged area, sometimes with dolomitic facies. The limestones usually contain silicified fossils.

Cenozoic Units

Tertiary
(Predominantly Miocene)

Hiko Tuff

The Hiko Tuff consists of rhyolitic ash flows and generally forms the basement for the older Kane Wash Tuff units. The tuff consists of approximately 50% sanidine and anorthoclase phenocrysts with minor plagioclase, quartz, biotite, and amphibole (Spatz, 1988).

Older Kane Wash Tuff

The older Kane Wash Tuff is divided into two members by Novak (1985); an older member designated "O", and a younger member, "W". These units, although bearing the name Kane Wash Tuff, are thought to have been derived from another volcanic center to the southwest of the Kane Springs Wash area (Novak, 1985). The basal member, O, is a compound cooling unit of fayalite-bearing rhyolite ash flow tuff (Novak, 1985). The second, thicker member of the older Kane Wash Tuff, W, is identical in composition to the first member, and is characterized by a prominent white, nonwelded base.

Younger Kane Wash Tuff

The younger Kane Wash Tuff consists of three members, designated from oldest to youngest, V1, V2, and V3 by Novak (1985). This unit represents the first extrusions from the Kane Springs Wash caldera. It is also the most extensive unit in the study area. Member V1 is generally a densely welded crystal-rich tuff that grades from a nonwelded ash-rich rhyolitic base to an upper densely welded trachytic tuff. The unit contains approximately 25% sanidine and 3-5% mafic phenocrysts (Novak, 1985; Spatz, 1988). Member V2 is a comendite ash flow tuff that grades from a crystal-poor comendite base to a trachytic top. It consists of 15% sanidine and quartz phenocrysts with accessory mafics. Member V3 is mineralogically identical to V2. The distinguishing feature of the V3 member is a thicker base.

Gregerson Basin unit

The Gregerson Basin unit was mapped by Scott et al. (1988) as a successor to the Kane Wash Tuff V2 unit mapped by Novak (1985). The unit is found in the northwest portion of the study area. It contains up to 25% phenocrysts in the upper zone, consisting of 60% sanidine, 25% quartz, and 15% hedenbergite, fayalite, and ilmenite (Scott et al., 1988).

Post Caldera Trachyte Lavas

The following volcanic units, with the exception of the younger basalt lavas, were erupted within the caldera. The first of these was a porphyritic trachyte, which occurs along the southeast edge of the caldera. The trachyte contains

anorthoclase phenocrysts up to 2 cm long, along with minor clinopyroxene, olivine, and quartz xenocrysts rimmed by clinopyroxene (Novak, 1985).

Central Syenite Complex

The Central Syenite Complex is a circular dome of extrusive to subvolcanic syenite (Novak, 1985) located within the central eastern portion of the caldera. Porphyritic fine-grained syenite is the most extensive unit within the syenite complex. This unit is composed of 20% anorthoclase and 3% clinopyroxene phenocrysts in a fine grained matrix of alkali feldspar and quartz (Novak, 1985).

Early Moat (Ferroedenite) Rhyolite Lavas

The early moat high-silica lavas were extruded in a moat, or low area, lying near the north rim of the caldera. The lavas consist of phenocrysts of sodic sanidine, quartz, and ferroedenite (an Iron-rich amphibole) with minor mafics, including titanomagnetite, ilmenite, and zircon (Novak, 1985).

Intracaldera Trachybasalt to Alkali Basalt Lava Flows

The trachyandesite lavas, as they are referred to by Novak (1985), are most commonly basaltic in composition. They outcrop in an extensive area along the southwestern caldera margin. Trachyandesite lavas typically contain phenocrysts of

plagioclase and olivine or clinopyroxene in a fine grained matrix of the same minerals (Novak, 1985). Novak also states that olivine is the dominant phenocryst phase in the basalts, while plagioclase is dominant in the trachyandesites.

Late Moat (Topaz) Rhyolite Lavas

Late moat rhyolites occur in relatively small outcrops in several parts of the study area. The largest rhyolite dome outcrops along the southwestern margin of the caldera. The domes are high in silica and contain phenocrysts of sanidine, plagioclase, resorbed quartz, annite, fayalite, and fer-roedenite with minor mafics (Novak, 1985).

Late Basalt Lavas

Olivine-rich basalt is found most extensively in the proximity of the trachyandesite lavas near the southwestern margin of the caldera. The basalts are found throughout the study area, and tend to cap many of the mesa-like hills within the caldera.

Granite Porphyry

A granitic intrusive stock was mapped by Tschanz and Pampeyan (1970) south of Delamar, an abandoned mining town north of the study area. The stock is found in the central northern portion of the study area, and is surrounded by Cambrian limestone and dolomite. Tschanz and Pampeyan describe the stock as an altered porphyritic potassic granite composed

predominantly of altered orthoclase and microcline phenocrysts with a small amount of quartz in a fine grained groundmass of the same minerals. The mafics have been replaced by iron oxides.

Chapter Two

Data Acquisition, Processing and Instrumentation

The TIMS Instrument and Data

The Thermal Infrared Multispectral Scanner (TIMS) is a cross-track airborne scanner which measures emittance in six channels between 8 and 12 micrometers. The TIMS was flown in a NASA Lear Jet over the study area at approximately 11:00 am PST on September 14, 1987. The TIMS specifications for the data acquired over the Kane Springs Wash study area are presented in Appendix 1. The TIMS channels are:

	Band center (um)	Bandpass (um)
CH 1	8.33	8.11 - 8.55
CH 2	8.77	8.58 - 8.96
CH 3	9.12	9.00 - 9.25
CH 4	9.90	9.66 - 10.15
CH 5	10.73	10.33 - 11.13
CH 6	11.41	11.28 - 11.55

The TIMS has a linear array of six mercury-cadmium-telluride detector elements, cooled by liquid nitrogen in order to achieve maximum sensitivity. The noise equivalent temperature difference ranges between $0.1^{\circ}C$ to $0.3^{\circ}C$ (Palluconi and Meeks, 1985). Line-by-line calibration is achieved by two internal reference sources, one set at a low temperature, and one at a high temperature. A mirror views the cold reference at the beginning of each scan, and the hot reference at the end of the scan.

Blackbody reference source temperatures and gain must be set before data acquisition. The blackbody reference source temperatures are adjusted so that they include the total range of brightness values expected for a particular scene. The temperatures were set at 10 and 45 degrees celsius for the Kane Springs Wash data.

Gain is a multiplication factor used to modify the spread of values in a scene. A low gain is used for a very bright scene in order to keep all the data within a usable range. The gain was set at 2 for the Kane Springs Wash data.

An important parameter of the TIMS instrument is the spectral responses of the filters. The filters allow only specific wavelength regions to be measured by each detector, thus defining the channels. The filter responses are sensitive to detector alignment and the specific detectors used. Thus, whenever the instrument is serviced or modified, the spectral responses can change. The TIMS filter responses for August 26, 1987 are presented in Appendix 11.

Image Processing

The TIMS data used for this project was obtained from the Jet Propulsion Laboratory (JPL). Calibration techniques were applied to the data at JPL using a program called TIMSCAL. The corrections included convolving the data with measured spectral bandpasses (see Appendix 11), gain, and offset and reduction of the data to physical units of radiance (photons/ $sec/cm^2/SR$). Convolving the data with the bandpasses, gain, and offset is performed in order to account for individual detector response. The object of the reduction to physical units is to translate the DNs for each scan line into physical

units using the internal reference sources and to account for scan to scan differences in the operation of the instrument (Palluconi and Meeks, 1985). No atmospheric corrections were applied to the data.

Further image processing was performed on a VAX-based IDIMS system at the Mackay School of Mines. The decorrelation stretch technique was used to produce an image in which hues represent emissivity variations and intensity variations represent temperature differences. A decorrelation stretch is produced by calculating the eigenvalues and eigenvectors which produce new components having zero correlation. This is followed by variance equalization and an inverse transformation back into the original color space. Appendix Two describes the process in detail.

The Fourier Transform Infrared Spectrometer
(FTIR)

An Analect Instruments Model 6200 FTIR spectrometer located at the Jet Propulsion Laboratory was used to gather biconical reflectance data. The spectra were acquired in the mid-infrared region (2.3 to 20 micrometers) from variably coated and freshly broken rock surfaces collected at the study area. Each spectrum represents the average of 100 scans of the reflected beam from the sample ratioed against the average of 100 scans of the reflected beam from a gold standard. Spectrometer specifications are given in Appendix 5.

Si-C sandpaper coated with a thin layer of gold was used as the standard for all spectral measurements (after Nash, 1986). The purpose of a standard is to reflect background radiation into the detector in order to eliminate the added

radiation from spectral measurements. An ideal standard should be coated with a consistent gold layer, but because of the irregularity of the sandpaper surface, this criterium is not met satisfactorily by the standard used. If the standard does not reflect 100%, when it is ratioed against any sample the sample contrast will be reduced since the background will not have been properly accounted for.

The FTIR utilizes a biconical reflectance attachment consisting of two off-axis paraboloid mirrors positioned below a specially designed rotating sample stage. The stage rotates the sample in 0.36 degree steps after each scan so that the source beam, a 1 mm diameter spot, can scan a large portion (approximately 3.5 cm) of the rock surface.

The biconical attachment does not have an adjustable focus. Instead, the focus is preset for a perfectly flat surface. The rock surfaces were not perfectly flat, thus sample topography usually prevented focussing of the source beam. The effect of not focussing the beam is reduced magnitude of reflectance. Although specific features are still present and in the same places, they will not be consistent in magnitude, even between like samples. This effect is very important and should be taken into account when analyzing the spectra.

The reflectance spectrometer was not sealed or purged of water vapor during any of the measurements presented in this paper. The effect of water vapor is evident in all of the spectra, and is most visible in the 6 to 8 um region as small fluctuations of the spectra (see Appendix 12 for reference spectrum).

The Portable Field Emission Spectrometer
(PFES)

The portable spectroradiometer used to collect passive emission data of the Kane Springs Wash samples was designed and built at the Jet Propulsion Laboratory (Hoover and Kahle, 1986). Specifications of the instrument are given in Appendix 6. Spectral measurements were made at the Jet Propulsion Laboratory in Pasadena, California, on top of building 183, which houses the geology group (Figure 2). A higher position reduced reflected and emitted thermal infrared radiation from surrounding surfaces. The measurements were collected over a period of approximately 4 hours (1 to 5 pm) on January 25, 1989. The sky was clear over Pasadena (except minor smog), and the temperature was approximately $65^{\circ}F$. Two blackbodies were used for calibration of the data; a cold blackbody (chilled by ice), and an ambient temperature blackbody. Blackbody temperatures were monitored before each measurement using a standard voltmeter and thermocouples. Each spectrum was measured four or five times and averaged to assure reproducibility and reduce noise in the system.

The emittance of all materials will approximate that of a blackbody at certain frequencies (Hoover and Kahle, 1986). Blackbody spectra calculated with Planck's equation (varying the temperature) were fitted to the sample spectra at frequencies where the sample was emitting near that of a blackbody, so that the sample and blackbody were at approximately the same temperature. The spectra were then ratioed according to the emissivity equation:

$$e = W \text{ realbody} : W \text{ blackbody}$$
$$(\text{at thermal equilibrium})$$

Where e = Emissivity

    W = Radiant spectral emittance

Portable Field Emission Spectra of coated and fresh rock surfaces of five rock types are given in Appendix 13.
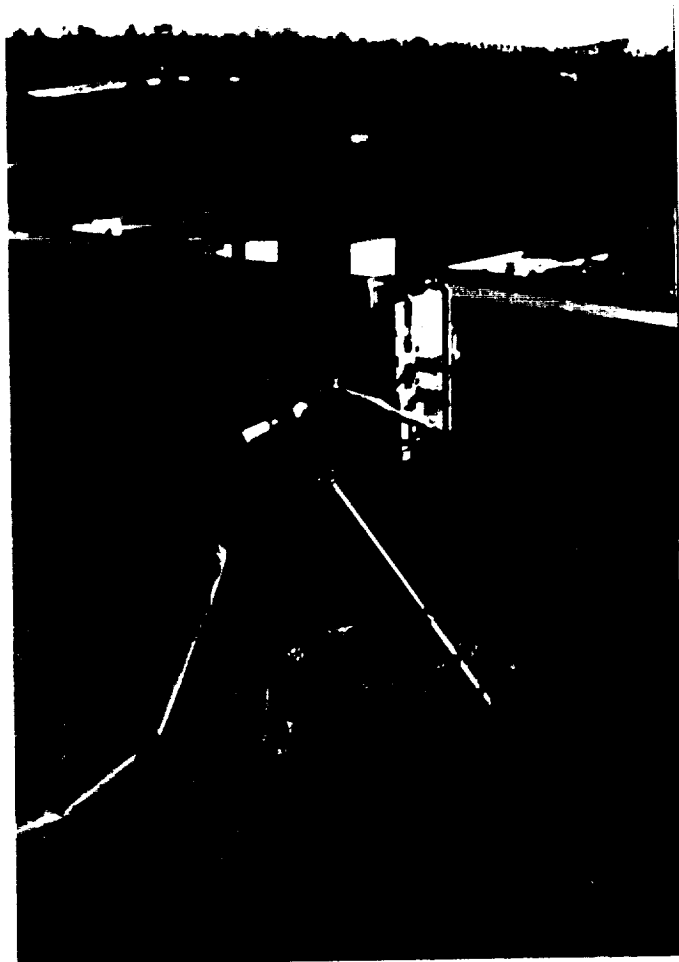
Figure 2. Photograph of the Portable Field Emission
Spectrometer at the Jet Propulsion Laboratory.

Chapter Three

Image Interpretation

Thermal Infrared Imagery

Thermal infrared imagery consists of two major variables: temperature and emissivity. Temperature is dominant, as shown in the unenhanced TIMS data (Figure A, Appendix Two). High DN values are associated with southeast facing slopes. These slopes are being heated by the morning sun. Low DN values are found in shadowed areas. Emissivity is a measure of how well a body radiates energy. Thermal infrared radiation is selectively absorbed at certain frequencies by the vibrations produced in molecular bonds, such as those between silicon and oxygen in silicate minerals. The absorption features are diagnostic, and can be used to identify specific minerals in laboratory spectra. Wavelength dependent emissivity variations are also present in TIMS data, and can be enhanced with special image processing techniques (see Appendix Two). Appendix Three describes basic thermal infrared principles in more detail.

Interpretation of the Decorrelation Stretched Image

The decorrelation stretch displays temperature as intensity, while emissivity is expressed as hue (Kahle et al., 1980). The colors in a decorrelation stretched image thus can be related to the position of the reststrahlen feature representative of the materials at the ground surface (rock, soil, and vegetation).
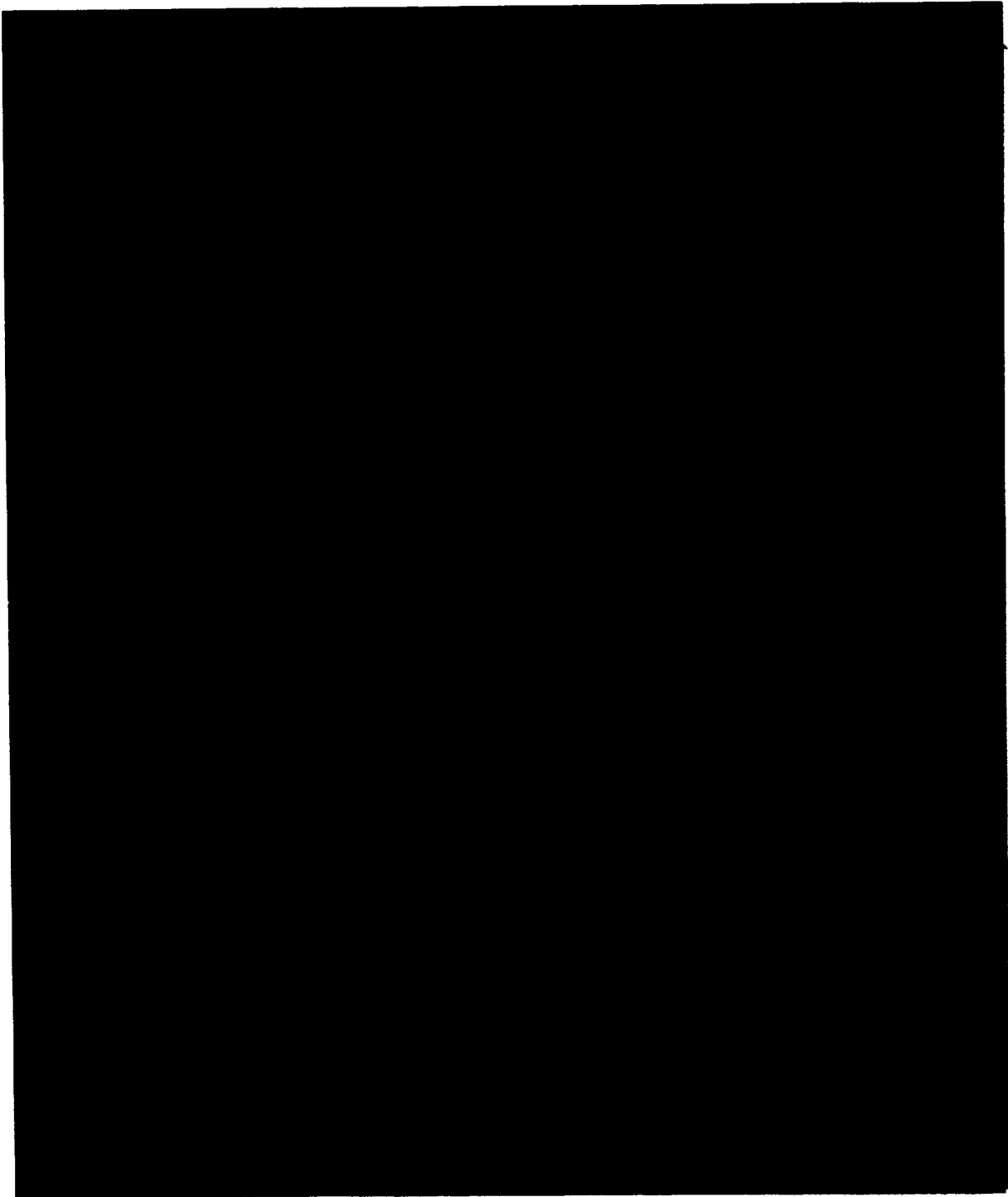
Figure 3.   Decorrelation Stretched TIMS image (531 in RGB).

The decorrelation stretched TIMS image (531 in RGB, Figure 3) allowed inference of mineralogy, and thus lithology, based on the emissivity differences. The mineralogy of samples collected throughout the study area was determined through petrographic analyses (Appendix 4). These mineralogic analyses will be used as a basis for hue interpretation in the following discussion.

Cambrian and Upper Cambrian limestone and dolomite and the Devonian Simonson Dolomite and Guilmette Formation exhibit distinct royal blue to blue-green signatures on the image. The $CaCO_3$ emissivity minimum occurs at approximately 11.3 um, and thus has a higher emissivity value in TIMS band 1, which has been assigned a blue color. Interbedded sandstones within larger limestone units (Upper Mississippian clastics ?) exhibit yellow hues due most likely to quartz signatures (absorption near 8.0 um) mixed with $CaCO_3$ signatures in pixels.

Younger Paleozoic limestones and dolomites appear blue-green to yellow-green and royal blue, respectively. Chert-rich limestones, which have more of a quartz component and thus a lower TIMS channel 1 emissivity, account for the difference in hue between these units and the lower Paleozoic limestones and dolomites.

The Hiko Tuff has a distinctive mottled red signature. A red hue indicates that the Hiko is quartz- (or tectosilicate) rich. Quartz-dominated tuffs appear red due to absorption in channel 1 and high emissivity values in channel 5. Spatz (1988) described the Hiko as being approximately 50% sanidine / anorthoclase with "some" quartz.

The older Kane Wash Tuff members O and W are represented by a red to gray signature. The O and W consist of phenocrysts of sanidine / anorthoclase, fayalite, pyroxene, and quartz (Spatz, 1988). The signature is probably a combination of the emission minima of the stronger bonded tectosilicates and the weaker bonded nesosilicates and inosilicates, resulting in low emissivity throughout the spectrum, and a corresponding neutral color.

The younger Kane Wash Tuff units, V1, V2, and V3 are not separable on the image, which is to be expected, since all three units are mineralogically similar. The V members, which are sodium sanidine-dominated tuffs, appear yellow due to longer wavelength absorption (i.e more green values) as compared with quartz.

Post caldera trachyte lavas are pink on the image. Anorthoclase is the major mineral component of this unit. Anorthoclase, when an important constituent in rocks, produces a red hue. The trachytes also contain augite and olivine in minor amounts, which appear to be affecting the emissivity minima by shifting it to slightly longer wavelengths, thus producing a pink hue.

The Central Syenite Complex, where not vegetated, is characterized by a red hue. The dominant mineral anorthoclase appears to cause short wavelength absorption, similar to that of quartz.

Early Moat rhyolite domes, where not vegetated, are represented by yellow to yellow-orange hues. Sodium sanidine and quartz are major components of this unit, thus reststrahlen features are a combination of absorption features

found near 9.0 (channel 3) and 8.5 um (channel 1), respective-
ly (Salisbury et al., 1987). Yellow signatures are produced
by high emissivity values in channel 5 (red) and moderate
values in channel 3 (green).

Trachyandesite lavas have dominantly purple to magenta
hues. This unit is composed primarily of a plagioclase,
augite, and olivine-rich groundmass, which results in shorter
wavelength reststrahlen features than basalt, and is thus
separable from basalt in the image.

Late moat rhyolite lavas exhibit a yellow hue in the
image. This unit cannot be distinguished from the early moat
rhyolite or the younger Kane Wash Tuff, but is distinctive
because it lies in an area dominated by basalt and trachy-
andesite.

Basalt lava, because of its olivine- and augite-rich
composition, displays a reststrahlen feature in TIMS band 5
resulting in a dark blue signature on the decorrelation
stretched image. Several regions of dark blue have been iden-
tified as basalt through field reconnaissance. These regions
have not appeared on any previous geologic maps of the area.

A granite porphyry stock produced a unique orange
signature in the image. Potassium feldspar is dominant in this
unit (up to 40 %). The emissivity minimum of potassium feld-
spar occurs at a slightly longer wavelength than quartz
(Salisbury et al., 1987), producing the orange hue.

Alluvial areas, including the Kane Springs Wash, Delamar
Valley, and the Gregerson Basin, are varied in hue. Rocks in
the washes can be traced back to their former exposures in

either the Delamar mountains or the Meadow Valley Mountains. Limestone exposed in the south-central image area (Figure 5) is an excellent example. The limestone-dominated wash can be traced back to the outcrop from which it was derived in the southern Delamar Mountains. The yellow portions of the Gregerson Basin can likewise be traced back to the younger Kane Wash Tuff from which it was derived in the northwestern corner of the image.

Discussion

This section will be a comparison of a geological interpretation map of the TIMS image (Plate 2, in back jacket, summarized in Figure 5) with the compilation map of all previous geologic maps of the study area (Plate 1, also in back jacket, summarized in Figure 4). The interpretation map has been field checked.

The TIMS image was helpful for distinguishing compositionally distinct lithologies. Basalt was easily located because of its unique dark blue color. Two basalt units in Plate 2 have not previously been mapped. These occur along the northeastern caldera margin and west of the caldera lying on older ash flows (compare with Plate 1).

Many of the intracaldera units can be correlated between Plates 1 and 2. The syenite complex is roughly comparable between the maps, as is the post caldera trachyte, basalt and

Figure 4. Summary of previous geologic mapping in the Kane Springs Wash study area (see Plate 1 for more detail).

Explanation

Qal	Alluvium
Tb	Basalt
Tl	Late Moat rhyolite
Tbta	Trachyandesite
Te	Early Moat rhyolite
Tip	Intracaldera ash flow tuff
Tc	Syenite
Tf	Post caldera trachyte
Tbx	Talus breccia
Tvy	Younger volcanics
Tgp	Granite porphyry
Tvt	Tuffs & tuffaceous sediments
Tkv	Kane Wash Tuff
Tpt	Precaldera trachyte
Tkow	Pre-Kane Wash Tuff
TKc	Older clastics
PPl	Permian-Pennsylvanian limestone
Msc	Upper Mississippian clastics(?)
Dg	Devonian Guilmette Formation
Dsi	Devonian Simonson Dolomite
Op	Ordovician Pogonip Group
Cu	Cambrian limestone/dolomite

Figure 5. Summary of the interpretations made from the TIMS image (see Plate 2 for more detail).

trachyandesite, and the late moat (topaz) rhyolite. Kane Wash
Tuff found in the caldera is also similar to that shown on
Plate 1.

Other intracaldera units were ambiguous in the imagery
or were vegetated. These units included the Early Moat
(ferroedenite) rhyolite domes, and portions of the Syenite
complex and the Pre-caldera trachyte. The Early Moat rhyolite
domes are completely masked by vegetation in their more
northern exposures. The same is true of the northernmost
exposures of the syenite.

Many of the extracaldera units correlate with previous
geologic mapping. Light brown to brown-orange colors in Plate
1 represent ash flow sheets extruded from the Kane Springs
Wash caldera, which were mapped as one unit by Novak (1984),
but as two units by Tschanz and Pampeyan (1970). The hues
which represent these units on the TIMS decorrelation stretc-
hed image correspond with Tschanz and Pampeyan's map. The
westernmost ash flows (light red in Plates 1 and 2), part
referred to as the Gregerson Basin unit by Scott et al.
(1988), are red to pink in the image, and are more felsic (see
Geologic Units section) in composition than the younger Kane
Wash Tuff (light brown in Plates 1 and 2). Older ash flows are
shown as brown-orange colors in Plates 1 and 2. The latter
corresponds to the pre-caldera Hiko Tuff, and has not been
mapped in the southwestern part of the imaged area. This area
has been field checked, and is similar to the Hiko Tuff found
elsewhere.

The granite porphyry located in the north-central map
area correlates between the two maps. The more extensive area

shown in Plate 2 is due to the weathering of the porphyry and the spread of talus further than the actual outcrop.

Paleozoic limestones and dolomites, mapped predominantly in the southern imaged area and surrounding the granite porphyry in the northern part of Plates 1 and 2, are shown more accurately in Plate 2 than in the geologic map of Lincoln county. Sandstone interbeds within limestones in the western Meadow Valley Mountains (southeastern corner of Plates 1 and 2) are mappable with the TIMS image.

Chapter Four

The Effects of Rock Coatings on
Mid-infrared Spectra and Implications for TIMS
Interpretations

Previous Investigations

Rock coatings have been studied by many researchers in the past in the form of desert varnish (Potter and Rossman, 1977, 1979a, 1979b; Elvidge, 1979; and others, see Appendix 7) and as silica-rich coatings on volcanic rocks (Curtiss et al., 1985; Farr and Adams, 1984; Kahle et al., 1989). Few remote sensing-oriented studies of coatings, mainly at visible and near-infrared wavelengths, have been ventured in any detail (Watson, 1970; Elvidge and Collet, 1982; Adams et al., 1984; Buckingham and Summer, 1983; Kahle et al., 1989; Spatz, 1988; and Bartholomew et al., 1989). Nine studies have reported on the mid-infrared spectra of rock coatings (Chenevey, 1989; Kahle et al., 1989; Bartholomew et al., 1989; Potter and Rossman, 1979a, 1979b; Christensen et al., 1986; Kahle et al., 1986; Kahle, 1987; and Podwysocki et al., 1987).

Compositional studies of rock coatings (see references above) have concluded that the major constituents are manganese oxide, iron oxide, and clay. The minerals birnessite, hematite, and mixed layer illite-montmorillonite were identified by Potter and Rossman (1979a) for desert varnish collected throughout the western United States. Iron oxides and manganese oxides were found to be spectrally flat in the

8 to 12 um region (Potter and Rossman, 1979a, 1979b), thus clays were the only spectrally distinct minerals composing the coatings.

Rock coatings collected in the Carlin, Nevada area were analyzed spectrally in the 8 to 12 um region by Podwysocki et al. (1987). They found that the characteristic emittance minimum of quartz shifted to longer wavelengths due to the clay component of the coatings.

Bartholomew et al. (1989) studied varnished and unvarnished quartzite, sandstone, and diorite. They measured samples with the same FTIR spectrometer that was used for this study. Their spectra showed a varnish feature at 9.7 um which they correlated with illite/smectite and/or kaolinite clays in the varnish.

Kahle et al. (1986) found that mid-infrared spectral features of quartzite are completely masked when desert varnish is heavily coating the rock. They attributed the coating features to clay.

Christensen et al. (1986) presented an opposing view of the effects of rock coatings on mid-infrared spectra. They show that a rock coating 50 um thick, although obscuring identification of a rock in visible and near-infrared wavelengths, is transparent in the mid-infrared region.

Rock coatings at the Kane Springs Wash area have been studied in detail by Spatz (1988). The following is a summary of his results.

SEM/EDX, X-ray diffraction, visible and near-infrared spectroscopy and petrographic techniques were employed to examine and analyze samples of rock coatings collected from the Late Moat (topaz) rhyolite, basalt, syenite, and Hiko Tuff. Thin section and SEM observations showed the coatings to be discontinuous encrustations, generally ranging in thickness from less than 5 um to 50 um, but not usually exceeding 5 um. Iron, manganese, silicon, and aluminum are the major elemental constituents. Minor elements include titanium, calcium, potassium, and sodium.

Spatz's laboratory data, collected with the techniques described above, indicated that iron and manganese-rich amorphous compounds make up the coatings. No coating phases were detected in transmission spectra of the Kane Springs Wash samples. X-ray diffraction patterns of two Kane Springs Wash samples showed possible clay features. Spatz stated that "poorly ordered mixed-layer illitic clay" possibly existed in several samples.

The Present Rock Coating Study

The plan of research for this study involved several steps. The first step was specimen collection at the study area. Rock coatings in the Kane Springs Wash area are very discontinuous, thus the strategy was to collect samples according to a qualitative scale:

Very heavy - 80% to 100% cover to the unaided eye.

Heavy   - 60% to 80% cover

Moderate   - 40% to 60% cover

Light   - 10% to 40% cover

Fresh   - Freshly broken, interior of the rock

Two sets of coatings collected with the above criteria were obtained from each major lithologic unit in the study area supporting rock coatings. Each sample was collected from a different part of the study area to insure data integrity.

The second step of the research methodology was to analyze the variably coated samples with mid-infrared spectrometers. A Fourier Transform Infra-Red (FTIR) spectrometer and the Portable Field Emission Spectrometer (PFES), both at the Jet Propulsion Laboratory, were used to measure the rock surfaces. Approximately 100 spectra were analyzed with the FTIR and 10 with the PFES. Fifty-nine of the FTIR spectra representing eleven lithologic units are presented in Appendix 12. The spectra are grouped according to rock type and are displayed from 6 um to 14 um. The most extensively coated sample appears at the bottom of each graph, and progressing upward, succeeding samples with decreasing extent of coating. The spectrum at the top of each graph is that of a freshly broken surface. Ten PFES spectra are presented in Appendix 13.

The third step is to analyze each group of spectra and determine what influence rock coatings have on the spectra of fresh rock surfaces. Step 3 is presented below.

The mineralogy of each rock type (Appendix 4) and the mineralogy of coatings found in the study area (Spatz, 1988) are known. Mineralogy is the dominant factor controlling the

position of reststrahlen bands, thus the interpretation of the reflectance spectra is based on published spectra of minerals (Salisbury et al., 1987). This spectral library is also advantageous since the spectra were measured with a biconical configuration, similar to that of the FTIR used for this project.

Table Two shows the spectral features found in the FTIR spectra of heavily coated samples. Comparison of the features at 8.8 um, 9.5 um, and 11.0 um with the Salisbury et al. (1987) spectral library shows a near match for these features with illite/smectite and nontronite clays. The illite/smectite spectral features are presented in Table Two for comparison with the FTIR data. Other diagnostic features for illite/smectite occur at 6.6 um and 7.2 um. These features may possibly exist in many of the study area spectra, but due to atmospheric effects (water absorption), they are masked. The absorption feature at 8.6 um is due to the remnant quartz influence in the spectra of the more felsic rocks. All of the spectra displaying the 8.6 um absorption feature contain quartz.

The match with illite/smectite conforms to the expected result, which is clay dominance in the spectra of coatings. The clay signature is significantly different than that of many of the fresh surfaces. The difference between the fresh rock reflectance peak and that of the coating was as great as 1.35 um for the Topaz rhyolite (KSW-9). The average difference was approximately 0.95 um for the five lithologies that showed significant deviations from the fresh spectra. Six of the

Table Two

Spectral Features
Found in Coated Sample Spectra (FTIR)

Feature	Samples
Shoulder/small peak at 8.2 um	1, 2, 5, 6, 7, 9, 12, 13, 25
Absorption at 8.6 um	1, 5, 9, 13, 25
Small shoulder at 8.8 um	2, 5, 9, 10, 13
Major peak at 9.5 um	All spectra
Small peak at 11.0 um	2, 5, 9, 10, 13

Illite/Smectite Spectral Features
(Packed surface, 35% illite; from Salisbury et al.,1987)

Small peak	6.6 um
Slight shoulder	7.2 um
Absorption	8.0 um
Shoulder	8.8 um
Major peak	9.4 um
Small peak	11.0 um

eleven units did not show a significant deviation of the coated rock spectra from that of the fresh. All six have large feldspar components (KSW-1, 10, 12, 13, 14, and 24, see Appendix 4), and only two of the six contain quartz, but in small quantities. The feldspars present in the study area rocks (orthoclase, sanidine, and plagioclase; anorthoclase not available) generally have a reflectance maximum near the major 9.5 um peak characteristic of clays (See Appendix 8).

Two sets of coated and fresh samples from the study area were analyzed by John Salisbury at the U.S. Geological Survey (USGS) in Reston, Virginia. The spectra were acquired at 4 cm^{-1} resolution using a Nicolet 5DXB reflectance spectrometer with an integrating sphere attachment. The directional hemispherical measurements (Figure 6) were analyzed using a spectral matching algorithm developed by Nicolet. A derivative method was utilized, which compares spectral curve changes rather than point by point comparison. The curves were then compared to the USGS mid-infrared spectral library. The best fits for the coated surfaces were illite/smectite and nontronite. These data support the conclusion of dominance of clay features in the coating spectra.

Spectra acquired with the Portable Field Emission Spectrometer (PFES) agreed, in general, with data collected with both of the reflectance spectrometers. However, the PFES did not have the resolution of the reflectance spectrometers, and the data were noisy.

The spectral data show that rock coatings, if present in sufficient quantity, can mask the signatures of the rock they coat. The effect of a clay-dominated signature is a shift in wavelength of the reststrahlen feature in the 8 to 12 um

region. Since the coating (clay) spectrum exhibits a reststrahlen feature near 9.5 um, some of the mafic lithology signatures measured with the TIMS will not be affected by a rock coating, even though the rock signature is masked. Generally, The most felsic (i.e. quartzites) and most mafic lithologies (i.e. dunites) will be affected most, since their emission minima occur at the low and high extremes of the 8 to 12 um window. Their reststrahlen features would be shifted to longer and shorter wavelengths, respectively.

The rock coatings in the Kane Springs Wash area are very discontinuous (Spatz, 1988) and are in a constant state of instability. Therefore, although coatings are present in mixed pixels, they do not completely mask the rock signatures found in the TIMS imagery of the Kane Springs Wash study area.
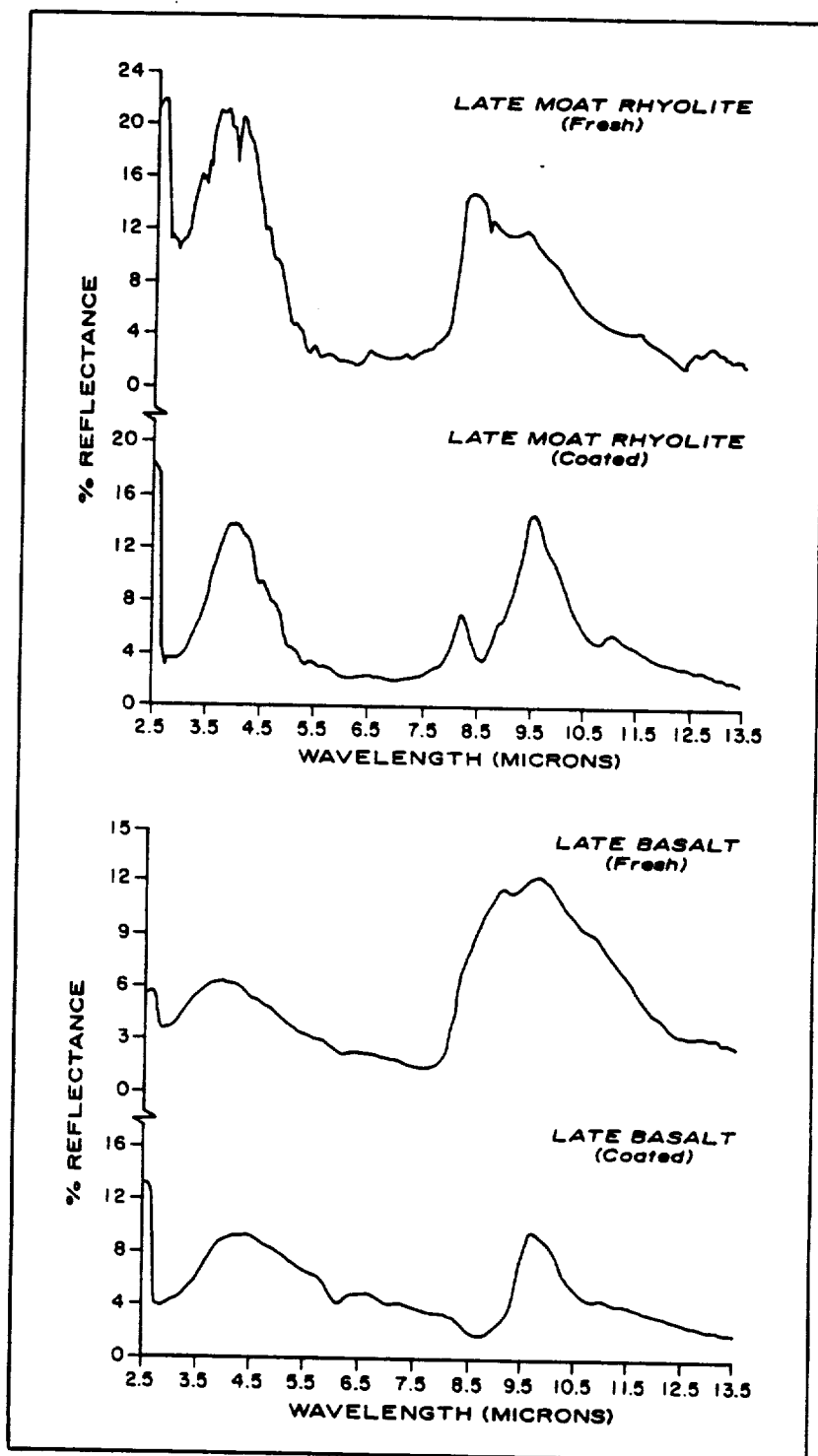
Figure 6. Directional hemispherical reflectance spectra of two sets of coated and fresh samples.

Chapter Five

The Effects of Vegetation on the Kane Springs Wash
TIMS Measurements

Introduction to the Vegetation Study

Chapter Seven is subdivided into two sections. The first section is a review of vegetation studies in the mid-infrared region. The second section is a study of the effects of vegetation on TIMS data of the study area.

Mid-infrared remote sensing studies of vegetation have, in the past, focussed primarily on temperature variations (Fuchs and Tanner, 1966; Goetz et al, 1983; Langran, 1985; Sader, 1985; Pelletier and Ochoa, 1985; Hatfield et al., 1986; Sabins, 1987). Gates and Tantraporn (1952) and Wong and Blevin (1967) first proved the existence of unique mid-infrared spectral features of plants, but with low spectral resolution reflectance data. Recent high-resolution spectral studies (Salisbury, 1986; Salisbury and Milton, 1988; Elvidge, 1988) have uncovered species-specific features and shown the possible usefulness of mid-infrared spectral (and possibly TIMS) data for plant species discrimination. The present study utilizes TIMS data to investigate the effects of vegetation on thermal infrared imagery acquired in a desert region.

Section I

Results of Previous Investigations

Most of the previous studies of vegetation in the thermal infrared have concentrated on canopy temperatures measured with broad bands in the 8 to 12 um window. Plants with high transpiration rates are cooler than ambient temperatures due to evaporative cooling of their leaves. Plants with low transpiration rates are warmer than those with high transpiration rates. Langran (1985) observed that surface temperatures are cooler over vegetated areas than over nonvegetated areas using daytime thermal infrared measurements, and that surface temperatures vary with percent vegetation cover. Sader (1985) noted that the TIMS appeared to be able to detect differences in surface temperature related to green leaf biomass. Pelletier and Ochoa (1985) found that diseased, water stressed, and maturing crops demonstrate a greater range in diurnal thermal response than unstressed vegetation. Day-night radiant temperature differences have been used to discern between green deciduous vegetation and soil (Sabins, 1987). Vegetation produces a cool signature relative to soil during the daytime, and a warmer signature at nighttime. A higher nighttime radiant temperature results from the insulating effect of vegetative cover and the high heat retention of water in leaves.

Spectral variations of vegetation found in the mid-infrared region are unlike those in the visible and near infrared. Visible and near-infrared spectra of green vegetation are dominated by chlorophyll and water absorptions, with variation between species being largely expressed as intensity

differences rather than as species specific absorptions. In contrast, species specific spectral features are being identified in the mid-infrared region (Salisbury, 1986; Salisbury and Milton, 1988), perhaps related to differences in the organic composition of the leaf cuticular layer.

Mid-infrared plant reflectance data were first published by Gates and Tantraporn (1952). Their biconical measurements were made in seven single wavelength bands between 3.0 and 25.0 um. The low spectral resolution of their instrument did not allow an accurate measurement of leaf spectral features. They reported reflectances of less than 10% for an angle of 65° for leaves in the region beyond 2.0 um. Wong and Blevin (1967) used seventeen bands between 2.0 and 14.0 um to measure the biconical reflectance of leaves. Again, the resolution was too low to accurately identify species-specific features, however, both Gates and Tantraporn (1952) and Wong and Blevins (1966) noted reflectances of less than 10% for all their samples.

Recent work with high resolution reflectance data has verified the presence of diagnostic spectral features of plants. Gates (1980) published leaf spectra of three species. No explanation of the leaf features or measurement technique was given, but he noted that the average reflectance was 0.01% for black spruce and 0.03% for broad leaf plants. Salisbury (1986) published biconical reflectance spectra of four plant species in the 8 to 14 um region. He hypothesized that reflectance peaks in mid-infrared leaf spectra were associated with strong hydrocarbon bands of the waxy cuticle superimposed on larger water absorption bands.

Elvidge (1988) published mid-infrared spectra of dry plant materials. The spectra were measured with biconical reflectance, as all the previous studies. The major contribution of this study was the presentation of spectra of individual organic compounds common to all plant material. Elvidge concluded that a basic ligno-cellulose spectrum existed for dry plant materials. This ligno-cellulose spectrum could be modified by the presence of compounds such as tannins or terpenes.

Nicodemus (1965) and Wong and Blevin (1967) show that only hemispherical reflectance measurements can be used to correctly calculate emissivity according to Kirchoff's Law (E = 1 - R). Biconical reflectance strongly biases the direction of primary reflection, while hemispherical reflectance allows a measurement of energy reflected over the total surface of the sample. The primary reflectance is not directionally biased in hemispherical data. Although theoretically incorrect, biconical reflectance spectra have been compared to emission measurements by Bartholomew et al. (1989), and a close approximation was found. Salisbury and Milton (1988) also compared biconical to hemispherical reflectance spectra and determined the two to be qualitatively the same.

Salisbury and Milton (1988) published the first directional hemispherical reflectance measurements of plants in the mid-infrared spectral region. Species-specific spectral features were found for six plant species (Figure 7). Reflectance features were attributed to the cuticular layer of the leaf, as Salisbury (1986) concluded.

Section II

Vegetation Effects on
TIMS Imagery

The TIMS has a noise equivalent temperature difference of $0.1^{\circ}C$ to $0.3^{\circ}C$ at $300^{\circ}K$ (Palluconi and Meeks, 1985). Kahle and Goetz (1983) showed that this sensitivity is equal to a noise equivalent emissivity change of 0.002 to 0.006. This means that an emissivity difference of 0.002 to 0.006 between surface materials at $300^{\circ}K$ will produce a signal change equal to system noise. Many hemispherical reflectance spectra of leaves show features with magnitude changes greater than 0.002 or 0.006 (Figure 7), thus emissivity variations of vegetation should be measurable with the TIMS, assuming canopy geometry does not reduce spectral contrast.

Vegetation in the Study Area

The study site ranges in elevation from approximately 3000 feet in the Kane Springs wash to near 7500 feet in the adjacent Delamar Mountains. Vegetation is stratified, from _Atriplex confertifolia_, _Ambrosia dumosa_, _Ceratoides lanata_, _Larrea tridentata_, _Yucca brevifolia_ and others in the washes to _Pinus monophylla_, _Juniperus osteosperma_, and _Artemisia tridentata_ in the mountains (see Appendix 9 for full listing of vegetation types, Figure 8 for a generalized vegetation map of the study area). Dense growth is found in the highest parts of the mountains. A Landsat Thematic Mapper color composite
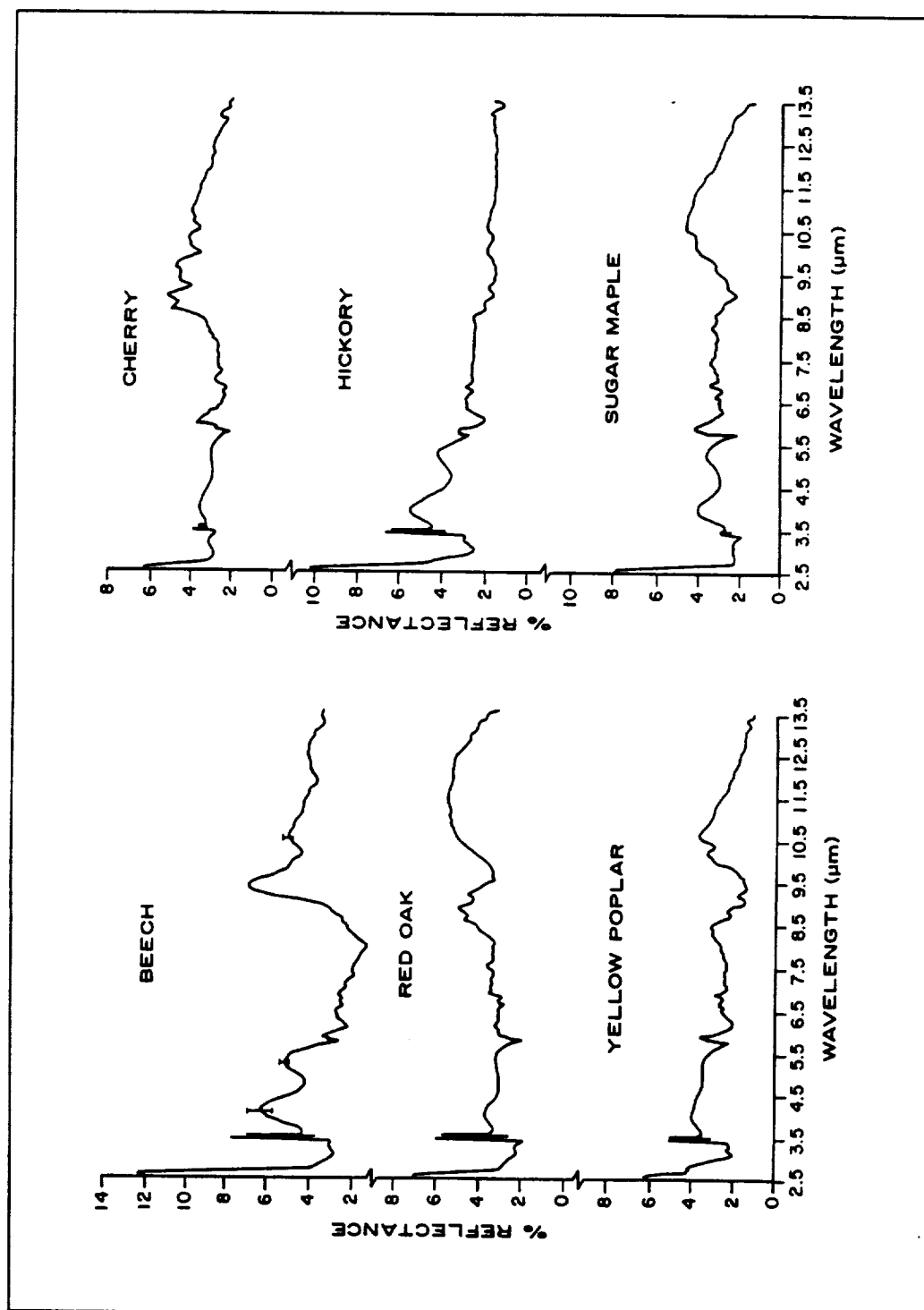
Figure 7. Directional hemispherical reflectance spectra of leaves of six different
broad-leafed tree species. Each spectrum is an average of the spectral
reflectance of at least ten leaves (from Salisbury and Milton, 1988).
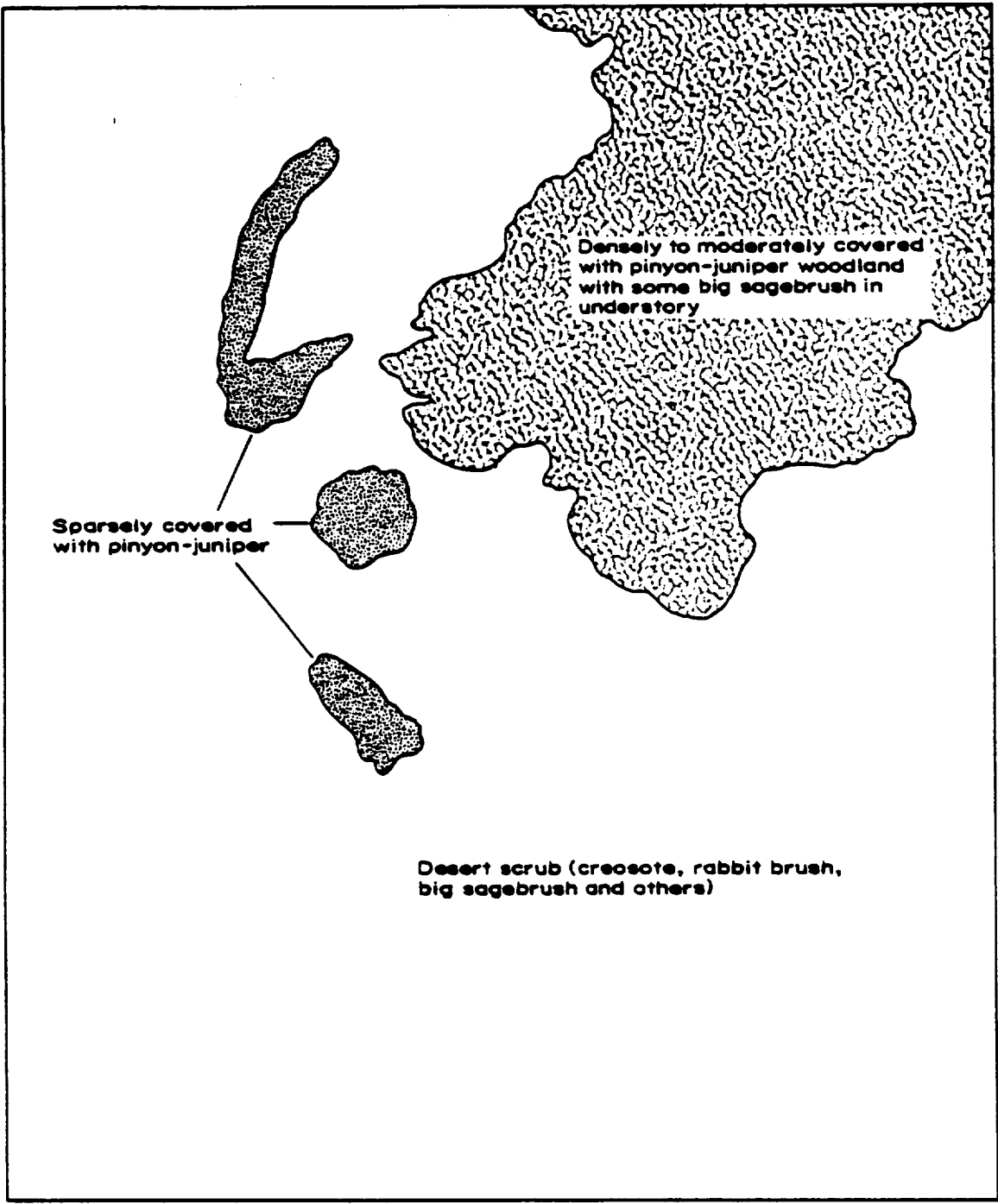
Figure 8. Generalized vegetation map of the study area.

and ratio image (Figures 9 and 10, respectively) show the location and relative amounts of vegetative cover over in the study area.

Interpretation of Vegetation Thermal Variations

Thermal response variations of vegetation in the study area were analyzed using calibrated TIMS data in integer format. Ten 3 x 3 pixel sites were chosen; five represent vegetation-influenced areas and five represent nonvegetated areas. Landsat imagery, color infrared aerial photography, and field reconnaissance were used as the basis for site selection. The representative vegetated / nonvegetated pixel pairs were chosen for their similarity in elevation, solar heating, and underlying lithology. Three lithologic units are represented by the five pairs: the Early Moat (ferroedenite) rhyolite, the Syenite complex, and a granite porphyry. Appendix 10 shows the means, standard deviations, and variances for each site in all six TIMS channels. Two statistical tests were performed on the data, an F-test (variance comparison), and a T-test (mean comparison).

An F-test was performed on each of the pairs in order to test the hypothesis:

$$H_o : (\text{variance 1} / \text{variance 2}) = 1.$$
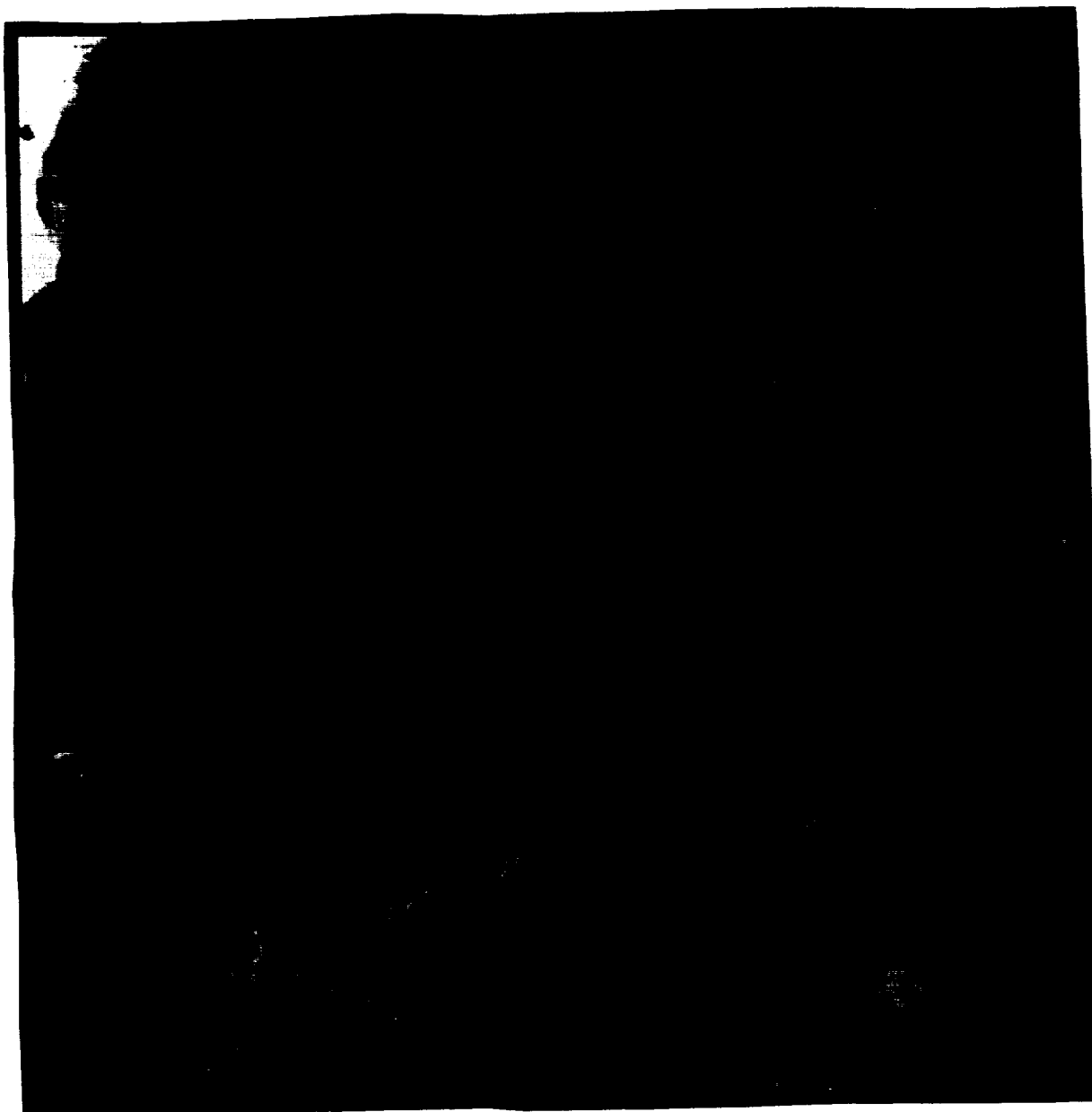
Figure 9. Landsat TM color composite (541 in
RGB) of the Kane Springs Wash area.
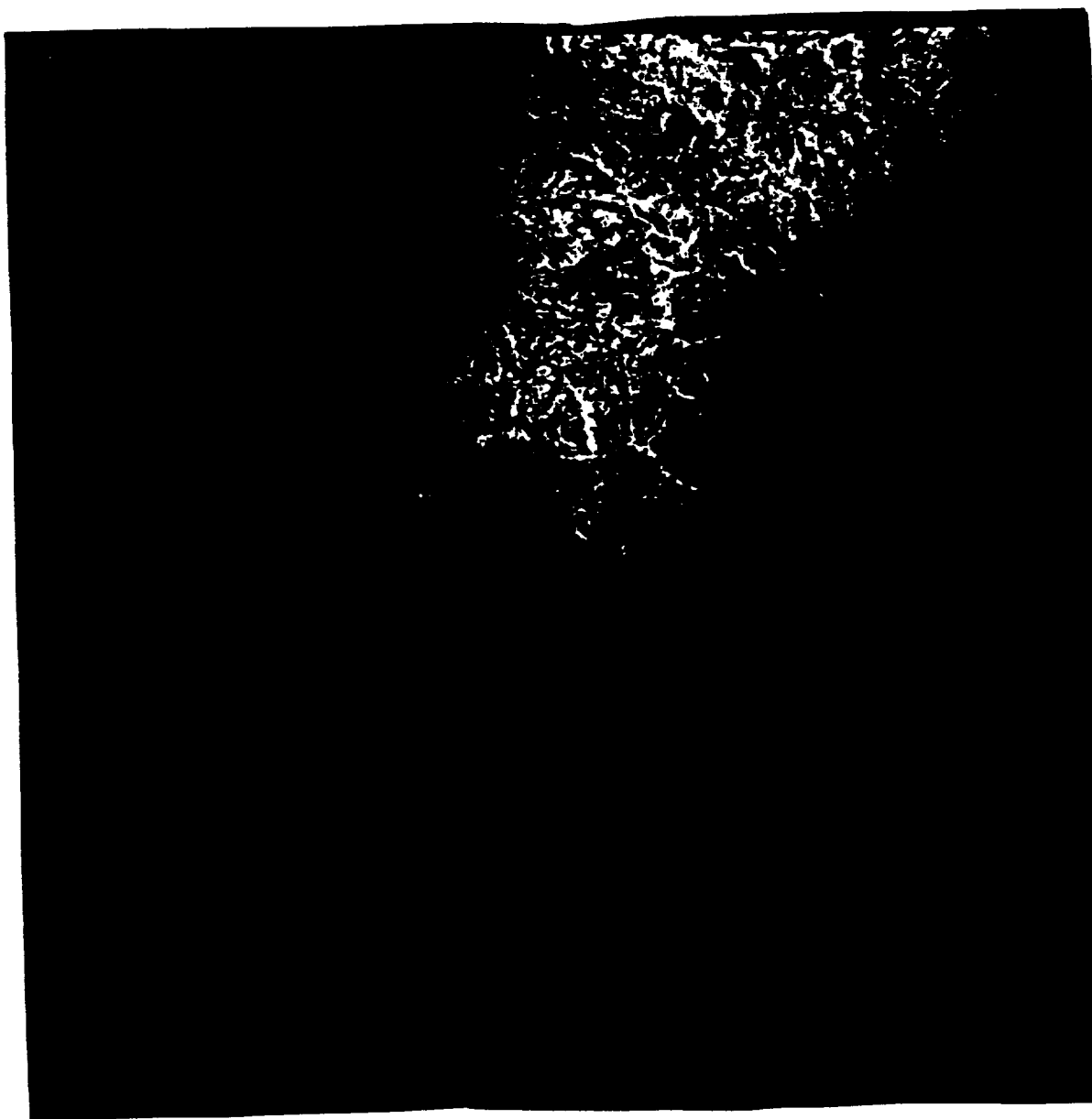
Figure 10. Landsat TM 4 / 3 ratio of Kane Springs
Wash study area.

H_o will be rejected in favor of

$$H_1 : (\text{variance 1} / \text{variance 2}) > 1$$

if (variance 1 / variance 2) > c, where c is defined as:

$$c = F_a (n-1, m-1).$$

The c value was obtained from a standard F distribution table at a 95% confidence level. The F-test data are presented in Appendix 10. The results of the F-test show that vegetated sites produce smaller variances relative to nonvegetated sites. The result is understandable, since nonvegetated areas consist of rock and soil, which produce a more variable signature than a vegetation canopy. The variances of some of the data were equal. Variances of the granite porphyry pairs, in particular, were not significantly different. This result may be due to the sparseness of vegetation on the granitic outcrops.

The brightness values for vegetated sites are generally lower than those for non-vegetated sites (Appendix 10). Empirically, vegetated areas should produce lower temperatures than non-vegetated areas due to evapotranspirative cooling, as shown by Langran (1985). Temperature is dominant in TIMS imagery, thus the calibrated data should be sensitive to vegetation evapotranspiration. The T-test was used to test the hypothesis that H_1: Mean (vegetated) - Mean (unvegetated) >

0, or that the means of the vegetated site data are significantly greater than those of the nonvegetated site data. Since the F-test showed that some variances were the same and some were different, two T-tests were used. The first T-test assumes the variances are different:

$$T = \frac{mean\ 1 - mean\ 2}{(Var\ 1\ /\ n\ +\ Var\ 2\ /\ m)^{1/2}}$$

$$Degrees\ of\ freedom = \frac{(Var\ 1\ /\ n\ +\ Var\ 2\ /\ m)^2}{\frac{(Var\ 1\ /\ n)^2}{n\ -\ 1}\ +\ \frac{(Var\ 2\ /\ m)^2}{m\ -\ 1}}$$

T_a was found in a standard T-test table using the calculated degrees of freedom and a 95% confidence level. The results of the first T-test are presented in Appendix 10.

The second T-test assumes that the variances are not different:

$$SP = \left[\frac{(n\ -\ 1)\ Var\ 1\ +\ (m\ -\ 1)\ Var\ 2}{(n\ +\ m\ -\ 2)}\right]^{1/2}$$

$$T = \frac{\text{Mean 1} - \text{Mean 2}}{SP (1 / n + 1 / m)^{1/2}}$$

Where   SP = Pooled standard deviation

T_a was found in the T-test table using the degrees of freedom calculated according to: n + m - 2 (= 16, since n = m = 9), with a 95% confidence level. The results of the second T-test are presented in Appendix 10.

The two T-tests showed that the means of the data are significantly different. Means in the first four channels of the Early Moat rhyolite 1 pair are the only exception. The exception is due to the unusually large variance difference between the vegetated and nonvegetated sites, which increases the denominator in the first T-test, and produces a low T value.

Interpretation of the Decorrelation Stretch Vegetation Signature

Vegetation appears to be affecting emission data measured in the highest parts of the study area. The dominant desert species in the higher parts of the Delamar Mountains are Pinus monophylla, Juniperus osteosperma, and Artemisia tridentata. These desert species possess needle clusters or small leaves, which produce multiple reflections of emitted energy within the canopies of individual plants (Salisbury and Milton,

1986). It is speculated that this multiple scattering will tend to make the plants appear to radiate as blackbodies. However, green leaves form only a small part of the volume and weight of the above ground biomass in the pinyon-juniper community. Wood and bark comprise the vast majority of the biomass in these areas. Thus the spectral signatures of wood and bark are key to interpreting the signature of vegetation in the decorrelation stretched TIMS image.

Spectra of dry plant material from desert species has been measured and published by Elvidge (1988). A selection of these spectra are presented in Figure 11. Reststrahlen features found in the 8 to 12 um region are due predominantly to ligno-cellulose. These features (reflectance maxima) occur consistantly near the 10.3 - 11.0 um region, which corresponds to TIMS channel 5. Elvidge's spectra were acquired with the same FTIR spectrometer used for the coating analysis in this paper (see Chapter Two). This instrument utilizes a biconical setup. The data, therefore, cannot be converted to emissivity in the most strict sense of Kirchoff's Law (E = 1 - R). However, a general interpretation of emissivity variations can be derived from the reflectance spectra. The Elvidge spectra show a low emissivity in what corresponds to TIMS channel 5. If the interpretation is carried even further, to the decor-relation stretch (531 in RGB), this would mean lower red values. Signatures that would normally be represented by yellow in the decorrelation stretch image (i.e. rhyolites) would appear green when covered with vegetation. This appears to be the case in the northern parts of the Delamar Mountains, where vegetation is masking what is mapped as rhyolite. Similarly, purple signatures (i.e. basalts) would appear blue. This also seems to correspond to image hues. Red hues, or signatures due to a dominance of tectosilicates in the rocks,

will appear dark. Various shades of these hues will appear in any image due to the variability of vegetative cover. More work on this subject is needed to confirm these preliminary findings.
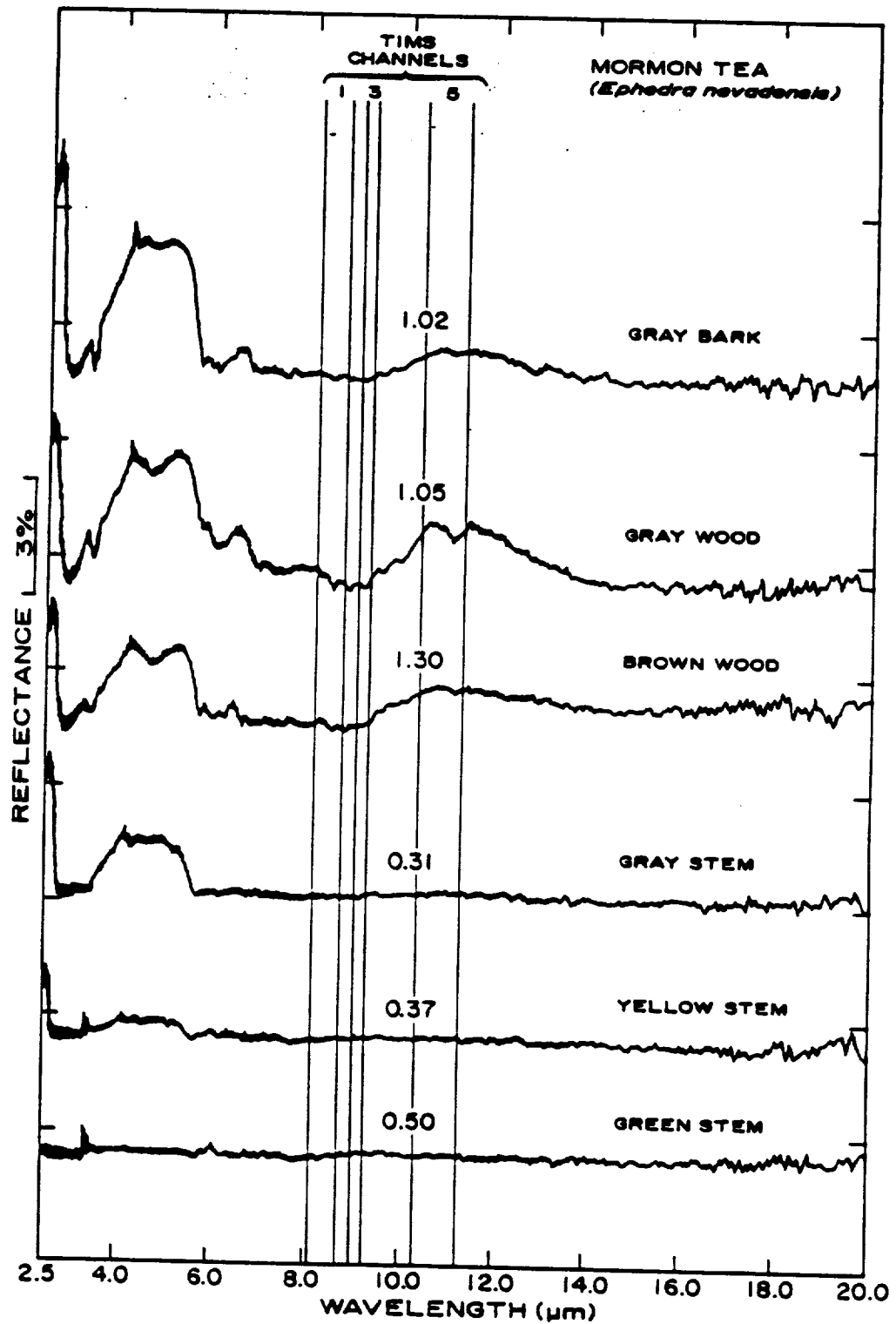
Figure 11.   Spectra of dry plant material (2.5 to 20.0 um) from three desert species: Mormon Tea, Big Sagebrush, and Pinyon Pine (Elvidge, 1988).
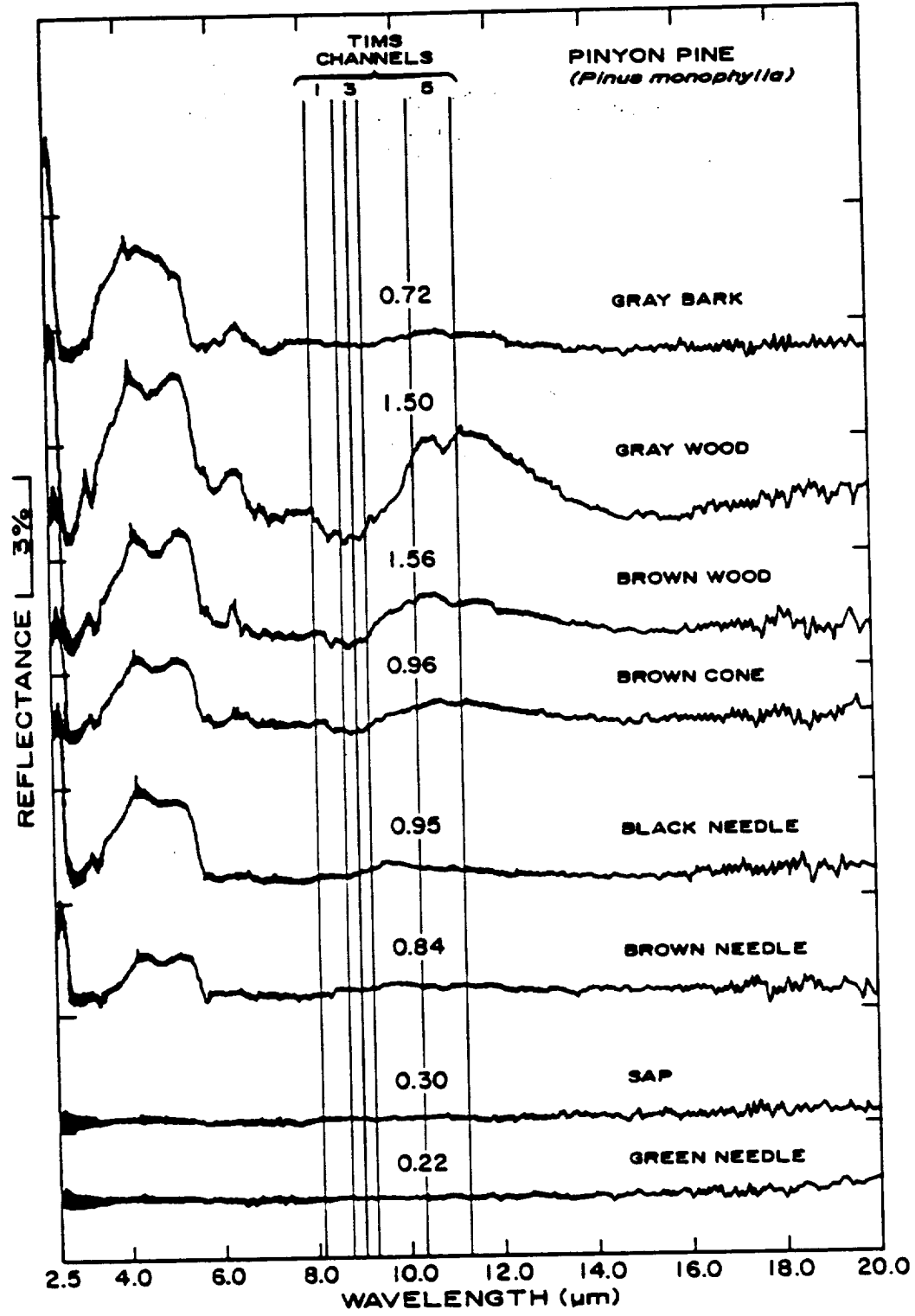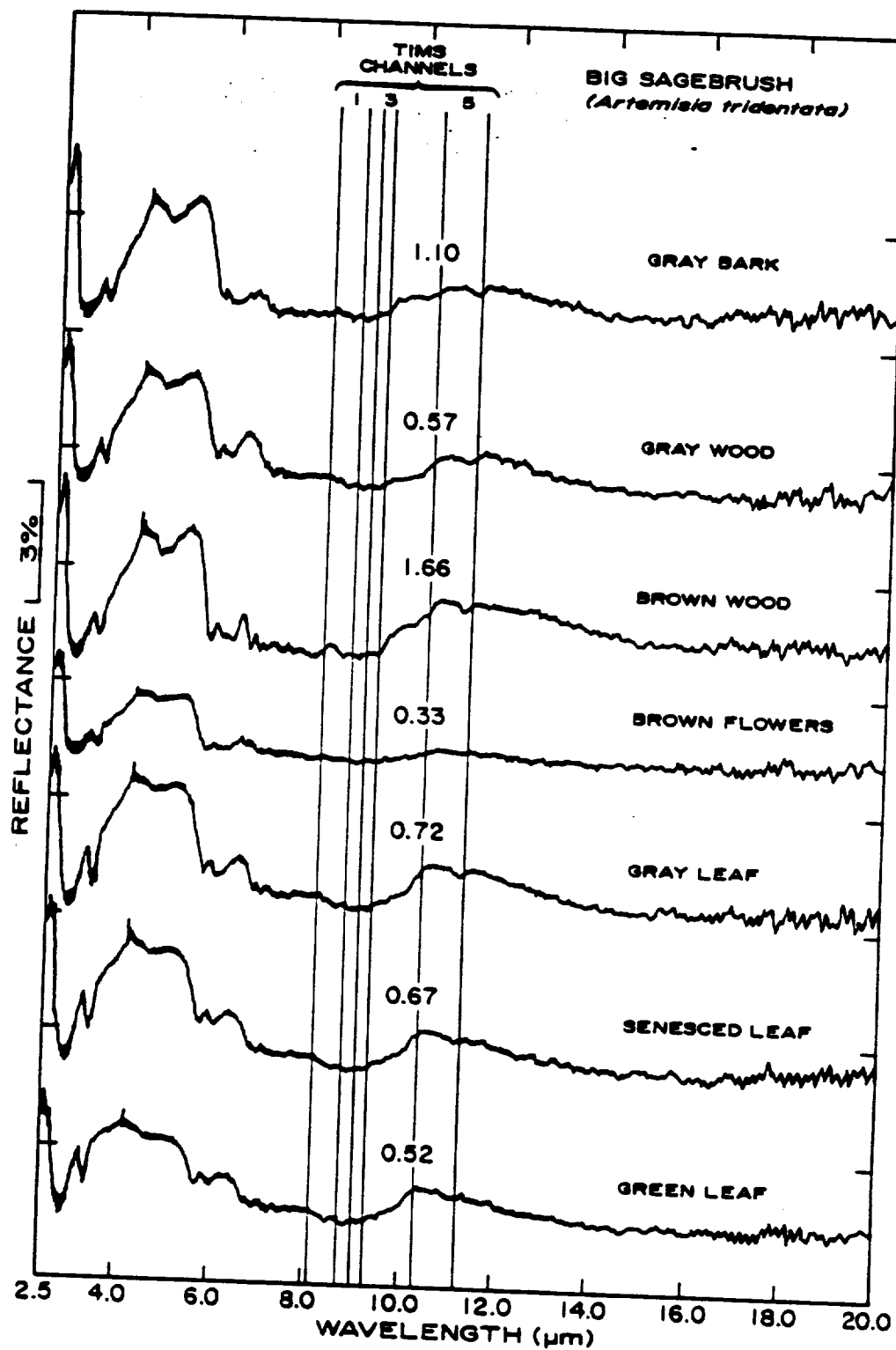
Figure 11, continued

Figure 11, continued

Chapter Six

Conclusions

TIMS imagery processed with a decorrelation stretch technique proved to be of assistance in geologic mapping of the study area. Several units not appearing on previous maps, notably a basalt, an ash-flow tuff, and 10 m thick sandstone interbeds in limestone were mapped with the thermal infrared imagery on a small scale.

Laboratory spectra of rock coatings obtained from volcanic rocks in the study area showed a dominance of spectral features attributed to illite/montmorillonite mixed-layer clays. When present in sufficient quantity, rock coatings can mask rock signatures measured with the TIMS by shifting the reststrahlen feature. The reststrahlen feature of rocks composed primarily of tectosilicates shifts to longer wavelengths, while the reststrahlen feature of rocks composed only of nesosilicates is predicted to shift to shorter wavelengths. Some mafic rocks, although completely coated, do not show spectral differences due to the close proximity of the reststrahlen features of the mafic minerals and the clays.

Mid-infrared studies of vegetation have, in the past, focussed on temperature variations. Vegetation-influenced pixels possess lower brightness values than non-vegetated pixels due to evapotranspirative cooling. Vegetated areas also produce smaller variances relative to nonvegetated areas. Discrepancy in the latter finding occurs when vegetation is sparse.

Vegetation, in the form of dry plant material, appears to be affecting emission data measured in the Kane Springs Wash study area. The effect is a lowering of the emissivity in TIMS channel 5 relative to channels 1 and 3. Units with sparse vegetation, which are yellow in the decorrelation stretched data (531 in RGB), such as rhyolites, appear green in more heavily vegetated areas due to the decreased red (channel 5) component. Basalt, which normally appears purple, has a brighter blue signature when covered with vegetation. Units with red hues appear darker when vegetation is present.

The TIMS is useful for reconnaissance geologic mapping on a small scale. The spatial resolution used for our flight (30 m) was high enough to discriminate small features, such as 10 m wide sandstone interbeds, in mixed pixels. Discrimination between compositionally distinct lithologies can be accomplished with TIMS, even if the differences are very subtle (i.e. between the Kane Wash tuff and the Hiko tuff).

The only drawback to the geologic use of the TIMS is the influence of vegetation on the imagery. Vegetation cover cannot exceed approximately 25% in order to observe lithologic variations using standard processing techniques. Such sparse vegetation cover occurs only in limited areas of the world (i.e. arid lands). Thus, the areas where TIMS can be used effectively for lithologic discrimination is restricted. However, vegetation influence may be removed in areas of moderate vegetation cover via a vegetation index formed with red and near infrared data (Elvidge, 1985). This could extend the areas over which multispectral thermal infrared data can be used for lithologic discrimination.

Rock coatings are not a major problem for lithologic discrimination in the Kane Springs Wash area. The coatings do not form a continuous veneer in southeastern Nevada. However, in certain regions of the world desert varnish is present over large portions of the available rock surfaces (i.e. the Australian shield) and could possibly pose a problem for satellite and aircraft thermal infrared data interpretation.

The TIMS proved to be a powerful tool for reconnaissance geologic mapping. However, the instrument could be improved by increasing the signal to noise ratio. A better signal to noise ratio would improve the decorrelation stretch image. The TIMS could also be improved by increasing the spectral resolution. Dominant mineralogical content of imagery units may be determined from high resolution emittance spectra using spectral matching algorithms similar to those employed for AVIRIS and AIS data.

The successful application of TIMS data for mapping lithologies and subtle mineralogic differences has paved the way for the development of plans to place multispectral thermal infrared sensors on NASA's first Polar Orbiting Platform (POP-1). The Jet Propulsion Laboratory is scheduled to build a Thermal Infrared Ground Emission Radiometer (TIGER), which will have 14 channels in the 3 to 13 um region. Japan is planning a Intermediate and Thermal Infrared Radiometer (ITIR), which will have channels similar to that of the TIMS. These instruments will permit multispectral thermal infrared data to be acquired in any area of the world and are expected to provide major advances in our capability to map lithologic units in a global manner.

References

Adams, J.B., Curtiss, B., and Shipman, H., 1984. Weathering processes, and remote sensing for mineral and rock types in the Goldfield-Cuprite area, Nevada; G.S.A. remote sensing field trip, Reno, Nevada, November, 1984.

Bartholomew, M.J., Kahle, A.B., and Hoover, G., 1989. Infrared spectroscopy (2.3 to 20 micrometers) for the geologic interpretation of remotely sensed multispectral thermal infrared data; International Journal of Remote Sensing, Vol.10, No.3, pp.529-544.

Buckingham, W.F., and Sommer, S.E., 1983. Mineral characterization of rock surfaces formed by hydrothermal alteration and weathering - application to remote sensing; Economic Geology, Vol.78, pp.664-674.

Chenevey, M.J., 1989. Geologic interpretation using thermal infrared imagery and the effects of vegetation and rock coatings on image interpretations; to be published in the proceedings of the ASPRS Image Processing '89 conference, May 1989, Reno, Nevada.

Chenevey, M.J., and Perry, J.J., 1989. Thermal infrared imagery applied as an aid in geologic mapping of a volcanic terrane; proceedings of the 1989 International Geoscience and Remote Sensing Symposium, Vancouver, B.C., July 10-14, 1989.

Christensen, P.R., Kieffer, H.H., Chase, S.C., and LaPorte, D.D., 1986. A thermal emission spectrometer for identification of surface composition from earth orbit; in Goward, S.N, Taranik, J.V., chairmen. Commercial applications and scientific research requirements for thermal infrared observations of terrestrial surfaces, Rpt. of the Joint EOSAT/NASA Thermal Infrared Working Group, NASA, Washington, D.C., and Earth Observation Satellite Co., Lanham, MD.

Cook, E.F., 1965. Stratigraphy of Tertiary volcanic rocks in eastern Nevada; Nev. Bur. Mines Geol., Vol.11, 61p.

Curtiss, B, Adams, J.B., and Ghiorso, M.S., 1985. Origin, development, and chemistry of silica-alumina rock coatings from the semi-arid regions of the island of Hawaii; Geochimica et Cosmochimica acta, Vol.49, pp.49-56.

Elvidge, C.D., 1979. Distribution and formation of desert varnish in Arizona; unpublished M.Sc. thesis, Arizona State University, 109p.

Elvidge, C.D., and Collet, C.J., 1981. Desert varnish in Arizona: distribution and spectral characteristics; in ASP technical papers, 80's era of change, Fall technical meeting, San Francisco, Sept. 9-11.

Elvidge, C.D., 1985. Separation of leaf water and mineral absorption in the 2.22 um Thematic Mapper band; unpublished PhD dissertation, Stanford University.

Elvidge, C.D., 1988. Thermal infrared reflectance of dry plant materials: 2.5-20.0 um; Rem. Sens. of Environ., Vol.25, pp.1-21.

Estep-Barnes, P.A., 1977. Infrared spectroscopy; in Physical Methods in Determinative Mineralogy, 2nd edition, J. Zussman, ed., Academic Press, New York.

Farr, T.G., and Adams, J.B., 1984. Rock coatings in Hawaii; Geol. Soc. Amer. Bull., Vol.95, pp.1077-1083.

Fuchs, M. and Tanner, C.B., 1966. Infrared thermometry of vegetation; Agronomy Journal, Vol. 58, pp. 597-601.

Gates, D.M., 1980. Biophysical Ecology, Springer-Verlag, New York, pp.235-238.

Gates, D.M., and Tantraporn, W., 1952. The reflectivity of deciduous trees and herbaceous plants in the infrared to 25 microns; Science, Vol.115, pp.613-616.

Gillespie, A.R., 1985. Lithologic mapping of silicate rocks using TIMS; in The TIMS Data User's Workshop, June 18 and 19, 1985, Kahle, A.B., and Abbott, E, eds., Jet Propulsion Laboratory Pub. 86-38, California Institute of Technology, Pasadena, Calif., pp.29-44.

Gillespie, A.R., Kahle, A.B., and Walker, R.E., 1986. Color enhancement of highly correlated images. I. Decorrelation and HSI contrast stretches; Rem. Sens. of Environ., Vol.20, pp.209-235.

Goetz, A.F.H, Rock, B.N., and Rowan, L.C., 1983. Remote sensing for exploration: an overview; Economic Geology, Vol.78, pp.573-604.

Hatfield, J., Carlson, T., Choudhury, B., Dozier, J., Gallo, K., Goward, S., Malila, W., Merritt, E., 1986. Evapotranspiration / Botany panel report; in Goward, S.N, Taranik, J.V., chairmen. Commercial applications and scientific research requirements for thermal infrared observations of terrestrial surfaces, Rpt. of the Joint EOSAT/NASA Thermal Infrared Working Group, NASA, Washington, D.C., and Earth Observation Satellite Co., Lanham, MD.

Hoover, G., and Kahle, A.B., 1986. A Portable Spectrometer for Use From 5 to 16 Micrometers; Jet Propulsion Laboratory Pub. 86-19, California Institute of Technology, Pasadena, Calif., 53p.

Hunt, G.R., 1980. Electromagnetic radiation: The communication link in remote sensing, in B.S. Siegal and A.R. Gillespie, (eds.), Remote Sensing in Geology, J. Wiley and Sons, New York, 702 p.

Hunt, G.R. and Salisbury, J.W., 1974. Mid-infrared spectral behavior of igneous rocks; Environ. Res. Paper 496-AFRCL-TR-74-0625, 142 p.

Hunt, G.R. and Salisbury, J.W., 1975. Mid-infrared spectral behavior of sedimentary rocks; Environ. Res. Paper 510-AFRCL-TR-75-0256, 49 p.

Hunt, G.R. and Salisbury, J.W., 1976. Mid-infrared spectral behavior of metamorphic rocks; Environ. Res. Paper 543-AFRCL-TR-76-0003, 67 p.

Kahle, A., Madura, D. and Soha, J., 1980. Middle Infrared Multispectral Aircraft Scanner Data: Analysis for Geologic Applications; Applied Optics, 19, p. 2279-2290.

Kahle, A.B., and Goetz, A.F.H., 1983. Mineralogic information from a new airborne thermal multispectral scanner; Science, Vol.222, pp.24-27.

Kahle, A.B., Christensen, P., Crawford, M., Cuddapah, P., Malila, W., Palluconi, F., Podwysocki, M., Salisbury, J., and Vincent, R., 1986. Geology panel report; in Goward, S.N, Taranik, J.V., chairmen. Commercial applications and scientific research requirements for thermal infrared observations of terrestrial surfaces, Rpt. of the Joint EOSAT/NASA Thermal Infrared Working Group, NASA, Washington, D.C., and Earth Observation Satellite Co., Lanham, MD.

Kahle, A.B., 1987. Surface emittance, temperature, and thermal inertia derived from Thermal Infrared Multispectral Scanner (TIMS) data for Death Valley, California; Geophysics, Vol.52, No.7, pp.858-874.

Kahle, A.B., Gillespie, A.R., Abbott, E.A., Abrams, M.J., Walker, R.E., Hoover, G., and Lockwood, J.P., 1989. Relative dating of Hawaiian lava flows using multispectral thermal infrared images: a new tool for geologic mapping of young volcanic terranes; Journ. of Geophys. Res., Vol.93, No.B12, pp.15,239-15,251.

Langran, K.J., 1985. Monitoring vegetation recovery patterns on Mount St. Helens using thermal infrared multispectral data; in The TIMS Data User's Workshop, June 18 and 19, 1985, Kahle, A.B., and Abbott, E, eds., Jet Propulsion Laboratory Pub. 86-38, California Institute of Technology, Pasadena, Calif., pp.53-54.

Lyon, R.J.P., 1965. Analysis of rocks by spectral infrared emission (8 to 25 microns); Economic Geology, Vol.60, pp. 715-736.

Lyon, R.J.P, and Green, A.A., 1975. Reflectance and emittance of terrain in the mid-infrared (6 to 25 um) region; in Infrared and Raman Spectroscopy of Lunar and Terrestrial Minerals, C. Karr, (ed.), Academic Press, New York, 375 p.

Nash, D.B., 1986. Mid-infrared reflectance spectra (2.3 - 22 micrometers) of sulfur, gold, KBr, MgO, and halon; Applied Optics, Vol.25, pp.2427-2483.

Nicodemus, F.E., 1965. Directional reflectance and emissivity of an opaque surface; Applied Optics, Vol.4, No.7, pp.767-773.

Noble, D.C., 1968. Kane Springs Wash volcanic center, Lincoln county, Nevada; in Nevada Test Site, Geol. Soc. Amer. Mem. 110, E.B. Eckel (ed.), pp. 109-116.

Novak, S.W., 1984. Eruptive history of the rhyolitic Kane Springs Wash volcanic center, Nevada; Journal of Geophysical Research, Vol.89, pp. 8603-8615.

Novak, S.W., 1985. Geology and geochemical evolution of the Kane Springs Wash volcanic center, Lincoln county, Nevada; unpublished PhD dissertation, Stanford University.

Palluconi, F.D. and Meeks, G.R., 1985. Thermal Infrared Multispectral Scanner (TIMS): An investigator's guide to TIMS data; Jet Propulsion Lab. Publ. 85-32.

Pelletier, R.E, and Ochoa, M.C., 1985. Applications of TIMS data in agricultural areas and related atmospheric considerations; in The TIMS Data User's Workshop, June 18 and 19, 1985, Kahle, A.B., and Abbott, E, eds., Jet Propulsion Laboratory Pub. 86-38, California Institute of Technology, Pasadena, Calif., pp.57-58.

Podwysocki, M.H., Brickey, D.W., and Salisbury, J.W., 1987. Remote compositional mapping of rocks using reflected and emitted radiance; in Summaries of the fifth thematic conference: Remote sensing for exploration geology, Reno, Nevada, p.122-123.

Potter, R.M., and Rossman, G.R., 1977. Desert varnish: the importance of clay minerals; Science, Vol.196, pp.1446-1448.

Potter, R.M., and Rossman, G.R., 1979a. The manganese- and iron- oxide mineralogy of desert varnish; Chemical Geology, Vol.25, pp.79-94.

Potter, R.M., and Rossman, G.R., 1979b. Mineralogy of manganese dendrites and coatings; American Mineralogist, Vol.64, pp.1219-1226.

Sabins, F.F., 1987. Remote sensing - principles and interpretation: San Francisco, W.H. Freeman, 449p.

Sader, S.A., 1985. Investigation of forest canopy temperatures recorded by the thermal infrared multispectral scanner at H.J. Andrews Experimental Forest; in The TIMS Data User's Workshop, June 18 and 19, 1985, Kahle, A.B., and Abbott, E, eds., Jet Propulsion Laboratory Pub. 86-38, California Institute of Technology, Pasadena, Calif., pp.57-58.

Salisbury, J.W., 1986. Preliminary measurements of leaf spectral reflectance in the 8-14 um region; Int. Jour. of Remote Sensing, Vol.7, pp.1879-1886.

Salisbury, J.W., Walter, L.S., and Vergo, N, 1987. Mid-infrared (2.1 - 25 micrometers) spectra of minerals: First Edition; USGS Open File Report 87-263.

Salisbury, J.W., and Milton, N.M, 1986. Spectral reflectance of tropical plant leaves in the 8-14 um region; in Summaries of the fifth thematic conference: Remote sensing for exploration geology, Reno, Nevada, p.16.

Salisbury, J.W., and Milton, N.M., 1988. Thermal infrared (2.5- to 13.5-um) directional hemispherical reflectance of leaves; Photogram. Eng. and Remote Sensing, Vol.54, No.9, pp.1301-1304.

Salisbury, J.W., Walter, L.S., and D'Aria, D., 1988. Mid-infrared (2.5 to 13.5 um) spectra of igneous rocks; USGS Open File Report 88-686.

Scott, R.B., Swadley, W.C., and Novak, S.W., 1988. Preliminary geologic map of the Delamar Lake quadrangle, Lincoln county, Nevada; USGS Open File Report 88-576.

Soha, J.M. and Schwartz, A.A., 1978. Multispectral histogram normalization contrast enhancement; Proc. 5th Canadian Symposium on Remote Sensing, Victoria, BC, Canada, pp.86-93.

Spatz, D.M., 1988. Genetic, spectral, and Landsat Thematic Mapper imagery relationships between desert varnish and tertiary volcanic host rocks, Southern Nevada; un-published PhD dissertation, University of Nevada-Reno.

Tschanz, C.M, and Pampeyan, E.H., 1970. Geology and mineral deposits of Lincoln county, Nevada; Nev. Bur. Mines Bull. 73, 187 p.

Vincent, R.K. and Thompson, F., 1972. Spectral compositional imaging of silicate rocks; Journal of Geophysical Research, 77, pp.2465-2472.

Vincent, R.K., Rowan, L.C., Gillespie, R.S., and Knapp, C., 1975. Thermal infrared spectra and chemical analyses of twenty-six igneous rock samples; Remote Sensing of Environment, 4, pp. 199-209.

Walter, L.S., and Salisbury, J.W., 1989. Thermal infrared (8 to 12 um) spectral characterization of igneous rocks; submitted for publication.

Watson, K., 1973. Periodic heating of a layer over a semi-infinite solid; Jour. of Geophys. Res., Vol.78, N.26, pp.5904-5010.

Wong, C.L., and Blevin, W.R., 1967. Infrared reflectances of plant leaves; Australian Jour. of Biol. Sci., Vol.20, pp.501-508.

Appendix One

The TIMS Instrument
Specifications for the 9-14-87 Overflight
of the Kane Springs Wash Area

(Partly from Palluconi and Meeks, 1985)

Number of channels 6

Channel locations .... CH1 8.11 - 8.55 um

    (for 8-26-87)   CH2 8.58 - 8.96 um

                             CH3 9.00 - 9.25 um

                             CH4 9.66 - 10.15 um

                             CH5 10.33 - 11.13 um

                             CH6 11.28 - 11.55 um

Channel sensitivity (NedT) .... $0.1\ ^{\circ}C$ to $0.3\ ^{\circ}C$

Field of view .... 76°

Instantaneous field of view ...... 2.5 mrad

Pixel size (GIFOV) .... appx. 28 m

Reference sources .... Low: $10\ ^{\circ}C$

                                  High: $45\ ^{\circ}C$

Altitude (AMT) .... 39,600 ft

Time of day (flight) .... 11:00 am PST

Operator of Lear Jet .... NSTL

Appendix Two

Image Processing

Calibrated TIMS data was acquired from the Jet Propulsion Laboratory. All subsequent image processing was performed on the Mackay School of Mines Vax 11/780-based Interactive Digital Image Manipulation System (IDIMS) software. Figure A shows the calibrated TIMS data (531 in RGB) before enhancement. The image data was compressed at the ends of the scan lines as a consequence of the large field of view (approximately 76°) of the TIMS instrument. A panoramic correction was applied to the image using the IDIMS function SCANFIX. A decorrelation stretch technique (Soha and Schwartz, 1978; Gillespie et al., 1986) is used to discriminate lithology in the TIMS image. This technique is explained below.

The Decorrelation Stretch

The original TIMS data is highly correlated (Figure B). Color composites and contrast stretching techniques usually employed with moderately correlated data, such as that of Landsat, are of no use with TIMS data in RGB space. A decorrelation stretch technique employs principle components to enhance subtle differences in the imagery. An IDIMS session of the decorrelation stretch technique is presented at the end of this appendix. Bands 1, 3, and 5 were used for the present analysis.

Figure A. Calibrated TIMS data (531 in RGB) before the
decorrelation stretch.
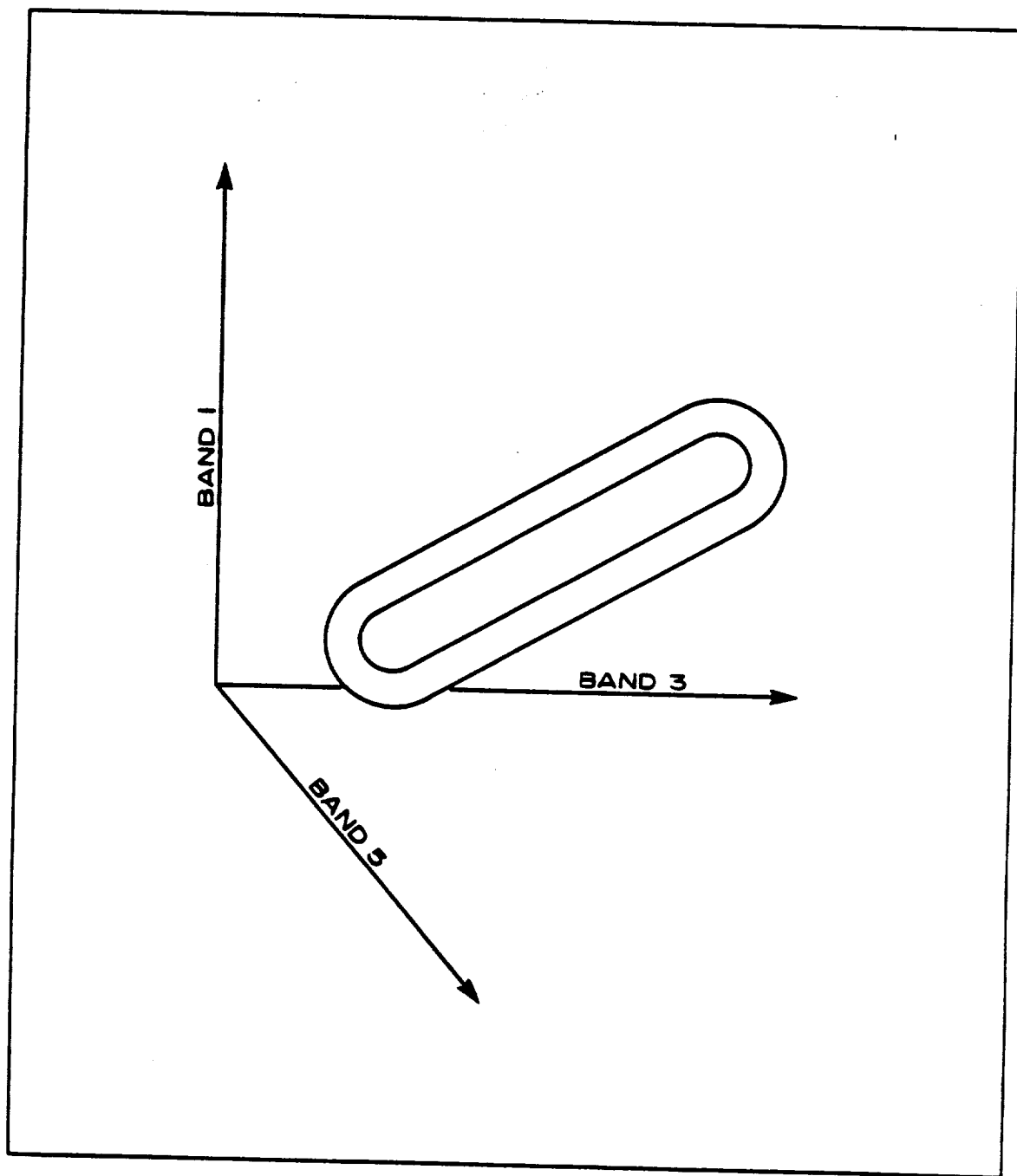
Figure B.   Ideal representation of the original three channels of TIMS data.

The initial step is the Karhunen-Loeve (principle components) transformation, which is applied to the original three bands of data. Principle components (PC) space is represented in Figure C. The axis with the highest variance is assigned to PC 1. The axes with the second and third highest variances are assigned to PC 2 and PC 3, respectively. Each axis is mutually perpendicular to the last. The IDIMS function KLTRANS (Karhunen-Loeve Transformation) uses a statistics file calculated with the IDIMS function ISOCLS. The statistics file consists of a 3 x 3 covariance matrix (for three bands) which displays the variance of the data along the diagonal. KLTRANS uses the covariance matrix to determine eigenvalues and eigenvectors and produces a 5 x 3 matrix:

		Band 1	Band 3	Band 5
		Mean 1	Mean 3	Mean 5
Eigenvalues:		EV 1	EV 2	EV 3
Eigenvectors:	PC 1	EVR 1	EVR 2	EVR 3
	PC 2	EVR 1	EVR 2	EVR 3
	PC 3	EVR 1	EVR 2	EVR 3

Eigenvalues (EV) are simply the values of the PCs; the highest eigenvalue corresponds to the first PC. Eigenvectors (EVR) are "weighting factors" applied to the PCs derived from the bands with the most variance. Note that the PC transformation subtracts the means of the original data in order to center the data cluster about the origin. The PC's are calculated as follows:
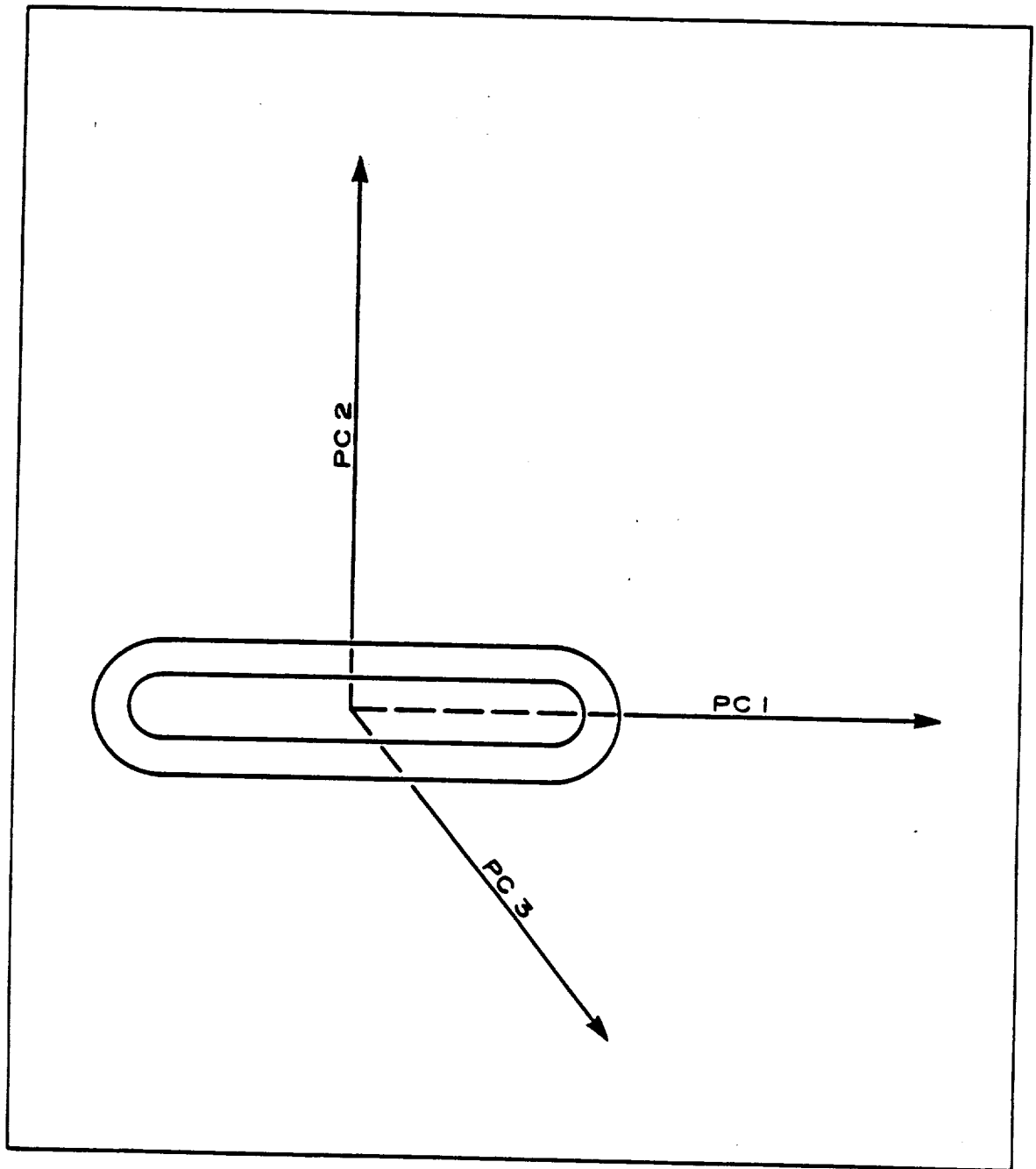
Figure C. TIMS data after principle components transformation.

Appendix Two, continued

PC 1 (pixel 1) = EVR 1 (DN 1) + EVR 2 (DN 2) + EVR 3 (DN 3)

      Where   DN 1 = The first pixel value in channel 1

                     DN 2 = The first pixel value in channel 3

                     DN 3 = The first pixel value in channel 5

This procedure takes place for every pixel in the original data to produce the PC 1 data set. PC's 2 and 3 are calculated using the same method.

A gaussian stretch is applied to PC 2 and PC 3 in order to equalize the variance of each to PC 1 (temperature). PC 1 is not stretched because temperature does not need to be enhanced in the image. This step is shown ideally in Figure D. Stretching PC 2 and PC 3 enhances noise inherent in the higher order principle components. A filter was convolved with PC2 and PC3 in order to remove horizontal striping in the images:

                0 0 0
                1 1 1
                0 0 0

The next step is to return to RGB space via a reverse PC transformation, which is applying the PC transformation a second time. The PC transformation always subtracts the means. This step is to be avoided in the reverse PC transformation, thus the means (set to zero), and the transposed transformation matrix (consisting of eigenvectors) are entered by hand. The original means are added back in when the reverse PC transformation is finished in order to shift the data cluster back to its original position (Figure E). The final product is shown in Figure 3, Chapter Three (5 3 1 in RGB).
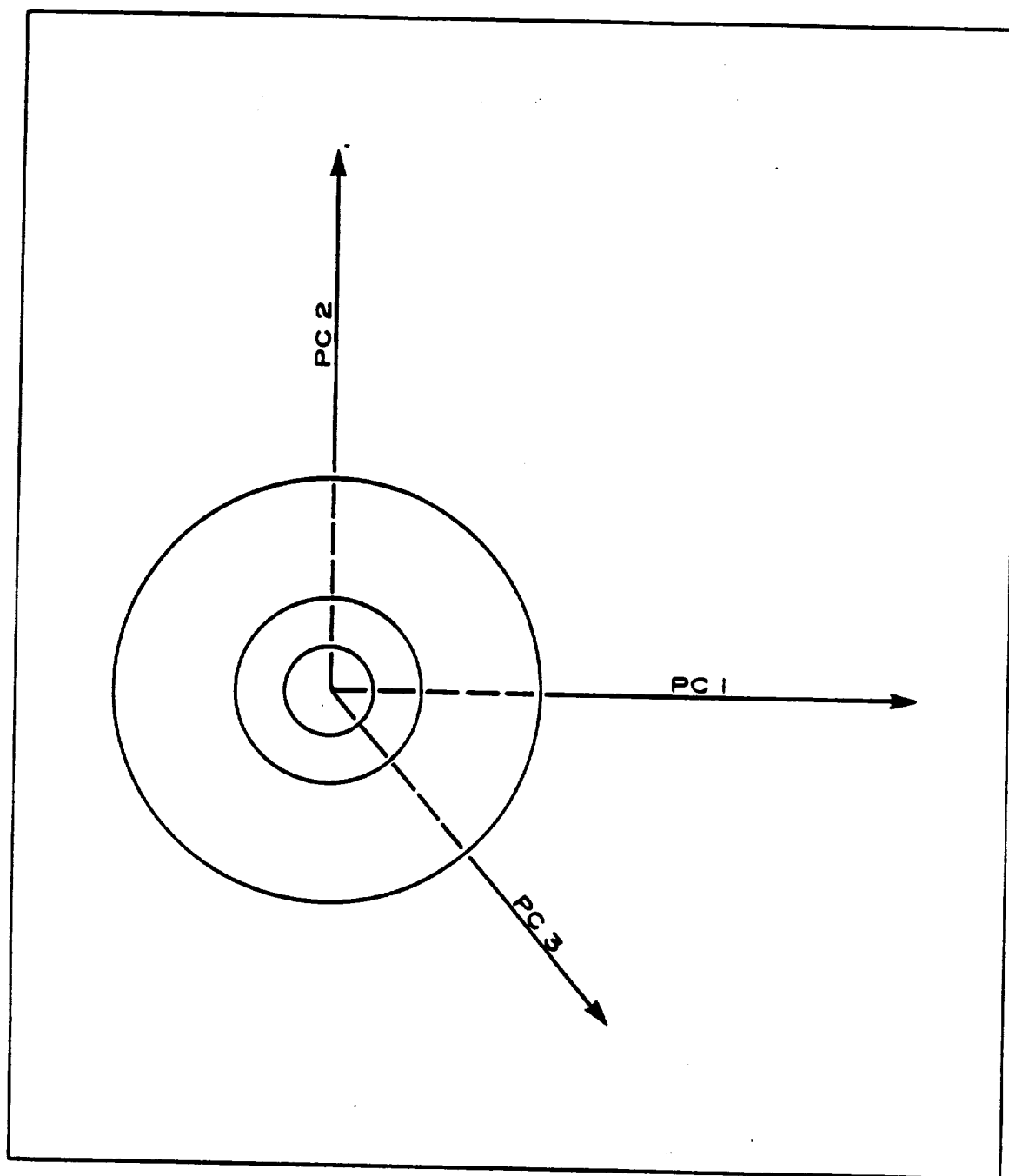
Figure D.   Ideal product of the gaussian stretch
of principle components 1, 2, and 3.
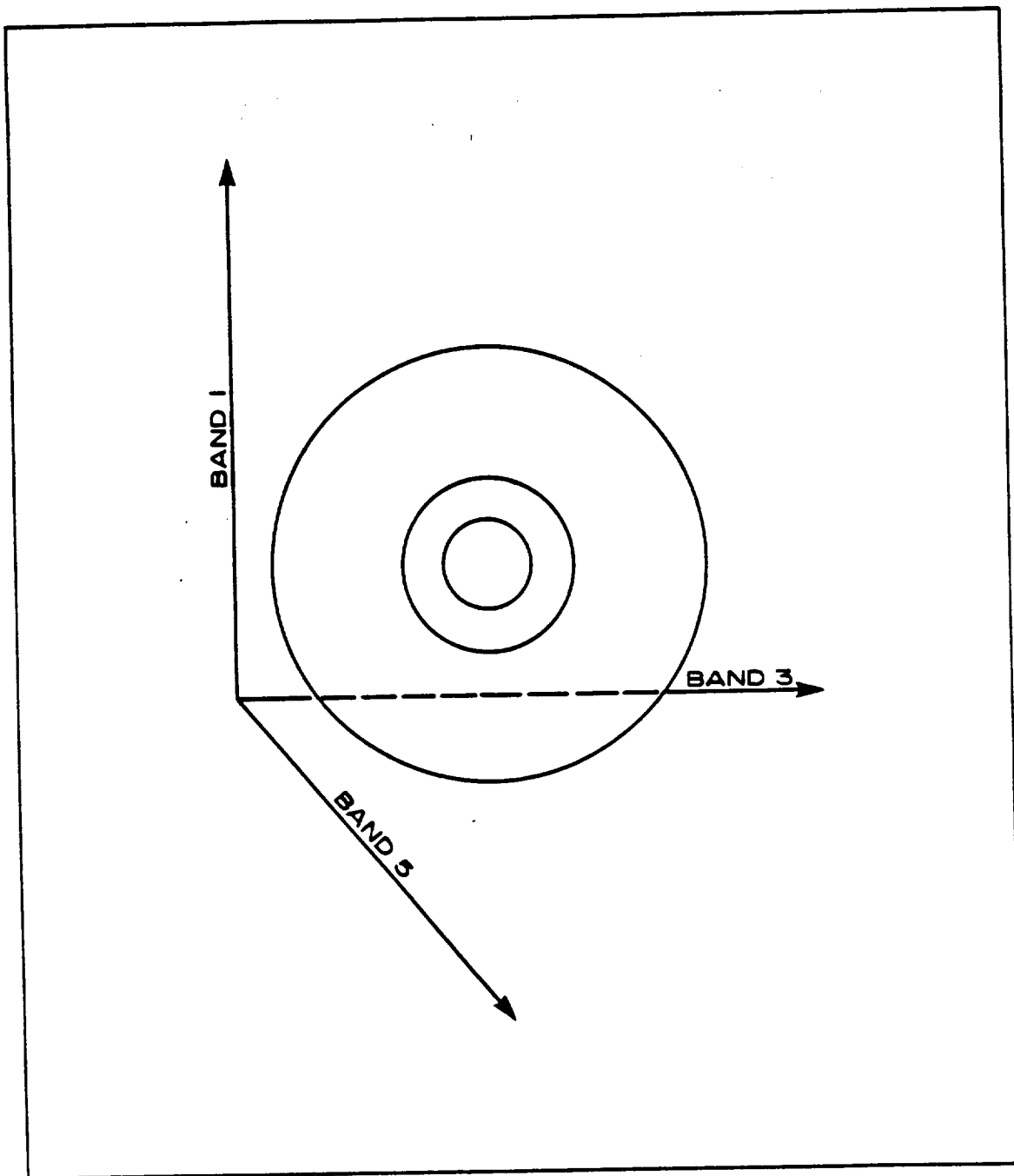
Figure E. Ideal product of the reverse principle components transformation. Note means added back in.

Appendix Two, continued

The Decorrelation Stretch Procedure

Input > ISOCLS
   ISTOP = 0

          * ISOCLS calculates statis-
            tics for the image "Input"

Input > KLTRANS > Input.PC Tmat
   Nbands = 3
   Datatype = 4

          * KLTRANS is the forward
            PC transformation

Input.PC > REDIST > Input.GAU
   Shape = Gauss
   Outype = Same

          * REDIST is used to stretch
            the PCs in order to
            equalize their variances

Input.GAU > KLTRANS > Rpcout
   Tsource = Term
   Nbands = 3
   Means: 0.0 0.0 0.0
   Tmatrix: T (1,1) > T (1,3)
          T (2,1) > T (2,3)
          T (3,1) > T (3,3)

          * "Reverse" principle
            components transformation

          * Since the means are
            subtracted by the KLTRANS
            function, want to
            specify 0.0 mean values

          * The transposed transfor-
            mation matrix is input
            by hand

> CONSTANT > Mean1
   Datatype = 4

          * Constant images are created
            in order to add the means

Appendix Two, Continued

```
Bands = 1                         back into the image data
NL = XXX                          (this is done for all three
NS = XXX                          bands)


Rpcout [1] Mean1 > ADD > Meanadd  * The means are added back
                                    in (this is done
                                    for all three bands)
Meanadd1 ... > UNITE > Unitemeans


Unitemeans > SCALE > Output       * The image is scaled
                                    and converted to byte
                                    format
```

Appendix Three

Thermal Infrared Considerations

All radiation contacting a surface is either reflected, absorbed, or transmitted into the material. This relationship is shown by Kirchoff's Law, which states:

$$\text{Reflectivity + absorptivity + transmissivity} = 1.$$

Transmissivity is negligible for an optically thick material, such as rock, so the formula can be reduced to:

$$\text{Reflectivity + absorptivity} = 1.$$

Therefore, a material with a high reflectivity will have a low absorptivity and thus a low emissivity at thermal infrared wavelengths.

Thermal infrared emission data are dominated by temperature and, to a lesser degree, by emissivity. Emissivity is a property of all materials, and is a measure of the ability of a material to absorb or emit radiation. A perfect absorber and emitter of thermal infrared radiation is known as a blackbody.

Appendix Three, continued

The radiant spectral emittance of a blackbody is defined by the Stefan-Boltzmann law:

$$W(bb) = \sigma T^4 ,$$

Where

W(bb) = Radiant spectral emittance of a blackbody

σ = Stefan-Boltzmann constant = 5.67×10^{-12} W cm^{-2} K^{-4}

T = Kinetic temperature, in degrees kelvin.

Emissivity is defined by the equation:

$$e = W(rb) : W(bb),$$

where

e = Emissivity

W(rb) = Radiant spectral emittance of a realbody.

Therefore, the radiant spectral emittance of a real body is:

$$W(rb) = e \; \sigma T^4$$

Appendix Three, continued

Everything above absolute zero emits radiation. The wavelength of maximum emission depends on the temperature of the object (Figure G). This relationship is shown by Wien's Displacement Law, which states the following:

Wavelength of maximum emission = 2987.4 um ^{O}K / T^O K

where   Wavelength = Wavelength of maximum emittance, in micrometers

T = Temperature of the object, in degrees kelvin

2897.4 = Wien's constant

Atmospheric Considerations

Atmospheric gasses such as hydrogen and oxygen absorb and emit radiation in the mid-infrared region. The 8 to 12 um region of the mid-infrared is least affected by atmospheric gasses (Figure H), and therefore is of most use for remote sensing applications. Water absorption near 8.3 um and ozone absorption near 9.8 um (Gillespie, 1985) are the only distractions in the 8 to 12 um window. Through this window, emission of photons from the earth's surface can be measured.

Appendix Three, continued

Mid-Infrared Mineral Spectra

The 8 to 12 um portion of the electromagnetic spectrum corresponds to the region of fundamental Si-O vibrational frequencies. These vibrations affect the emissivity of minerals, which is wavelength dependant. Emissivity minima over a given wavelength range are referred to as reststrahlen features. The features occur in different parts of the spectrum depending on the strength of the silicate bonds, reflected in the degree of polymerization of the Si-O tetrahedra (Lyon, 1965; Lyon and Green, 1975).

Weaker overtone and combination tone bands caused by interfering fundamentals are present in the thermal infrared wavelength region, but affect measurements much less and occur at wavelengths shorter than the unhindered fundamental bands (Salisbury et al., 1987). Strong Si-O bonds possess high vibrational frequencies, thus reststrahlen minima occur in the shorter wavelength portions of the spectrum. Tectosilicates, (i.e. quartz), the strongest-bonded of silicate structures, tend to display emissivity minima near 9 um, and nesosilicates (isolated tetrahedra), the weakest-bonded of the silicates, display minima near 11 um (Estep-Barnes, 1977). Variations in reststrahlen minima exist between tectosilicates. Quartz, for instance, has a shorter wavelength minimum than feldspar (Gillespie, 1985). This difference is due to the presence of divalent cations in the feldspars (Walter and Salisbury, 1989).
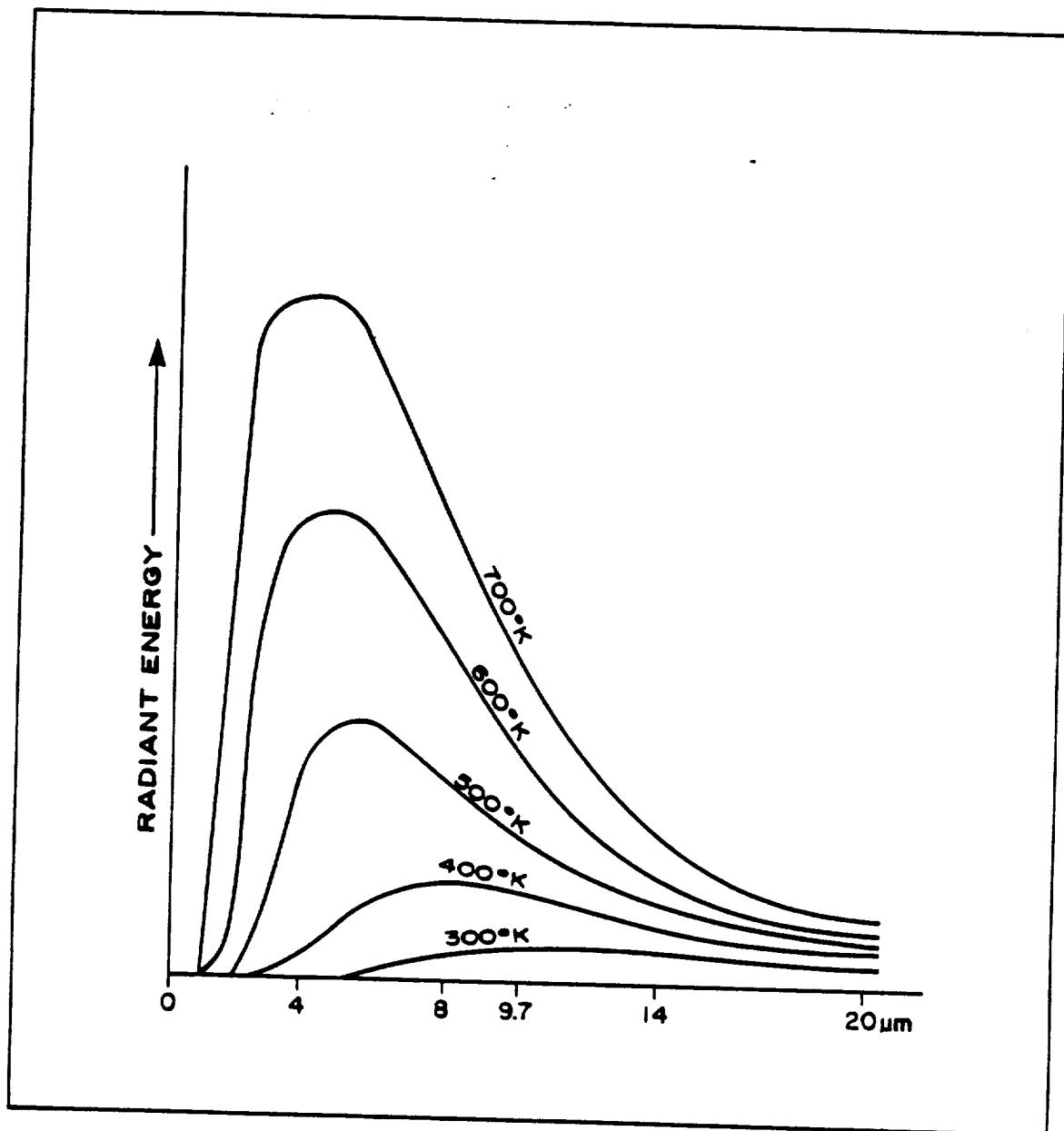
Figure G.   Planck blackbody curves.

85
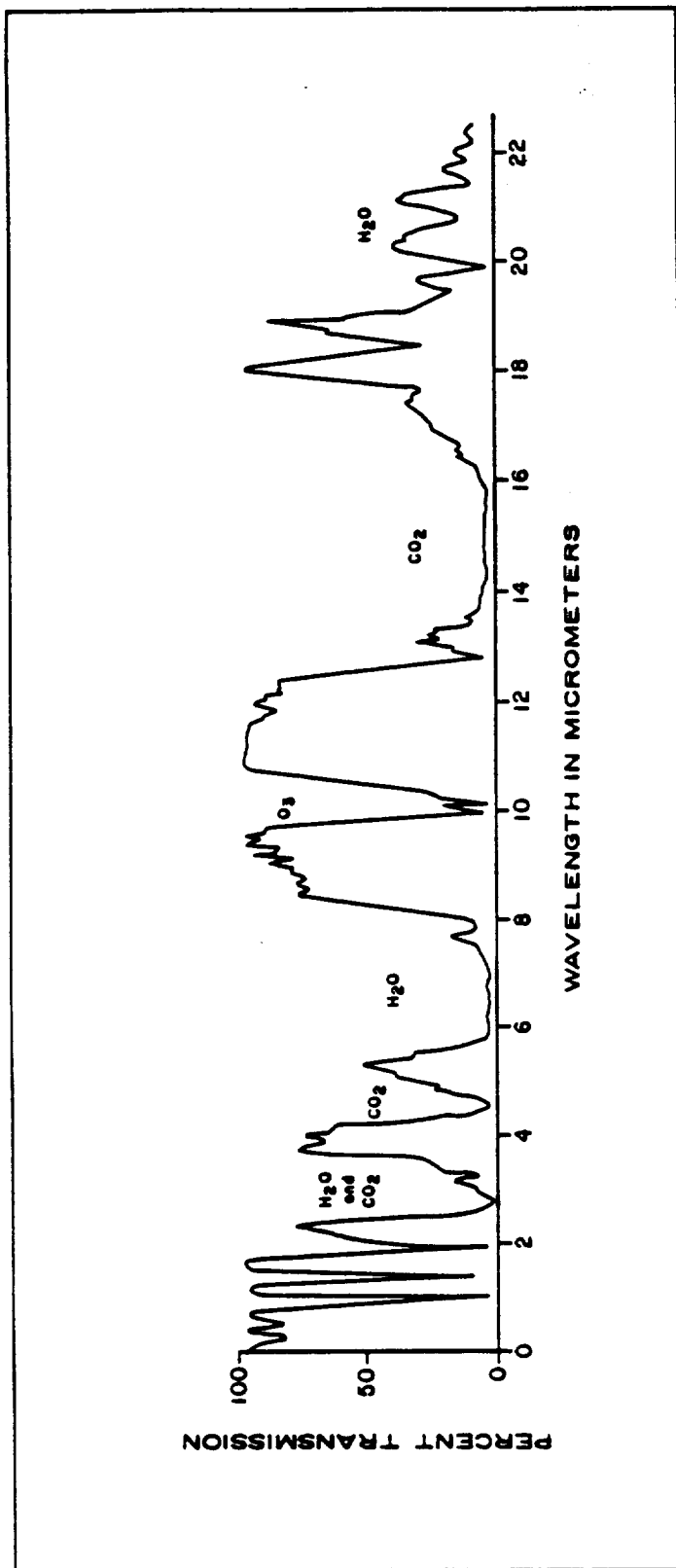
Figure H. Atmospheric transmission in the 0 to 22 um region. The six TIMS channels are located in the 8 to 12 um region. Note ozone absorption near 10.0 um.

Appendix Three, continued

Several factors not inherent in the mineralogy of a
sample that may influence rock spectra at mid-infrared wave-
lengths are porosity (as a function of grain size), and im-
purities such as hydrocarbons (Salisbury et al., 1988).

Rock spectra are dominated by surface scattering, or
direct "specular scattering" off surfaces, coupled with volume
scattering, or scattering resulting from penetration of
optically thin grains and surface topography (John Salisbury,
Personal communication, 1989). The scale of roughness of the
surface is important in the latter process. Diffuse and
specular reflection refer to processes which are part of both
surface and volume scattering. They are not unique to either,
and will be used in this context. Biconical reflectance
measurements (i.e. FTIR measurements) oversample the specular
component and undersample the diffuse.

Appendix Four

Dominant mineralogy of the major geologic units
Compiled from Novak (1985), Spatz (1988)
and present work

Unit	Mineralogy
Hiko Tuff .... (KSW-1)	50% Sanidine/ Anorthoclase 25% Plagioclase 15% Biotite <5% Kspar
Kane Wash Tuff (O member) .... (KSW-6)	40% Sanidine / Anorthoclase 10% Quartz 1-2% Fayalite 1-2% Pyroxene - Minor biotite 50% groundmass of glass and sericite
Kane Wash Tuff (W member) .... (KSW-7)	25% Sanidine / Anorthoclase - Minor pyroxene - Minor quartz 75% unrecognizable groundmass
Kane Wash Tuff (V series) .... (KSW-2)	7-15% Na-sanidine 1-7% Quartz 1% Hedenbergite 1% Fayalite
Early moat rhyolite .... (Ferroedenite rhyolite) (KSW-5)	15% Na - Sanidine 15% Quartz Minor ferroedenite
Late moat rhyolite .... (Topaz rhyolite) (KSW-9)	15% Sanidine, Quartz, Plagioclase(Ab90), Biotite, Ferroedenite, Fayalite

Appendix Four, Continued

Granite porphyry ....40% Kspar
              35% Plagioclase
              25% Quartz
               - Minor biotite
              Groundmass:
                Kspar
                Plagioclase
                Quartz

Post caldera trachyte .... 20-35% Anorthoclase
 (KSW-12)   - Augite
              - Olivine
             <1% Quartz (sometimes)

Syenite complex .... 35% Anorthoclase
 (KSW-13, 14, 25)   5% Quartz
              5% Clinopyroxene
               (sometimes)
              - Minor amphibole

Trachyandesite ....15% Plagioclase and
 (KSW-24)   augite (P>A)
              Groundmass:
                Plagioclase
                Augite
                Olivine

Basalt .... 5% Plagioclase and
 (KSW-10)   augite (P>A)
              Groundmass:
                Plagioclase
                Augite
                Olivine

Limestone .... $CaCO_3$ + minor SiO_2

Dolomite .... Dolomite
               $CaCO_3$

Sandstone .... Quartz

Appendix Five

The Fourier Transform Infrared Spectrometer
(FTIR)

Instrument Parameters

*	Spectral resolution	4 wavenumbers
*	Spatial resolution	1 mm^2
*	Reference	Gold coated SiC paper, 600 grit
*	Spectral range	2.3 to 20 micrometers
*	Technique	Biconical reflectance
*	Biconical reflectance	2 off-axis paraboloid mirrors, rotatable
*	Detector	Liquid nitrogen cooled HgCdTe
*	Sample stage	
	Rotation	0.36 degrees per step
	Sample size	7.5 cm diameter
		5 cm high

Appendix Six

The Portable Field Emission Spectrometer
(PFES)

Instrument Parameters

*   Spectral range   5 to 14.5 micrometers
*   Measures   Radiant spectral emittance
*   Spectral resolution   0.1 to 0.2 micrometers
*   NEdT   0.65 degrees for a blackbody at 24° C
*   Field of view 15°, circular
*   Detector   HgCdTe
*   Filter wheel specifications

Three segments:

Segment 1: Substrate: Quartz
Range: 2.5 to 4.5 um
Transmittance: 27%

Segment 2: Substrate: Germanium
Range: 4.4 to 8.0 um
Transmittance: 32%

Segment 3: Substrate: Germanium
Range: 7.9 to 14.5 um
Transmittance: 35%

*   Storage   3 1/2 inch diskettes on portable lap top computer

Appendix Seven

References for Desert Varnish Studies

Allen, C.C., 1978. Desert varnish of the Sonoran Desert - optical and electron probe microanalysis, Jour. of Geol., Vol.86, pp.743-752.

Blake, W.P., 1905. Superficial blackening and discoloration of rocks especially in desert regions, Am. Inst. Min. Engineers Trans., Vol.35, pp.371-375.

Borns, D.J. et al, 1980. The role of micro-organisms in the formation of desert varnish and other rock coatings: SEM study, Geol. Soc. Amer. Abst. with Prog., Vol.12, p.390.

Dorn, I.R., and Oberlander, T.M., 1982. Rock varnish, Prog. in Phys. Geog., Vol.6, pp.317-367.

Engle, C.G., and Sharp, R.P., 1958. Chemical data on desert varnish, Geol. Soc. Amer. Bull., Vol.69, pp.487-518.

Hooke, R.LeB., Yang, H., and Weiblen, P.W., 1969. Desert varnish: an electron probe study, Jour. Geol., Vol.77, pp.275-288.

Hunt, C.B., 1954. Desert varnish, Science, Vol.120, pp.183-184.

Hunt, C.B., 1961. Stratigraphy of desert varnish, U.S. Geol. Survey Prof. Paper 424B, pp.B194-B195.

Knauss, K.G., and Teh-Lung, K, 1980. Desert varnish: potential for age dating via uranium-series isotopes, Jour. of Geol., Vol.88, pp.95-100.

Lakin, H.W. et al, 1963. Variation in minor-element content of desert varnish, U.S. Geol. Survey Prof. Paper 475-B, pp.B28-B31.

Appendix Seven, continued

Laudermilk, J.D., 1931. On the origin of desert varnish, Am.
     Jour. Sci., Vol.21, pp.51-66.

Merrill, G.P., 1898. Desert varnish, U.S. Geol. Survey Bull.
     150, pp.389-391.

Watson, R.D., 1970. Surface-coating effects in remote sensing
     measurements, Jour. of Geophys. Res., Vol.75, N.2,
     pp.480-484.

White, C.H., 1924. Desert varnish, Am. Jour. Sci, Vol.7, 5th
     ser., pp.413-420.

Appendix Eight

**Spectral Features of Feldspar Minerals
Found in the Study Area Samples**
(From Salisbury et al., 1987)

<u>Albite</u>

8.20 um (shoulder)

8.60 (major peak)

9.00 (minor peak)

9.45 (major peak)

9.78 (major peak)

12.70 (minor peak)

13.00 (minor peak)

13.35 (minor peak)

13.75 (minor peak)

<u>Anorthite</u>

8.40 um (major peak)

8.90 (subtle shoulder)

9.50 (minor peak)

10.40 (major peak)

11.80 (minor fluctuations)

13.15 (minor peak)

13.60 (minor peak)

<u>Sanidine</u>

6.00 um (minor peak)

6.55 (minor peak)

8.35 (major peak)

8.60 (major peak)

9.40 (major peak)

14.00 (minor peak)

<u>Orthoclase</u>

6.00 um (minor peak)

6.55 (minor peak)

8.35 (shoulder)

8.60 (major peak)

9.40 (major peak)

14.00 (minor peak)

Appendix Nine

Vegetation in the Kane Springs Wash Study Area
(Nancy Milton, Paul Tueller, David Charlet,
Personal comm., 1989)

Delamar Valley _____

Ceratoides lanata

Grayia spinosa

Oryzopsis hymenoides

Yucca brevifolia

Lycium andersonii

Delamar Mountains _____

Pinus monophylla

Juniperus osteosperma

Ephedra nevadensis

Purshia glandulosa

Artemisia tridentata

Artemisia tridentata vaseyana

Artemisia nova

Coleogyne ramosissima

Prunis andersonii

Quercus gambella

Amelanchier sp.

Leptodactylon pungens

Arctostaphylos patula

Appendix Nine, continued

Kane Springs Wash_____

Larrea tridentata

Ambrosia dumosa

Ceratoides lanata

Atriplex confertifolia

Quercus gambelli

Gregerson basin _____

Artemisia tridentata

Chrysothamnus vicidiflorous

Chrysothamnus nauseosus

Purshia tridentata

Burn areas _____

Crysothamnus sp.

Ephedra nevadensis

Purshia glandulosa

Bromus tectorum (higher elevations)

Bromus rubens (lower elevations)

Appendix Nine, continued

Upper washes _____

        Pinus _monophylla_

        Juniperus _osteosperma_

        Quercus _gambelli_

        Prunis _amgdelus_

        Purshia _tridentata_

        Arctostaphylos _patula_

        Ribes _cereum_

        Cercocarpus sp.

        Ephedra _nevadensis_

        Eriogonum sp.

        Amelanchier _alnifolia_

Lower washes _____

        Atriplex _canescens_

        Sedzana (?) _mexicana_

        Hymenoclea _salsola_

Others_____

        Rhus _trilobata_

        Scrub _oak_

Appendix Nine, continued

Others, continued _____

    Quercus turbinella
    Prunis amagdalus

Appendix Ten

Statistical Parameters
of the
Vegetated / Nonvegetated Pixel Groups

Rock type		Band	Mean	Std Dev	Variance
Early moat	Veg.	1	3555.3	99.1	9821.7
rhyolite 1		2	3820.9	88.5	7839.1
		3	4013.8	104.3	10886.6
		4	4569.7	116.9	13673.7
		5	4841.8	119.6	14311.1
		6	4755.4	63.4	4015.5
	Nonveg.	1	3781.8	487.6	237766.1
		2	4036.3	511.8	261954.7
		3	4221.1	505.4	255461.6
		4	4926.8	600.0	360054.4
		5	5212.7	543.3	95201.9
		6	5357.4	426.2	81674.5
Early moat	Veg.	1	3415.7	37.5	1405.5
rhyolite 2		2	3688.7	44.3	1965.7
		3	3876.9	38.9	1510.4
		4	4443.8	52.2	2727.7
		5	4712.5	42.0	1764.0
		6	4663.0	62.2	3871.0
	Nonveg.	1	4474.7	180.4	32565.2
		2	4777.2	168.6	28414.2

Appendix Ten, continued

Rock type		Band	Mean	Std Dev	Variance
Early moat		3	4977.2	171.2	29295.9
rhyolite 2		4	5727.3	179.5	32207.0
		5	5893.9	204.6	41884.9
		6	5655.8	114.5	13122.9
Syenite 1	Veg.	1	3662.3	57.9	3363.2
		2	3944.2	88.4	7813.4
		3	4121.3	53.9	2910.0
		4	4697.4	73.7	5432.0
		5	4995.0	54.6	2981.2
		6	4873.1	49.2	2418.4
	Nonveg.	1	4706.0	125.9	15873.9
		2	5007.2	128.8	16582.2
		3	5213.2	131.8	17379.9
		4	5960.2	147.7	21831.2
		5	6167.3	138.1	19083.0
		6	5784.1	101.7	10347.4
Syenite 2	Veg.	1	3771.0	96.6	9335.7
		2	4051.4	93.4	8721.5
		3	4231.3	98.7	9739.7
		4	4885.4	104.9	11005.0
		5	5110.5	121.5	14757.3
		6	4917.5	39.5	1557.8
	Nonveg.	1	4475.5	181.2	32845.5
		2	4769.8	194.0	37655.2
		3	4934.4	188.6	35575.5

Appendix Ten, continued

Rock type		Band	Mean	Std Dev	Variance
Syenite 2		4	5727.1	191.3	36580.9
		5	5950.9	171.5	29417.6
		6	5658.4	51.6	2667.8
Granite	Veg.	1	3517.0	86.3	7446.5
porphyry		2	3790.4	91.3	8344.5
		3	3973.8	89.9	8089.4
		4	4574.1	105.3	11091.1
		5	812.4	94.8	8981.8
		6	4690.0	82.2	6758.0
	nonveg.	1	4173.4	108.6	11802.9
		2	4434.9	124.7	15564.6
		3	4654.8	115.1	13250.4
		4	5394.8	129.9	16893.2
		5	5619.3	112.4	12643.7
		6	5361.0	107.2	11492.5

Appendix Ten, continued

Results of F- and T-tests
F-Test (Variance comparison) Data

$$c = F_{0.05}(8,8) = \underline{3.44}$$

Site	Band	Vegetated Variance	Nonvegetated Variance	F Value	H_o Rejected?
Early Moat Rhyolite 1	1	9821.7	237766.1	24.2	Yes
	2	7839.1	261954.7	33.4	Yes
	3	10886.6	255461.6	23.5	Yes
	4	13673.7	360054.4	26.3	Yes
	5	14311.1	295201.9	20.6	Yes
	6	4015.5	181674.5	45.2	Yes
Early Moat Rhyolite 2	1	1405.5	32565.2	23.2	Yes
	2	1965.7	28414.2	14.4	Yes
	3	1510.4	29295.9	19.4	Yes
	4	2727.7	32207.0	11.8	Yes
	5	1764.0	41884.9	23.7	Yes
	6	3871.0	13122.9	3.4	No
Syenite 1	1	3363.2	15873.9	4.7	Yes
	2	7813.4	16582.2	2.1	No
	3	2910.0	17379.9	6.0	Yes
	4	5432.0	21831.2	4.0	Yes
	5	2981.2	19083.0	6.4	Yes
	6	2418.4	10347.4	4.3	Yes
Syenite 2	1	9335.7	32845.5	3.5	Yes
	2	8721.5	37655.2	4.3	Yes

Appendix Ten, continued

Site	Band	Vegetated Variance	Nonvegetated Variance	F Value	H_0 Rejected?
Syenite	3	9739.7	35575.5	3.6	Yes
2	4	11005.0	36580.9	3.3	No
	5	14757.3	29417.6	2.0	No
	6	1557.8	2667.8	1.7	No
Granite	1	7446.5	11802.9	1.6	No
porphyry	2	8344.5	15564.6	1.9	No
	3	8089.4	13250.4	1.6	No
	4	11091.1	16893.2	1.5	No
	5	8981.8	12643.7	1.4	No
	6	6758.0	11492.5	1.7	No

T-Test (Mean comparison) Data

Site	Band	T Value	T_a Value	Means Significantly Different?
Early Moat	1	1.366	1.833	No
Rhyolite	2	1.244	1.860	No
1	3	1.205	1.833	No
	4	1.752	1.833	No
	5	2.000	1.833	Yes
	6	4.191	1.860	Yes

Appendix Ten, continued

Site	Band	T Value	T_a Value	Means Significantly Different?
Early Moat	1	17.237	1.833	Yes
Rhyolite	2	18.735	1.833	Yes
2	3	18.807	1.833	Yes
	4	20.601	1.833	Yes
	5	16.964	1.833	Yes
	6	22.847	1.746	Yes[*]
Syenite	1	22.575	1.796	Yes
1	2	20.417	1.746	Yes[*]
	3	22.997	1.796	Yes
	4	22.944	1.782	Yes
	5	23.676	1.812	Yes
	6	24.189	1.782	Yes
Syenite	1	10.291	1.782	Yes
2	2	10.007	1.782	Yes
	3	9.909	1.782	Yes
	4	11.575	1.746	Yes[*]
	5	11.995	1.746	Yes[*]
	6	34.193	1.746	Yes[*]
Granite	1	14.202	1.746	Yes[*]
porphyry	2	12.504	1.746	Yes[*]
	3	13.985	1.746	Yes[*]

Appendix Ten, continued

Site	Band	T Value	T_a Value	Means Significantly Different?
Granite	4	14.718	1.746	Yes[*]
porphyry	5	16.461	1.746	Yes[*]
	6	14.901	1.746	Yes[*]

[*] T-Test assumes that the variances are not different (for all others, the T-Test assumes that the variances are different).

Appendix Eleven

TIMS Filter Responses
for August 26, 1987

TIMS Channel I

TIMS Channel 2

C-6

TIMS Channel 3

TIMS Channel 4

TIMS Channel 5

PERCENT TRANSMISSION

WAVELENGTH (MICRONS)

TIMS Channel 6

PERCENT TRANSMISSION

WAVELENGTH (MICRONS)
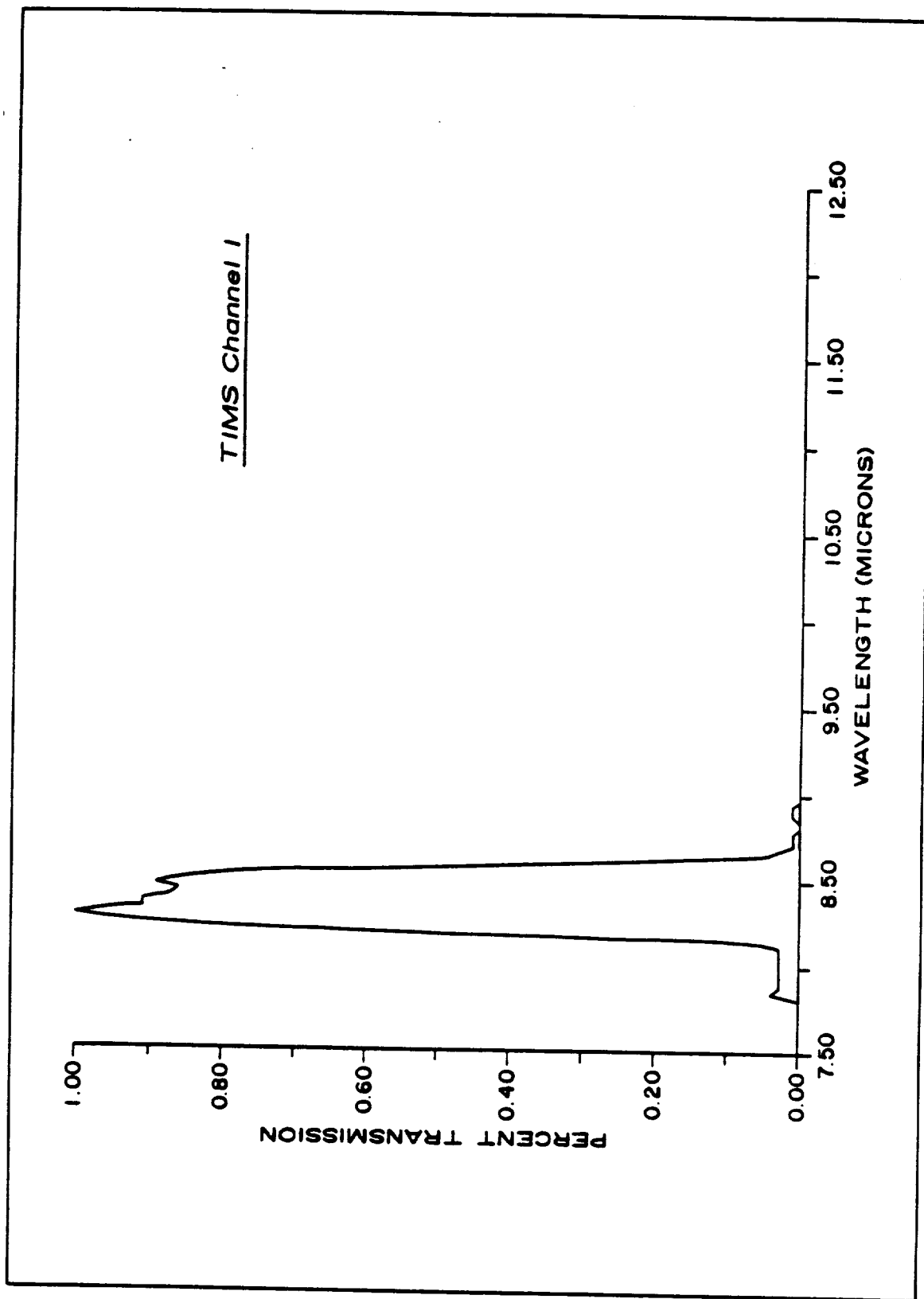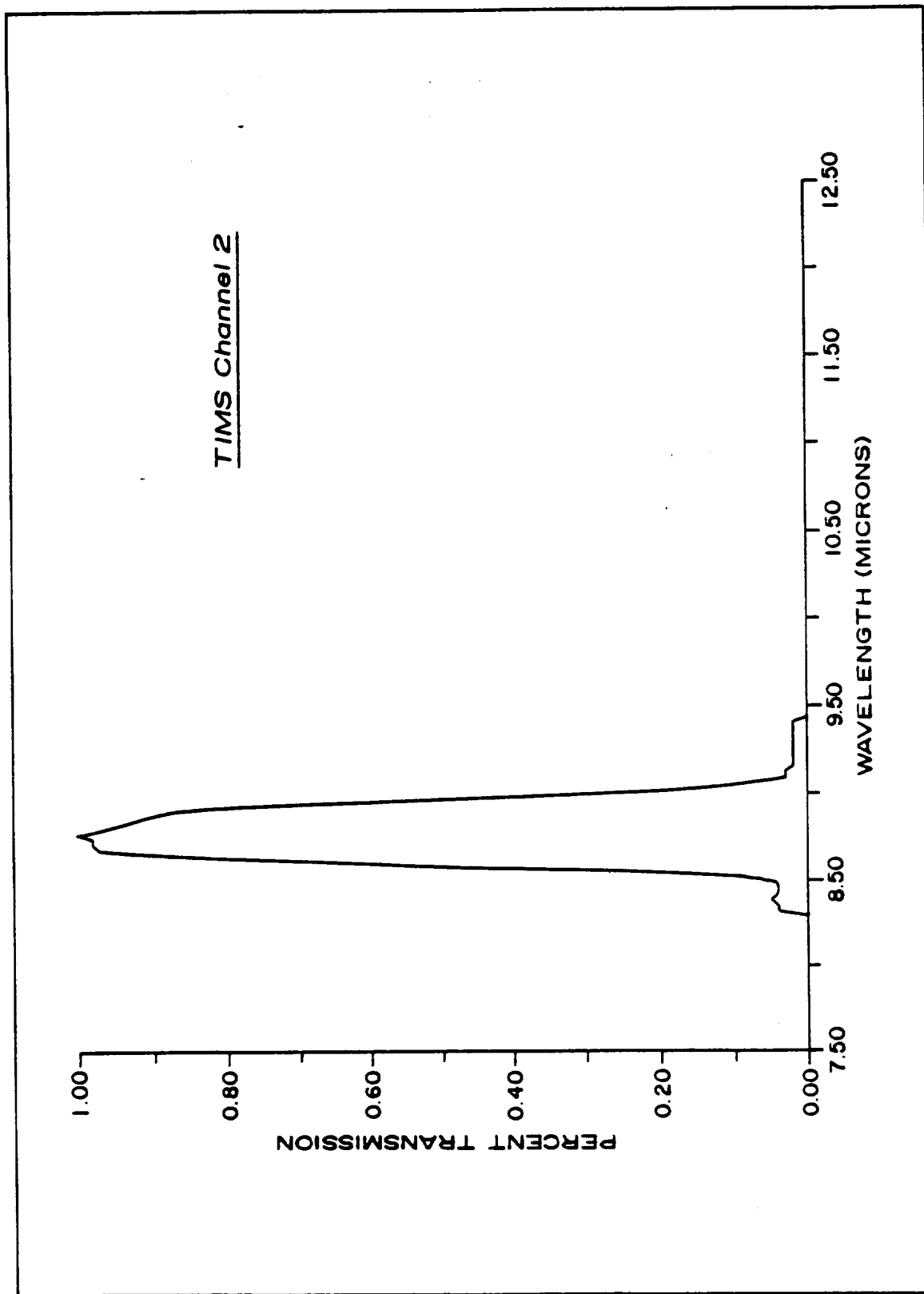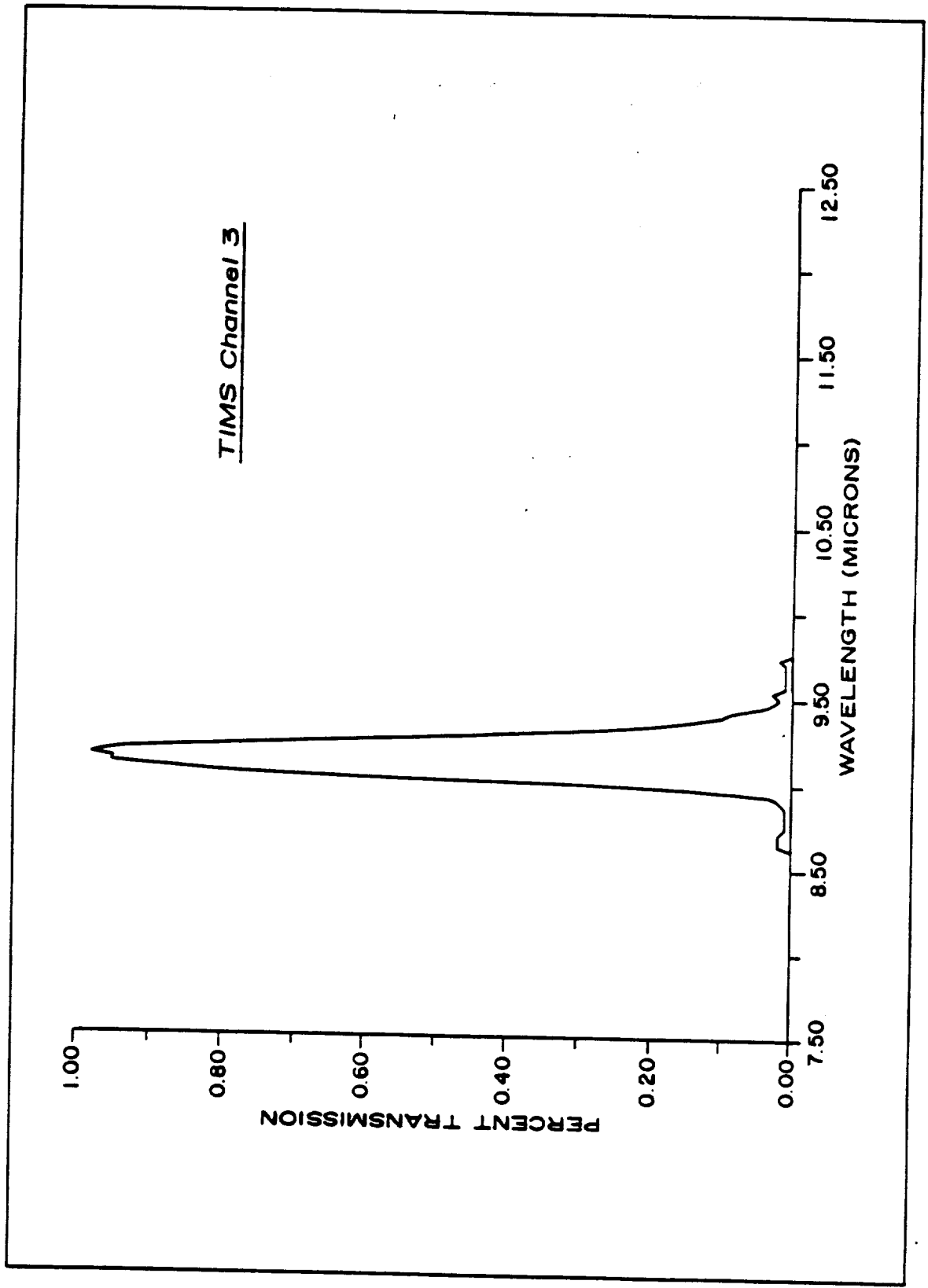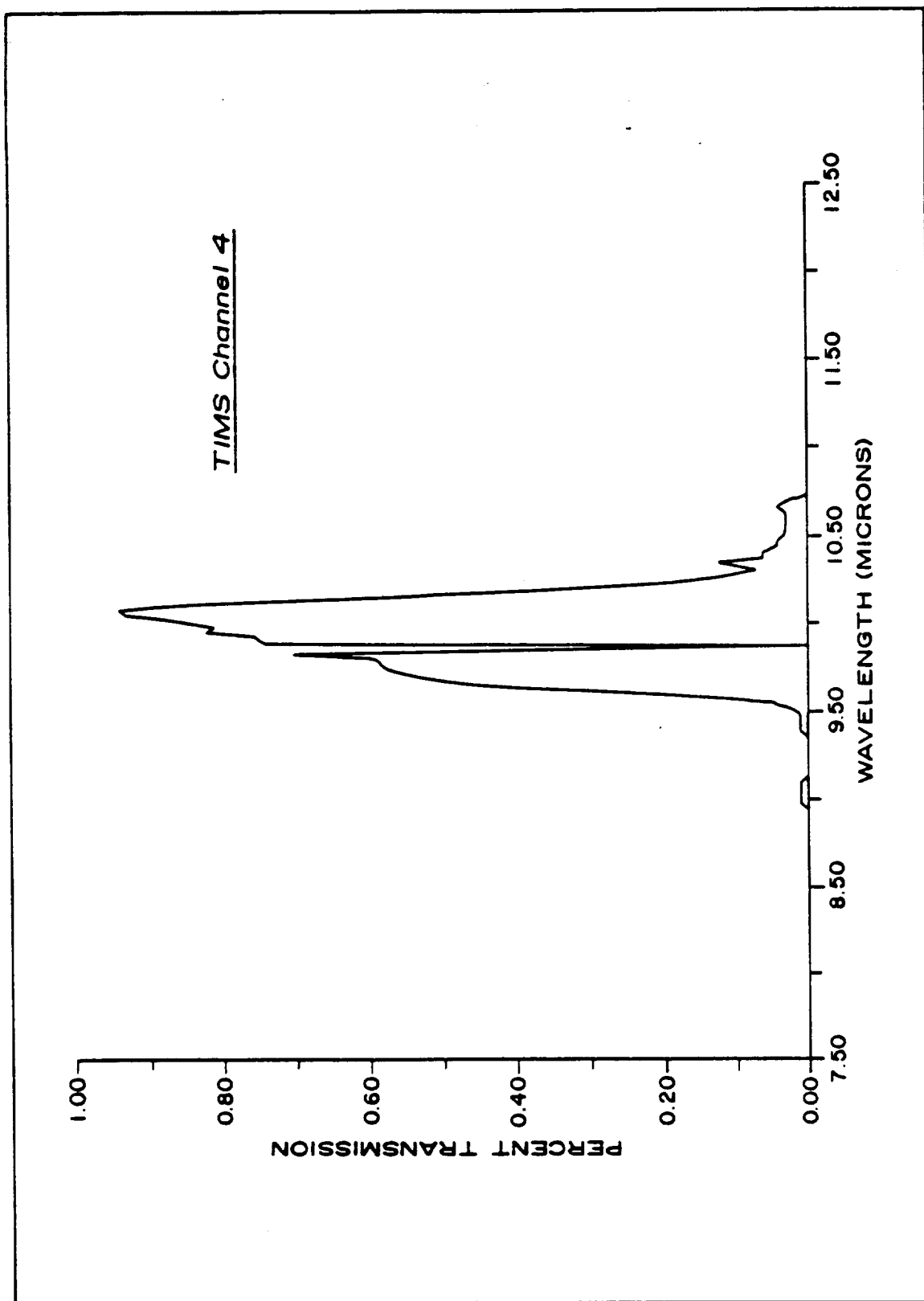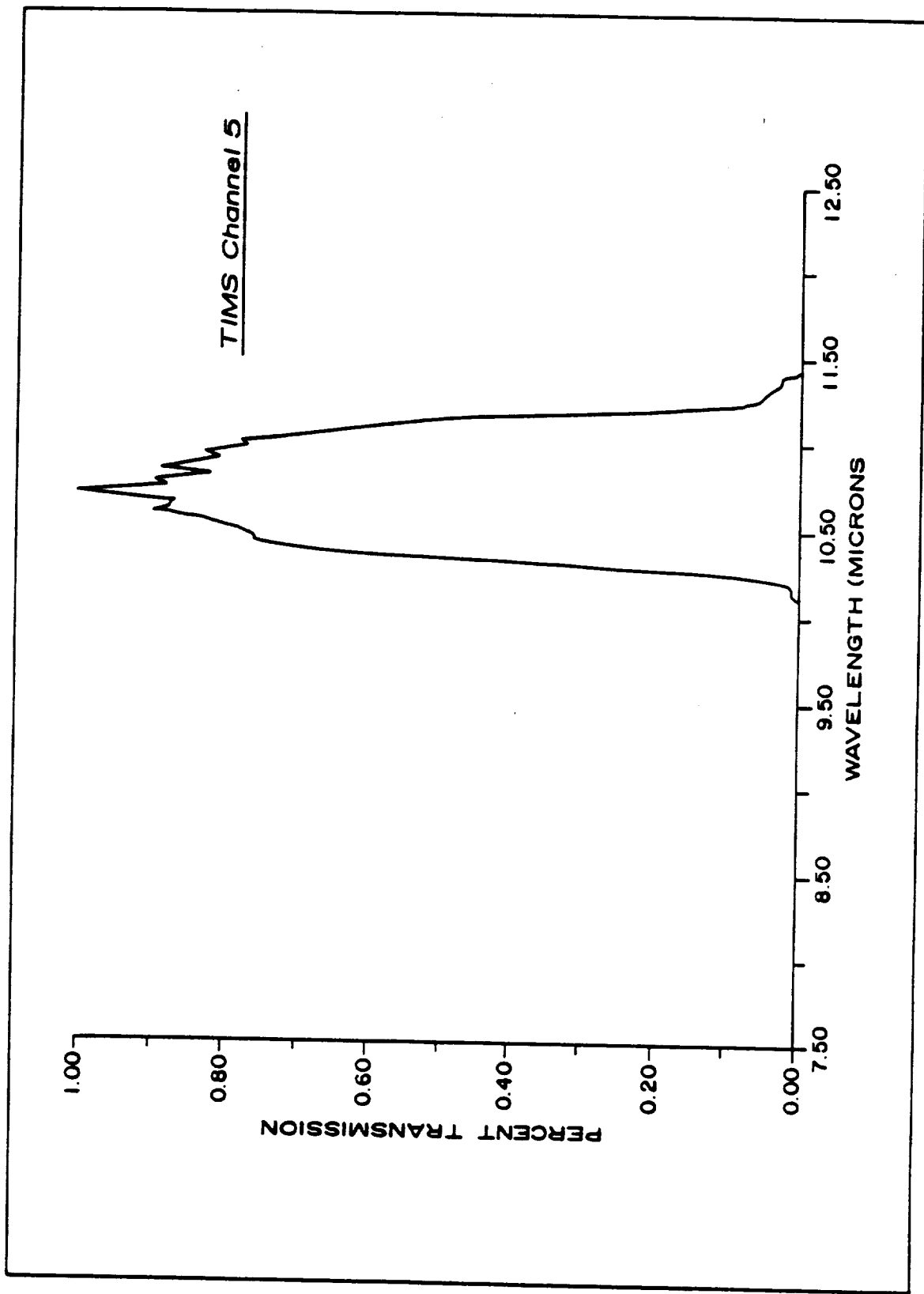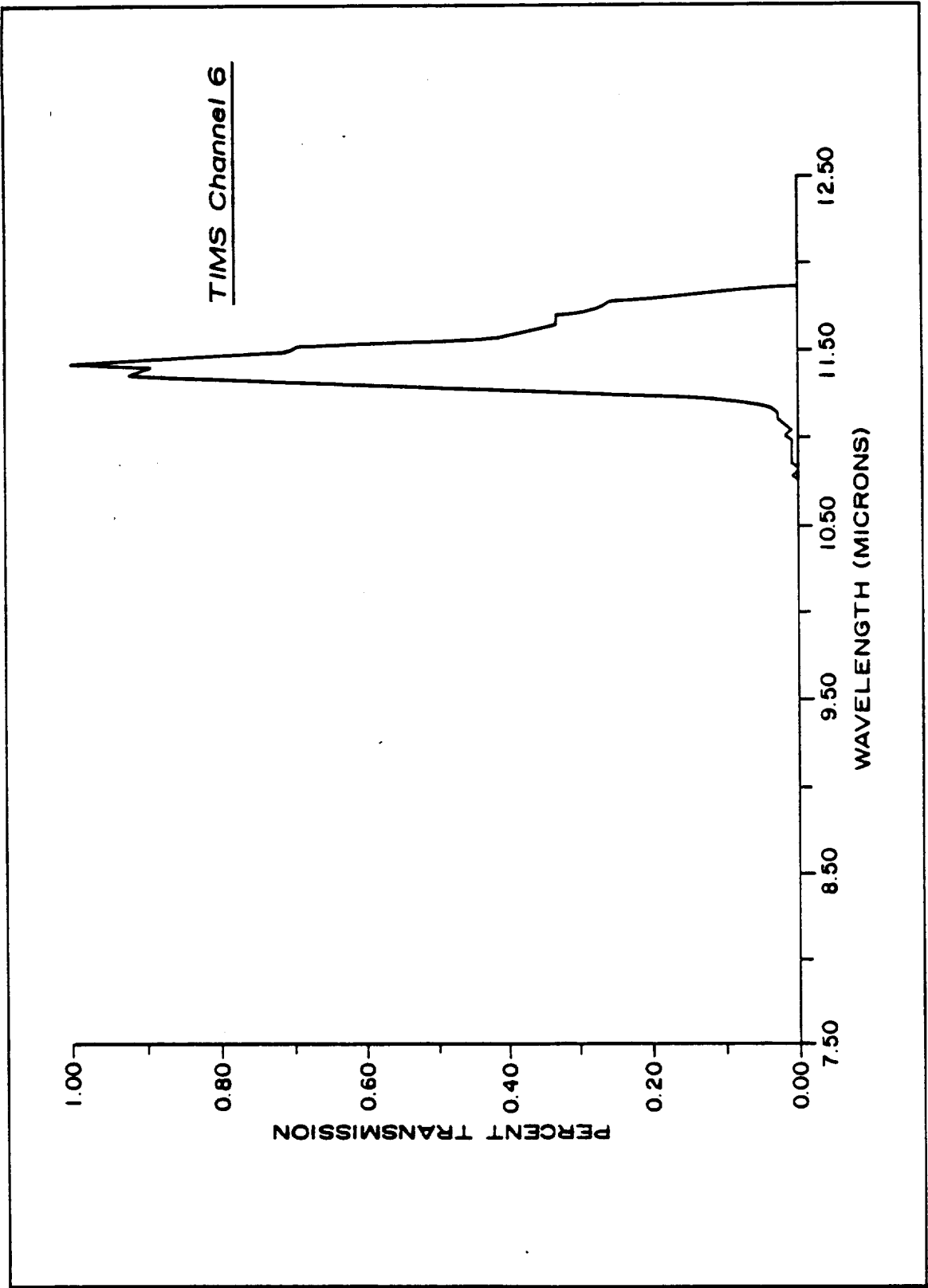
Appendix Twelve

Fifty-nine spectra of variably coated rock surfaces
grouped by rock type

Gold Standard
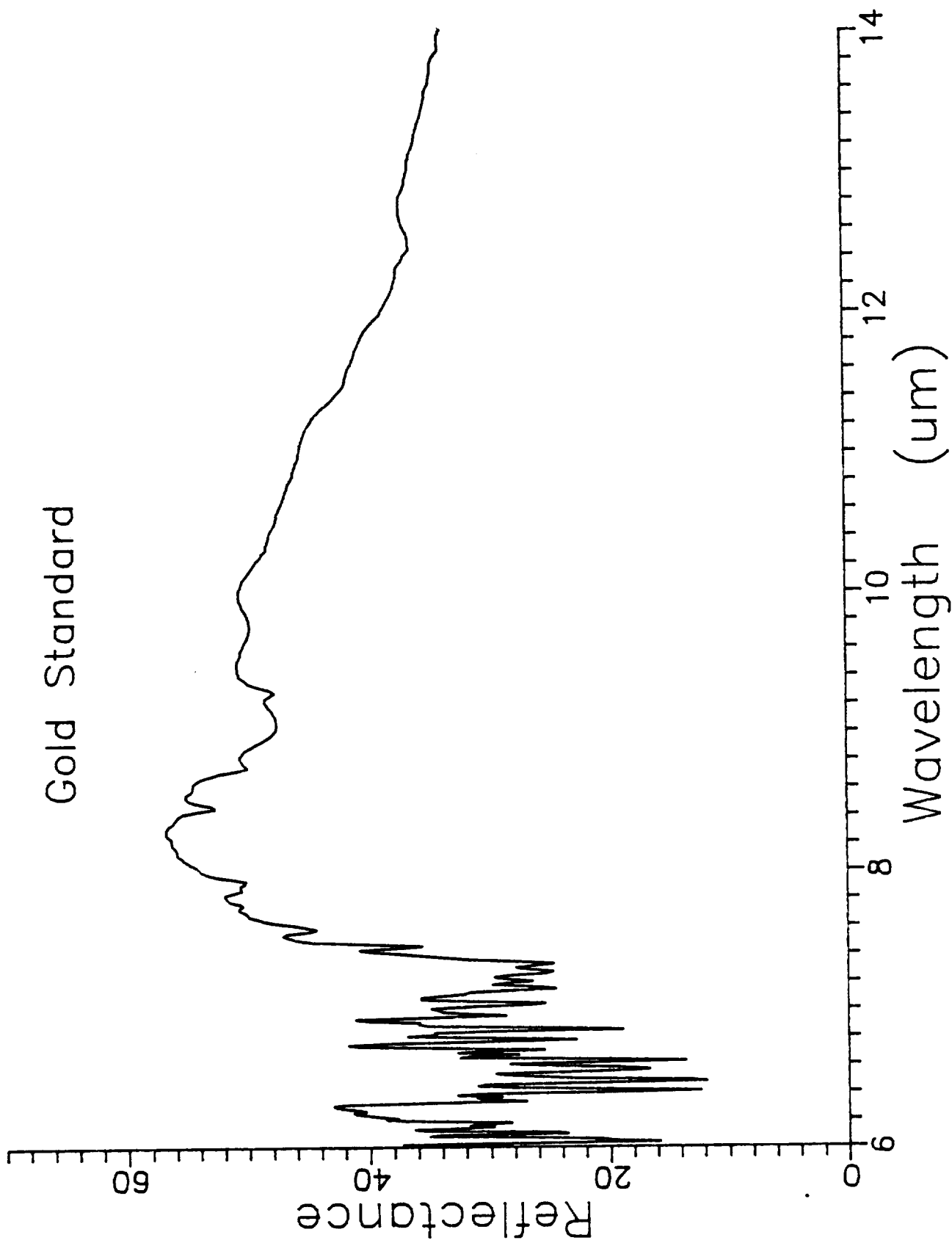
KSW-1 Hiko Tuff
Relative extent of varnish

Relative Reflectance

Wavelength (um)
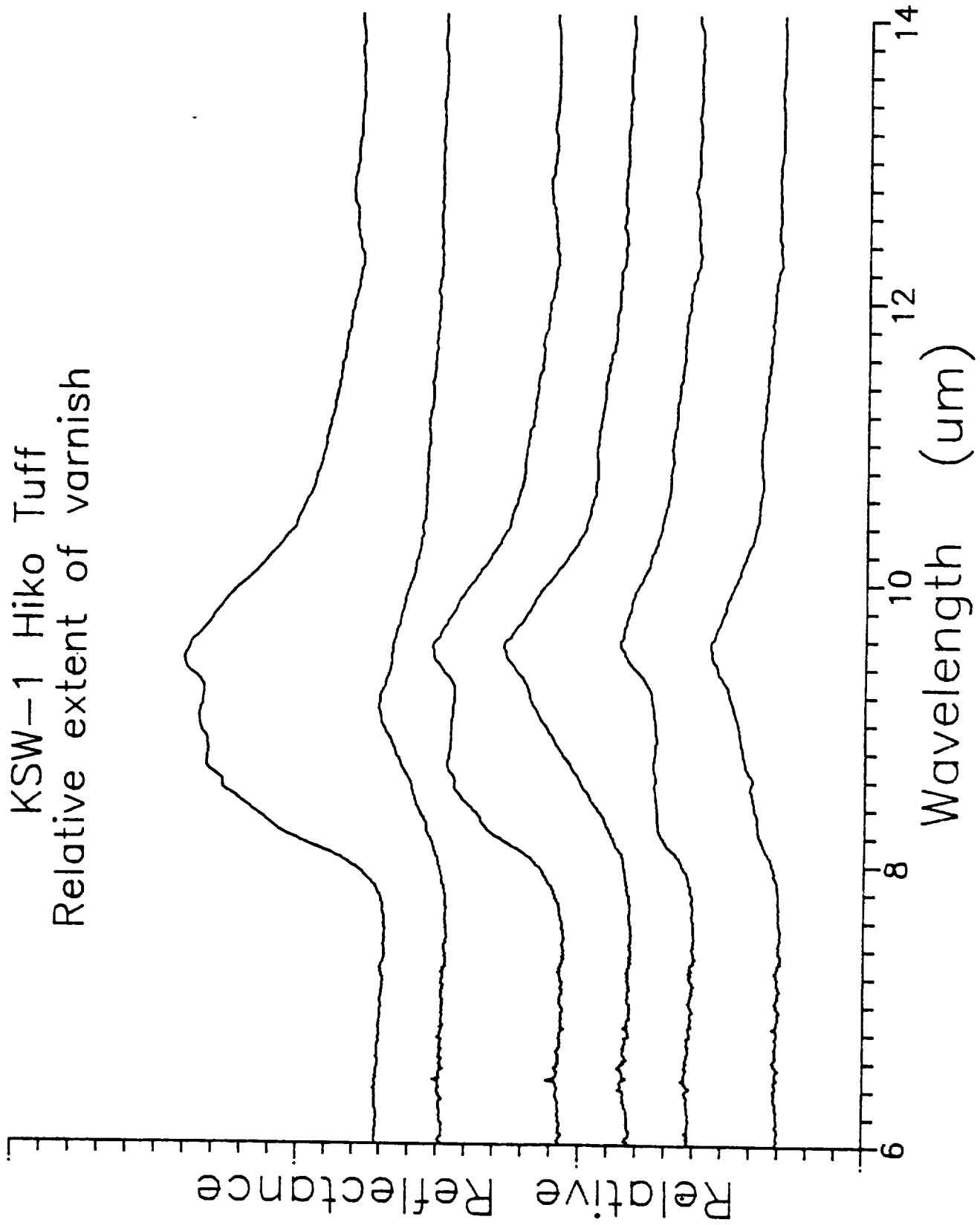
KSW-2 Kane Wash Tuff (V)
Relative extent of varnish

Wavelength (um)

Relative Reflectance
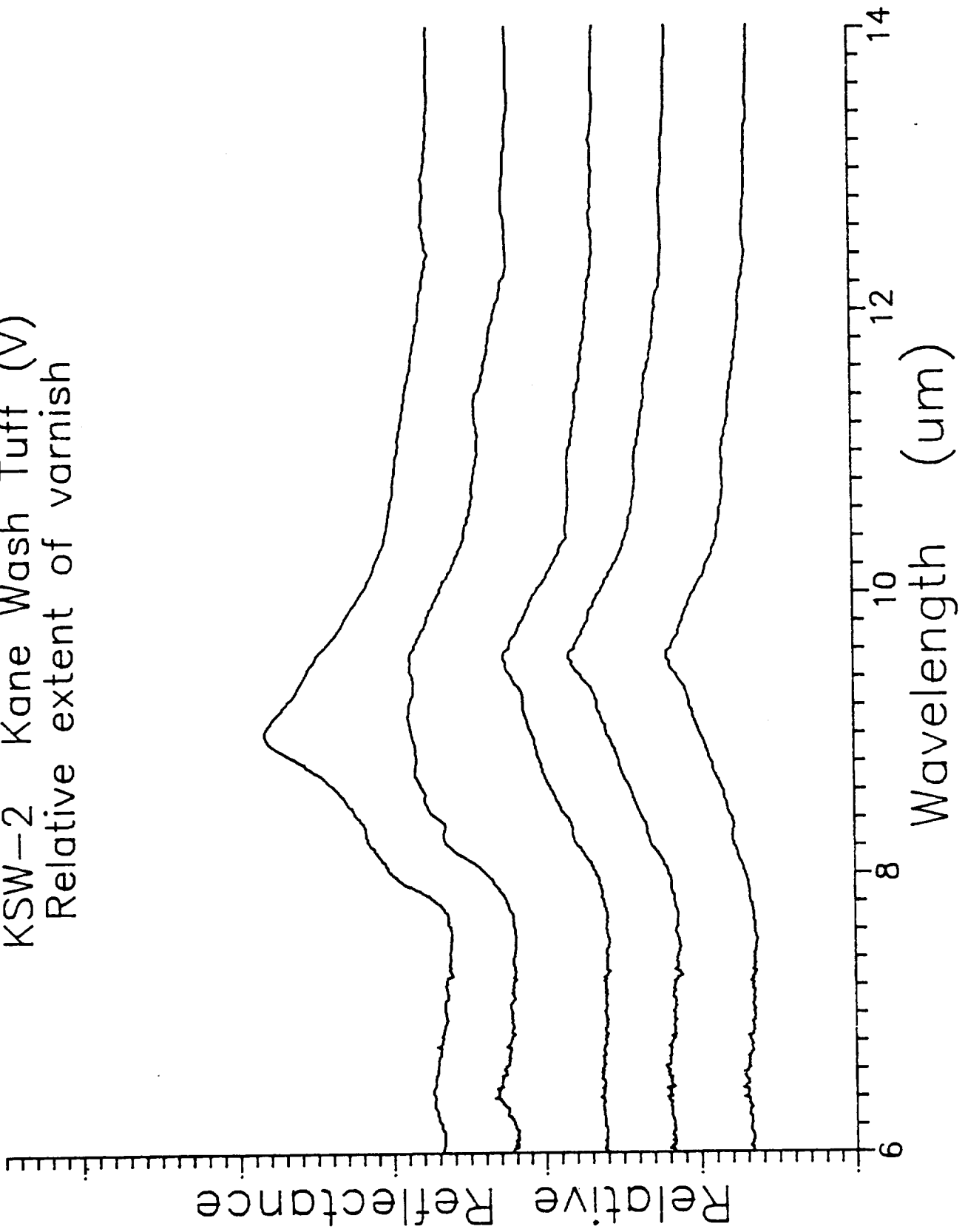
KSW-5   Ferroedenite Rhyolite
Relative extent of varnish

Relative Reflectance

Wavelength (um)
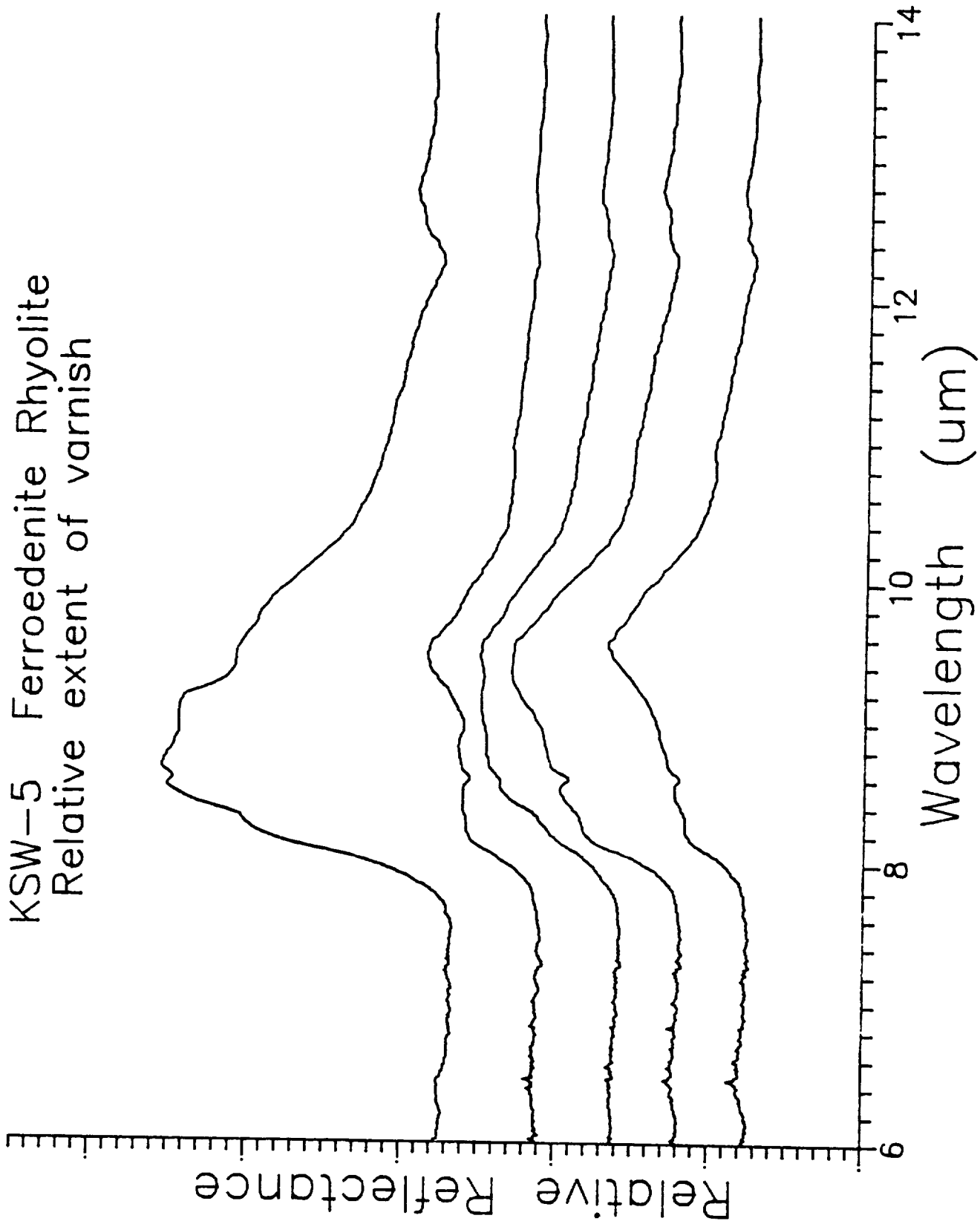
KSW-6 Kane Wash Tuff (O Member)
Relative extent of varnish

Relative Reflectance

Wavelength (um)
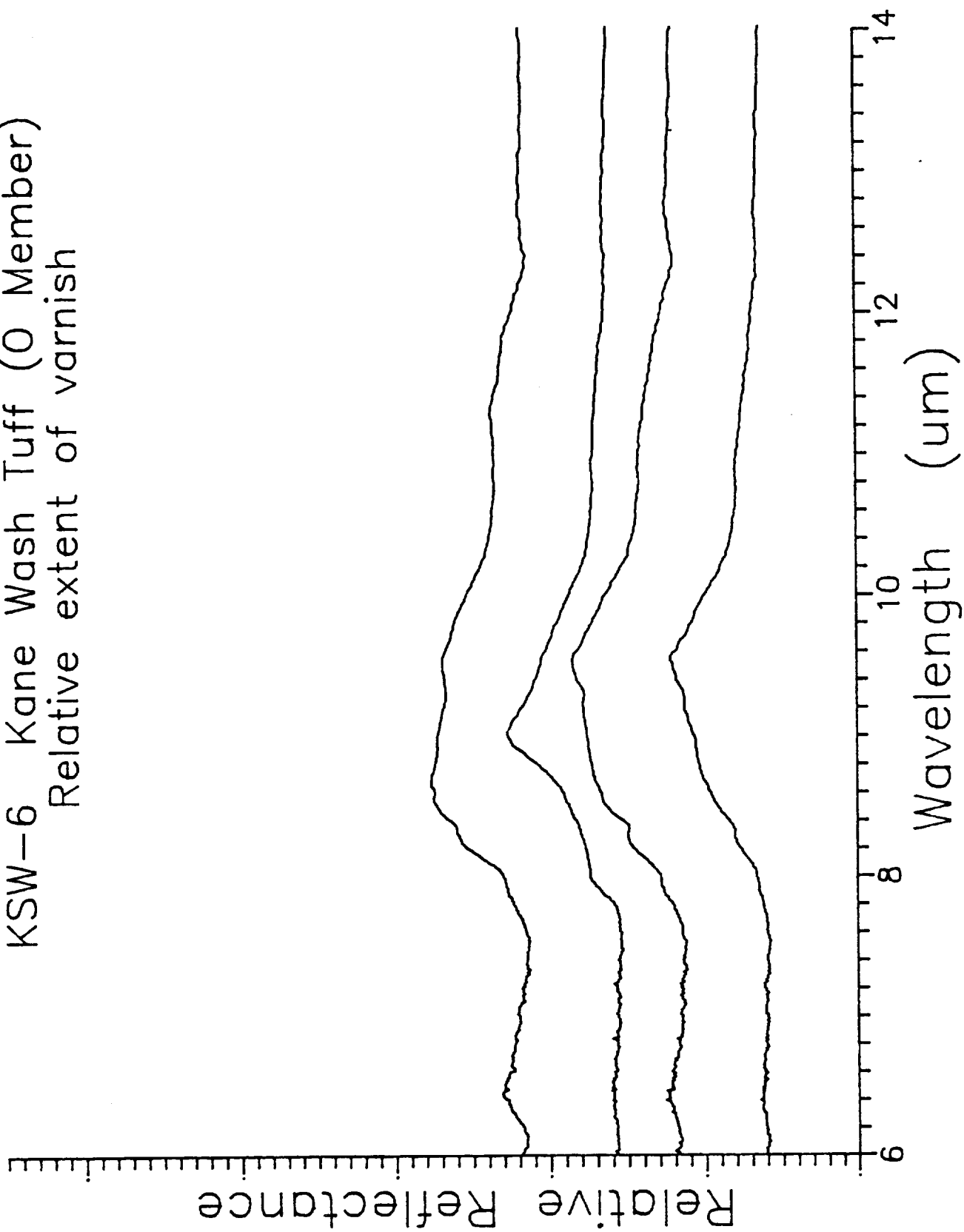
KSW-7 Kane Wash Tuff (W Member)
Relative extent of varnish

Relative Reflectance

Wavelength (um)
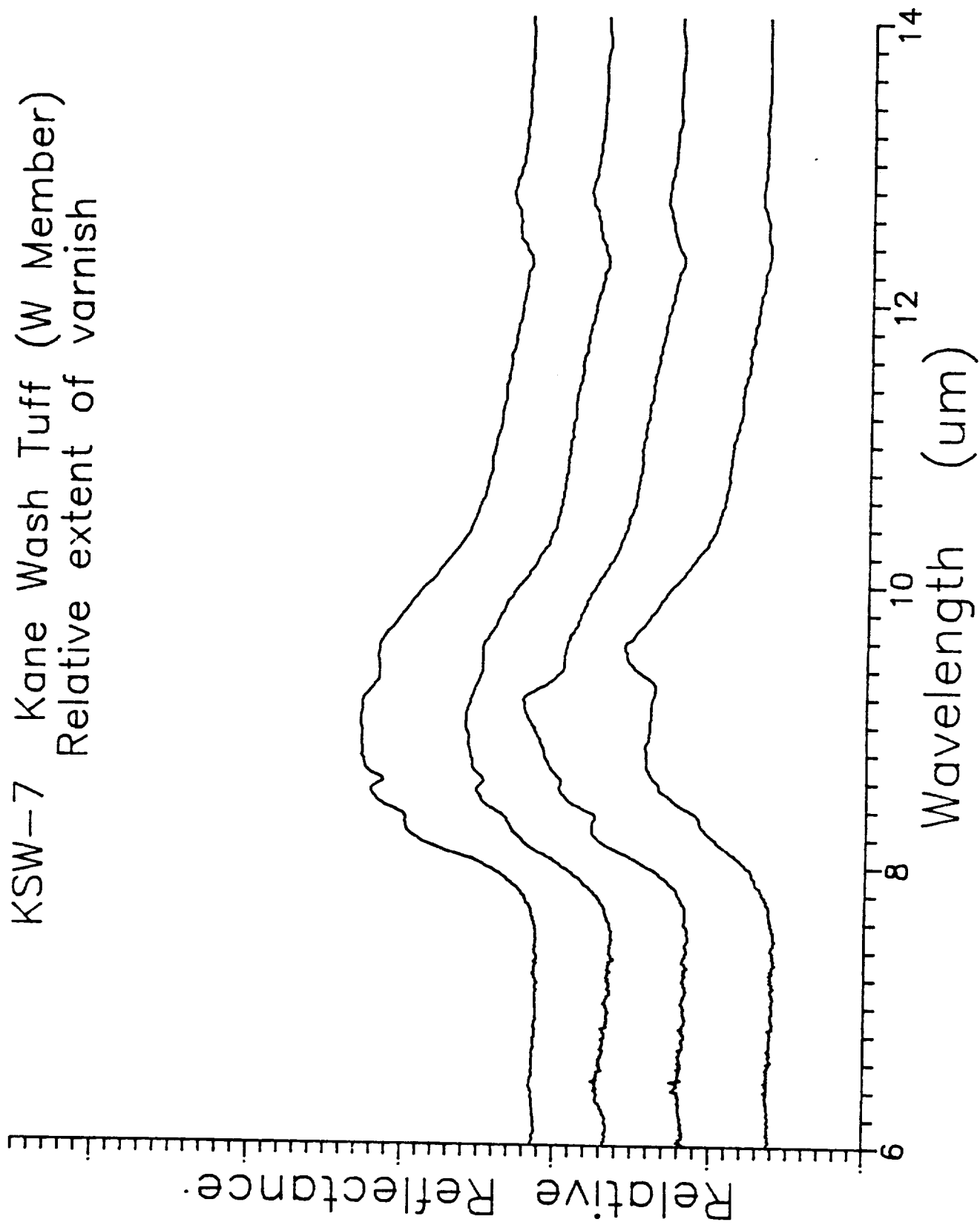
KSW-9 Topaz Rhyolite
Relative extent of varnish
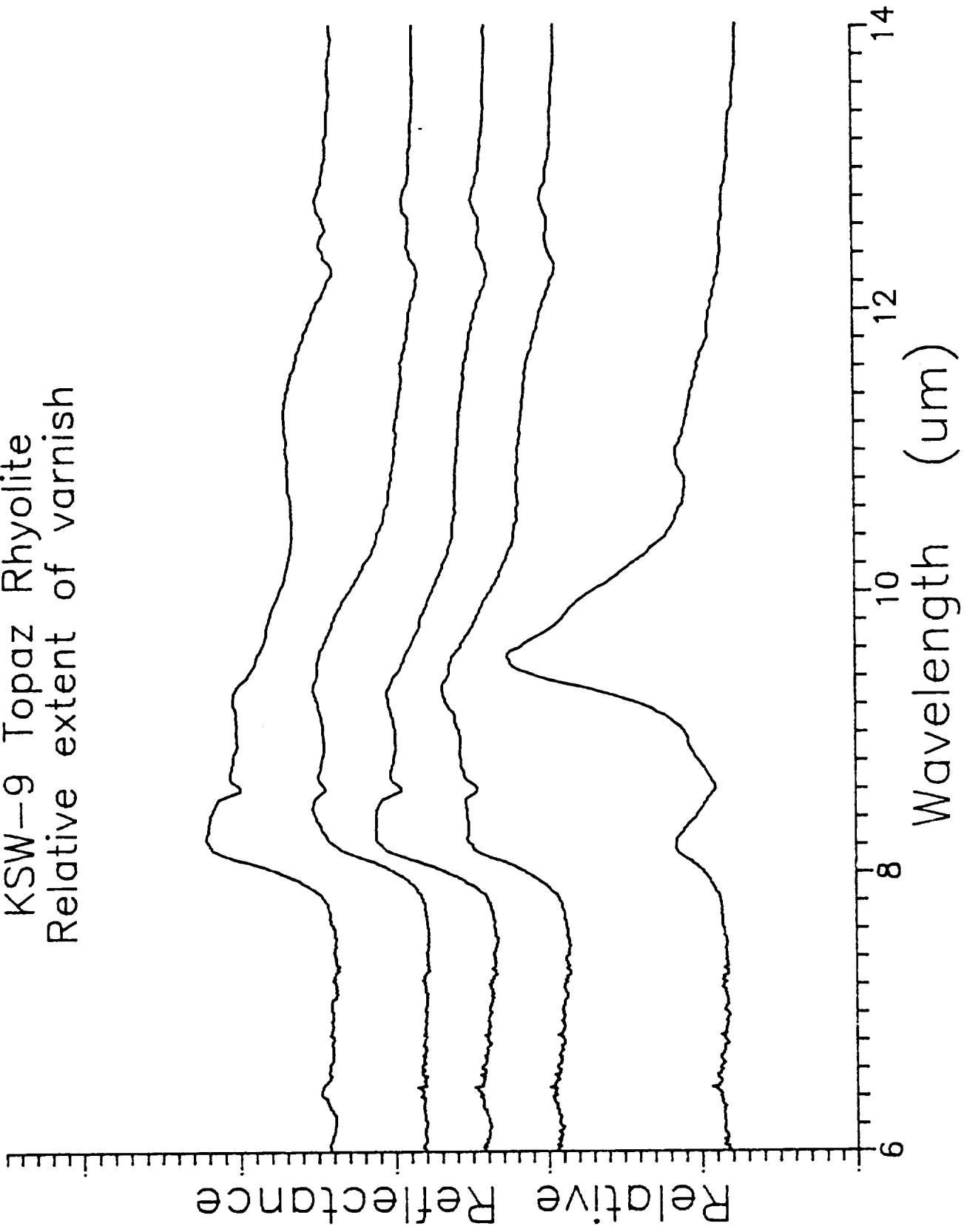
KSW-10 Late Basalt
Relative extent of varnish

Relative Reflectance

Wavelength (um)
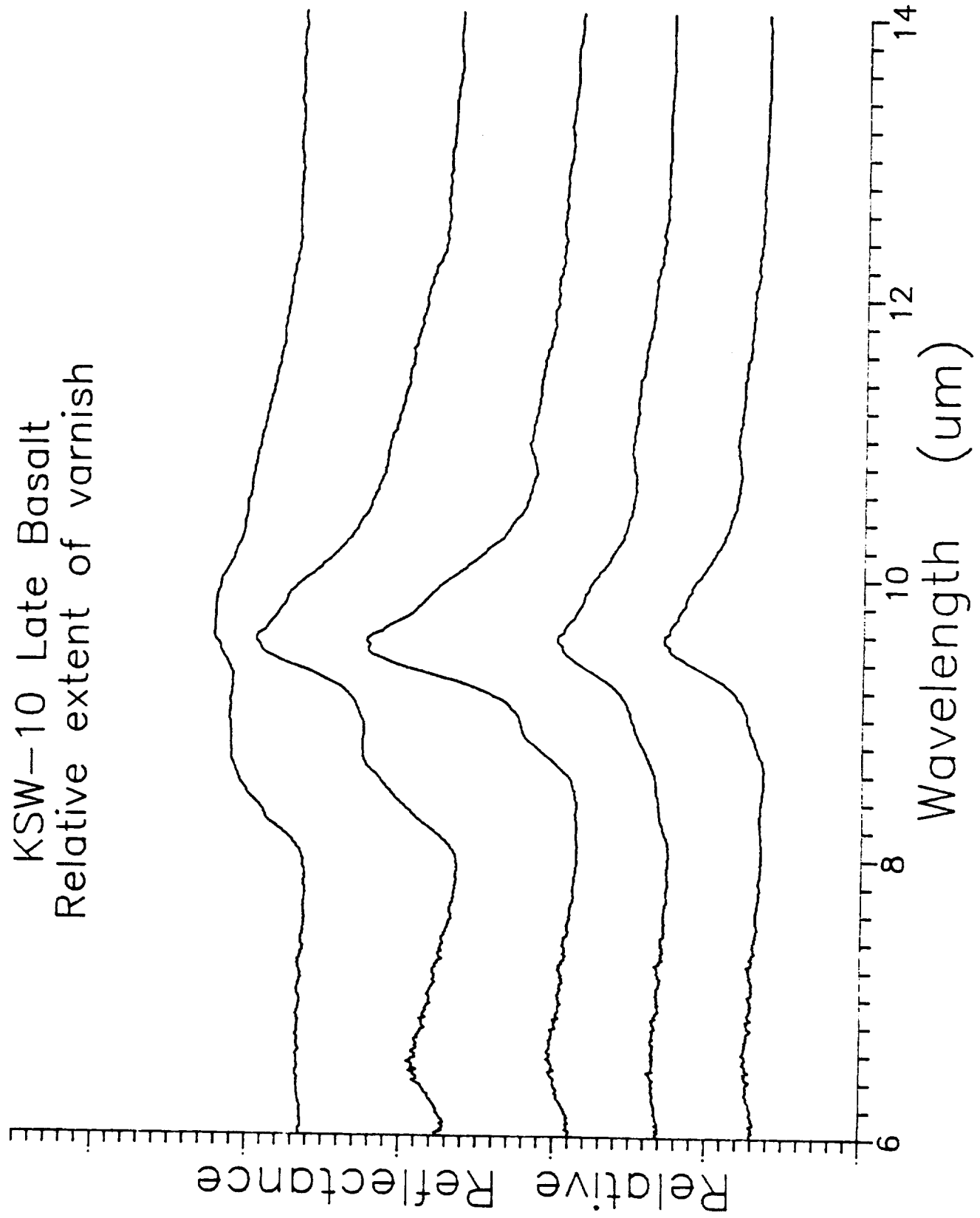
KSW-12 Post Caldera Trachyte
Relative extent of varnish

Relative Reflectance

Wavelength (um)
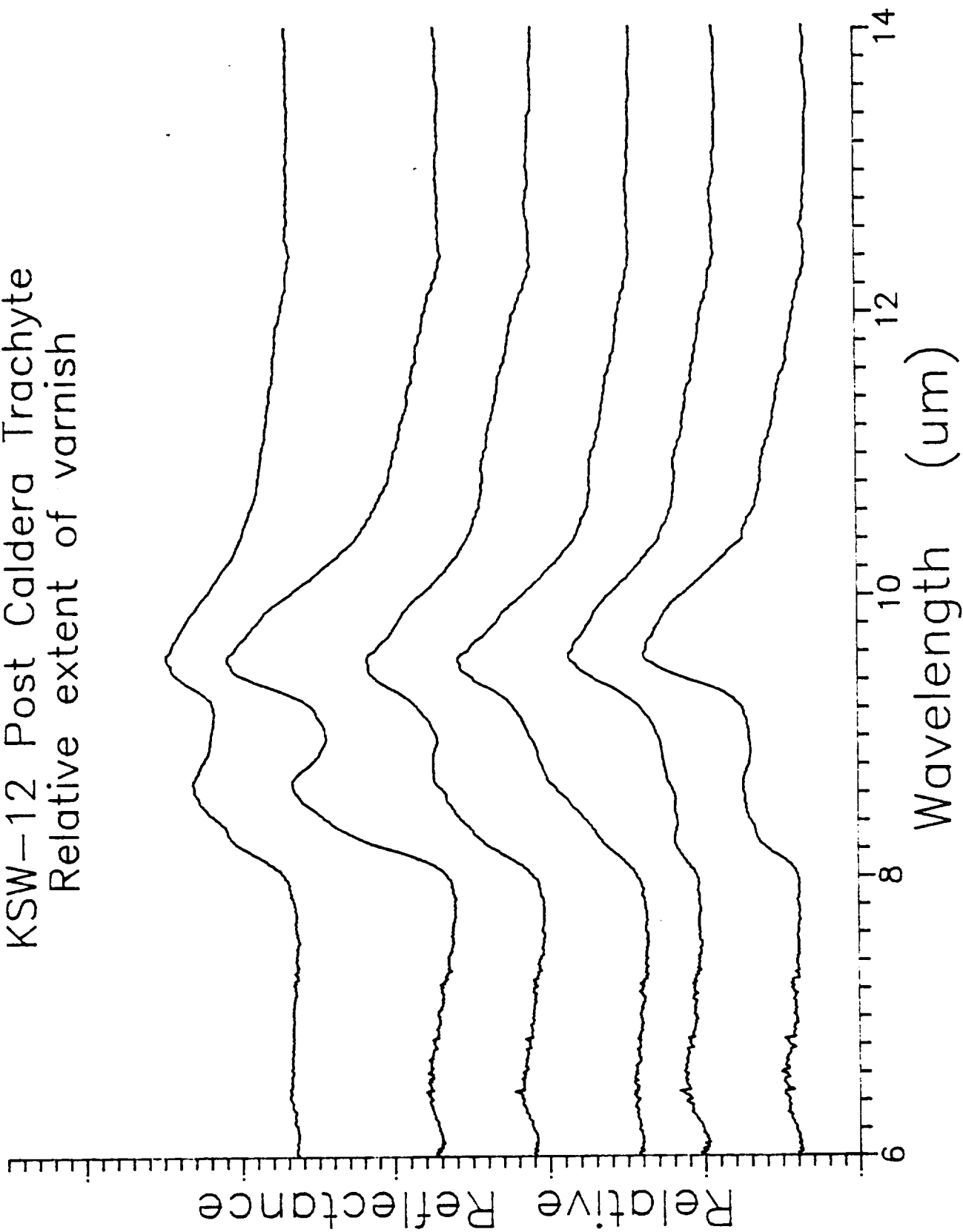
KSW-13 Fine Grained Porphyritic Syenite
Relative extent of varnish

KSW-14 Fine Grained Porphyritic Syenite
Relative extent of varnish

Relative Reflectance

Wavelength (um)
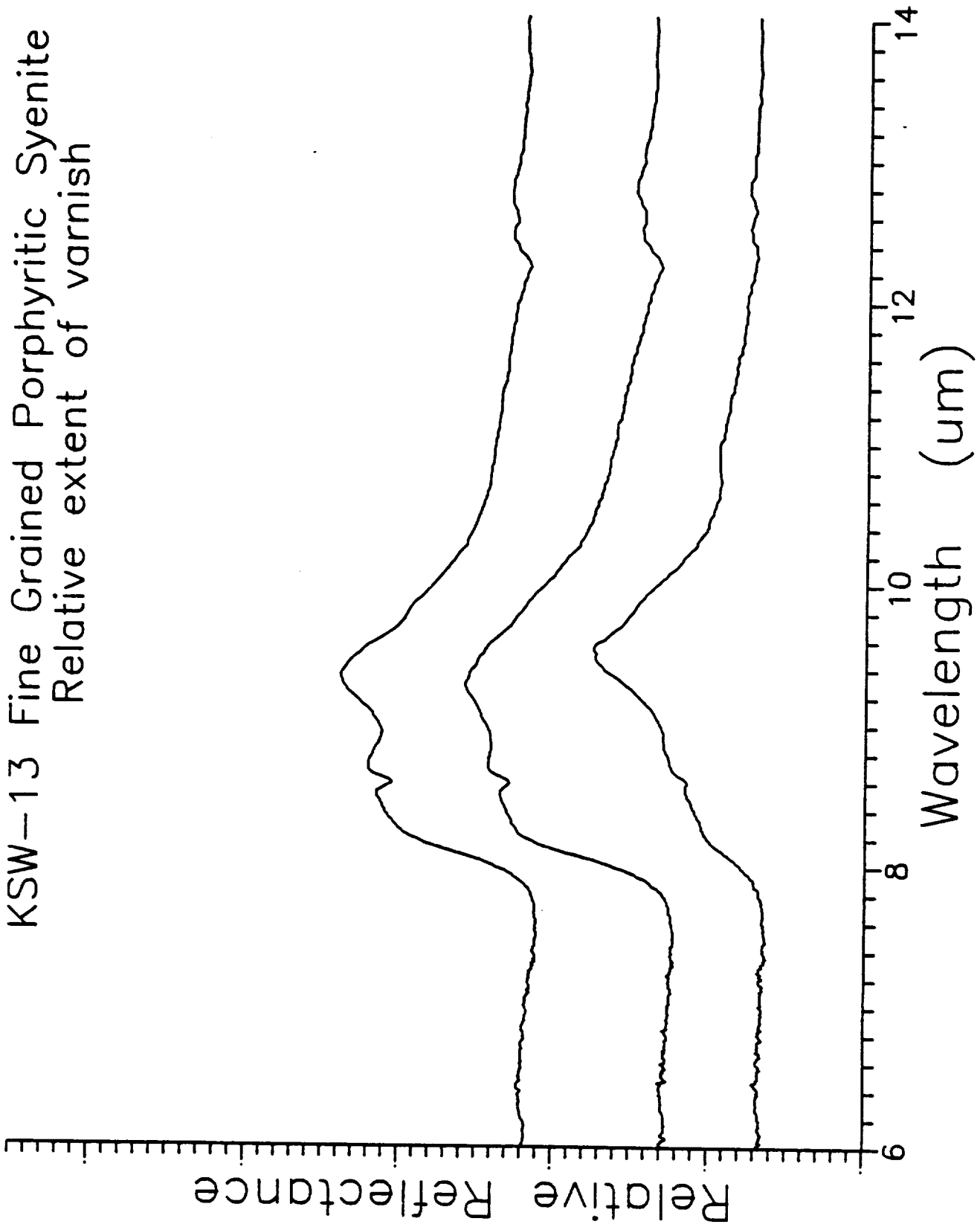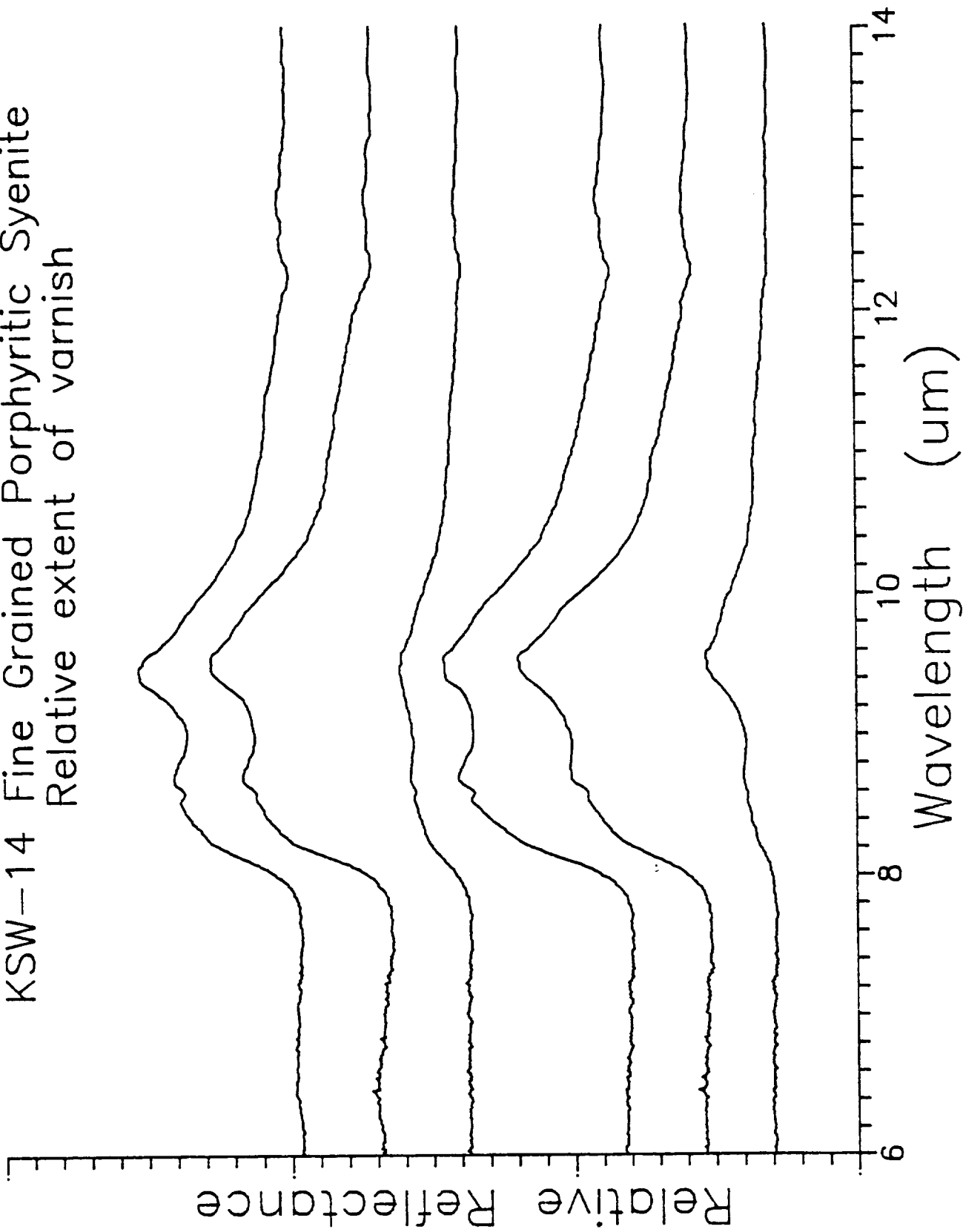
KSW-24 Trachyandesite
Relative extent of varnish

Wavelength (um)

Relative Reflectance

KSW-25 Seriate Syenite
Relative extent of varnish
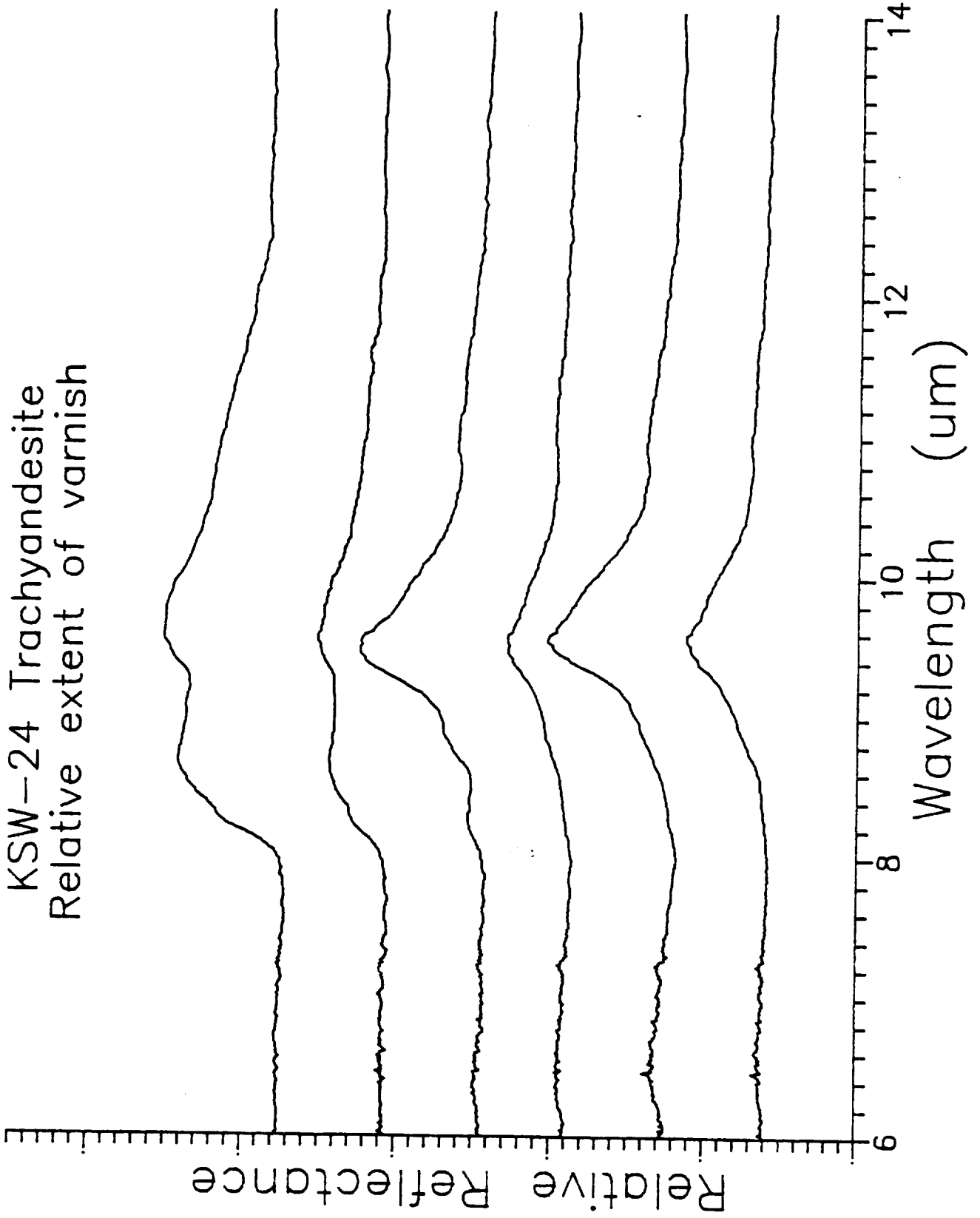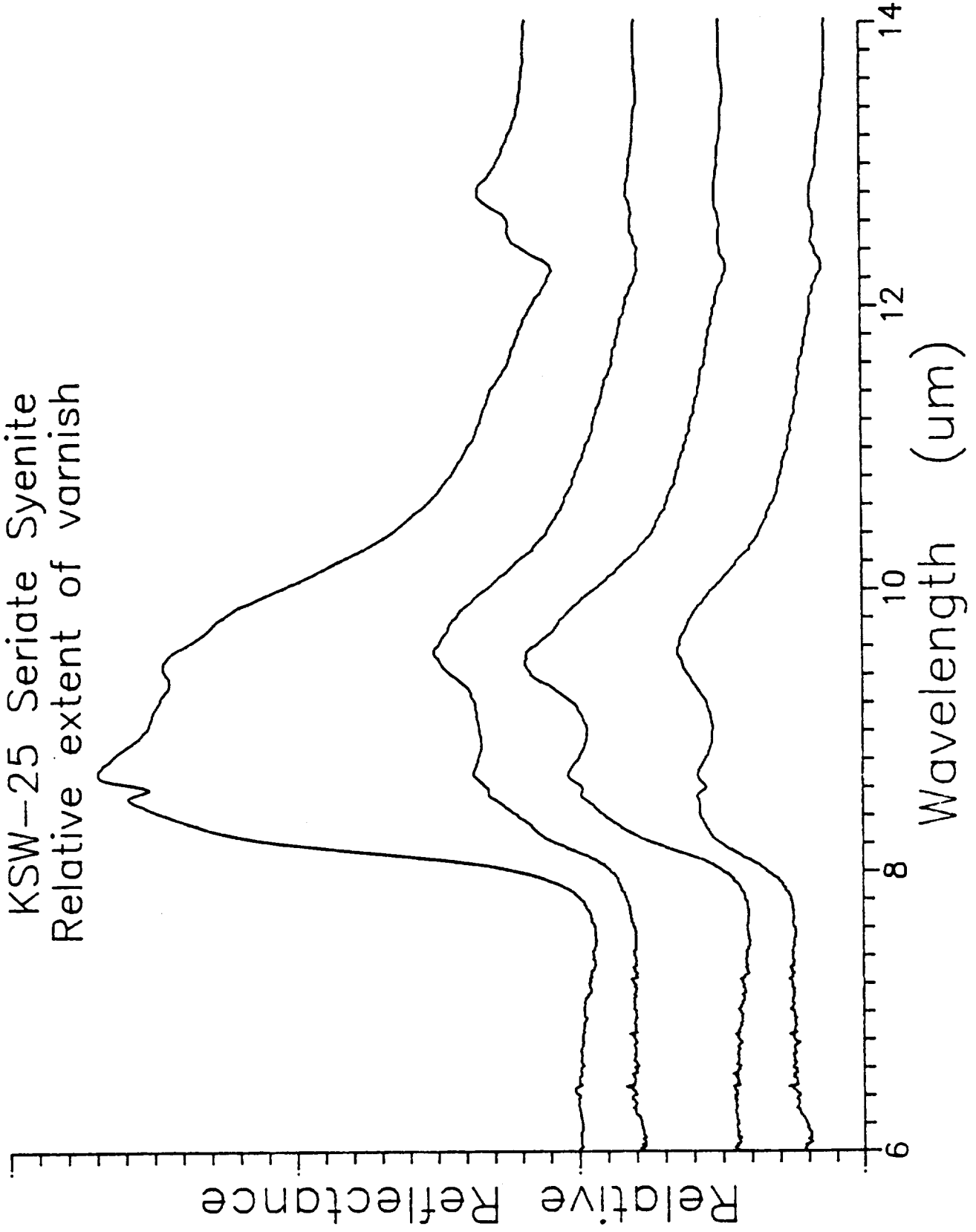
Appendix Thirteen

PFES spectra of coated and fresh surfaces
of five rock types
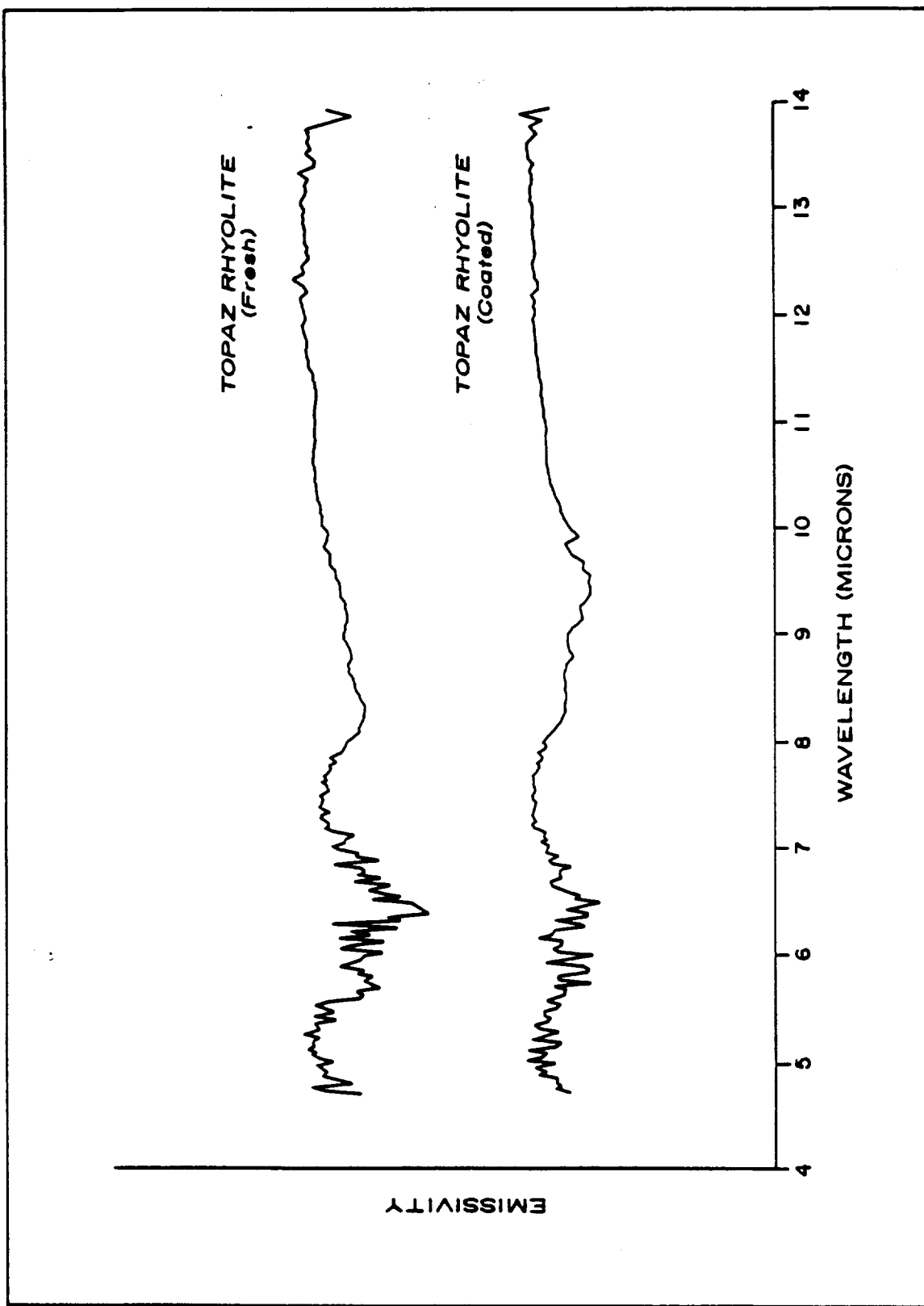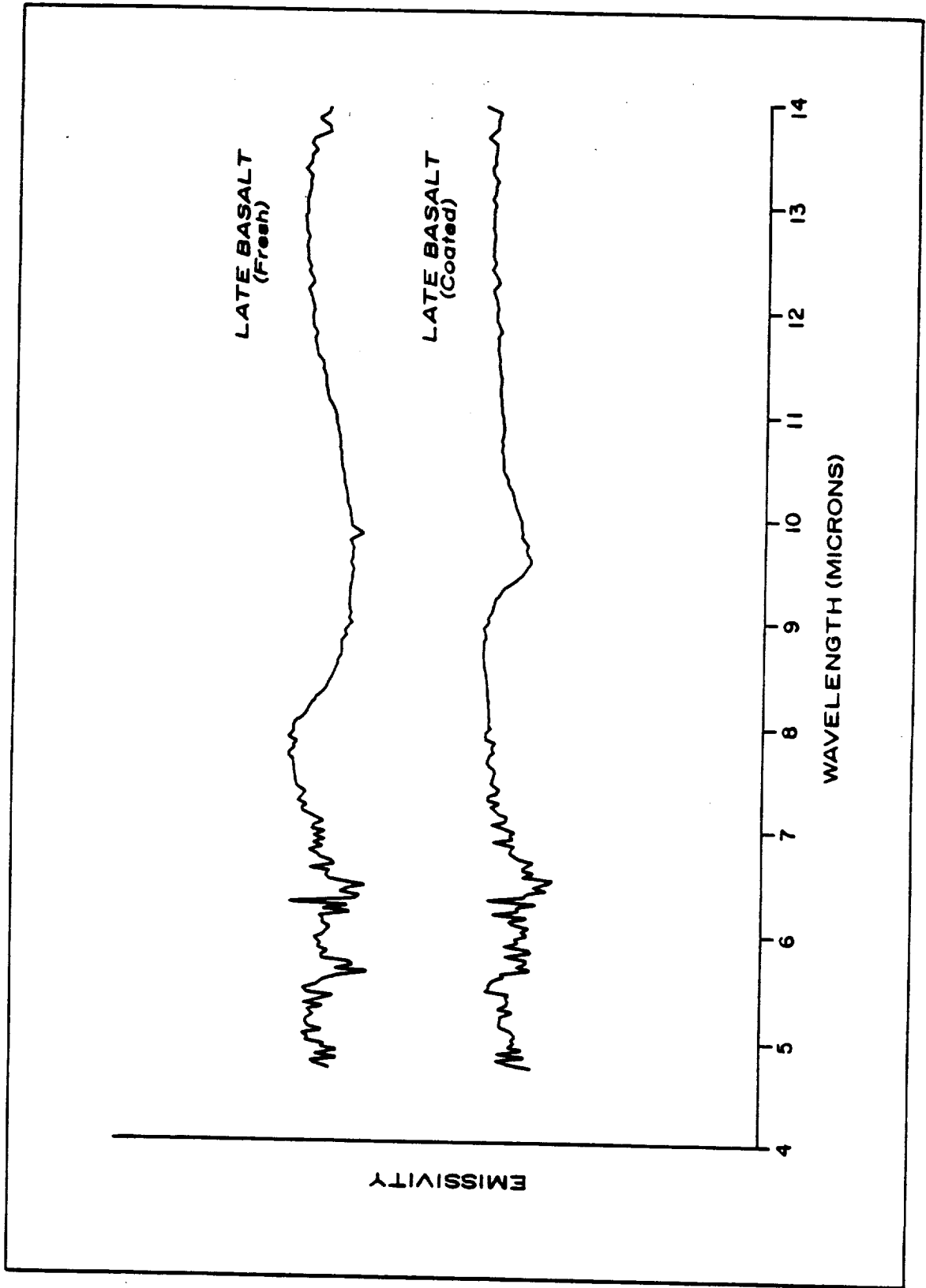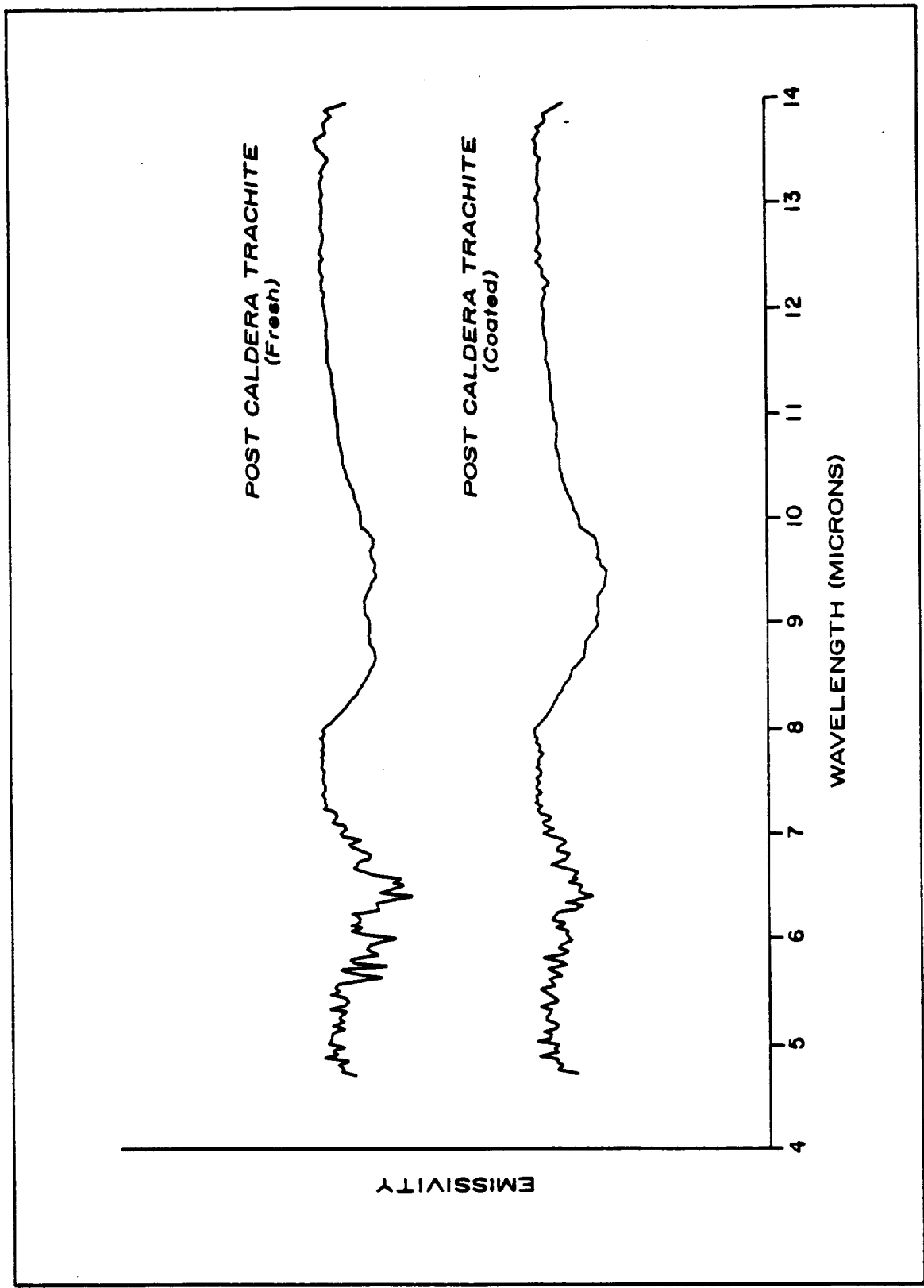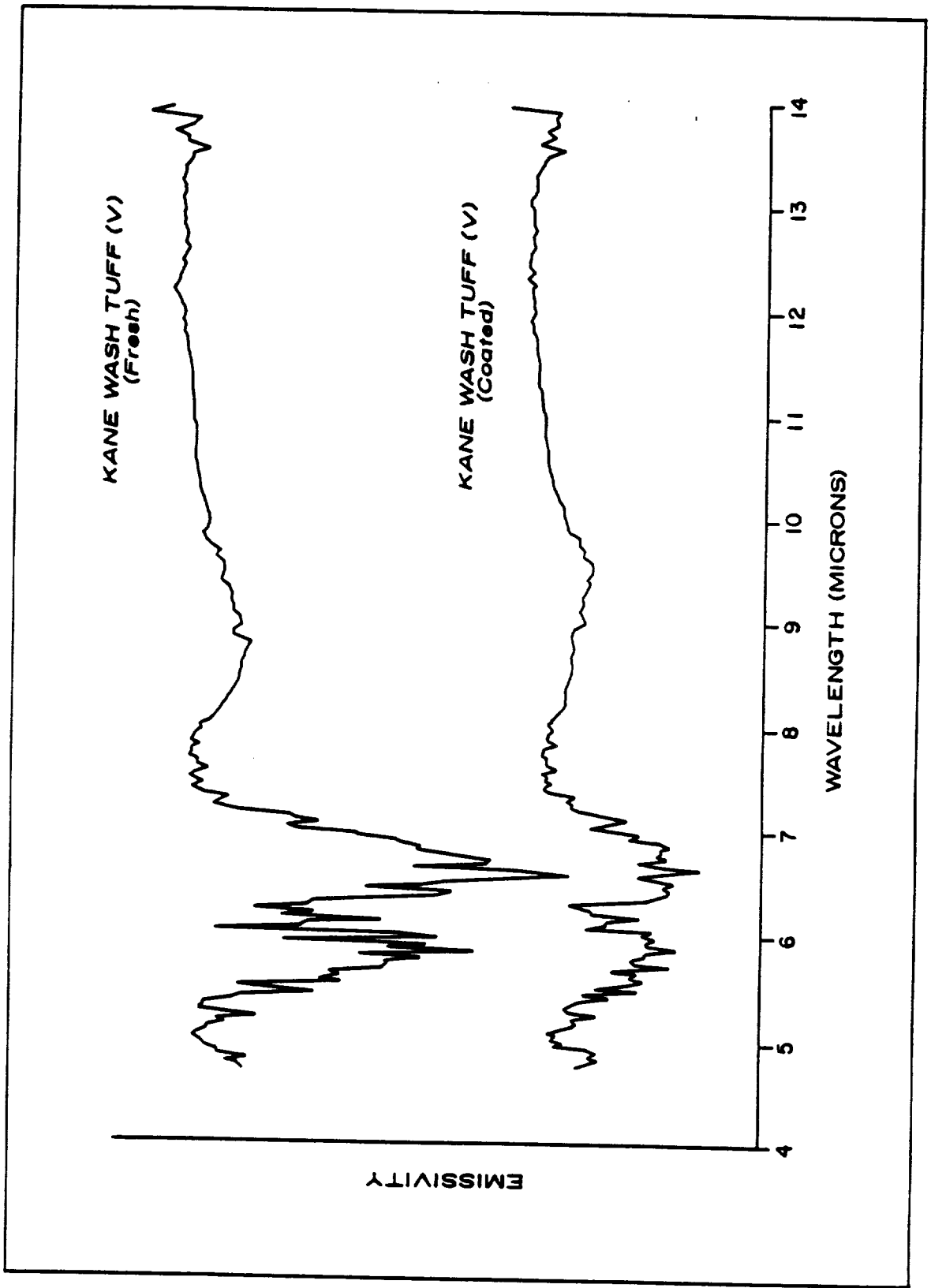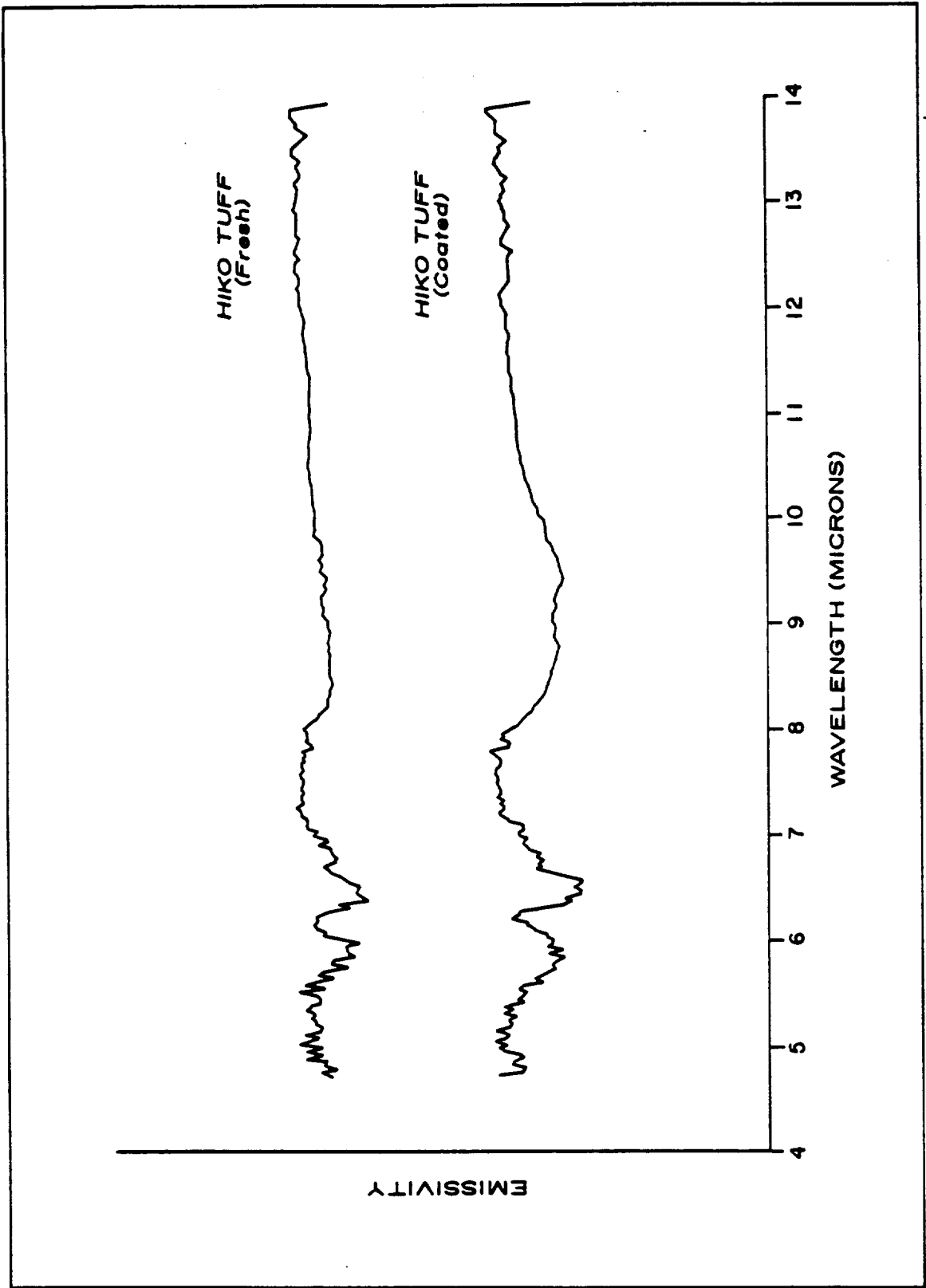
TOPAZ RHYOLITE
(Fresh)

TOPAZ RHYOLITE
(Coated)

EMISSIVITY

WAVELENGTH (MICRONS)

LATE BASALT
(Fresh)

LATE BASALT
(Coated)

EMISSIVITY

WAVELENGTH (MICRONS)

POST CALDERA TRACHITE (Fresh)

POST CALDERA TRACHITE (Coated)

EMISSIVITY

WAVELENGTH (MICRONS)

KANE WASH TUFF (V)
(Fresh)

KANE WASH TUFF (V)
(Coated)

EMISSIVITY

WAVELENGTH (MICRONS)

HIKO TUFF (Fresh)

HIKO TUFF (Coated)

EMISSIVITY

WAVELENGTH (MICRONS)

PART III

PART III

INTERREGIONAL COMPARISONS OF DESERT VARNISH

David M. Spatz, Principle Author
Mackay School of Mines
University of Nevada, Reno
Reno, Nevada 89557

TABLE OF CONTENTS

LIST OF FIGURES AND TABLES

INTERREGIONAL COMPARISONS OF DESERT VARNISH

INTRODUCTION

After conducting a detailed examination of desert varnish (varnish) on volcanic rocks at three study sites in southern Nevada and evaluating the influence of varnish on Landsat imagery (Spatz et.al, 1987a, 1987b, 1988; Spatz and Taranik, 1989), comparisons were made with varnishes from other semiarid regions. This interregional investigation was conducted in order to determine how generally conclusions drawn from the southern Nevada study may be applied to other regions as well. Of particular interest were 1) the lateral distribution of varnish at the hand sample and outcrop scale, 2) thicknesses of varnishes and the relative proportions of thick laminated occurrences to thin impregnating films, 3) the relative proportions of surfaces with well developed mature varnish accumulations to surfaces with poorly developed varnish, 4) presence and nature of weathering rinds and dark secondary bands of Ca enrichment, and 5) implications for Landsat imagery based on applications developed from the southern Nevada investigation.
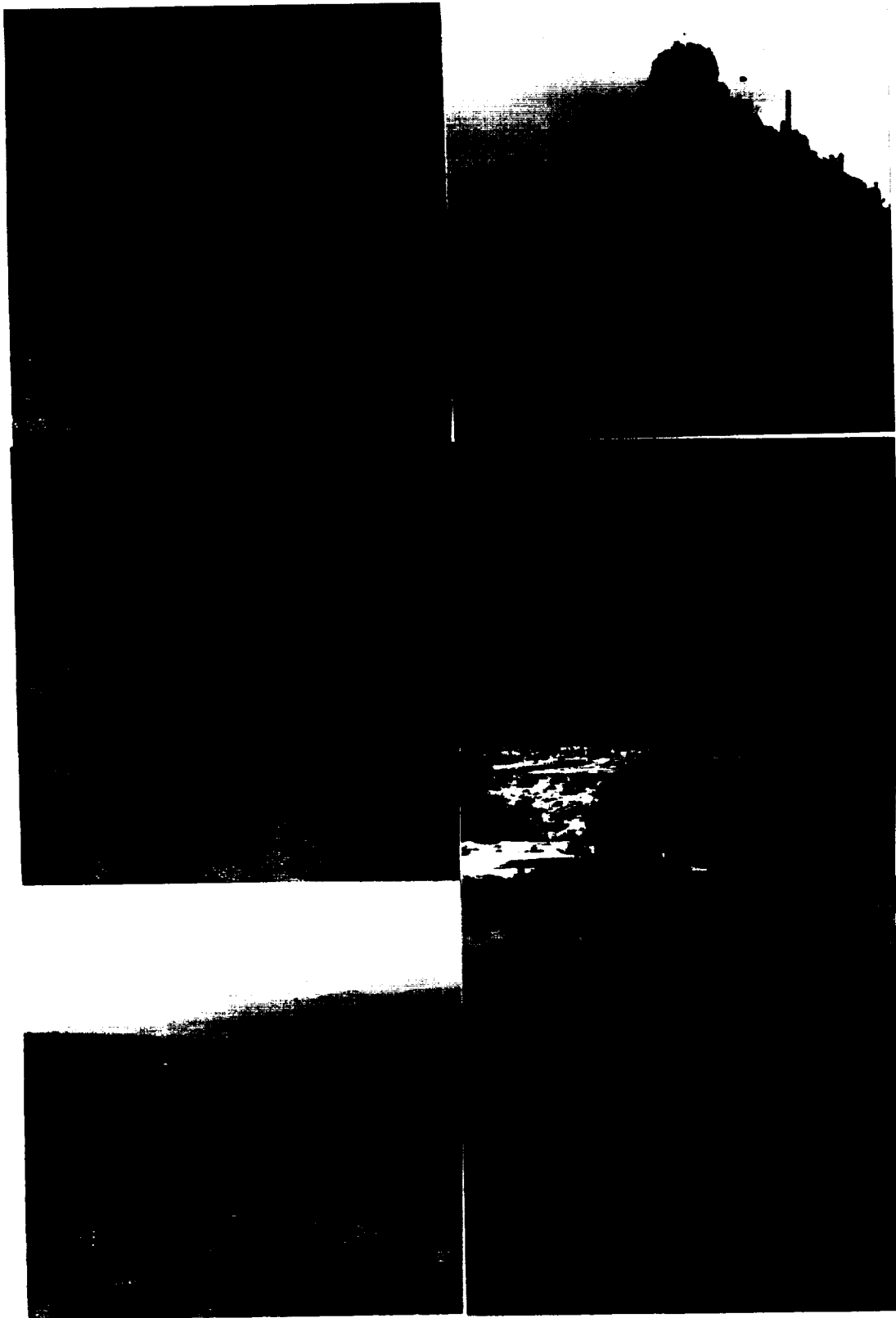
STUDY AREAS

Four semiarid regions were examined, photographed and sampled.
These sites include the Mojave Desert of southern California, the
Sonoran Desert of western Arizona, the Colorado Plateau of
northern Arizona and southeastern Utah, and the steppe of eastern
Africa. Figure 1 contains typical scene photographs of these
areas, and Figures 2 and 3 show sample locations.

MOJAVE DESERT. The Mojave Desert (Figures 1 and 2) is an arid
to semiarid region defined physiographically by mountain ranges
uplifted along the San Andreas fault on the southwest and the
Garlock fault on the northwest. The region is disrupted
tectonically by faults which parallel these two regional
structural breaks. The area is dominated by Basin and Range
topography, characterized by low ranges that separate undrained
valleys. Vegetation is sparse, even more so than in southern
Nevada, and soil and rock exposures predominate at most sites.
Grasses, sage, and other low growth are the principle plants.

Dibblee and Hewett (1966) have summarized the geology of the
Mojave Desert. The area is underlain by widespread exposures of
Precambrian gneisses, schists, granites and granitic rocks. The
Precambrian rocks are overlain unconformably by Paleozoic marine
sedimentary strata exposed primarily in the northeast part of the
province. Mesozoic andesite flows and subvolcanic intrusive
masses and other more felsic intrusions are present in the

Figure 1. Scene photographs, representing typical terrain within the Mojave Desert, Sonoran Desert, and east African study sites. Upper Left: Chocolate Mountains, Mojave Desert, southeastern California. Upper Right: Growler Mountains, northwest of Ajo, Arizona. Middle Left: Tucson Mountains, Gates pass, southwest of Tucson, Arizona. Middle Right: Jurassic Entrada Sandstone, 15 mi south of Moab, Utah. Lower Left: Olduvai Gorge, northern Tanzania. Lower Right: Ngorongoro crater, northern Tanzania.

SOUTHWESTERN U.S.A.
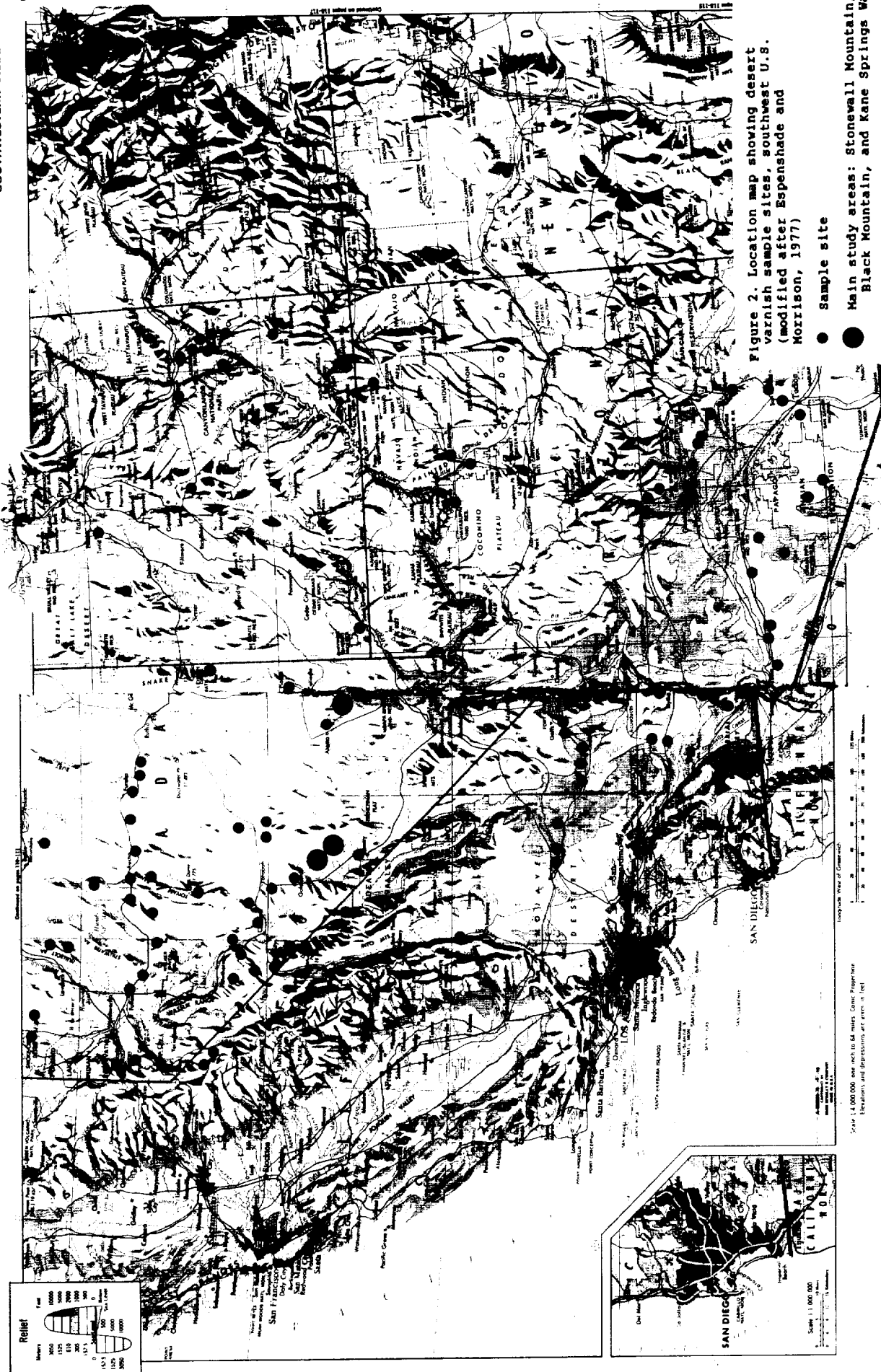
Figure 2. Location map showing desert
varnish sample sites, southwest U.S.
(modified after Espenshade and
Morrison, 1977)

• Sample site

● Main study areas: Stonewall Mountain,
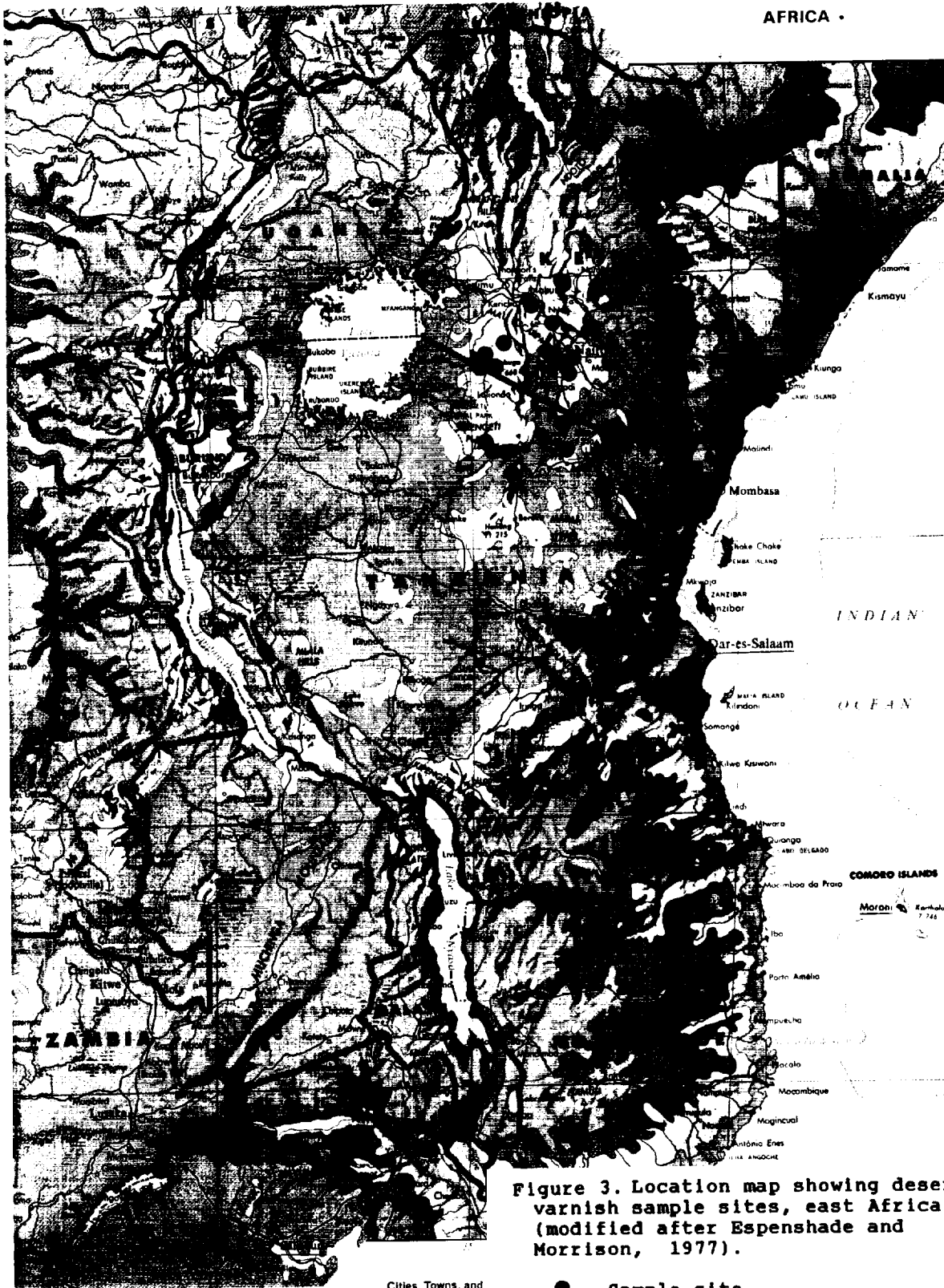   Black Mountain, and Kane Springs Wash

AFRICA ·

Figure 3. Location map showing desert
varnish sample sites, east Africa
(modified after Espenshade and
Morrison, 1977).

Cities, Towns, and   ●   Sample site

central Mojave. Nonmarine middle to late Tertiary volcanic and sedimentary rocks are widespread. The volcanic rocks range in composition from rhyolite through andesite to basalt, erupted from vents and fissures later filled with volcanic plugs. Unconsolidated Quaternary alluvium occupies the broad valleys. The consolidated basement section has been faulted and folded into a west to northwest trending structural grain during the late Tertiary to early Quaternary.

SONORAN DESERT. The Sonoran Desert of western and southern Arizona occupies the southern extension of the Basin and Range Province and is characterized by alternating linear mountain ranges and broad alluvium filled valleys (Figures 1 and 2). Precipitation is generally 5 to 10 inches annually, and desert vegetation is dominated by cactus varieties.

The geology of Arizona has been summarized by Hayes (1969). Lower Precambrian strata, consisting of metavolcanics and metasediments are exposed in the northwest trending ranges along the northern and northeastern fringes of the Sonoran Desert. Upper Precambrian strata, composed dominantly of shallow marine clastic sediments, occur in isolated ranges. The early Paleozoic experienced shallow sea transgression from both the northwest and the southeast, filling geosynclines that would collect transgressive and regressive successions of shale, sandstone and limestone throughout the era. A northeast trending highland, that transects the Sonoran Desert and separated the two

geosynclines, collected the thinnest strata. Throughout the majority of Mesozoic time the Sonoran Desert region of Arizona was largely terrestrial, and most rock formations of the era are fluvial clastics. Major plutonism occurred during the era, however, and is represented today largely by metamorphic core complexes. The late Cretaceous and early Cenozoic Periods were punctuated by the Laramide orogeny, which resulted in major tectonic disturbance, mountain building, intrusive and volcanic activity and mineral deposition. This crustal strain continued throughout much of the Cenozoic, which is marked by faulting, folding, plutonism and volcanism as well. The broad valleys throughout the Sonoran Desert are filled largely with unconsolidated Quaternary gravels.

COLORADO PLATEAU. The semiarid climate of the Colorado Plateau (Figure 1) produces 5 to 10 inches of precipitation annually. Terrain is marked by buttes and mesas with isolated mountain ridges and peaks. Vegetation is predominantly grasses, sage and other scattered low brush and scrub juniper and pine.

The geology of Utah has been summarized by Tooker and Stewart (1969). The Colorado Plateau of southeastern Utah is underlain almost exclusively by Mesozoic terrestrial sedimentary rocks, deposited under semiarid and oxidizing conditions. The section is dominated by Triassic and Jurassic Formations, including from oldest to youngest the Moenkopi, Chinle, Kayenta, Navajo, Carmel, and Entrada. These deposits are comprised of sandstone and other

fine continental clastics. They include crossbedded dune deposits and tend to be buff to rusty red in color. Although this section is faulted and folded and intruded by Tertiary granitic bodies in places, they appear largely subhorizontal and undeformed. Of course, the region includes broad sections of unconsolidated Quaternary alluvium.

STEPPE OF EAST AFRICA. Throughout much of Kenya and Tanzania (Figures 1 and 3) are broad semiarid provinces of steppe climate with local savannah zones. The steppes are broad plains with gentle rolling hills and occasional volcanic mountains (Mount Kilimanjaro, for example). They are mantled with relatively continuous grass cover with scattered umbrella and yellow bark acacia trees. Much of the steppe receives about 4 to 5 inches of rainfall annually with larger amounts at transition zones with savannahs.

A summary of the geology of Africa is given by Derry (1980). Most of Kenya and Tanzania, where the study took place, is underlain by Precambrian metamorphic rocks, including granitic gneisses and biotite schist. The Precambrian basement is rifted along the presently active Great Rift Valley. The rift has resulted in voluminous extrusion of volcanic deposits, including felsic ash flow tuffs and andesitic to basaltic lavas. Several high stratavolcanos developed, including Mount Kilimanjaro, the highest mountain in Africa.

SAMPLE SITES

Sample sites are shown in Figures 2 and 3. Observations at each site focused on the nature and distribution of desert varnish; associations of desert varnish with outcrop properties and other rock coatings including vegetative cover; thickness, distribution and continuity of varnish; and weathering characteristics of host rocks. Most sites were photographed and samples were collected at many. Over 50 sites were examined in the Mojave and Sonoran Deserts and the Colorado Plateau and numerous other examples of desert varnish have been observed elsewhere in the Basin and Range Province, mostly in Nevada (Figure 2). Approximately 20 sites were examined in eastern Africa.

FIELD CHARACTERISTICS OF DESERT VARNISH

Photographs of outcrops exhibiting desert varnish from the Mojave Desert are shown in Figure 4. Photos of varnish bearing outcrops from the Mojave and Sonoran Deserts and the Colorado Plateau are shown in Figure 5, and photographs from the East African study site are presented in Figures 6 and 7. Varnish occurrences from these areas are quite similar to varnishes from our detailed study sites in southern Nevada. They are characterized by an extremely variable degree of development,

Figure 4. Photographs, showing well developed desert varnish on outcrops in the Mojave Desert, southeastern California. Upper Left: dacitic flows, Newberry Mountains, 5 miles west of Newberry Springs. Upper Right: ash flow tuff, Chemehuev Mountains off Highway 95. Middle Left: Triassic-Jurassic metasediments, Coxcomb Mountains off Highway 177. Middle Right: dacitic ash flows, 10 miles north of Vidal Junction off Highway 95. Lower Left: coarse granite in background, fine granite in foreground, Chuckwalla Mountains, Desert Center. Lower Right: exfoliated ash flow, 10 miles south of Palo Verde off Highway 78.

Figure 5. Photographs, showing well developed desert varnish on outcrops from the Mojave and Sonoran Deserts and the Colorado Plateau. Upper Left: densely welded ash flow tuff, Chocolate Mountains, Mojave Desert off Highway 78. Upper Right: ash flow tuff at Roll Arizona. Middle Left: granitic gneiss 8 miles west of Apache Junction, Arizona. Middle Right: Permian Coconino Sandstone at the rim of the Grand Canyon. Lower Left: Jurassic Entrada Sandstone 12 miles northwest of Moab Utah off Highway 163. Lower Right: Entrada sandstone 4 miles north of Moab off Highway 163.
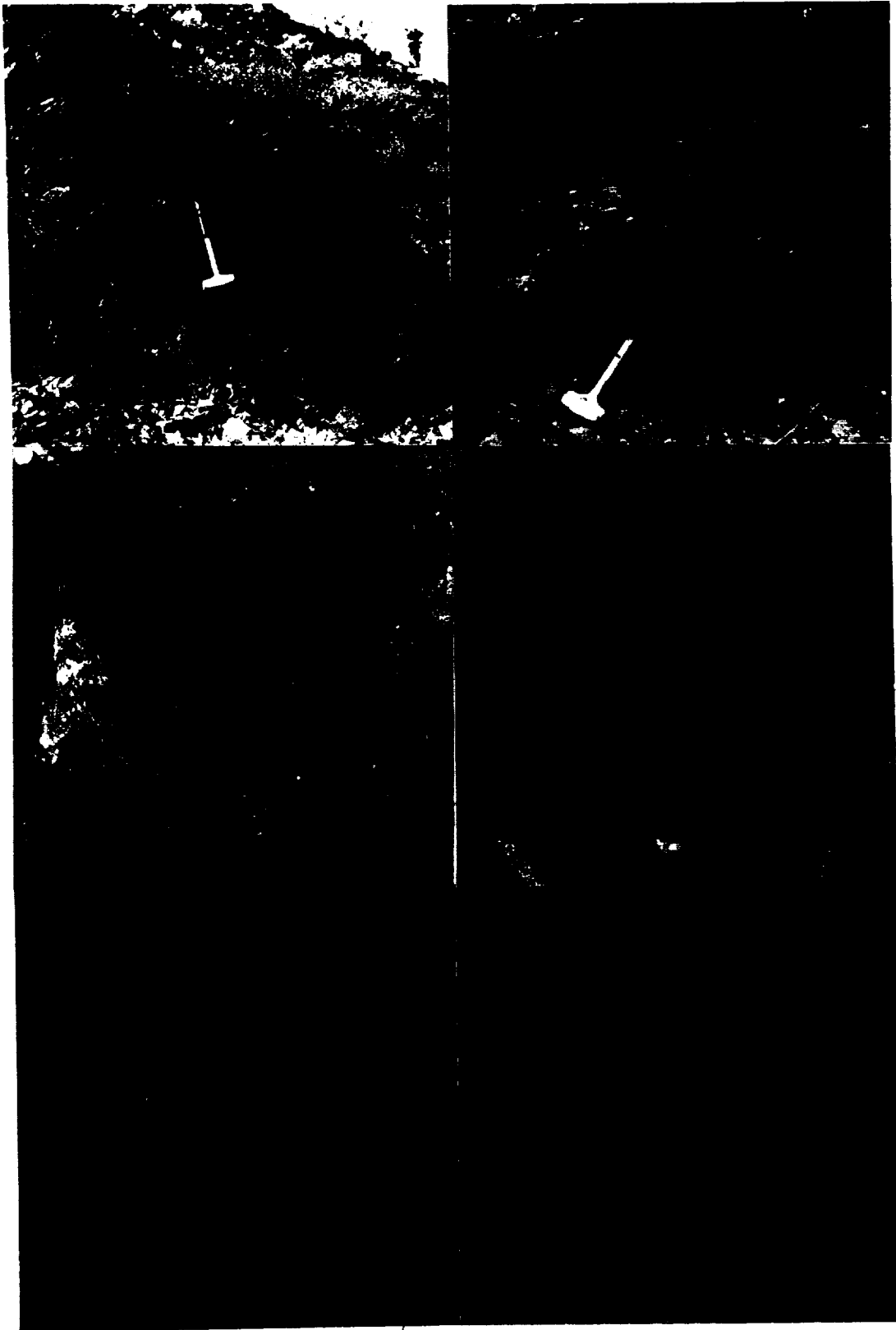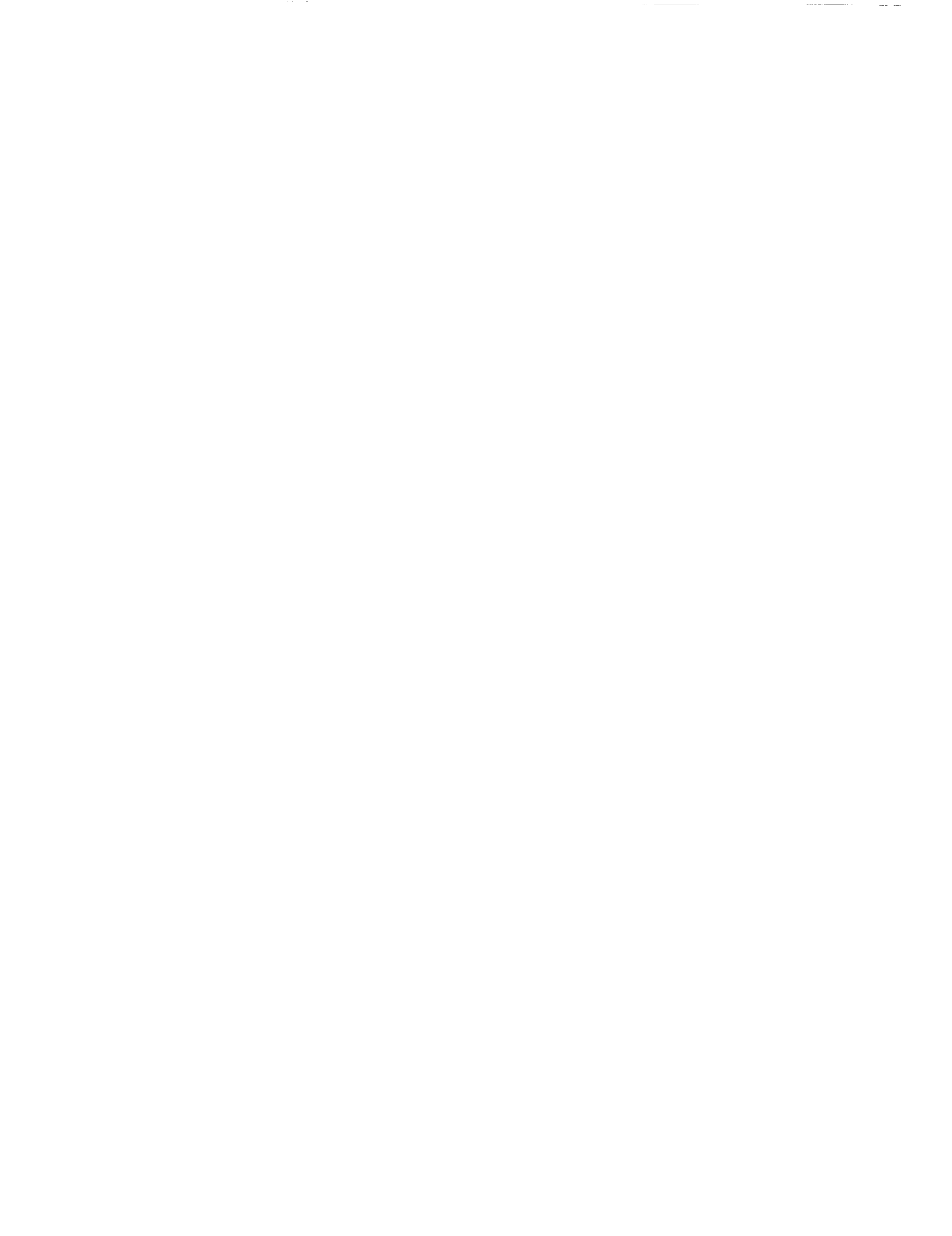
Figure 6. Photographs of outcrops from the Serengeti, southwest
Kenya and northwest Tanzania. Upper Left: mafic metavolcanics on
the Sand River at the border between Kenya and Tanzania, showing
well developed desert varnish adjacent to unvarnished surfaces
exhumed by exfoliation slabs. Upper Right: sandstone with thin Fe
rich varnish, Masai Mara, southwest Kenya. Middle Left: well
developed desert varnish on andesite, south shore of Lake Nakuru,
Kenya. Middle Right: close-up of varnish on andesite, south shore
of Lake Nakuru, Kenya. Lower Left: granite inselberg at Naabi Hill
in the Serengeti, northwest Tanzania, showing organic dominated
streaks intermixed with some desert varnish. Lower Right: lava beds
with well developed desert varnish, Seronera Valley in the northern
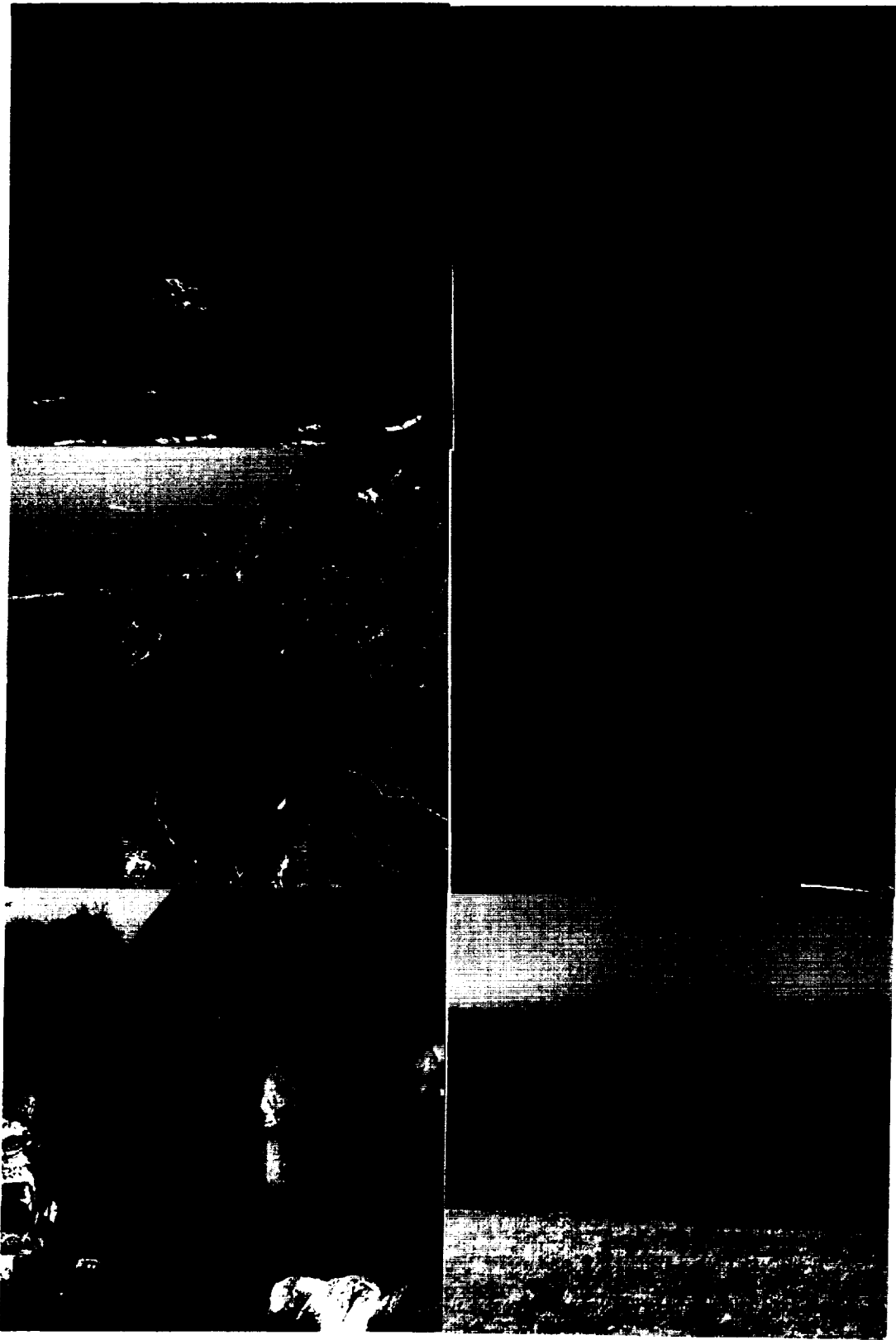Serengeti, northwest Tanzania.

Figure 7. Photographs of outcrops from Kenya and Tanzania, showing variable development of desert varnish. Upper: volcanic ash deposit, 8 miles south of Nairobi, Kenya. Middle Left: sandstone boulder near Olduvai Gorge, northwest Tanzania. Middle Right: basaltic andesite, showing well developed desert varnish west rim of Ngorongoro Crater (collapsed caldera). Lower: volcaniclastic with admixed desert varnish and organic growth, inner rim of Ngorongoro Crater, northwest Tanzania.
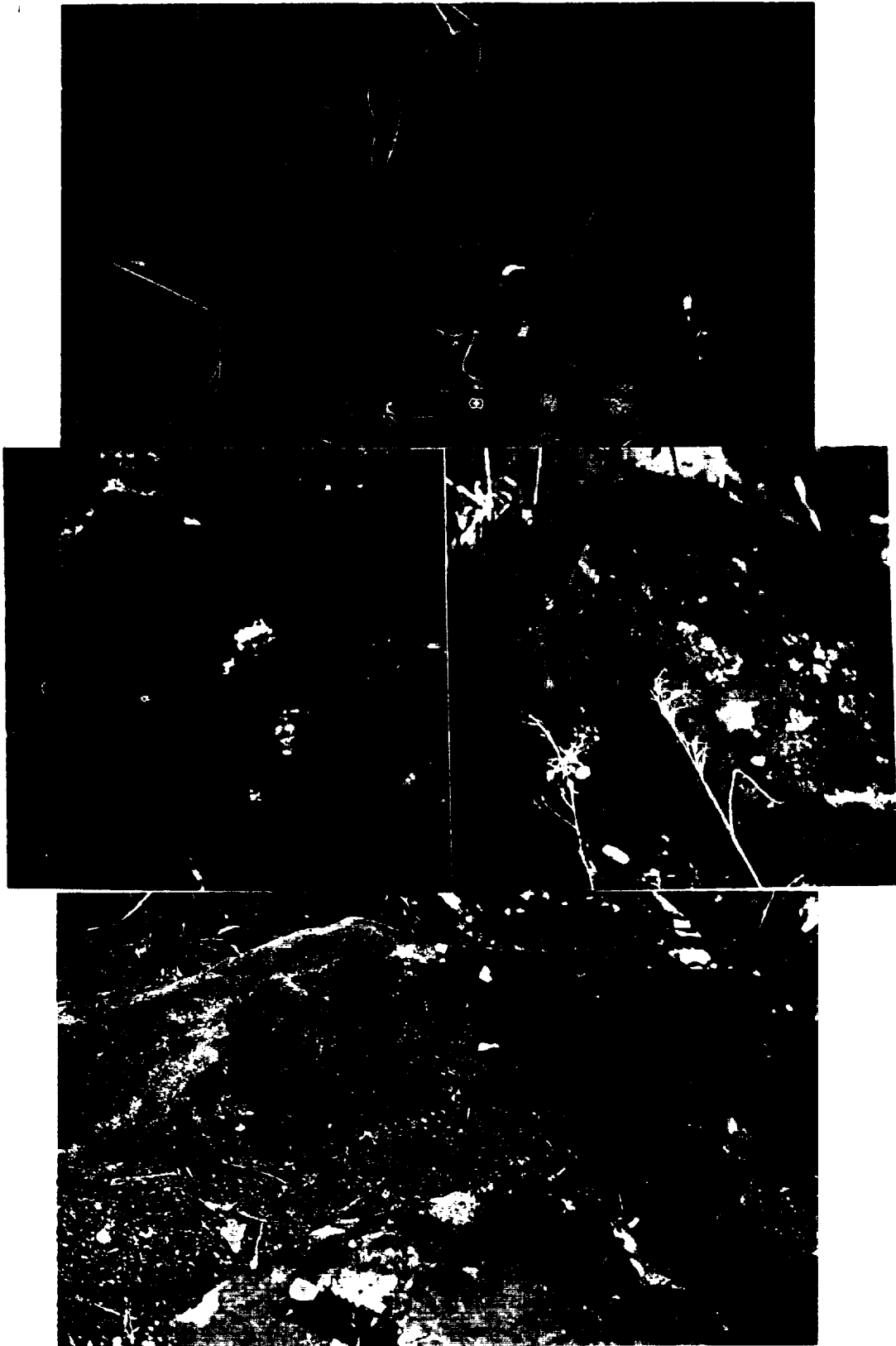
abrupt discontinuity and thin impregnating films that ride on unstable surfaces. Exfoliation slabs spall off the outcrops carrying mature varnish accumulations with them and periodically exhuming unvarnished but weathered surfaces. Denser more resistent formations and beds host the more mature and extensive varnish deposits. Varnish is deposited more consistently on the vertical and subvertical rock slopes so that horizontal views contain much more consistent varnish cover than vertical or overhead views which are imaged by Landsat.

SOUTHWEST U.S. Even though desert varnish development in the Mojave Desert of southern California is quite mature (Figures 4 and 5) and somewhat more extensive than varnishes in southern Nevada, the degree of development is no thicker or darker than the "heavy" deposits described from southern Nevada. The difference is that there is more continuous "heavy" varnish occurrences in the Mojave. There seems to be a limit on how thick and mature a varnish can eventually develop to, and the limit is probably set largely by the stability of the rock surfaces and the time it takes for exfoliation slabs to develop and spall off the outcrop, or the time it takes for mineral grains to dislodge. Ash flow tuffs and the fine clastic and granular rocks with more mafic tendencies tend support the more mature varnish coatings.

From a horizontal view the hillsides and vertical to steeply sloping rock surfaces are often very dark with varnish, and steeply dipping strata like the Triassic-Jurassic sediments of

the Coxcomb Mountains (Figure 4) tend to weather into enechelon ridges one above another upslope so that from a distance it is chiefly the subvertical outcrop surfaces that are visible. On the outcrop, however, the ridges are observed interleaved with subhorizontal surfaces mantled with soil, fine detritus and grasses (Figure 4, middle left). Rock surfaces are unstable and mature desert varnish accumulations are continually being removed on exfoliation slabs, exposing unvarnished surfaces (Figure 4). Some of the exfoliation slabs are extremely thin (2-3mm thick, Figure 4, middle right) and may appear to be desert varnish crusts to a careless observer.

Coarse granular rocks like medium to coarse grained granite tend to support weakly developed varnish, since surface crystals are continually being dislodged, and the surface remains too unstable and ephemeral for mature varnish accumulations (Figure 4, lower left). Finer varieties of granite, however, may support quite extensive varnish cover, particularly if there is a mafic or dioritic tendency (Figure 4, lower left). Figure 4 (lower left) shows a coarse granite with poorly developed desert varnish in contact with a fine dioritic granite, supporting well developed varnish. This relationship suggests that the varnish on the finer granitic variety is due partly either to its more stable surface, or to derivation of varnish components from the underlying diorite substrate, or both, rather than due to an external supply difference, since the two units are juxtaposed. At one locality in the Mojave - the Chemehuev Mountains (Figure

4, upper right) - an ash flow tuff boulder supported an extremely thick (3mm) desert varnish deposit in a shallow bowl-like depression (discussed in more detail in the following section).

Occurrences of desert varnish at the outcrop scale in the Sonoran Desert of southwest Arizona (Figure 1, upper right and middle left and Figure 5, upper right and middle left) appear identical to varnishes of southern Nevada. Distinct weathering rinds and Ca enrichment layers just below leached zones at the rock surface were observed in ash flow tuff formations at several locations, including Roll, the Saucedo Mountains and 5 miles NW of Sells.

Desert varnish development on the terrestrial sandstones and mudstones of the Colorado Plateau are shown in Figures 1 (middle right) and 5 (lower right and left). Varnishes from the Colorado Plateau appear different in several general respects. Firstly, they are redder in color, reflecting the reddish hues of their underlying host rocks. Varnishes in general seem to be more or less darker, redder, or purplish, if the host rocks possess those respective tones or hues, a property expected since varnishes are typically amorphous and translucent. The redder hue is also likely due to high Fe/Mn ratios in the varnishes since water and dust surrounding these units is likely enriched in Fe oxide rich detritus weathered from the red bed host rocks. Secondly, varnishes from the Colorado Plateau form vertical streaks on cliff faces apparently in response to deposition from water runoff. Varnishes tend to develop to more mature levels on the

more resistent sandstone interbeds in many of the formations. These beds form higher relief ledges that protrude slightly from the cliffs and slopes (Figure 1, middle right). The less resistent interbeds do not support significant varnish.

EAST AFRICA. Field examples of desert varnish from east Africa are shown in Figures 6 and 7. Occurrence of desert varnish in this steppe climate appears very similar to varnish occurrences in the semiarid regions of the southwest U.S. The east African steppe is largely grass covered and grades into fairly lush savannahs. Moreover, the terrain is largely flat rolling hills (Hemingway's "green hills of Africa"). Thus, outcrop is restricted, which leads to limited occurrences of desert varnish. In addition, the equatorial climate is conducive to biological activity on rock surfaces, and dark growths of fungus and bacteria are common in places (Figure 6, lower left and Figure 7, bottom). Fungus and bacterial growth concentrates within streaks on steep outcrop slopes along water runoff pathways (Figure 6, bottom left) and on flat surfaces where water stagnates after showers. Some secondary coatings are mixtures of organic and desert varnish growth.

DESERT VARNISH MORPHOLOGY

The form and habit of desert varnishes observed in the Mojave

and Sonoran Deserts, on the Colorado Plateau, and in east Africa are identical to the varnishes studied in detail from southern Nevada, with a few isolated and rare exceptions. In the main, varnishes tend to occur as thin films than impregnate the surface, typically to a depth of 1mm or less. It is difficult to locate coherent accumulations in thin section that can be analyzed by microprobe (Figures 8 and 9). Thick accumulations usually occur in small recesses in the rock surface (Figure 8, bottom); however they may overlap onto adjacent protuberances (Figure 9, bottom). Some of the thick deposits are laminated (Figure 9, bottom) in response to cyclic deposition of more Mn or Fe+Mn rich coatings.

A remarkably thick deposit of varnish was sampled in the Mojave Desert (Figure 8, bottom). Megascopically, the deposit resembles asphalt. It is about 3mm thick, black with disseminated mineral and lithic grains, and forms a distinct layer with a sharp contact with the underlying ash flow tuff. The deposit covers an area of about 10x10cm, feathering out laterally into typical varnish cover. Thin section observation and SEM-EDX imagery (Figure 8, bottom) shows that the layer is composed chiefly of felsic mineral grains and felsic lithic fragments with a very thin film of desert varnish matrix in the interstices. The layer is bound both against the rock and at the air interface by encrusting desert varnish layers. Apparently an older exposed surface with mature desert varnish was covered by rock detritus which was cemented in place by desert varnish films, then covered

Figure 8. SEM backscatter (primary electron) images of polished rock sections with desert varnish coatings. Samples are from the southwest U.S. Brighter tones represent backscatter from higher atomic number elements. Thus, Fe and Mn rich minerals and desert varnish are bright in these images. The red letters correspond to SEM-EDX compositional probes tabulated in Tables 1 and 2. Upper Left: ash flow tuff from the Sonoran Desert, Roll, Arizona; scale 1mm = 37 micrometers. Upper Right: ash flow tuff, 5 miles northwest of Sells, Arizona in the Sonoran Desert; scale 1mm = 12 micrometers. Middle Left: Entrada Sandstone on the Colorado Plateau, 15 miles south of Moab, Utah; scale 1mm = 4 micrometers. Middle Right: densely welded ash flow tuff, Chocolate Mountains, Mojave Desert, southeast California; scale 1mm = 25 micrometers. Bottom: ash flow tuff, Chemehuev Mountains, Mojave Dessert, southeast California, showing the thick asphalt-like desert varnish deposit, bounded at both the air and rock interfaces by bright Fe+Mn rich desert varnish, but the layer between is largely felsic material. Thin desert varnish films stain this entire layer dark, so that megascopically it appears to be an extremely thick desert varnish layer.
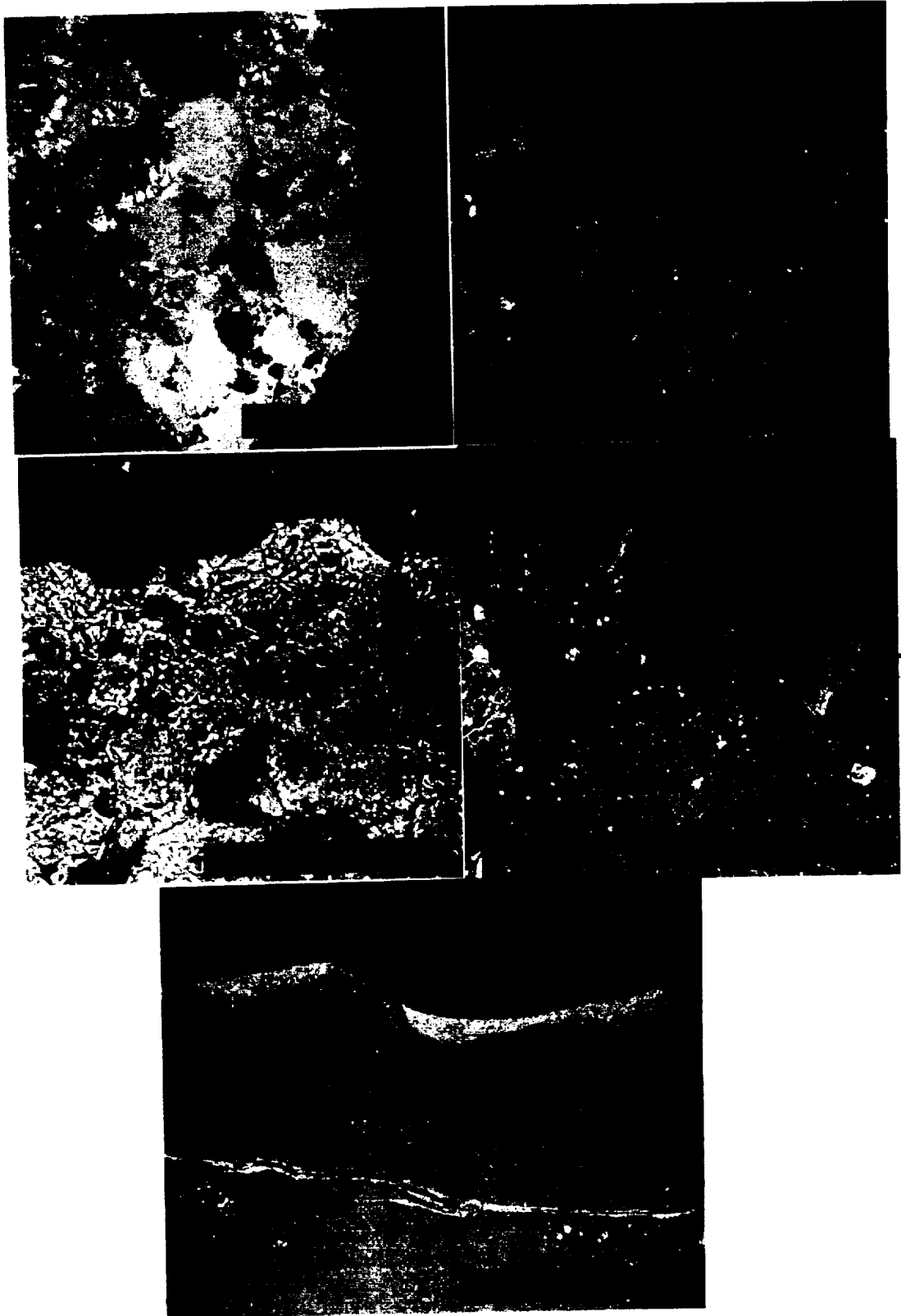
Figure 9. SEM backscatter images of polished rock sections with desert vanish coatings. Bright tones represent backscatter intensities from higher atomic number elements, including the Fe and Mn in desert varnish. Upper: andesite from the south shore of Lake Nakuru, west Kenya; scale 1mm = 12 micrometers. Middle: basaltic andesite with a well developed, thick desert varnish coating from the west rim of Ngorongoro Crater (collapsed caldera), northwest Tanzania; scale 1mm = 25 micrometers. Lower: ash flow tuff south of Nairobi, Kenya. Desert varnish on this unit is unusually thick and well developed, even though the rock is poorly welded, porous, and pumiceous rich; scale 1mm = 37 micrometers.

by another desert varnish accumulation to its present state.

DESERT VARNISH COMPOSITION

SEM-EDX (scanning electron microscope with an energy dispersive X-ray system) was used to probe several polished sections of rock surfaces hosting desert varnish (Tables 1 and 2). Desert varnish samples from the southwest U.S. (Table 1) contain about 31% to 46% combined Fe+Mn. Exceptions include the sandstone sample from the Colorado Plateau which contained 8.98% Fe+Mn and the lower zone of varnish (Figure 8, bottom) that demarks the unusually thick asphalt-like deposit on the ash flow in the Chemehuev Mountains which contains 72.02% Fe+Mn with 60.84% Mn. Varnishes on the red bed sandstones of the Colorado Plateau are very thin and typically poorly developed, due to the relatively rapid erosion of surface sand grains. The varnishes are very thin. The relatively high Fe/Mn ratio (1.30) is not surprising since these rocks contain abundant iron oxide cement. The varnish zone of this sample may have included some clay component, which could account for the high Si and Al content.

The unusually high Mn value reporting from the varnish zone in the ash flow tuff from the Mojave Desert (Figure 8, bottom and Table 1) may have originated during an earlier period, prior to deposition of the overlying thick clastic zone containing the varnish cement, or it might possibly have been developed by

ENTRADA SANDSTONE
MOAB, UTAH

ELEMENT	WEIGHT %	OXIDE %
NA	0.01	0.01
MG	1.13	1.87
AL	10.87	20.55
SI	29.34	62.12
K	3.58	4.21
CA	0.51	0.71
TI	0.93	1.55
MN	3.03	3.91
FE	3.94	5.07
O	47.05	
TOTAL	100.00	100.00

O COMPUTED BY STOICHIOMETRY

03-AUG-89   13:55:13

ASH FLOW TUFF
CHEMEHUEV MOUNTAINS

ELEMENT	WEIGHT %	OXIDE %
NA	2.02	0.03
MG	2.17	3.45
AL	7.79	18.49
SI	14.82	38.80
K	1.71	2.06
CA	0.88	1.23
TI	1.01	1.68
MN	8.36	11.44
FE	26.91	34.62
O	36.53	
TOTAL	100.00	100.00

O COMPUTED BY STOICHIOMETRY

03-AUG-89   13:52:02

ASH FLOW TUFF
ROLL, ARIZONA

ELEMENT	WEIGHT %	OXIDE %
NA	0.01	0.01
MG	0.49	0.81
AL	8.36	15.79
SI	17.59	37.63
K	2.74	3.30
CA	1.85	2.59
TI	0.84	1.41
MN	11.39	14.71
FE	18.47	23.76
O	38.27	
TOTAL	100.00	100.00

O COMPUTED BY STOICHIOMETRY

03-AUG-89   13:55:21

BSAM: RESULT OF ANALYSIS OF BULK SAMPLE
SPECTRUM: C8B2

ELEMENT	WEIGHT %	OXIDE %
NA	0.97	1.31
MG	0.01	0.01
AL	2.27	4.29
SI	6.87	14.70
K	2.49	2.99
CA	0.54	0.75
TI	2.35	3.92
MN	47.12	60.84
FE	8.69	11.18
O	28.70	
TOTAL	100.00	100.00

O COMPUTED BY STOICHIOMETRY

03-AUG-89   13:52:11

WELDED ASH FLOW TUFF
CHOCOLATE MOUNTAINS

ELEMENT	WEIGHT %	OXIDE %
NA	0.02	0.02
MG	0.45	0.75
AL	11.70	22.11
SI	18.98	40.61
K	2.12	2.56
CA	1.11	1.56
TI	0.68	1.14
MN	10.70	13.81
FE	13.56	17.45
O	40.67	
TOTAL	100.00	100.00

O COMPUTED BY STOICHIOMETRY

03-AUG-89   13:55:29

ASH FLOW TUFF
SELLS, ARIZONA

ELEMENT	WEIGHT %	OXIDE %
NA	0.02	0.03
MG	0.28	0.46
AL	10.15	19.19
SI	18.43	39.42
K	1.86	2.24
CA	1.19	1.67
TI	0.80	1.34
MN	16.63	21.47
FE	11.03	14.19
O	39.61	
TOTAL	100.00	100.00

O COMPUTED BY STOICHIOMETRY

03-AUG-89   13:52:19

Table 1. SEM-EDX compositional probes of desert varnish. SEM sample sites are shown on Figure 8 in red letters for each of the corresponding analyses in this table. Fe and Mn oxides were computed as FeO and MnO.

ANDESITE
LAKE NAKURU

BSAM: RESULT OF ANALYSIS OF BULK SAMPLE

SPECTRUM: 201A / **SPECTRUM: 301B** / **SPECTRUM: 401A**

ELEMENT	WEIGHT %	OXIDE %		ELEMENT	WEIGHT %	OXIDE %		ELEMENT	WEIGHT %	OXIDE %
NA	0.22	0.03		NA	0.02	0.02		NA	1.25	1.68
MG	0.01	0.01		MG	0.18	0.29		MG	2.07	3.44
AL	4.53	8.74		AL	13.35	26.18		AL	2.73	5.59
SI	15.54	33.25		SI	22.44	48.01		SI	10.33	22.12
K	2.40	2.39		K	2.17	2.61		Y	0.09	0.47
CA	18.89	26.43		CA	1.82	1.43		CA	2.17	7.24
TI	1.40	2.34		TI	1.08	1.67		TI	0.93	1.56
MN	7.35	9.46		MN	4.30	5.55		MN	29.28	37.81
FE	17.86	16.30		FE	11.06	14.23		FE	20.13	25.98
C	26.57			O	43.96			O	31.54	
TOTAL	100.00	100.00		TOTAL	100.00	100.00		TOTAL	100.00	100.00

O COMPUTED BY STOICHIOMETRY (201A) — 16-AUG-89 11:01:20 5-AUG-89

O COMPUTED BY STOICHIOMETRY (301B) — 10:57:27 16-AUG-89

O COMPUTED BY STOICHIOMETRY (401A) — 10:52:05

BSAM: RESULT OF ANALYSIS OF BULK SAMPLE

SPECTRUM: 201B / **SPECTRUM: 301C** / **SPECTRUM: 401B**

ELEMENT	WEIGHT %	OXIDE %		ELEMENT	WEIGHT %	OXIDE %		ELEMENT	WEIGHT %	OXIDE %
NA	3.73	5.03		NA	0.04	1.13		NA	0.03	0.04
MG	2.00	0.01		MG	0.01	0.01		MG	0.01	0.01
AL	8.06	15.22		AL	13.18	24.98		AL	5.50	10.39
SI	28.67	61.33		SI	17.27	36.94		SI	14.40	30.80
K	4.49	5.41		K	1.49	1.90		K	0.59	0.71
CA	3.47	4.86		CA	1.00	1.40		CA	1.00	2.63
TI	0.33	0.55		TI	3.48	5.01		TI	0.78	1.30
MN	0.34	0.44		MN	3.89	5.02		MN	22.49	29.04
FE	5.56	7.15		FE	17.88	23.00		FE	19.50	25.00
O	45.05			O	40.97			O	34.83	
TOTAL	100.00	100.00		TOTAL	100.00	100.00		TOTAL	100.00	100.00

O COMPUTED BY STOICHIOMETRY (201B) — 16-AUG-89 11:01:29 16-AUG-89

O COMPUTED BY STOICHIOMETRY (301C) — 10:59:16 16-AUG-89

O COMPUTED BY STOICHIOMETRY (401B) — 10:52:13

**BASALTIC ANDESITE
NGORONGORO CRATER**

BSAM: RESULT OF ANALYSIS OF BULK SAMPLE

SPECTRUM: 301A / **SPECTRUM: 301D** / **SPECTRUM: 401C**

ELEMENT	WEIGHT %	OXIDE %		ELEMENT	WEIGHT %	OXIDE %		ELEMENT	WEIGHT %	OXIDE %
NA	0.02	0.02		NA	0.97	1.30		NA	0.67	0.90
MG	0.17	0.29		MG	0.50	0.82		MG	0.01	0.01
AL	9.50	17.96		AL	7.20	13.60		AL	9.06	17.13
SI	18.25	39.04		SI	12.84	27.47		SI	31.01	66.34
K	1.44	1.73		K	0.87	1.04		K	4.19	5.05
CA	1.25	1.75		CA	1.51	2.11		CA	0.46	0.64
TI	0.82	1.37		TI	1.44	2.41		TI	0.51	0.84
MN	7.67	9.90		MN	17.19	22.19		MN	1.05	1.35
FE	21.71	27.93		FE	22.59	29.06		FE	6.01	7.73
O	39.16			O	34.91			O	47.03	
TOTAL	100.00	100.00		TOTAL	100.00	100.00		TOTAL	100.00	100.00

O COMPUTED BY STOICHIOMETRY (301A) — 16-AUG-89 10:57:19 16-AUG-89

O COMPUTED BY STOICHIOMETRY (301D) — 10:59:24 16-AUG-89

O COMPUTED BY STOICHIOMETRY (401C) — 10:52:22

Table 2. SEM-EDX compositional probes of desert varnish and rock substrate on samples from east Africa. Spectrum letters A, B, C, and D correspond to the letters on the respective SEM backscatter images in Figure 9. Fe and Mn oxides were computed as FeO and MnO.

enrichment from Mn rich waters permeating laterally along the interface between the rock and the asphalt-like zone.

Combined Fe+Mn content of desert vanishes from east Africa (Table 2) ranges from 26% to 64%. Si and Al are the other chief constituents. Ti is enriched in varnishes on the basaltic andesite and ash flow tuff. The high Fe+Mn content of the exceptionally thick deposit of varnish on the ash flow tuff may be caused by progressive leaching of alkali cations over time from the varnish in addition to progressive enrichment by Fe and Mn. The Fe/Mn ratios on the mafic rocks - basaltic andesite and andesite - reach 2.8 and 1.8, respectively, supporting observations from work on varnishes from southern Nevada that the higher the mafic tendency of the host the higher the Fe/Mn ratios, suggesting that varnish compositions are dependent to some degree on host rock compositions, and that the host rocks may indeed be source rocks for some of the Fe and Mn in varnish.

COMPARISONS WITH SOUTHERN NEVADA

Some comparisons between desert varnishes from the Mojave and Sonoran Deserts and the steppe of east Africa have been drawn throughout the sections above. This section recaps and summarizes the similarities and differences, organized by 1) distribution, continuity and thickness, 2) weathering rinds and secondary zones of enrichment and 3) compositions.

LOCAL DISTRIBUTION OF DESERT VARNISH. Desert varnish distribution, accumulation, continuity and thickness at the microscopic, hand sample and outcrop scale is very similar from region to region, conforming to the detailed observations described for the varnishes in southern Nevada. Desert varnish is characterized by extreme discontinuity of thin films that form mottled patches at micrometer scales when viewed microscopically. Tonal consistency appears to encompass larger areas when viewed from distances of a few feet, but even within patches of very heavy varnish cover smaller zones are present with thinner varnish cover, and essentially unvarnished mineral grains are randomly and commonly exposed.

More resistant and older surfaces develop darker more mature varnish deposits. The proportion of "heavy" and "very heavy" varnish relative to less extensive deposits is greater in the Mojave Desert of California and western Arizona than in southern Nevada; however, deposits of varnish thicker than the "very heavy" degrees developed in southern Nevada do not seem to occur in the Mojave except in very isolated and rare situations. There appears to be a physical constraint on the age of varnish that is controlled by the stability of rock surfaces in semiarid climates. Outcrops are continually exfoliating carrying the mature varnish cover off the outcrop. Mineral grains eventually dislodge from rock surfaces as well.

Thick, laminated and encrusting types of varnishes are uncommon in comparison to the more typical thin films that

comprise the majority of varnish cover. They tend to reside in minute recesses, although they occasionally extend over zones of higher relief.

WEATHERING RINDS AND SECONDARY ZONES OF ENRICHMENT. The weathering characteristics of rock surfaces and the relationship they bear to the desert varnish they host is similar from region to region. Weathering rinds develop on all rocks and vary from very distinct with relatively sharp contacts on many of the ash flow tuffs, other volcaniclastics and metasedimentary units at one extreme, to rinds with rather diffuse contacts on dense volcanic rocks, to nebulous and indistinct weathering rinds on coarse rocks like coarse-grained granite and sandstone at the other extreme. The upper surfaces of the weathering rinds are typically lighter in color than the rest of the rock, and we can assume from our work with similar bleached surfaces of well studied rocks from southern Nevada, prima facie, that they too are leached zones. The weathering rinds are commonly enclosed within exfoliation slabs.

The dark secondary zone of Ca enrichment and cementation, chief evidence for the solution-evaporation pump model we conceived for initial extraction of Fe and Mn from host rocks and incorporation into the desert varnish layer, was observed on porous volcanic rocks from both the Mojave and Sonoran Deserts. These observations indicate that the evaporation pump model is an inclusive model for all of the southwest U.S.

COMPOSITION. There appears to be little compositional variation between desert varnishes from each of the study regions. Varnishes are composed chiefly of Fe, Mn, Si, and Al, and occur in amorphous compounds with varying amounts of clay and mineral/lithic detritus. Our analytical work indicates that true oxide minerals of Fe and Mn are typically absent. Varnishes from all regions tend to contain some alkalis and Ti. The Fe/Mn ratios in varnishes from all the regions are dependent on host rock composition: the higher the mafic tendency of the host, the higher the Fe/Mn ratio.

CONCLUSIONS AND IMPLICATIONS FOR REMOTE SENSING

Results of this interregional investigation and comparison of desert varnishes has important implications for the detection of varnish on Landsat and other visible and near IR remote sensing systems and the influence of varnish on the imagery signatures of host rocks. Of general significance is the implication that conclusions drawn from the southern Nevada investigation are applicable to the entire semiarid southwest U.S. and the steppe of east Africa and likely applicable as well to other semiarid regions of the world. Of more specific significance are:

1) Varnish maturity and thickness are controlled by short-lived rock surfaces that exfoliate or weather,

degrading the surface and aborting further varnish accumulation. Thus the "heavy" to "very heavy" varnish deposits described in the southern Nevada study prevail as the most advanced varnish developments in other semiarid regions as well.

2) Varnishes tend to be highly discontinuous, occurring principally as thin films rather than encrusting laminations.

3) The influence of desert varnish on host rock signatures in the visible and near infrared region of Landsat is limited by (1) and (2) above, limited increasingly so as wavelengths increase, since lower energy radiation seems to penetrate slightly further through the translucent varnish films, reflecting to a greater extent primary rock spectral properties. Thus, the longer wavelength false color composites such as 3-5-7 images and principle component images tend to contain superior lithologic information.

4) For the same reasons, 5/2 ratio values should increase over felsic units with extensive desert varnish cover, leading to high tonal contrast over these units on 5/2 images.

5) The similar varnish compositons and varnish-host

compositional relationships from region to region and the presence of the dark bands or secondary zones of cementation indicate that the solution-evaporation pump model may be an appropriate explanation for the initial extraction of Fe and Mn from porous ash flow tuffs and other host rocks and initial supply to the desert varnish zone throughout the southwest U.S. and other semiarid regions as well.

6) The spectral characteristics of varnish would be expected to be similar from region to region. Thus, 5/7 ratios should be somewhat lower over units with extensive desert varnish cover, but compositional differences among varnishes are too narrow to permit differentiation of units based on the varnish itself.

REFERENCES

Dibblee, T.W. and Hewett, D.F., 1966, Geology of the Mojave Desert region in Mineral Resources of California, Calif. Div. of Mines and Geol. Bull. 191, pp.62-66.

Espenshade, E.B., editor, and Morrison, J.L., associate editor, 1977, Goode's World Atlas, Rand McNally and Company, Chicago, pp.112-114 and 217.

Hayes, P.T., 1969, Geology and topography [of Arizona] in Mineral and Water Resources of Arizona, Ariz. Bur. of Mines Bull. 180, pp.35-58.

Spatz, D.M., Taranik, J.V., and Hsu, L.C., 1987a, Influence of mineral coatings and vegetation on TM imagery over Tertiary caldera lithologies, Basin and Range province, western U.S., ASPRS Technical Papers, Fall Convention, Reno, Nevada, 4-9 October, pp.13-25.

Spatz, D.M., Taranik, J.V., and Hsu, L.C., 1987b, Desert varnish on volcanic rocks of the Basin and Range province - composition, morphology, distribution, origin, and influence on Landsat imagery in Proceedings of the Twenty-First Symposium on Remote Sensing of Environment, ERIM, Ann Arbor, MI, October 26-30, pp.843-852.

Spatz, D.M., Taranik, J.V., and Hsu, L.C., 1988, Differentiating volcanic rock assemblages using Landsat TM data - influence of petrochemistry and desert varnish: Advances in Space Research, Vol.9, No.1, Peragamon Press, Elmsford, N.Y., pp.93-98.

Spatz, D.M. and Taranik, J.V, 1989, Regional analysis of Tertiary volcanic calderas, western U.S., using Landsat Thematic Mapper imagery: Remote Sensing of Environment, vol.28, pp.215-230.

Tooker, E.W. and Stewart, J.H., 1969, Stratigraphy [of Utah] in Mineral and Water Resources of Utah, Utah Geological Survey Bull. 73, pp.19-25.

PART IV

PART IV

AIRBORNE SCANNER (GERIS) IMAGERY OF THE KANE SPRINGS WASH VOLCANIC CENTER, LINCOLN COUNTY, NEVADA

David Spatz and William Aymard, Principle Authors
Mackay School of Mines
University of Nevada, Reno
Reno, Nevada 89557

TABLE OF CONTENTS

FIGURES AND TABLES

AIRBORNE SCANNER (GERIS) IMAGERY OF THE
KANE SPRINGS WASH VOLCANIC CENTER, LINCOLN COUNTY, NEVADA

INTRODUCTION

Airborne imaging spectrometry (GERIS) was flown at the Kane Springs Wash volcanic center. Data from one flight line of Geophysical Environmental Research Inc.'s imaging spectrometer (GERIS) was collected.

GERIS is a narrow band, 64 channel, visible/near-infrared imaging spectrometer (Appendix A). Single band, false color composite, and Chebyshev coefficient images were produced and correlated where possible with mapped lithologies and other surface cover. The GERIS imagery was then compared with Landsat Thematic Mapper imagery of the same area. This qualitative and preliminary investigation may be significant to those interested in geologic mapping and in comparing the new narrow band airborne sensors with Landsat. Most geologic studies with GERIS and other narrow band visible/near-infrared sensors involve specific mineral detection, including phyllosilicate, carbonate, and sulfate mineralogy. Basically, this imaging spectrometric approach plots curves for comparison with a reference library of known mineral

spectra. Application of these sensors to general geologic mapping problems has been limited.

PURPOSE

The purpose of the GERIS survey was to collect imagery within narrow intervals of the visible/near-infrared spectrum that might enhance contrast among the volcanic rock assemblages at Kane Springs Wash or help differentiate units with variable amounts of desert varnish cover. Airborne imaging at Kane Springs Wash in the thermal infrared using the TIMS (Thermal Infrared Mapping System) spectrometer suggested that clay minerals in desert varnish might be the cause of some imaging characteristics of some rock units. If so, the narrow band advantage of GERIS could provide an imaging advantage over Landsat Thematic Mapper (TM) imagery due to the spectral sensitivity of GERIS at the clay absorption peak around 2.2 micrometers. For the same reason, carbonate minerals in weathering rinds might also be detectable and lead to imagery units with lithologic correlation. Moreover, the steep slope apparent in the field spectra for surfaces with "heavy" varnish cover and for some of the more "evolved" late stage volcanic differentiates between TM bands 5 and 7 might lead to better imaging resolution with narrow band intervals. Finally, the improved

spatial resolution of GERIS could provide differentiation advantages among the volcanic units.

LOCATION AND FLIGHT LINE

The Kane Springs Wash volcanic center is located in southern Lincoln County, Nevada, approximately 110 air km NNE of Las Vegas (Figure 1) in the Delamar Mountain Range. Access to the Kane Springs Wash caldera is by excellent graded dirt road that connects Caliente with Federal Highway 93 about 30 km south of Alamo. Access within the Kane Springs Wash study site is by unimproved and often very poor dirt roads. The northern part of the GERIS study site is accessed by unimproved dirt roads from Highway 93 about 30 km west of Caliente. Roads within the study site are sparse, poor, and unimproved. Topographic relief is moderate to high. Elevations vary from about 1070 to 1980m.

The GERIS flight line was about 35 km long and was flown at a N20E bearing along the NW flank of the Delamar Mountains (Figure 2). The scanner swath resulted in an image width of about 7.5 km. Flight altitude was 20,000 feet. Details of the GERIS instrument are given in the following section.

INSTRUMENTATION

The GERIS scanner (Appendix A) has a total of 64 channels, 63 spectral data channels and one gyroscope channel. Appendix B lists the channels and corresponding band positions in the electromagnetic spectrum. Channels 1 through 24 cover, continuously, the 433.6 nm to 971.8 nm spectral region with bandwidths of 23.4 nm. Channels 25 to 31 cover, continuously, the 1.08 micrometer to 1.8 micrometer region with bandwidths of 0.12 micrometer. Channels 32 through 63 cover, continuously, the 1.986 micrometer to 2.496 micrometer region with bandwidths of 16.43 nm. GERIS has a single aperture with three separate spectrometers for the three separate detector arrays. This makes perfect image pixel registration possible. The scanner has three instantaneously changeable aperture sizes, corresponding to 2.5, 3.3, and 4.6 mRAD IFOV's. The ground resolution at 20,000 ft. aircraft altitude is 18, 24, 36 meters square with IFOV's of 2.5, 3.3 and 4.6 mRAD, respectively. The data has 12 bit digital resolution and 16 bit dynamic range. No gain and offset adjustment is necessary. The signal-to-noise ratio in the 400-1100 nm region is as high as 5,000 and in the 1.4-25 micron region, it is about 500.

The data collected was calibrated, geocorrected and analyzed with standard band, band ratio, and color composite imagery techniques as well as by use of Chebyshev polynomial coefficients.
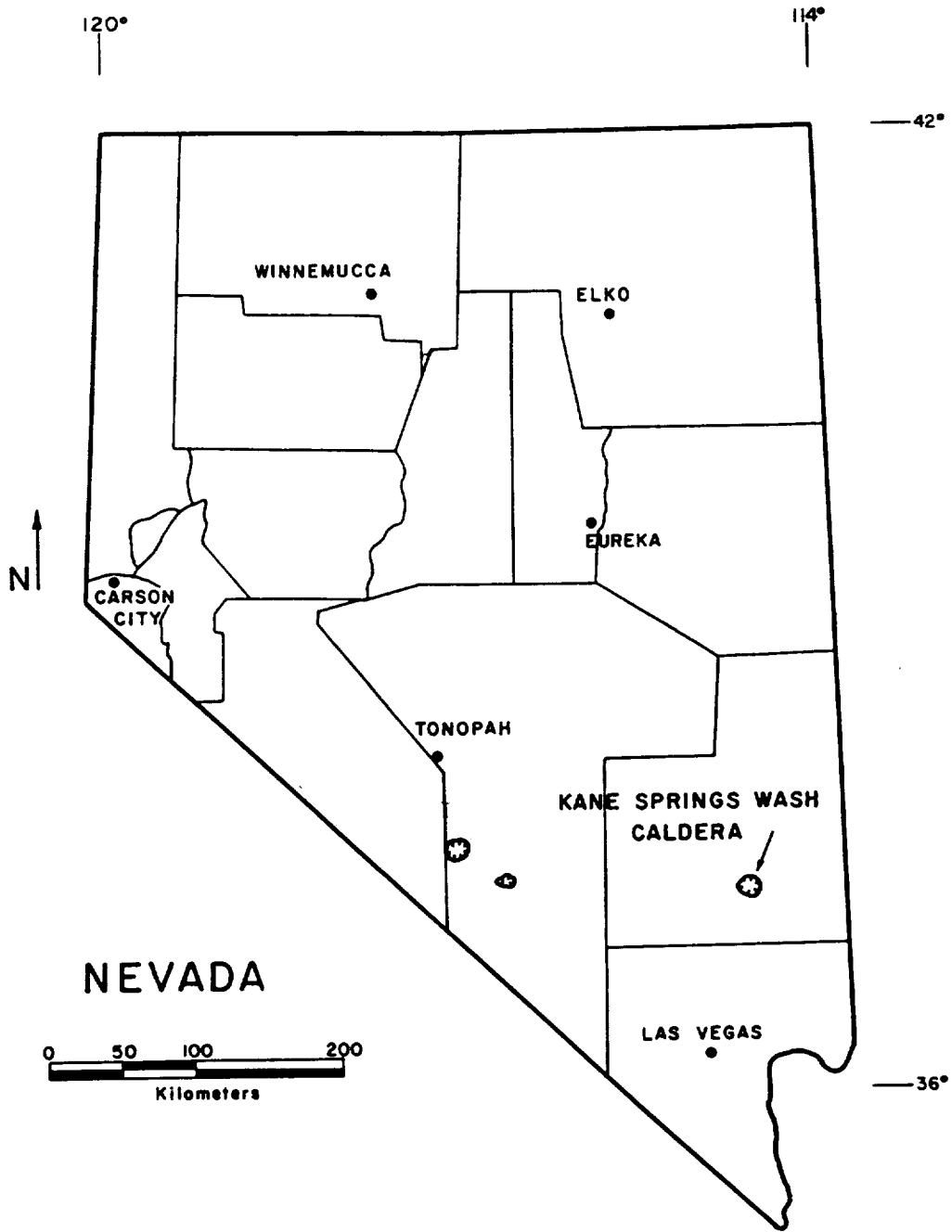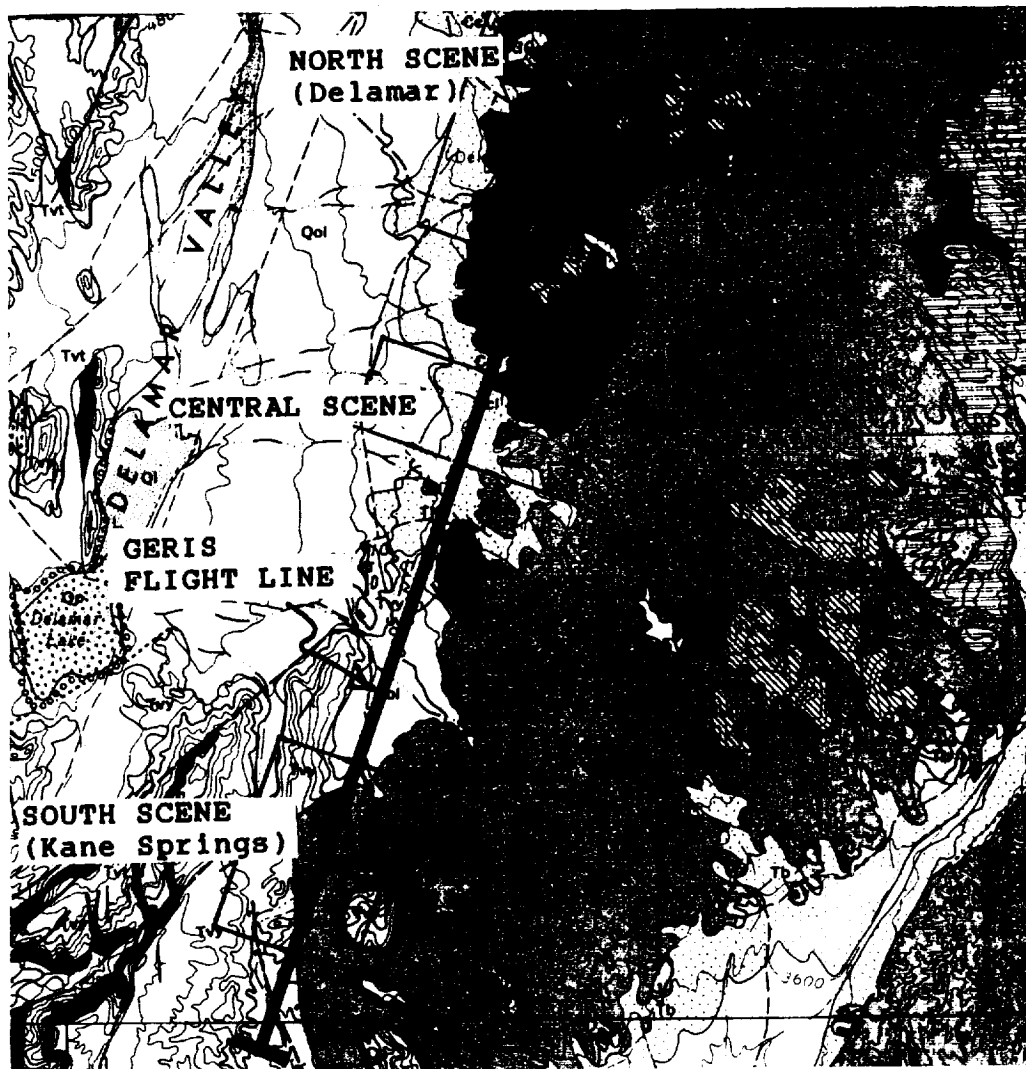
FIGURE 1. Location of the study sites within Nevada, U.S.A.: Kane Springs Wash caldera,

Figure 2. Geologic map of the northwest flank of the Delamar Mountains, including the Kane Springs Wash volcanic center at the south. The GERIS flight line is depicted with a heavy black line (modified after Tschanz and Pampeyan, 1970).

EXPLANATION
T-Tertiary, K-Cretaceous, €-Cambrian, Qal-younger alluvium, Tvt-tuffs and tuffaceous sediments, Tvb-spheroidal weathering ignimbrite, Tvr-rhyolite complex, Tvy-younger volcanics, Tb-basalt, Tgp-granite porphyry, Tr-rhyolite and microgranite dikes, Td-diorite, TKvu-volcanic rocks, undifferentiated, TKc-older clastic rocks, €pm-Prospect Mountain Quartzite, €p-Pioche Shale, €hp-Highland Peak Formation, €c-Chisholm Shale, €cl-Lyndon Limestone. Scale=1:250,000. North is top of page. Heavy lines and dashes are faults (U=up side, D=down side).

IMAGE CALIBRATION

Several image processing techniques were used to effectively calibrate all the data sets. They included the following:

1. SLOPE CORRECTION. A computer program was written to correct the general slope of the image along the scan line (Appendix C). The slope distortion was produced by slight unevenness of the two reflecting mirrors in the scan head of the GERIS instrument.

2. DESTRIPING. A computer program was written to destripe the image. Striping was introduced into the scan data and resulting imagery by detector differences in the head of GERIS.

IMAGE REGISTRATION

Registration is the process of geometrically aligning data sets from which geological and geophysical and other terrain information may be extracted. The registration procedure involves two main steps. First, ground control

points must be selected. Second, the data set (image) must be registered to a UTM projection through an affine polynomial transformation.

GROUND CONTROL POINTS (GCP). Twelve uniformly spaced GCP were selected and digitized on each of the two topographic maps used. These points have known latitude and longitude coordinates as well as known UTM coordinates. The corresponding line and sample number of the points in each of the images used and the map coordinates were noted and listed for the production of a transformation matrix. When improperly performed, the selection of GCP becomes the principle source of error in the registration process. The magnitude of the error is driven by three main factors: 1) map scale, 2) digitizer resolution and 3) human error. In order to minimize error, the following precautions were taken:

1. Only 7.5 degree topographic maps (1:24,000) were used.

2. A very high resolution digitizer was utilized to digitize the ground control points from topographic maps (Calcomp 9100, resolution of 0.0005 inch).

3. The points were digitized several times and the results averaged. These actions produced an accuracy of about 0.31 pixels in both x and y directions.

REGISTRATION TO UTM. Once ground control points were

selected, regression analysis was applied to determine the coefficients for the transformation. These transformation coefficients were used to warp the original images into a UTM projection. For the study area an affine transformation was used. For areas larger than 250 kilometers, higher order polynomials may be used in order to obtain accurate registration. A computer program written by M. Crawford of ARCO for PC based systems was modified and used to calculate the transformation coefficients of the data set. The program uses the Affine Transformation:

$$X' = a1X + b1Y + c1$$

$$Y' = a2X + b2Y + c2$$

X and Y = input pixel coordinates

X' and Y' = output coordinates

GRID RESAMPLING. The grid scale produced by the affine transformation was determined by the original pixel size of each image. The grids were resampled using a cubic convolution algorithm.

FLIGHT LINE GEOLOGY

The GERIS airborne flight path coincided with the NE flank of the Delamar Mountains at the pediment/outcrop contact (Figure 2). Distortion in the data rendered some of the

imagery useless, but 3 subscenes were separated for evaluation. The south end of the line traversed the western margin of the Kane Springs Wash caldera. The geology of the Kane Springs Wash caldera (Figure 3), a Miocene eruption dated at 14 to 11 Ma was described in detail in Parts I and II of this report. The western part of the caldera, imaged by GERIS, is dominated by outflow ash sheets from the caldera. These ash flow tuffs are dominated by the Kane Wash Tuff, which is composed of 3 separate cooling units in this area. Underlying Kane Wash Tuff are two ash flow cooling units, O and W, assigned to the Kane Wash Tuff Formation by Noble (1968) but thought by Novak (1985) to have originated from another source. Underlying the O and W Tuffs and forming the oldest exposures at the center is the Hiko Tuff. The image encompasses a portion of the intracaldera deposits which include rhyolite ash flow tuffs, trachyandesite lavas, minor basalt, and a prominent topaz rhyolite flow dome. The caldera margin is overlapped by a talus breccia bed.

The central part of the flight line is underlain by volcanic rocks consisting largely of ash flow tuffs and by the Cambrian Highland Peak Formation, which consists of limestone and dolomite. Well developed alluvial fans with west pointing distributary channels dominate the central subscene.

The geology of the northern part of the flight line is

Legend:
- Alluvium
- Basalt
- Topaz rhyolite lava
- Biotite–rhyolite lavas
- Trachyandesite lavas
- Ferroedenite–rhyolite lavas
- Intracaldera rhyolite ash–flow tuffs
- Central syenite complex
- Post–caldera trachyte lavas
- Talus breccia
- Kane Wash Tuff
- Pre–caldera trachyte lavas
- Pre–Kane Wash rocks
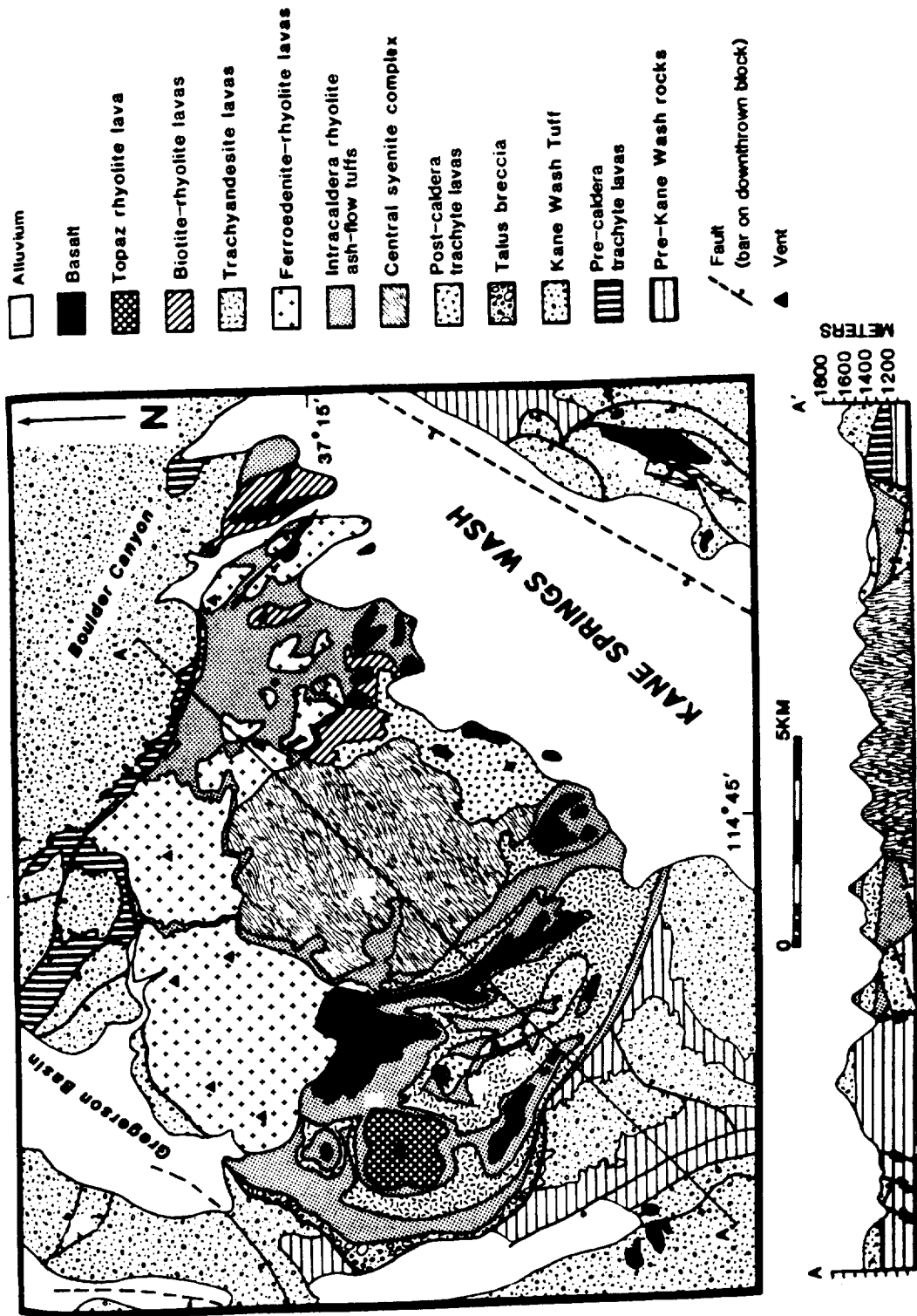- Fault (bar on downthrown block)
- ▲ Vent

Figure 3   Geologic map and cross section of the Kane Springs Wash volcanic center (after Novak, 1984).

dominated by the Cambrian Prospect Mountain Quartzite, a thin-bedded to massive, reddish brown to white quartzite. The Prospect Mountain Quartzite is overlain conformably by the Pioche Shale, which is overlain conformably by the Highland Peak limestone, both Cambrian in age (Tschanz and Pampeyan, 1970). The Paleozoic section strikes generally NNE and dips shallowly to moderately E. It is overlain unconformably by Tertiary volcanic flows along the northern, eastern and southern parts of the northern subscene. Rhyolite dikes and sills are present, and faulting is dominated by NW Trends. An important feature of the north subscene is an area of hydrothermal alteration that centers around the Delamar mining district in the central western part of the subscene. The old workings, including a large glory hole and mill tailings form a salient imagery unit (Figure 3, upper left and right). The Cambrian sedimentary section and Tertiary rhyolite dikes in the vicinity of the mined area are altered to argillic phase mineral assemblages, and the weathering of altered quartzite breccias has resulted in iron staining and zones with powdery quartz coatings.

IMAGERY INTERPRETATION

Three subscenes were lifted along the flight line where distortion was not too extreme. The subscenes used for

analysis and interpretation include north, central and south subscenes (Figure 2). Of the 63 bands GERIS measures (Appendix B), 14 were processed to correct for distortion and slope and used in individual band images and false color composites. The bands selected for processing (1, 4, 7, 11, 14, 18, 26, 30, 36, 40, 46, 49, 55, 63) are those located at spectral positions which should provide select information about rock assemblages and desert varnish, based on our experience with field spectra and Landsat TM and which should be advantageous for comparison with TM. Many images were reviewed and many hard copies made, but most exhibited redundant information. The images showing the greatest contrast and those with color units that correlated best with surface cover are shown in Figures 4 and 5. Ratioing was attempted without success. Other workers have expressed similar problems with ratioing GERIS bands. Evidently, each band is swamped with surface radiation, resulting is very small spectral differences. Ratio values are thus quite small, and resulting images contain virtually no contrast. Waveform analyses were also performed and output in imagery form. The waveform analysis is based on Chebyshev polynomials. Variations in the coefficients of the polynomial terms used to approximate the spectral curves form the basis for new pixel values used to produce the Chebyshev images (for more detail see Collins et al., 1981 and Marsh and McKeon, 1983).

Figure 4. GERIS narrow band imagery of the western edge of the Kane Springs Wash caldera and the western flank of the Delamar Mountain range. All images are contrast enhanced and color sequence is red-green-blue. Image tops point N20E. Scale: 1cm=0.7km. A. North Subscene, 36-46-7 color composite. B. North Subscene, 7-30-55 color composite. C. Central Subscene, 30-4-1 color composite. D. Central Subscene, 14-30-49 color composite. E. Central Subscene, 4-40-46 color composite. F. South Subscene, 7-4-1 color composite. G. South Subscene, 4-26-56 color composite. H. South Subscene, 36-46-56 color composite. I. South Subscene, 40-46-26 color composite. Cpm-Cambrian Prospect Mountain Quartzite. Chp - Cambrian Highland PeakFormation (limestone). T - mine tailings. TKvu - Tertiary volcanic rocks, primarily ash flow tuffs. Tkt - Tertiary Kane Wash Tuff. Tfd - Tertiary topaz rhyolite flow dome. B - Tertiary basalt.
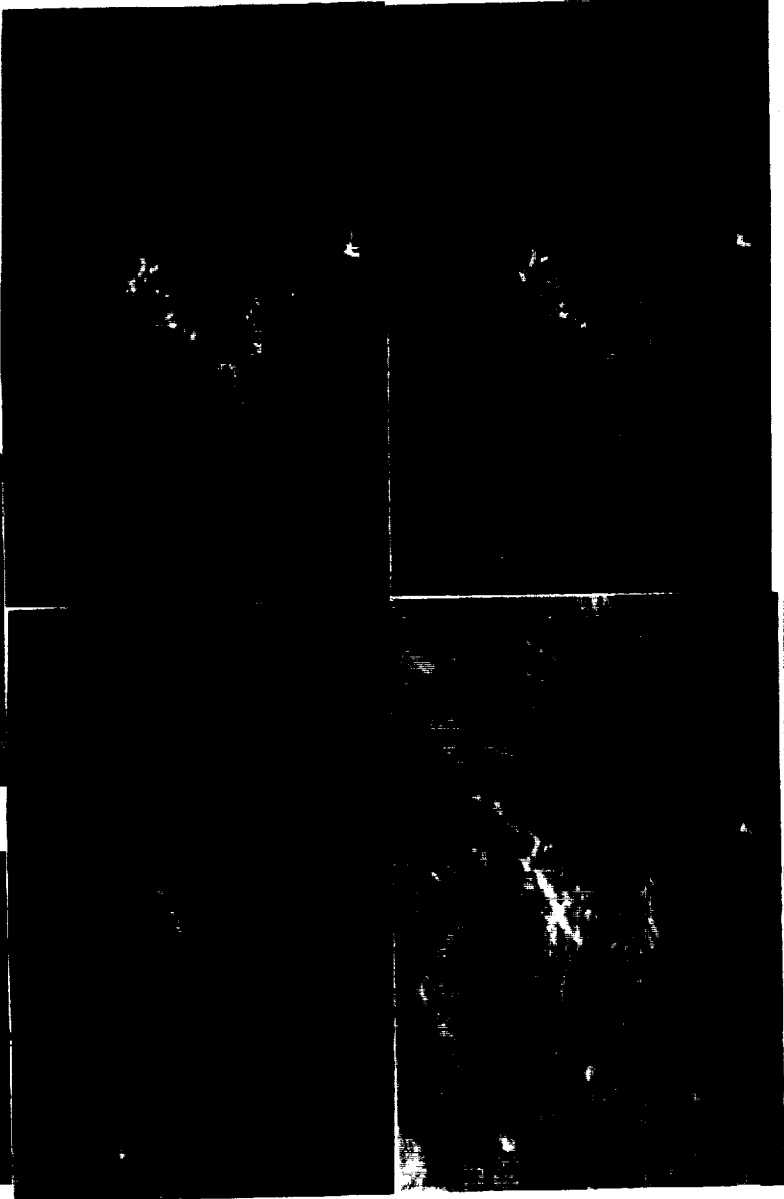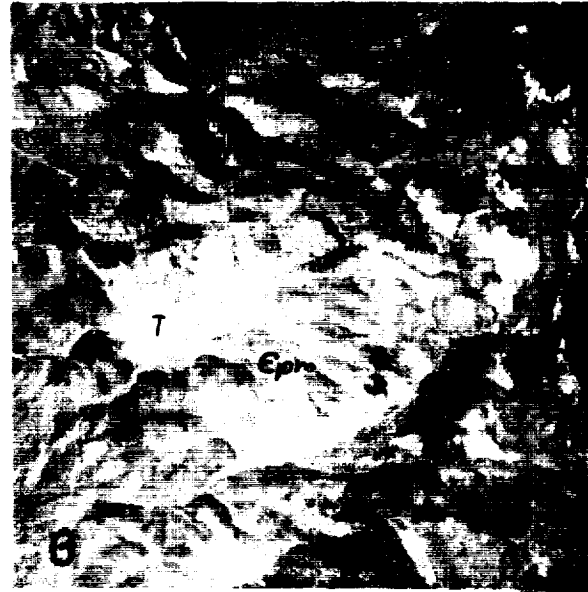
Figure 5. Chebyshev polynomial images of the GERIS spectra over the western flank of the Delamar Mountain range. All images are contrast enhanced and color encoded red-green-blue. Image tops point N20E. Scale: 1cm=0.7km. Upper Left: North Subscene, V7-I4-I2 color composite. Upper Right: North Subscene, V5-V3-I4 color composite. Middle Left: North Subscene, V2-I3-I10 color composite. Middle Right: Central Subscene, V7-V3-V1 color composite. Lower Left: South Subscene, V2-V3-V5 color composite. Lower Middle: South Subscene, V1-V2-V5 color composite. Lower Right: V3. V=visible, I=infrared.
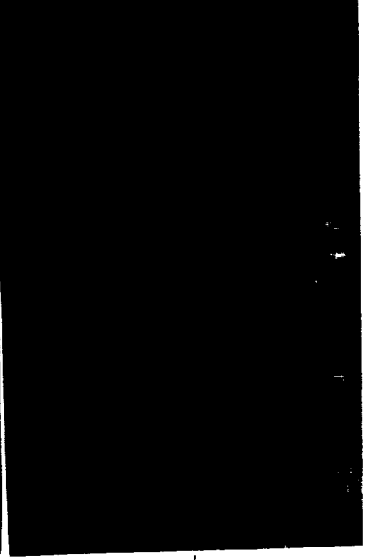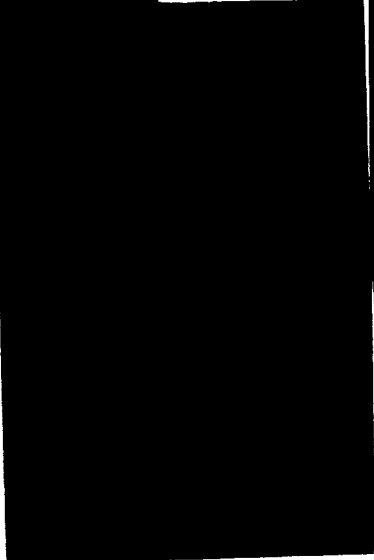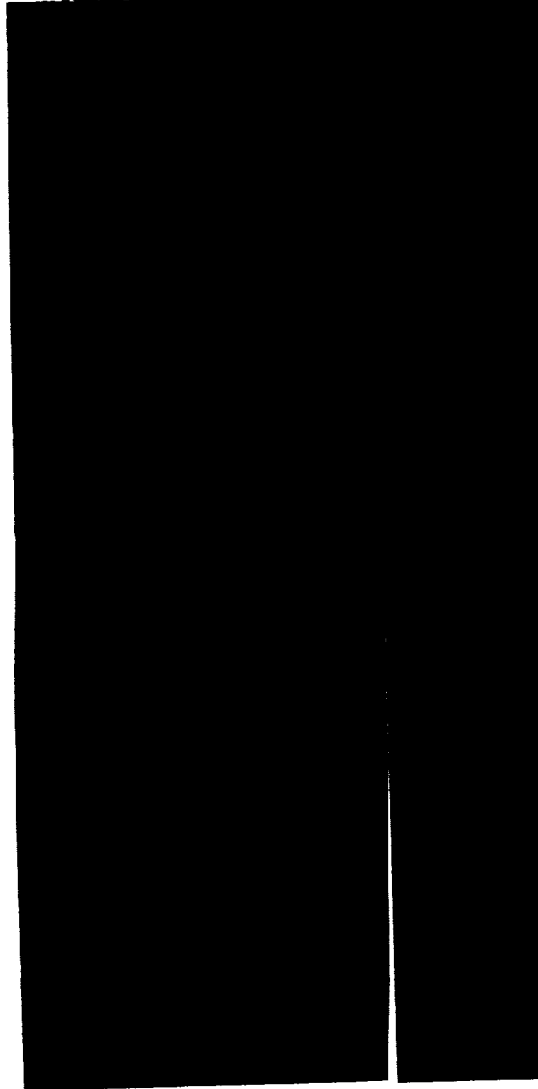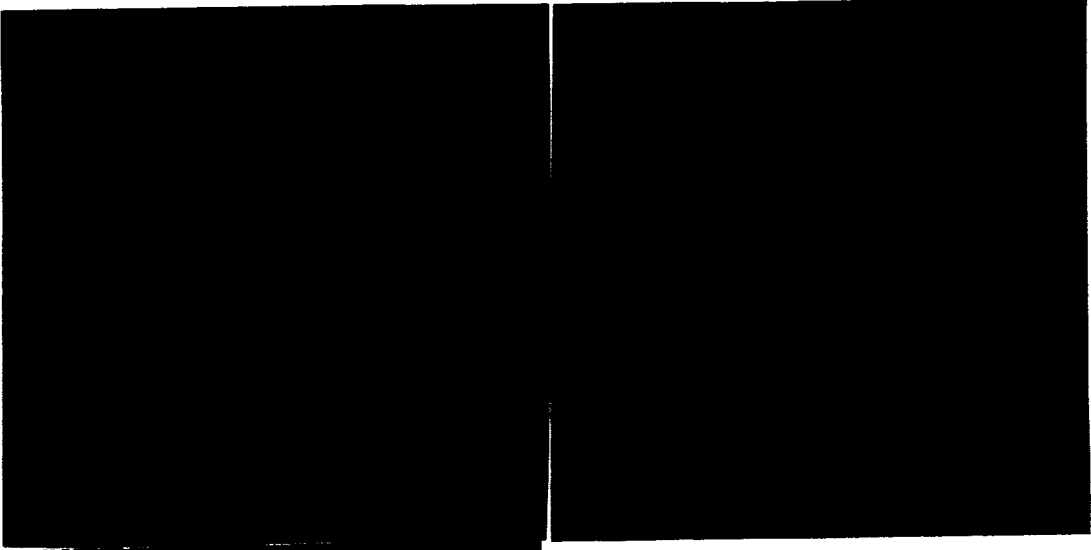
NORTH SUBSCENE. False color composite images - GERIS bands 36-46-7 and 7-30-55, colored red-green-blue - of the north subscene are shown in Figure 4 (upper left and right). Distinctive imagery units that correspond with mappable formations or rock assemblages include the bluish and cyan patches on the northern, eastern and southern fringes of the 36-46-7 image, which correlate with Tertiary volcanic flows, primarily ash flow tuffs. The volcanic beds and the alluvial fan they shed in the NW part of the image are relatively reflectant in band 46, due partly to a lack of secondary clay minerals, which are prevalent within the Delamar mining district and the central part of the image and to vegetation which caps areas of higher relief. The hydrothermally altered area is achromatic on the images. The Tertiary volcanics are reddish to orangy on the 7-30-55 image due to relatively high reflectances in bands 7 and 30. Band 7 is the longer wavelength region of the visible or what the eye perceives as red and probably is reflecting the slightly reddish color of weathered volcanics and incipient desert varnish cover. High values in band 30 are in response to the spectral separation so prominent around 1.6 micrometers which correlates with TM band 5. Felsic assemblages respond with relatively high values. Cambrian formations higher in the section, Pioche Shale and Highland Peak Limestone form elongate N-S patterns on the eastern fringe of the image. Highland Peak is orangy on the 7-30-55 image due to lower reflectance response in band

55, which is centered at 2.35 micrometers, where carbonate minerals absorb. Bluish hues on the 36-46-7 image and reddish hues on the 7-30-55 image along drainage channels correspond to riparian vegetation.

Composite Chebyshev images are shown in Figure 5. They tend to result in broad imagery units that correspond with vegetation zones. The dark blue zone on the V7-I4-I2 image and the red unit on the V5-V3-I4 (colored red-green-blue) image represents the densest vegetation in the subscene, where juniper and pinyon pine grow. The mine workings at the Delamar mine are quite distinctive on the V2-I3-I10 image. They are magenta due to relatively high reflectance values in V2 and I10. Similar hues in three patches in the NE quarter of the subscene represent hydrothermally altered areas in a fault block near the Culverwell mine.

CENTRAL SUBSCENE. The central subscene (Figure 2) is dominated by alluvium and a well developed alluvial fan. Outcrops of Highland Peak Formation exposed along the west flank of the Delamar Mountains are imaged in the NE portion of the subscene. The Highland Peak Formation is a succession of limestones, dolomites, and sandy dolomites. The section dips moderately to steeply ENE. The Highland Peak Formation in the subscene is characterized by NNW lineations that represent interbedded limestones and sandy dolomites. On the 30-4-1 image, colored red-green-blue, the limestone interbeds

are blue due to the high reflectance of limestones in the blue region of the electromagnetic spectrum. Limestones are reddish on the 4-40-46 image for the same reasons. In fact, the ability of the short visible wavelength bands to discriminate limestone lead to superior composite images using bands 1 to 4. The sandy dolomite interbeds in the Highland Peak exhibit relatively high reflectance values in all bands, leading to achromatic tones on the composite images. An alluvial terrace just west of Highland Peak exposures is also very light in tone due to distribution of sandy dolomite detritus over it. The reddish hues on the west side of the 30-4-1 image is a vegetation response. A recent alluvial fan, quite distinctive on the 30-4-1 and 4-40-46 image, is developed west of the Highland Peak exposure. Hues of the fan correspond with hues of the limestone beds, reflecting the source of the detritus that comprises the fan.

A Chebyshev image of the central subscene, color composite V7-V3-V1, colored red-green-blue, is shown in Figure 5. General patterns that correlate with vegetation, outcrop, and alluvium are depicted by this image, but little detail is apparent.

SOUTH SUBSCENE. The southern part of the data strip contained extreme distortion that could be rectified only partially. The color composite images thus contain wavy textures (Figure 4). South subscene imagery is marked by

distinctive white or yellowish imagery units that correspond with intracaldera ash flow tuff (Figure 4). One such occurrence is a small circular or cotton ball like exposure on the eastern edge of the image. Another occurrence forms a linear, feathery arcuate pattern in the center of the image that is concave upwards. On the 4-26-56 image, colored red-green-blue, intracaldera ash flow tuff is yellow due to the lack of reflectance in band 56 caused perhaps by absorption of secodary calcareous deposits and clay developed in these porous beds. The wide, sinuous, light brown zone in the SW quarter of the image correlates with the caldera flank breccia deposit. Dark tonal contrast in patches extending south of the white cotton ball like exposure of intracaldera tuff are exposures of trachyandesite which is dark and relatively nonreflectant throughout the visible and near-infrared. A small circular patch of basalt, also dark on these images, borders and mirrors the circular patch of intracaldera tuff. The Kane Wash Tuff ash flow sheet occurs in the north, west and south parts of these images where scan distortion is extreme. It does form a distinct imagery unit, however, in the northern half of the images. The unit is greenish yellow on the 7-4-1 and 4-26-56 images, reddish on the 36-46-56 image and purplish on the 40-46-26 image all colored red-green-blue. The reddish hue on the 36-46-56 image could be due to poor reflectance in 46 and 56 due to clay in the well developed desert varnish it tends to support and to carbonate deposits

in the weathering rinds. Moreover, felsic units are usually bright on images in the 1-2 micrometer range, such as band 36 or band 26 which helps create the purplish image that corresponds with the unit on the 40-46-26 image and the greenish hue on the 4-26-56 image. The western edge of the topaz rhyolite dome is framed just within the eastern fringe of the images. The dome is fairly indistinct but responds similarly to the Kane Springs Tuff with which it is genetically related. The rhyolite flow dome was deposited immediately following the outpouring of the Kane Wash Tuff and is very similar in composition. The two units tend to parallel one another in imagery characteristics on Landsat TM as well.

Chebyshev coefficient images are shown in Figure 5. Intracaldera ash flow tuff is conspicuous on the V2-V3-V5 and V1-V2-V5 images. The topaz rhyolite is outlined on the SE fringe of the V1-V2-V5 image in a speckled red semicircle. A similar pattern marks exposures of Kane Wash Tuff on the western fringe of this image. Topaz rhyolite is bright on the V3 image, and north of it along the NE fringe of the subscene ferroedinite-rhyolite lavas respond similarly.

COMPARISON WITH LANDSAT THEMATIC MAPPER IMAGERY

Figures 6, 7 and 8 exhibit Landsat 5 Thematic Mapper imagery of the area covered by the GERIS flight line. The

imagery is discussed in the following text by subscene.
Landsat TM imagery of the area covered by the south subscene,
the Kane Springs Wash caldera, has been described by Spatz,
Taranik, and Hsu (1987a, 1987b, and 1989) and Spatz and
Taranik (1989). Thermal infrared imagery of the area has been
discussed by Chenevey (1989), Chenevey and Perry (1989) and
in Part II of this report.

NORTH AND CENTRAL SUBSCENES. Comparison of TM Band 2 with
TM Band 5 (Figure 6) over the North study site demarks the
exposure pattern of Prospect Mountain Quartzite quite well.
The unit is markedly brighter on the Band 5 image than on the
Band 2 image due likely to relatively deeper penetration of
Band 5 wavelengths and the resulting lithologic response of
this very light toned quartzite. Band 2 wavelengths are
absorbed to a greater extent by desert varnish that develops
on this resistant rock. The TM 3/1 ratio image and the
principle component 3 image (Figure 6) highlight the old
Delamar Mining district tailings in bright tones as well as
other areas of extensive hydrothermal alteration to the ENE.
A similar correlation was observed on the GERIS Chebyshev V2-
I3-I10 image (Figure 5). The tailings at Delamar are dark on
the 5/7 image (Figure 6, middle right), surrounded by light
tones that correlate with an argillic alteration halo around
the old gold mines. The low 5/7 values produced by the
tailings may be due to anomalous metal in the tailings. Bright

Figure 6. Landsat 5 Thematic Mapper images of the western flank of the Delamar Mountain range. All images are full resolution 512x512 subscenes and are contrast enhanced. Image tops point about N10E. Upper Left: Band 2 image. Upper Right: Band 5 image. Middle Left: 3/1 ratio image. Middle Right: 5/7 ratio image. Lower: principle component 3 image. Cpm - Cambrian Prospect Mountain Quartzite. Chp - Cambrian Highland Peak Formation (limestone). TKvu - Tertiary volcanics, mainly ash flow tuffs. Qal - Quaternary alluvium.

5 TM DELAMAR BAND 2 512

Qal

Mine
Tailings   Єpm

Qal   Єpm

Єhp

Єhp
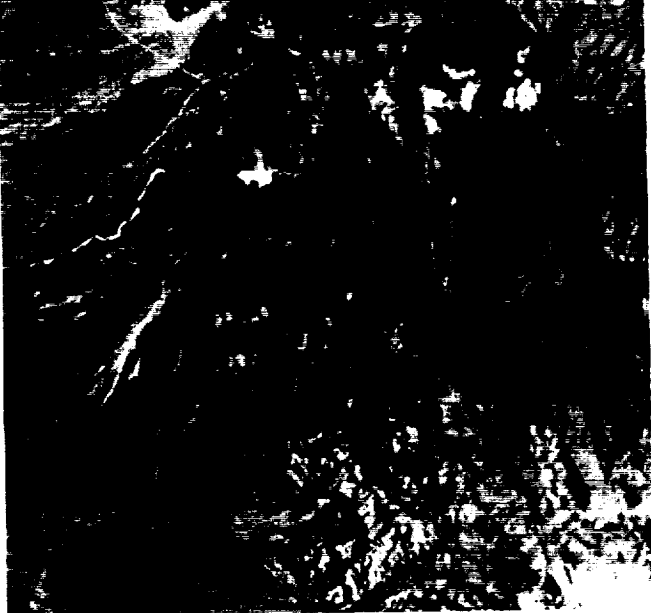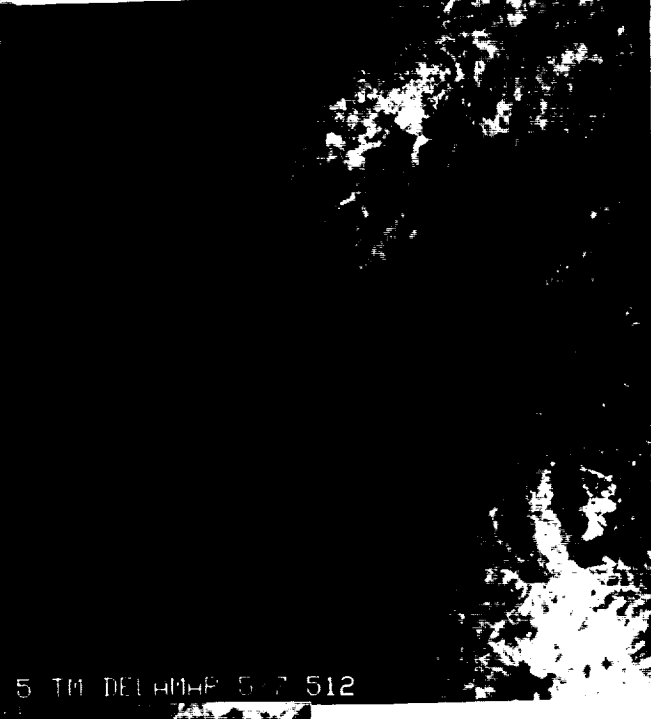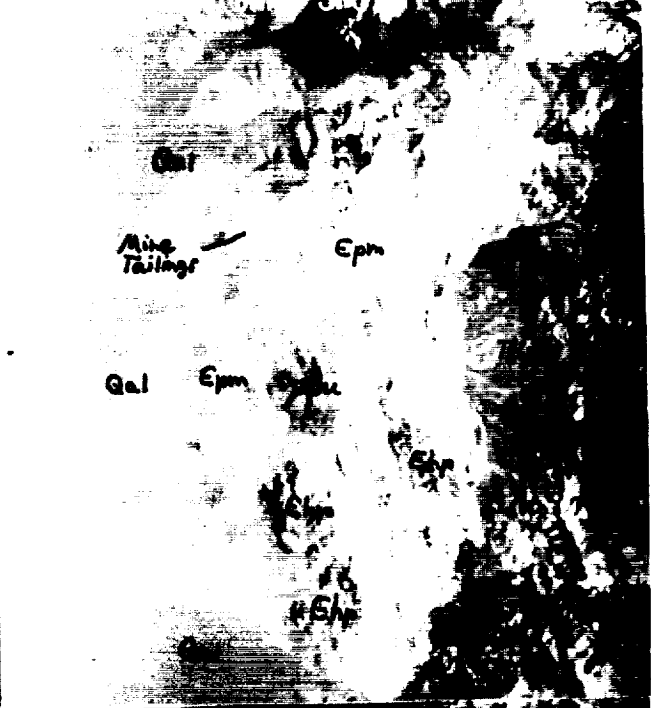
T TM DELAMAR 4 1 512

5 TM DELAMAR 5 7 512

Figure 7. Landsat 5 Thematic Mapper images of the western flank of the Delamar Mountain Range. All images are full resolution 512x512 pixel, contrast enhanced color composites and encoded red-green-blue. Image tops point N10E. Upper Left: 2-4-5 image. Upper Right: 3-5-7 image. Middle Left: principle component 2-3-4 image. Middle Right: principle component 2-4-5 image. Lower: principle component 1-2-3 image. Cpm - Cambrian Prospect Mountain Quartzite. Cp - Cambrian Pioche Shale. Chp - Cambrian Highland Peak Formation (limestone). TKvu - Tertiary volcanics, mainly ash flow tuffs. Qal - Quaternary alluvium.

5 TM DELAMAR BAND 2 4 5 RGB 512

5 TM DELAMAR BAND 2 3 4 RGB 512

Figure 8. Landsat 5 Thematic Mapper imagery of the western edge of the Kane Springs Wash caldera (south subscene). Image tops point N10E. All images are full resolution 512x512 pixel. Upper Left: 3-5-7 color composite encoded red-green-blue. Upper Right: Band 2 image. Middle Left: Band 5 image. Middle Right: 3/1 ratio image. Lower: 5/7 ratio image. Tkw - Tertiary Kane Wash Tuff. Rfd - Tertiary topaz rhyolite flow dome. B - Tertiary basalt.
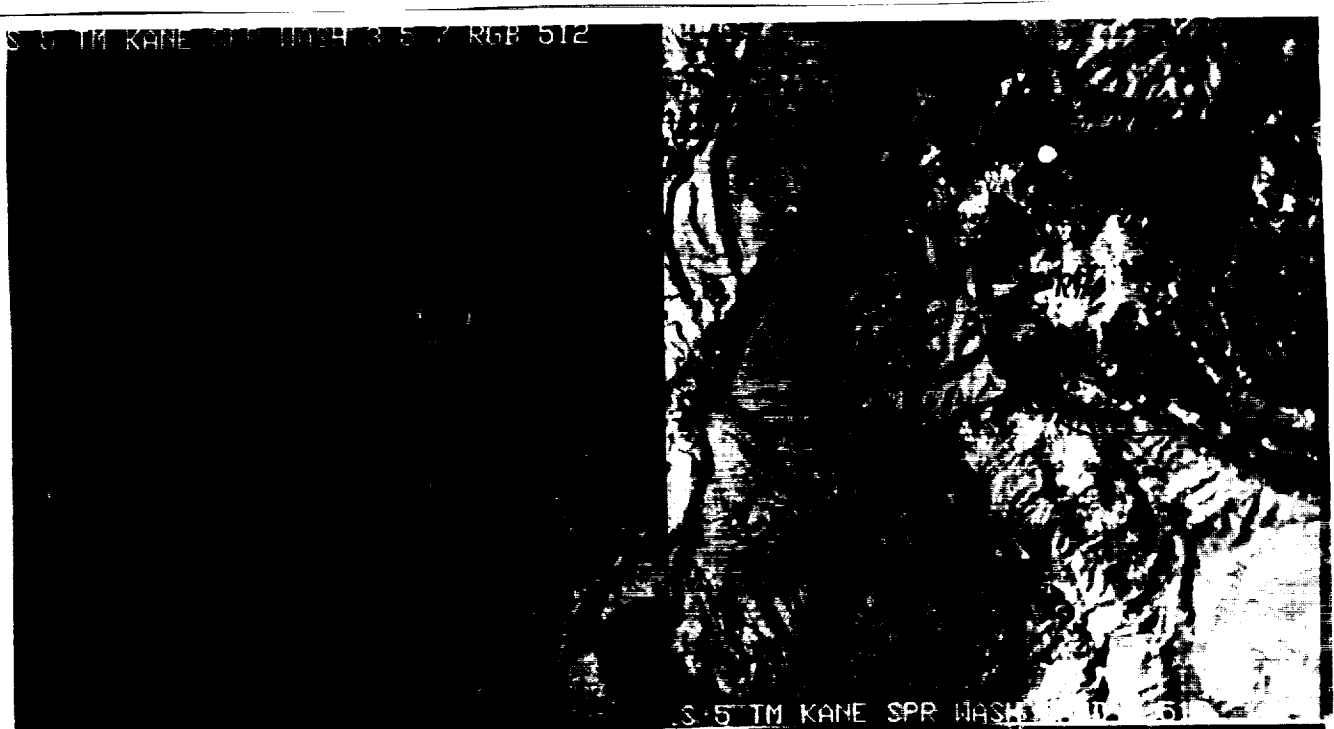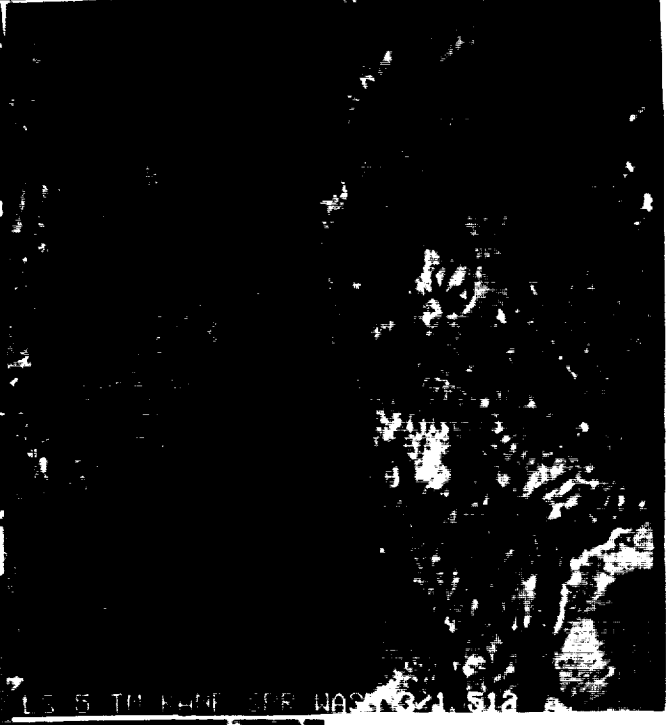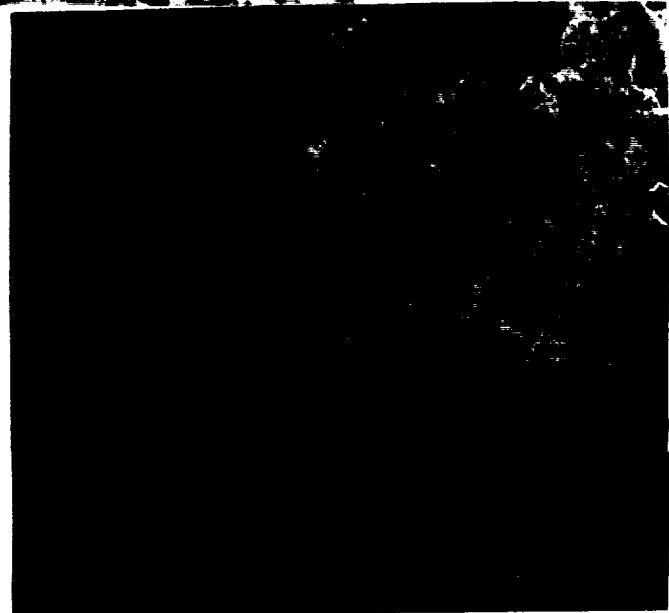
3/1 values produced by the tailings reflect a high iron oxide content. A prominent NNW structural gain caused by moderately NE dipping strata is prominent on the Landsat images (Figures 6 and 7), but not so apparent on the GERIS images.

Lithologic correlation in the Landsat principle component images (Figure 7) is high. Lithologic units are labeled on Figure 6, middle left. This exhibit can be referenced for imagery-lithology correlations on the other images as well. Striking correlations on the principle component 2-3-4 image (Figure 7, middle left) include: Highland Peak Formation (yellow), Pioche Shale (blue), Prospect Mountain Quartzite (mottled moss, mustard, lavender) and Tertiary volcanics (mottled pink and magenta). Imagery unit-lithology correlations are similarly striking on the principle component 2-4-5 image (Figure 7, middle right). Alluvial fans respond differently, spectrally, depending on source lithologies and extent of desert varnish.

SOUTH SUBSCENE. The south subscene covers the western part of the Kane Springs Wash caldera. The geology of this area (Figure 3) was described by Noble (1966), Novak (1984) and in Parts I and II of this report, and Landsat TM imagery units were described in detail in Part I. Individual Band 2 and 5 images, 5/7 and 3/1 ratio images, and a 3-5-7 false color composite image are shown in Figure 8. Distinctive units on these images are the Kane Wash Tuff and the Topaz Rhyolite,

both related in the volcano-tectonic history of Kane Springs Wash by close emplacement timing and similar petrochemical properties. These two volcanic assemblages exhibit similar hues and tones. Note that they are quite dark on the 5/7 image (Figure 8, bottom) due likely to a trace element suite that includes magmatically "incompatible" elements and to relatively well developed desert varnish which also leads to steep spectral slopes in the near infrared region between TM Bands 5 and 7 and to low 5/7 values. The GERIS image of the south subscene covers a smaller area (Figure 5). Many of the imagery units on the TM images are also distinguishable, as well, on the GERIS images.

SUMMARY AND CONCLUSIONS

Application of GERIS imagery to geologic mapping, identification of distinct lithologic units and rock assemblages, and to the detection of desert varnish was reviewed at the Kane Springs Wash volcanic center and along the western flank of the Delamar Mountains. Data suffered from heavy scan distortion but three areas with moderate distortion were extracted from the flight line for study. Individual band images, false color composite imagery and Chebyshev coefficient images were processed. Comparisons were made between the GERIS imagery and Landsat TM. The study is

qualitative and preliminary.

The GERIS imagery units seem to correlate best with fairly broad areas, representing general cover types: areas with heavy vegetation, outcrop, alluvial fans and Quaternary gravel. Individual lithologic units are distinguishable in places but no consistent lithologic correlation is apparent in either individual band images, color composites, or Chebyshev imagery. The significant result is that the GERIS imagery does not provide very useful information for geologic mapping purposes with the exception of the mine tailings at the Delamar mining district which may be reflecting a unique alteration mineral or metal content. Structural and textural properties resulting from structural grain are indistinct on the GERIS images.

In contrast, imagery units on Landsat TM images correlate well with lithologic units, and structure is much more apparent. One explanation may be that the broad bands of TM essentially average spectra over a broader range of the spectrum than the GERIS scanner, resulting in a broader spectral characterization of rock types and some surface cover types. The ability of TM to ratio seems a distinct advantage, particularly for applications of 5/7 ratios to identification of evolved volcanic differentiates, 5/2 and 5/7 ratios for detection of desert varnish and 3/1 ratios for detection of iron oxides.

REFERENCES

Chenevey, M.J., 1989, Geologic interpretation using thermal infrared imagery and the effects of vegetation and rock coatings on image interpretation: proceedings, ASPRS Image Processing Conf., May, Reno, Nev. 10p.

Chenevey, M.J. and Perry, J.J., 1989, Thermal infrared imagery applied as an aid in geologic mapping of a volcanic terrane: proceedings, IGARSS, July 10-14, Vancouver, B.C., Canada, 10p.

Collins, W., Chang, S.H., and Kuo, J.T., 1981, Infrared airborne spectroradiometer survey results in the western Nevada area: Columbia Univ., Aldridge Lab. Appl. Geophysics, Final Rept. to NASA, Contract JPL 955832, 61p.

Marsh, S.E. and McKeon, J.B, 1983, Integrated analysis of high-resolution field and airborne spectroradiometer data for alteration mapping: Econ. Geol., vol. 78, pp. 618-632.

Noble, D.C, 1968, Kane Springs Wash volcanic center, Lincoln County, Nev.: GSA Mem. 110, p.109-116.

Novak, S.W., 1984, Eruptive history of the Kane Springs Wash volcanic center, Nevada: Jour. Geoph. Res., v. 89, pp. 8603-

8615.

Spatz, D.M., Taranik, J.V. and Hsu, L.C., 1987a, Application of TM imagery to mapping volcanic rock assemblages at Tertiary calderas, Basin and Range province: IGARSS '87, Internat. Geos. and Rem. Sens. Sym. Digest, Ann Arbor, Mich., May 18-21, pp. 1299-1308.

Spatz, D.M., Taranik, J.V. and Hsu, L.C., 1987b, Influence of secondary mineral coatings and vegetation on TM imagery over Tertiary caldera lithologies, Basin and Range province, western, U.S. in Technical Papers, American Society of Photogrametry and Remote Sensing, Fall convention, Reno, Nev., Oct. 4-9, pp. 13-25.

Spatz, D.M., Taranik, J.V. and Hsu, L.C., 1989, Differentiating volcanic rock assemblages using Landsat Thematic Mapper data - influence of petrochemistry and desert varnish: Advances in Space Res., vol. 9, no. 1, pp. 93-98.

Spatz, D.M. and Taranik, J.V., 1989, Regional analysis of Tertiary volcanic calderas, western U.S., using Landsat Thematic Mapper imagery: Remote Sen. of Environ., vol. 28, pp. 215-230.

Tschanz, C.M. and Pampeyan, E.H., 1970, Geology and mineral deposits of Lincoln County, Nev.: Nev. Bur. Mines and Geol. Bull. 73, 188p.

APPENDIX A
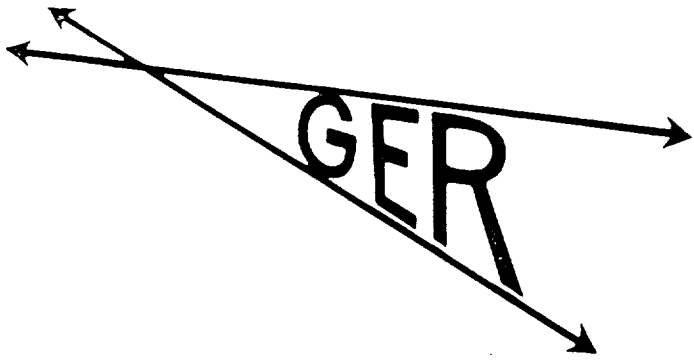
GER HIGH SPECTRAL AND RADIOMETRIC RESOLUTION SCANNERS

FOR INDUSTRY AND OTHER MAPPING

USED FOR SURVEYS OR FOR SALE TO CUSTOMERS

GER Airborne Scanner

Optics Block Diagram

Detector Array
1   32

Detector Array
1   8

Detector Array
1   32

Detector Array
1   24

Visible Near Infrared Spectrometer

Near Infrared Spectrometer

Infrared Spectrometer

Far Infrared Spectrometer

400 nm to 1100 nm

1.4 micron to 1.8 micron

2.0 micron to 2.5 micron

3 micron to 12 micron

GER Airborne Scanner

90°

20,000 feet

IFOV 3.3 mRAD

78 feet
24 meters

40,000 feet
7.6 miles

Aperture Size	IFOV	Ground Spot Size
0.015°	2.5 mRAD	18 M square
0.020°	3.3 mRAD	24 M square
0.030°	4.5 mRAD	35 M square

Scan Parameters

And Other Spot Sizes Available

GEOPHYSICAL ENVIRONMENTAL RESEARCH CORP.

111 8TH AVENUE
ROOM 1007

SCANNER SYSTEMS

* 400nm to 2.5 microns, 63 channels
* 400nm to 14 microns, 24 channels

GER 63 CHANNEL SCANNER BANDS

VISIBLE/NEAR INFRARED

BAND 1 to 24	499nm to 1083nm 25.4nm Bandwidth

NEAR/INFRARED

BAND 25 to 31	1.08 micron to 1.80 micron 120nm Bandwidth

INFRARED

BAND 32 to 63	1.980 micron to 2.494 micron 16.5nm Bandwidth

SCANNER FEATURES

BAND NUMBERS	* 64 with selectable wavelengths
DYNAMIC RANGE	* 16 bits * All gains and offsets permanently set. * Radiometrically calibrated with results repeatable to better than 1 percent from flight-to-flight. * To 10,000 counts 400 to 1100nm * To 6,000 counts 1.4 to 2.5 microns
SIGNAL-TO-NOISE	* To 5000 at 400 to 1100nm * 100 to 500 at 1.4 to 2.5 microns (500 + new detectors)
I FOV	* Selectable ** 2.5 mRAD ** 3.3 mRAD ** 4.6 mRAD ** Others
PIXELS PER SCAN	* Selectable ** 512 Pixels ** 1024 Pixels ** Others
SCAN SPEED	* Selectable ** 1 to 50 scans per second

RECORDING	* Computer tape, 9 track, 6250 BPI * New tape gives greater dimensions of recording
SPECIAL FEATURES	* Special electronics eliminate all other scanner noise — system is detector noise limited. * All channels acquired simultaneously resulting in perfect band-to-band registration. * Continuous spectral curves in each pixel * Analysis ** Selected bands ** Waveform in all bands

DATA CALIBRATION

READ AIRCRAFT TAPE	Data translated from aircraft system to computer format.
CORRECT EACH SCAN LINE TO THE ZERO SIGNAL (DARK) LEVEL	Removes all "STRIPING" effects.
SEPARATE BANDS	Sharpens image by removing signal lag.
ELECTRONIC TIME CONSTANT CORRECTION	Separates the interleaved data into 63 images.
ROLL CORRECTION	Calculates aircraft roll from the system gyro and corrects each pixel to remove roll from the image.
RADIOMETRIC RADIATION	Corrects instrument counts to radiance. This calibration is traceable to the Bureau of Standards Radiance Source.
CHEBYSHEV TRANSFORMATION	Transforms 53 band data into polynomial coefficients that are sensitive to changes in spectral waveforms.

THERMAL SCANNER
BAND 1-24

400nm to 14 microns
* Present System
    ** 9 thermal spectral bands
    ** 1 3 to 5 micron band
    ** 1 8 to 12 micron band
    ** 1 400nm to 1 micron band

APPENDIX B

TABLE 1

GER. CORP. SCANNER RADIANCE CORRECTION FUNCTION

CHANNEL	WAVELENGTH (NM)	RADIANCE CORRECTION FUNCTION
1	5366.60010	0.828E-02
2	5649.60010	0.481E-02
3	5932.60010	0.449E-02
4	6215.60010	0.369E-02
5	6498.60010	0.333E-02
6	6781.60010	0.323E-02
7	7064.60010	0.297E-02
8	7347.60010	0.291E-02
9	7630.60010	0.294E-02
10	7913.60010	0.269E-02
11	8196.60059	0.281E-02
12	8479.60059	0.308E-02
13	8762.60059	0.294E-02
14	9045.60059	0.283E-02
15	9328.60059	0.301E-02
16	9611.60059	0.293E-02
17	9894.60059	0.350E-02
18	10177.60059	0.319E-02
19	10460.60059	0.406E-02
20	10743.60059	0.457E-02

CHANNEL	WAVELENGTH (NM)	RADIANCE CORRECTION FUNCTION
21	11026.60059	0.478E-02
22	11309.60059	0.641E-02
23	11592.60059	0.611E-02
24	11875.60059	0.950E-02
25	10800.00000	0.248E-01
26	12000.00000	0.600E-03
27	13200.00000	0.429E-03
28	14400.00000	0.393E-03
29	15600.00000	0.525E-03
30	16800.00000	0.603E-03
31	18000.00000	0.345E-03
32	19729.69922	0.470E-03
33	19891.89844	0.544E-03
34	20054.09766	0.566E-03
35	20216.29688	0.523E-03
36	20378.49609	0.532E-03
37	20540.69531	0.575E-03
38	20702.89453	0.574E-03
39	20865.09375	0.603E-03
40	21027.29297	0.588E-03
41	21189.49219	0.618E-03
42	21351.69141	0.651E-03
43	21513.89063	0.640E-03

CHANNEL	WAVELENGTH (NM)	RADIANCE CORRECTION FUNCTION
44	21676.08984	0.696E-03
45	21838.28906	0.691E-03
46	22000.48828	0.706E-03
47	22162.68750	0.731E-03
48	22324.88672	0.803E-03
49	22487.08594	0.811E-03
50	22649.28516	0.781E-03
51	22811.48438	0.789E-03
52	22973.68359	0.762E-03
53	23135.88281	0.797E-03
54	23298.08203	0.779E-03
55	23460.28125	0.853E-03
56	23622.48047	0.911E-03
57	23784.67969	0.964E-03
58	23946.87891	0.973E-03
59	24109.07813	0.109E-02
60	24271.27734	0.114E-02
61	24433.47656	0.123E-02
62	24595.67578	0.131E-02
63	24757.87500	0.128E-02

The table of the radiance calibration function is shown above. The instrumwnt counts are multiplied by the radiance function.

APPENDIX C

```fortran
C
C          PROGRAM TO CORRECT FOR THE SLOPE OF A COLLINS 64-CHANNEL
C          IMAGE IS THE GENERAL SLOPE OF THE IMAGE ALONG A SCAN LINE
C          DIRECTION CAUSED BY SLIGHT UNEVENESS OF THE TWO REFLECTING
C          MIRRORS IN THE SCAN HEAD OF THE GER INSTRUMENT.
C                         WRITTEN BY DR. SHENG-HUEI CHANG
C                         GER INC., NEW YORK, NY
C                         ADAPTED TO THE UNR VAX BY WILLIAM AYMARD
C                         FEBRUARY 21, 1989
C
       CHARACTER FIL*50, FIL1*50
       REAL*4 ASUM1(500)/500*0./
       REAL*4 ASUM3(500)/500*0./, AINST, YY(512)
       INTEGER*2 A1(512)
       INTEGER*4 IAA
C               VARIABLES ST=1ST SCANLINE, ND= LAST SCANLINE OF
INPUT FILE
C               STL=1ST SCANLINE, NTL=LAST SCANLINE, INTV=INTERVAL
OF SLOP
C               CORRECTED IMAGE
       WRITE (6,*) ('ENTER THE NAME OF THE INPUT FILE')
       READ (5,101) FIL
       WRITE (6,*) ('ENTER THE NAME OF THE OUTPUT FILE')
       READ (5,101) FIL1
  101  FORMAT (A50)
C
       OPEN (7,FILE=FIL,STATUS='OLD',ACCESS='DIRECT',SHARED)
                                           O    P    E    N
(8,FILE=FIL1,STATUS='NEW',ACCESS='DIRECT',RECL=256,SHARED)
C
       WRITE (6,*) ('ENTER FIRST SCANLINE, LAST SCANLINE OF INPUT
FILE')
       READ (5,*) ST,ND
       WRITE(6,*)('ENTER 1ST LINE, LAST LINE INTERVAL FOR SLOPE
FILE')
       READ (5,*) STL,NDL
          INTV=1
C
          ILT = ND-ST+1
          ILL = NDL-STL
          LINE = 0
C
       DO 10 I=STL,NDL,INTV
          LINE = LINE+1
C      WRITE (*,900) LINE
       READ (7,REC=I) A1
               DO 20 II=51,85
                  ASUM1(LINE) = ASUM1(LINE)+FLOAT(A1(II))/35
   20          CONTINUE
               DO 30 II=441,475
                  ASUM3(LINE) = ASUM3(LINE)+FLOAT(A1(II))/35
   30          CONTINUE
          IF (MOD(I,50).EQ.0) WRITE (*,110) I
  110     FORMAT (' SCAN LINE NO.',I6,' WAS READ')
```

```
      10        CONTINUE
C
           SUM1=0
           SUM2=0
           SUM3=0
           DO 40 J=1, LINE
               SUM1 = SUM1+ASUM1(J)/LINE
               SUM3 = SUM3+ASUM3(J)/LINE
      40        CONTINUE
C
C      CORRECTION POINT BETWEEN 58-488
C
        SLOP = (SUM3-SUM1)/(458. -68.)
        AINST = 1. -SLOP*256.
        WRITE (*,*) 'SUM1=',SUM1,'   SUM3=',SUM3,'    SLOP=',SLOP,'
INT=',AINST
        DO 50 JJ=1,512
            YY(JJ)=SLOP*FLOAT(JJ)+AINST
      50    CONTINUE
C        WRITE (*,*)YY
C
C      DO SLOP CORRECTION
C
        DO 60 IL=ST,ND
            READ (7,REC=IL)A1
                DO 70 II=1,512
                    IAA = A1(II)-INT(YY(II))
                    IF (IAA.LE.0) THEN
                        IAA = 0
                        ELSE IF (IAA.GE.25000) THEN
                            IAA = 0
                            ELSE
                    ENDIF
                    A1(II)=IAA
      70    CONTINUE
C        ILL=IL-ST+1?
            WRITE (8,REC=IL)A1
            IF (MOD(IL,50).EQ.0)WRITE(*,*)'   LINE=',IL,' DONE'
      60    CONTINUE
C 900  FORMAT ('LINE NO. =',I6)
        STOP
        END
```

```
C
C       PROGRAM TO CORRECT FOR DE-STRIPPING OF A COLLINS 64-CHANNEL
C       IMAGE CAUSED BY DETECTOR DIFFERENCE IN THE SCAN HEAD OF THE
C       GER INSTRUMENT.
C                   WRITTEN BY DR. SHENG-HUEI CHANG
C                   GER INC., NEW YORK, NY
C                   ADAPTED TO UNR VAX 11/780 BY WILLIAM AYMARD
C                   FEBRUARY 22, 1989
C
        INTEGER*2 AA(512),BB(512)/512*-9999/
        INTEGER*2 IDET1(512,10),IDET2(512,10),IDET3(512,10)
        INTEGER*2 IDETT(512,40),IDET4(512,10)
        CHARACTER NAME*40,NAME1*40,ADI*40
        WRITE(*,*)'ENTER THE INPUT FILENAME'
        READ(*,200)NAME
        WRITE(*,*)'ENTER THE OUTPUT FILENAME'
        READ(*,200)NAME1
  200   FORMAT(A40)
        WRITE(*,*)'ENTER THE START AND END LINE # (I1,I2)'
        READ(*,*)IL1,IL2
        OPEN(12,FILE=NAME,STATUS='OLD',ACCESS='DIRECT')
C
        OPEN(13,FILE=NAME1,STATUS='NEW',ACCESS='DIRECT',RECL=256)
C
C       USE LINE 3 TO 22 (20 LINES) TO CALCULATE DETECTOR DIFFERENCE
C
        DO 25 IL=3,22
          ILL=IL-2
          IM=INT((ILL-1)/4)+1
          WRITE(*,*)ILL,IM
          READ(12,REC=IL)AA
            DO II=1,512
              IDETT(II,ILL)=AA(II)
              IF(MOD(ILL,4).EQ.1)IDET1(II,IM)=AA(II)
              IF(MOD(ILL,4).EQ.2)IDET2(II,IM)=AA(II)
              IF(MOD(ILL,4).EQ.3)IDET3(II,IM)=AA(II)
              IF(MOD(ILL,4).EQ.0)IDET4(II,IM)=AA(II)
            ENDDO
   25     CONTINUE
C
C       CALCULATE STANDARD DEVIATION ANS AVERAGE
C
        CALL AVERSTD(IDETT,20,50,450,AVT,STTD)
        CALL AVERSTD(IDET1,5,50,450,AV1,STT1)
        CALL AVERSTD(IDET2,5,50,450,AV2,STT2)
        CALL AVERSTD(IDET3,5,50,450,AV3,STT3)
        CALL AVERSTD(IDET4,5,50,450,AV4,STT4)
        WRITE(*,*)AVT,STTD,AV1,STT1,AV2,STT2,AV3,STT3,AV4,STT4
C
C
C       DO DE-STRIPPING CORRECTION
C
        SA=STTD
        MA=AVT
```

```
            READ(12,REC=1)AA
            WRITE(13,REC=1)AA
            READ(12,REC=2)AA
            WRITE(13,REC=2)AA
            DO IL=3,IL2
            IRL=IL-2
            READ(12,REC=IL)AA
            IF(MOD(IRL,4).EQ.1) THEN
            SI=STT1
            MI=AV1
            ELSE IF(MOD(IRL,4).EQ.2) THEN
            SI=STT2
            MI=AV2
            ELSE IF(MOD(IRL,4).EQ.3) THEN
            SI=STT3
            MI=AV3
            ELSE IF(MOD(IRL,4).EQ.0) THEN
            SI=STT4
            MI=AV4
            ELSE
            ENDIF
C           WRITE(*,*)'SA=',SA,' SI=',SI,' MA=',MA,' MI=',MI
            DO II=1,512
            AAA=INT(FLOAT(AA(II))*SA/SI+(MA-MI*SA/SI))
            IF(AAA.LE.0)AAA=0
            IF(AAA.GT.32760)AAA=0
            AA(II)=AAA
            ENDDO
        WRITE(13,REC=IL)AA
        IF(MOD(IL,50).EQ.0)WRITE(*,*)' LINE',IL,' IS DONE'
        ENDDO
C
        WRITE(*,*)'ALL DONE !! '
  999   STOP
        END
C
C       AVERAGE AND STANDARD DEVIATION OF WHOLE ARRAY ( TWO D )
C
        SUBROUTINE AVERSTD(BB,INN,IP1,IP2,AV,STD)
        INTEGER*2 BB(512,40), INN,IP1,IP2
        REAL*4 ASUM,AASUM,AV,STD
        ASUM=0.
        AASUM=0.
        DO IL=1,INN
        DO 10 I=IP1,IP2
        AASUM=AASUM+FLOAT(BB(I,IL))*FLOAT(BB(I,IL))
   10   ASUM=ASUM+FLOAT(BB(I,IL))
        ENDDO
        I1=(IP2-IP1+1)*INN
        AV=ASUM/I1
        SQ1=(AASUM-ASUM*AV)/(I1-1)
        IF(SQ1.LT.0)SQ1=0
        STD=SQRT(SQ1)
        WRITE(*,*)'AVER=',AV,' STD DEV=', STD
```

```
      20    CONTINUE
            RETURN
            END
C
```